NASA Conference Publication 3290

Proceedings of the Fourth International Conference and Exhibition: World Congress on Superconductivity

Volume I

Proceedings of a conference and exhibition held at Marriott Orlando World Center, Orlando, Florida, June 27 - July 1, 1994

1994

NASA Conference Publication 3290

Proceedings of the Fourth International Conference and Exhibition: World Congress on Superconductivity

Volume I

Kumar Krishen and Calvin Burnham, Editors
Lyndon B. Johnson Space Center
Houston, Texas

Proceedings of a conference and exhibition held at Marriott Orlando World Center, Orlando, Florida, June 27 - July 1, 1994

1994

This publication is available from the NASA Center for AeroSpace Information, 800 Elkridge Landing Road, Linthicum Heights, MD 21090-2934 (301) 621-0390.

The World Congress on Superconductivity

The World Congress on Superconductivity (WCS) was formed in Houston in 1987 by a group of volunteer engineers and scientists interested in increasing the focus on this emerging technology field of superconductivity. The leadership of the WCS, a non-profit 501(c)3 organization, is comprised of individuals from several major technical societies such as the Engineers Council of Houston, the American Chemical Society, IEEE, etc. This group is augmented by leaders of the international research, academic, science, government and business communities who serve on the Advisory Board or ad hoc committees. Since its inception, the Advisory Board has been global in scope with technologists from such countries as Japan, Russia, Switzerland, etc., actively involved in steering the direction of our programs.

The goals of the WCS have been to establish and foster the development and commercial application of superconductivity technology on a global scale by providing a non-adversarial, non-advocacy forum where scientists, engineers, businessmen and government personnel can freely exchange information and ideas on recent developments and directions for the future of superconductive research.

To date, four international conferences have been completed since 1987. These conferences were attended by over fifteen hundred delegates from thirty-six nations. The success of these conferences is remarkable in light of the fact that the WCS has no staff and must rely on monetary donations from the private sector, foundations and government agencies. In addition, thousands of man-hours have been donated by the WCS volunteer staff in the organizing of this activities. WCS is especially thankful for the assistance of Dr. Kumar Krishen as program chairman and the support from NASA which makes this activity possible.

Because of the unique nature of the WCS and its success, the organization is sanctioned by the United Nations and is a member of the UN's Advance Technology Alert System. The WCS was awarded Leadership Houston's International Corporate award for its Munich conference in 1992.

Plans are currently underway for the 5th International Conference of the World Congress on Superconductivity, which will be held in July 1996 in Budapest, Hungary. This meeting will coincide with the 1,100 year anniversary of Hungary. For more information on this meeting and WCS activities, please contact Calvin Burnham, President, World Congress on Superconductivity, P.O. Box 27805, Houston, TX 77227-7805; telephone 713-895-2500; fax 713-469-5788; e-mail: 70425.501@compuserve.com

Page intentionally left blank

CONTENTS

Introduction xiii

VOLUME 1

Session: **PLENARY, ROUNDTABLE AND KEYNOTE**
Session Chair: **Dr. Kumar Krishen**

Korea's Developmental Program for Superconductivity ..... 3 -1

Progress of Applied Superconductivity Research at Materials Research Laboratories, ITRI (Taiwan) ..... 10 -2

Progress in Superconductivity: The Indian Scenario ..... 24 -3

Superconductivity in Russia: Update and Prospects ..... 37 -4

Preparation, Structure and Superconductivity of High-T_c Compounds (Research of High Temperature Superconductors in Hungary) ..... 48 -5

High -T_c Superconductors: Technical and Commercial Challenge ..... 56 -6

Technical and Commercial Challenges in High T_c SQUIDs and Their Industrial Applications ..... 60 -7

Session: **ACCELERATOR TECHNOLOGY**
Session Chair: **Dr. Siegfried Wolff**

The LHC Magnet System and Its Status of Development ..... 65 -8

Status of High Temperature Superconductor Development for Accelerator Magnets ..... 75 -9

Development Work for a Superconducting Linear Collider ..... 84 -10

Session: **POWER AND ENERGY**
Session Chair: **Prof. Istvan Kirschner**

Today's Research Development on the Application of the Superconductivity Transport System in Japan ..... 96 -11

Measurement and Calculation of Levitation Forces Between Magnets and Granular Superconductors ..... 106 -12

ESR, Sims and Temf of an Y-Ba-Cu-O Superconductor ..... 116 -13

Serial and Parallel Power Equipment with High-Temperature Superconducting Elements ..... 126 -14

Session: **PERSISTENT MAGNETIC FIELDS**
Session Chair: **Dr. Roy Weinstein**

Stability, Mechanical Considerations, and AC Loss in HTSC Monoliths, Coils and Wires ..... 138 -15

Aspects of Passive Magnetic Levitation Based on High T_c Superconducting YBCO Thin Films ..... 148 -16

Hybrid Superconductor Magnet Bearings ..... 157 -17

Progress in HTS Trapped Field Magnets: J_C, Area, and Applications ..... 158 -18

The Superconducting MHD-Propelled Ship Yamato-1 ..... 167 -19

Session: **PERFORMANCE CHARACTERIZATION**
Session #1 Chair: **Dr. R. K. Pandey**
Cochair: **Dr. U. Varshney**

Electric Field Effect in Superconductor-Ferroelectric Structures ..... 180 -20

Oxide Perovskite Crystals for HTSC Film Substrates Microwave Applications ..... 188 -21

Texturing of High T_c Superconducting Polycrystalline Fibers/Wires by Laser-Driven Directional Solidification in a Thermal Gradient 198 22

Heavy Fermion Behaviour Explained by Bosons ..... 209 -23

Session #2 Chair: **Dr. R. K. Pandey**
Cochair: **Dr. U. Varshney**

An Electron Tunneling Study of Superconductivity in Amorphous SN_{1-x} Cu_x Thin Films ..... 222 -24

Changes in the Superconducting Properties of High-T_c Ceramics Produced by Applied Electric Fields 232 25

Effect of Nb_2O_5 and V_2O_5 Addition on the Superconducting Properties of $YBa_2Cu_3O_y$ Thin Films ..... 241 -26

Transparent Magnetic State in Single Crystal $Nd_{1.85}$ $Ce_{0.15}$ CuO_{4-y} Superconductors 250 27

Processing and Property Evaluation of Metal Matrix Superconducting Materials 260 28

Session: **PHYSICAL PROPERTIES**
Session PP-1 Chair: **Prof. Valeri Ozhogin**
Cochair: **Prof. Evgenii Z. Meilikhov**

Electronic Properties of Y-BA-Cu-O Superconductors as Seen by Cu and O NMR/NQR ..... 273 -29

Quaternary Borocarbides - New Class of Intermetallic Superconductors 283 30

Electronic Structure and the Van Hove Singularity Scenario in High-T_c $HgBa_2$ $CuO_{4+\delta}$ Superconductors ..... 298 -31

Boson Localization and Universality in $YBa_2Cu_{3-x}M_xO_{7-\delta}$ ..... 308 -32

Thermomagnetic Phenomena in the Mixed State of High Temperature Superconductors ..... 318 -33

Spectroscopy of Infrared-Active Phonons in High-Temperature Superconductors ..... 328 -34

Session PP-2 Chair: Prof. Valeri Ozhogin
Cochair: D. Brinkman

Flux Pinning Characteristics and Irreversibility Line in High Temperature Superconductors ..... 337 -35

Effects of Neutron Irradiation on the London Penetration Depth for Polycrystalline $Bi_{1.8}$ $Pb_{0.3}$ Sr_2 Ca_2 Cu_3 O_{10} Superconductor ..... 347 -36

The Thermopower in the Temperature Range T_c-1000K and the Band Spectrum of Bi-Based Superconductors ..... 354 -37

Nonequilibrium Transport in Superconducting Filaments ..... 359 -38

Session: FABRICATION METHODOLOGY
Session Chair: Dr. U. Balachandran

High T_c Superconductors Fabricated by Plasma Aerosol Mist Deposition Technique ..... 372 -39

Partial Melting of Bulk Bi-2212 ..... 382 -40

Correlation Between Fabrication Factor and Superconducting Properties of the Tl- and Bi- Based High T_c Superconductor 391

VOLUME 2

Session: SUPERCONDUCTIVE MAGNETIC ENERGY STORAGE (SMES) UTILITY INTEREST GROUP
Session Chair Dr. Phillip Baumann
SMES1: Technical Session

Policy Issues Inherent in Advanced Technology Development 400

SMES 2: Technical Session

Financial Options Methodology for Analyzing Investments in New Technology 405

SMES: Redefining the Path to Commercial Demonstration 410

Modular Transportable Superconducting Magnetic Energy Systems 416

Session: **THIN FILMS**
Session Chair: **Prof. Tomoji Kawai**

Optimization of the Deposition Conditions and Structural Characterization of $Y_1Ba_2Cu_3O_{7-x}$ Thin Superconducting Films....423

Growth and Analysis of Highly Oriented (11_n) BCSCO Films for Device Research....433

Structural, Transport and Microwave Properties of 123/Sapphire Films: Thickness Effect....440

Scanning Micro-Hall Probe Mapping of Magnetic Flux Distributions and Current Densities in $YBa_2Cu_3O_7$ Thin Films....447

Angular Dependence of Critical Current Density and Magnetoresistance of Sputtered High-T_c-Films....457

Correlations Between Critical Current Density, j_c, Critical Temperature, T_c, and Structural Quality of $Y_1B_2Cu_3O_{7-x}$ Thin Superconducting Films....467

Session: **HIGH TEMPERATURE MATERIALS**
Session #1 Chair: **Prof. Mikio Takano**

The Oxygen Content of the High-Temperature Superconducting Compound $Bi_{2+x}SR_{3-y}$ $CayCu_2O_{8+d}$ with Respect to Varying Ca and Bi Contents....483

P_b Solubility of the High-Temperature Superconducting Phase $Bi_2Sr_2Ca_2Cu_3O_{10+d}$....490

Superconductivity Theory Applied to the Periodic Table of Elements....500

Chemical Stabilization and High Pressure Synthesis of B_a-Free Hg-Based Superconductors, (Hg, M) Sr_2 $Ca_{n-1}Cu_nO_y$ (n = 1~3)....510

Session #2 Chair: **K. Kishio**

A New Series of Oxycarbonate Superconductors $(Cu_{0.5}C_{0.5})$ $_mBa_{m+1}$ Ca_{n-1} $Cu_nO_{2(m+n)+1}$....522

High Pressure Synthesis and Magnetic Studies of Quasi One Dimensional Systems Sr_{n-1} Cu_{n+1} O_{2n} (n = 3, 5)....529

Influence of Calcium on Transport Properties, Band Spectrum and Superconductivity of $YBa2Cu3O_y$ and $YBa_{1.5}$ $La_{0.5}$ Cu_3O_y....537

Structure and Superconductivity in $(Bi_{0.35}$ $Cu_{0.65})$ $Sr_2YCu_2O_7$ and Related Materials....546

Structural, Dynamical and Electronic Properties of $CaCuO_2$....555

Session: **DEVICE APPLICATIONS**
Session Chair: **Dr. Yoshifusa Wada**

High-Performance Passive Microwave Survey on Josephson Junctions 568

Josephson Frequency Meter for Millimeter and Submillimeter Wavelengths 574

Josephson Junction Spectrum Analyzer for Millimeter and Submillimeter Wavelengths 585

Nondestructive Testing (NDT) of Metal Cracks Using a High T_c rf-SQUID and Eddy Current Method 594

High Temperature Superconductors Applications in Telecommunications 601

HTS Thin Films: Passive Microwave Components and Systems Integration Issues 611

Session: **WIRE FABRICATION**
Session Chair: **Dr. K. C. Goretta**

Development of Practical High Temperature Superconducting Wire for Electric Power Applications 624

Mechanical Properties of High-Temperature Superconducting Wires 633

Progress in Development of Tapes and Magnets Made From Bi-2223 Superconductors 639

High Temperature Superconductors as a Technological Discontinuity in the Power Cable Industry 650

Improvement of Critical Current Density in Thallium-Based $(Tl,Bi)Sr_{1.6}Ba_{0.4}Ca_2Cu_3O_X$ Superconductors 661

Session: **GRANULAR SUPERCONDUCTORS**
Session Chair: **Prof. Manu S. Multani**

Introduction of Artificial Pinning Centres in "$Bi_2Sr_2CaCu_2O_8$" Ceramics 677

Tape Casting and Partial Melting of Bi-2212 Thick Films 686

Effect of Microwave-Enhanced Superconductivity in $YBa_2Cu_3O_7$ Bi-Crystalline Grain Boundary Weak-Links 694

Effects of Oxygen Stoichiometry on the Scaling Behaviors of $YBa_2Cu_3O_x$ Grain Boundary Weak-Links 703

Effect of Particle Size and Particle Size Distribution on Physical Characteristics, Morphology and Crystal Structure of Explosively Compacted High-T_c Superconductors 712

Percolation Effect in Thick Film Superconductors (Using a Bi(Pb)SrCaCuO Based Paste to Prepare a Superconducting Planar Transformer) 722

Line Group Techniques in Description of the Structural Phase Transitions in Some Superconductors 730

Session: POSTERS

Macroscopic and Bulk-Controlled Elastic Modes in an Interaction of Interstitial Alcali Metal Cations Within a Face-Centered Cubic Crystalline Fullerine 739

Thallium 2223 High T_c Superconductor in a Silver Matrix and Its Magnetic Shielding, Hermal Cycle and Time Aging Properties 743

The Role of Silver in the Processing and Properties of Bi-2212 753

A Study on the Superconducting Properties of $YBa_2Cu_{3-x}Nb_xO_y$ Thin Films 762

Growth and Micro Structural Studies on Yittria Stabilized Zirconia (YSZ) and Strontium Titanate (STO) Buffer Layers 770

INTRODUCTION

Page intentionally left blank

INTRODUCTION

The World Congress on Superconductivity (WCS) is a nonprofit organization dedicated to the universal promotion of research, development, and applications of superconductivity technology. Through open meetings and conferences, it provides forums for the world community to share technological and research results in the field of superconductivity and to discuss the translation of these results into applications which will benefit all of the world's population. The WCS established the Award of Excellence to recognize the contributions of organizations and individuals within the industry. Since 1988, nineteen individuals and organizations have received this recognition.

The WCS presented its first two International Conferences and Exhibition World Congresses on Superconductivity in 1988 and 1990, with a combined attendance of approximately 1,000 delegates from 16 countries. Its third conference, attended by more than 400 scientists, technologists, and managers from thirty six nations, was held in Munich, Germany in September 1992. Proceedings from these three conferences have been published and distributed worldwide.

The Fourth International Conference and Exhibition World Congress on Superconductivity was held June 27-July 1, 1994 in Orlando, Florida. It was sponsored in large part by the National Aeronautics and Space Administration's Johnson Space Center. More than 120 presentations were scheduled for the more than 200 delegates from 30 nations who attended this year's conference. I believe this conference provided the most comprehensive worldwide review of high temperature superconductivity research and its applications to date (table 1). The exchange of information and ideas and the identification of technical and commercial challenges which occurred during the conference are bound to significantly advance this revolutionary technology.

The substantial progress which has been made in the field of superconductivity was reflected in the conference presentations: the number of elements used in the search of superconductivity has increased to eight; the reported critical temperatures have increased to 164°K; and a new thallium-based compound, reported by Professor Z.Z. Sheng, is expected to provide further insight into the mechanisms that govern the complex phenomena of superconductivity. Additionally, significant progress was reported with theoretical and modeling efforts which will accelerate research and development of new materials and devices, and with magnetic field capacity and electrical current capacity. The parameters for these capacities are now quoted at 77°K at 2.2 Tesla and 100,000 Amps/cm^2, respectively.

The commercial applications of superconductivity are progressing rapidly, with magnets, SQUIDS, transformers, thin films, wires, and several devices now available commercially. And the worldwide interest in the exploration of this revolutionary technology continues to grow.

To create the uniquely efficient superconductor many production components must be orchestrated. Teaming the exact mix and proportion of elements, arranging the different layers of elements in the appropriate order, and achieving the right environment and temperatures in which to cook the elements are essential.

Any technology which enhances our quality of life truly is super and I believe superconductivity will do just that. This revolutionary technology will be an integral part of future achievements which will produce great benefits for humans.

Table 1. Schedule of Events - Fourth World Congress on Superconductivity

Sunday, June 26, 1994 - 1:30 PM - 7:00 PM Registration: 7:00 PM - 9:00 PM Reception				
Monday, June 27, 1994 - 8:30 AM - NOON INTERNATIONAL UPDATE				
1:30 - 5:30 PM	1:30 - 5:30 PM	1:30 - 5:30 PM		
Accelerator Technology	Power/Energy Applications	Persistent Magnetic Fields		
7 PM - 9 PM ROUNDTABLE DISCUSSION - "Technical and Commercial Challenges"				
Tuesday, June 28, 1994 - 8:30 AM - Noon				
Physical Properties 1	Performance Characterization 1	SMES 1		
LUNCHEON Noon - 1:30 PM				
1:30 - 5:30 PM	1:30 - 5:30 PM	1:30 - 5:30 PM	1:30 - 5:30 PM	1:30 - 5:30 PM
Medical Applications	Physical Properties 2	Performance Characterization 2	Fabrication Methodology 1	SMES 2
Wednesday, June 29, 1994 - 8:30 AM - Noon				
Granular Superconductors 1	Thin Films	SMES 3		
Afternoon free for tours or sightseeing				
Thursday, June 30, 1994 - 8:30 AM - Noon				
WCS-5 Planning	Device Applications Chair	High-Temperature Materials 1		
1:30 - 5:30 PM	1:30 - 5:30 PM	1:30 - 5:30 PM		
Wire Fabrication Technology	Device Applications Chair	High-Temperature Materials 2		
AWARDS BANQUET 7:00 PM - 9:00 PM				
Friday, July 1, 1994 - 8:30 AM - Noon				
Granular Superconductors 2	Poster Session 1	Poster Session 2		
Meeting ends at Noon				

The process involved in developing superconductors is an excellent example of the great results that can be achieved by successfully teaming different elements. It should symbolize for us the advances we are capable of when we work together. Most of the technological advances made in this field in recent years are the result of teamwork. One of the objectives of this conference was to promote global teaming which transcended geographic and national barriers and helped to advance science and technology related to superconductivity. Since we collectively share the challenge of advancing teamwork and cooperation, we hope that several dialogues were initiated during this conference.

Some of the many enthusiastic researchers, technologists, and program directors who helped develop this conference are listed in table 2. The speakers for the opening session, held on the morning of June 27, 1994, are listed below.

Mr. Calvin Burnham Welcome	President, WCS
Dr. Kumar Krishen Opening Remarks	Program Chair, WCS
Dr. Gye-Won Hong	Korea
Dr. R.S. Liu	Republic of China
Prof. Manu S. Multani	India
Dr. Naoki Koshizuka	ISTEC, Japan
Dr. Wei Kan Chu	TCSUH, U.S.
Dr. Valeri Ozhogin	Russia
Prof. Z.Z. Sheng	University of Arkansas, U.S.

I would like to thank Mr. Calvin Burnham, Mr. Glenn Carraux, Dr. Jim Salinas, Dr. Tsuneo Nakahara, and Dr. Z.Z. Sheng for their exhaustive efforts in organizing and implementing this international event. The roundtable discussion on technical and commercial challenges was organized by Dr. Tsuneo Nakahara and chaired by Dr. Ken-ichi Sato. The brief presentations and responses given by the panelists stimulated a wide-ranging question and answer session. The panelists for the roundtable discussion included Dr. Ken-ichi Sato from Osaka Research Laboratory, Dr. M. Takano from Kyoto University, Dr. D. Lu from Midwest Superconductor, Inc., Dr. Wei-Kan Chu from TCSUH, and Dr. Istvan Vajda from the Technical University, Hungary. Dr. Usha Varshney chaired the session on Thin Films and Ms. Yelena T. Oltarzhevskay chaired the session on Device Applications. I would like to thank them both as well as all of the roundtable panelists for their contributions. Finally I would like to thank Dr. C.W. (Paul) Chu for the illuminating keynote address he presented at the conference, Dr. Istvan Kirchner for his review of the work being done in Hungary, and Professor Vladislav V. Lemanov of the Russian Academy of Sciences for the keynote address he presented at the Awards Banquet. I am sure that the depth and breadth of Prof. Lemanov's knowledge provided a wholely unique perspective for the 250 in attendance at the banquet.

Table 2. WCS List of Program Organizers

Program Chairman

Dr. Kumar Krishen
NASA Lyndon B. Johnson Space Center
Mail Code: IA4
Houston, TX 77058 U.S.A.

Technical Area Chairmen

HIGH-TEMPERATURE MATERIALS
Prof. Mikio Takano
Institute of Chemistry
Kyoto University
Gokasho, Uji-city
Kyoto 611 JAPAN

PHYSICAL PROPERTIES
Dr. Valeri Ozhogin
Doctor of Sciences, Professor
Kurchatov Institute of Atomic Energy
123182 Moscow RUSSIA

THIN FILMS
Prof. Tomoji Kawai
Institute of Scientific & Industrial Research
University of Osaka
81, Mihogaoka, Ibaraki-chi
Osaka, 567 JAPAN

PERFORMANCE CHARACTERIZATION
Dr. R. K. Pandey
Center for Electrical Materials
Dept. of Electrical Engineering
Texas A&M University
College Station, TX 77843-3128 U.S.A.

C-60 BASED SUPERCONDUCTORS
Dr. John L. Margrave
Butcher Professor of Chemistry
Rice University
P. O. Box 1892
Houston, TX 77251 U.S.A.

DEVICE APPLICATIONS
Dr. Yoshifusa Wada
Research & Planning Dept.
International Superconductivity Technology
Eishin Kaihtsu Bldg.
34-4, Shimbashi S-Chome
Minato-Ku, Tokyo 105 JAPAN

PERSISTENT MAGNETIC FIELDS AND SHIELDING
Dr. Roy Weinstein
Institute for Beam Particle Dynamics
IBTD-5506
University of Houston
Science Research Center, Room 632
Houston, TX 77204-5506 U.S.A.

WEAK LINK EFFECTS & FLUX MOTION
Dr. Kishin Moorjani
Applied Physics Laboratory
The John Hopkins University
John Hopkins Road
Laurel, MD 20723 U.S.A.

FABRICATION METHODOLOGY
Dr. Kazumasa Togano
National Research Institute for Metals
1-2-1, Segen, Tsukuba
Ibaraki, 305 JAPAN

Table 2. WCS List of Program Organizers (Concluded)

Technical Area Chairmen

SPACE APPLICATIONS
Dr. M. Sokoloski
Science and Technology Corp.
409 Third Street S.W.
Washington, DC 20024
Fax: 202-488-5364
Phone: 202-863-0012

Dr. Frank W. Patten
Defense Advanced Research Projects Agency
3701 North Fairfax Drive
Arlington, VA 22203-1714 U.S.A.

ACCELERATOR TECHNOLOGY
Dr. Siegfried Wolff
PMAG
DESY
Postfach
22603 Hamburg GERMANY

COMPUTER APPLICATIONS
Dr. Ushio Kawabe
Central Research Laboratory
Hitachi, Ltd.
Kokubunji, Tokyo 185 JAPAN

FUTURE R&D DIRECTIONS
Mr. Arthur J. Murphy
Jet Propulsion Laboratory - California
Institute of Technology
4800 Oak Grove Drive
Pasadena, CA 91109 U.S.A.

SUPERCONDUCTING ENERGY STORAGE
Dr. Phillip Baumann
5910 No. Central Expressway
Suite 1000
Dallas, TX 75206 U.S.A.

MEDICAL APPLICATIONS
Dr. Ian R. Young
GEC Research Hirst Research Center
Elmstree Way
Borehamwood
Hertfordshire WD6 1RX
UNITED KINGDOM

GRANULAR SUPERCONDUCTORS
Prof. Manu S. Multani
Tata Institute of Fundamental Research
Homi Bhabha Road
Bombay 400 005 INDIA

POWER/ENERGY APPLICATIONS
Prof. Istvan Kirschner
Roland Eotvos University
Dept. of Low Temperature Physics
H-1088 Budapest VII, Puskin u. 5-7
HUNGARY

WIRE FABRICATION TECHNOLOGY
Dr. K. C. Goretta
Ceramics Section
Argonne National Laboratory
MCT-212
Argonne, IL 60439 U.S.A.

TECHNICAL & COMMERCIAL CHALLENGES
Dr. Tsuneo Nakahara
Sumitomo Electric Industries, Ltd.
1-3 Shimaya 1-Chrome
Konohana-ku, Osaka 554, JAPAN

Throughout my thirty year career, first with Kansas State University, then with Lockheed Electronics Company and now with the National Aeronautics and Space Administration (NASA), I have supported the space program. The paramount missions of NASA have always ignited my imagination and my determination. Today one of the key missions for NASA is researching the universe: its origin and growth, its formation of bodies and systems, and its governing processes. Another mission of this Agency is to explore the evolution of life within the universe. Through the efforts of many nations, we have come to realize the critical link between human life and the global environment, and, as an extension of this, between the phenomena that underlie the nature of our universe. NASA's current mission addresses the need to expand our knowledge about our universe, as does research in the area of superconductivity. This research will provide a means to characterize unique phenomena which might otherwise be unobservable. We hope that these proceedings will help identify ways to advance the performance and applications of high temperature superconductors.

Kumar Krishen, Ph.D.
Program Chairman
World Congress on Superconductivity

Plenary, Roundtable, and Keynote

Chair: Dr. Kumar Krishen

Page intentionally left blank

Korea's Developmental Program for Superconductivity

Gye-won Hong, Dong-Yeon Won, Il-Hyun Kuk, Jong-Chul Park*

Korea Atomic Energy Research Institute
P.O. Box 105, Yuseong, Taejeon, 305-600, Korea
Korea Standards Research Institute
P.O. Box 102, Yuseong, Taejeon, 305-600, Korea

S1-76
313251
7 P.
342188

1. Introduction

Superconductivity research in Korea was firstly carried out in the late 70s by a research group in Seoul National University (SNU), who fabricated a small scale superconducting magnetic energy storage system under the financial support from Korea Electric Power Company(KEPCO). But a few researchers were involved in superconductivity research until the oxide high Tc superconductor was discovered by Bednorz and Mueller.[1)]

After the discovery of YBaCuO superconductor operating above the boiling point of liquid nitrogen(77K)[2)], Korean Ministry of Science and Technology(MOST) sponsored a special fund for the high Tc superconductivity research to universities and national research institutes by recognizing its importance. Scientists engaged in this project organized "High Temperature Superconductivity Research Association(HITSRA)" for effective conducting of research. Its major functions are to coordinate research activities on high Tc superconductivity and organize the workshop for active exchange of information. During last seven years the major superconductivity research has been carried out through the coordination of HITSRA. The major parts of the Korea's superconductivity research program were related to high temperature superconductor and only a few groups were carrying out research on conventional superconductor technology, and Korea Atomic Energy Research Institute(KAERI) and Korea Electrotechnology Research Institute(KERI) have led this research.

In this talk, the current status and future plans of superconductivity research in Korea will be reviewed based on the results presented in interim meeting of HITSRA, April 1-2, 1994, Taejeon, as well as the research activity of KAERI.

2. Research Activities in Korea

After the first workshop held on July 6, 1987, HITSRA has organized 18 workshops to promote research activities on high Tc superconductivity and share the results. Recent research results presented at interim meeting of HITSRA are summarized as follows:

(1) film : High quality YBCO thin films were reported by many groups using RF sputtering, laser ablation, chemical vapor deposition etc. But there was no report on Bi- and Tl-based thin film. Currently the research activites are concentrated on development of devices applying film such as HTSC dc SQUID, Josephson junction device, filter, resonator, antenna, flux transformer etc. Several research groups reported the successful fabrication of the HTSC dc SQUID and Josephson step edge junction. Korea Standards Research Institute(KSRI) and Goldstar central research laboratory lead the research in this field.

(2) bulk : Researches on fundamental properties of HTSC superconductor such as superconductivity theory, thermodynamics, kinetics, mechanical and magnetic properties etc were carried out for Y-, Bi- and Tl-base materials. Several groups are executing the research on Hg-base compound and KSRI and Pohang Institute of Science and Technology reported the successful formation of Hg-1212 and Hg-1223 oxides using ampoule method and obtained a Tc of about 130K. They are trying to fabricate Hg-base compound in thin film. The study on fabricating high magnetization YBCO material for application on fly wheel and current lead is also carried out by several groups with different techniques such as extrusion and laser melt pedestal growth,

isothermal peritectic process, quasi melt process, melt texture growth etc.

(3) wire/tape : There were several reports on the superconducting tape of Bi-2212/Ag and Bi-2223/Ag composites showing a relatively good critical current density in the order of 10^4 A/cm^2 in 1 m length and KAERI and KERI reported preliminary results on multi-filamentary wire of 7, 49 and 108 filaments. KERI also reported the preliminary result on Tl-1223/Ag composite tape.

It was noticeable that trends of superconductivity research in Korea was changed from fundamental research to application technique and government emphasized the importance of joint R & D between industry and national research institute.

3. Superconductivity Research Activities in KAERI

Since the high Tc superconductivity research in Korea started in 1987, KAERI has played leading role by presenting several important results on material development and its application. In previous articles[3,4], it was pointed out that 105K Pb-doped BiSrCaCuO, Bi-2223/Ag composite superconducting tape, high Jc YBaCuO film, high magnetization YBaCuO bulk superconductor and high speed rotating system(75,000 rpm in air) using superconducting bearing by melt processed YBCO superconductor were firstly fabricated by KAERI in Korea. Some important results were reported on characteristics of Bi-2223 compound formation [5-8], mechanisms of YBCO formation[9-15] and preparation of YBCO film by CVD process[16,17]. We reported the formation of high Jc YbBaCuO film on various substrates at 650 ℃ without using any other excitation source[18-20]

Very recently, we have developed new process for fabricating BSCCO/Ag composite using silver powder instead of silver tube[21], which has many advantages such as ; ability of fabricating large composite with high critical current density, ability of fabricating complicated shape with less difficulty than powder in tube method, possibility of changing silver sheath composition easily

by adding suitable alloying element powder to silver powder, good controllability of BSCCO powder packing density etc. Through repeated cold rolling and annealing at 840 ℃ in air, Ag/Bi-2223 composite with a thickness of 0.1 mm and a width of 40 mm was obatained. The Ag/Bi-2223 composite with large dimension was fabricated into complex H-patterned and helical shape having a high current carrying capacity(Jc = 3,500 A/cm^2 at 77K, 0T, Ic = 4.5 A for a specimen with a width of 3 mm). Currently the test for applying this composite as antenna, magnetic shield and wire are being carried out together with the experiments for deciding optimum process condition.

For last several years, we also have put large effort to understand the flux pinning behavior and increase the quality of melt processed YBCO specimen for developing application device such as fly wheel, current lead and superconducting magnetic bearing. Some important result were reported : the behavior of 211 particle growth in different melt composition[22], the abnomalous magnetization of 123[23], and effect of various additives on the growth of 123 matrix.[10,14]

In order to develop the key technology in the field of nuclear energy, Korean government set up an long term national R&D program in 1992 and its major categories are as follows ;

- Nuclear fuel cycle technology
- Waste management
- Radiation and RI application through the use of KMRR
- Nuclear basic research
- Nuclear safety research.

The development of superconducting magnet for superconducting magnetic energy storage and nuclear fusion is classified as one of the important topics of nuclear basic research program. And superconductivity research team and fusion research team are responsible for that. From 1992, we have extended

our research activity to the development of superconducting magnet and fabricated a superconducting magnet with high homogeneity of 10 ppm in 5 cm dsv through cooperation with Kurchatov Institute of Atomic Energy(KIAE). The goals on the magnet technology in KAERI are summarized as follows:

1992 - 1995 : Magnet for basic research and preliminary design of magnet for medium size tokamak

1995 - 1998 : Fabrication of proto type magnet for medium size tokamak and SMES

1998 - 2005 : Fabrication of magnet for medium size tokamak.

To achieve the goals successfully, it is very important to have a wide international cooperation and we are willing to have a close relationship with any institute which keep the advanced magnet technology.

4. Superconductivity Research Program in Korea

The MOST recognized the importance of superconductivity research and decided to support its activities continuously. Therefore the third phase of three years base national program on superconductivity research started in 1993. In third phase program, the higher priority was given to the application techniques and joint research among national research institute, universities and industries are emphasized. It is planned that the technical bases for implementing the HTSC material to practical application is established in this period and next phase program is mostly oriented to industrialization of those techniques.

Until 1992, superconductivity research activities in Korea had been concentrated on high Tc superconductor and little attention was paid on conventional superconductor. But from 1992, the research on the application of conventional superconductor has been carried out intensively by KAERI and KERI. The major fields of interest are superconducting magnetic energy

storage, power transmission cable, superconducting motor and generator, superconducting magnet with high homogeneity and high field and superconducting magnet for medium size tokamak. MOST recognizes the importance of conventional superconductor technology for large scale application and KEPCO also showes deep interest to the application of superconductivity to electric power system and support related research. It is expected that the priority of superconductivity research will greatly increase as far as the development of application technique keeps current pace of improving.

5. Conclusion

Superconductivity research in Korea, which was initiated by the discovery of high Tc superconductor, is extending its area to the conventional superconductor and their application such as SMES, nuclear fusion, MRI etc. To achieve the reseach goals effectively, HITSRA coordinates the researches on HTSC materials and their applications continuously. To carry out the research successfully, Korean government encourages cooperation between national research institute and industry as well as international cooperation with foreign institution.

References

1. Bednorz and Mueller, Z. Phys., B64, 189(1986)
2. C.W. Chu et al., Phys. Rev., B35, 405 (1987)
3. D.Y. Won and H.G. Lee et al., ed. C.G. Burham, 2nd World Congress on Superconductivity, Sept. 10-13, Houston, Texas, 30(1990)
4. D.Y. Won and H.G. Lee, Appl. Superconductivity, 1(3-6), 191 - 197, 1993.
5. H.G. Lee and D.Y. Won et al., Appl. Phy. Lett., 54, 23 (1989)
6. C.J. Kim and D.Y. Won et al., J. Am. Cer. Soc., 75, 570 (1992)

7. C.K. Rhee and D.Y. Won et al., Jpn. J. Appl. Phy., 28, L1137 (1989)
8. H.G. Lee and D. Y. Won et al., Jpn. J. Appl. Phy., 28, L1151 (1989)
9. H.G. Lee and D.Y. won et al., proc. 3rd Int'l Symp. superconductivity, Sendai, Nov. 6-9, Japan, 789 (1990)
10. C.J. Kim, et al., J. Mat. Sci. Lett.,11, 346-348 (1992)
11. H.J. Lee, et al., J. Mat. Sci. Lett., 11, 1562-1565 (1992)
12. C.J. Kim et al., Mat. Lett. 11(8-9) 241-246 (1991)
13. C.J. Kim et al., J. Materials. Research, 7(9) 2349-2354 (1992)
14. C.J. Kim et al., J. Materials Science Letters, 11, 831-834 (1992)
15. C.J. kim et al., Materials Letters, 14, 268-273 (1992)
16. H.G. Lee et al., Jpn. J. Appl. Phy., 30(9A) 1977 (1991)
17. H.G. Lee et al., proc. 4th Int'l Symp. superconductivity, Tokyo, Oct. 14-17, Japan, 727 (1991)
18. H.G. Lee et al., Applied Superconductivity, 1(3-6) 807-814 (1993)
19. H.G. Lee et al., Jpn. J. Appl. Phy., 31(2B) L157 (1992)
20. H.G. Lee et al., proc. 5th Int'l Symp. superconductivity, Kobe, Nov. 16-19, Japan, 951 (1991)
21. H.G. Lee, submitted to Cryogenics
22. H.G. Lee et al., J. Am. Cer. Soc.,(in press)
23. C.J. Kim et al., submitted to Materials Lett.,

PROGRESS OF APPLIED SUPERCONDUCTIVITY RESEARCH AT MATERIALS RESEARCH LABORATORIES, ITRI (TAIWAN)

R. S. Liu and C. M. Wang

Materials Research Laboratories, Industrial Technology Research Institute,
Hsinchu, Taiwan, R.O.C.

Abstract

A status report based on the applied high temperature superconductivity (HTS) research at Materials Research Laboratories (MRL), Industrial Technology Research Institute (ITRI) is given. The aim is to develop fabrication technologies for the high-T_c materials appropriate to the industrial application requirements. To date, the majorities of works have been undertaken in the areas of new materials, wires/tapes with long length, prototypes of magnets, large-area thin films, SQUIDs and microwave applications.

1. Introduction

High temperature superconductivity (HTS) research at Materials Research Laboratories (MRL), Industrial Technology Research Institute (ITRI), was started from Feburary 1987. The goals for the high-T_c superconductivity research at MRL/ITRI are as follows :

- Search for new high-T_c materials.
- Develope techneques for mass production of superconducting and homogeneous with small particle size powders .
- Establish long length and high-J_c wire fabrication techneques.
- Fabrication of high-T_c superconducting current lead and magnet.
- Establish high quality and large area superconducting thin film fabrication techneques.
- Thin film application researches in SQUIDs and microwave devices.

Therefore, the simplest target for the HTS research at the MRL/ITRI is to develop fabrication technologies for the high-T_c materials appropriate to the industrial application requirements. To date, the majorities of works have been undertaken in the areas of new materials, wires/tapes with long length, prototypes of magnets, large-area thin films, SQUIDs and

microwave applications. The concept of the metal-superconductor-insulator transition has been applied to fine-tune the optimal T_c's for new high-T_c superconducting material systems. Superconductivity up to 135 K has been achieved in the Hg-containing cuprates. The process for producing a single pancake Bi-2223 coil which can generate a magnetic field of ~ 437 Gauss at 77 K and self field has been set-up. High quality YBCO thin films ($T_c \geq 88$ K and $J_c \geq 10^6$ A/cm^2 at 77 K) with diameter around 2 inches have been made by laser ablation and hot-wall sputtering. SQUIDs and Microwave devices (such as resonator) have also been developed. This research is mainly supported by the Ministry of Economic Affairs (R.O.C.). In Table 1 we list the budget and manpower of the HTS research at the MRL/ITRI. Moreover, several local companies have joined the research program with the MRL/ITRI since 1988 indicating that the industry in Taiwan has perceived what a magnificant impact would be if HTS products are commercialized.

Table 1. The budget and manpower of the HTS research at the MRL/ITRI supported by the Ministry of Economic Affairs.

Fiscal Year (FY)	Budget (US$ in million)	Manpower (person)
FY 90	2.650	28
FY91	3.313	33
FY92	2.630	33
FY93	2.362	32
FY94	1.637	23

Some of our recent achievements on the HTS research at the MRL/ITRI are summarized as the following sections.

2. The chemical control of high-T_c superconductivity

The substitutional chemistry of a wide range of cuprate superconducting materials has been investigated at the MRL/ITRI with the general aims of optimising the ctitical temperature, current density, phase purity, chemical stability and ease of synthesis. Here, we demonstrate a typical example based on the chemical control of high-T_c superconductivity through the metal-superconductor-insulator transition. Bulk superconductivity, up to 110 K, in the system $(Tl_{0.5}A_{0.5})(Ca_{0.8}R_{0.2})Sr_2Cu_2O_7$ (A = Pb or Bi; R = Y or rare earth elements) has been reported.[1-4] This septenary system has the highest T_c among the thallium cuprate systems with the so-called 1212 structure. The structure of the 1212 phase $(Tl_{0.5}Pb_{0.5})Sr_2(Ca_{1-x}Y_x)Cu_2O_7$ can be described in terms of an intergrowth of double rock salt-type layers [({Tl/Pb}O)(SrO)] with double $[Sr(Ca,Y)Cu_2O_5]$ oxygen deficient perovskite layers, formed by sheets of corner-sharing CuO_5 pyramids interleaved with calcium and/or yttrium ions as shown in Fig. 1. The structure of $(Tl_{0.5}Pb_{0.5})(Ca_{1-x}Y_x)Sr_2Cu_2O_7$ resembles that of the 90 K superconductor $YBa_2Cu_3O_7$: the (Tl,Pb)-O layers replacing the Cu-O chains, Sr cations replacing Ba cations and Ca cations partially substituting for yttrium ions. The parent compound $TlSr_2CaCu_2O_7$ is itself a metal, but exhibits no superconductivity at temperatures down to 4 K. The nominal Cu valency of this compound is 2.5+. On the basis of earlier studies of superconductivity in cuprates, one might believe that this system has an excess of hole carriers in the conducting CuO_2 layers, which gives rise to a so-called "over-doping" state. Such a condition can be efficiently modified chemically by the stepwise substitution of Tl^{3+} by Pb^{4+}, by the substitution of Ca^{2+} by Y^{3+}, or, indeed, by the dual substitutions, Tl^{3+}/Pb^{4+}, Ca^{2+}/Y^{3+}. A representation of the entire electronic structure phase diagram[5] of $(Tl_{1-y}Pb_y)Sr_2(Ca_{1-x}Y_x)Cu_2O_7$ is given in Fig. 2. Both the $(Tl_{1-y}Pb_y)Sr_2CaCu_2O_7$ and $TlSr_2(Ca_{1-x}Y_x)Cu_2O_7$ systems have the highest T_c (~ 80 K) for y ~ 0.5 or x ~ 0.7. However, the $(Tl_{0.5}Pb_{0.5})Sr_2(Ca_{1-x}Y_x)Cu_2O_7$ system exhibits superconductivity over the homogeneity range x = 0 ~ 0.5, with the superconducting transition temperature showing a maximum of 108 K at x = 0.2. Across the homogeneity range x = 0.6 ~ 1.0, the material also undergoes a metal - insulator transition at temperatures above T_c. It is to this part of the electronic phase diagram that we have found; we have aslo characterized a range physical property measurements across the entire homogeneity range x = 0 to x = 1.0.

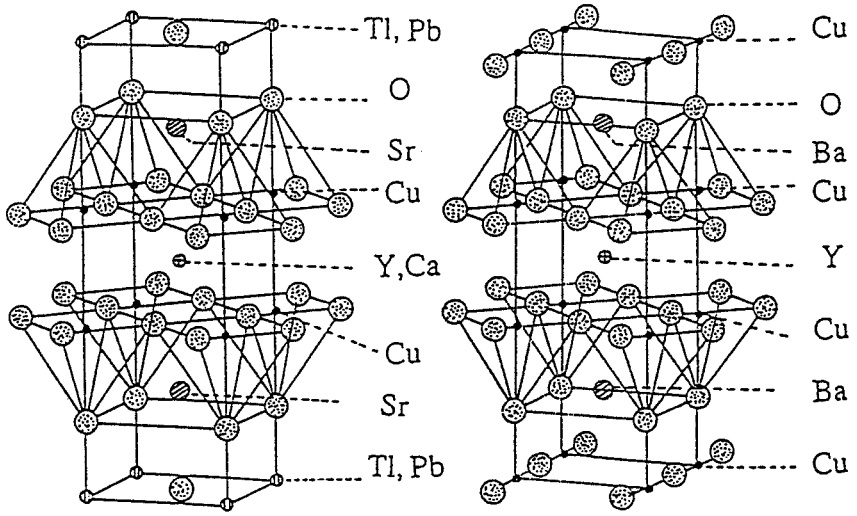

Fig. 1. A representation of the crystal structures of $(Tl_{0.5}Pb_{0.5})Sr_2(Ca_{1-x}Y_x)Cu_2O_7$ and $YBa_2Cu_3O_7$.

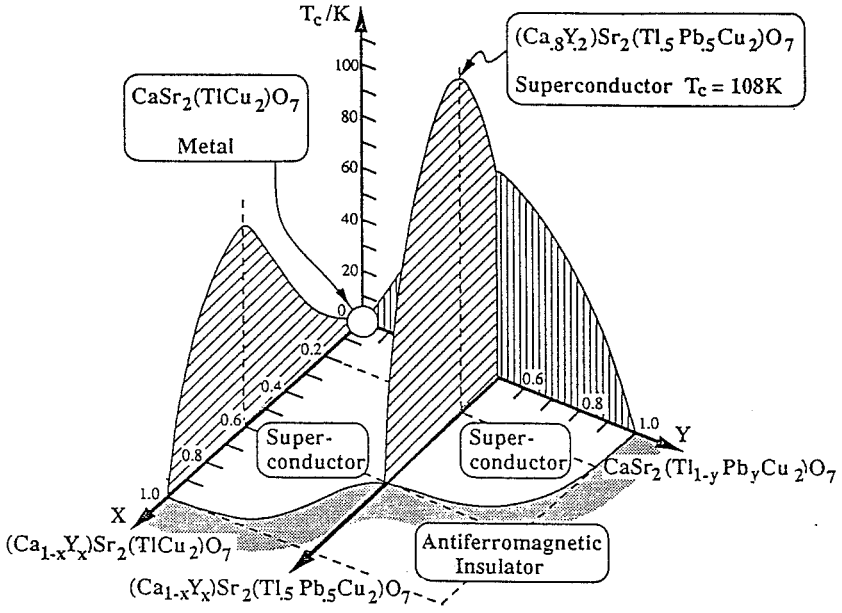

Fig. 2. Metal - Superconductor - Insulator phase diagram for the system $(Tl_{1-y}Pb_y)Sr_2(Ca_{1-x}Y_x)Cu_2O_7$.

(2) Fabrication of Bi-2223 tapes and their applications in magnets and motors

Ag-clad tapes with the $(Bi,Pb)_2Sr_2Ca_2Cu_3O_{10}$ (hereafter referred to as Bi-2223) composition were prepared by the PIT (powder-in-tube) technique. Calcined powders were prepared by coprecipitation method.[6] The metal nitrate salts of $Bi(NO_3)_3 \cdot 5H_2O$, $Pb(NO_3)_2$, $Sr(NO_3)_2$, $Ca(NO_3)_2 \cdot 4H_2O$ and $Cu(NO_3)_2 \cdot 3H_2O$ were weighted in the mole ratio 1.7/0.4/1.8/2.2/3.2 respectively, and dissolved in ethylene glycol with nitric acid finally. The mixture of the metal nitrate solution was added to the $H_2C_2O_4/Et_3N$ solution with virgorous stirring. During the coprecipitation process, the pH value of the solution was controlled to 1.5±0.2 by the addition of Et_3N. The precitant of the pale blue powder was filtered and then dried at 120 °C. The dehydrated powders were then calcined at 800 °C, each particle contains Bi, Pb, Sr, Ca, Cu in appropriate ratios of cation stoichiometry. The calcined powder with the mainly $(Bi,Pb)_2Sr_2CaCu_2O_8$ (Bi-2212) phase was then packed into a silver tube, with 12 mm in outer diameter and 10 mm in inner diameter. The composite was then drawn to about 1.0-1.5 mm in outer diameter in a 15 % of area reduction per pass. Multifilamentary wires were prepared by feeding the drawn mono-core wires to a silver tube, and repeated the above drawing process. After drawing, the wire was cold rolled into a tape with thinkness about 0.15 mm. The rolled tape was then sintered at 835-840 °C for 25 - 50 h in air. After first sintering, the sintered tape was re-rolled into the thinner tape with thickness and width of 0.12 mm and 4 mm, respectively. Pancake coils were fabricated from these re-rolled tapes. Four monocore tapes were co-wound in parallel with insulation (used to separate each turn) to form a coil. Inorganic adhesive (alumina paste) was used as insulator and binder. The coil was then annealed at about 830 °C for 50-70 h in air and slow cooled to room temperture in order to transfer the Bi-2212 phase into the Bi-2223 phase.[7,8] Transport critical currents were determined by the dc four-probe technique with a criterion of 1 μV/cm. A hall effect magnetometer (Oxford model 5200) was used to determine the central magnetic field (B_0) generated by pancake coils at 77 K.

In Fig 3 we show a pancake coil co-wound by four 7 meter Bi-based tapes. The coil has a critical current (I_C) of 26.3 A in the self-field and can generate a B_0 of 437 G at 77 K. Prototypes of HTS pancake coil magnets have also been fabricated. Figure 4 represents a photograph of the magnet stacked by four Bi-2223 pancake coils, a B_0 of 847 G at 77 K can be obtained.

Figure 5 shows a cross-sectional micrographs of Ag-sheathed 61-filamentary superconducting wires (a) intermediate stage and (b) final shape. The value of critical current density (J_C) of this tape was 1.3 x 10^4 A/cm^2 at 77 K. In Fig. 6 we show the overview of a HTS DC motor consisted of armature (copper rotor) and magnetic field winding (HTS coil). The react-and-wind coil was fabricated by winding three 1.8 meter 19-filamentary tapes on an iron

core with diameter of 2.5 cm. The rotating speed of the fan was 1,700 rpm, as transport curent was 8.7 A.

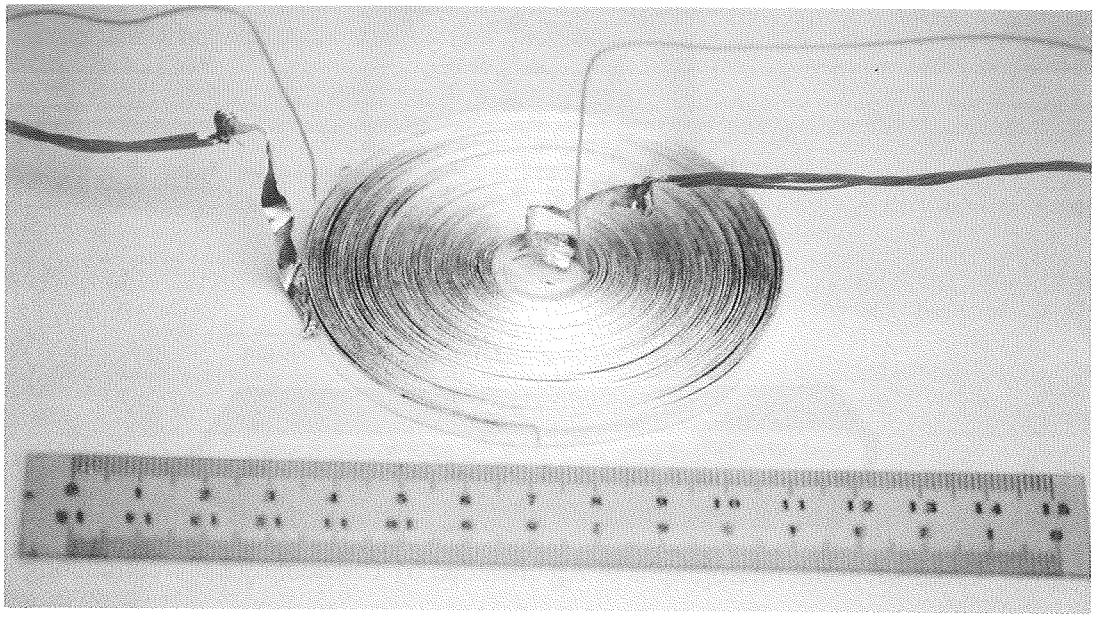

Fig. 3. A HTS pancake coil co-wound by four 7 meter Bi-based tapes, generating a center magnetic field (B_o) of 437 G at 77 K.

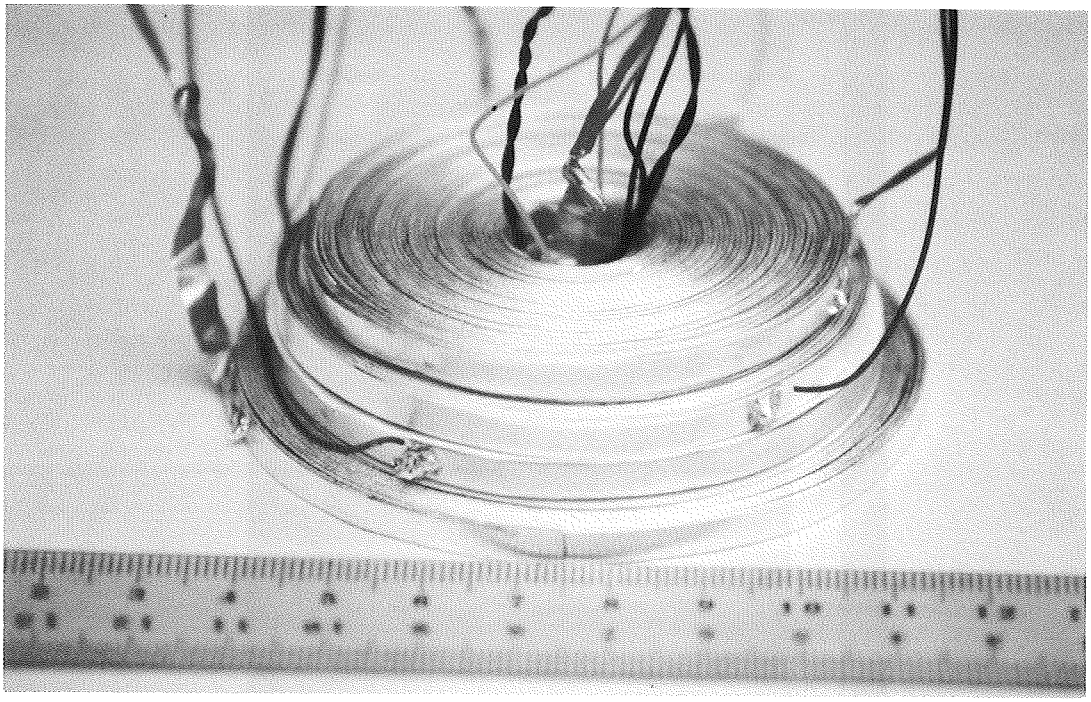

Fig. 4. A prototype of HTS magnet stacked by four pancake coils generating a center magnetic field (B_o) of 847 G at 77 K.

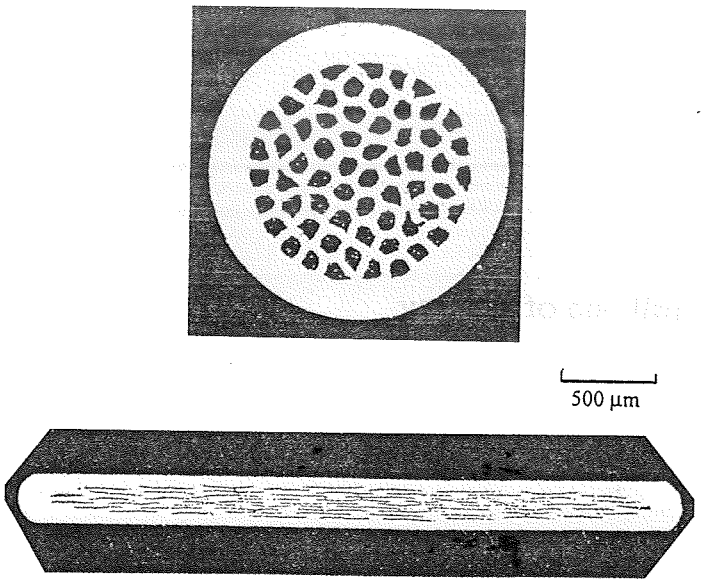

Fig. 5. Cross-sectional micrographs of Ag-sheathed 61-filamentary superconducting wires (a) intermediate stage and (b) final shape, having a $J_{c(77\ K)} \sim 1.3 \times 10^4$ A/cm^2.

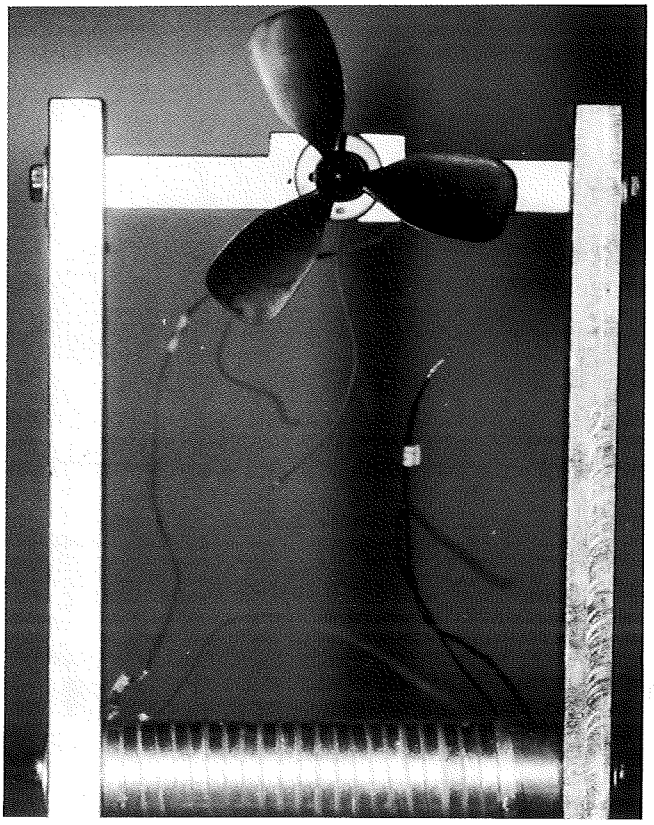

Fig. 6. A prototype of HTS DC motor prepared by winding sintered Ag-sheathed 19-filamentary tapes on an iron core to generate magnetic field, the fan speed reaching 1,700 rpm.

(3) Fabrication of large-area Y-Ba-Cu-O Thin Films

(a) Hot-wall sputtering technique[10)]

High quality epitaxial $YBa_2Cu_3O_{7-x}$ (YBCO) thin films have been prepared reproducibly by various deposition techniques at the MRL/ITRI. Due to the high substrate temperature and high oxidizing environment ($P_{O2} > 0.01$ Torr) required for in-situ growth of superconducting YBCO films, well-controlled substrate temperature is still one of the key factors in growing high quality thin films. The problem of short-life of the substrate heater has been encountered in the growing process frequently and results in the controling difficulties of substrate temperature and uniformity of temperature on the large area substrates. Therefore, we develop a hot-wall DC sputtering deposition system, where the substrate is heated by a tube-furnace "outside" the deposition system.

The schematic picture of the hot-wall sputtering system is shown in Fig. 7. The deposition chamber was made of a quartz tube. The target was made by a solid state reaction of Y_2O_3, $BaCO_3$ and CuO with a stoichiometric ratio of Y:Ba:Cu=1:2:3. The sputtering gas was 50%Ar-50%O_2 and the total gas pressure was 1.5 torr. The gas pressure was controlled by an automatic control valve. The target-to-substrate separation was 2 cm. The sputtering current and voltage were 0.2-0.4 A and 150-200V respectively and the target dimension is 40 mm in diameter and 4 mm in thickness. The thickness of the films was 150-500 nm and deposition rate was 0.05-0.1 nm/s. After deposition, the deposition chamber was immediately back-filled with oxygen to 1 atm and the films were furnace-cooled to below 100°C in flowing oxygen.

Composition of the films grown at substrate temperatures of 750-780 °C was the same as that of the target with a stoichiometric ratio of Y:Ba:Cu=1:2:3 analysised by Rutherford Backscattering Specroscopy (RBS). High-quality YBCO films with $T_{c(zero)}$'s of 90 K and $J_{c\ (77\ K)}$'s in excess of 1 x 10^6 A/cm^2 have been grown on sapphire (with a buffer layer of MgO or YSZ), $LaAlO_3$, MgO, $SrTiO_3$ and YSZ substrates. The films are highly oriented with the c-axis perpendicular to the surface of the substrate.

Recently, we have scaled up the hot-wall sputtering system to grow YBCO films on two-inch substrates. The variations of the thickness and composition of the films are within 14% and 10% respectively. $T_{c(zero)}$'s in excess of of 88 K and $J_{c(77\ K)}$'s of (1.6-3.2)x10^6 A/cm^2 can be obtained on two-inch YBCO/MgO thin films.

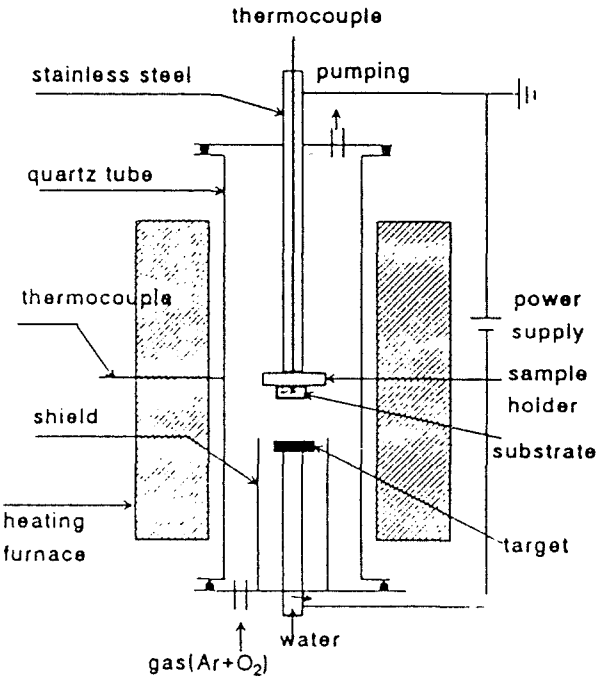

Fig. 7. Schematic picture of the hot-wall sputtering system.

(b) Pulsed laser ablation technique

Pulsed laser ablation (PLD) has become a widely used technique for fabricating oxide superconducting thin film due to the advantages of tolerance of high background oxygen pressures and reproducing target composition.[11,12] Recently, high temperature superconducting thin films have been expected to have great potential on the applications of wireless communication in the next centry. Hence, the development of large-area and high quality superconducting thin films will play the most important role on producing high quality microwave devices in the future. Therefore, how to make use of the formal experiences on "small-area" for preparing high quality and "large-area" thin films by PLD is the main goal of the research.

A KrF pulsed laser system (248 nm, 25 ns and 1.5 J/cm^2), as shown in Fig. 8, has been used to fabricate YBCO thin films. After carefully examining the effects of substrate temperature, laser fluence, target conditioning and target-substrate distance etc on superconducting properties, high quality Y-Ba-Cu-O superconducting thin films have been successfully prepared on (100)$LaAlO_3$ substrates. The optimal growth condition of YBCO thin films is listed as following:

Base pressure : less than 1 x 10^6 torr
Substrate temperature : 730 °C
Repetition rate : 5 Hz
Laser energy density : 1.5 J/cm^2
Target-substrate distance : 4.5 cm
N_2O gas pressure : 0.26 torr (during deposition)

$T_{c(zero)}$'s and $J_{c(77K)}$'s in excess of 88 K and 1 x 10^6 A/cm^2 respectively can be obtained routinely.

In consideration of the uniformities of the composition and thickness in large-area, we made lots of efforts on speed of target rotation, position of laser spot and nozzle geometry design[13], variation of composition and thickness within ±15% in a two-inch $LaAlO_3$ substrate have been obtained.

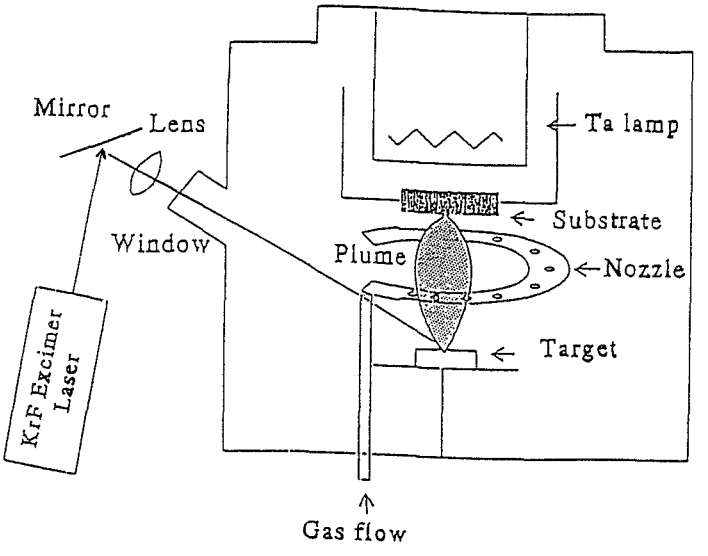

Fig. 8. Schematic picture of the laser ablation system.

(4) High-Tc superconducting devices

(a) Superconducting quantum interference devices (SQUIDs)

Among the "high T_c" weak link structures investigated, the most common are natural grain boundaries, however, they are generally randomly distributed, resulting in multiple junctions.[14] To avoid this problem, one of the ways for making single grain boundary

junctions, epitaxial films deposited on bicrystal substrate, has been suggested and shows some optimistic results on sensitivity and noise-reduction.[15,16]

We have also successfully developed the fabrication technologies of DC-SQUIDs with highly reproducibility.[17,18] The $Tl_2Ba_2Ca_2Cu_3O_{10}$ (Tl-2223) DC-SQUIDs, patterned by standard photolithography techniques, show modulation depth (peak to peak) up to 90μV, as shown in Fig. 9. After the successful development of the bi-epitaxial grain boundary Josephson junction at the MRL/ITRI. YBCO bi-crystal DC-SQUIDs with magnetic field modulation in excess of 1μV can be obtained, as shown in Fig. 10.

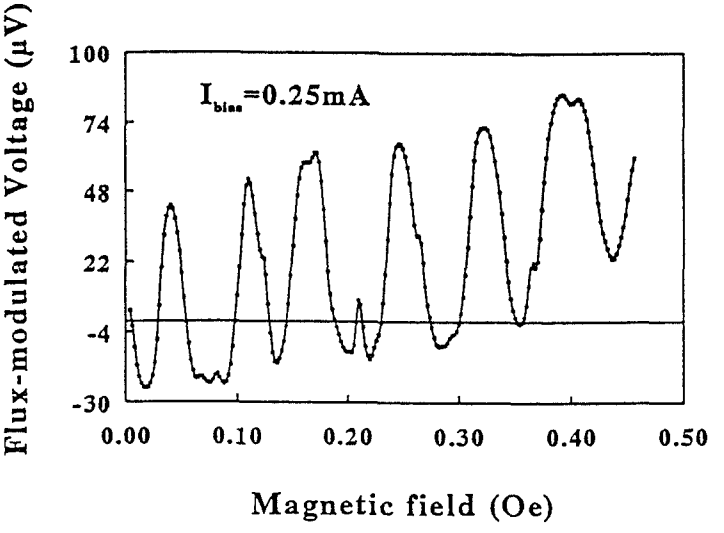

Fig. 9. Typical voltage-flux characteristic of Tl-2223 DC-SQUID at 77 K, showing the modulation depth (peak to peak) of around 90μV.

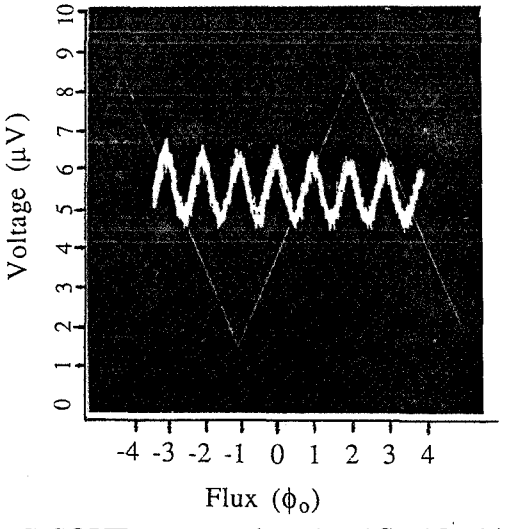

Fig. 10. A YBCO DC-SQUID prepared on (100)$SrTiO_3$ bi-crystal substrate. magnetometer at 77 K, showing the magnetic field modulation of around 1.2μV.

(b) High-T_c superconducting resonators

We have successfully fabricated and charaterized coplanar 2-port transmission line resonators, suggested by Porch et al[19], using superconducting $Tl_2Ba_2CaCu_2O_8$ thin films on (100) $LaAlO_3$ substrates. These films were prepared by rf-sputtered Ba-Ca-Cu-O precursor films followed by Tl-diffusion technique. The resonator pattern were made by standard photolithography techniques and chemical wet etching ($HCl : H_2O = 1 : 30$). The resonators were finally examined by a Wiltron 360 Network Analyzer. It was found that the unloaded quality factor (Q_o) of linear- and meander-type resonators are larger than 5×10^3 (5 GHz) and 1.2×10^4 (1.6 GHz) at 77 K respectively, as shown in Fig. 11. According to the relation[20] of the surface resistance (R_s) proportional to the square of frequency (f^2), R_s of the film at 10 GHz was estimated to be about 800 μΩ, which is much lower than that of 20 mΩ of commercial Au films.

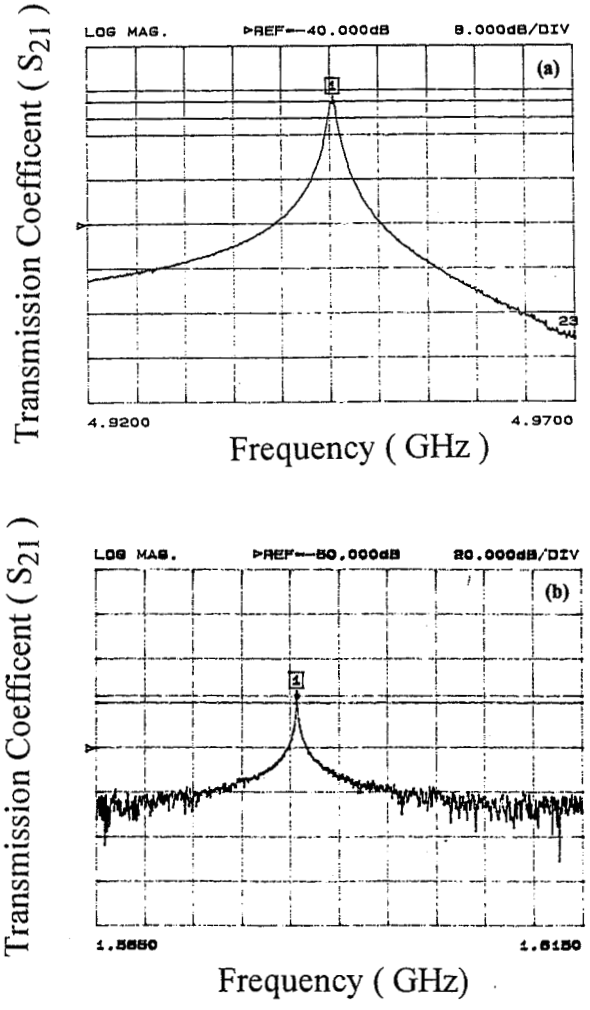

Fig. 11. Magnitude of the transmission coefficent versus frequency for (a) linear-type (b) meander-type Tl-2212 resonators.

Acknowledgements

The authors would like to thank the Ministry of Economic affairs for the financial support of the HTS research at the MRL/ITRI. We also wish to thank Dr. H.C. Lei, Dr. K. Chen, Mr. R. J. Lin and Dr. C. J. Huang for the help to organise this manuscript.

References

1) R. S. Liu, J. M. Liang, S. F. Wu, Y. T. Huang, P. T. Wu and L. J. Chen, Physica C **159**, 385 (1989).
2) P. T. Wu, R. S. Liu, J. M. Liang, Y. T. Huang, S. F. Wu and L. J. Chen, Appl. Phys. Lett. **54**, 2464 (1989).
3) J. M. Liang, R. S. Liu, Y. T. Huang, S. F. Wu, P. T. Wu and L. J. Chen, Physica C **165**, 347 (1990).
4) Y. T. Huang, R. S. Liu, W. N. Wang and P. T. Wu, Jpn. J. Appl. Phys. **28**, L1514 (1989).
5) R. S. Liu, P. P. Edwards, Y. T. Huang, S. F. Wu and P. T. Wu, J. Solid State Chem. **86**, 334 (1990).
6) D. S. Shy, W. H. Lee, and R. S. Liu, Proceedngs of the 1994 Annual Conference of the Chinese Society for Materials Science **1**, 290 (1994).
7) Y. T. Huang, S. F. Wu, and D. S. Shy, Proceedngs of the 1994 Annual Conference of the Chinese Society for Materials Science **1**, 332 (1994).
8) K. Chen, L. Horng, H. S. Koo, C. Y. Shei, L. P. Wang, C. Chiang, T. J. Yang, W. H. Lee, and P. T. Wu, Appl. Phys. Lett. **59**, 1635 (1991).
9) K. Chen, L. Hormg, C. H. Tai, J. C. Wei, T. J. Yang, and J. T. Lue, Chinese J. Phys. **31**, 1049 (1993).
10) R. J. Lin and L. J. Chen, Appl. Phys. Lett. **62**, 105 (1993).
11) D. Dijkkamp, T. Venkatesan, X. D. Wu, S.A. Shaheen, N. Jisrawi, Y. H. Min-Lee, W. L. Mclean and M. Croft, Appl. Phys. Lett. **51**, 619 (1987).
12) M. C. Foote, B. B. Jones, B. D. Hunt, J. B. Barner, R. P. Vasquez and L. J. Bajuk, Physica C 201, 176 (1992).
13) C. M. Chang, H. C. Lai and R. J. Lin, Proceedngs of the 1994 Annual Conference of the Chinese Society for Materials Science **1**, 328 (1994).

14) B. Oh, R. H. Koch, W. J. Gallagher, V. Foglietti, G. Koren, A. Gupta, and W. Y. Lee, Appl. Phys. Lett. **56**, 2575 (1990).
15) D. Dimos, P. Chaudhari J. Mannhart, and F. K. LeGoues, Phys. Rev. Lett. **61**, 219 (1988).
16) R. Gross, P. Chaudhari, M. Kawasaki, m. B. Ketchen, and A. Gupta, Appl. Phys. Lett. **57**, 727 (1990).
17) T. L. Chen, S. F. Wu, Y.C. Chen and R. J. Lin, Proceedngs of the 1993 Annual Conference of the Chinese Society for Materials Science, 7-5 (1993).
18) Y. C. Chen, T. L. Chen, R. J. Lin, and S. F. Wu, Chinese Journal of Physics **31**, 1109 (1993).
19) A. Porch, M. J. Lancaster, R. G. Humphreys and N. G. Chew, Presented at Applied Superconductivity Conference, Chicago, Aug. 23-28, 1992.
20) M. R. Namordi, A. Mogoro-Campero, L. G. Turner and D. W. Hogue, IEEE Trans. Microwave Theory Tech. **39**,1468 (1991).

Single Spin
53-76
313319
13 p.
34081

PROGRESS IN SUPERCONDUCTIVITY: *THE INDIAN SCENARIO*

Manu Multani
Tata Institute of Fundamental Research, Bombay 400 005, India

V.K. Mishra
Department of Science & Technology, Government of India, New Delhi 110 012, India

India has made rapid progress in the field of high temperature superconductivity, beginning at the time of publication of the *Zeitschrift für Physik* paper by Bednorz and Müller. Phase I of the program was conceived by the Department of Science & Technology of the Government of India. It consisted of 42 projects in the area of basic research, 23 projects in applications and 4 short-term demonstration studies. The second phase started in October 1991 and will run through March 1995. It consists of 50 basic research programs and 24 application programs. The total investment, mainly consisting of infrastructural development to supplement existing facilities and hiring younger people, has amounted to about Indian Rupees 40 crores, equivalent to about US$ 13 million. The expenditure for the period 1992-1997 shall be upto about Rs. 27 crores, equivalent to about US$ 9 million. The basic idea is to keep pace with developments around the world.

It is noteworthy to remark that during the above-mentioned period several books have been published. Some of the titles are: ***Chemical Aspects of High Temperature Superconductivity,*** edited by C.N.R. Rao (World Scientific Publishing Company, Singapore, 1991), ***Superconductivity Today,*** C.N.R. Rao and T.V. Ramakrishnan (Wiley Eastern, 1992), ***Proc. of the International Conference on Superconductivity,*** edited by S.K. Joshi, C.N.R. Rao and S.V. Subramanyam, a Series (now in its 13th. volume) entitled ***Studies in High Temperature Superconductors,*** edited by A.V. Narlikar, ***Thallium-Based High Temperature Superconductors,*** edited by J.V. Yakhmi and A.M. Hermann (Marcel-Dekker, New York, 1994), ***Selected Topics in Superconductivity - A Flavor of Current Trends,*** edited by L.C. Gupta and M.S. Multani (as part of a nine-volume series on **Frontiers in Solid State Sciences,** World Scientific Publishing Company, 1993-1995), ***Physical and Material Properties of High Temperature Superconductors,*** edited by S.K. Malik and S.S. Shah (Nova Science Publishers, Inc., New York, 1992), ***Theoretical and Experimental Approaches to High Temperature and Conventional Superconductors,*** edited by L.C. Gupta (Nova Science Publishers, New York, 1991)

One of the highlights of our achievements is the discovery of borocarbides as superconductors. Prof. R. Nagarajan, the main discoverer of this new family, is giving a separate talk on this. So I shall not dwell on it. We shall outline below the main achievements of the past two to three years.

SYNTHESIS AND CHARACTERIZATION

Thin Films

The growth of high quality high-T_c superconductor films on semiconductor substrates is an important step towards the possible marriage of two technologies. A recent study by the Poona University group was the realization of Y-123/YSZ epitaxial configuration on Si (100) by pulsed laser ablation without the chemical removal of the native surface oxide. The crystalline characteristics of the deposited films have been studied by x-ray diffraction (XRD), high resolution transmission electron microscopy (HREM) and Rutherford backscattering (RBS) techniques. Typically, the superconducting films of thickness 500 nm deposited on silicon with 150 nm epitaxial Y-ZrO_2 buffer layer have T_c as high as 88 K and J_c of $2x10^5$ A/cm^2 at 77 K for a 5 μm bridge pattern (using the same KrF excimer laser as for pulsed laser deposition).[1]

The group has deposited superconducting thin films as well as buffer layers using the KrF excimer laser (λ = 248 nm). The substrates include Y-ZrO_2 , $LaAlO_3$, $LiNbO_3$, $Gd_3Ga_5O_{12}$ and Si (100). Detailed studies addressing such issues as epitaxy, interface reactions, grain structure and coupling have been carried out. Effects such as those of dopants, devices and other physical properties will be described later in this talk in the relevant sections. The characterization was done at the laboratory of one of the authors (MM).[2] A group at the Bhabha Atomic Research Center (BARC, Bombay) has been growing single crystal substrates.

Granularity of HTSC (bulk as well as thin) materials is a characteristic disadvantage of the layered superconductors. While one single crystal grain of an HTSC film can support a $J_c \geq 10^7$ A/cm^2 at 77 K, most bulk materials measurements show 3 to 4 orders of lower critical current density. Thin epitaxial films have improved these values considerably - but not quite close to the intrinsic value of a single crystal. A group at the Tata Institute of Fundamental Research has prepared Ag-doped (5 wt.%) and undoped Y-123 films by PLD.[3] The excimer laser fluence was 3 J/cm^2 The growth of the film was carried out at 200 mTorr oxygen, a target-substrate distance of 5 cm and a laser repetition rate of 10 Hz. A normal oxygen cool in 500 Torr oxygen was provided as post deposition oxygenation. The group found that Ag-doping considerably improves the microstructure, leading to larger and well-aligned grains with narrower grain boundaries. A 10 μm wide microbridge led to a $J_c = 1.4x10^7$ A/cm^2 at 77 K on (100) $SrTiO_3$. Implications of this for devices is discussed in the appropriate section.

Innovative design and development for producing *in situ* superconducting thin films and make property-structure-deposition parameter correlations have been made by a group at the Indian Institute of Science (I.I.Sc., Bangalore). A technique with the acronym HOST (High pressure oxygen sputtering technique) was developed and *in situ* superconducting Y-123 films have been successfully prepared. To prove the superiority of HOST over the conventional sputtering techniques, detailed investigations have been carried out on HOST plasma by studying the *I-V* characteristics and by carrying out Langmuir probe studies and optical emission spectrometry (OES). These studies have revealed that in high pressure oxygen plasma at elevated substrate temperatures, negative oxygen ion energy was extremely small and the number of ions near the substrate were also small. This clearly explains why the negative oxygen ions cannot disturb the composition of the films in HOST. It was also observed that the

positive ion population was more in this technique and, hence, deposition rates were high.

Y-123 films have been deposited on MgO, $SrTiO_3$, and $LaAlO_3$ by HOST. Auger and RBS channeling studies have indicated that the films are stoichiometric and perfectly oriented. The films were uniform (better than 1 percent) over an area of I $cm.^2$. The challenging task of depositing large-area (60 mm or more) films has begun with the design of Facing Target Sputtering (FTS). Investigations have been carried out to study the effect of target diameter, target-substrate distance, operating pressure, inter target distance, *I-V* characteristics, Langmuir probe studies, negative bias voltage on the substrate, and a variety of other parameters are being studied for optimal deposition rate and quality.

A significant aspect of the research by another group at the I.I.Sc. has been the synthesis, purification and characterization of all the organometallic precursors needed for the CVD process. Initially, dipiraoxylmethanates (DPM) of Y, Ba and Cu were synthesized. These have been used by other investigators as well. More recently, a new β-diketonate precursor has been synthesized for each metals. These precursors, the keto-carboxylates, have been found to be very useful and, perhaps, better than the DPM precursors. The processes for the synthesis and purification of the various precursors have been scaled up to yield usefully large (10 grams) quantities. Due to polymerization-related problems with Ba precursors, only poor quality high-T_c have been obtained so far by MOCVD.

A group at the National Physical Laboratory (NPL, New Delhi) has achieved very good epitaxial films of the Y-123 system by the technique of dc magnetron sputtering. These films have been grown *in situ* on the following substrates: $SrTiO_3$ (100), $LaAlO_3$ (100), MgO (100), YSZ (100) and the *r*-plane of sapphire.[4] The sputtering gas consisted of a flowing mixture of argon and oxygen (in the ratio 2:1) at pressures varying between 200 to 1600 mTorr. The effects of sputtering gas pressure and the substrate temperature in the on-axis geometry (30 mm distance) were characterized by XRD, SEM, RBS, VSM, *R-T* and χ_{ac} *-T*.

The value of the critical current has been estimated as a function of the magnetic field using Bean's modified critical state model. The typical values of J_c at zero field and 12 kOe are $2.2x10^7$ and $1.6x10^6$ A/cm^2 at 77 K

Fullerenes and Related Systems

The Indira Gandhi Center for Atomic Research (IGCAR, Kalpakkam) group has synthesized C_{60} and C_{70} along with the alkali dopants, K and Rb. Some preliminary studies have also been made on co-doping K with Pb or Bi. The nominal compositions were PbK_2C_{60} and BiK_2C_{60} were prepared in the vapor phase reaction, starting with the stoichiometric constituents. XRD and χ_{ac}-*T* measurements indicate that while Pb and Bi are incorporated in the *fcc* lattice, there is no appreciable change in T_c unlike in the case of Tl-doped samples. On doping C_{60} samples with Yb it is seen that Yb_2C, Yb_3C_{60} and Yb_6C_{60} are formed. The observed superconductivity below 5.4 K is due to the *fcc* compound with the least Yb.(See ref.5 and citations therein)

The group of one of the authors (MM) in collaboration with the Poona University group has also been looking a Raman scattering from thin films of carbon-60 clusters with admixtures

of the carbon-70. The 488 nm Ar^+ radiation in the backscattered geometry has been used to characterize the different bonding types. Diamond films have been the focus of study by the two groups with respect to novel synthesis techniques. We have achieved formation of diamond films by laser-induced reactive quenching at the liquid-solid interface between a suitability organic liquid such as cyclohexane (in view of its stereochemical aspects) and a well-characterized substrate such as tungsten. A nanosecond laser pulse is made incident on a thin layer of cyclohexane or decalin supported on a tungsten foil. An area of 5 mm x 5 mm is thermally shocked in the scan mode by the laser pulses. The evidence from glancing angle XRD, TEM and laser Raman spectroscopy show, conclusively, the formation of hexagonal and cubic diamonds on the surface of tungsten. The choice of the organic liquid is found to be crucial.

A second group at NPL has recently published a paper reporting on the observation of imperfect carbon cage structures of C_{60} by high-resolution scanning tunneling microscopy.[6] The imperfect carbon cages have been resolved to the finest detail, which, for the first time, provide adequate confirmation of a variety of defect structures predicted by molecular dynamics simulations. From the conductance spectra by in the STS mode, one observes that the gap between the HOMO and LUMO for the clusters is decreased with the presence of defects. From the value of 1.5 eV for the perfect cage, the imperfect cage can lead to gap values of 0.3 eV or even lower, perhaps to zero value.

Powders and Compacts

A new technique called the pyrophoric process has been developed to synthesize ultrafine powders of the Y-123 system. The nanoparticles (40 nm) and have been observed to sinter to 99% density by processing the pellets at much lower temperatures (880 C) and shorter lengths of time (1 hr.) than other processes, *viz.*, the conventional ceramic process or the coprecipitation technique.

C-axis oriented Y-123 whiskers have been synthesized to fabricate whisker-reinforced Y-123 composite, which show partial *c*-axis orientation after sintering and a J_c value of 1440 A/cm^2 at 77 K.

In collaboration with the University of Florida group, the author's (MM's) group at has invented the method of synthesizing high density (about 97% of single-crystal density) of Y-123 ceramics with a large Meissner fraction (90% unoptimized). The technique involves the use of microemulsions which has been the focus of many studies reported in the past decade by chemists as well as physicists. The microemulsion-derived powders sintered with explosive grain growth from about 40 nm to about $50x10^3$ nm (along the longer axis of the ellipsoids). There are ramifications for high *Jc* in bulk superconductors from these studies.

The IGCAR group has designed a vacuum calcination method for the synthesis of high temperature superconductors. The essence lies in decomposition of precursors (from the co-precipitation, citrate, or sol-gel routes) in the quick removal of the CO_2 which would otherwise react with the Y-123 to form $BaCO_3$, Y_2O_3, CuO and $Y_2Cu_2O_5$, depending on the temperature. The reduced pressure calcination circumvents this by more effective removal of the carbon

dioxide. Presently, synthesis of upto 150 grams of Y-123 powder per batch has been standardized. The process parameters are well understood and there should be no difficulty in scaling up the process for 500 grams batch size. An annual production upto 100 kg of well-characterized material is well within reach.

A new semi-wet route to the synthesis of Pb-doped Bi-2223 powders free from contamination by the 2201 and 2212 stoichiometries has been developed. This process requires 48 hours to complete. By following the sequence of the thermochemical reactions, it is shown that Ca_2PbO_4 and 2212 formed in the early stages of reaction, in conjunction with CuO, play the most crucial role in accelerating the formation of the 2223 phase.[7]

The Defence Metallurgical Research Laboratory (DMRL, Hyderabad) has synthesized Y-123 powder which leads to sintered compacts with high current densities and levitation properties using quenched melt growth (QMG) and modified QMG techniques. The group has also prepared Y-123 sputtering targets of high quality.

Towards New Superconductors

It was recently shown that $YSr_2Cu_3O_7$, which is not otherwise possible to prepare under ambient conditions, can be stabilized by the incorporation of oxyanions such as carbonate, sulfate and phosphate. Such oxyanion derivatives of the 123 cuprates are rendered superconducting by the partial substitution of Y by Ca, Sr by Ba, or by the substitution of carbonate by nitrate. It has been noted that $YSr_2Cu_{2.8}(PO_4)_{0.2}O_y$ is stable in the orthorhombic structure, but the material is non-superconducting. The group has found that increasing the hole concentration through partial substitution of Y by Ca typically by 30 atomic percent renders the complex system superconducting (T_c 40 K). Once again, by incorporating the 0.2 phosphate group in the Cu site of orthorhombic $YBaSrCu_3O_7$, a stable tetragonal derivative with a transition temperature of 47 K has been prepared. The T_c increases to 70 K by 30 atomic percent substitution of Y by Ca. The IR spectrum of this system confirms the presence of the phosphate group in the C_{2v} symmetry. This observation is significant since no other stable 123-type cuprate is known to be formed in the Y-Ca-Sr-Cu-O system under the experimental conditions employed; let alone exhibit superconductivity.

When the Cu(1) site in orthorhombic $YBaSrCu_3O_{7-}$ (T_c = 80 K) is partly substituted by the carbonate ion (upto 50%), the crystal structure becomes tetragonal and electron diffraction pattern shows evidence for $2a$ x $2c$ superstructure; the material, however, is not superconducting. The same is true when Y is partly replaced by Ca as in $YCaBa_2Sr_2Cu_5(CO_3)O_y$. When the CO_3 group is partly by the NO_3 group as in the $YCaBa_2Sr_2Cu_5(CO_3)_{1-x}(NO_3)_xO_y$, the structure remains the same but superconductivity is retained. The IR spectroscopic studies show that both, CO_3 and NO_3 coordinate strongly and are not present as free ions in these oxyanion cuprate derivatives. Cu K-EXAFS studies on the carbonate and carbonato-nitrate derivatives confirm the presence of oxyanions in the place of CuO_4 units in the Cu-O chains.

Incorporation of the BO_3^{3-} stabilizes the $YSr_2Cu_3O_7$ but the borate derivative is not superconducting. Neither is superconductivity obtained by partial substitution of Y by Ca. Superconductivity appears, however, when Sr is partially replaced by Ba. Now, dramatically,

50 atomic percent replacement of Y by Ca remains superconducting. The borate ion is coordinated to Cu, reducing its point group symmetry. Observation of superconductivity in the borate derivatives prepared under ambient conditions is noteworthy.

The important point to note is that the cuprate family compounds are, essentially, being *fine-tuned* to observe subtle changes in the electronic properties. Such an approach can lead to an identifiable mechanism of the new ceramic superconductivity. It can also lead to higher or well-tailored transition temperatures. The derivative, $Tl_{0.5}Pb_{0.5}Sr_4Cu_2(SO_4)O_y$, has been synthesized with the same motivation. Infrared spectra show that the sulfate ion is present as a bidentate ligand as expected from the structural space group, P4/mmm. (See refs. 8, 9 and citations therein)

Coatings

Plasma spraying of high-T_c superconductors offers some scope for large scale processing. The results of work done at Bharat Heavy Electricals Ltd. (BHEL, Hyderabad) are reported. Essentially, in the plasma spray process, feed stock material in the form of powder is injected into a high-temperature, high-velocity, plasma stream. The temperatures have been estimated to be in the region of 4000-12,000 K while the velocities may lie in the vicinity of 100-200 m/s. These fast-moving molten droplets form a deposit (coating) when they are suddenly stopped by a relatively cold substrate. We can, therefore, see that the heat and momentum transfer from the plasma jet to the powder particles are of crucial importance for achieving good coatings. The arc current, plasma gas composition and flow, and particle size of the feed stock powder are the primary parameters which need to be optimized. Substrate distance from the gun nozzle and the substrate temperature are also relevant parameters as they dictate the speed with which solidification takes place on impact and govern porosity and micro cracks in the deposited coating.

Tapes

BHEL has also been engaged in the design and development of tapes. Silver-sheathed tapes were fabricated using the Bi-2223 system. The tapes were processed to final thickness by direct rolling as well as by repeated rolling with intermediate heat treatment. The rolling reduction rate was also varied to find its effect on the final properties. The critical current measured at 77 K could be enhanced from 2770 A/cm^2 for directly rolled tapes to 12,500 A/cm^2 by repeated rolling under identical conditions. In repeatedly rolled tapes the J_c - B variations were found to be much lower in comparison to the directly rolled tapes. Texture evaluation using angular dependence of the magnetoresistance showed the *a-b* plane orientation to be along the rolling direction..

The powder-in-tube technique using an Ag sheath has emerged as the only viable method for fabricating long lengths of flexible HTSC tapes. The Bi:Pb ratio in the above 2223 system was 1.8 : 0.4. The average particle size of the powder was about 2 μm. The BHEL group has now completed angular magnetoresistance (AMR) studies to garner useful information regarding the texture in the tape described above.The magnetic field is provided by suitably chosen gap distance between two NdFeB permanent magnets. The gap is adjusted so that the uniform field is more than H_{c1} of the Bi-2223 system (where Bi is partially

substituted by Pb). The fixture for changing the field direction is such as to change the angle (θ) between the transport current (in the plane of the tape) direction and the applied magnetic field direction. The range covered is $0 \leq \theta \leq 180$. The BHEL group has completed a study along with the Argonne National Laboratory and the Regional Research Laboratory (Trivandrum) on the influence of initial composition and processing parameters on the critical current density of BPSCCO PIT process tapes.

TOWARDS DEVICES

The etch kinetics of Y-123 films have been investigated for fabrication of 2 μm width microbridges by photolithography. The films have been etched to form different patterns of micron dimensions. It has been shown that Y-123 could be patterned down to micron dimensions by controlled wet etching using EDTA as an etchant and by lift-off technique. Lift-off technique requires fewer number of processing steps and avoids exposure to chemical etchants. EDTA is an admirably suitable etchant. The critical current density has been found to increase with decreasing linewidths which is due to decreasing number of weak links in the active microbridge area.

The same group at the Indian Institute of Technology (IIT, Kharagpur) has now been able to grow 5 monolayer thick 2201 and 2212 phases of BSCCO either singly or one on top of the other by the atomic layer deposition (ALD) process . In this method, the group has sequentially evaporated Bi and Cu from K-cells and SrO and CaO from e-beam guns onto MgO (100) substrates heated to 700 C. During the deposition, oxygen gas containing 10% atomic oxygen (generated by dc. discharge inside a U-shaped tube with a very fine hole in the bent portion which allows the atomized gas into the chamber) was allowed to impinge on the heated substrate. The 2201 film was deposited first on the substrate followed by the 2212 film so as to prevent interdiffusion and consequent reaction between the MgO and the 2212 film. The films have been found to be perfectly *c*-axis oriented. Tunneling measurements are in progress.

The group has also deposited BSCCO 2201 and 2212 films on PLZT-coated $Si/SiO_2/Si_3N_4$ substrates by the ALD process. The PLZT, depending on its processing conditions, can be used either as a dielectric or a conductor. *In situ* RHEED analysis shows excellent *c*-axis growth of the PLZT layer. Further studies on Si/PLZT/BSCCO/PLZT/BSCCO films are in progress.

Some degree of success has been obtained by a group at NPL in the design, fabrication of an rf-SQUID.[10] It is well known that a dc-SQUID is difficult to synthesize because of the requirement of two weak links having the same critical current. Moreover, the observation of an rf-SQUID behavior does not require a direct contact, so the problem of contact resistance can be eliminated. These SQUIDs were prepared from screen-printed films of Y-123 and Bi-2223 (with a small contamination of the 2212 stoichiometry). The voltage-flux characteristics of both the SQUIDS show oscillations with the period of the flux quantum,ϕ_o. These oscillations correspond to the area of the SQUID loop and are observed upto 85.1 K in the Y-123 system (central hole of 350 μm radius with a suspended microbridge of dimensions 200x400

μm^2) and upto 98 K in the Bi-2223 system (with a central hole of 40 μm with a microbridge of 150x120 μm^2). The field sensitivity of the first system comes out to be $\sqrt{S_B}=\sqrt{(S\phi/A)}=5.2x10^{-12}$ T/Hz in the white noise region. For the second system the corresponding value is $7.9x10^{-12}$ T/Hz. The latter system is also found to be more stable with several thermal cycles between liquid nitrogen and ambient temperatures that the former system.

The IGCAR group has developed SQUID sensors using the Nb-Al_2O_3-Nb sensor using the slit wafer geometry. A whole set of photomasks involving a minimum feature size of 4 μm has been designed and fabricated. This device geometry enables fabrication of SQUID sensors with an integrated input coupling coil which couples the picked-up signal into the SQUID. The coupling efficiencies exceed 80-85%, a value difficult to achieve with other types of device design. Since the fabrication foundry can handle wafers upto 75 mm diameter, a large number of devices can be obtained in each batch.

The Poona University group has succeeded in using Zn doping for tuning of the operating temperature of a bolometer based on Y-123 thin films.[11] The advantage of Zn doping lies in the fact that $(1/R)(dR/dT)$, which is the highest at the mid-point of the resistive transition for the new ceramic superconductors, does not decrease substantially as for other dopants. Thus the T_{co} can be tailored to specific values, such as, for example, at the boiling point of liquid nitrogen. In fact, T_c is hardly affected upto doping level of $x = 0.3$ which drives the transition temperature down to 52 K.

A novel approach has been adopted by a group at the Banaras Hindu University (BHU, Varanasi) for enhancing the intergrain and intragrain critical currents in bulk Y-124. The low intragrain critical current densities are due to inadequate flux pinning in the native cuprate high temperature superconductors. This situation can be remedied by developing appropriate flux pinning centers such as by local structural perturbations are strong and isolated, and their sizes are comparable to the short coherence lengths (0.4 - 3 nm). It has been found that the Y-124 dissociates above 915 C (for times as short as 10, 30 and 60 seconds) and the dissociated/transformed phase is always based on Y-124 even though it contains minority phases such as Y-123, Y-125, interfaces of these with the parent matrix phase, and stacking faults. The 30-second dissociated sample exhibits critical current densities about 11 times higher than for the virgin Y-124 at 77 K. The correlations with the microstructures have been described and discussed. The same group, along with the group at NPL (New Delhi) has observed the rf-SQUID effect in thin films (obtained by spray pyrolysis) of Tl-Ca-Ba-Cu-O. Two films have been chosen for the SQUID characterization. One is mainly the 2122 phase with needle-like grains.The other consists of the well-connected platy phase of the 2223 stoichiometry. The SQUID has been operated in the flux-locked-loop mode. The 2223 stoichiometry thin film exhibits better flux noise performance.

At the Central Electronics & Engineering Research Institute (CEERI, Pilani) a superconducting magnetic resistor and S-FET device-like structures have been developed using the sputtering technique.

PHYSICAL MEASUREMENTS

In spite of the tremendous efforts by researchers around the globe, the mechanism of high-T_c superconductivity has thus far remained a mystery. Amongst the different approaches followed to unfold the mechanism, an important one has been the study of the influence of intelligent substitutions in the new ceramic superconductors different microscopic and macroscopic aspects of superconductivity. Within the broad context of this approach, the role of magnetic impurities has been of particular interest. Unfortunately, in the high transition temperature superconductors it has been difficult to isolate the direct positive or adverse effects of dopants (magnetic or otherwise) from their indirect effects realized *via* their influence on such aspects as the orthorhombicity, oxygen stoichiometry, oxygen-vacancy ordering, etc.. A few facts have emerged from the vast body of substituent data which need not be reiterated here. But it may be noted that theoretical attempts to understand dopant effects on T_c depression are scarce. It has been argued that the depression of the transition temperature can be understood to be due to spin flip scattering within the Abrikosov-Gorkov theory formulated for the strong coupling situation if it is assumed that (1) the Cu^{2+} on CuO_2 planes are highly localized and antiferromagnetically correlated even in the superconducting state and are, therefore, harmless, (2) a vacancy or an extra spin produced by a dopant acts as a magnetic scatterer.[12]

The IIT Kharagpur group has studied the electrical transport properties on the Y-123 films grown by rf. magnetron sputtering for understanding the dimensionality and inter-layer coupling between CuO_2 layers. The films (200 nm thick) on MgO or $SrTiO_3$ substrates, had a J_c of 1.5×10^6 A/cm^2 at 77 K. The temperature dependence of the nonlinear current-voltage characteristics near the superconducting transition temperature have been analyzed for dimensionality crossover from 2D to 3D as suggested by the Kosterlitz-Thouless (KT) transition. The resistivity behavior near the transition temperature has been found to be governed by the activated thermal dissociation of the vortex-antivortex pairs as revealed by the exponential dependence of resistance on $\sqrt{T}$. However, deviation at temperatures away from T_c have been observed and are under investigation.

A group at I.I.Sc. along with the IGCAR group has made an interesting study of pressure-induced bandgap reduction, orientational ordering and reversible amorphization in single crystals of C_{70} using the techniques of photoluminescence (PL) and Raman scattering. These researchers were the first to measure the pressure-induced red-shift of the bandgap using the PL technique. These experiments yielded dE_G/dP = 0.138 eV/GPa. Later, the optical reflectivity and optical absorption measurements have confirmed this value. Using the bulk modulus K_o of 18 GPa, the hydrostatic deformation potential, which is related to the electron-phonon coupling constant, is $d_0 = dE_G/d(lnV)$ = 2.5 eV. The measurement on C_{70} indicates the hydrostatic deformation potential to be 2.15 eV. The slope changes in the pressure dependence of the peak positions and linewidths of the Raman modes associated with the intramolecular vibrations at 1 GPa mark the known *fcc* rhombohedral orientational ordering temperature. Group theory predicts 53 Raman-active modes corresponding to the species $12A_1' + 22E_2' + 19E_1'$ of the point group D_{5h} for the C_{70} molecule. In solid C_{70}, the selection rules predict many more Raman-active modes. Solid C_{70} transforms to an amorphous phase at P 20 GPa which reverts back to the starting crystalline phase on decompression, as evident from the

Raman lines associated with the intramolecular vibration and the PL. This implies that the C_{70} molecules are stable at least upto 31 GPa. This is in contrast to the irreversible amorphization in solid C_{60} at pressures greater than 22 GPa. The workers have rationalized this difference on the basis of different pressure dependence of the c-c distance between neighboring molecules.[13]

It is worth recalling a study made by two members of IGCAR along with the Texas group of C.W. Chu, the Princeton group and the Lawrence Livermore group.[14] They found a correlation between the local charge-density and superconductivity through positron annihilation studies. The temperature dependence between 10 and 300 K of the positron lifetime was measured in the $YBa_2(Cu_{1-x}M_x)_3O_{7-\delta}$ with 0.8, *M* Zn or Ga and x = 0.0 to 0,07. In the undoped and Ga-doped samples, the positron lifetime in the Bloch state, τ_b , was observed to decrease below T_c. In the Zn-doped samples, a dramatic x-dependent temperature variation of τ_b was observed below the transition temperature for x = 0.01 to an increase of the lifetime for x>0.02. It is established from the experimental data that the positron density distribution (PDD) plays a crucial role. A decrease in lifetime is observed when the positrons probe the chains and an increase is observed when the positrons probe the CuO_2 layers. The decrease in the lifetime below the transition temperature implies an increase in electron density at the site of the positron, viz., the Cu-O chains. A simple physical picture to understand this is to invoke that there is a local transfer of electron density between the layers and the chains in the superconducting state. Such a proposal can account for the temperature dependence in the Zn- and Ga-doped systems if we take the PDD into account correctly. The calculated PDD shows that the weight of the positron density shifts from the Cu-O chains to the CuO_2 layers due to Zn doping. A transfer of electron density from the layers to the chains will in this case lead to a decrease in the electron density at the site of the positron and this can account for the observed increase in the lifetime below the transition temperature. In the Ga-doped system, the PDD is seen to be on the chains and a decrease in the lifetime is seen below the critical temperature; once again this is consistent with the notion of electron density transfer from the layers to the chains. Besides, this model explains the observed decrease in $\Delta\tau_b$ with increased doping concentration. An electron transfer from the layer to the chain in the superconducting state can be viewed as an increase of the charge state of Cu in the layers from 2+ to 3+. With partial replacement of Cu by Zn or Ga such a charge transfer can be expected to be suppressed, leading to a decrease in the magnitude of the $\Delta\tau_b$ with increased Zn or Ga doping.This basic approach has been extended to a number of HTSC systems and a comprehensive paper.

The group at the Saha Institute of Nuclear Physics (SINP, Calcutta) has been active in theory as well as experiment. A recent study involves the resistivity anisotropy in Y-substituted Bi-2212 system.[15] The group has grown undoped and doped Bi-2212 single crystals and measured the resistivity in the *ab*-plane and along the *c*-axis. The normal state ρ_{ab} is linear in T with positive slope for all samples. The data are interpreted in terms of the Matthiessen rule: $\rho = m^*/(ne^2\tau_{imp}) + m/ne^2\tau_{ph})$. The x = 0 and x = 0.1 samples show a metallic temperature dependence which agrees with the prediction made earlier by Kumar and Jayannayar for the *c*-axis resistivity, $\rho_c(T)$, and the resistivity anisotropy,ρ_c/ρ_{ab}, at room temperature. The value of the relaxation time that emerges from the fittings of the data to the Matthessen rule is almost of the same order ($\sim 10^{-14}$ sec) as obtained from optical conductivity measurements by Romero *et al.*.

The SINP group has also studied the excess conductivity of the Bi-2212 system as a function of the carrier concentration. The analysis shows that the system is highly anisotropic and the interlayer coupling strength decreases very rapidly with the decrease of the hole concentration. In the low-hole concentration region, T_c depends strongly on the interlayer coupling as compared to that in the optimum- and heavily-doped region. From the value of the interlayer coupling, out-of-plane coherence length and dimensional crossover temperature are estimated.

The Madras University group has been involved in Mössbauer[16] and Positron Angular Correlation[17] studies. A recent study focused on the 1D-ACPAR measurements on the Y-123 (with varying oxygen content) and the Y-124 systems have been analyzed. It is revealed from this work that the Umpklapp components of the second and third Brillouin zones appear in all superconductors. In the insulating compounds of the Y-123 system, they are less prominent. Otherwise the band structure features of all these samples are strikingly similar. In conclusion, the authors note that there is qualitative accord between the measured and calculated spectra, signifying the reasonable description of the ground state and the Fermi surface of the new superconductors.

The group of at the Center for Advanced Technology (CAT, Indore), a group at TIFR and co-workers at the Bhabha Atomic Research Institute (BARC, Bombay) have been concentrating in the past few years on the dc and ac hysteresis effects on granular samples of the new ceramic superconductors. A recent study involves the minor ac hysteretic study of Y-123. The results have implications for intergrain and intragrain response for hard type-II superconductors. When the external dc field B_{dc} is zero, hysteresis is seen as B_{ac} is raised from zero and higher odd harmonics are observed in the magnetization. The absence of even harmonics is indicated by the symmetry of the hysteresis loop. When B_{dc} is non-zero a response is also observed at higher even harmonics and the concomitant asymmetry of the minor hysteresis loop is stressed to be the signature of the field-dependent critical current density $J_c(B)$. It is shown for the first time that the shape of these loops is a function of the history of application of the cycling field. A model based on the two-component nature of an HTSC pellet has been put forward to explain the ac and dc history effects.[18,19]

THEORY

Prof. S.S. Jha has worked out a mathmatical outline of the generalized pairing theory for the layered HTSCs for, both, singlet and triplet pairing. For the spin-singlet case, a distinction is made between intra-layer and inter-layer pairing by using different coupling constants (phenomenological) for the two situations. The actual nature of the exchange mechanism (whether electronic charge fluctuations, spin fluctuations, ionic excitations, etc.) are not specified. It is shown how superconductivity at high Tc can arise in this type of materials. The singlet pairing theory appears to be more promising. It is suggested that no single exchange mechanism may be operative and the phonon exchange mechanism may be only playing a supporting role.[20]

Prof. G. Bhaskaran has clarified the application of RVB theory to HTSCs. The author introduces basic ideas of RVB theory by defing the RVB state and the nature of excitations. Some exactly solvable models having the RVB ground states are given, followed by approximate methods (mean field theory and slave boson gauge theory). The theory is then applied to explain some general properties of HTSCs, the interlayer tunneling mechanism and to calculate the NMR relaxation times.[21]

NEUTRON SCATTERING

Neutron profile refinement has been carried out for most polycrystalline HTSCs at the DHRUVA reactor at Trombay. The results of these investigations are reviewed within the context of the current structural models and some novel structural features are highlighted.[22]

SUPERCONDUCTING SYSTEMS

Superconducting Generator

Recognizing the important role of superconductivity in future technologies and products such as generators, BHEL has taken up the development of a 5 MVA Superconducting Generator under the National Superconductivity Program. As a forerunner to this, a 200 KVA laboratory model of the generator has been successfully developed at the Corporate R&D Headquarters at Hyderabad. The prototype is undergoing several commissioning trials. The rotor has been wound with Nb-Ti wire, producing peak magnetic field of 4 Tesla. For cooling the rotor windings, a closed-cycle liquid helium plant with liquid nitrogen pre-cooling system has been installed. The potential advantages of the Superconducting Generator are reduction in size and weight, improvement in efficiency, possibility of operating at larger capacities and higher voltages, and improvement in steady-state stability.

Superconducting High-Gradient Magnetic Separator

Magnetic separations is one of the largest industrial applications of magnetism, next to motors and generators. It is used for separation of paramagnetic and diamagnetic particles as well as non-magnetic materials, and finds extensive applications in mineral processing industries. The magnetic field intensity achievable through conventional magnetic separators is upto about 2 Tesla, and the magnetic field gradient is of the order of $1x10^3$ or $2x10^3$ Tesla/meter. With the advent of superconducting magnets, even larger magnetic field gradients such as about 10^5 Tesla/meter are achievable with negligible increase in power consumption. In view of these advantages, this area was promoted in India also. Projects for the design & development and laboratory trials of superconducting high-gradient magnetic separators have achieved some degree of success at BHEL & NPL[23] and the Atomic Minerals Division of the Department of Atomic Energy have now been completed. The system has been installed and successfully operated at the Corporate R&D Division of BHEL at Hyderabad.

At BHEL, using the superconducting high-gradient magnetic separator, a number of experiments have been carried out on ball clay, magnesite, synthetic rutile and iron ore slime. Iron oxide impurities in ball clay could be brought down from 1.5% to 0.5% from 1.0% to 0.5% in magnesite, from 2.5% to 0.5% for synthetic rutile, enrichment of iron ore slime

enrichment to 70% from 60%, all processes in a single pass. These results have proved the efficacy of the system in separating weakly magnetic impurities of micron size from crushed basic minerals. The throughput is about 1 ton/hour for the crushed mineral ore while it about 5 tons/hour for the slurry.

This development marks the first step in the endeavors towards commercial application of superconducting technology in an industrial environment. Another prototype equipment development has been started by BHEL and the Electronics Corporation of India Ltd. (ECIL, Hyderabad)

References

1. R.D.Vispute, S.M.Kanetkar,K.C.Rajkumar, A.Madhukar, N.Parikh and B.Patnaik: *Physica C* 199 (1992) 59
2. S.B.Ogale, R.D.Vispute and S.M.Kanetkar: *Indian J.of Pure & Appl.Phys.*30 (1992) 666
3. D.Kumar, M.Sharon, R.Pinto, P.R.Apte, S.P.Pai, S.C.Purandare, L.C.Gupta and R.Vijayaraghavan: *Appl.Phys.Lett.*62 (1993) 3522
4. R.Chandra, A.K.Gupta,and V.Kumar: *Indian J.of Pure & Appl.Phys.* 32 (1994) 133
5. C.S.Sunder et al., *Indian J.of Chem.* 31 (1992) F92
6. A.V.Narlikar, S.B.Samanta and P.K.Dutta: *Proc.Royal Soc.London A* 444 (1994) 325
7. D.Pandey, A.K.Singh and A.P.Singh: *Physica C* 204 (1992) 179
8. R.Nagarajan, S.Ayyappan and C.N.R.Rao: *Physica C* 220 (1994) 373
9. R.Mahesh, R.Nagarajan and C.N.R.Rao: *Solid State Commun.* 90 (1994) 435
10. S.Khare, A.K.Gupta and N.Khare: *Indian J.of Pure & Appl.Phys.* 32 (1994) 39
11. S.B.Ogale, M.Vedawyas, G.S.T.Bendre and S.M.Kanetkar: *Appl.Phys.Lett.*61 (1992) 2105
12. S.B.Ogale, D.D.Chougale, S.M.Kanetkar, P.Guptasarma and M.S.Multani: *Solid State Commun.* 89 (1994) 13. N.Chandrabas, A.K.Sood, D.V.S.Muthu, C.S.Sunder, A.Bharathi, Y.Hariharan and C.N.R.Rao: *Solid State Commun.*
14. Y.C.Jean et al., *Phys.Rev.Lett.* 64 (1990) 1593
15. J.B.Mandal, S.Keshri and B.Ghosh: *Physica C* 216 (1993) 195
16. S.Srinivasan, V.Sridharan and T.Nagarajan: *Bull.Mater.Sci.*14 (1991) 697
17. T.Nagarajan, S.Sivasankaran, D.Ravichandran and K.Nandhini: *Mater.Sci.Forum* 105-110 (1992) 767
18. S.B.Roy, S.Kumar, A.K.Pradhan, P.Chaddah, R.Prasad, N.C.Soni and K.Adhikary: *Pramana-J.Phys.*41 (1993) 5119. S.B.Roy, S.Kumar, A.K.Pradhan and P.Chaddah: *Physica C* 218 (1993) 476
20. S.S.Jha in: *Frontiers in Solid State Sciences, Vol.1: Selected Topics in Superconductivity*, eds: L.C.Gupta and M.Multani (see references therein)
21. G.Bhaskaran in: *ibid*
22. A.Sequeira: *Physica C* 174 (1991) 311
23. B.V.Mohan, G.Swaminathan, H.R.Balu, K.A.Durga Prasad, Y.S.Reddy: *Proc. Intermag 93*, Stockholm, April 13-16, 1993

The authors apologise for omissions because of lack of space in this proceedingspublication and the presentation which was only for twenty minutes

54-76
313337

to be published in Proceedings of 4th World Congress
on Superconductivity, June 27-July 1, Orlando, FL, USA

SUPERCONDUCTIVITY IN RUSSIA: UPDATE AND PROSPECTS

V. Ozhogin
Editor-in-Chief of "Superconductivity: Physics, Chemistry, Technology" journal
RRC "Kurchatov Institute", 123182 Moscow, Russia

Introduction. The researches in high temperature superconductivity in the FSU had been organized and financed since 1988 through **a special State Program**, the scheme being retained for Russia after the regretable decomposition of SU. The scientific supervision is being carried out by the Scientific Council under the chairmanship of Academician Yu. Osipyan. The Council consists of four sections conditionally named "Physics", "Chemistry", "Weak Currents" and "High Currents" and headed by I. Shchegolev (Inst. of Solid State Phys., Chernogolovka), Yu. Tret'yakov (Moscow State Univ.), V.Lemanov (Phys.-Tech. Inst., St.-Petersburg), and N. Chernoplekov (RRC "Kurchatov Inst."), respectively. **I am deeply grateful to each of them for highly valuable discussions of corresponding chapters of this review**.

During the 2 years that passed between the 3d and the 4th World Congresses on Superconductivity, the tendency survived towards curtailing the number of research groups working in the field of high temperature superconductivity and, accordingly, towards cutting back the number of publications on the subject. This process is due basically to the fact that this problem is given up by random people deprived of sufficient financial support and is kept up by high-grade professionals. Therewith the quality of publications raises and their subject matter becomes more and more purposeful. The situation in Russia is developing in the same direction, if only a little bit slower, partly because of less rigid approach to the financing problem. Thus, **in 1993 the HTSC State Program coordinated the activities within 275 projects**, while in 1992 there were 340 of them and 402 in 1991.

Major Research Guidelines. The investigation of high-Tc superconductors is hindered, first of all, by **their equilibrium crystal structures being seemingly always intrinsically deficient**. Some of lattice sites in these structures remain unoccupied which inevitably makes the lattice partially disordered. That is why more and more attention has been paid of late to a possibly thorough analysis of the real structure of the compounds under investigation, their phase composition, etc.

Next, the properties of high-Tc superconductors are in many senses **unusual even in the normal state**. It has been found that anomalies originate because of a strong interaction between electrons in Cu-O planes. However there is still no definite answer to the basic question of whether this electron-electron interaction contributes to the onset of the superconducting state and if so, in what way. To clarify this vague question the mechanism of current carrier formation in Cu-O planes is being studied theoretically and experimentally. A feasibility of realizing nontrivial scenarios of superconductivity is examined, different methods are used for gaining the information on the quantity and symmetry of the superconducting order parameter, etc.

Another stream of works on HTSC worthy of mentioning involves a study into their mixed state predicted by A. Abrikosov as early as in 1957. A giant single-axis anisotropy of electron properties of high-Tc superconductors results in **nearly laminated structure of Abrikosov vortices** which changes essentially their dynamics and the process of their interaction with different defects and dopants. The analysis of these problems creates the basis for a search for possible ways of raising the critical current of high-Tc superconductors, improvement of noise parameters of HTSC-based devices, etc.

1992-93 Developments of Primary Importance.

Ph.1. The precision x-ray structure analysis of $YBa_2Cu_3O_x$ single crystals with various oxygen content held at the Institute of Crystallography of the Russian Academy of Sciences (RAS), Moscow, (head: V.Simonov) has revealed that **there are only three thermodynamically equilibrium phases of this compound**, namely, a dielectric tetragonal phase of the $\mathbf{YBa_2Cu_3O_6}$ composition with T_c = 0K, an orthorhombic phase II of the $YBa_2CuO_{6.5}$ composition with T_c = 60K and an orthorhombic phase I of the $YBa_2Cu_3O_7$ composition with T_c = 92K. Single crystal with $6<x<6.5$ is not, strictly speaking, single crystal but is built of blocks of the tetragonal phase and the orthorhombic phase II, while single crystal with $6.5<x<7$ is built of blocks of

orthorhombic phases I and II. On variation of the oxygen index the relation between the volumes of the blocks varies.

Ph.2. Several research teams gained important results concerning the properties and **the role of the electron-electron interaction in HTSC**.

One of the manifestations of this interaction is the existence of large strongly correlated fluctuations of electron spins whose existence is reliably established in various experiments. Superconducting pairing owing to spin fluctuations is one of few real alternatives to the conventional electron-phonon mechanism of superconductivity. Most of the theories analyzing the pairing via spin fluctuations predict the origination of so-called d-wave Cooper pairs with a weaker space symmetry rather than s-wave pairs inherent in conventional superconductors. In this connection the clarification of the type of the superconducting pairing not so long ago seemed almost decisive for answering the question of the mechanism of HTSC. In fact, the alternative s- or d-wave pairing ceases to look so meaningful now when there is a very important work made at the Kurchatov Institute (head: Yu. Kagan) late in 1992 which theoretically proves electron spin fluctuations being capable of leading under certain conditions to the formation of s-wave type Cooper pairs.*)

The absence of noticeable anisotropy of a superconducting gap in single crystals of different HTSC systems **directly indicative of the s-wave pairing** was revealed in direct tunnel measurements held in the Moscow State University (head: Ya. Ponomarev) and the Physical Institute, RAS, Moscow (head: S.Vedeneev).

A new approach to this field of problems is offered in the work fulfilled at the Institute of Solid-State Physics, RAS, Chernogolovka (head: V.Timofeev) which searched into reflections of the IR-radiation from the La_2CuO_{4+x} crystals in the insulating phase **under optical pumping of nonequilibrium current carriers**. It has been found that the **carriers** being formed **are strongly bounded due to their spins entering into strong interactions with the spins of copper electrons** (all the phenomena occur in Cu-O planes).

Ph.3. In the work performed at the Kurchatov Institute, Moscow (head: A.Taldenkov) a change in the thermal resistance of a superconductor on switching of the magnetic field has been attributed to phonon scattering by Abrikosov vortices. By means of measuring the effect magnitude the authors show that **Cooper pairs** in crystals of systems Tl-Ba-Cu-O and Bi-Sr-Ca-Cu-O **are always formed by the electrons of one**

*) The same (!) result was obtained independently and a little bit later by J. Appel and A.W.Overhouser.

and the same plane, while in the Y-Ba-Cu-O system the situation varies depending on the oxygen content. In the $YBa_2Cu_3O_7$ phase, for example, superconducting pairs may consist of electrons belonging to adjacent planes. This conclusion is in agreement with other numerous factors known in this respect.

In a sense the same effect of phonon interaction with Abrikosov vortices has been registered in quite a different way in the work of the Institute of Physical Problems RAS, Moscow (head: N.Zavaritskii). Here the appearance of **electric voltage under a sound wave action** was detected in a HTSC sample when in the mixed state. The effect results from phonons dragging the vortices.

Section 2: CHEMISTRY

Within the framework of the Project headed by B.Popovkin (Moscow State University) E.Antipov and S.Putilin synthesized, resting on an original method of the crystal-chemical approach to the HTSC phase structure, **a new family of superconductors** based on complex copper and mercury oxides: $HgBa_2CuO_{4+\delta}$ (T_c = 94 K) and $HgBa_2CaCu_2O_{6+\delta}$ (T_c = 127 K). The latter has a parabolic T_c dependence on the copper oxidation degree. It is the first compound with T_c above 100 K which possesses superconducting properties under deficient and excessive number of holes.

Of late the same researches independently and simultaneously with Swiss scientists have synthesized one more compound of this family, namely **$HgBa_2Ca_2Cu_3O_{8+\delta}$ with the record-high critical temperature of 134 K** increasing up to 158 K at 150-200 kbar, which inspires a hope for synthesizing this phase under the normal pressures by means of selecting proper dopants. The latter member synthesized of the new family, $HgBa_2Ca_3Cu_4O_{10+\delta}$, has a lower T_c value of 133 K - a tendency similar the last members of the bismuth and thallium families. Within the scope of the same Project a new compound, $Eu_{1.6}Sr_{1.8}Ce_{0.6}Cu_3O_{8+\delta}$ (and its samarium analog), have been also synthesized with T_c = 36 K.

On the basis of the **$Sr_2CuO_2CO_3$ phase, earlier found** by E.Antipov's group, a number of laboratories in different countries have produced at present a lot of **oxicarbonate HTSC** akin to oxide HTSC phases. Among other results of a search for new HTSC phases let me point out synthesis of an ordered polytype of Bi-2212 and Bi-2201 phases, namely, $Bi_4Sr_4CaCu_3O_{14+\delta}$ with T_c = 85 K (Project headed by N.Evtikhiev and A.Bush, Moscow Institute of Radio Electronics and Automation). Let me stress out here that the information of **these two results first were published in the "Superconductivity: Physics, Chemistry, Technology" journal** and then they were

"rediscovered" by Western investigators. It's a very serious hint for me as an Editor-in Chief!

Procedures have been developed for separation of individual fullerens of C_{60} and C_{70} on modified sorbents (silica gel, modified with diphenylsilile groups, or graphite) which accelerate noticeably the separation process (Project headed by M.Vol'pin, Institute of Element-Organic Compounds, and Project headed by A.Dityatiev, Science and Research Center of Chemical Technologies). **Methods of extraction of higher (up to C_{200}) fullerens and metalfullerenides have been devised**. In order to raise T_c a search for new endohedral metalfulleren complexes and methods of their testing is being performed.

Along with physical methods of HTSC film deposition the State Program supports the development of **chemical methods of films manufacturing**, such as aerosol pyrolysis, a sol-gel technique. Special attention has been paid to the fundamentals of the chemical vapor deposition (CVD) method, most suitable for epitaxial HTSC film production, and its MetalOrganic modification (MOCVD).

The results of the researches performed under Projects headed by A.Kaul', Moscow State University, and Project headed by F.Kuznetsov, Institute of Inorganic Chemistry, the Siberian Branch of RAS, indicate at **indubitable perspective technological character of the MOCVD method**. Superconducting properties of films are by no means worse than of those produced by physical methods, that is, films have been produced with the MOCVD method had the critical temperature $T_c > 90$ K, critical current density j_c (77 K) $> 10^6$ A/cm^2 and surface resistance R_s (77 K, 10 GHz) < 500 μOhm). This method has made it possible to achieve deposition rate of 30 μm/h while retaining high critical parameters of HTSC films and produce high-quality films on substrates of 100 cm^2 in area.

The major promising directions of developing this methods in the nearest years to come seem to be the following:

a) a search for **new metalorganic precursors**; clarification of chemical transformations of precursors in the vapor phase;

b) development of single-source systems of precursor evaporation as the most straightforward method to achieve **high reproducibility of the deposition process**; development of the *in situ* methods of the deposition process control;

c) mathematical **modeling of the deposition** process;

d) **investigation into the pinning mechanism** in MOCVD films, directed synthesis of films with preset distribution and prevailing type of pinning centers;

e) production of **heterostructures** containing HTSC layers.

Researchers of the Institute of General and Inorganic Chemistry RAS (Project headed by V. Nefedov) analyzed changes occurring in HTSC ceramics and thin films after a long-term (10 days) exposure to the electrical current action and found that **passing the current is accompanied with redistribution of the content of active oxygen** (enrichment near the positive electrode) and impurities; the concentration of the HTSC phase increases in the middle of the sample and the critical current drops. It has also been found that the epitaxial films degrade much slower than nonepitaxial ones do.

Section 3: WEAK CURRENTS

The works carried out by this Section in last two years covered the following problems:

1. **Substrate** manufacturing for HTSC film deposition, a search for new crystalline materials to be used as substrates and perfecting the quality of existing materials;

2. **Control and optimization** of the methods of high-quality HTSC film production, including those on large-diameter substrates;

3. Elaboration of a reproducible production **process for Josephson junctions, development of SQUIDs**;

4. Development of **bolometers** of high sensitivity;

5. Application of HTSC materials in **microwave devices**;

6. Manufacturing of multilayer structures of the "metal-insulator-superconductor" type and analysis of the **electric field** (or polarization) **effect** on electrical properties of a superconductor;

7. Working out a production process for micron-scale superconducting structures on the basis of **high-Q tunnel transitions** Nb-AlO_x-Nb (low temperature superconductivity).

The following results may be regarded as the most significant for each of these problems (**at the end of each paragraph a name for proper references is offered**):

1) Buffer layers made of cerium oxides (CeO_2, a=5.411Å (100) and a=3.826Å (110); Ce_2O_3, a=3.891Å; $CeAlO_3$, a=3.767Å) well chemically and chrystallographically compatible with YBCO films (a=3.824Å) have been found to be particularly promising. It opens up perspectives of producing microwave and other devices on **large area HTSC material** (integrated variant). Eu.Gol'man, St.-Petersburg Electro-Tech. Inst.

2) HTSC film were produced by molecular-beam epitaxy on substrates of up to 76 mm in diameter. Smooth-surface films of 10 cm in diameter were laser deposited on Al_2O_3 substrates without a sublayer. **The critical current densities in the films run up**

to 10^7 A/cm^2 at 77 K. An average surface resistance value in the films is 0.5 mOhm (77 K, 10 GHz). Double-coat films were produced on Al_2O_3 substrates. On Si substrates with a sublayer films with T_c = 3.5x10^6 A/cm^2 (at 77K) are produced. M.Predtechenskii, Inst. of Thermal Physics, Novosibirsk.

3) A reproducible production process for Josephson junctions on bicrystalline substrates has been worked out. The voltage-current characteristics have marked Shapiro steps up to the 4-th order. The VvsI characteristics obtained register the highest for the moment characteristic voltage $V_c = j_cR_N$ = 1 mV. **For the first time** the existence of Josephson junctions of the "HTSC - semiconductor - HTSC" type was experimentally corroborated.

Realized are **DC SQUIDs** with the flux sensitivity (1.2 - 1.5)x10^{-5} $\Phi_o/Hz^{1/2}$ in the incoming signal band of 30-10,000 Hz and the slew rate up to 10^4 Φ_o/sec. On using an external magnetic flux concentrator the field sensitivity makes 6.6x10^{-13} T/$Hz^{1/2}$. Two dimensional magnetic flux scanners based on LTSC and HTSC d.c. squids have been worked out. M.Kupriyanov, Moscow State Univ.

RF SQUIDs have been made with a 100x100 μm quantization loop and a magnetic flux concentrator of 3 mm in diameter. The measurements revealed that the spectral noise density diminishes rapidly with the frequency increase and for frequencies above 3 Hz attains the fixed level of 6.5x10^{-5} $\Phi_o/Hz^{1/2}$. The power sensitivity was 5.6x10^{-29} J/Hz and the field sensitivity made 2.3x10^{-13} T/$Hz^{1/2}$ (at 3 Hz). S.Gaponov, Inst. Appl. Phys., Nizhnii Novgorod.

4) A layout is calculated and a production process is elaborated of **antenna microbolometers** on $NdGaO_3$ substrates with a threshold sensitivity of 1.6x10^{-11} W/$Hz^{1/2}$ and time constant 30x10^{-7} sec.

The following receiving devices have been worked out and manufactured: **a double-channel receiving device** based on HTSC bolometers for scientific researches in the IR and submillimeter ranges and a four-channel receiving device based on antenna microbolometers for investigations in thermonuclear plasma in the submillimeter range.

A bolometer of a new type has been suggested with the operation principle based on the temperature dependence of the kinetic inductance for a strip resonator.

Further investigations envisage a study of **ultrafast electron processes** in thin HTSC films and an elaboration of receiving and commutating devices with extremely high speed of response (involving a mechanism of electron heating in the resistive state). Eu.Gershenzon, Moscow Pedagogical Institute.

5) Film resonators are already available with the Q-factor (at 10 GHz) **three times better than that for copper** devices.

Suggested and investigated is an electrically small antenna for the frequency range of about 2 GHz. The antenna has a radiator sized 0.07 of the wavelength and a compact matching system (resonator) sized 20x13x2 mm^3. The calculated efficiency has turned out to be **75% for HTSC materials and 14% for copper (at 77 K)**. O.Vendick, St.-Petersburg Electro-Tech. Institute.

6) **The electric field effect in multilayer "superconductor-insulator-metal"** (SIM) structures open up new prospects of investigating into physical properties of HTSC materials and provide the grounds for posing the question of HTSC field-effect transistor development. A production process has been worked out for multilayer structures where $SrTiO_3$, $PbTiO_3$ - $PbZrO_3$ and $SrTiO_3$- $BaTiO_3$ films are used as insulators (ferroelectrics). With ferroelectric 0.5 mm films of $PbZr_{0.75}Ti_{0.25}O_3$ solid solutions the dielectric constant (at 1 kHz) was found to be ~600, the loss tangent 0.02 and the remanent polarization was 24 $\mu C/cm^2$ at the cohercivity field of 80 kV/cm^2. V.Lemanov, St.-Petersburg Phys. Tech. Institute.

7) The manufacturing practice for **high-quality submicron Nb - AlO_x - Nb transitions** has been optimized. A production process of multilayer superconducting structures on the basis of such transitions has been developed which ensured the manufacturing of microcircuits with the spread in parameters below 7% for transitions sized 3x3 μm^2 and the level of integration 10^3 per chip.

Threshold parameters of one-quantum digital elements were experimentally analyzed. The number of "error-free switchings" was more than 10^{15} for the buffer cascade and not less than 10^{14} for the NOT element. V.Kosheletz, Inst. of Radio Electronics, Moscow.

Section 4: HIGH CURRENTS

Realization of high expectation of the Technical Revolution connected with the HTSC practical application are obviously dragged out by **the absence of large-scale production of long-lengh wires** and current-carrying elements on their basis. The difficulty in working out corresponding technological processes consists in the necessity of meeting (over the whole volume of HTSC wire) the three classical requirements of ensuring high current-carrying ability:

- no weak links between crystallites;
- favorable pinning structure; and
- formation of a crystallographic structure with well-expressed texture along the expected transport current direction.

A success in solving the problem is undoubtedly feasible only on the basis of a sufficiently deep insight into the nature of HTSC materials and its interconnection with the microstructure and phase composition of samples.

Thus, in Project headed by I.Voloshin, Energy Institute, Moscow most promising melt-textured HTSC samples with the critical current density of about 10^5 A/cm^2 were analyzed. Magnetic field and temperature dependencies of the critical current density were studied. The investigation was performed with **an original noncontact technique** worked out by the Project participants ensuring the variations of the magnetic domain structure of the indicating film contacting with the sample. A nontrivial result has been obtained, namely, the magnetic flux penetration in well-textured samples occurs through macroscopic strip of the scale of about 1 mm rather than via crystallite boundaries.

As to HTSC wires, the majority of the technology teams in Russia are successfully developing the "powder-in-tube" method which looks most promising for the moment. Current-carrying ability values (0 T, 77 K) at the level of 10^4 A/cm^2 for Bi-2223 based wire are quite common but the transition to greater lengths results in noticeable decreasing of the critical transport current. The most advanced, to my mind, are the works performed at the All-Russia Research Institute of Inorganic Materials, Moscow, head: A. Nikulin. The critical current density of their short-length (5 cm) Bi-2223 wires runs to 3.5×10^4 A/cm^2 in the self field and at 77 K featuring **high reproducibility** and relatively weak decreasing of current-carrying ability on the application of an external magnetic field.

Perspective and, by all means, **pioneer method of long-length high-current HTSC composite wire production** is a technology being jointly developed within the scope of Project headed by V.Kruglov by the researchers from the RRC "Kurchatov Institute", Moscow, and Moscow Institute of Steels and Alloys. The technology is based on the high temperature gas-dynamic extrusion of amorphous or crystallized semiproducts produced by pumping of the melt into silver containers followed by operations of drawing, rolling and thermal treatment, see Fig.

This process ensures a nearly theoretical density of the HTSC core, low contamination of crystallite boundaries, a possibility of introducing structure variations within a broad range and at any stage of the technological process and a multi-axial loading principle with one-shot extrusion deformation degrees up to 98%. In consequence it is possible to produce **long-length (up to 10 m) wire stretches** with a high degree of homogeneity along the whole length (as confirmed by weak smearing of the V vs I characteristics, not exceeding those of commercial niobium-titanium alloys) and with high transport properties yielding the critical current densities for Bi-2212

based compounds (4.2 K) of the order of 10^5 A/cm^2 and $7x10^4$ A/cm^2 in the fields of 5 T and 8 T, accordingly.

A research team from the Moscow State Technology University (head: Drs. O.Polushchenko) has produced bulky highly textured rods and plates based on the 1-2-3 compound with the critical current density above 10^4 A/cm^2 at the liquid nitrogen temperature and 1 T magnetic field. It allowed specialists from the Moscow Aviation Institute (head: L.Kovalev) to devise prototypes of a new face-type hysteresis motor (stature diameter: 60 mm; power: >10 W) and a synchronous jet-propulsion stepping motor with an external diameter of 108 mm.

Good progress in the development of a so-called "topological generator" has been made by a group headed by Yu.Baurov from the Central Science and Research Institute of Machine Building, Moscow. They designed a generator on the basis of bulk ceramics as well as films. In the produced prototype generator of this type sized 80 mm in diameter and 100 mm in length the current in the closed circuit was about 10 A at 77 K. The experience acquired in the course of tests allows one to hope that it is possible to design a high current (1,000 A) topological generator using the now available technology for HTSC elements manufacturing.

The Project headed by Eu.Krasnoperov, RRC "Kurchatov Institute", Moscow, envisages working out "hybrid" magnetic systems. Outer sections are superconducting and inner ones are resistive water-cooled. The total stationary field will be 30 T. An outer section is made of niobium-titanium wires and comprises 16 compounded modules. During the tests of a section the field in the center was 4.9 T which is 0.5 T higher than the calculated value. The water-cooled section consists of two "polyhelix"-type optimized windings connected in series. Their production has been launched. The contribution of the superconducting section into the total field will make 9-10 T and that of the water-cooled section will be 20 T.

The realization of this project (which is inhibited by serious financial difficulties) will provide a means of carrying out physical investigations in stationary magnetic fields up to 30 T. Evidently, it is of primary necessity for studying the properties of HTSC materials.

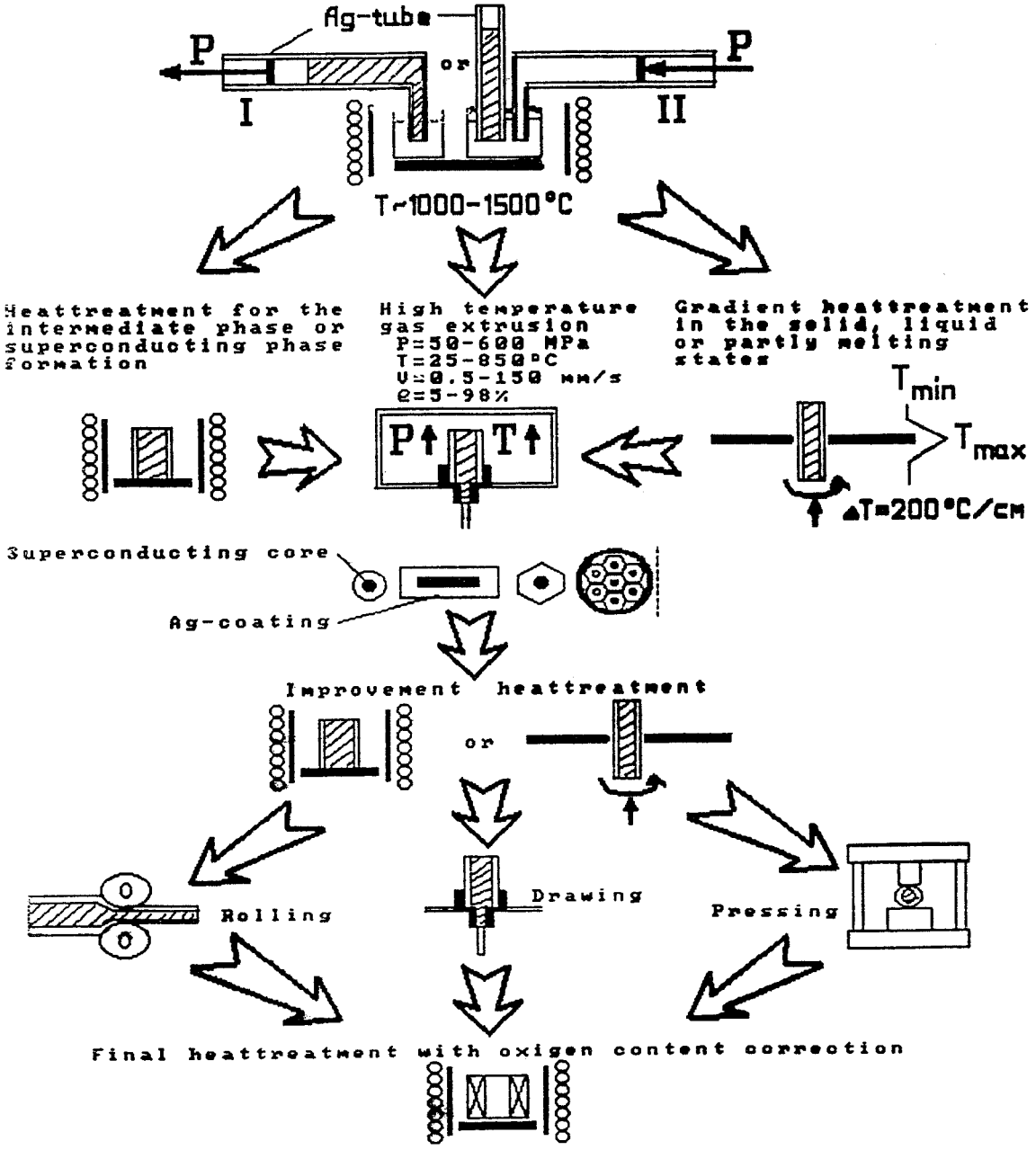

Figure 1.- NoveL method of the LongLength current carrying HTSC structures formation.

SINGLE SCAN
S5-76
313355
8 P.

PREPARATION, STRUCTURE AND SUPERCONDUCTIVITY OF HIGH-T_c COMPOUNDS

(Research of high temperature superconductors in Hungary)

I. Kirschner

Department for Low Temperature Physics, Eötvös University, Budapest, Hungary

Abstract

In this paper the main directions, methods and results of the investigation of high-T_c superconductors in Hungary are briefly summarized. The fundamental idea of this research is to study the effect of starting conditions on the microstructure of samples and the influence of the latter one on their superconducting parameters. The investigation concerning technical development is also mentioned.

Introduction

At the beginning of this century the fundamental gravitation experiments of Loránd Eötvös and his collaborators made the Hungarian physics to be well-known. Numerous famous results are connected to his name, namely the Eötvös-pendulum (which has an importance in the research of raw materials too), Eötvös-effect and Eötvös-law, etc.

Before the 2nd World War the physical investigation was concentrated in the universities and some big companies, dealing mainly with the applied research referring to the actual needs of the industry. In this way important results have been achieved in the field of research of metals (in particular of wolfram), noble alloys, and physical basis of the production of incandescent lamps and high-power electrical equipments.

Many Hungarian originated physicists and chemists left their native country and worked in the forefront of scientific research in different places of the world. Among them Jenő Wigner (nuclear physics), Ede Teller (nuclear physics), Miklós Kürti (low temperature physics), János Kemény (discovery of basic language of computers), László Tisza

(thermodynamics), Zoltán Bay (radar technology), Frigyes Bárány (vestibular system), Tódor Kármán (mechanics, who was the founder of Jet Propulsion Laboratory), Dénes Gábor (holography), Leó Szilárd (nuclear physics), György Békésy (research of hearing), János Neumann (mathematics), János Polányi (dynamics of chemical process), Kornél Lánczos (mathematical physics), György Hevesy (nuclear chemistry, isotope-traces), Albert Szent-Györgyi (biochemistry) and Bálint Telegdi (nuclear physics) are the most known. The excellent scientific results of Wigner, Gábor, Szent-Györgyi, Hevesy, Békésy, Bárány and Polányi were acknowledged by Nobel-prize.

During the years of fifties a new research and development system was established, having four sections, namely university departments, institutes of the academy of sciences, industrial research institutes and local research and development centers of different companies.

The physical research broadened significantly and the directions covered almost all of the main fields of physics, e.g. quantum-mechanics, solid state physics, thermodynamics, nuclear physics, optics, astrophysics, elementary particles, statistical physics, laser physics, relativity theory, etc.

Some groups were successful in different areas of physical research, namely in the investigation of cosmic rays, molecular spectroscopy, crystal growth, elementary particles, low energy nuclear physics, evolution of the world, magnetism, neutron physics, quantum chemistry, etc. having internationally respected results.

Activity and co-operation in high-T_c superconductivity

The solid state physics and materials science have a rather old tradition in Hungary, and numerous Hungarian research institutions (universities, academic institutes and industrial research centers) act in different fields of condensed matter physics. During this research, remarkable results obtained concerning metals, alloys, semiconductors, surfaces and technical application of the results of the fundamental study. This activity provided the basis of the research of low temperature phenomena, first of all superconductivity.

The main themes of our superconductivity research were the investigation of the magnetic properties of conventional superconductors, namely In-Bi, In-Tl, In-Pb, Sn-Bi, and Sn-Sb alloys, the study of compounds and alloys having an importance from the point of view of application, building magnets and small-scale cable sections, the investigation of the

pinning properties and the use of the irreversible thermodynamics to describe the features of superconductors.

In the last years, after the discovery of the high-temperature superconductivity, we turned mostly to the investigation of the phenomena of these new superconducting compounds.

The investigation of the high-temperature superconductivity was started in Hungary in January 1987, based on our former experiences obtained in the course of the research of the conventional superconductors, which began in 1963.

(1). In a small country, like Hungary, the co-operation plays a very important role in the research work, so we have organized a very wide cooperation inside and outside Hungary concerning this field of science. This contains the following institutions:

1. Eight laboratories of the Eötvös University, Budapest, (Department for Low Temperature Physics, Department of Atomic Physics, Department for General Chemistry, Department for Mineralogy, Laboratory for Nuclear Chemistry, Department for Petrology and Geochemistry, Laboratory for Surface Physics and Department for Analytical Chemistry),
2. Central Research Institute of Silicate Industry,
3. Five laboratories of the Budapest Technical University (Physical Institute, Reactor, Department of Electrical Machines, Institute of Mechanical Technology and Department of Electronics Technology),
4. Central Research Institute for Chemistry,
5. University of Debrecen (Institute for Experimental Physics),
6. Institute for Research of Metals,
7. Central Research Institute for Physics,
8. Research Institute of Electrical Industry,
9. EPOS-PVI Electrical Inc.,
10. University of Veszprém (Department of Silicate Chemistry),
11. Research Institute of Technical Physics,
12. National Bureau of Standards,
13. Nuclear Research Institute of the Hungarian Academy of Sciences,
14. Ministry of Industry (Ganz Electric, Budapest Iron and Steel Company, Kőbánya Porcelain Works, Microelectronics Ltd, Metalltech Ltd),
15. Committee of Technical Development;

16. Finland: Wihuri Physical Laboratory (University of Turku), Microelectronics Laboratory (University of Oulu),
17. Great Britain: Center for HTSC (Imperial College of Science and Technology, London), Department of Physics (Glasgow University),
18. Germany: Institut für Festkörperforschung (KFA, Jülich), Lehrstuhl für Tieftemperaturphysik (Humboldt University, Berlin), Forschungszentrum (Geesthacht), Hammelwerke Sensor GmbH (Scheweningen), Physikalisches Institut (University Erlangen-Nürnberg, Erlangen),
19. The Netherlands: Physics Department, (University of Amsterdam), Physical Institute (University of Nijmegen),
20. Russia: Institute for Physical Problems (Moscow), Institute of High Temperature Research (Moscow),
21. Austria: Physikalisches Institut (University of Vienna),
22. Egypt: Department for Physics (Ain Shams University, Cairo),
23. USA: Institute of Chemistry, Drexel University, Philadelphia, etc.

(2). We have developed a complex basis for preparation of samples, which included university laboratories, academic institutes, industrial research centers and local industrial research-development sections. The preparation work covers different profiles, containing different methods form the solid state reaction, through explosion procedure or screen printing, until laser ablation.

(3). In the frame of the above mentioned co-operation we have sent superconducting samples to Italy, Germany, England, The Netherlands, Russia, Austria for investigation and provided more, than 100 Hungarian schools with them giving the possibility for the demonstration of the impressive HTSC effects.

(4). A specific governmental financial support helped us to increase the level of investigation and made possible to carry out some experiments of that kind, which could not be done earlier due to the lack of certain up-to-date experimental equipments.

Research and results in the field of HTSC

The research performed in Hungary in this field is basically experimental, it has, however, some theoretical and application aspects, as well.

(1). The investigation can be treated as a complex one, because it concerns all of the main directions in question, namely the sample preparation, physical properties and possible technical applications.

(2). This study covers all of the known families of HTSC compounds. The properties of La-Ba-Cu-O, Y-Ba-Cu-O, Bi(Pb)-Sr-Ca-Cu-O, Tl-Ca-Ba-Cu-O and in the latest time Hg-Ba-Ca-Cu-O superconductors have been investigated. Different substitutions of ions and doping processes were also performed, which is demonstrated as follows: Sr → Ba, Eu or other RE → Y, Fe or Sn → Cu, F → O_2 and addition of Ag or LiF, in order to change the physical or mechanical parameters of the basic superconducting compounds.

(3). The bulk samples, thick films and thin layers are equally in our interest from the point of view of investigations.

(4). High-T_c superconductors, suitable to different specific purposes, (e.g. magnetic screening) were elaborated, as elastic foils, rods and filaments, using organic and inorganic filling materials.

(5). Certain improvements of the experimental technique were also performed concerning the measurement of thermoelectromotive force, critical currents, a.c. resistivity and susceptibility.

(6). During the different directions of investigation we used a rather wide spectrum of the research methods, namely:

1. SEM, 2. X-ray, 3. TEM (HRTEM, SAED), 4. micro-probe, 5. EDS, 6. EPMA, 7. STM, 8. TG, 9. DTA, 10. resistivity measurements, 11. susceptibility, 12. SQuID-technique, 13. ESR, 14. NMR, 15. thermodynamic cross-effect (TEMF, Hall), 16. magnetic (hysteresis), 17. dilatation, 18. SIMS, 19. detection of vortex movement, 20. ESCA, 21. Mössbauer-spectroscopy, etc.

(7). The applied methods provide scientific information on the physical properties of the samples, namely:

1. character of the superconducting transition (metallic, semiconducting, percolative), 2. sharpness of it, 3. effect of preparation (starting materials, their mixture, heat treatment), 4. temporal stability or instability (possible change in structural, electrical and magnetic properties), 5. effect of external circumstances, 6. quantity of superconducting material in specimens, 7. number, quality and share-rate of s.c. phases, 8. place and change of ions, 9. type of charge carriers, 10. degree of oxidation, 11. chemical co-ordination, 12. properties of surfaces and grains, 13. critical parameters (T_o, T_c T_d, H_{ci}, J_{ci}, ξ, λ, κ), 14. phonon-

electron coupling, 15. gap, 16. conclusion on the fundamental superconducting mechanisms, 17. data for unit cells and their deformation, 18. anisotropy, 19. mechanical properties, dilatation, elasticity, 20. influence of thermal cycling, 21. corrosion, degradation, etc.

(8). Due to the limited length of this paper only a few concrete results of the Hungarian HTS-research can be enumerated to demonstrate the scope of it:

1. Just from the beginning we made the electrical and magnetic measurements together to obtain a good chance to evaluate the Meissner's state volume of samples.
2. We have investigated in detail some important questions of high-T_c compounds, namely the preparative chemistry consequences on Y-Ba-Cu-O superconductors, the possible role of percolation effects in establishment of superconductivity, characteristic parameters of Tl-Ca-Ba-Cu-O compounds based on a very wide spectrum of preparation methods, surface structure of different samples by STM method, effect of thermo-mechanical and water corrosion, proximity effect, complex study of Bi-based samples, effect of neutron irradiation, diamagnetism above T_c, effect of particle size on the mechanism of the development of HTSC, improvement of the plastic properties of samples, etc.
3. Similarly to other laboratories, we also observed superconductivity at higher, than usual T_c in an Y-based, temporally unstable specimen in April, 1987, but in contrast with other results, the value of its T_c was only 105 K.
4. The elaboration of superconducting ceramic magnets with a new energy feeding, small-scale electrical rotating machines, cryogenic liquid level sensors, magnetic field detectors and magnetically screening elastic foils, rods and thin filaments can be mentioned among our works for the purpose of technical development.
5. Some Hungarian researchers were dealing with the study and application of Josephson's tunnelling and with the high-T_c SQuID experiment having some new and valuable information on these questions and on their application in measuring technique.
6. The employment of the Mössbauer-spectroscopy to find out the details of structure and some fine effects represents an important contribution to the HTSC-research in Hungary. It was very wide, and based on replacing sites by ^{151}Eu, ^{119}Sn, ^{57}Fe and ^{57}Co nuclides in order to get information about site preference, structural changes, temporal instability and change of the phonon properties.
7. Hungarian researchers have attained remarkable results in the investigation of fullerenes, certain part of those can be superconducting. If the chains of C60 molecules contain some alkaline metals (e.g. K, or Rb), they can develop in the form of filaments and produce

electrically conducting polymer-crystals, which show a metallic behaviour. This research is also accomplished in an international (American and Swiss) co-operation. The structure of fullerenes of different kinds of conductivity are under investigation in Hungary, using unlike methods, e.g. ESR-, IR-, and Mössbauer-spectroscopy. These investigations include alkaline fullerenes, fullerene polymers and ligandum-containing fullerenes as well.

8. Optically induced changes of the magnetic properties, created by laser beam in La-Ba-Cu-O superconductors have been observed. According to our investigation, the light-induced change of the magnetic moment strongly depends on the temperature at low temperatures. The results obtained in the magnetic field of 1-26 Oe suggest, that the observed effects have contributions from the weakening Josephson's junctions under illumination and from the additional part of the optically induced flux creep, which depends on the applied magnetic field.
9. In order to examine the fine details of superconducting-normal or normal-superconducting transition, a new, so-called thermometric mapping method was elaborated. By the essence of this method, the samples are submitted to a large and variable temperature gradient, which broadens significantly the transition to reveal its gradual nature. This procedure is in a strong contrast with the conventional electrical and magnetic measuring practice of superconductivity, where a homogeneous temperature distribution is used generally to avoid the uncertainty of results. The method is sensitive enough to detect not only the fine structure of the transition, or to select the unlike properties of different specimens, but to trace the change of the features of a given sample too.

(9). Comparing to the international research of HTSCs, we investigated firstly some important questions of this field, which were as follows:

1. building high-T_c superconducting ceramic magnets, 2. synthesis and application of a new precursor $Ba_2Cu_3O_5$, 3. investigation of the corrosion effects, 4. elaboration of the thermometric mapping method, 5. Mössbauer-study of Tl-based superconductors, 6. cryogenic liquid level sensor based on TEMF, 7. a new method for preparing Y-based superconductors, 8. observation of the fine structure of S-N or N-S transition, and 9. elaboration of a microwave magnetic field detector. At the same time Hungarians were among the first groups to measure TEMF, to develop ceramic HTSCs workable by machine-tool, to elaborate elastic foils, rods and filaments and to build small electrical rotating HTSC machines.

Publications

In the course of investigation of high-T_c superconductors we have reached internationally respected results, published over 150 scientific papers, elaborated some patents and introduced the fundamental phenomena of high-temperature superconductivity into the education of universities and secondary schools. Among them, we have the exact number of the publications of one of the Hungarian high-T_c laboratories. This is the Department for Low Temperature Physics, Eötvös University, which published 75 scientific papers, 3 patents and 15 studies and dissertations on the methods, results and applications between 1987 and 1993.

Conclusions

On the basis of the facts analyzed in this paper, certain conclusions can be drawn, as follows:

1. A small country can also be effective in the field of a given branch of scientific research, if the aim is chosen right, the powers are concentrated rationally and the co-operations are organized operatively [1].

2. Hungarian scientists attained significant results in different areas of high-T_c superconductivity and contributed successfully to the world-wide research, because they utilized effectually the internal and the possibilities of international co-operations [2].

References

1. I. Kirschner, J. Bánkuti, M. Gál and K. Torkos, Phys. Rev. **B36.** 2313. 1987.
2. I. Kirschner, S. Leppävuori, R. Laiho, A.D. Caplin, T. Kármán, E. Lähderanta, G. Zsolt, A. Uusimäki, J. Laverty, T. Porjesz, I. Halász and Gy. Kovács, Zeitschr. Phys. **B78.** 381. 1990.

SINGLE SCAN
56-76
313 385

HIGH-T_c SUPERCONDUCTORS: TECHNICAL AND COMMERCIAL CHALLENGE

I. Kirschner[1], E. Horváth[2], I. Vajda[3], L. Bencze[4] and N. Göbl[4]

(1) Department for Low Temperature Physics, Eötvös University, Budapest, Hungary
(2) EPOS-PVI, Inc., Budapest, Hungary
(3) Department of Electrical Machines, Technical University, Budapest, Hungary
(4) Research Institute for Electrical Industry, Budapest, Hungary

Abstract

Some basic questions of the way, which leads from the discovery of high-T_c superconductors to their applications is surveyed. The influence of high-T_c superconducting technology on the industrial and social development is also briefly analysed.

General

The main problems are how the results of the scientific research can be transferred into technology and in what extent this process can be useful for the society.

Postulation: Superconductivity, as a phenomenon of extremely or ideally lossless state should revolutionize not only the electrical or electronical industry, but through them it should change various segments or sections of technology and the life style of the society too.

The fact: There are certain obstacles (requirement of cooling, critical parameters themselves, a.c. losses, etc.) those make difficult to introduce the physical findings, results and developments into technology.

Disappointments: Some potential users, even professionals (engineers, managers, etc.) are often deeply disappointed when they are aware of the difficulties.

Financing : Both of basic and technical researches require sponsors who are able and eager to invest money into a scientific program without the requirement of making profit within a short term. Governments and companies of developed countries wish to sponsor these themes, but in an other part of countries there is a lack of money to support the superconductivity research.

Usefulness: The new technology induced by the research of superconductivity results in new and efficient modes of production. This leads to bring forth new values for the society.

Superconducting products

Fifty years were necessary after the discovery of conventional superconductivity [1] until the first attempt [2] to elaborate some magnetic application of this phenomenon. The main difficulty is represented by complicated and expensive liquid helium technique which strongly limits the spread of low-temperature superconductors.

A qualitatively new situation appeared by the discovery of high-temperature superconductivity [3], for which the simple and cheap cooling provided by liquid nitrogen is sufficient. Until this date five groups of oxide ceramics can be taken into consideration from the point of view of technical employment, namely La-Ba-Cu-O, Y-Ba-Cu-O, Bi(Pb)-Sr-Ca-Cu-O, Tl-Ca-Ba-Cu-O and Hg-Ba-Ca-Cu-O families having intervals of critical temperature T_c of 32-40 K, 80-92 K, 85-110 K, 60-125 K and 90-150 K, respectively. As far as the other two main parameters are concerned, the upper critical magnetic field H_{c2} falls into interval of 50-200 T, while the transport critical current density J_c extremely depends on the morphological character of the samples [4], having values of 100-300 A/cm^2 for bulk materials, 10^3-10^5 A/cm^2 for melt-textured thick films and 10^5-10^6 A/cm^2 for high quality thin layers.

The reliable and controlled best values of J_c for 100-200 m long wires and tapes are 50000-100000 A/cm^2 for Y-based, 50000-150000 A/cm^2 for Bi-based materials, while 10000-20000 A/cm^2 can be reached for very pure Tl-based short samples. Since some of these superconductors can work in a very high (5-25 T) magnetic field, the possibility of their use for different electrotechnical purposes can be taken to be acceptable.

The problem of rigid and brittle properties of these ceramics and the question of long time stability seems to be soluble.

The most probable applications of these materials concern not only the electrical industry, but the electronics, signal processing, computer technique and informatics too, as is listed in the followings [5]:

1. building magnets and magnetic shieldings,
2. generators, electrical transport lines, magnetic energy storage,

3. fault current limiters,
4. heavy-duty bearings,
5. magnetically levitated machines,
6. sensors for temperature, pressure, magnetic field, frequency, voltage, current, liquid level, radiation, etc.,
7. signal detectors and processors,
8. electronical chips,
9. high frequency receivers, mixers and antennas,
10. fast computers,
11. bolometers and nuclear particle detectors, etc.

New developments: Proposals and experiments regarding technical applications of high-T_c superconductors should compete with existing and reliable products. The new products should have some advantages to substitute the present ones.

Most successful applications have been developed in those fields of technology, where there are no real competitive counterparts.

Commercial challenge

The commercial challenge arises when superconducting products are at the society's disposal in an appropriate quality and quantity and they should be distributed among the demanding institutions and persons by selling and buying. Nowadays we are far from this point, but the society must be prepared to this one, because the new materials, products, instruments and equipments will change the style and quality of the life.

Superconductivity and society

How to influence the society in order to accept easier the novel and unique results of the science and technology?

We think there is a lack of a thorough analysis of economic and social effects of the technology of superconductivity. This analysis must be accomplished by ourselves and its results should be submitted to the decision-making persons.

It is obvious that we are responsible to introduce the teaching of basic and applied

aspects of superconductivity into the education of the universities and secondary schools or to improve their education. Numerous projects aimed at the application of superconductivity are planned to be partly or fully completed by the end of this century. By this time the students who will study the superconductivity in the next years will come to work into the industry, economy, etc., and perhaps they would be more susceptible to new technologies, like superconductivity.

References

1. K. H. Onnes, Comm. Phys. Lab. Univ. Leiden N° **119**. 122. 1911.
2. J. E. Kunzler, E. Buehler, F. S. L. Hsu and J. H. Wernich, Phys. Rev. Lett. **6**. 89. 1961.
3. J. G. Bednorz and K. A. Müller, Zeit. Phys. **B64**. 189. 1986.
4. I. Kirschner, Appl. Supercond. **1**. 1785. 1993.
5. I. Kirschner, S. Leppävuori, T. Porjesz, A. Uusimäki and T. Kokkomäki, Sensors and Actuators **A41**. 58. 1994.

Stock Sam
5-4-96
313427

Technical and Commercial Challenges in High Tc SQUIDs and Their Industrial Applications

Roundtable Discussion Session
The Fourth World Congress on Superconductivity

D. F. Lu
Midwest Superconductivity Inc.
Lawrence, KS 66049

A SQUID is the most sensitive device for measuring changes in magnetic flux. Since its discovery in the sixties, scientists have made consistent efforts to apply SQUIDs to various applications. Instruments that are the most sensitive in their respective categories have been built, such as SQUID DC susceptometer that is now manufactured by Quantum Design, pico-voltmeter which could measure 10^{-14} volts, and gravitational wave detectors. One of the most successful applications of SQUIDs is in magnetoencephalography, a non-invasive technique for investigating neuronal activity in the living human brain. This technique employs a multi-channel SQUID magnetometer that maps the weak magnetic field generated by small current when information is processed in brain, and its performance is marvelous.

All the wonders of SQUIDs have been realized using low temperature superconducting (LTS) SQUIDs that must be cooled using liquid helium. Since the discovery of high temperature superconductors in 1986, people have long expected to replace LTS SQUIDs with their high Tc counterparts in some applications, or to find new applications for high temperature superconducting (HTS) SQUIDs. A HTS SQUID is capable of working at liquid nitrogen temperature, which is far more advantageous to liquid helium in terms of cost and in terms of possibility for field applications. Many efforts have been made to take advantage of HTS SQUIDs. Various types of HTS thin film or bulk SQUID magnetometers and gradiometers have been studied. The best HTS SQUID is very competitive with its LTS counterpart in properties and performance. However, there has not been any real commercial application of HTS SQUIDs yet. Despite the promising features of HTS SQUIDs, there are still many challenges ahead before HTS SQUIDs can be widely used in commercial products. In this short paper, we would like to briefly discuss some of the issues that people need to be concerned with when trying to use a HTS SQUID in a particular application.

First of all, people have to ask themselves in what type of applications that a HTS SQUID has advantages over other techniques. Although a SQUID device is more sensitive, the cost involved is generally higher and the requirement of knowledge to operate a SQUID device is more stringent. Therefore, people need to determine for themselves how competitive a SQUID device is compared with other techniques. How much better is it to use a HTS SQUID in a particular application than those currently used systems? How much improvement can we expect over other techniques if we use a HTS SQUID in that application? Is the improvement substantial that it can be easily accepted and adopted by end users? As Weinstock always points out, one should not use a SQUID-based instrument when a simpler technology will suffice [1].

Suppose that a SQUID is a necessity for an application, should a HTS SQUID be used? For instance, can a HTS SQUID replace a LTS SQUID in susceptometers, gravitational wave detectors without or with only little compromise? Compared with LTS SQUIDs, HTS SQUIDs have only one big advantage. That is, it has a higher transition temperature and it can work at liquid nitrogen temperature instead of liquid helium temperature. This is much preferred economically, and it does open doors to a lot of possible uses of HTS SQUIDs. However, as pointed out by John Clark, a SQUID working at this temperature will never achieve as good a resolution as can their counterparts working in liquid helium [2].

At the same time, since high temperature superconductors are ceramics, they are much more difficult to process than low temperature superconductors. A superconducting transformer made of high Tc wires similar to low Tc transformers, which helps to place SQUIDs in a magnetically shielded environment, has not been realized. A HTS SQUID gradiometer cannot be made as symmetric as a LTS SQUID gradiometer, which achieves one part per million in symmetry. Thus, it will be very hard for HTS SQUIDs to replace LTS SQUIDs for sensitive measurements.

Nevertheless, we need to realize that there are still many other applications in which the sensitivities of HTS SQUIDs will suffice. For these applications, we must take full advantages of high transition temperatures of HTS SQUIDs. If they are combined with small size cryocoolers, portable HTS SQUID devices may become possible for field and industrial applications. This cannot be accomplished with LTS SQUIDs.

Of course, to apply HTS SQUIDs for field or industrial applications, many practical matters need to be taken care of. The immediate concern for field applications is that a SQUID is subject to environmental noises, such as interference from powerline, machinery, electronic equipment, and etc. It is not like those biomagnetic instruments and those scientific instruments where almost everything, such as SQUID sensors, superconducting transformers, and even the sample, is enclosed in a magnetic shielded room. Therefore the field sensed by the SQUID sensors is very small, and is all the information people want. Everything detected is useful. For field or industrial applications, there is no shielded room to use. Otherwise it cannot be portable or the cost involved is too much. Without any shielding, the SQUID is exposed to a large environmental field or interference. The interference in general is alternating fields which render a SQUID magnetometer simply not usable since most of SQUID electronics has a range of only $\pm 500\Phi_0$, while the flux produced by the interference may be hundreds times larger. The SQUID electronics just has to reset itself too frequently to be usable. HTS SQUID gradiometers may be used. However, they are also influenced by the interference due to limited symmetry. This difficulty has to be overcome for HTS SQUIDs to have a big market. Techniques may involve redesign or modification of electronics.

The large environmental noise also affects the properties of a SQUID itself. In almost all the LTS SQUID applications, the SQUID is placed in a shielded chamber and the surrounding field is tiny. The measured signal is transformed by a superconducting transformer with the pick-up coil placed outside the shielded chamber. But for high temperature superconductors, such a flexible superconducting transformer cannot be fabricated yet. A HTS SQUID has to be exposed to external field, even with thin film transformers. When it is exposed, many of its properties may change depending on the magnitude of the field. For instance, the critical current in the junction may vary with the applied field, which will certainly affect the SQUID properties. At the same time, for high temperature superconductors, flux trapping may be quite important in large field, thus causing large noises.

It is usually expected that a device with a HTS SQUID performs better than those without SQUIDs in many applications. It should be able to do what the current systems cannot do. It should be able to detect even smaller signals. While talking about possible benefits they may obtain with a SQUID, people often tend to omit the fact that the signal to noise ratio is reduced for small signals. Although the noise may be smaller than currently detectable signal, will it overwhelm the expected smaller signal detectable only by SQUIDs? If it does, the sensitivity of SQUIDs cannot be fully utilized. People need to find a way to reduce the noise further to improve the signal to noise ratio. I will take nondestructive testing of metal as an example. The conventional eddy current method is not able to detect small cracks at a depth greater than 0.5 inches. We are working on using a HTS SQUID as a sensor to replace the coil sensor in conventional eddy current method for detection of small cracks at large depth. Since our target crack (hereafter the target) is farther from the coil than the crack (hereafter the crack) that can be detected using conventional eddy current method, the current density induced at the target is smaller than that at the crack. Similarly, since the target is also farther from the sensor than the crack, the field change

generated by the target decays faster than by the crack. Because of these factors, the signal from the target is much smaller. However, the noise level remains the same. The effect of change in lift-off, the distance between the coil or sensor and the sample, is still large with the eddy current method. If such a change in lift-off cannot be controlled, it will generate a noise that may be much greater than the signal generated by the target. Useful signal will be buried in the noise. This may be more important practically than the noise of a SQUID system.

There are of course many other things people need to consider and discuss for specific applications. There is a bright future for SQUID applications in industry, there are also a lot of things to be done before it becomes a reality. Overall, researchers have to study the particular applications they are interested in, and make all necessary adjustments to build usable devices.

I sincerely thank the organizing committee for inviting me to speak at the "Roundtable Discussion Session." I am also grateful to Prof. K. W. Wong for valuable suggestions. Finally, I would like to thank Midwest Superconductivity Inc. for the support.

References:

1. H. Weinstock, *Physica C* **209**, 269 (1993)
   H. Weinstock, *IEEE Trans. Mag.* **27** 3221 (1991)
2. J. Clarke, *Scientific American*, August Issue, p. 46 (1994)

Accelerator Technology

Chair: Dr. Siegfried Wolff

Page intentionally left blank

THE LHC MAGNET SYSTEM AND ITS STATUS OF DEVELOPMENT

Maurizio BONA, Romeo PERIN, Jos VLOGAERT
CERN, CH-1211 Geneva 23 Switzerland

S8-76
3/2.8.90
10 P. 313482

Abstract
CERN is preparing for the construction of a new high energy accelerator /collider, the Large Hadron Collider (LHC). This new facility will mainly consist of two superconducting magnetic beam channels, 27 km long, to be installed in the existing LEP tunnel.
The magnetic system comprises about 1200 twin-aperture dipoles, 13.145 m long, with an operational field of 8.65 T, about 600 quadrupoles, 3 m long, and a very large number of other superconducting magnetic components.
A general description of the system is given together with the main features of the design of the regular lattice magnets. The paper also describes the present state of the magnet R & D programme. Results from short model work, as well as from full scale prototypes will be presented, including the recently tested 10 m long full-scale prototype dipole manufactured in industry.

1. Basic choices and main constraints of the LHC Collider

The new machine, a high-energy accelerator collider, consists essentially of a double ring of high-field superconducting magnets installed, together with the other machine components, in the same 27 km long underground tunnel, which houses the existing LEP collider [1]. Particles circulating in counter sense in the rings can be brought to collide in intersecting points.
The main performance parameters of the LHC for proton-proton and for Pb ion collisions are given in Table 1.
As the circumference of the LHC is fixed by the LEP tunnel, and the available cross-sectional space is limited, there has been from the start a quest for compact magnets operating at the strongest possible field to reach the highest collision energies. The dimensions of single magnets operating at the projected field level exclude the possibility to install two separate magnetic rings. This constraint has led to the development of the two-in-one concept in which two sets of magnetic excitation windings are placed in a common yoke and cryostat assembly, leading to smaller cross-sectional dimensions and to a more economic solution [2].
It was also decided that, for the LHC, coils wound from NbTi alloy operating at superfluid helium temperatures will be used.

	C.m. energy for B = 8.65 T [TeV]	No. of bunches	Particles per beam	Luminosity [cm^{-2} s^{-1}]
pp	14	2835	$4.7\ 10^{14}$	10^{34}
Pb ions	1150	496	$4.7\ 10^{10}$	$1.8\ 10^{27}$

Table 1: Main parameters of the LHC [1]

2. The LHC main magnet system

About 24 km of the LHC ring will be occupied by superconducting magnets of various types. The long arcs, covering approximately 20 km of the circumference are composed of "standard cells", a bending focusing configuration which is periodically repeated 192 times around the ring. The magnet system for the LHC has been described extensively elsewhere [14, 15].
One half of an arc cell has a length of 51 m and contains three 13.145 m long bending magnets and a 6.5 m long short straight section. In the straight section are installed: the 3.05 m main quadrupole, a beam position monitor and two corrector magnets, one with

combined dipole/sextupole windings and the other one with tuning quadrupole and octupole windings. Spool pieces containing sextupole and decapole correctors are attached to each main dipole to correct the field errors of these magnets.
Dipoles and main quadrupoles of the two rings are combined into "two-in-one" units, each pair having a common yoke and cryostat. In the present design multipole correctors are assembled concentrically on a common beam pipe.
In addition to the regular arcs, there are other magnets in the dispersion suppressor section, and on either side of each crossing point.Table 2 shows the types and numbers of superconducting magnets.
The LHC magnets will be one of the most massive applications of superconductivity. The quantity of conductor will be about 1400 t of which ~ 400 t will be NbTi alloy. The mass to be kept at 1.8 K temperature will be about 30'000 t distributed over a 27 km circumference.

2.1 Main dipoles

The design of the dipoles is made to meet the following requirements:
- Operational field: 8.65 T.
- Magnetic length: 13.145 m.
- Coil inner diameter: 56 mm.
- Distance between the axes of the apertures: 180 mm.
- Overall diameter of cold mass: ≤ 580 mm.

The resulting main parameters are listed in Table 3.
The coils are formed of two layers made with keystoned cables of the same width but of different thickness, resulting from the wanted grading of current density for optimum use of the superconducting material. The proposed filament size allows the fabrication of superconducting wires by single stacking process. The persistent current sextupole components (defined as $\Delta B/B$ at a radius of 10 mm) at injection field (0.56 T) are -3.56×10^{-4} and 0.18×10^{-4} respectively for these filament diameters.Table 4 shows the dipole strand and cable characteristics.

Type	Nominal strength	Magnetic length (m)	Number
Regular lattice			
Main dipoles	$B_0 = 8.65$ T	13.145	1280
Main quadrupoles	G = 220 T/m	~3.05	376
Tuning quadrupoles	G = 120 T/m		
+ octupoles	$B^{III} = 1 \times 10^5$ T/m3	0.72	768
Combined correctors			
Dipole	B = 1.5 T		
6-pole	$B^{II} = 3000$ T/m^2	1.0	768
Sextupole correctors	$B^{II} = 5700$ T/m^2	~0.10	1280
Decapole correctors	$B^{IV} = 4.6 \times 10^7$ T/m^4	~ 0.10	1280
Interaction regions			
Twin-aperture quads	G = 220 T/m	3.7 to 8.0	130
Single-aperture quads	G = 225 T/m	6.9	24
Separation dipoles	$B_0 = 5.2$ T	9.0	6

Table 2: Type and number of superconducting magnets

2.2 Lattice Main Quadrupoles

The main quadrupoles are designed to provide a 220 T/m field gradient over a magnetic length of 3.01 m, on the basis of the two-in-one configuration with Ø 56 mm coil aperture and distance between aperture axes of 180 mm.

The main parameters and the cable characteristics are listed in Tables 5.and 6. Their constructional features are very similar to that of the already built prototypes. The two layer

coils will be wound from the same superconducting cable in the double pancake style. This technique avoids the inter-layer splices which, being numerous in the quadrupole, would be a significant load to the cryogenic system.

Operational field	8.65	T
Coil aperture	56	mm
Magnetic length	13.145	m
Operating current	12 000	A
Operating temperature	1.9	K
Coil turns per beam channel		
inner shell	30	
outer shell	52	
Distance between aperture axes	180	mm
Outer diameter of cold mass	560	mm
Overall length of cold mass	14085	mm
Outer diameter of cryostat	980	mm
Overall mass of cryomagnet	29	t
Stored energy for both channels	7.2	MJ
Self-inductance for both channels	110	mH
Resultant of e-magn. forces in the 1st coil quadrant ΣFx (1.80 MN/m)	23.7	MN
inner layer ΣFy (- 0.15 MN/m)	- 2.0	MN
outer layer ΣFy (- 0.62 MN/m	- 8.2	MN
Axial e-magn. force on magnet ends	0.55	MN

Table 3: Dipole parameters

	Inner Layer	Outer Layer
Strand		
Diameter (mm)	1.065	0.825
Cu/Sc ratio	1.6	1.9
Filament size (mm)	7	6
Twist pitch (mm)	25	25
Critical current (A)		
10 T, 1.9 K/9 T, 1.9 K	$\geq$ 510	$\geq$ 370
Cable		
Number of strands	28	36
Cable dimension		
width (mm)	15.0	15.0
thin/thick edge (mm)	1.72/2.06	1.34/1.60
Transposition pitch (mm)	110	100
Critical current (A)		
10 T, 1.9 K/9 T, 1.9 K	$\geq$ 13750	$\geq$ 12880

Table 4: Dipole strand and cable characteristics

2.3. Insertion Magnets

There are a total of 166 special quadrupoles in the LHC insertions and straight sections differing in type, length and integrated gradient. Of this total, 114 magnets are of the lattice quadrupole type having the same cross-section but with three different lengths. The other

ones are special magnets, based on a 70 mm aperture coil which is being developed for the low-beta quadrupoles. In the experimental insertions, these are single aperture units, while for other insertions a two-in-one version is being designed, which may, however, operate at 4.5 K.

Operational field gradient	220	T/m
Coil aperture	56	mm
Magnetic length	3.01	m
Operating current	11470	A
Operating temperature	1.9	K
Turns per coil		
inner layer	4+6	
outer layer	10	
Distance between aperture axes	180	mm
Yoke, outer diameter	444	mm
Self-inductance (both apertures)	8.8	mH
Stored energy (both apertures)	580	kJ

Table 5: Main parameters of LHC lattice quadrupole magnets

Strand diameter (mm)	0.825
Number of strands	28
Cable dimensions	
width (mm)	11.60
thin/thick edge (mm)	1.348/1.60
Transposition pitch (mm)	95
Critical current at 9 T, 1.9 K (A)	≥ 10060

Table 6: Characteristics of the cable for the quadrupoles

The low-beta quadrupoles are single-bore units, 6.1 and 6.9 m long. The LHC performance depends critically on their field quality, especially on the higher order random multipole errors at low field. In order to obtain this field quality and to provide additional space for the cone of secondary particles emanating from the collisions, a novel design based on a graded coil with an aperture of 70 mm [4], wound from NbTi keystoned cables has been proposed. The design gradient of the magnet is 250 T/m for an excitation current of 5200 A. The design concept is presently being verified on a 1.3 m model magnet which is being developed in collaboration with an industrial firm.

2.4 Other Magnets

The strengths of all other magnets, i.e. tuning quadrupoles and octupoles, sextupoles and correction dipole, sextupole and decapole corrector spools are lower than those of the previous design for which prototypes have been successfully built and tested or are in the construction phase. Therefore the further R & D work on them will aim at simpler and more economical solutions.

3. Status of the LHC magnet development

The programme was mainly focused on the standard cell components and in particular on the dipoles, but included study and construction of several other magnets and items.

3.1 Quadrupoles

Two full size quadrupole magnets of final aperture (56 mm) and length (3.05 m) have been designed and built by CEA-Saclay, using s.c. cables and structural parts made in industry. Their design and construction are described in [10].
These magnets have undergone tests at 1.9 K and magnetic measurements at CEA-Saclay by the end of 1993. Both prototypes have reached the design current, the first magnet after one quench, the second one after three quenches.
After testing, the first prototype has been delivered to CERN where it is presently being installed into a "short straight section", which is an assembly of quadrupoles, sextupoles and all other types of correction magnets. This will be the first element to form the test string (one half standard cell) of the LHC which is expected to be ready for testing by end 1994.
The collaboration between CERN and CEA-Saclay has permitted to develop a set of tooling in view of the mass production to be performed in industry.

3.2 Dipoles

The R & D effort covers:

- Superconducting cables.
- Short single-aperture and twin-aperture models (~ 1.3 m long).
- Long twin-aperture prototypes (~ 10 m long).

3.2.1 Superconducting cables

Twenty-four kilometres of cable for the inner coil shell made of 26, Ø 1.29 mm strands, and 42 kilometres of cable for the outer coil shell, made of 40, Ø 0.84 mm strands, have been developed and produced by the five European manufacturers and at present satisfy all main technical requirements. The current densities in the non-copper part of the strand cross-section, taken from the finished cables at the 3 σ limit in the distribution curve of production, are 980 A/mm^2 at 8 T, 4.2 K, for the inner layer and 2000 A/mm^2 at 6 T, 4.2 K, for the outer layer. The results of the models show that the short sample quenching field of the dipole (B_{SS}) is close (within ~ 2%) to the cable short sample limit determined from strands extracted from the cables.
The total quantity produced, 14 t, is a significant amount and gives confidence that the required quality can be maintained in mass production.

3.2.2 Model magnets

A number of models of the main dipoles have been made and successfully tested [5, 6, 7]. Two magnets were built in Japan by KEK in collaboration with industrial companies. All other magnets were entirely built by European companies except one which was assembled at CERN using industry made coils and other components.
At 4.3 K, the conductor short sample limit of this magnet was attained at the second quench and no retraining occurred after thermal cycles.
At 2 K the magnet had the first quench above 9 T central field, reached 9.5 T in five quenches and finally attained the record field of 10.5 T. After thermal cycles to room temperature all quenches were above 9.75 T.

3.2.3 Ten metre long magnets

A magnet, named TAP, with a CERN twin structure but coils identical to those of the HERA dipole (75 mm aperture) was built in industry and successfully tested at CEA-Saclay at the nominal temperature of 1.9 K at which the conductor short sample limit of 8.3 T was reached [8].

Subsequently, the construction of seven higher field (cable width 17 mm), 10 m long magnets was launched in four firms or consortia. All these magnets have the same type of coils, but three slightly different mechanical structures [15].
The present status of manufacturing/testing of these higher field prototypes, referred to as MBP, is well advanced. The first one,named MBP/A #1 (CERN-INFN 1) and funded by INFN (the Italian "Istituto Nazionale di Fisica Nucleare"), has satisfactorily passed a thorough campaign of tests and measurements , and is now ready for installation in the test string [13, 15]. The next chapter will deal with this magnet. The second prototype MBP/A #2 (CERN-INFN 2) is now being tested at CERN.

4. The first tested full scale dipole prototype

4.1 General

In the present chapter a brief description is given of the main design and manufacturing aspects of the first full scale prototype MBP/A #1.
A collaboration on applied superconductivity set up between CERN and INFN in the second part of the eighties, has permitted to launch the construction of the first two full scale prototypes about 8 months in advance with respect to the CERN self-financed magnets. INFN placed their orders for the manufacture of the various components with Italian industry. The overall technical responsibility for the these prototypes remained with CERN. As already explained in [14, 15], it should be stressed that this R&D program was the first attempt done by CERN to develop full length prototypes directly in Industry (after the positive experience with short models), without passing through a phase of in-house development followed by a technology transfer.

4.2 Technological development

At the time when the programme was launched, in spring 1990, the only results available at CERN were those of the two single-aperture 1 m long models referred to as 8TM1 and 8TM2 made with HERA type strand. The twin-aperture models (MTA1), were the first attempt to explore the two-in-one structure; they have been tested in latespring-summer 1991. Development of the TAP magnet, which permitted to assess the problems related to a 10 m long magnet, although at lower field and with larger aperture, was still going on; this magnet was tested at end 1991 - beginning 1992.
The above facts clearly indicate the difficulty of carrying out the construction of these prototypes without disposing of the results of the previous steps of the R&D programme. This was particularly true for the first full scale magnet, the MBP/A #1 prototype whose design evolved from the initial concept to the final one passing through a number of modifications suggested by the results of intermediate phases [12]. Fig. 1 shows the final cross-section of the magnet.

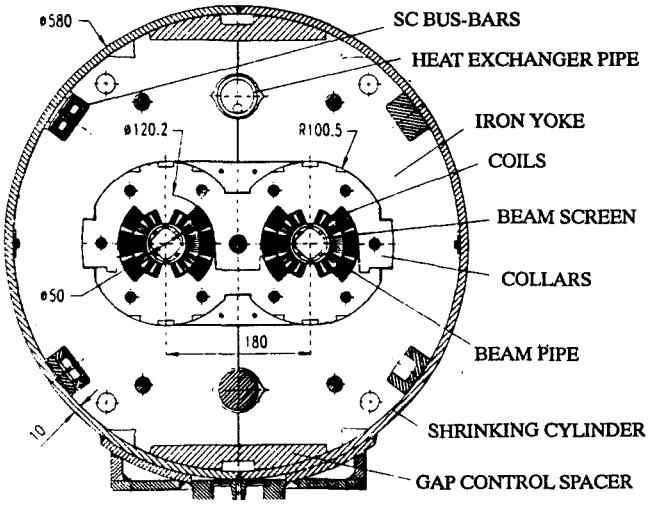

Fig. 1. Final cross-section of the first full scale prototype MBP/A #1 (CERN-INFN 1)

4.3 From design to fabrication

The design principle has already been described in [9, 11]. It is largely based on the kinematics of the structure during the cool-down from room temperature to the operating temperature of 1.9 K. The structural design calculations [11] were therefore aiming at the definition of a cross-section which would behave as expected. Detailed design analysis showed that very tight tolerances were required in the fabrication of coils and of the other magnet components. This has required strict control of the manufacturing techniques, both at the level of fabrication of the magnet itself and of the procurement of parts with the sub-contractors. A typical tolerance for the main parts like coils, collars and yoke laminations is of the order of a few tens of μm.

The collars and yoke laminations, made respectively of Al alloy and of soft steel, were obtained by fine blanking which required development of special tools and punching techniques to cope with the characteristics of the materials.

To optimize coil production and the so-called "coil collaring"(i.e. clamping the coils with their structural supports), a complete dummy coil-collar assembly was fabricated. This allowed to set-up the main parameters for the coil winding, coil curing and elastic modulus measurement operations. The main new difficulties related to these operations reside in the fact that the cables were much stiffer compared to previously made magnets and that the aperture diameter was only 50 mm. While winding and curing the first layer (fabricated with dummy cables) took months, the typical time for winding and curing of a layer of the superconducting coils for prototype MBP/A #3 was of the order of only three days.

Magnet collaring was a fundamental operation carried out under a press at loads between 6 to 10 MN for meter of press length. The average compressive azimuthal stresses in the coils were:

80 MPa in the inner layers
55 MPa in the outer layers

Preparation of the collaring operation and calibration of the pre-stress in the coils required about one month for the dummy assembly and about one week for prototype MBP/A #1. Prototypes MBP/A #2 and MBP/A #3, fabricated by the same manufacturer of prototype MBP/A #1, required less than one day (one shift) to be collared. Collaring of the mass production dipoles should not take more than a few hours.

Another interesting development was the setting-up of the procedure for welding the outer containment structure of the magnet, made of two stainless steel half cylinders joint together, so as to ensure the wanted pre-stress on the coil/collar/yoke assembly (Fig. 2). This

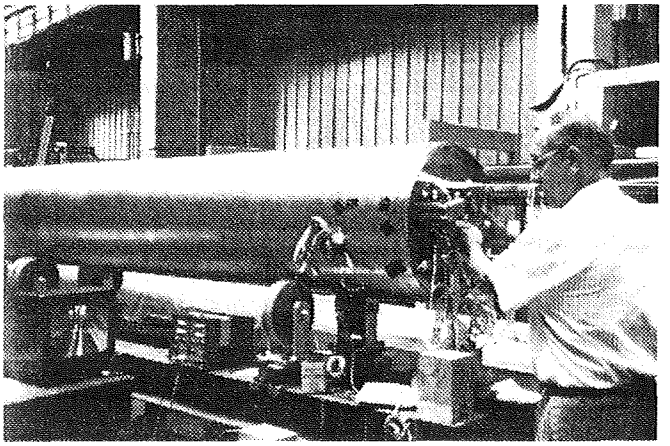

Fig. 2 . Inspection of the magnet apertures, after welding of the external shrinking cylinder.

required the fabrication of three complete models (about 400 mm long, having the real cross-section of the magnet), which were cooled to liquid nitrogen temperature to verify the kinematical behaviour of the magnet. A major design modification was introduced [9], consisting of two sets of Al bars, placed between the yoke halves, which permit a precise control of the geometry after welding and during thermal cycles. The wanted (and achieved) tensile stress in the shrinking cylinder was about 190 N/mm2.
Before being put into the cryostat, the cold mass was pressure tested at 26 bar, to assess its soundness with respect to the maximum pressure increase during a quench (max expected pressure 20 bar). It also passed a leak tightness test which proved that the leak rate was less than 10^{-9} mbar/ls. These tests were repeated after insertion of the cold mass into its cryostat.

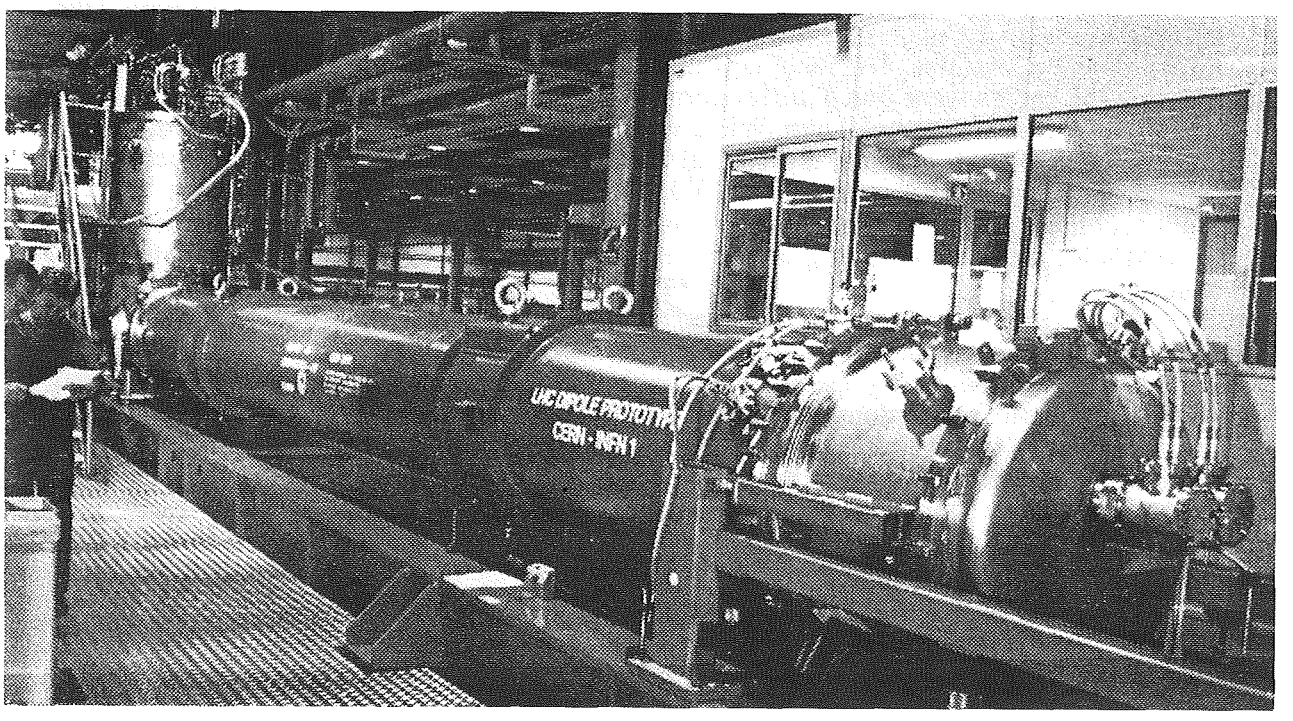

Fig. 3 . Prototype MBP/A #1 (CERN-INFN 1) on its test bench at CERN.

4.4 Testing at CERN
The first prototype was shipped to CERN in February 1994 . After one month of preparation it was mounted on the new test station (see Fig 3), developed at CERN to test the prototype dipoles. On April 1994 the magnet went through its first quenches. The first quench (see fig.4), occurred at a field slightly above the nominal field of the LHC machine, which is 8.65 T. On the third quench the magnet reached 9 T.
The magnet was then warmed-up to insert anti-cryostats in the cold bore apertures to perform precise magnetic measurements. An intense campaign of magnetic measurements was carried out [13], which showed excellent field quality in both apertures.
Following these magnetic measurements, testing was resumed on mid June 1994. The magnet behaved particularly well. It did not not show any "retraining" after the thermal cycle to room temperature and reached a field of 9.5 T after some quenches. Fig. 4 resumes the training history of the magnet.

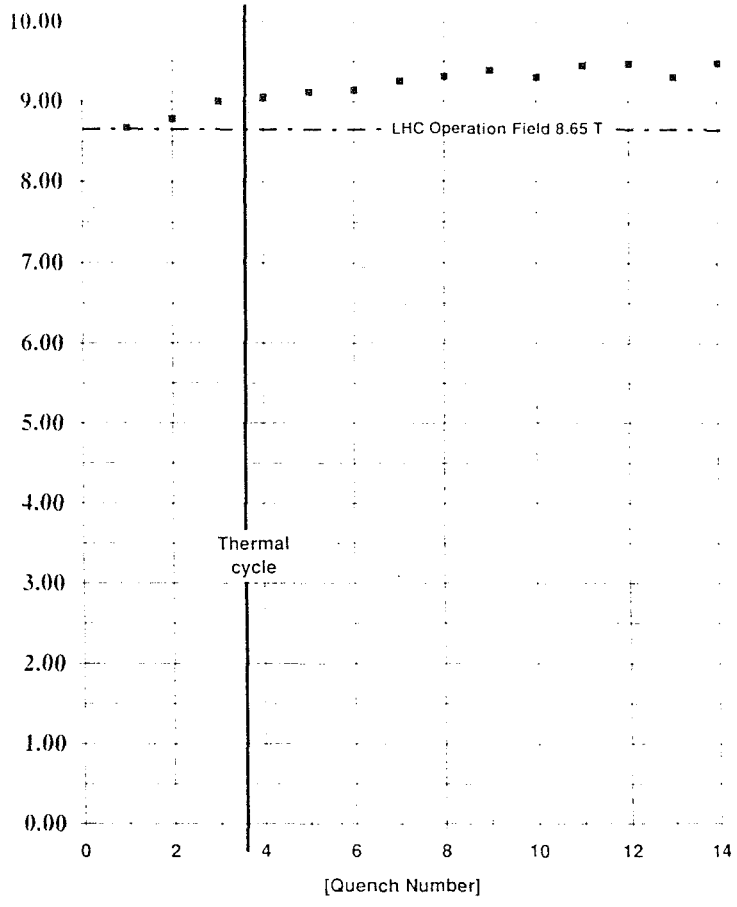

Fig. 4 . Quench history of the MBP/A #1 (CERN-INFN 1) prototype during the first and second test campaigns.

The results obtained so far with prototype MBP/A #1 are very encouraging indeed.They permit to be confident on the capability to build the LHC advanced technology magnets in industry. The evolution of the design of the LHC machine has led to dipole magnets with an increased magnetic length of 13.145 m, having a 56 mm diameter aperture. Although the increased length, together with the fact that they will be sligthly curved, will require some development, the larger aperture coupled with a smaller and hence less stiff cable should make the final magnets easier compared to the already successfully tested prototype MBP/A #1.

5. Future programmes

A decision concerning the approval by CERN Council of the LHC accelerator is expected to be taken soon . If a positive decision is taken in 1994 it is expected that, after finalization of the R&D programme and evaluation of a number of pre-production units, the mass production of the s.c. magnets will start in 1997.

6. Conclusion

The R&D programme for the superconducting magnets for the LHC is approaching the end of the first very important phase in which the following points have been confirmed:

- The technical choices for the LHC magnets are sound, including the twin-aperture configuration.
- The field levels of the LHC machine and the required field quality have been achieved in model magnets and in 10 m long prototypes made in industry.

These facts represent a encouraging base for the second phase of the R&D programme, which is aimed at finalizing the magnet design and construction techniques for the mass production.

Acknowledgment
Several National Institutions and Laboratories have contributed in an important way to the reported R & D work, which received a very substantial support from industry. The LHC Magnet Team gratefully thanks them all.

References:
[1] The LHC Study Group, "LHC, The Large Hadron Collider Accelerator Project", CERN /AC/93(LHC), November 1993.
[2] D. Leroy, R. Perin, G. de Rijk, W. Thomi, "Design of a High-field Twin-aperture S.C. Dipole Model", IEEE Trans. on Magn., vol. 24, March 1988, pp. 1373-76.
[3] A. Asner, R. Perin, S. Wenger, F. Zerobin, "First Nb3Sn, 1 m Long Superconducting Dipole Model Magnets for LHC Break the 10 T Field Threshold", Proc. 11th Int. Conf. on Magnet Techn., Tsukuba, 1989, pp. 36-41.
[4] R. Ostojic, T.M. Taylor, "Design and Construction of a One-Metre Model of the 70 mm Aperture Quadrupole for the LHC Low-b Insertions", presented at MT13, Victoria, Canada, 20-24 September 1993.
[5] M. Bona, D. Leroy, R. Perin, P. Rohmig, B. Szeless, W. Thomi, "Design, Fabrication Variants and Results of LHC Twin-Aperture Models", IEEE Trans. on Magn., vol. 28, pp. 338-341, Jan. 1992.
[6] D. Leroy et al., "Test Results on 10 T LHC Superconducting One-Meter Long Dipole Models", IEEE Trans. on Applied Superconductivity, March 1993, vol. 3, No. 1, pp. 614-621.
[7] A. Yamamoto et al., "Development of 10 T Dipole Magnets for the Large Hadron Collider", IEEE Trans. on Applied Superconductivity, March 1993, vol. 3, No. 1, pp. 769-772.
[8] M. Granier et al., "Performance of the Twin-Aperture Dipole for the CERN LHC", Proc. EPAC92, Berlin, March 1992.
[9] E. Acerbi, M. Bona, D. Leroy, R. Perin, L. Rossi, "Development and Fabrication of the First 10 Metre Long Superconducting Dipole Prototype for the LHC", presented at MT13, Victoria, Canada, 20-24 September 1993.
[10] J.M. Baze et al., "Design and Fabrication of the Prototype Superconducting Quadrupole for the CERN LHC Project", IEEE Trans. on Magn., Jan. 1992, vol. 28, pp. 335-337.
J.M. Rifflet et al., "Status of the Fabrication and Test of the Prototype LHC Lattice Quadrupole Magnets", presented at MT13, Victoria, Canada, 20-24 September 1993.
[11] M. Bona, D. Perini, "Finite Element Structural Analysis of the 10 m Long Dipole Prototype Magnet for the LHC", IEEE Trans. on Magn., Vol. 28, Jan. 1992, p. 358. Paper presented at MT12 Conference, Leningrad, June 1991.
[12] J. M. Rifflet et al.,"Cryogenics & Mechanical measurements of the first two LHC lattice quadrupole prototypes", presented at EPAC Conference, London, 27 June-1July, 1994.
[13] M. Bona, D.Leroy, R. Perin, P. Sievers, L.Walckiers, E. Acerbi, L. Rossi,"Results, of tests and measurements of the first CERN-INFN 10 m long superconducting dipole prototype for the LHC", presented at EPAC Conference, London, 27 June-1July, 1994.
[14] R. Perin, "Status Report on the LHC Magnets", presentes at World Congress on Superconductivity, Munich, Germany, 1991. Applied Superconductivity Vol. 1, Nos 10-12, pp 1487-1502, 1993.
[15] R. Perin, "Status of the Large Hadron Collider", presented at MT13 Conference, Victoria, Canada, 20-24 September 1993.

S9-76
3/3523

Status of High Temperature Superconductor Development for Accelerator Magnets

H. Hirabayashi
KEK, National Laboratory for High Energy Physics
1-1, Oho, Tsukuba-shi, Ibaraki-ken, Japan 305

3/29/91
9P.

1) Abstract

High temperature superconductors are still under development for various applications. As far as conductors for magnets are concerned, the development has just been started. Small coils wound by silver sheathed Bi-2212 and Bi-2223 oxide conductors have been reported by a few authors.

Essential properties of high T_c superconductors like pinning force, coherent length, intergrain coupling, weak link, thermal property, AC loss and mechanical strength are still not sufficiently understandable.

In this talk, a review is given with comparison between the present achievement and the final requirement for high T_c superconductors, which could be particularly used in accelerator magnets.

Discussions on how to develop high T_c superconductors for accelerator magnets are included with key parameters of essential properties.

A proposal is also given how to make a prototype accelerator magnet with high T_c superconductors with prospect for future development.

2) Introduction

Since the discovery of superconductivity by K. Onnes in 1911, the record of critical temperature (T_c) had been updated slowly by the middle of 1980s. The speed of updating the record of T_c was remarkably increased after the discovery of the oxide superconductors in 1986, as shown in Figure 1. The highest record of T_c is approximately 134K for Hg-Ba-Ca-Cu-O[1].

The oxide superconductors which have high critical temperatures are generally called high T_c superconductors. In recent years, enormous amounts of research concentrated on high T_c superconductors all over the world.

In addition to basic studies on superconductivity, various applications to films, tapes and wires have also been intensively studied. However, the high T_c materials are not well-understood in the viewpoints of solid-state physics and industrial production.

Characteristics of metallic and inter-metallic superconductors, which have low T_c, are also improved continuously. Copper stabilized Nb-Ti wires have become applicable for the magnets in the region of 10T with superfluid helium cooling. A15 compound as Nb_3Sn copper stabilized superconductor has become also applicable for magnets of 12T at 4.5K with liquid helium cooling.

The superconducting cables commonly used for accelerator dipole and quadrupole magnets in the range of several teslas are Nb-Ti Copper cables and practically operated at 4.5K with liquid helium cooling. Some magnets are wound with copper stabilized Nb_3Sn wires for actual operation around 12T at 4.5K. Nevertheless, it is difficult to use these wires and cables in the operation beyond 15T.

Recently, it was found that some oxide superconductors are applicable up to 30T at 4.2K[2] as shown in Figure 2. This is quite attractive in application to generate a very high magnetic field.

Figure 3 shows the T_c of the metallic and the oxide superconductors. A15 intermetallic compound superconductor shows intermediate values between those of metallic and oxide superconductors in Tc and Hc.

3) Present status of high T_c superconducting wires and cables

There are three types of high T_c superconducting wires and cables, e.g., Bi-, Y- and Tl-based materials. Among these materials, Bi-based ones are considered as a main stream of development. Specially, Bi-2223 and Bi-2212 are studied by many researchers.

Bi-based silver sheathed Bi-2223 and Bi-2212 have been remarkably developed as the high T_c wires and cables for magnets.

G. J. Yurek has manufactured multi-core, tape-shaped wires using a combination of the metallic precursor method, and the silver-sheath method[3] and the technique to produce about 300m long wires has been established. The wire J_c is reported to be around 50A/mm^2 at 20K in 5T for 3m long wires, and J_c=37A and 24A at 77K in 0T for 30m and 300m long cables, respectively.

P. Haldar *et al.*, reported the results of the test of short samples at 4.2K, 27K and 77K under magnetic fields up to 20T.[4]

Quite recently, T. Hikata *et al.*, reported the result of 1km-class silver-sheathed Bi-based superconducting wires.[5] They made monofilamentary and 61-multifilamentary wires. A J_c of 40A/mm^2 was achieved for 1,080m long wire. An anisotropy for the direction of external magnetic fields was found in J_c. They measured the parameter (J_c×length). The maximum value was (J_c×length)=9.91×10^{10}[A/m] for 623m long wire. Figure 4 shows the 1080m long high T_c tape wound in a coil.

Pancake coils wound with high T_c wires and cables were studied by S. Meguro.[6] He studied the temperature dependence of J_c of Bi-2212 wire in magnetic fields and showed the possibility to operate the Jelly Rolled Bi-2212 silver sheathed superconductor below 20K.

Among high T_c superconductors available at present, it seems, only Bi-based silver sheathed conductors have suitable characteristics for accelerator magnet application. Bi-2212 silver sheathed tapes were significantly improved in J_c with the formation of the high c-axis orientation of laminated grains and reached $J_c \approx$ 350A/mm^2 at 77K with zero external magnetic field. However, J_c was lowered down to $\approx$ 4A/mm^2 at the same temperature with an external field of 1T. The large magnetic field dependence is not suitable for accelerator magnet application at 77K. Further study is necessary to find the method to satisfy both requirements of high J_c and I_c.

On the other hand, this highly c-axis oriented Bi-2212 high T_c superconducting tape could survive since it shows high $J_c \approx$ 20A/mm^2 with the external magnetic field as high as 30T, if it is cooled down to 4.2K.

The J_c of high T_c superconductor around several tesla is still much lower than that of metallic superconductors which are presently used as accelerator magnets.

4) Requirements for superconducting wires and cables of accelerator magnets

The advantage of using high T_c materials for accelerator magnets is that the refrigeration system for high T_c magnets is much simpler than that for conventional metallic superconducting magnets. Quench protection from the heat load due to beam radiation is also expected to be easier.

The requirements for accelerator magnets are complicated since they must be determined after a delicate adjustment of various parameters which are not always compatible with one another. We discuss an overview of common requirements for 10T-class superconducting magnets which are desirable for a multi-TeV accelerator.

The beam size of the accelerator is preferred to be as small as reasonably achievable by optimizing the beam optics and improving a beam cooling technique, since the costs have risen remarkably for large scale magnets. A small magnet for a high field requires a high current density. The current density of $400A/mm^2$ in the windings is a reasonable goal, which requires the current density of more than $1000A/mm^2$ in the wires. This implies that the electric insulation must endure 100-150MPa at low temperatures. The choice of insulation materials and the manufacturing technique must be improved to achieve these conditions.

5) Proposed high T_c superconducting accelerator magnet cables

As mentioned in the previous section, requirements for superconducting wires and cables of accelerator magnets are remarkably severe. Further improvement is necessary for the production of high T_c superconductors for this application.

A possible solution to apply high T_c superconducting wires for accelerator magnets is to make a so-called superferric magnet as shown in Figure 5. In this configuration, the superconducting coil is cooled down together with the magnetic iron and enables us to assemble accelerator magnets below 2T. However, wires and cables are required to have much more mechanical strength and much better performance for the application to accelerator magnets which can be operated in the magnetic field larger than 2T, e.g. 5 to 10T.

One possible way to develop such wires and cables with high T_c superconductors is to combine the longitudinal *in-situ* and radial Jelly Rolled structures of the wire strands. The longitudinal *in-situ* structure within the coherent length of polycrystals in metallic wire will improve the J_c along the wire length and the Jelly Roll will also improve the J_c deterioration with external magnetic field. We believe that such a structure of high T_c superconducting wires should be created and tested for the future application to accelerator magnet.

6) Conclusions

Superconducting accelerator magnets require high T_c cables which show a high J_c and I_c with a strong magnetic field.

A proposed solution for these requirements is to develop the Jelly-Rolled Bi-2212 silver sheathed round wires. The multi-layer and round shape cross-sectional structure could be another solution for high J_c and I_c requirements. The J_c characteristics of this type of wires will be heavily deteriorated above 20K, therefore it is suitable for magnet operation at temperatures below 20K.

Another solution to develop accelerator magnet wire and cable would be found in a further study of the *in-situ* structure in high T_c polycrystal superconductors by adjusting their coherent length in appropriate metallic sheaths and/or stabilizers.

From the viewpoint of accelerator magnet application, we expect the development of high T_c superconducting wire with high J_c, I_c and lengths over 1 km in near future.

It is still very hard to see how high-T_c superconducting wires could be operated with high-J_c and high-I_c at the temperature around 70K. Further study of high T_c superconductors are strongly desired.

7)Acknowledgments

The author is grateful to Drs. K. Sato of SEI and S. Meguro of FEC for their kind suggestions. He is also grateful to staff members of Cryogenics Center of KEK for the preparation of this paper.

8)References

1) A. Schilling et al., Nature **363**, 56(1993).
2) M. Mimura et al., Advances in Superconductivity V, eds. Y. Bando and H. Yamauchi, Springer-Verlag (ISS'92), p.693-696, and private communication.
3) G. J. Yurek, Advances in Superconductivity VI, eds. T. Fujita and Y. Shiohara, Springer-Verlag (ISS'93), p.3-8.
4) P. Haldar et al., Advances in Superconductivity VI, eds. T. Fujita and Y. Shiohara, Springer-Verlag (ISS'93), p.605-608.
5) T. Hikata et al., Proceedings of the 1994 International Workshop on Superconductivity, Jun. 6-9, 1994, Kyoto, Japan, p.69.
6) S. Meguro, private communication.

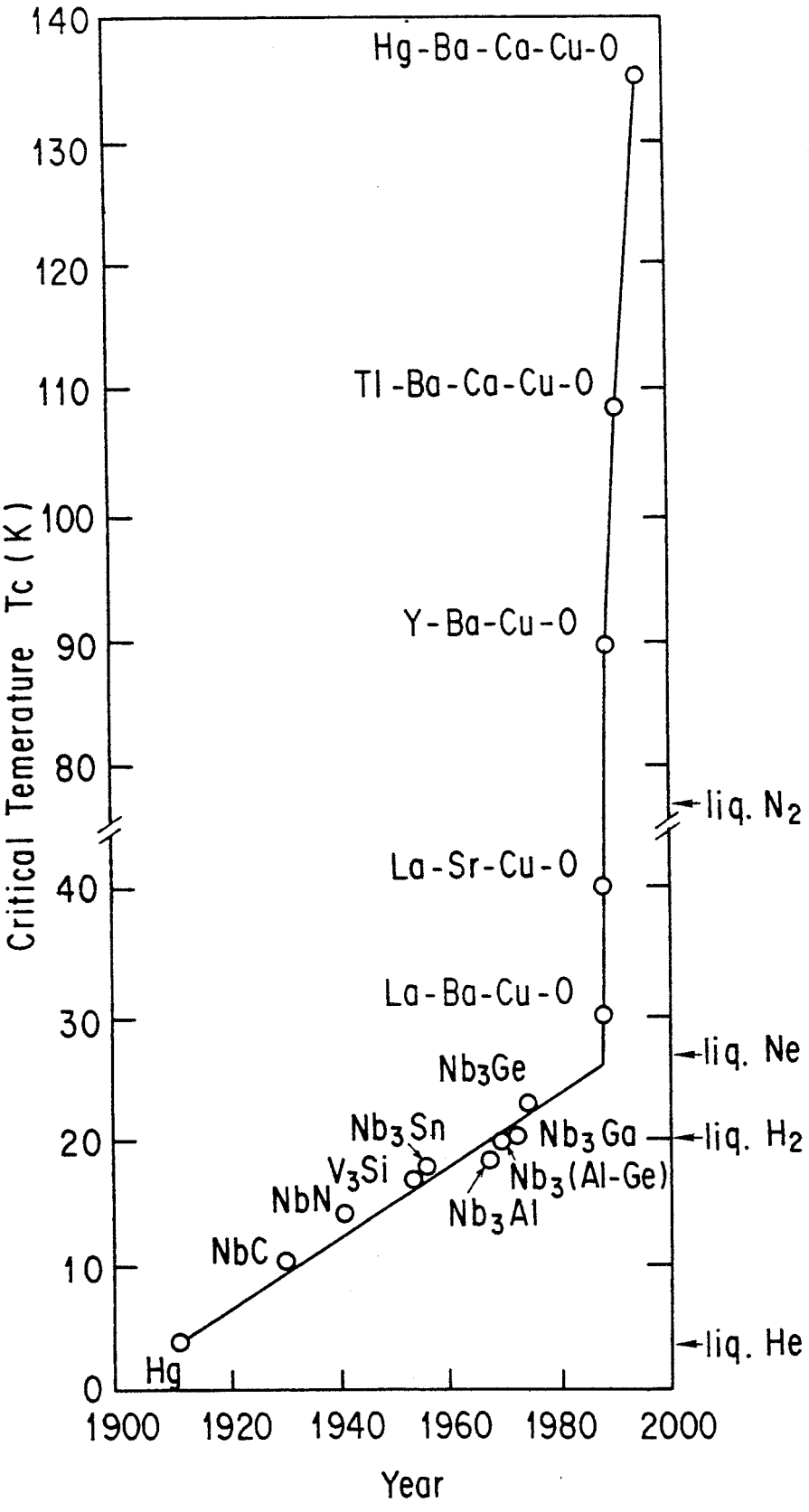

Figure 1.- History of updating the record of critical temperature of Superconductors.

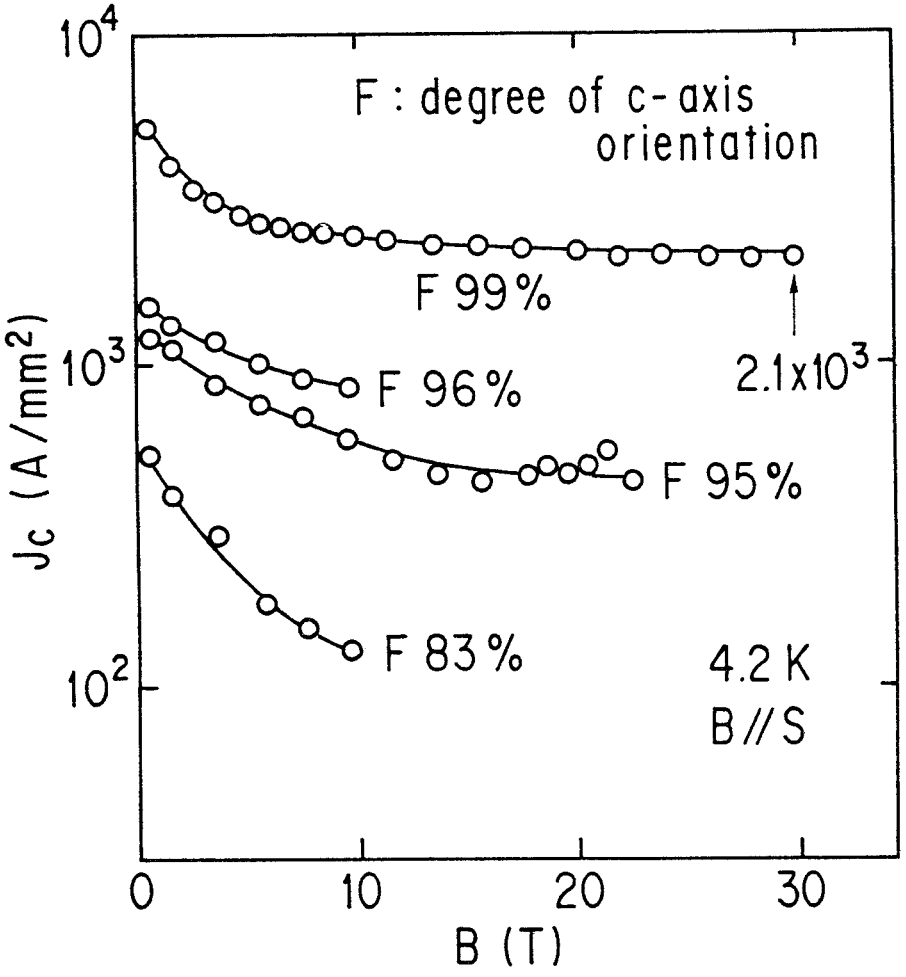

Figure 2.- Dependence of J_c of Bi-2212 on magnetic field at 4.2K.

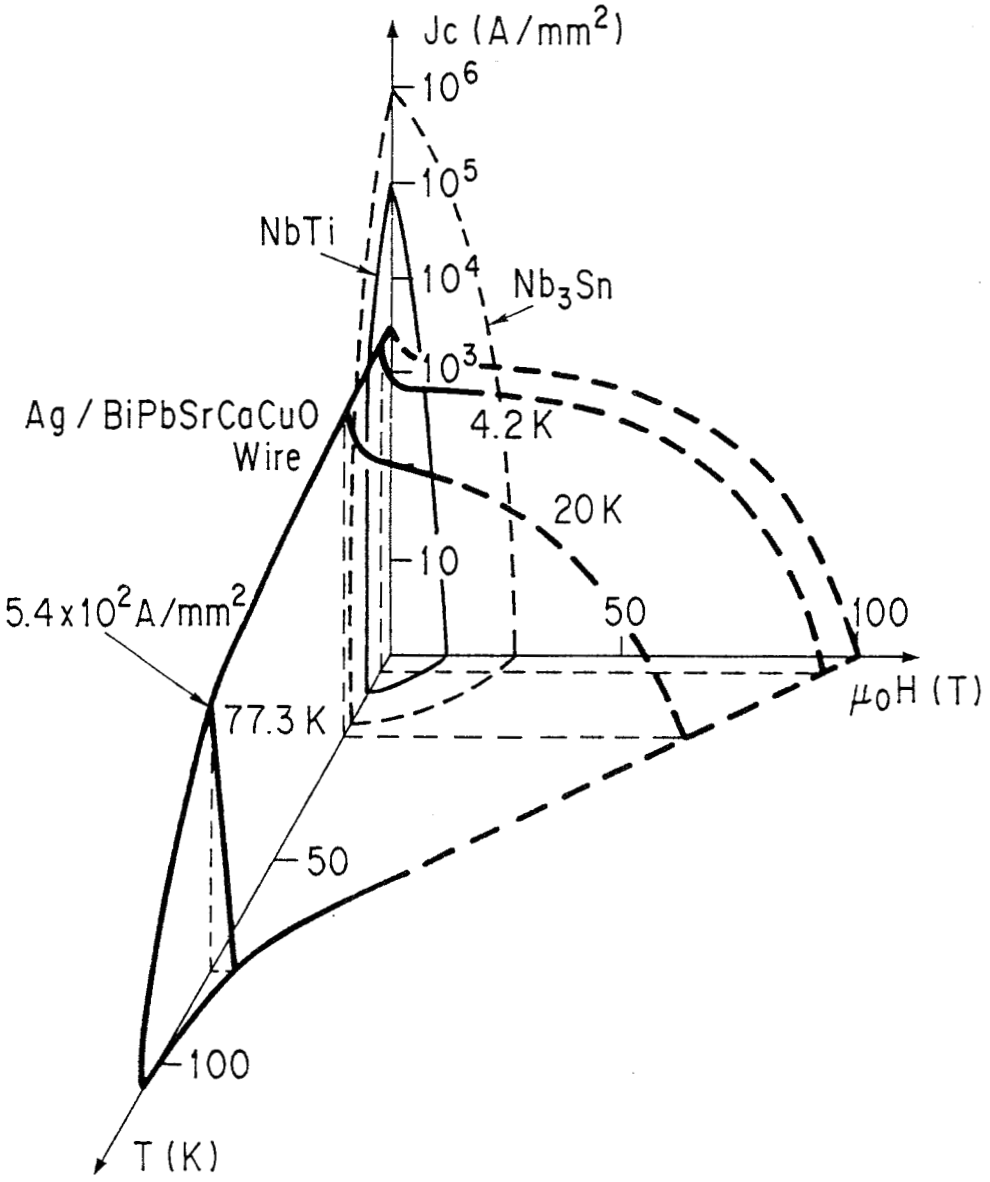

Figure 3.- Critical values of superconductors.

FABRICATION OF LONG LENGTH WIRES

61-MULTI FILAMENTARY WIRES		Jc	JcxL
		A/mm^2	10^{10} A/m
100 m-CLASS LONG WIRE	74 m	267	1.98
	100 m	261	2.61
1,000 m-CLASS LONG WIRE	623 m	159	9.91
	1,080 m	40.2	4.34

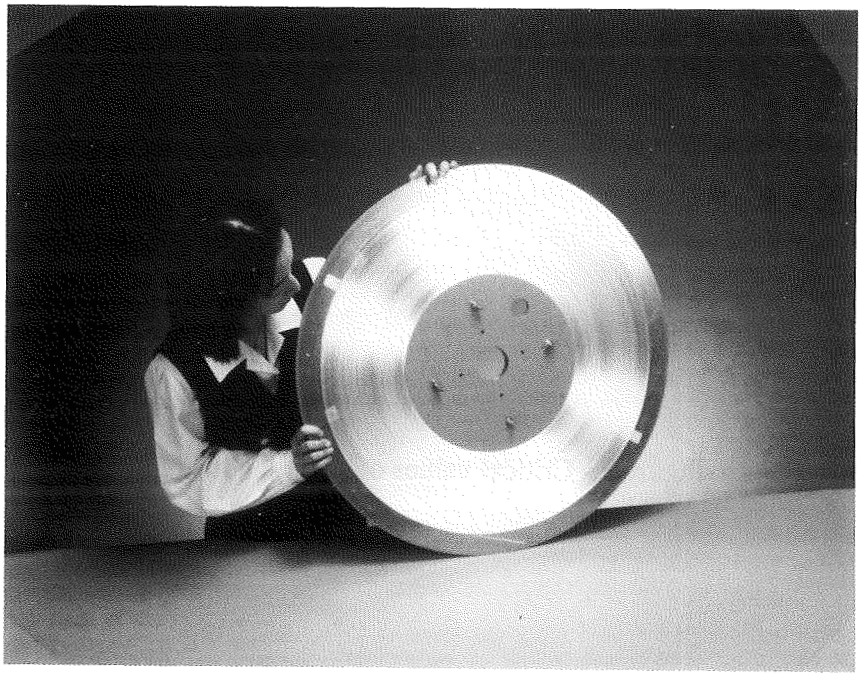

Figure 4.- 61-multifilamentary long high T_c superconducting wire.

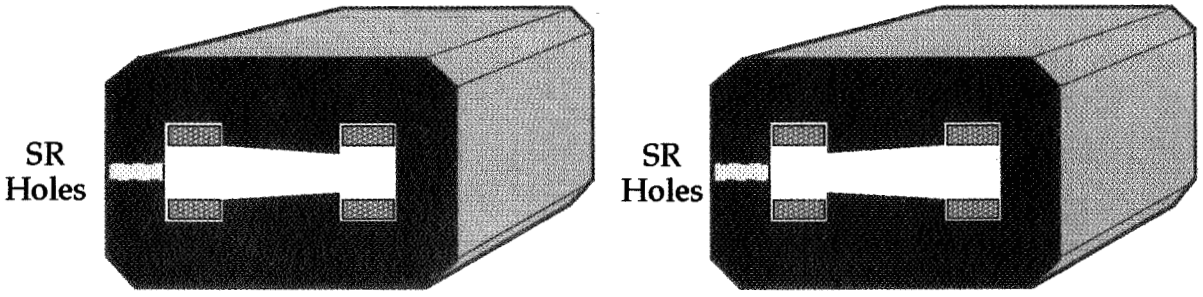

High Tc Superconducting
Alternating Gradient Synchrotron Magnets
with Cold Iron

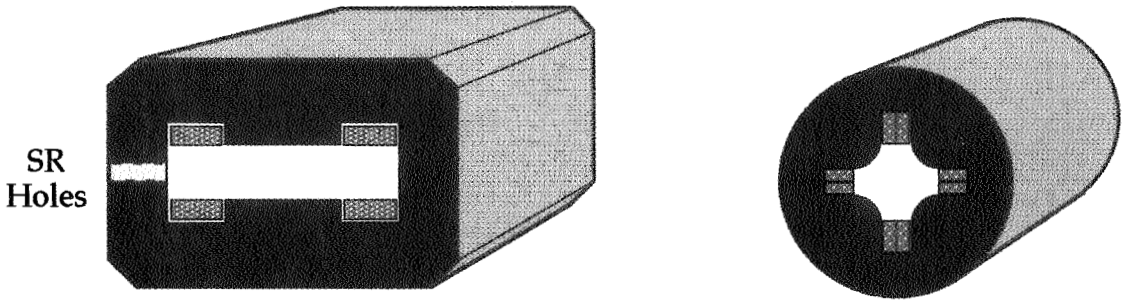

High Tc Superconducting Magnets with Cold Iron

Figure 5.- Superferric magnets with cold irons.

SINGLE-SCAN

5/0-76

313528

Development Work for a Superconducting Linear Collider

Axel Matheisen, for the TESLA collaboration
Deutsches Elektronen Synchrotron DESY
Notkestraße 85
D-22603 Hamburg

Introduction

For future linear e+e- colliders in the TeV range several alternatives are under discussion (Ref.1). The TESLA approach (Ref. 2) is based on the advantages of superconductivity. High Q values of the accelerator structures give high efficiency for converting RF power into beam power. A low resonance frequency for the RF structures can be chosen to obtain a large number of electrons (positrons) per bunch. For a given luminosity the beam dimensions can be chosen conservatively which leads to relaxed beam emittance and tolerances at the final focus .

Each individual superconducting accelerator component (resonator cavity) of this linear collider has to deliver an energy gain of 25 MeV/m to the beam. Today s.c. resonators are in use at CEBAF/USA, at DESY/Germany, Darmstadt/Germany; KEK/ Japan and CERN/Geneva. They show acceleration gradients between 5 MV/m and 10 MV/m. Encouraging experiments at CEA Saclay and Cornell University showed acceleration gradients of 20 MV/m and 25 MV/m in single and multicell structures (Ref. 3,4)

In an activity centered at DESY in Hamburg/Germany the TESLA collaboration is constructing a 500 MeV superconducting accelerator test facility (TTF) to demonstrate that a linear collider based on this technique can be built in a cost effective manner and that the necessary acceleration gradients of more than 15 MeV/m can be reached reproducibly.

The test facility (Fig 1) built at DESY covers an area of 3.000 m^2 and is devided into 3 major activity areas: - The testlinac , where the performance of the modular

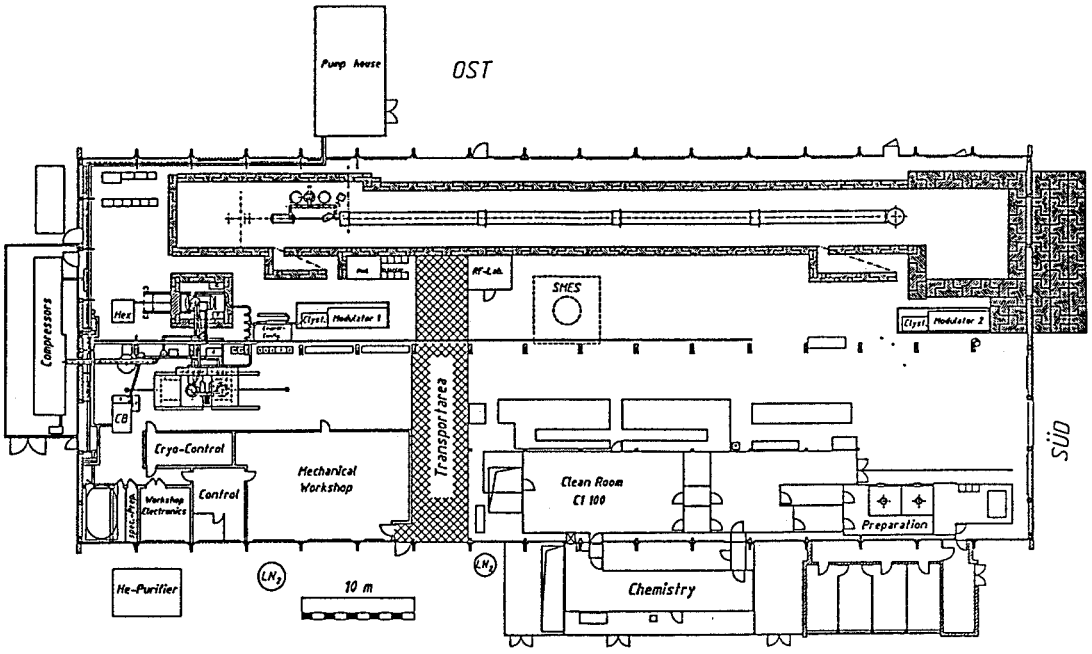

Fig 1 Cross-section of the TTF facilities and the planned 500 MeV linac

components with an electron beam passing the 40 m long acceleration section can be demonstrated.
- The test area, where all individual resonators are tested before installation into a module.
- The preparation and assembly area, where assembly of cavities and modules take place.
We report here on the design work to reach a reduction of costs compared to actual existing superconducting accelerator structures and on the facility set up to reach high acceleration gradients in a reproducible way.

Design Issues of the Accelerator Components

Cryostat

Today´s designs of superconducting accelerator units fulfill the requirement of their application in storage rings. Small numbers of resonators and large number of cold to warm transitions per cryo unit result from the requirements of the circular storage rings. The number of transitions yields high heat load budgets and additional manufacturing costs for each transition.
Both numbers , investment- und heat budget costs can be reduced by having a large number of resonators connected to each other without any transition to the 300 K level.
The TESLA design splits a cryo unit of 144 m length into 12 subunits (cryomodules), each 12m long. One cryo module will house an assembly of 8 cavities . Fig. 2 shows a transverse cross section at one of the support posts. The resonators, each being equipped with its individual Helium tank and tuning system, hang on a 350 mm stainless steel tube (TYP DIN 1.4429) which acts as a Helium pumping line and girder tube for the resonators as well. The 4.2 K/80 K radiation shields, made from aluminium, and the 4.2/80 K He distribution lines are also connected to this tube.

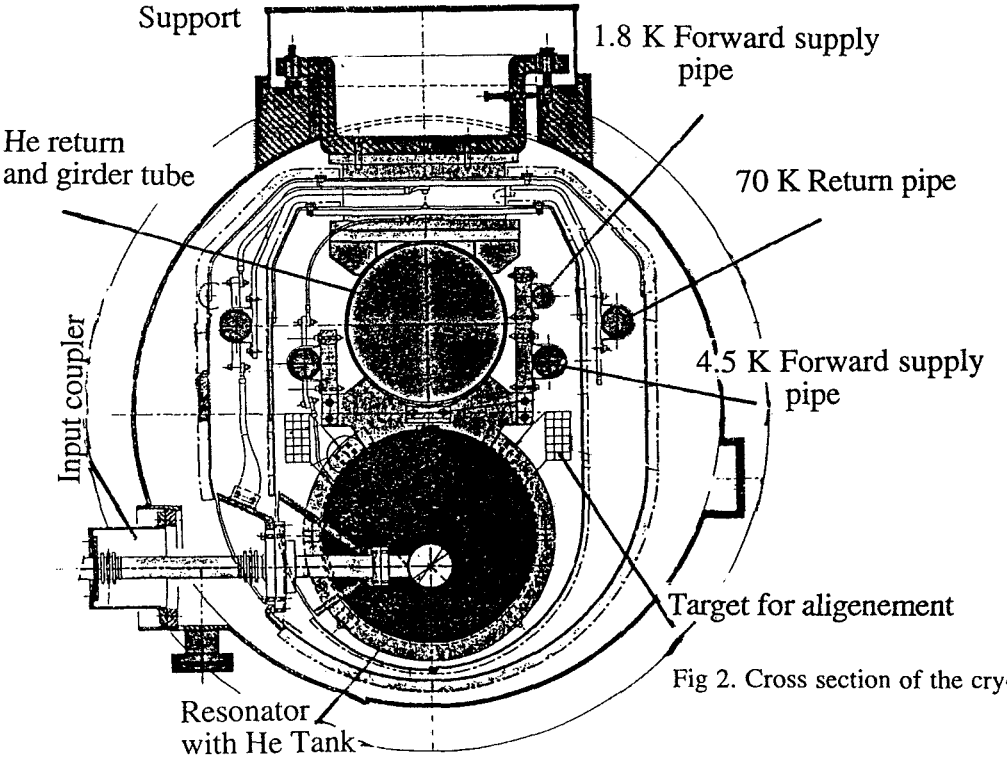

Fig 2. Cross section of the cryostat

Three posts, made from carbon fiber , take the gravitational forces of the girder tube to the rigid vacuum vessel made from carbon steel . For this design the static heat loss at 1.9 K is calculated to be 0.4 W/m . This will be a reduction by a factor of ten compared to the actual existing storage ring designs.

Cavity

Besides the increase of acceleration gradients cost reduction during fabrication is needed in order to make s.c.cavities a competitive alternative to warm structures. A large amount of cost intensive manufacturing is related to the auxiliaries like power input couplers, higher order mode (HOM) damping couplers and tuners connected to each cavity. A compromise between reduced costs by an increased number of cells per cavity, the excitation of higher order modes and the appearance of trapped modes has to be made.

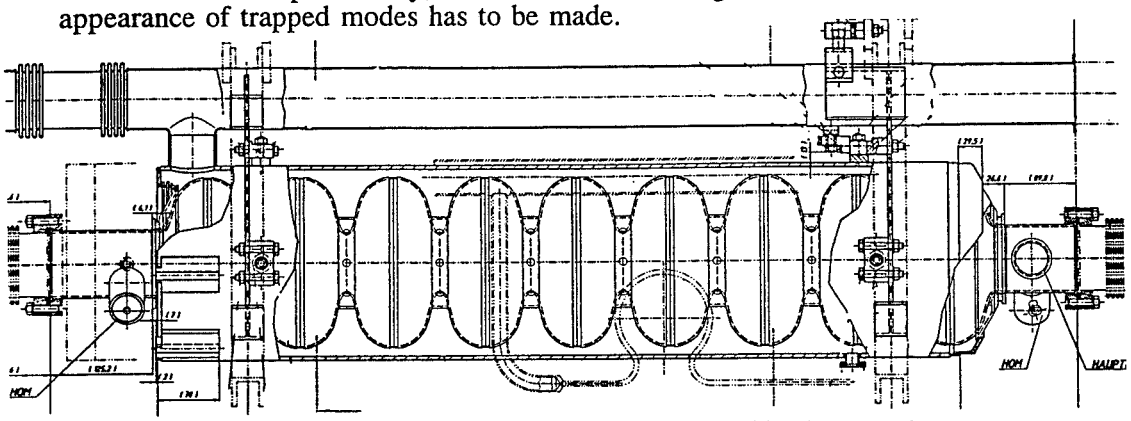

Fig.3 Longitudinal cross section of the TESLA resonator covered by the He tank

The TESLA resonator (Fig. 3) is built from 9 cells with an eigenfrequency of 1.3 GHz .The RF power is fed in by the input coupler, perpendicular to the beam axis, while the HOM modes are damped by two couplers on each side of the cavity. The geometry of this resonator results in the numbers listed in Table 1. The resonators will be made from high thermal conducting 2.8 mm thick niobium sheet material (RRR >300) by deep drawing and electron beam welding technique. To reduce the number of cost-intensive welds, new technologies are investigated in addition.The HOM couplers are extruded in one step from a Nb pallet to their final shape , while the beam pipes are machined from sheet material by spinning. Using these technologis a total number of 5 welds and several intermediate production steps like chemical etching and calibration are eliminated. Further investigations on seamless cells and resonators are made in the collaboration.

f	1300 [MHz]
(R/Q)	1030 [Ω]
Ep/Eac	2
Hp/Eac	42.2 [Gs/MV/m]
$k_{c\text{-}c}$	1.87 %
$f_{\pi} - f_{\pi-1}$	.7 [MHz]
long. loss K	9.24 [V/pC]

Table 1. TESLA cavity parameters

Tuning

For an optimized energy transfer to the beam, all resonators have to have the resonance frequency within an accuracy of some Hz. Room temperature adjustment errors result in frequency variations of +-200kHz. To ajust the static frequency shift slow reacting tuners are installed in the vacuum at the 80 K level. A lever arm system driven by a stepping motor via an elliptical gearbox acts on

the cavity. By elongation and contraction of the structure this arangement allows a frequency adjustment of +- 4 Hz
Electromagnetic forces act on the resonator surface during RF pulses. Due to these Lorentz forces, a fast displacement of the walls (10^{-4} mm at Eacc = 25 MV/m) will occur at every RF pulse . This displacement results in a frequency shift of 1.2 kHz to be compared with a bandwidth of the loaded cavity of 360 Hz. Stiffening rings between each cell reduce this fast displacement down to a frequency shift of 600 Hz (360 Hz by the cavity +300 Hz by the tank), which will be tolerable for the RF system.

Power coupler

The RF power transferred to the beam will be 200 KW /cavity in pulses of 2 msec length with a repetition rate of 10 Hz. Sixteen cavities are driven in parallel by one 4.5 MW klystron. Besides the power transfer the input power coupler has to separate the resonator vacuum of 10^{-10} mbar at 1.8 K and the atmospheric pressure at 300 K. Two ceramic windows, as shown in Fig. 4, are integrated, one at a temperature level of 80 K, to separate the clean cavity vacuum from the insulation vacuum and the second at room temperature for the

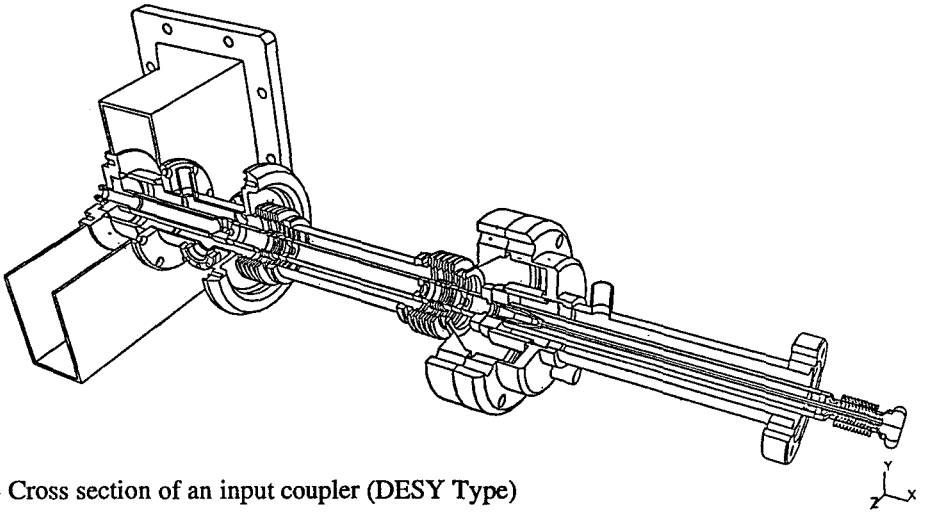

Fig.4 Cross section of an input coupler (DESY Type)

transition to atmospheric pressure. The separation of the vacua allows a dust free assembly and sealing of the resonator in the cleanroom independently from the assembly of the coupler in the cryomodule .The heat loads introduced to the 1.8 K and 4.2 K level by this coupler will be 0.61 W for static- plus dynamic losses.

HOM Couplers

Two different designs of HOM couplers are studied. Fig.5 shows the coaxial type coupler design which is fixed to the beam pipes by EB welding. The fish hook coupler design flanged to the beampipe is shown in Fig. 2 . These two versions have to be compared in respect to costs, handling and reliability.

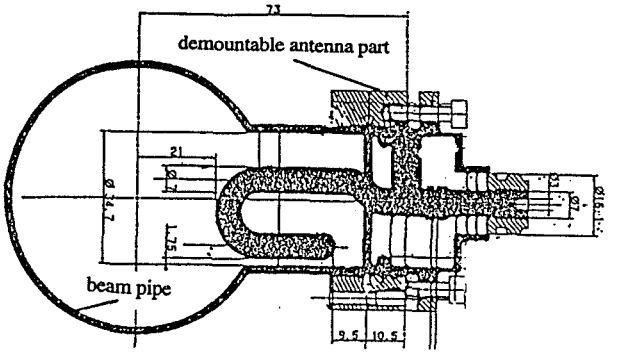

Fig.5 Demountable HOM coupler

Infrastructure

Experimental Hall

The TESLA Test Facility is located in an experimental hall of about 3.000 m^2 ground area (see Fig. 1). Half of this space will be occupied by the test linac described later.The second part of the hall is supplied with equipment for tests, assembly and surface treatment of all linac components. The most important components of this infrastructure are a cleanroom and the surface treatment area, which cover 1/4 of the space.

1.8 K test area

To reduce dynamic losses due to BCS surface resistance, the resonators will be cooled down to 1.8 K . The necessary cooling is supplied by a refrigerator of 200 W cooling power at 1.8 K.
To test and qualify the resonators before insertion in the cryomodule, three test cryostats are installed. Two vertical dewars for tests of resonators not equipped with the helium tank allow RF processing of resonator defects by high peak power processing (HPP). In case of appearance of defects, limiting a single resonator below the goal of 20 MV/m, a surface temperature mapping setup can be attached to the cavity in order to study and localize the limitation.
The two clystrons for supplying the testlinac with RF power are located next to the cold test area. The power distribution system of one klystron allows to feed each test cryostat with pulses of 2 MW power for HPP of resonators.

Cleanroom and assembly area

The most important components of the TTF infrastructure are a cleanroom including an ultra pure water supply, a chemical etching facility and a furnace for postpurification of niobium.
In order to reach the necessary cleanliness for high gradient resonators, the standards of electronic industry are applied in a cleanroom of 300 m^2 space (Fig.6). A class 100 ASTM area of 100 m^2 space is installed to assemble individual cavities and align the resonators to a cryomodule string under dust free conditions. Inside this cleanroom 2*20 m^2 of class 10 ASTM are installed for assembly of critical components connected to the resonators. Access to this area is provided by the sluices for personal and material separately.These sluices are equipped with ionized air guns for cleaning and particle counters for monitoring. In the class 10.000 area a separate space of 70 m^2 is used for high quality surface cleaning and treatment (chemistry area).

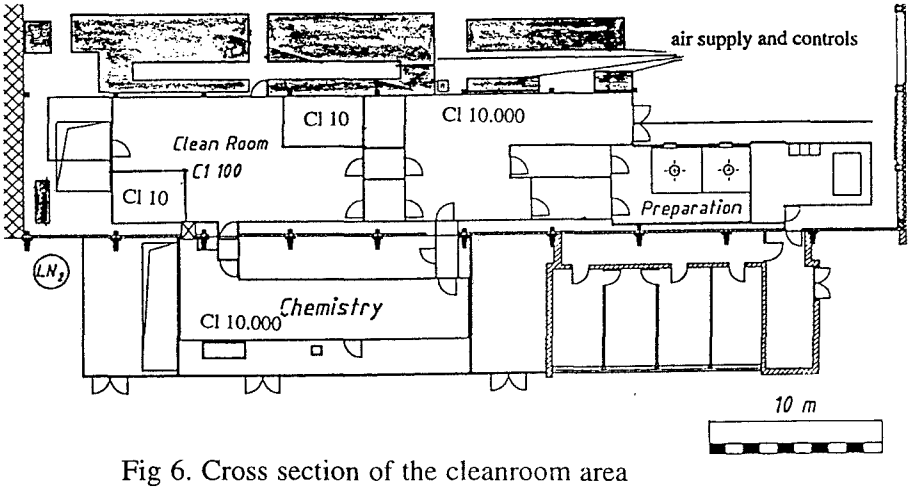

Fig 6. Cross section of the cleanroom area

Ultra pure water and ultra pure nitrogen gas lines,coming from separate plants, are connected to this area. An ultrasonic bath of 400 l capacity, a rinsing basin of 400 l capacity as well, a preparation area and a high pressure rinsing cabinet allow to clean the cavities and handle all sophisticated parts which have to be adopted to the resonators during final assembly. Remote controlled oil free pumping stations are located outside the cleanroom to establish the vacuum and leak checks under dust free conditions.

Chemistry

Inside the chemistry area a cabinet for surface treatment by etching of the niobium is installed. The acid in use is a chemical mixture of $HF/HNO_3/H_3PO_4$ (*1) in a 1/1/2 volume mixture. The acid is circulating in a closed loop between the storage tanks and the cavity. The storage tanks are located in a separate area outside the cleanroom . The pumps, pumping lines (made from PVDF) and filter elements (0.2 µm size) of the chemistry distribution system fulfill the standards of the electronic industry .

Two different acid treatments are foreseen. The outside treatment removes the niobium-titanium surface layer after the postpurification of the niobium in the furnance whereas the inside treatment with highest quality requirements is used for the preparation of the inner RF surface.The separation of the two treatments is guarantieed by two independent piping circuits in the chemistry distribution system. In addition, separate cabinets for supply and disposal of acid are installed .

The temperature of the acid can be set between 5 C^o and 20 C^o with a massflow up to 20 l/min. The process and the safety interlocks are controlled by a computer to reach high safety and reproducibilty standards. After the etching process the cleaning procedure is finished by an ultrapure water rinse and drying in an ultra clean nitrogen atmosphere.

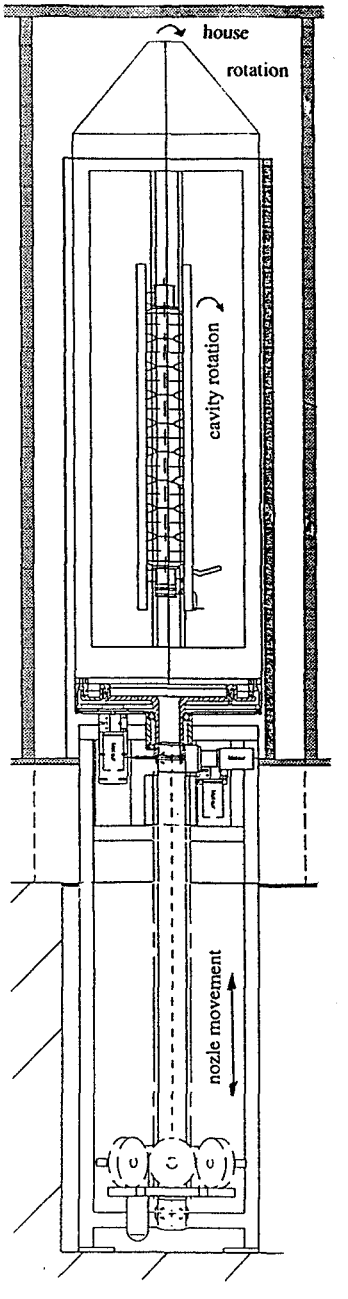

Fig.:8 Cross section of the high pressure rinsing station

Ultra pure water

An ultra pure water plant (UPW) supplies the processes with water of L= 18.2 MΩ cm under particle free conditions .The UPW circuit is equipped with reverse osmosis precleaning, a polisher stand with two mixed bed ion exchangers, point of use particle filters and ultra violet light source to avoid bacteria contamination. A permanent circulation in the pipes, the storage tank and the filters via a separate feedback line provides a minimization of existing death volumina. The storage tank of 4.000 l capacity allows to discharge large quantities of the ultra pure water in short time periodes . The quality of the water is perma-

nentely checked by inline resistivity measurement and a liquid particle counter.

High pressure rinsing and HPP stand

Today, most existing cavities are limited due to electron emission by the RF power consumption of these electrons. A strong reduction of non resonant electron loading was observed after application of high pressure rinsing (HPR) of the surface (Ref. 6) and a treatment of the emitters by high peak power processing (HPP) (Ref. 7)

For HPR a pumpingstation is installed to pressurise the ultra pure water up to 200 bar. A volume of 18 l/min is pressed through 6 one mm diameter nozzles and attacks emitters by the stored energy of the water (Fig.8).

Electron emitting sources, not removable by acid treatment or HPR, can be eliminated by high peak power processing. Pulses of 2 MW power and a puls length of 150 µsec are formed with the klystron. Through a rectangular wave guide and a doorknob ceramic window transition to a coaxial input coupler, the power is transmitted to the cavity. Here acceleration fields up to 100 MV/m can be established during the pulse. These fields lead to strong emission of electrons accompanied by local heating of the emitter. One example of an emitting area after the impact of the HPP RF is shown in Fig.7

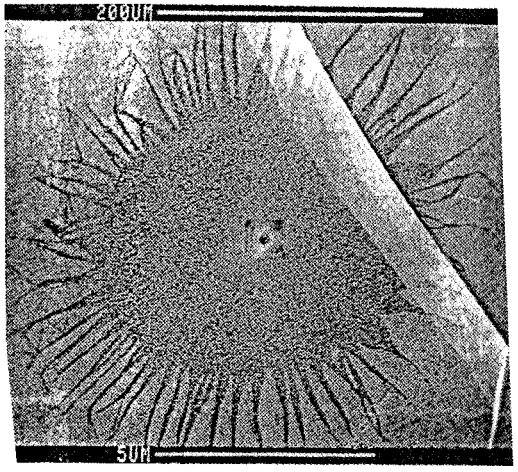

Fig 7. Starburst of an emitter after HPP impact

UHV furnace

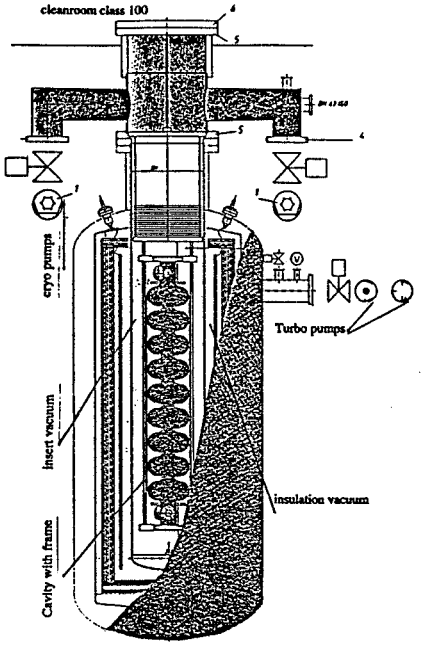

For effective HPP and thermal stabilization of defects, a good thermal conductivity of the niobium bulk material is required (Ref. 9). The UHV oven, as shown in Fig. 8, is installed in the cleanroom of class 100 ASTM . Titanium is evaporated and sprayed on to the niobium at a temperature of 1.400 C^{o} in an vacuum atmosphere of 10^{-7} mbar. The oven is installed in the class 100 area of the cleanroom to retain dustfree conditions for this postpurification as well.

Fig.:9 View of the UHV oven

Comissioning

Two prototype resonator (No-001 and No-002) are fabricated with tools and manufacturing prescriptions foreseen for the production of the 40 TTF resonators. They are in use as commissioning devices for the test facility setup at DESY. To check fixtures, cleanroom assembly , transport systems, test cryostat and computer software, the resonator No-002 was etched,assembled and tested at CEA SACLAY in France, The etching of 100 μm was done by dipping the resonator into an acid tank. Final rinse and assembly of a high Q antenna set up was done under dust free conditions. An acceleration field of Eacc= 6.3 MV/m was measured after this procedure. The maximum field was limited by the available RF power due to heavy fieldemission. After a transportation of about 1000 km the cavity was disassembled and connected to the HPP antenna set up in the DESY cleanroom. During the reproduction measurement with the DESY HPP test stand no degradation , compared to the previous test, was observed.
Resonator No-001 is in use for commissioning of the chemistry plant. A removal of 100 μm was done at an acid temperature of 5 C^{o}. The measurement at 1.8 K showed a limitation at Eacc = 8.5 MV/m due to heavy field emission which can be processed by RF impact. The commissioning of the klystron and the HPP test stand will be done with this cavity without any manipulation on the resonator inbetween.

Test linac

A test linac with a 40 m long accelerator section will be built. This test linac can not provide all parameters of the potential TESLA 500 (Ref. 5). A list of the most important parameters of TESLA 500 and a comparison to the test linac is given in table 1. The TTF linac consists of a 250 keV room temperature injector , a short s.c. structure (15 MeV), followed by a beam analysis area and an optics matching system. The linac itself consists of 4 cryomodules followed by the 500 MeV beam analysis area. Two different types of injectors are planned. Type one will provide the TESLA design current, but not the large bunch spacing. Type two is intended to deliver the bunch spacing and intensity as foreseen in the TESLA 500 machine.

Table 2. TESLA 500-TTF linac parameters

Parameter	TESLA 500	TTF linac
Linac Energy	250 GeV	500 MeV
Accelerating Gradient	25 MV/m	15 MV/m
Quality Factor Q_0	5×10^9	3×10^9
No. of Cryo Modules	many	4
Single Bunch $\Delta E/E$	1.5×10^{-3}	$\approx 10^{-3}$
Bunch to Bunch $\Delta E/E$	10^{-3}	$\approx 5 \times 10^{-3}$
Beam Current	8 mA	8 mA
Macro Pulse Length	0.8 ms	0.8 ms
Injection Energy	10 GeV	10-15 MeV
Lattice β	66 m	12 m
Bunch Rep.Frequency	1 MHz	216 / 1 MHz
Bunch Population	5×10^{10}	$0.023/5 \times 10^{10}$
Bunch Length, rms	1 mm	0.3 / 1 mm
Emittances $\gamma\sigma^2/\beta$	20, 1 μm	3.7 / ??? μm
Beam Size, Injection	60, 20 μm	≈1 mm
Beam Size, End of Linac	50, 12 μm	??? mm

Outlook

The TESLA test facility is built up at DESY by the TESLA collaboration. A total of 40 s.c. resonators will be built and shall accelerate an electron beam up to 500 MeV. The test linac will be installed until 1997 and will give informations about beamparameters, costs and the acceleration gradients for application of superconducting resonators in TeV machines like TESLA 500. Major parts of the hardware necessary for surface treatment and and test of the s.c. structures are in place at the TTF and will be commissioned during 1994.

References:
Ref1. LC 92 ECFA workshop on e+e- linear colliders June 92, Garmisch Partenkirchen
Ref2. A proposal to construct and test prototype superconducting RF structures for linear collider, DESY (April 92)
Ref.3 H. Padamse, priv. communication
Ref.4 B.Aune priv. communication
Ref.5 The TESLA test facility (TTF) - a description of the superconducting 500 MeV linac, H.Weise, EPAC 94 London, to be published
Ref.6 D.Bloess, priv.communication
Ref.7 High peak power processing studies od 3 GHz niobium cavities, J.Graber et al., IEEE particle accelerator conference 91, San Francisco, Vol. page. 2420
Ref.8 H. Padamse, priv.communication.
Ref.9 R.W.Roeth et. al., Proceedings of the second EPAC, EPAC 90, Nice, Vol. 2, Page 1097

*1 components of the acide mixture : HF 40% quality selectipur
HNO_3 65 % quality selectipur
H_3PO_4 85 % quality selectipur

OMIT THIS
PAGE

THIS PAGE INTENTIONALLY LEFT BLANK

Page intentionally left blank

Power and Energy

Chair: Prof. Istvan Kirschner

SINGLE SCAN

51-76

31355

Today's Research Development on the Application of the Superconductivity Transport System in Japan

Yoshihiro Kyotani
TECHNOVA Inc.
Tokyo Japan

Abstract

At the Miyazaki test track today, the new test vehicle, MLU002N, is under test run to obtain necessary data for Yamanashi test track where the construction is underway, the test vehicle has been ordered and the first tunnel was completed in December ' 93.

Superconducting magnetohydrodynamic drive ship,MHDS, "Yamato 1" has completed its experiment in '92 and it is now under preparation to exhibit to the public in '94. Furthermore, to promote the research development of MHDS, the detailed discussion is underway on the magnetohydrodynamic drive equipment as well as the research on the future scheme.

Neither an automobile nor railway but a new transport system called EQUOS LIM CAR(ELC) has been proposed. By using the rotating magnetic field, it will levitate on the aluminum like reaction plate. On the normal road, it will run by rolling the wheels like an electric car but on the highway, it will levitate on the guideway resulting to less noise, less vibration and pollution free drive. To understand the concept of the ELC, the model was built and experimented by using permanent magnet. The same model was donated to the MUSEUM OF SCIENCE AND INDUSTRY in Chicago and was displayed to the public. Today, the trial superconducting magnet has been made and the research development of the subsystem is underway.

Research development of superconducting elevator, equipment for the launching of spaceship, tube transportation system and others are in progress for the superconducting applied transportation system.

SUPERCONDUCTING MAGNETICALLY LEVITATED RAILWAY

Today in Japan, under the supervision of the Ministry of Transportation and with the cooperation of universities and enterprises, Central Japan Railway Company, Japan Railway construction Corporation and Railway Technical Research Institute are promoting the development of the Superconducting Magnetically Levitated Railway, hereunder called SG-Maglev.

Each concerned are aiming as an immediate objective to complete the Yamanashi Test Track. On the other hand, at , Miyazaki Test Track, experiments are progressed by Railway Technical Research Institute to obtain necessary information for Yamanashi Test Track.

In September,' 93, Symposium on ' 93 Central Super Express on the Railway Academic Conference was held at Yokohama with a theme of "Central Super Express and Community".

Miyazaki Test Track: In December '79, 10 meters long weighing 10 tons of test car, ML500, has recorded a high speed of 517 km/h at the Miyazaki test track. With this test, passengers loadable test car, MLU001 with 3 carriage cars,were trial manufactured.

By using MLU001, it has been confirmed that the travel stability will increase when the connection cars are added and also traveling characteristics were obtained. In September '82, manned testing run has started. Then in February '87, after increasing the capacity of electric power supply facilities, I was onboard on the 2 carriage car and reached the high speed of 401 km/h.

In March '87, to promote more practical use of test car, MLU002 was completed and exhibited to the domestic and international related media by Japan National Railways(JNR). In November '89, it has reached the high speed of 394 km/h.

In the case of MLU001, superconducting coils are placed equally in chain under the car while with MLU002, superconducting coils are concentrated under the front and back edge of the car. In considering the concept of the commercial cars, this was due to reduce the air resistance and the magnetic field effect to the passengers. On the other hand, instead of placing levitate coils on the running track of the guideway as an opposite direction levitation, the research on placing levitate coils at the side of the wall levitate method is under study.

Not only of the concentrated placement but also to stimulate the test of the side wall levitate method test started in June '91. As a result, the block of side wall levitate method was further extended to obtain necessary information for the Yamanashi test track but in October, same year, MLU002 had a fire accident and became inapplicable.

The fire accident of MLU002 was a regret but with the effort of the people concerned and the enthusiasm of many people related to the materialization of SC-Maglev, the new MLU002N was manufactured and started its test from January '93. MLU002N has a length of 22m, width 3m and weighs 19 tons. In February '94, MLU002N has recorded high speed of 431 km/h at Miyazaki test track.

Yamanashi Test Track: West of Tokyo between Sakaigawa Mura, Higashi Yashiro Gun, Yamanashi Pref. and Akiyama Mura, Minami Tsuru Gun, of same prefecture is the extension of 42.8 km Yamanashi test track now under construction. (Fig.1) In order to speed-up the commencement of the test run, the proceeding block of 18.4 km were decided and started its construction .

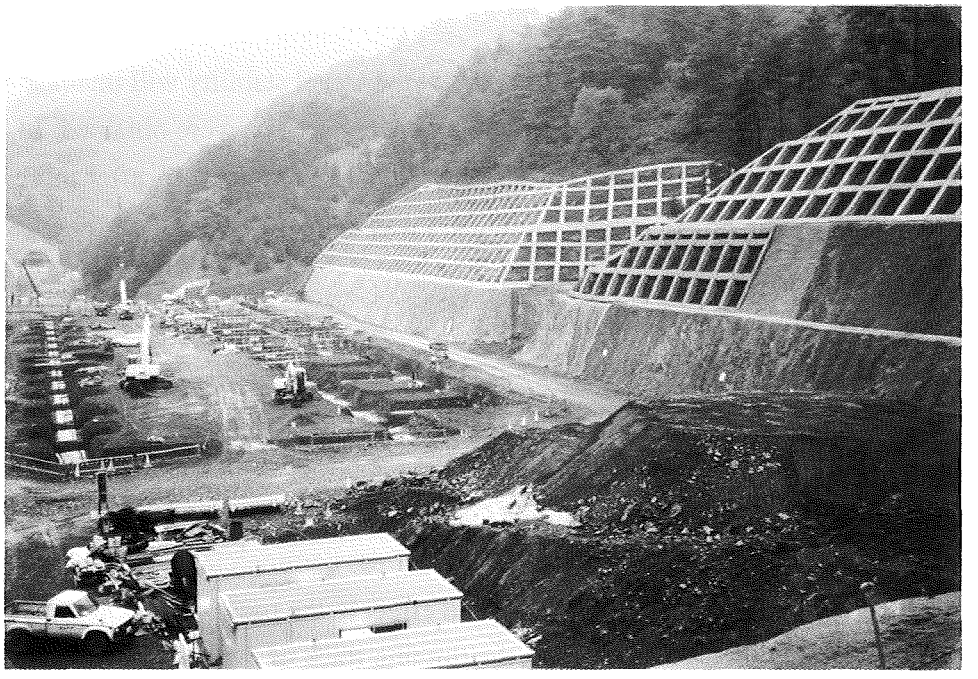

Fig.1 Yamanashi Test Track, Under construction

The standard construction technologies are, maximum speed, 500 km/h, minimum curved line radius, 8,000 m, maximum grade 4%, center track interval, 5.8 m. As to the main construction work, about 35 km are tunnels, 8 km out of tunnel,1 test center, 2 substations and 1 train base.

According to the information as of April '94, progress of land purchase situation on the proceeding block is 92 %, tunnel excavating situation on the proceeding block is 95 %, that is, 15 km have completed its excavation out of about 16 km. Proceeding block will start its test In Spring '96 and is scheduled to complete its test by '98.

As for the test cars,the manufacturing of 2 composed train of 5 carriage cars and 3 carriage cars are underway and each are cars composed of connecting flatcar.

TUBE TRANSPORTATION SYSTEM(TTS)

While the research development of Tokaido Super Express Line was on progress, there was a need for further research about the train's air dynamics and the space security of the train. I had the same thought while research development was in progress at the time of SC-Maglev and so I thought about running it in the vacuum tube. After a very rough estimation, the conclusion was that if the speed reaches over 600 km/h, the effect of vacuum tube will be larger and therefore the development of the SC-Maglev, aiming its maximum speed to 500 km/h, will not adopt the vacuum tube system.

But, recently the global issues of green house effect and the environmental as well as energy problems became a big issue.

So, I have proposed a Tube Transportation System (TTS) having the section as shown on Fig.2.

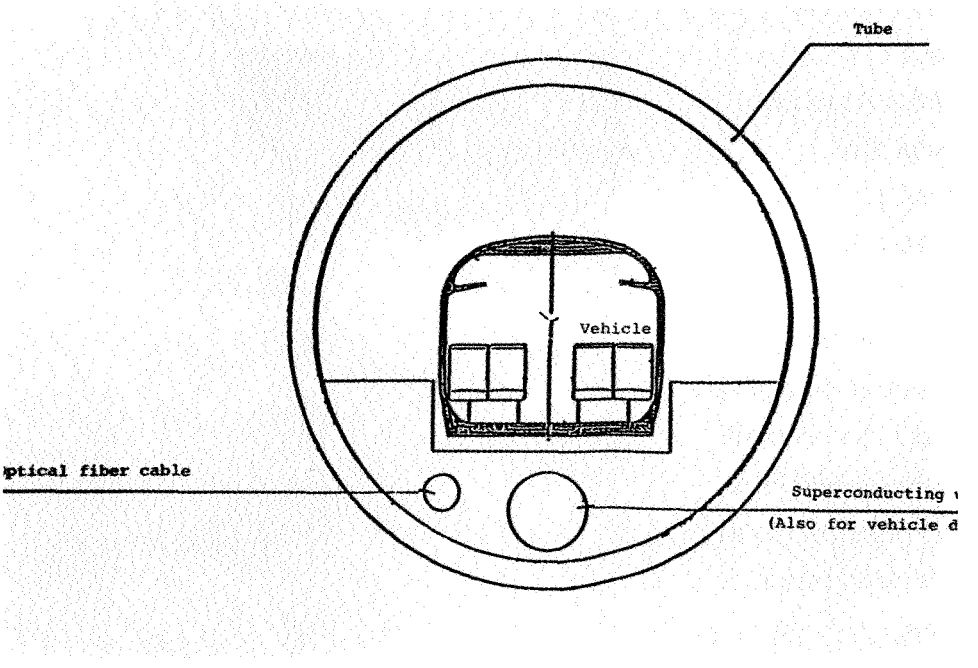

Fig . 2 Section of Tube Transportation System

This system is to store carriage of passengers and products using SC -Maglev, transfer of electric power using superconducting(SC) power transmission and transfer of information by using optical information transfer cable.

In order to examine in detail, optimistic supposition like maximum speed 3,700 km/h, minimum radius 10,000 m and maximum grade 4 % were obtained .

First, 3 routes connecting Tokyo and London was considered , via Northern route, passing through Central China' s Central route or via Yellow Sea and coast of Indian

Ocean route of South route. The route Tokyo and London is a route connecting East and West, so the route of South and North was also considered. To connect with the above studies, hypothesis of London and Buenos Aires route was considered.

Then, in order to plan the development of the countries deeply involved to Japan Sea, Pacific Rim Japan Sea Concept was proposed and investigated. Then, adding the views of those people of China and Taiwan, who have the strong interest on this Japan Sea Rim Concept, a hypothesis route shown in Fig.3 has been investigated. We call it "East Asia Corridor Route" tentatively. The total distance of this new route will be 10,000 km, the distance of mountain tunnel occupies 24.8 %, under water tunnel will be 17.0 %. The objective of time around this route will be 3 hours.

The commercialize opening of tunnel link between Britain and France channel this year will be the starting point of this concept .

In order to materialize this concept, the cooperation of professionals of superconductive and macroengineering as well as experts from many fields are essential but above all major necessity will be to raise the awareness of this concept to many people of the world.

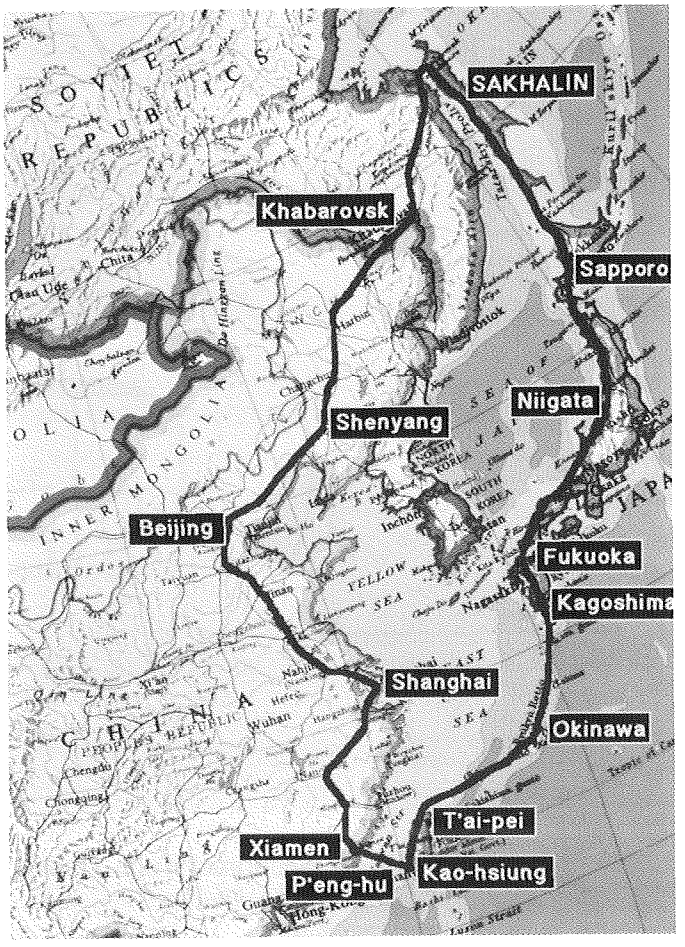

Fig.3 East Asia Corridor Route

SUPERCONDUCTING MHD PROPELLED SHIP

Japan Foundation for Shipbuilding Advancement , later called 'Ship and Ocean Foundation" has started its research development of SC-MHDS and as result of the basic research, it has reached to the point of corroboration, building and testing the demonstration ship "Yamato 1".

"Yamato 1"will be mentioned at the other session. I had an opportunity to take the wheel of this ship and was surprised of its quiet and smoothness which entertained a big dream on the future of this SC-MHDS.

Research development of "Yamato 1" had a great purpose in the expansion of large superconducting magnet and cryogenic device. In order to further promote this research development to suit the lighter and powerful superconducting magnet, there still is a need to research the formation device such as cryogenic device.

The success of "Yamato 1", as a complete new propulsion system, has great expectation and concern. On the other hand, how this development will embodiment in the stage of future development, it is necessary to forecast the future view on technology, transport system,and the need of society now. Having these as a base, to establish condition to possess SC-MHDS in future, the target will be on island route for tourism and urban route for passengers. As a model of the ship, double bodied supporting type lift for tourism and submarine type for urban life and are shown as an example on Fig.4.

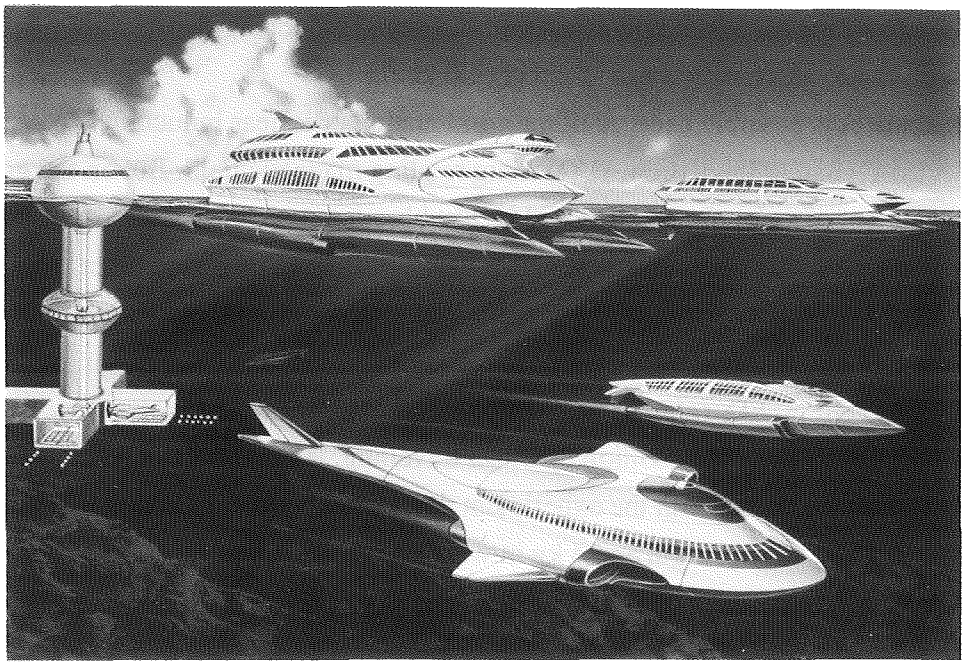

Fig.4 Future Ship

EQUOS LIM CAR(ELC)

Railroad, in a broad sense guided ground transportation, is a transportation system that runs with something by a ground guided system and has an advantage to run safely on a high speed with connected carriage but the guided line(rail)is limited and cannot move freely. On the other hand, automobiles have an advantage to run freely but has to head the vehicle to the direction by holding the steering wheel, which has a limit to the speed in human driving. Also, it is difficult to drive connecting many cars like a carriage. So I have investigated a vehicle having the advantage of both railroad and automobile.

Intelligent of many countries are making a research and soon automobiles will be electrified and automated. This direction is without fail definite and it would be an opportunity to make research development of "new vehicle" which is neither an "automobile" nor a "railroad".

From the experience of the research development of small SC-motor with SC-Maglev, I have thought that the future automobile will be an electric car and its implant will be rotating SC-motor or linear motor and therefore, I thought of combining these two motors for this new vehicle.

When driving in the city it will run as an usual automobile, rotating the wheels with rotating superconductive motor which will result to no vibration, noiseless and pollution, free. But on the highway, when the rotation of wheel is speeded, vehicle will levitate and run with high speed. At this moment the guide power works in between the ground and the car and it will direct without anyone touching the steering wheels. It is not a dream to reach maximum speed of 500 km/h.

This concept is possible because of the combination of Linear Induction Motor (LIM) and Electro-Dynamic Levitation (ED) using rotating magnetic field. But on the ground an arrangement of a electric conductor plate like aluminum plate is required.

A vehicle with this new concept is called EQUOS LIM CAR and in order to confirm the possibility of this concept, we have made and experimented a model shown in Fig.5 with EQUOS RESEARCH CO. On this experiment, permanent magnet was used to see the wheel travelling, ED, rotating magnetic field transfer with LIM propulsion

We have confirmed the condition of wheel travelling, levitation, levitated travelling, landing, wheel travelling with the experiment device of about 26 m.long guideway with a model car of 50 cm in length and 4 kg in weight.

So far, we made research investigation on cryogenic device, onboard electric source as well as research on superconducting magnet needed for the future vehicle. Even for the guide, the research and experiment on the basic experiment device have only started. In order to make practical use of ELC,the best solution will be to make further research development and to let many people to know and be acquainted with this new vehicle. As a result, it is necessary to continue the research development of superconducting magnet, cryogenic device, electric source device, simultaneous use of permanent magnet and to make use of this concept, for example by promoting the development of a vehicle at the amusement park and to develop racing cars .

Also, to design the model of this concept is not as difficult to produce as it is thought. It is like remodeling the commercialized automobile. As to the guideway, it is more simple than producing railroad model. If a circuit race course with the model automobile could be made, it will be more enjoyable.

As for the automobiles, we are approaching to the age of genuine object. Not only electrified but without stirring wheel automobile free to travel anywhere with super high speed levitated travelling which will be enjoyable. ELC can make this dream come true and what is more, it can also run on non conductive guideway.

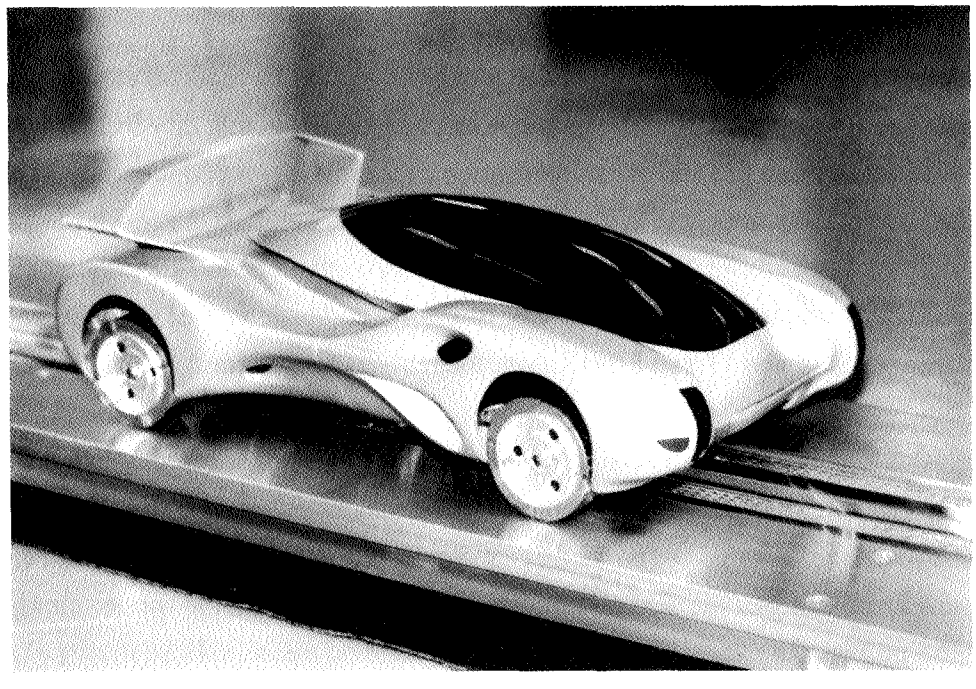

Fig . 5 Conceptual Model of EQUOS LIM CAR

SUPERCONDUCTING CORRIDOR

So far I have mentioned the major transportation system applying superconductive. For the development of large machinery as well as transportation system, the sustenance test of actual structure is needed. Since the same thing could be said for the applied equipment of superconductive, the large scale test installation and support of big financial capital are needed.

The cities in the past have collected all kinds of functions and many people gathered to make use of its convenience which formed a city. There are cities developed as a center for politics, administration, economics, commercial, industries, transportation and tourism. Furthermore in order to develop the region, countries around the world are considering to form a distinguished city furnished with special faculty. For example, Hong Kong has developed as the free port for economy and the second and the third Hong Kong are considered.

High technologies and new materials as well as superconductive will provide affect on future technology, industry or even in a broad sense economy. The research development of high technologies and new materials must be opened to the public all over the world for the need to promote further research development.

Gathered the thoughts as mentioned above, I have proposed a thought of one city and named and announced it as a "Superconducting City".

Later, part of content was published in a magazine and I have received a commission on research investigation as to the application of superconducting city from Iwaki City in Fukushima Prefecture and as an interim report, I drew a superconducting city concept based on Iwaki City. With this concept drawing, adding the result of investigation research related to the underground development and superconducting magnetically propulsion ship from Power Reactor And Nuclear Fuel Development Corporation, Ship and Ocean Foundation, the revised concept drawing is shown on Fig. 6.

Below SMES is SC-Maglev and down left is the picture of superconducting linear elevator. The building under the water is the terminal for submarine type SC-MHDS and the link to the ground for passengers and cargoes will be SC-linear elevator. The sky scraper building in the center has a height over 1,000m, and the former elevator will have the problem of rope weight and have to change on the way. If SC-linear elevator is used, there will be no need to change lift on the way because there will be no rope used and also, it can pass over like a railroad and can reduce the surface area occupied. In Japan, other than SC-linear elevator research development of normal conducting linear elevator is in process.

The small picture at the right top of the drawing is the amusement park applying superconductive and the building at the right is the hospital equipped with superconductive applying equipment and the building on the left to the amusement park is the information transmission center equipped with superconductive applied equipments.

It is my dream to build a city where research development is free and I would like to open this city to the world as a liberal city of technologies where any people are free to enter for the happiness of the humankind around the World.

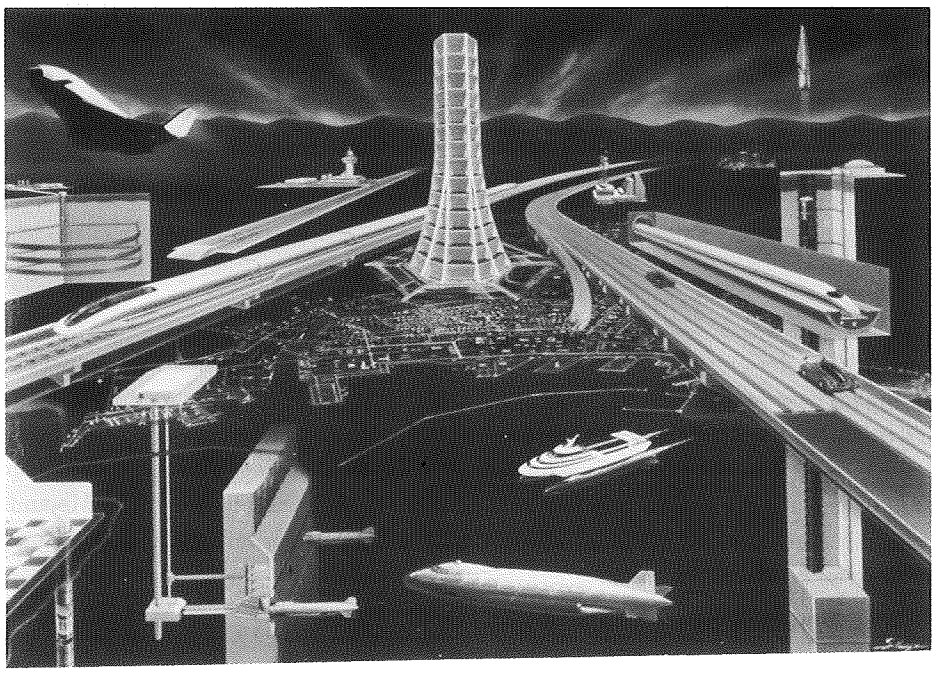

Fig.6 Superconducting Corridor

CONCLUSION

The application of superconductive is ranging in the wide field. Especially the transportation field is expected to make a big change. If the high temperature superconductive is to materialize, the change will make further development. It will be my most concerned and appreciation, if the application of superconductive leads to the solution of the global issues of environment and energy.

Silver Scan
S12-76
313623

MEASUREMENT AND CALCULATION OF LEVITATION FORCES BETWEEN MAGNETS AND GRANULAR SUPERCONDUCTORS

T.H. JOHANSEN, H. BRATSBERG, M. BAZILJEVICH, P.O. HETLAND and A.B. RIISE

Department of Physics, University of Oslo.
P.O. Box 1048, Blindern, 0316 Oslo 3, Norway.

Abstract – Recent developments indicate that exploitation of the phenomenon of magnetic levitation may become one of the most important near-term applications of high-T_c superconductivity. Because of this, the interaction between a strong permanent magnet(PM) and bulk high-T_c superconductor(HTSC) is currently a subject of much interest . We have studied central features of the mechanics of PM-HTSC systems of simple geometries. Here we report experimental results for the components of the levitation force, their associated stiffness and mechanical ac-loss. To analyse the observed behavior a theoretical framework based on critical-state considerations is developed. It will be shown that all the mechanical properties can be explained consistently at a quantitative level using a minimum of model parameters.

1. INTRODUCTION

A quantitative understanding of how the nonuniform fields of permanent magnets(PMs) magnetizes bulk high-T_c superconductors(HTSCs) stands central in developing levitation-type applications like frictionless bearing for rotors, torque couplers, vibration dampers etc.[1-3] It is also a key to understand how replicas of magnetic structures can be made using HTSCs.[4] One approach to these issues is to investigate various aspects of the magnetic force acting between PMs and HTSCs.

From magnetomechanics[5] a PM producing a field $\mathbf{B}_a$ will experience a force from a volume V of magnetization $\mathbf{M}$ equal to

$$\mathbf{F} = \int_V (\mathbf{M} \cdot \nabla)\, \mathbf{B}_a \, dV \ . \tag{1}$$

Thus the force results from two distinct factors; i) the magnitude of the magnetization which in the case of superconductors is determined by the distribution of persistent shielding currents, and ii) the degree of inhomogeneity in the applied field. Since the field produced by PMs of simple shapes can be readily computed, one should in principle be able to discuss all aspects of the levitation phenomenon once the magnetization behavior of the HTSC is at hand. However, in the literature one finds that analyses of this kind are most often carried out on a very general and qualitative basis. Although some model calculations have been reported[6-8] a physical picture that consistently describes at a quantitative level the various properties of the interaction is still lacking.

We have performed a series of measurements to reveal the detailed behavior of several central features of levitation forces. System configurations of sufficient simplicity were chosen in order to compare the observed behavior with analytical calculations. In this paper we describe the results of our investigation.

2. VERTICAL FORCE

The experimental set-up designed to measure the vertical force is shown in fig.1. The fully computerized apparatus uses a Mettler AE240 Delta Range electronic balance as force sensor. The

force versus distance measurements were done after the HTSC sample had been zero-field cooled to 77K in liquid nitrogen. Both the PM and HTSC were shaped as rectangular bars, and mounted in a configuration shown in detail below.

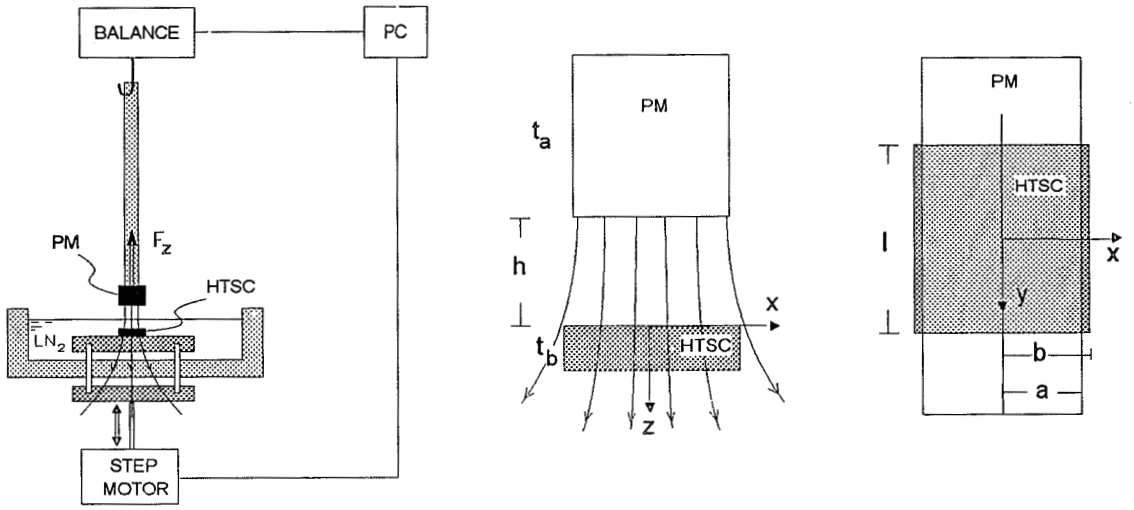

Figure 1: Apparatus to measure the vertical force between a PM and HTSC(left).
Magnet-superconductor configuration viewed along the y-axis(middle) and seen from above(right).

Using a step motor stage the force was measured while raising the HTSC towards the PM, starting from a distance $h = 20$ mm. At each point the collection of data was delayed in order to allow relaxations to decay below the 0.1mg resolution of the balance. At every millimeter the steady motion was interrupted for a reverse displacement of 15 μm. This added a set of minor loops in the F_z versus h curve. The result of the entire experiment is shown in fig.2(left).

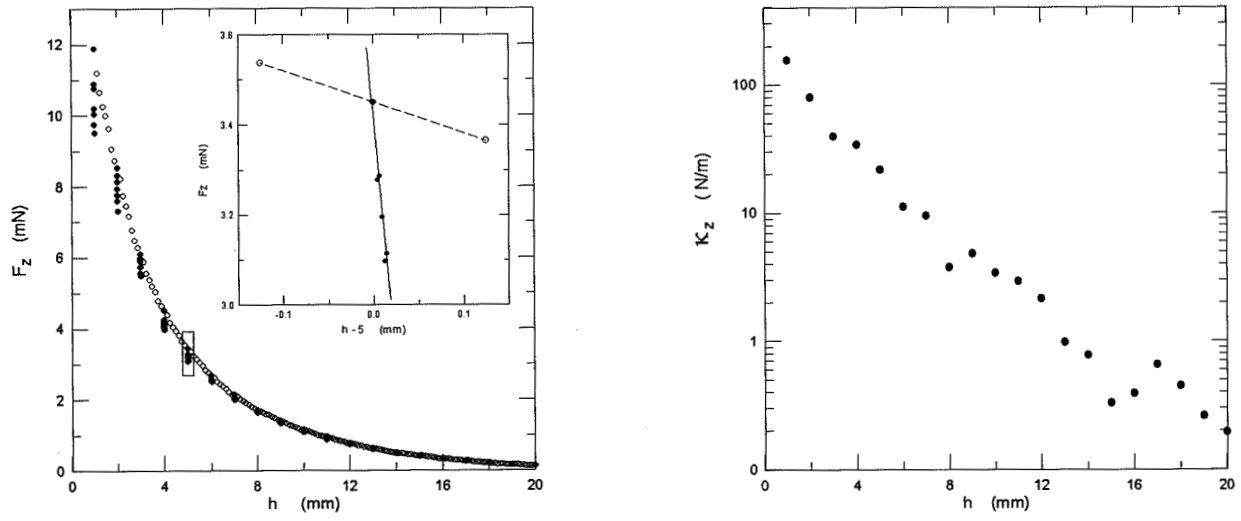

Figure 2: Vertical force as a function of PM-HTSC distance.(left) The insert shows a close-up of a minor loop. The magnetic stiffness versus levitation height is shown on the right.

The irreversible nature of the PM-HTSC interaction causes the minor loops to form an angle with the major curve. Thus, the spring constant, or stiffness, governing vibrational motion

needs to be determined separately. Note that hysteretic behavior can not be seen in the minor loops themselves, which make such small-amplitude oscillations essentially loss-free.[9] The vertical stiffness,

$$\kappa_z = -\frac{\delta F_z}{\delta h} ,$$

found as the slope of a line fitted to the individual minor loops is plotted in fig.2(right). The stiffness covers a range of 3 orders of magnitude, which makes it a parameter that varies much stronger than the force itself.

3. MODEL CALCULATION

The HTSC used in this study is made of $YBa_2Cu_3O_{7-\delta}$ prepared by a conventional sintering method. In order to construct a realistic model for our sample it is necessary to know, at least at a qualitative level, how an external field is penetrating the HTSC. In other words, what is the pattern of the induced shielding currents. An effective method to investigate this central point is to use a magneto-optic vizualization technique based on the Faraday effect in iron-garnet films with in-plane anisotropy.[10]. A plate serving as substrate for the thin indicator film is placed directly on the surface of the HTSC which is mounted in an optical cryostat. The contrast in the picture seen in a microscope with crossed polarizers gives an analoge representation of the perpendicular flux density at the HTSC surface.

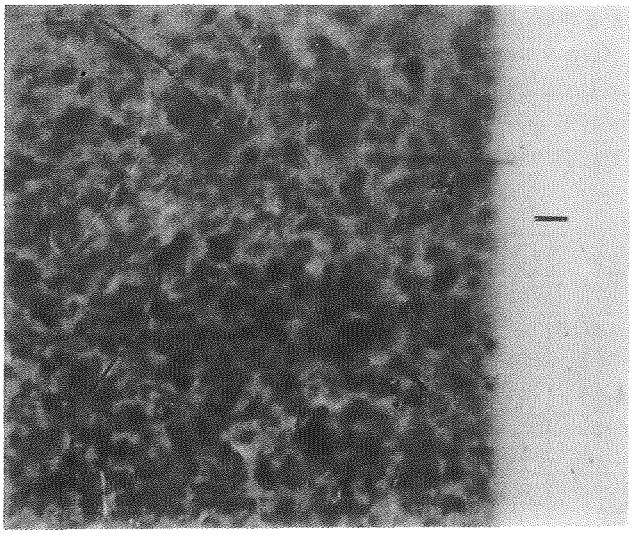

Figure 3: Magneto-optic image of flux penetration in our HTSC sample. The scale-bar is 100 μm long.

Figure 3 shows the image of our z.f.c. HTSC placed in an external field of 15mT at 15K. The edge of the sample is seen as the vertical line dividing the picture into two distinct regions. The uniform region to the right represents the intensity of the external field. In the left part one sees a complex structure of areas having nearly the same light intensity as outside the sample. The dark parts are regions of low flux intensity, i.e., where the superconductor is well shielded from the field. The HTSC can therefore be characterized as a magnetically porous material where the applied field leaks through the intergranular space, and thereby surrounding the grains which carry the shielding currents.

Evidently, it is formidable task in the calculation of levitation forces to account in detail for such complex magnetic structures as seen in the magneto-optic image. On the other hand, in the

present force experiments the size of the magnet is too large to feel the effect of individual grains, and one can therefore simplify the treatment by using a locally averaged magnetization. In the geometry of fig.1 this magnetization will be essentially vertical.

The dimensions of the HTSC sample are $t_b = 1.7$mm, $b = 3.4$mm and $l = 11.9$mm. The PM is made of Nd-Fe-B with a remanent induction of B_r=1.05T, and measures $a = 2.8$mm and $t_a = 6.0$mm. The length in the $y-$direction is 17mm, which is long compared to l, and hence the applied field is close to that of an infinitely long bar magnet, $\mathbf{B}_a = (B_x, 0, B_z)$, where

$$B_x(x,z) = \frac{B_r}{4\pi} \ln \frac{[(z+h)^2+(x+a)^2]\,[(z+h+t_a)^2+(x-a)^2]}{[(z+h)^2+(x-a)^2]\,[(z+h+t_a)^2+(x+a)^2]} \ , \tag{2}$$

$$B_z(x,z) = \frac{B_r}{2\pi}\left(\arctan\frac{z+t_a+h}{a+x} + \arctan\frac{z+t_a+h}{a-x} - \arctan\frac{z+h}{a+x} - \arctan\frac{z+h}{a-x}\right) . \tag{3}$$

Making use of the approximation $\mathbf{M} = M(x,z)\,\hat{\mathbf{z}}$, the vertical force component equals

$$F_z = l \int_0^{t_b} dz \int_{-b}^{b} dx\, M \frac{\partial B_z}{\partial z} \ . \tag{4}$$

In order to make the calculations analytically tractable we will treat the HTSC as a system consisting of a large collection of decoupled grains, each behaving in accord with the critical state model.[11] The presence of pinning centres causes a gradient in the internal induction, which by Ampere's law is associated with an azimuthal current of density j_c. Figure 4 illustrates schematically the model behavior at various stages of the levitations force experiment.

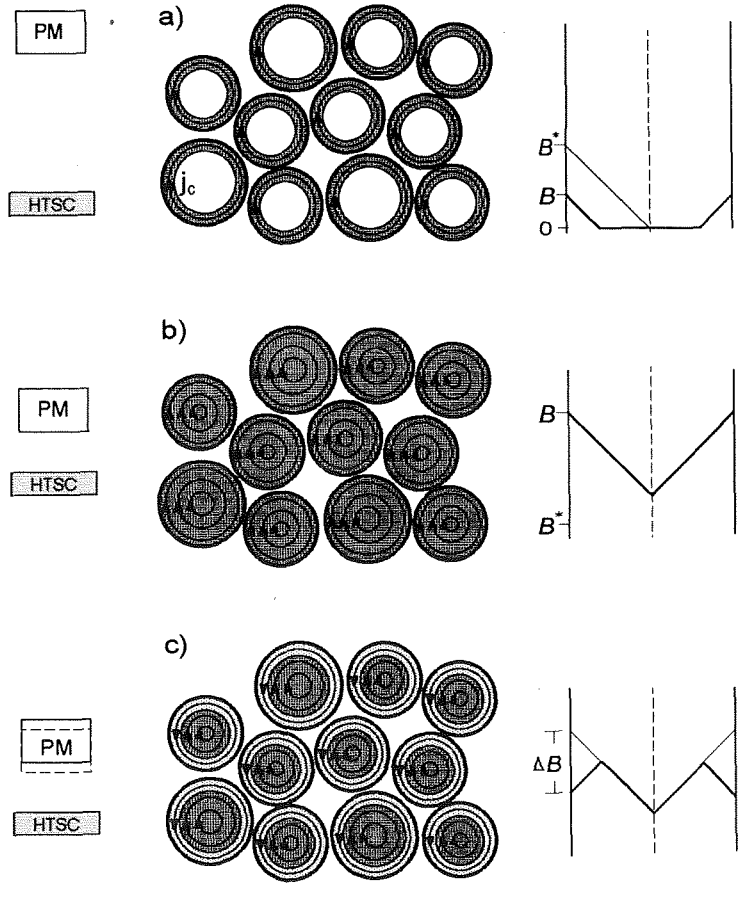

Figure 4: The decoupled grain model. a) Incomplete intra-granular flux penetration at a large PM-HTSC distance. b) At smaller distances the critical state is fully developed in the grains. c) After a small increase in PM-HTSC distance an outer layer of reversed j_c is formed.

Under conditions where essentially all grains are saturated with j_c, as in fig.4b, the magnetization can be considered uniform over the entire volume. In this case eq.(4) simplifies to

$$F_z = -M\ l \int_0^{t_b} 2\ B_x(b,z)\ dz\ . \tag{5}$$

Since the HTSC sample is relatively thin we make use of the approximation

$$F_z(h) = -2\,l\,t_b\,B_x(h)\ M\ , \tag{6}$$

where $B_x(h) \equiv B_x(b, t_b/2)$ in eq.(2).

Conditions of saturation can be expected to be realized at points on the enveloping part of the F_z versus h curve of fig.2 at the small-to-intermediate distances. Here the magnetization will be proportional to j_c. Since j_c is known to depend on the field it is instructive to make a parametric plot of $-M$, where

$$-M = \frac{F_z(h)}{2\,l\,t_b\,B_x(h)}\ , \tag{7}$$

against the applied field at corresponding values of h. This is done in fig.5, where the B-axis denotes the field at the centre of the sample, i.e., $B_z(h) \equiv B_z(0, t_b/2)$ in eq.(3).

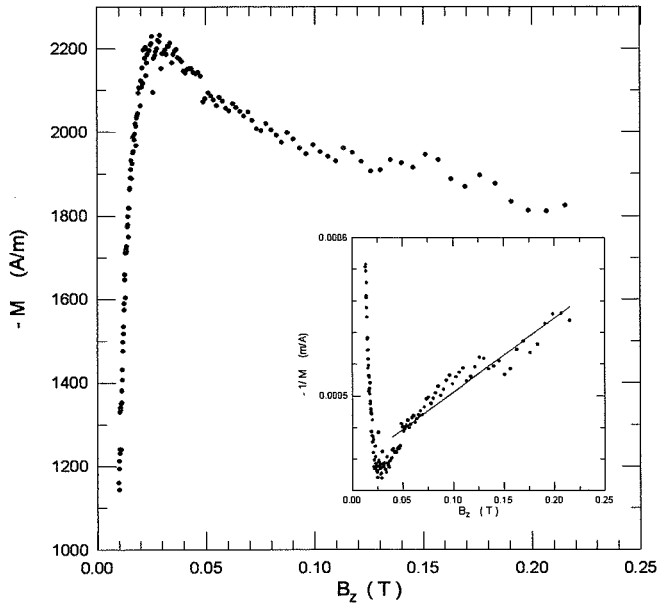

Figure 5: Parametric plot of the infered magnetization, eq.(7), against the applied field at the HTSC centre.

We see that $-M$ displays a clear peaked behavior, which can be understood as follows. As the HTSC approaches the PM the increasing applied field gradually magnetizes the grains. This gives rise to the steep positive flank of the curve. Saturation appears to occur near $B_z = 0.025$T, where $-M$ reaches its maximum. Above the maximum the field-dependence of j_c leads to a monotonic reduction in the magnetization. To quantify this behavior we use a form

$$-M = \frac{M_0}{1 + B_z/B_0}\ , \tag{8}$$

as in the Kim model.[12] The two parameters, M_0 and B_0, were determined by fitting a straight line to $1/M$ in the region indicated in the insert. This gave $M_0 = 2195$ A/m and $B_0 = 0.97$T.

By combining eq.(6) and (8) one can calculate the levitation force as function of the height h. The result is shown in fig.6 together with the enveloping part of the force data in fig.2. The

theoretical curve describes the behavior excellently from the smallest h and up to about 13mm. At larger distances a deviation starts appearing as a consequence of the non-saturation conditions, see fig.4a, existing at such small applied fields.

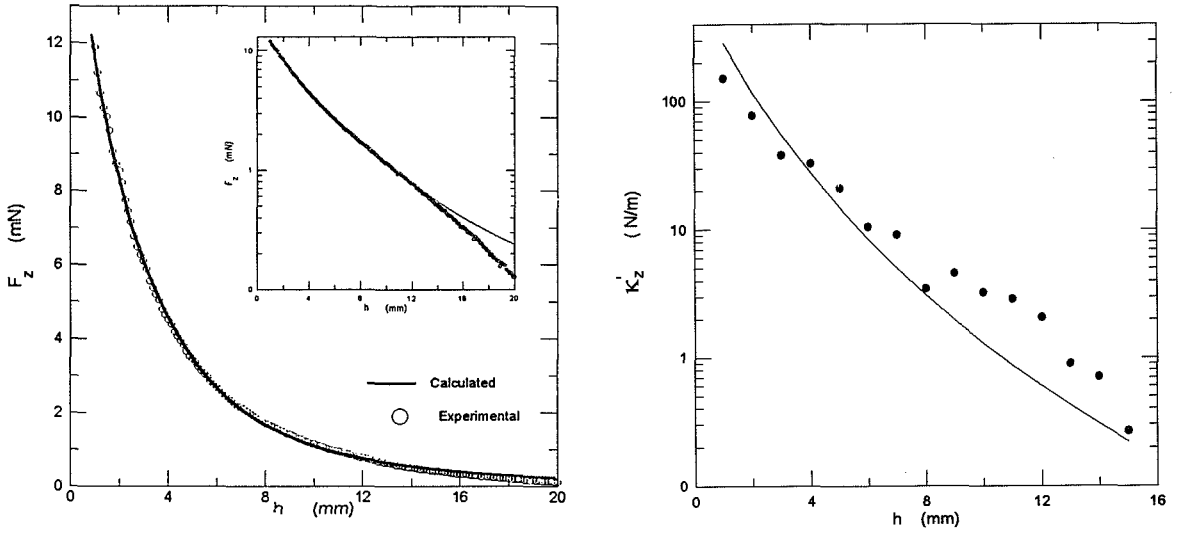

Figure 6: Measured levitation force together with fitted theoretical curve.(left) Semi-logarithmic plot of the vertical stiffness, κ', and the prediction of eq.(13).(right)

During the reversed vertical displacement producing the minor loops in fig.2, each grain will experience a reduction in the field. Some flux will pour out of the grain and establish in an outer layer a flux density gradient of opposite sign. As illustrated in fig.4c, this layer will now have j_c circulating in the reverse direction, giving a positive addition to the magnetization. If we for simplicity assumes that the grains have the shape of long cylinders the critical state model gives to first order

$$\mu_0 \Delta M_{grain} = |\frac{\partial B_z}{\partial z}| \, \Delta h \, . \tag{9}$$

After the PM-HTSC distance has been increased from h_0 to $h_0 + \Delta h$ the magnetization can then be written

$$M(h_0 + \Delta h) = M(h_0) + \frac{f_s}{\mu_0} |\frac{\partial B_z}{\partial z}| \, \Delta h \, , \tag{10}$$

where f_s is the volume fraction of the superconducting material. Again the force, $F_z(h_0 + \Delta h)$, can be found from eq.(4). If the state of magnetization at h_0 corresponds to saturation, i.e., $M(h_0) = -M_{sat}$, we get

$$F_z(h_0 + \Delta h) = l \int_0^{t_b} dz \int_{-b}^{b} dx \left(-M_{sat}(h_0) + \frac{f_s}{\mu_0} |\frac{\partial B_z}{\partial z}| \, \Delta h \right) \frac{\partial B_z}{\partial z} \, , \tag{11}$$

where the last gradient factor is evaluated for $h = h_0 + \Delta h$. Since the saturation magnetization varies slightly with $B_z(h)$ we write $M_{sat}(h_0)$ as $M_{sat}(h_0 + \Delta h) - (\partial M_{sat}/\partial h)_{h_0} \Delta h$. The first term here gives in eq.(11) the force at $h_0 + \Delta h$ on the enveloping curve. The two terms proportional to Δh quantifies how the stiffness deviates from the slope of the envelope. Using eq.(8) to represent M_{sat} one finds that the $\partial M_{sat}/\partial h$-term is negligibly small, leaving

$$\Delta F_z' = -\frac{f_s}{\mu_0} \, l \int_0^{t_b} dz \int_{-b}^{b} dx \left(\frac{\partial B_z}{\partial z} \right)^2 \Delta h \, , \tag{12}$$

to describe the angle of a minor loop. This irreversible reduction in the force gives the contribution to the stiffness

$$\kappa_z' = -\frac{\Delta F_z'}{\Delta h} = \frac{f_s}{\mu_0}\, 2\, l\, t_b \int_0^b \left(\frac{\partial B_z}{\partial z}\right)^2 dx\ . \tag{13}$$

Again, since our sample is thin we multiply here by t_b instead of integrating over z, and evaluate the gradient at $z = t_b/2$.

Using the data of fig.2(left) the experimental κ_z' was derived and compared with the theoretical result, eq.(13). Note that this comparison only allows for an adjustment of the prefactor,f_s, and is therefore a strong test of the physical model. Figure 6(right) shows the outcome of this procedure carried out for $h \leq 15$mm. The good quantitative agreement was obtained using $f_s = 0.8$, a most realistic value. The irreversible part κ_z' differs only very slightly from the full κ_z. Thus, from our analysis we conclude that the vertical stiffness is essentially independent of the actual magnetization of the HTSC. Geometrical parameters together with the gradient of the applied field are the most important.

4. HORIZONTAL INTERACTION

It is a well known feature of the PM-HTSC interaction that it can provide lateral stability, i.e., a horizontal restoring force will prevent e.g. a magnet to fall to one side when it is placed levitating above a superconductor. In a previous work we investigated[13] this stabilizing force together with the stiffness that governs lateral vibrational motion. We include these experimental results here to show that the theoretical framework developed in the previous section also describes the behavior of the horizontal interaction.

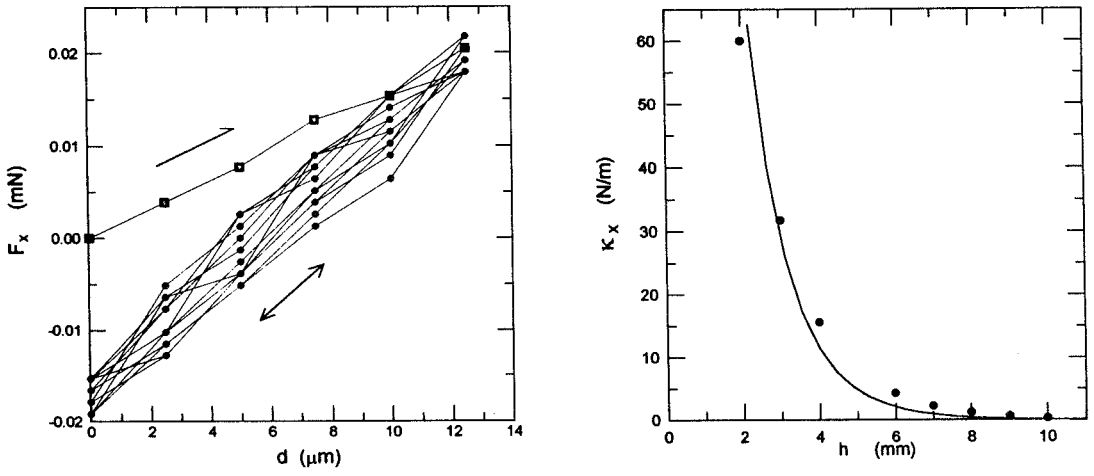

Figure 7: Horizontal restoring force versus displacement(left) together with experimental and theoretical horizontal stiffness, κ_x, as function of levitation height.(right)

Figure 7(left) shows the observed behavior of the lateral force during a virgin horizontal displacement followed by small-amplitude oscillations. The positive slope of the unique virgin branch quantifies the lateral stability of the system. On return to $d = 0$ the F_x becomes negative. The subsequent oscillations produce a linear force–displacement relation with a steeper slope that represents the lateral stiffness κ_x. The experiment was done using the same HTSC-PM system as in the previous sections, also now providing z.f.c. to 77K. The distance was here $h = 7$mm, and the

initial position, $d = 0$, corresponds to the symmetrical configuration of fig.1. The measurements were repeated at different distances to find the h-dependence of the stiffness, fig.7(right).

We calculate the lateral force from

$$F_x = \int_V M \frac{\partial B_x}{\partial z} dV = l\, t_b \int_{-b}^{b} dx\, M \frac{\partial B_z}{\partial x} . \tag{14}$$

where, as before, the thin sample approximation was used. Note immediately that for the initial symmetric position F_x vanishes since M is symmetric in x and $\partial B_z/\partial x \equiv g(x)$ is antisymmetric.

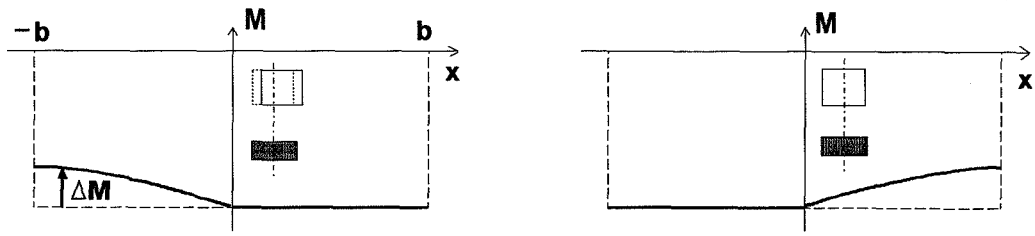

Figure 8: Profile of the magnetization after a lateral displacement of the magnet (left), and after completing one displacement cycle(right). In the model $\Delta M = f_s|\Delta B_z|/\mu_0$ is the deviation from uniform magnetization, $-M_{sat}$.

When the magnet is displaced a small distance d, the lateral shift in the field profile implies that B_z increases for $x > 0$ and decreases for $x < 0$. To 1. order the field change is

$$\Delta B_z = B_z(x-d) - B_z(x) = -g(x)\, d \ .$$

This will cause an asymmetry in $M(x)$ which we can evaluate as follows. Consider two grains located symmetrically on each side of $x = 0$. Initially, they both experience the same applied field, which we assume induces a negative magnetization corresponding to saturation. For the present range, $h \leq 10$mm, this is an assumption consistent with the analysis in section 3. After the lateral displacement the grain at $x < 0$, due to a field reduction, aquires an additional magnetization, $|\Delta B_z|/\mu_0$, whereas the grain at $x > 0$ remains in saturation since the field there has increased. The resulting M versus x is shown in fig.8(left). For $x < 0$ one has

$$M = -M_{sat} + \frac{f_s}{\mu_0}\, g(x)\, d \ .$$

One also has to take into account that the gradient $\partial B_z/\partial x$ has been shifted by d. To 1. order it is now $g(x-d) = g(x) - g'(x)\, d$, giving

$$F_x(d) = l\, t_b \left(\frac{f_s}{\mu_0} \int_{-b}^{0} [g(x)]^2\, dx \ - \ 2M_{sat}\, |g(b)| \right) d \ . \tag{15}$$

This describes the virgin force behavior, and represents a stabilization since the magnitude of the first term is much larger than the second.

To find the stiffness one needs to consider the effect of reversing the magnet motion. With the PM back to $d = 0$ the grain at $x < 0$ will have experienced one complete minor loop and has restored its state of saturation. On the other hand, a grain at $x > 0$ will experience a field reduction, and add a positive part to the magnetization. The new profile of M is shown in fig.8(right). Here the field gradient is once again the fully antisymmetric $g(x)$, and one gets

$$F_x(d=0) = -l\, t_b \left(\frac{f_s}{\mu_0} \int_{0}^{b} [g(x)]^2\, dx \right) d \ , \tag{16}$$

which describes the minimum force seen in fig.7(left)

By repeating this displacement cycle the magnetization will alternate between the profiles of fig.8, and F_x will oscillated linearly between the two extremum values given by eq.(15) and (16). The stiffness is therefore equal to

$$\kappa_x = \frac{F_x(d) - F_x(d=0)}{d} = 2\,l\,t_b\,\left(\frac{f_s}{\mu_0}\int_0^b [g(x)]^2\,dx - M_{sat}\,|g(b)|\right). \qquad (17)$$

The full line in fig.7(right) represents this expression using $f_s = 0.8$ and $M_{sat} = 1900\text{A/m}$ found in section 3. The weak field dependence of the saturation magnetization was neglected since the main contribution to κ_x lies in the integral term. Again, we find a quite acceptable quantitative agreement between our data and the model calculation, where no parameters were adjusted. Theoretically, κ_x is about twice the slope of the initial stabilizing force. Within the experimental uncertainty also this prediction is consistent with the observed behavior.

Experimentally it has been found that when the amplitude of vibrations increases the PM-HTSC interaction becomes more and more dissipative.[9] This also follows from Bean's model where the energy loss per cycle for a long cylinder in a parallel field equals[14]

$$W = \frac{2V}{3\mu_0}\left[\frac{2(\Delta B)^3}{B^*} - \frac{(\Delta B)^4}{(B^*)^2}\right] \text{ for } \Delta B \le B^* \text{ and } W = \frac{2V}{3\mu_0}\left[2B^*\Delta B - (B^*)^2\right] \text{ for } \Delta B \ge B^* \qquad (18)$$

Here ΔB is the amplitude of the external flux density, which in the mechanical case is determined by the displacement amplitude of the PM. In order to design an optimal vibrational damper for a given application one will probably need to tune the dissipation properties of the system. Note then that one way to vary the ac-loss at a given vibrational amplitude is to modify the full penetration field, B^*. This parameter is proportional to j_c, which again depends on temperature.

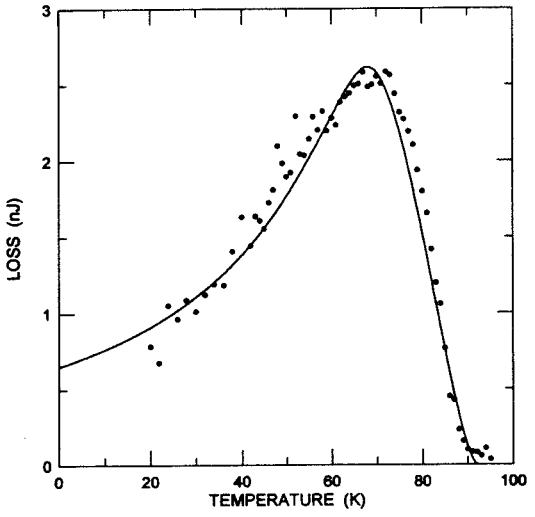

Figure 9: ac-loss per cycle in lateral vibrations of 50μm amplitude. The line represents the theoretical temperature dependence of the dissipation.

Figure 9 shows the result of a measurement series of the ac-loss in lateral vibrations maintained at a constant amplitude of 50μm over a range of temperatures. The dissipation was determined from the area of the force-displacement loops. As found also in numerous susceptibility measurements, the loss varies strongly with the temperature, having here a peak near $T^* = 70\text{K}$. At this maximum the magnitude of $j_c(T^*)$ is such that the 50μm displacement amplitude satisfies the condition $\Delta B = B^*$, where due to the distribution of grain sizes B^* must be understood in an

average sense. The expressions of eq.(18), modified by $V \rightarrow f_s V$ to account for the magnetic porosity of the HTSC, were fitted to our loss data. A temperature dependence of j_c of the form $j_c(T) \propto (1 - T/T_c)^p$ was assumed. Best fit was obtained for $p = 3/2$, and the result is seen in the graph as a full line. Again a very good quantitative agreement is obtained.

A detailed description of the loss experiment together with a more comprehensive theoretical analysis will be published soon.[15]

5. CONCLUDING REMARKS

Several key parameters characterizing the mechanics of magnetic levitation with HTSCs have been investigated experimentally and theoretically. We have shown that (1)the repulsive vertical force and its associated stiffness, (2) the lateral stabilizing force and the stiffness governing horizontal vibrations and (3) the temperature dependence of the mechanical ac-loss can be explained at a quantitative level and with a minimum of adjustable parameters. For the first time, analytical expressions for all these quantities have been derived consistently for a model system. By doing so it is brought out in detail how different parameters such as geometry and the magnetic response of the superconductor affect the behaviors.

In this work we chose to study a sintered HTSC instead of a melt-processed bulk sample. The reason is that melt-processed HTSCs tend to consist of grains many orders of magnitude larger than in sintered samples. Although large grains give rise to large levitation forces, it will also produce a local magnetization that varies over distances of the same scale as the size of the levitating magnet. To account quantitatively for the forces in such cases one probably needs to consider the detailed structure of weak links, or the large-scale flow pattern of the shielding currents in each individual HTSC sample. This problem was avoided here by averaging over many small grains.

The authors wish to thank prof. Y. Galperin for stimulating discussions. The financial support by The Research Council of Norway (Norges Forskningsråd) is gratefully acknowledged.

References

1. B.R. Weinberger, L. Lynds and J.R. Hull, Supercond. Sci. Technol. **3**, 381 (1990).
2. F.C. Moon, C.Golkowski and D. Kupperman, Appl. Supercond. **1**, 1175 (1993).
3. K.B. Ma, C.K. McMichael, M.A. Lamb and W.K. Chu, IEEE Trans. Appl. Supercond. **3**, 388 (1993).
4. I.-G. Chen, J. Liu, R. Weinstein and K. Lau, J. Appl. Phys. **72**, 1013 (1992).
5. see e.g., F.C. Moon, "Magneto-Solid Mechanics", New York, John Wiley & Sons, 1984.
6. F. Hellman, E.M. Gyorgy, D.W. Johnson Jr., H.M. O'Brian and R.C. Sherwood, J. Appl. Phys. **63** 447, (1988).
7. L.C. Davis, J. Appl. Phys. **67** 2631 (1990).
8. T. Torng and Q.Y. Chen, J. Appl. Phys. **73** 1198 (1993).
9. T.H. Johansen, H. Bratsberg, Z.J. Yang, S.J. Guo and B. Loberg, J. Appl. Phys. **70**, 7496 (1991).
10. A.A. Polyanskii, V.K. Vlasko-Vlasov, M.V. Indenbom and V.I. Nikitenko, Sov. Tech. Phys. Lett. **15**, 872 (1989).
11. C.P. Bean, Phys. Rev. Lett. **8**, 250 (1962).
12. Y.B. Kim, C.F. Hempstead and A.R. Strnad, Phys. Rev. **129**, 528 (1963).
13. T.H. Johansen, H. Mestl and H. Bratsberg, J. Appl. Phys. **75**, (1994).
14. R. B. Goldfarb, M. Lelental, C. A. Thompson in "Magnetic Susceptibility of Superconductors and Other Spin Systems" edited by R. A. Hein, T. L. Francavilla, D. H. Libenberg, New York, Plenum Press, 1991.
15. P.O. Hetland, H. Bratsberg and T.H. Johansen(to be published).

ESR, SIMS AND TEMF OF AN Y-Ba-Cu-O SUPERCONDUCTOR

I. Kirschner[1] , J. Giber[2] and I. Halász[3]

(1) Department for Low Temperature Physics, Eötvös University, Budapest, Hungary
(2) Department of Atomic Physics, Technical University, Budapest, Hungary
(3) Central Research Institute of Chemistry, Budapest, Hungary

Abstract

Superconducting transition comes into being between 92 K and 82 K in the samples having a Meissner's state value of 68 vol.%. The main material content has an orthorhombic unit cell of $Y_1Ba_2Cu_4O_8$ accompanied by low quantity CuO and a sporadic phase. A proof of anisotropic superconductivity, an unusually high Cu^- ion concentration and a temperature dependent transition of charge carriers have been observed.

Introduction

On the basis of our earlier research concerned high-T_c superconductivity [1-3], the study of different Y-Ba-Cu-O compounds has been continued in the direction to find out the influence of the exact composition, preparing technique and structure on the superconducting parameters.

In order to accomplish this task, superconducting specimens of the nominal composition of $Y_1Ba_2Cu_4O_8$ have been prepared for different investigations. The following points of view have played the main role in the sample preparation process:

1.the value of the compatible ionic radii, which has a range of 1.25-1.30,

2.the favourable substitution of yttrium (Y) with alkaline earths (AE)

3.the ratio of (Y+AE) to Cu, which is higher, than 0.5 in these experiments, moreover

4. the redox process and the mixed and variable valence of Cu.

Characterization of samples

During present investigations SEM, X-ray, resistivity measurement, ESR- and SIMS methods, moreover TEMF experiment have been applied for obtaining information

on the structure and superconducting properties of specimens.

The samples were prepared by solid-state reaction from pure chemicals of Y_2O_3, $BaCO_3$ and CuO with an appropriate rate. This mixture was pulverized and homogenized by an intensive grinding. The optimum reaction temperature was chosen by a thermogravimetric analysis as a value of 850 °C at which the first heat treatment was carried out for 9 h in oxygen atmosphere.

The lined picture obtained by an X-ray Guinier camera with quartz-monochromatized CuK_α radiation (DRON-2) on the reacted and pulverized mixtures show a fully microcrystalline structure without any amorphous phase.

The powders were then pressed by a pressure of 5 MPa into pellets and then were sintered again at temperature 850 °C for 9 h in oxygen atmosphere.

In the course of this preparation process, a slightly distorted, perovskite structure develops without oxygen deficiency.

The photographs taken by a scanning electron microscope (Jeol JXA-50A) on the samples demonstrate a homogeneous microstructure (Fig. 1). The forms of crystals are not sharp, from which a conclusion on a well-sintered state results.

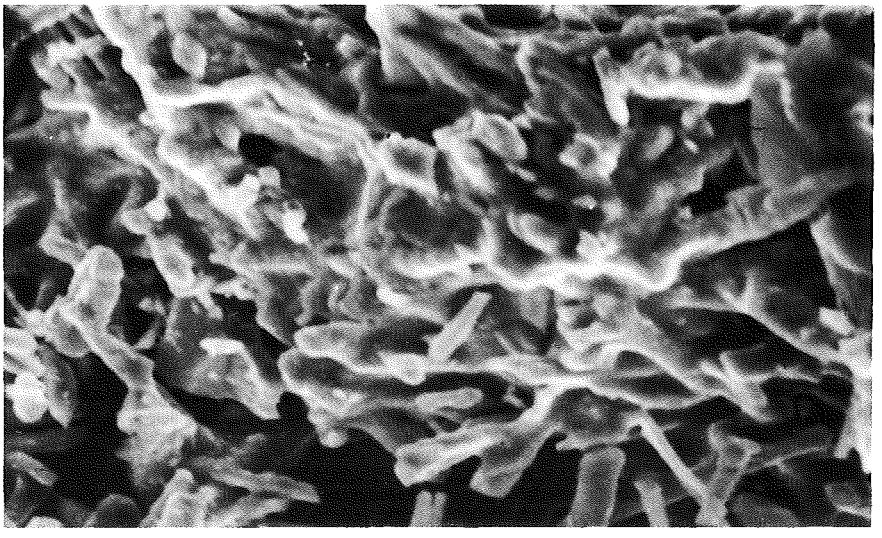

Fig 1. SEM photograph on a sample

The composition of specimens was investigated by X-ray diffraction method (Siemens D-500). This study provides a diffractogram (Fig. 2), demonstrating a nearly single-phase material having a main phase of $Y_1Ba_2Cu_4O_8$ and other compositions only in very low quantity. The majority phase of stoichiometry of Y:Ba:Cu=1:2:4 has an orthorhombic symmetry with lattice parameters a=3.83 Å, b=3.88 Å and c=27.22 Å

and this is responsible for the superconductivity. The minority phase is the well-known Cu-O of monoclinic unit cells. Finally, the peaks, which can not be indexed indicate the existence of an unidentified sporadic phase.

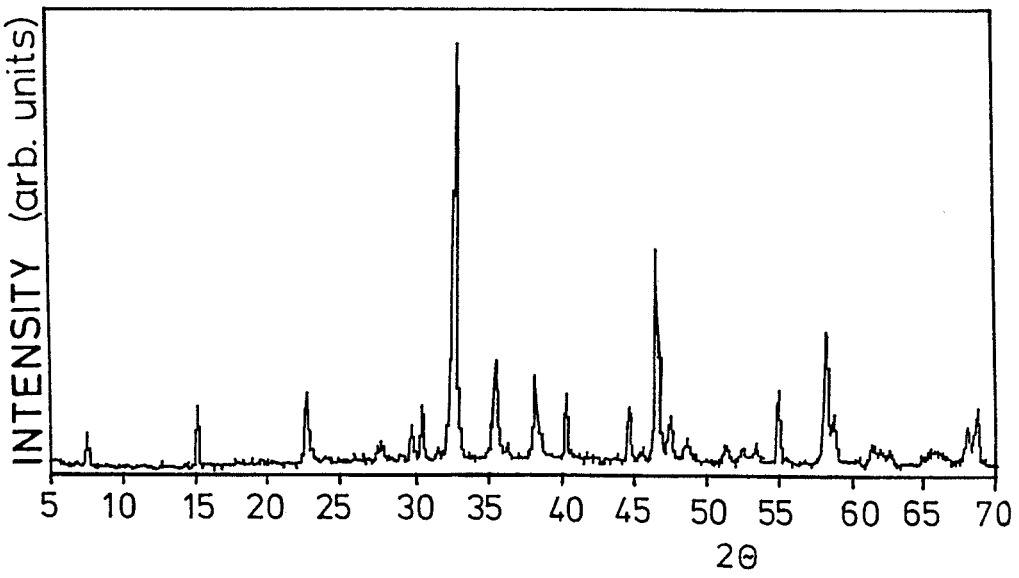

Fig 2. X-ray diffractogram of a sample

Since the (1,2,4) compound is an oxygen stoichiometric one [4], the number of oxygen atoms practically can not be changed. Therefore the lattice parameters determined by double Cu-O chains can also not easily be varied by substitution of other atoms. From this the higher thermal stability of the oxygen content follows, as compared to the (1,2,3) phase. As the experiments show, this statement is, however, valid only until a given temperature, and in the range above 850 K the (1,2,4) phase decomposes into (1,2,3) one and CuO.

Superconducting properties

The dependence of the resistance R on temperature T was determined by a conventional four-probe technique using evaporated gold contacts on the samples to which the electrical leads were soldered by silver paste. A typical R-T characteristic is shown in Fig. 3. The specimens show metallic behaviour in the whole temperature interval under investigation, having room temperature specific resistivity of ρ_{300}=8-11 mΩcm. As it can be seen, the sharp drop of the resistance starts at 92 K and zero-resistivity state sets in at 82 K.

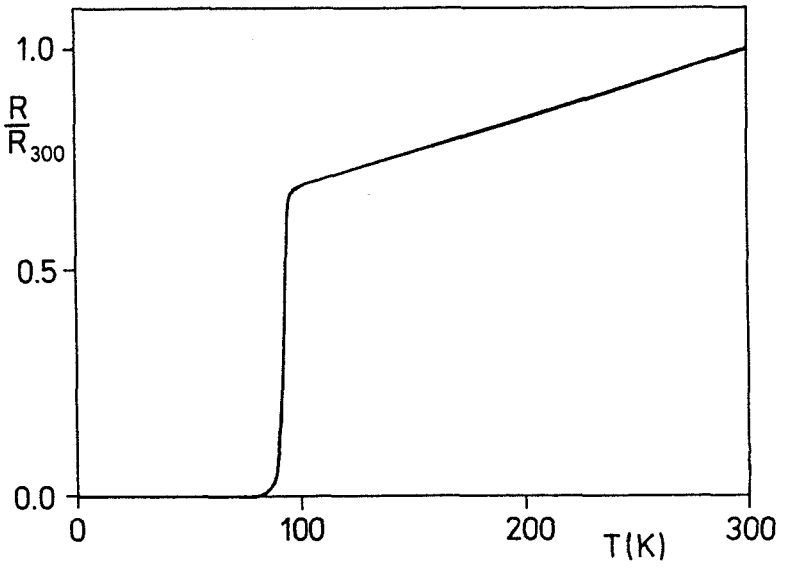

Fig 3. Dependence of the resistance on temperature of a sample

Double-coil dynamic magnetic measurements were performed on the samples forming prism of dimensions 2x2x12 mm^3. During these experiments an a.c. method was used in the frequency range of 5-150 kHz and at effective magnetic field interval of 0.1-27 Oe. As the investigation shows, 68 ± 4 vol.% of samples material is in pure Meissner's state at low temperatures (Fig. 4).

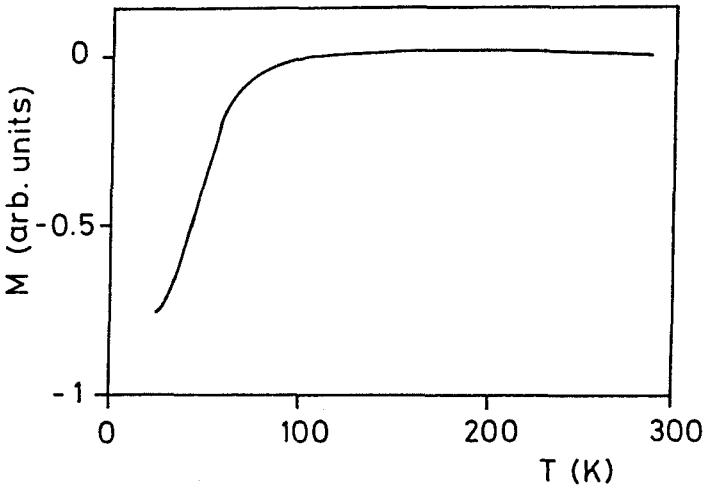

Fig 4. Typical a.c. susceptibility curve at 100 kHz

Superconducting transition has also been traced with an X-band (9.5 GHz) Electron Spin Resonance (ESR) equipment (ERS 200). ESR investigation hints at a strongly anisotropic and layered structure of the specimens. Above the temperatures of

dropping resistance, the samples have an ESR signal of asymmetrical shape (Fig. 5).

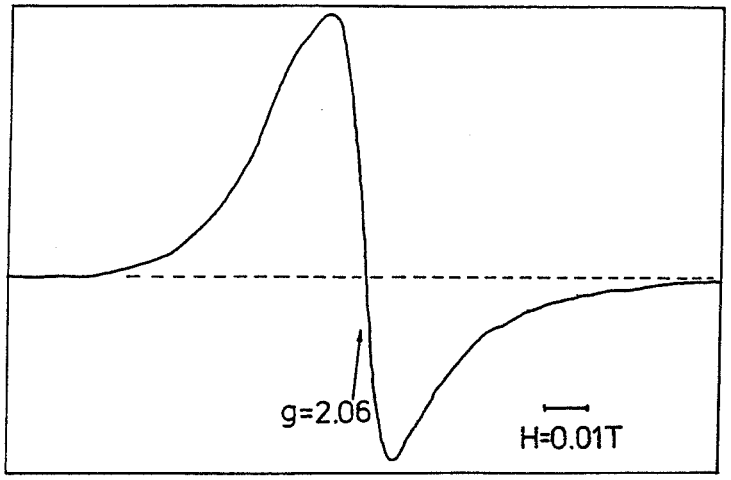

Fig 5. ESR signal of a sample

The center of the line corresponds to the gyromagnetic factor with average value of g=2.06 and its peak to peak width is 152 Oe. The shape of the signal slightly depends on the angle between pressing plane and direction of the magnetic field, thus it refers to an anisotropy in the samples and a tensorial character of g, which survives the pulverizing of the specimens.

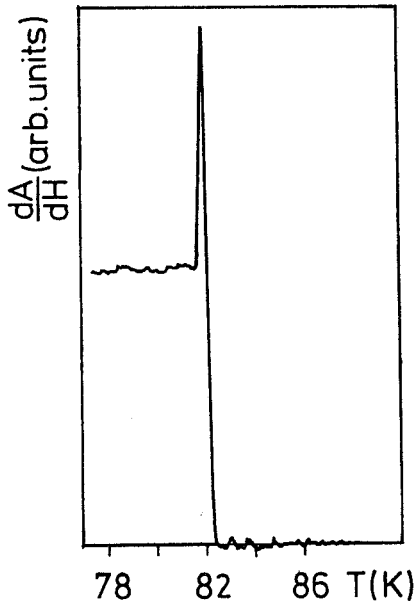

Fig 6. Temperature dependence
of the derivative of microwave absorption near T_c

During the transition to zero-resistivity state a sharp increase in the base-line level occurs at 82 K, although the ESR signal remains unchanged. The increase of the base-line level decreases with the static magnetic field.

This indicates a magnetic field dependent microwave absorption A, which is related to the dissipative behaviour of type II superconductivity of high-T_c superconductors. Figure 6 shows the temperature dependence of the first derivative of microwave absorption on static magnetic field near the zero-resistivity state. It demonstrates a drastic change in the absorption properties at the critical temperature, which reflects the transformation of the state in samples.

Detailed experimental investigation was carried out on the specimens by Secondary Ion Mass Spectroscopy (SIMS, type Balzers). Dynamic spectra were measured in argon and oxygen atmosphere at a monitor current of 1×10^{-6} A in a wide mass range. Fig. 7 and 8 show the positive and negative secondary ion spectra, respectively, taken on the characteristic mass range of 1 - 100 in argon atmosphere, where the peaks of main components and micro-impurities can be seen. In the higher mass range YO^+, BaO^+, Ba_2O^+ molecule ions and Dy^+, Yb^+, Pt^+ impurity ions appear as well.

According to the observation, the oxygen atmosphere increases the peak of Y^+ 4.7- times, Ba^+ 2.1- times and Cu^+ 3.5-times, indicating that the original material is not completely oxidized. This result is in agreement with earlier statement on oxidation state.

The existence of the high intensity Cu^- peak compared to the Cu^+ one, may be a very important point explaining the superconducting behaviour of this compound. The Cu^+/Cu^- ratio being here 10^{-1} is quite unusual comparing to the value of 10^2 in copper oxides and 2×10^2 in copper alloys.(Similar effect for metallic components was found only at noble metals, namely at Au and Pt). From this fact a significant interaction between Cu ions and electrons can be supposed, due to which the Cu atoms leaving the bulk material are surrounded by an excess electronic cloud. It means that less electrons can take place in the transport and so a positive charge carrier conductivity may occur. This supposition was controlled by TEMF measurement too.

Thermoelectric effect can also be detected in the granular and anisotropic superconductors creating a temperature difference between two sides of samples [5].

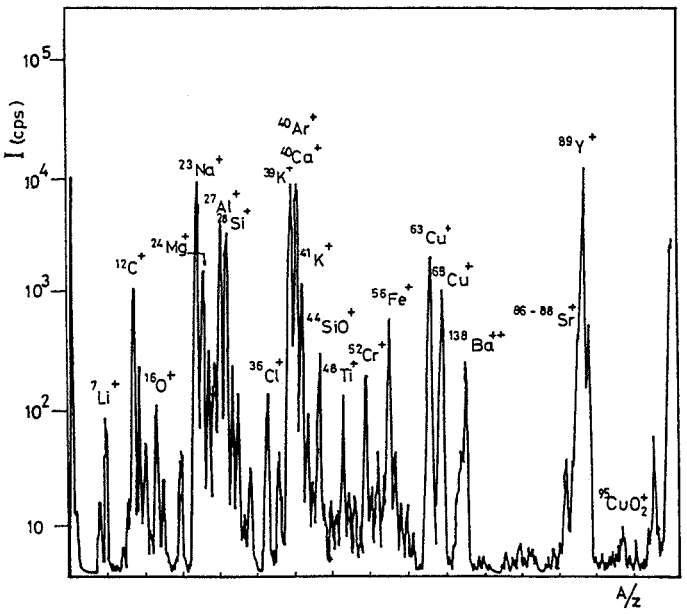

Fig 7. A positive SIMS spectrum of a sample with 3 keV Ar^+ bombardment (A=mass number, Z=particle charge number)

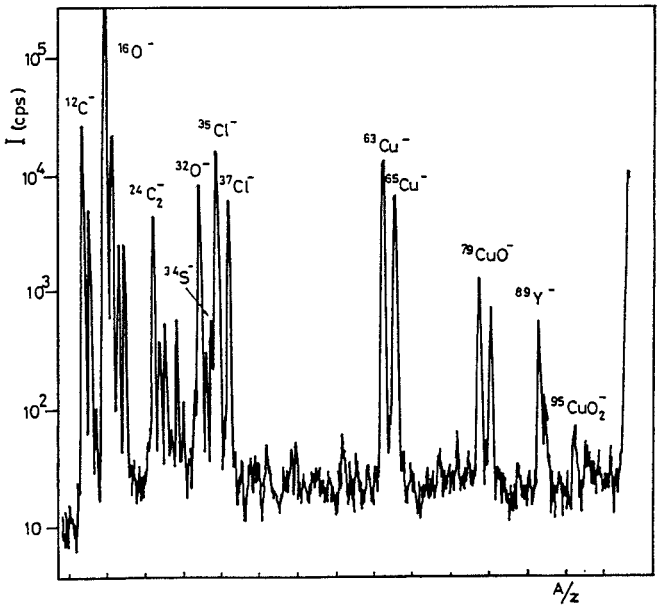

Fig 8. A negative SIMS spectrum of a samples with 3 keV Ar^+ bombardment (A=mass number, Z=particle charge number)

As Fig. 9 shows, the thermoelectric voltage has a negative sign and a slightly increasing tendency in its absolute value during the cooling stage without any external magnetic field in the temperature interval of 220-124 K. Below this temperature the TEMF is decreasing and reaches zero value at 82 K. After the zero value it has an increasing and later a decreasing branch of positive sign and ceases at about 50 K.

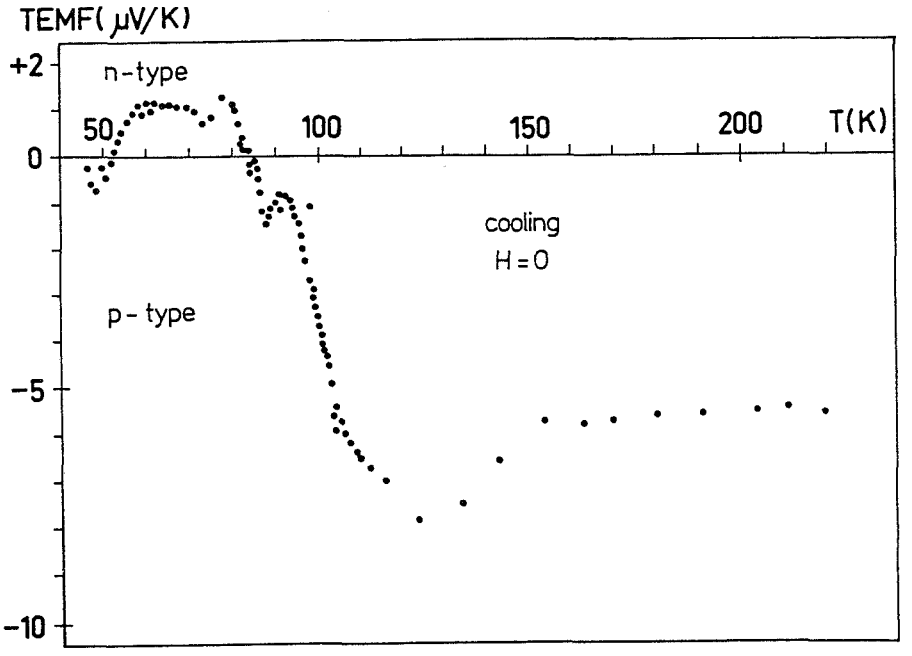

Fig 9. Dependence of TEMF on the temperature in the cooling stage without magnetic field

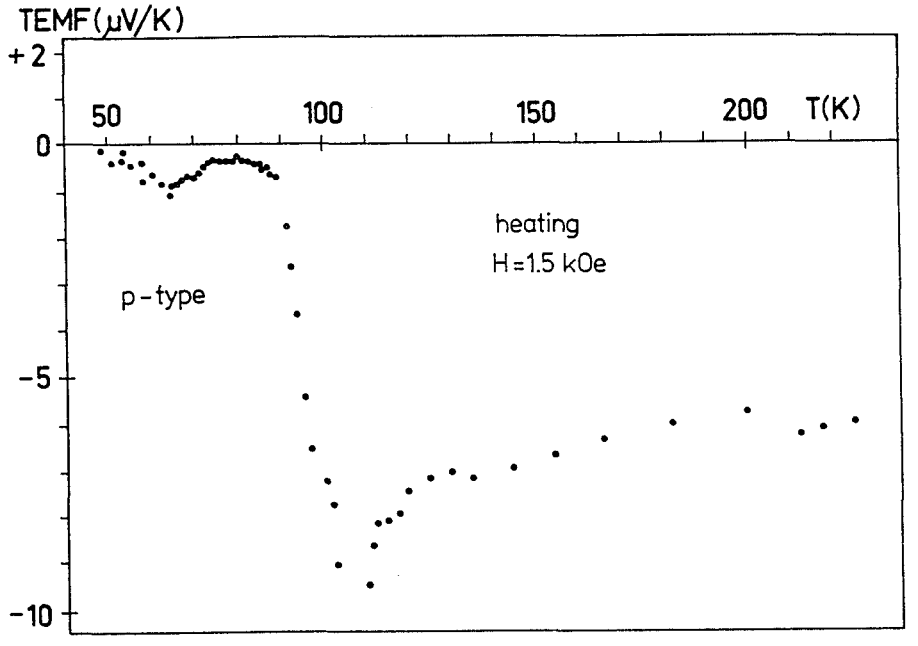

Fig 10. Dependence of TEMF on the temperature during heating process in an external magnetic field

Investigating this phenomenon during the heating stage in an external magnetic field of 1.5 kOe, the sign of TEMF is negative in the whole temperature range (Fig. 10).

Starting from 50 K, the curve of TEMF firstly has an increasing character in its absolute value until 110 K. At this point a sharp break then a moderate decrease and a saturation tendency in the investigated temperature interval (until 220 K) can be observed.

If a temperature gradient exists in the sample between two opposite surfaces, the charge carriers diffuse from higher-temperature side to the lower-temperature one until a stationary voltage difference established. In the case of p-type charge carriers the cold surface will be more positive and in the presence of n-type ones, more negative. This phenomenon represents a positive-negative transition of the charge carriers occurring at the temperature of zero-resistivity state. In contrast with this observation there is no change in dominant carriers during the heating stage in an applied external magnetic field.

Comparing the magnitude of the effect in other materials, the obtained voltage signals are generally higher, than those for metals and lower, than the thermal voltages belonging to semiconductors. The obtained TEMF values were independent from the materials (bronze, copper or nickel) of the measuring electrodes.

In consequence of granular and porous character of the high-T_c oxide superconductors a spatial fluctuation of the chemical potential and a phonon drag appear, which play together an important role in the formation of TEMF-curve at low temperatures (below 124 K), but they alone can not change the sign of thermoelectric voltage. In this way, the results of these experiments refer to a complicated mechanism, due to that the holes, the p $\leftrightarrow$ n transition and the electrons are together responsible for establishing superconductivity [6].

Thermoelectric voltage is affected by the relatively large electron-phonon interaction and the creation of superconducting pairs counteracts the diffusion of electrons (and so the thermoelectric effect), therefore a decrease of the absolute value of TEMF can be observed at low temperatures. In this way, the maximum of the positive branch is much smaller, than the values of the negative branch at higher temperatures, but it shows that the pairing process is not capable to cease fully the thermoelectric voltage in anisotropic superconductors in the transitional range.

Finally, we would like to point out, that this phenomenon can be explained in the framework of Ginzburg-Landau theory [7]. If, the power series of the superconducting free energy is completed by a new term, the Ginzburg-Landau equations will be able to imply the thermodynamic cross-effects, namely the thermoelectricity too.

Conclusions

From the analysis of recent investigation some conclusions can be drown:

1. Relatively low temperatures of the heat treatment can result in nearly single phase Y-(1,2,4) of reproducibility and long time stability.
2. Specific effects which can be detected by non-conventional methods of research can contribute to the explanation of the mechanism of high-T_c superconductivity in different compound.

References

1. I.Kirschner, J. Bánkuti, M. Gál and K. Torkos, Phys. Rev. **B36.** 2313. (1987).
2. R. Laiho, E. Lähderanta, L. Säisä, Gy. Kovács, G. Zsolt, I. Kirschner and I. Halász, Phys. Rev. **B42.** 347. (1990).
3. A. C. Bódi and I. Kirschner, Phys. Lett. **A181.** 479. 1993.
4. J. Karpinski, S. Rusiecki, E. Kaldis, B.Bucher and E. Jick, Physica **C160.** 449.(1989).
5. A. Mawdsley, H. J. Trodahl, J. Tallon, J. Sarfati and A. B. Kaiser, Nature **328.** 233. (1987).
6. T. Porjesz, T. Kármán, I. Kirschner, Gy. Kovács, G. Zsolt and H. Beyer, ICTP Report 87−278k, Trieste, 1987.
7. V. L. Ginzburg and L. D. Landau, Zh. Exp. i Teor. Fiz. **20.** 1064. (1950).

Single Scan
S/4-76
313656
qp. 342.943

Serial and Parallel Power Equipment with High-Temperature Superconducting Elements.

László Bencze[1], Nándor Göbl[1], Béla Palotás[2], István Vajda[3]

Summary

One of the prospective, practical applications of high-temperature superconductors is the fault-current limitation in electrical energy networks. The development and testing of experimental HTSC serial current limiters have been reported in the literature. A Hungarian electric power company has proposed the development of a parallel equipment for arc suppressing both in the industrial and customers' networks.

On the basis of the company's proposal the authors have outlined the scheme of a compound circuit that can be applied both for current limitation and arc suppressing. In this paper the design principles and methods of the shunt equipment are presented. These principles involve the electrical, mechanical and cryogenic aspects with the special view on the electrical and mechanical connection between the HTSC material and the current lead.

Preliminary experiments and tests have been carried out to demonstrate the validity of the design principles developed. The results of the experiments and of the technological investigations are presented.

---

[1] Research Institute of the Electrical Industry, Hungary

[2] Institute for Mechanical Technology and Materials Science; Technical University of Budapest, Hungary

[3] Department of Electrical Machines, Technical University of Budapest, Hungary

Address: Egry József utca 18, Budapest, H-1111, Hungary

Phone: 36.1.1666358

Fax: 36.1.1666358

E-mail: H9639VAJ@ella.hu

Introduction

A new project for the investigation of the possible application of high-temperature superconductors in electrical switch gear has been initiated and financed by a Hungarian power engineering company, ***EPOS-PVI, Rt.*** The organisational and functional structure of the project is shown in Figure 1.

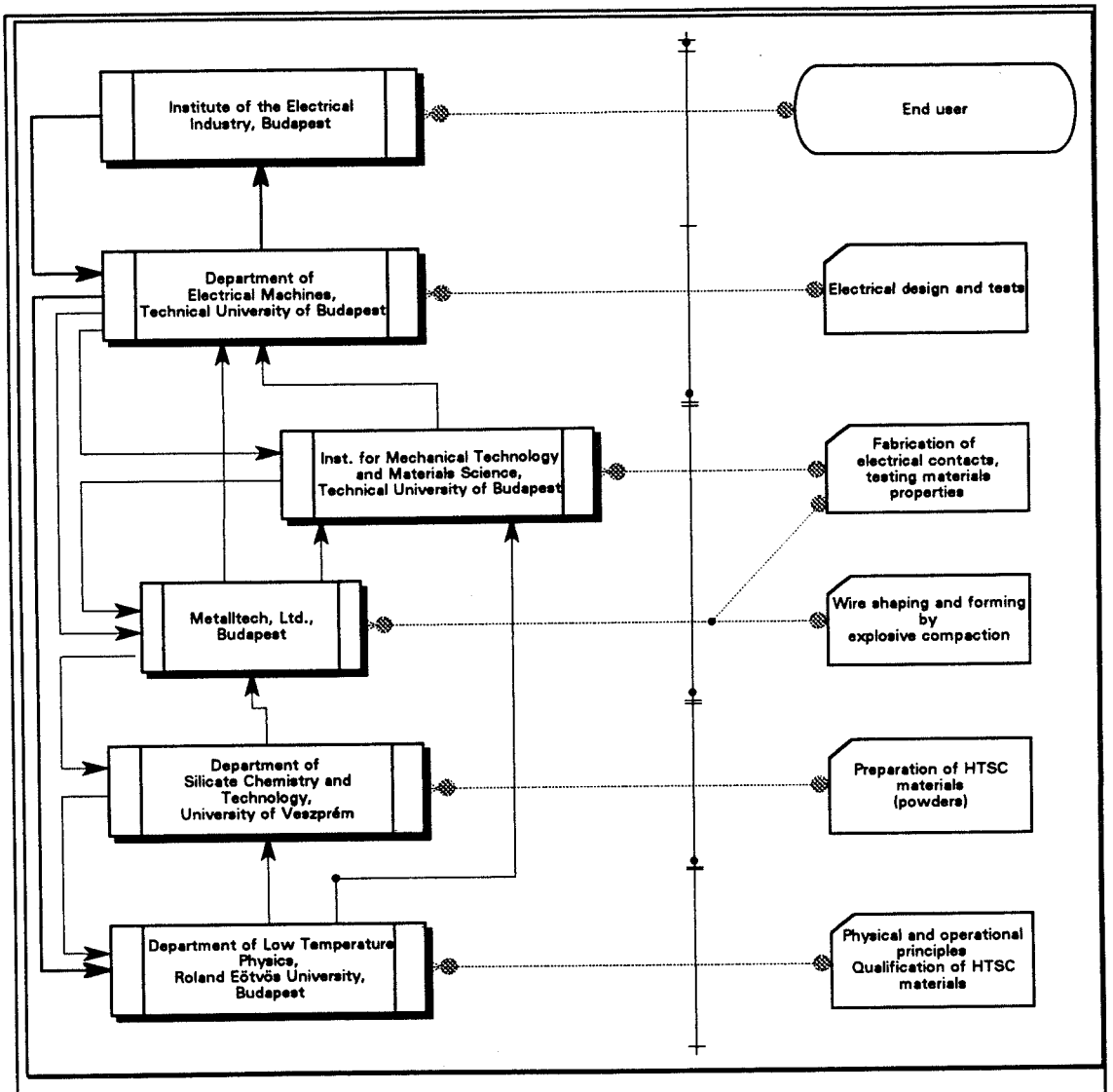

Figure 1

The structural chart of the co-operation

This project is in close connection with the one carried out at the Department of Electrical Machines, Technical University of Budapest, supported by the ***Hungarian Academy of Sciences (National Fund for Science and Research).*** The aim of this project is the development of a model of an HTSC electrical machine. In this frame a

numerical method and a software have been developed for the calculation of the magnetic field of superconductors [2], [3].

The work carried out in the frame of the Hungarian co-operation has attained an attention and interest from abroad. The national co-operation is planned to be elevated onto an international level.

Design principles

The device containing the HTSC element is connected parallel with the section of the network to be protected. The arrangement of the device for a single-phase network is shown on *Figure 2* [6].

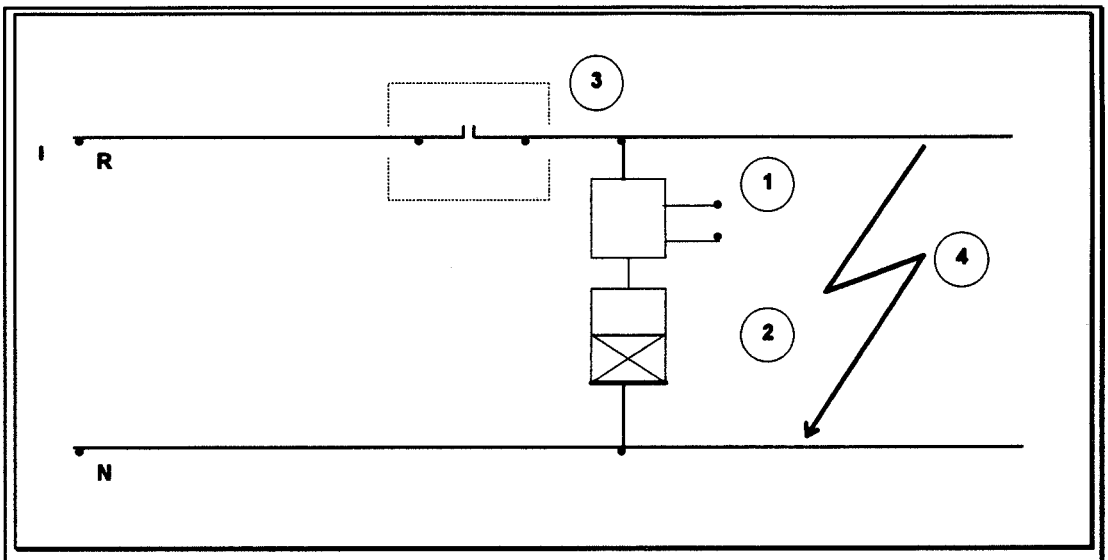

Figure 2

1-phase schematic arrangement

1 controlling element
2 HTSC-element
3 classical switch-gear
4 electric arc (short circuit

According to *Figure 2.* the device containing the HTSC element is connected parallel with the section of the network to be protected between the phase- and the neutral conductor. If, for example, an arc develops in the section of the network to be protected, then the protection system supplied with optical and electrical sensors detects the arc and gives a signal to the controlling element of the device containing the HTSC element. Due to the operation of the controlling element the HTSC element

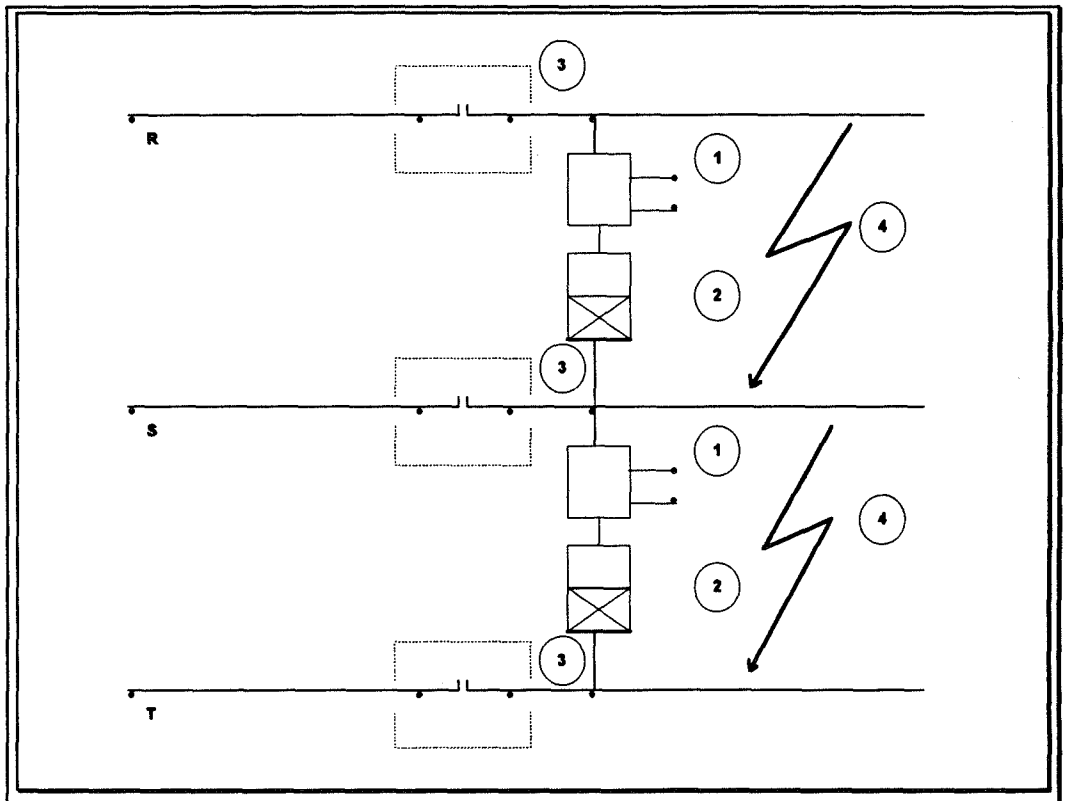

Figure 3

3-phase schematic arrangement
(legend according to Figure 2)

carries a given current. If the value of this current exceeds the critical current characteristic of the selected superconductor then the HTSC material goes from its superconducting state into its normal state. The HTSC material in its normal state behaves as a current limiter and, thus, decreases the current load of the traditional circuit breakers.

In the case of a three-phase network the device may be connected, for example according to *Figure 3*, between the line conductors.

Modelling of the superconducting-normal transition

One of the fundamental parameters of both of the operation and of the design of the switching device containing an HTSC element is the switching time, that is the time of the transition from the superconducting to the normal state (and back). Similarly it is essential to know the ratio of resistivities of the superconducting and the normal states.

For the investigation of the conditions, as the first step, a small sample of the device has been constructed since HTSC materials, at least at present, are characterised by relatively low critical current densities [4], [5]. The arrangement for the transition tests is shown in *Figure 4.*

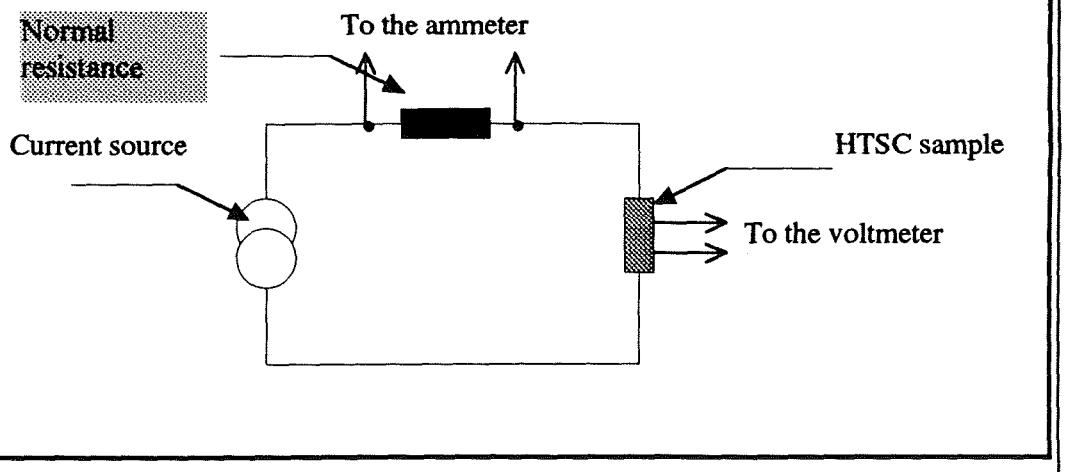

Figure 4

Scheme of the transition test arrangement

The HTSC sample has been fed from a current source giving an output current of triangular form. For a better evaluation the frequency of the current has been set to 10 Hz. The voltage proportional to the current and sampled with the frequency of 30 kHz has been registered and processed by a computerised measuring system.

To avoid the distortion of the results by the voltage drop on the current feed we have formed separate pairs of contacts for the current feed and the voltage signal.

For the evaluation of the switching speed we have used the results of measurements shown in *Figure 5.*

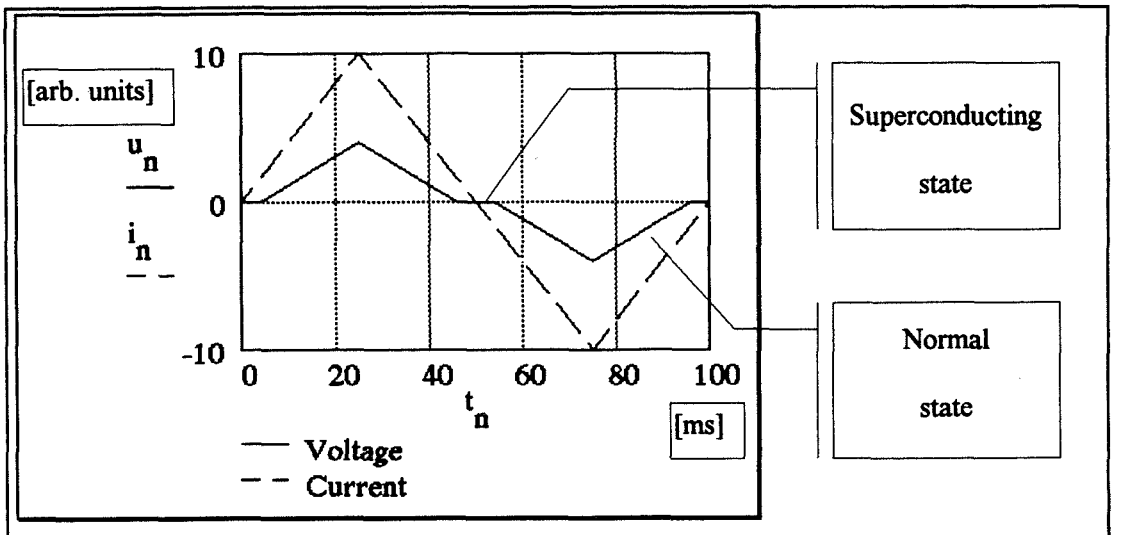

Figure 5

Measurement of the superconducting-normal state transition

It is clearly seen in the figure that in the moment when the current flowing through the sample has exceeded the critical value then a voltage drop has appeared momentarily indicating that the HTSC element has gone from its superconducting state into its normal state. Similarly, when the current has decreased below the critical value then the material has returned to its superconducting state.

According to the commonly accepted convention the sample is considered to be in its superconducting state if the voltage drop per unit length (in centimetres) is not more than 1 μV independently of the dimensions of the sample and of the current flowing through the sample. Consequently the ratio of the resistivities of the normal and the superconducting states of the sample may be considered to be practically infinite since the voltage drop on the sample in its superconducting state is practically zero.

The switching time of the sample both in the superconducting⇒normal state and the normal⇒superconducting state has been orders of magnitude less than 1 ms. This time period is critical for the arc suppressing.

Fabrication of HTSC material-metal contacts

One of the crucial points of the application of the HTSC materials in current limiters or circuit breakers is the possibility of fabrication contacts with satisfactory mechanical properties and contact resitivities [7].

In the frame of the project various welding and soldering methods are planned to be investigated. The first successful results in this respect have been achieved by electron beam evaporation and welding.

Figure 6 shows silver contacts evaporated by an electron beam on the surface of an YBaCuO rod.

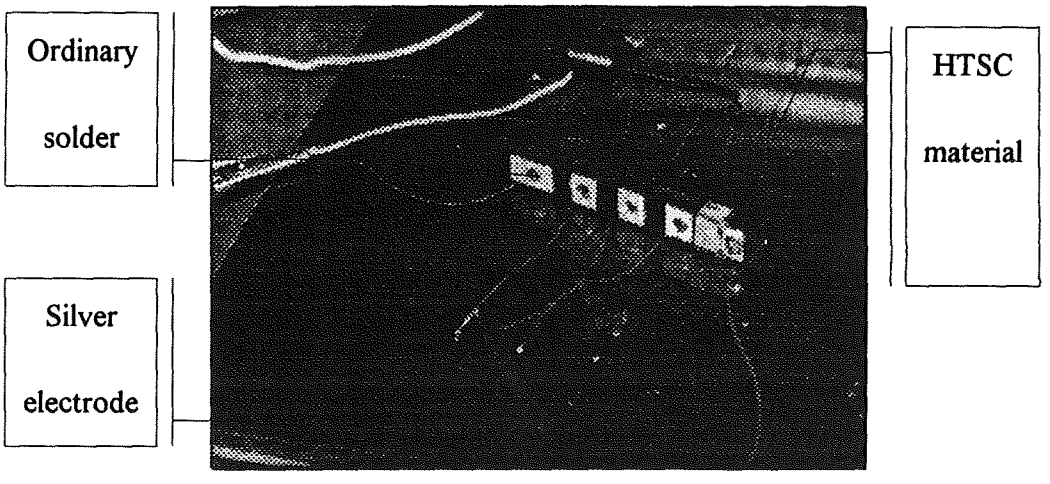

Figure 6

Electric contacts made by electron beam evaporation

Silver rods of Ø3 mm jointed to an YBaCuO plate by electron beam welding is shown in *Figure 7.*

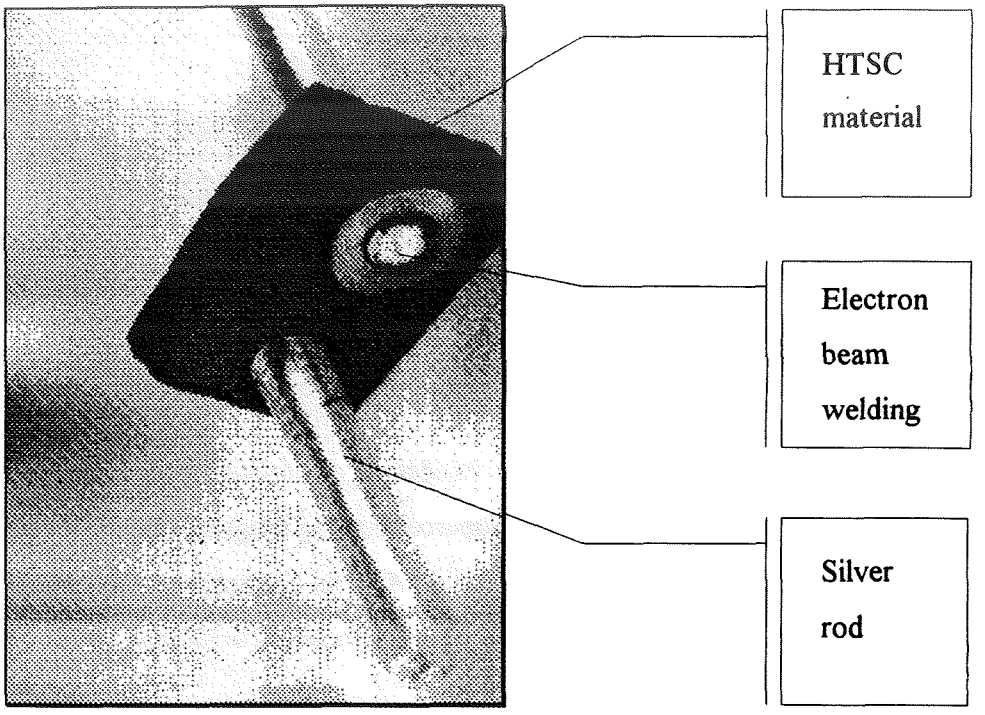

Figure 7

Electrical contacts made with electron beam welding

According to our investigations the welded contacts allow current loads that are orders of magnitude higher than what has been achieved by other technologies referred in the literature. The electron beam welding seems to be a suitable method of fabricating contacts of considerable cross section between HTSC materials and metals.

It is worth to be noted that we have made promising experiments in wire forming and contact making by the method of explosive powder compaction as well [1].

Conclusions

The design principles of a device containing an HTSC element and suitable to arc suppressing has been developed. A sample switch for the modelling of the superconducting⇒normal and the normal⇒superconducting transitions has been constructed and tested. Preliminary experiments regarding the technologies of contact making have shown promising results.

References

[1] *L. Bencze, A. Szalay, I. Vajda:* Fabrication of an HTSC Switch
Sensors and Actuators A, **41-42**, p. 70-73, (1994), (EUROSENSORS VII).

[2] *I. Vajda, K. Kovács:* Calculation of the Levitation Force of a High Temperature Magnetic Bearing,
International Conference on Electrical Machines, 5-8 Sept, 1994.

[3] *I. Vajda, L. T. Mohácsi, K.Kovács:* Modelling of the Superconductor for the Application in High Temperature Superconducting Magnetic Bearing,
The 3rd Japan-Hungary Joint Seminar on Applied Electromagnetics in Materials and Computational Technology, Budapest, 10-13 July, 1994.

[4] *I. Kirschner:* Requirements and Results of High-T_c Superconducting Wire and Tape Fabrication,
Applied Superconductivity, **1**, 10-12,. p. 1785-1789, 1993.

[5] *I. Kirschner:* HTSC Materials - Properties and Applications,
Research Report, Institute of the Electrical Industry, Budapest, 1994,
(In Hungarian).

[6] *K. Kovács:* A Study on the Controlling Methods of HTSC Shunt Devices,
Research Report, Institute of the Electrical Industry, Budapest, 1994,
(In Hungarian).

[7] *B. Palotás:* A Study on the Technologies Applicable for Making Contacts Between HTSC Materials and Metals,
Research Report, Institute of the Electrical Industry, Budapest, 1994,
(In Hungarian).

SKIP
THIS
PAGE

THIS PAGE INTENTIONALLY LEFT BLANK

Page intentionally left blank

Persistent Magnetic Fields

Chair: Dr. Roy Weinstein

OMIT THIS PAGE

STABILITY, MECHANICAL CONSIDERATIONS, AND AC LOSS IN HTSC MONOLITHS, COILS, AND WIRES

M. D. Sumption and E. W. Collings

Battelle Memorial Institute
505 King Ave, Columbus, OH 43201, USA

Abstract

For monolithic high-T_c superconductors (HTSCs) calculations are presented of: (1) the initial flux jump field, H_{fj}, in melt-processed YBCO based on a field- and temperature dependent J_c, and (2) the radial and circumferential stresses in solid and hollow cylinders containing trapped magnetic flux. For model multifilamentary (MF) HTSC/Ag strands calculations are presented of: (1) the limiting filament diameters for adiabatic and dynamic stability, and (2) the hysteretic and eddy current components of AC loss. Again for MF HTSC/Ag composite strands the need for filamentary subdivision and twisting is discussed.

INTRODUCTION

Large-scale applications of high-T_c superconductors (HTSCs) stem not only from their obviously high T_cs which offer the possibility of operation in liquid hydrogen, liquid nitrogen as well as refrigerated gases, but also from their high H_{c2}s when high operating temperature is not the primary consideration. The thermal properties central to stable conductor design are thermal conductivity, K(T), and specific heat, C(T). The former dominates at low temperatures and there dictates the choice of a dynamic stability criterion. Specific heat takes over at high temperatures where stability is controlled by adiabatic considerations. The much higher C(T) of materials at 77 K than at 4 K guarantees a much greater adiabatic flux-jump stability. Several effects related to stability, while present in LTSC materials, are much more prominent in HTSCs; for example, a much more pronounced ramp rate dependence of flux jumping (in non-stabilized samples).[1] In the first section of this paper, the field dependence of flux jumping in large monoliths of HTSC, and its associated adiabatic and dynamic aspects, will be considered. In the next section we calculate the Lorentz-force induced mechanical stresses that are present in flux-trapped solid cylinders of melt grown YBCO. We then go on to compare these results to those for hollow cylinders. The discussion on stability then concludes with a note on flux-jump- and cryo-stabilization of Ag-clad HTSC strands. The paper continues with a discussion of AC loss in multifilamentary HTSC/Ag composite strands. Using a model strand configuration, typical hysteretic and eddy current losses are compared with reference to practically attainable matrix resistivities and twist pitches. We conclude with a discussion of the particular properties of filamentary subdivision in HTSCs.

MAGNETIC STABILITY OF HTSC MONOLITHS

A well known expression for the initial flux jump field, is $H_{j0} = \sqrt{\{\pi^3 C(T)\Delta T_0\}}$, in which $\Delta T_0 \equiv J_c/(-dJ_c/dT)$. In its more widely used form, in which ΔT_0 is replaced by (T_c-T_b), a number of assumptions have been made: (1) J_c is linearly dependent on T, (2) J_c is field independent, and (3) the sample is isotropic. These assumptions are convenient, and have worked reasonably

well for LTSCs. However, Müller and Andrikidis[2] have recently developed an expression which takes into account the field dependence of J_c based on the Kim model, $J_c = J_{c0}H_0/(H+H_0)$. Field dependence of J_c has been considered before, both experimentally[3] and theoretically using a Kim-type model[4], although Müller et al.'s treatment[2] is the most complete.

Müller et al.'s expression for this modified flux jump field for a semi-infinite slab on the virgin run is given implicitly by

$$2\left[(|H_{fj}| - |H_e|)(|H_{fj}| + H_0) + (|H_{fj}| + H_0)(|H_e| + H_0)Ln\left(\frac{H_0 + |H_e|}{H_0 + |H_{fj}|}\right)\right] = H_{j0}^2 \qquad (1)$$

Here H_{fj} is the new flux jump field, H_e is an internal field due to previous flux jumps (we will set it to zero), and H_0 is the Kim model parameter. Curves derived from this expression in case (i) $\mu_0H_0 = \infty$ ($H_{fj} \equiv H_{j0}$), (ii) $\mu_0H_0 = 4$ T and (iii) $\mu_0H_0 = 0.1$ T are plotted in Fig. 1. We have chosen to plot H_{fj} for the virgin run, where we additionally require $H_e = 0$, since it does not involve the past history of the sample, and is easily compared to experimental results. Following Müller et al., in calculating Fig. 1 we assembled previously published[5] specific heat data from two temperature ranges -- 1-17 K and 30-100 K -- extrapolating them both to 26 K to complete the data set. This causes a discontinuity in slope of C(T) at 26 K and hence in the slope of the resulting H_{fj}.

It is noteworthy that the temperature dependence of H_{fj} responds strongly to the choice of the Kim field, H_0. It is also expected that the temperature dependence of J_c will also have a strong influence. We have noted from an inspection of several data sets for melt-processed YBCO that the combined temperature- and field dependence of J_c can be expressed in the form $J_c(T,H) = J_{c00}\exp(-T/T_s)H_0(T)/\{H_0(T)+H\}$. In particular, based on data from Maley et al.[6], we have deduced for their sample that $J_{c00} = 5.92 \times 10^5$ A/cm^2, $T_s = 19.87$ K, and $H_0(T) = a\text{-}bT$ (with $a = 2.504$ tesla, $b = 2.79\times10^{-2}$ tesla/K).

Ignoring for a moment the field dependence, the exponential form of $J_c(T)$ yields $\Delta T_0 = T_s$, leading to a "field-independent" H_{fj} of the form $\sqrt{\{\pi^3C(T)T_s\}}$. Next, an H_{fj} combining both J_c's exponential T-dependence and H_0's linear T-dependence was calculated. The new curve, also plotted in Fig. 1, covers just the region of exponentially fitted J_c data (up to about 80 K); at higher temperatures, J_c must decrease to zero more rapidly -- linearly would be a good approximation. The unusual shape of the final curve indicates that H_{fj} is sensitive to the full T-dependence of J_c. Indeed, in one of the first published papers on flux jumping, just such an effect was taken into account.[3] Given the wide temperature range over which HTSCs operate, and the wide variation in materials properties within it, inclusion of a T dependence as well as an H dependence is important for a quantitative description of flux jumping.

An interesting offshoot of the use of Kim-model-J_c field dependence is the prediction of a new flux jump regime -- that of the solitary flux jump. Flux jumping will occur when the field (or for a given d, J_c) becomes large enough. In the Bean model this can happen with equal likelihood anywhere around the M-H loop. However, for a Kim-type model, J_c (and thus field gradients) will be larger in some parts of the M-H loop than in others. In particular, two points on a Kim-type M-H loop which occur on the shielding branches, at relatively low fields (on opposite sides of the M-axis) have maximum overall field gradients. If we imagine following the trace of an M-H loop, once a flux jump is initiated at these high H-gradient

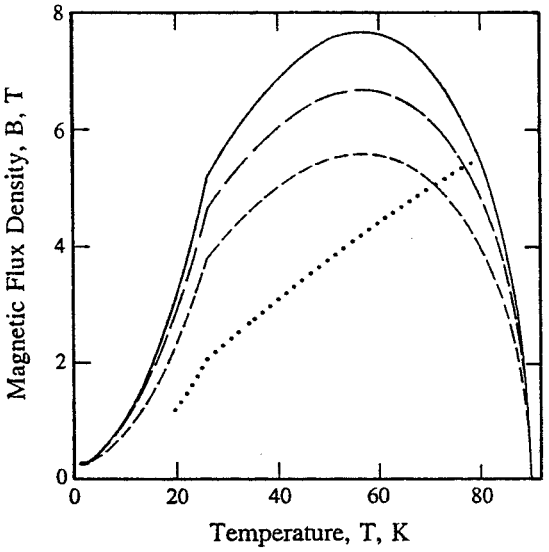

Figure 1. H_{fj} and H_{j0} vs T calculated for $\mu_0 H_0 = \infty$ (H_{j0}) (——), $\mu H_0 = 4$ T (— —), and $\mu H_0 = 0.1$ T (– – – –). Also shown is the result for $H_{fj} = H_{fj}$ (H,T) (• • • •, see text).

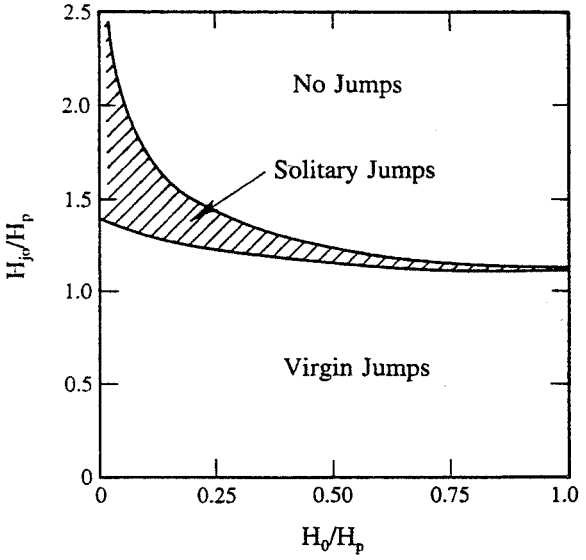

Figure 2. Illustration of the flux jump regimes. H_{j0}/H_p vs H_0/H_p for H_m/H_p =1, where H_p is the penetration field and H_m is the maximum field sweep amplitude. After Müller and Andrikidis.[2]

points, the total field difference is reduced. As H is increased (as we continue to sweep out the loop) the gradient cannot build back to its previously high value, since $J_c(H)$ is lower. We can then see that M-H loops executed in a certain range of temperature, and for certain H_0 values will exhibit pairs of "solitary" flux jumps. At lower temperatures, or as $H_0 \rightarrow \infty$, multiple flux jumps will occur (corresponding to the usual case). The solitary and multiple flux jumps regimes are displayed in Fig. 2. We note that the partial flux jump boundaries displayed in Fig. 1 will be extended somewhat by the solitary flux jump regime.

Another important idea which needs to be incorporated into the analysis of flux trapping samples is the influence of cooling on flux jump stability. It has been asserted that for slower ramp rates the ramp rate sensitivity of H_{fj} may be modified by dynamic cooling.[2] It seems clear that significant cooling will also occur along a direction orthogonal to the dimension along which the flux gradient is formed for flux trapping samples.[7] This suggests that the employment of a thin disk geometry may improve the stability of such samples.

It is also important to account for sample anisotropy. If H is parallel to c, then the problem is essentially isotropic. However, with H perpendicular to c, the stability will presumably be determined by the weaker of $H_{fj,a-b}$ and $H_{fj,c}$. However, this question has not been directly addressed.

STRESSES IN MELT GROWTH CYLINDERS AND POTTED MAGNETS ARISING FROM LORENTZ FORCES.

We have calculated the stress for a cylindrical superconductive sample used for flux trapping. While the literature concerning stresses in superconducting solenoids is extensive, we are unaware of any solutions for solid cylinders. This type of sample is shown in Fig. 3(a), with the field applied along the z-direction. Field independent J_c is assumed, and we have set the crystalline c-axis to be along the z-axis as well, in order to describe the configuration of

interest for flux trapping superconductors. Superconductive and mechanical properties will then be θ-invariant. We calculate the stresses after the sample has been set up in the full flux trapping state (presumably by field cooling), with the resultant flux profile shown in Fig. 3(b). The Lorentz force is given by $F = B_z J_c/10$ (in cgs-practical units). Using $dB/dr = 4\pi J_c/10$, the Lorentz force can be re-expressed as a function of position in the sample as

$$F(r) = \frac{4\pi J_c^2}{100}(R - r). \tag{2}$$

Following the procedure used to calculate the solenoidal solution[8,9], we start with the conditions of equilibrium for a 2-D θ-invariant problem in polar coordinates:

$$\frac{\partial}{\partial r}\sigma_r(r) + \frac{\sigma_r(r) - \sigma_\theta(r)}{r} + F(r) = 0. \tag{3}$$

The problem is similar to that of the spinning disk as described by Timoshenko.[10] Using his method we find the following expressions for the radial and circumferential (hoop) stress components, σ_r and σ_θ:

$$\sigma_r = \frac{1}{3}N_c R(2 + \nu)[R - r] - \frac{1}{8}N_c(3 + \nu)[R^2 - r^2],$$
$$\sigma_\theta = \frac{1}{3}N_c R(2 + \nu)R - \frac{1}{3}N_c R(1 + 2\nu)r - \frac{1}{8}N_c(3 + \nu)R^2 + \frac{1}{8}N_c(1 + 3\nu)r^2. \tag{4}$$

It can be shown that these expressions satisfy Eqn. 3, above. In cgs-practical units, $N_c = 4\pi J_c^2/100$, while in SI it is $\mu_0 J_c^2$. We have applied the boundary condition that $\sigma_r = 0$ at $r = R$. σ_r and σ_θ are shown as a function of r in Fig. 4 for a sample with $R = 1.27$ cm and $J_c = 10^9$ A/m^2. σ_θ drops monotonically with r to $(N_c R^2/12)(1-\nu)$ at the sample perimeter. σ_r, however,

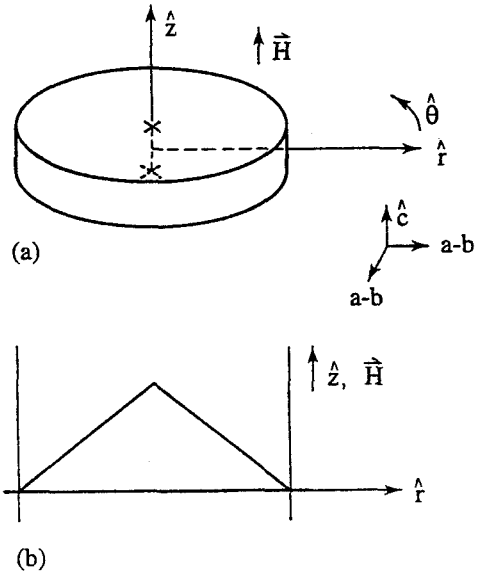

Figure 3. (a) Superconducting monolith with H∥c, and (b) Flux trapping profile.

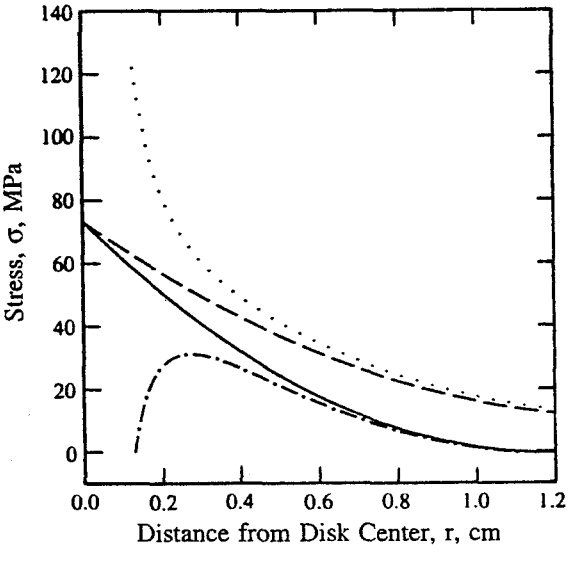

Figure 4. σ_r and σ_θ vs r for a solid superconducting disk (——σ_r,— —σ_θ), as well as one with a circular hole (—·—σ_r,·····σ_θ). Cylinder radius, R = 1.27 cm; hole radius, a = R/10; $J_c = 10^5$A/cm^2.

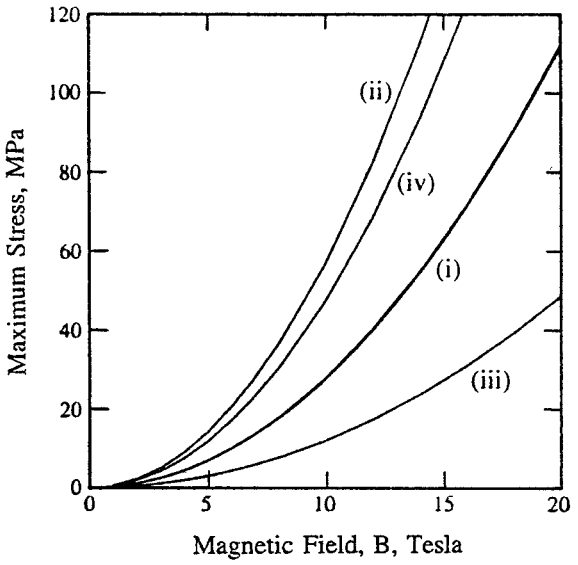

Figure 5. Maximum stresses for solid and axially perforated superconducting cylinders as functions of the maximum field (field at the center). (i) σ_r and σ_θ for the solid cylinder and σ_r for the axial pin-hole (a/R = 10^{-5}) cylinder; (ii) σ_θ for the latter; (iii) and (iv) σ_r and σ_θ, respectively, for the axially bored (a/R=10^{-1}) cylinder.

has a minimum at r = (8/9)R(1 + ν/2)/(1 + ν/3), and σ_r is negative in this region. Physically this represents the action of the hoop stresses set up in the outermost regions of the cylinder. At r = 0, σ_r and σ_θ are maximum and equal; they are given by

$$\sigma_{max} = \frac{\pi J_c^2 R^2}{600}(7 + 5\nu) \tag{5}$$

in cgs-practical units (A/cm^2, cm, dyn/cm^2). To convert to SI units (A/m^2, m, Pa) multiply the right hand side of Eqn. 5 by $100\mu_0/4\pi$ (= 10^{-5}, numerically).

Substituting ν = 0.3 in Eqn. 5 we find the maximum stress in the cylinder to be given by $\sigma_{max} \approx 0.35\mu_0 J_c^2 R^2$, which can be re-written in terms of maximum (r = 0) field, as $\sigma_{max} = 0.282 B_{max}^2$. For these last expressions it is convenient to use SI units where B_{max} is in tesla and σ_{max} is in MPa. This relation is shown in Fig. 5. The tensile strength of polycrystalline YBCO is about 15 MPa, while for a single crystal, it is closer to 60 MPa.[11] This translates into a maximum field of 14.5 T for crystalline YBCO, which is above the quench field at any temperature (see above). If, as an approximation, we set the tensile strength of any grain boundaries which might be present in this material to 15 MPa (that of the sintered material), then the maximum field is 7.29 T. This is only somewhat lower than the maximum quench field (≈10 T), and it is only exceeded by H_{fj} in a small region near 60 K (under certain assumptions). We may therefore expect that mechanical integrity is not a problem for these flux trapping superconductors. However, the strains associated with the stress values listed above may well degrade J_c, although we have not yet considered this.

Next we go on to consider the same sample, but with an axial hole of radius a. The boundary conditions in this case are σ_r = 0 at r = a and r = R. For the case of superconducting solenoids, Wilson[9] has developed an expression analogous to those above. If $J_{eff} = J_c$, these expressions can be re-written for comparison to the monolithic case as

$$\sigma_r(r,a,R) = \sigma_r(a=0) + \sigma_{add}$$

$$\sigma_\theta(r,a,R) = \sigma_\theta(a=0) + \sigma_{add} \tag{6}$$

where

$$\sigma_{add} = \frac{1}{3}N_c(2 + \nu)\left(\frac{Ra^2}{R + a}\right)\left[1 - q\frac{R^2}{r^2}\right] - \frac{1}{8}N_c(3 + \nu)a^2\left[1 - q\frac{R^2}{r^2}\right]$$

where q = 1 for σ_r and q = -1 for σ_θ. In the above treatment, hollow cylinders and potted Bi:HTSC/Ag pancake coils give the same results as solenoids. Plots for σ_r and σ_θ for a = R/10 are shown in Fig. 4 for comparison to the results for the monolith. We can see that the presence of the hole decreases σ_r, but increases σ_θ. In Fig. 5, curves of maximum σ_r and σ_θ (for a given internal B) are shown as a function of the internal field, B (which is assumed constant throughout the hole) and compared to the monolith results. For the case with the center hole, σ_θ still maximizes at the inner boundary, but σ_r maximizes somewhere within the structure, as shown in Fig. 4. As we can see in Figs. 4 and 5, with the introduction of a hole, σ_r becomes equal to or less than its counterpart for the monolith, while σ_θ becomes equal to or greater than its counterpart for the monolith. Thus, as shown in Fig. 5, in the limit of $a \rightarrow 0$, the maximum in $\sigma_{r,hole}$ is equal to the maximum value of $\sigma_{r,mono}$, while the maximum in $\sigma_{\theta,hole}$ is twice that of $\sigma_{\theta,mono}$. This agrees with the idea of stress enhancement around holes typically found in mechanics.

STABILITY IN MULTIFILAMENTARY STRANDS

Superconducting wires (strands) are generally produced in multifilamentary (MF) form. Low-T_c strands for accelerator magnet applications, for example, often consist of many thousands of filaments (e.g. 5,000 to 40,000); they are small in diameter to provide stability and low hysteretic loss, and twisted together to reduce eddy current loss to some fraction of the hysteretic value. As we shall see, in HTSC strands filamentary subdivision serves some of the above functions but also some additional ones. For practical reasons the number of filaments tends to be smaller and consequently the twisting requirement is less stringent. The first requirement in MF strand design is to prevent flux jumping. For NbTi, filaments smaller than about 100 μm in diameter are immune to it. This is also approximately true for HTSC strands at 4 K. But at 77 K they are adiabatically flux jump stable in diameters as large as several cm. In general, requirements other than stability tend to dictate the choice of filament diameter. For LTSCs these are low magnetization and low AC loss. For HTSCs the dominating requirement has to do with grain alignment. For example in the Ag-clad Bi:HTSC wires, alignment seems to take place when the superconductor "thickness" is less than about 50 μm. The following account demonstrates that this is certainly compatible with flux jump stability.

In calculating the filament diameter requirements for flux jump stability two alternative criteria may be applied -- the adiabatic and the dynamic. The former dominates if the heat capacity is high and cryocooling can be ignored; in the dynamic case heat conduction to a cryogen bath must be invoked. The maximum filament diameter under the adiabatic criterion (based on a slab calculation[12, p.134]) in c.g.s. units is

$$d_{ad} = \sqrt{10^9\left(\frac{3}{\pi}\right)C(T)\Delta T_0/J_c(T,H)} \qquad (7)$$

The dynamic criterion (based on a cylinder calculation[12, p.156]) yields

$$d_{dyn} = 2\sqrt{8\frac{K_{SC}}{\rho_{Ag}}\Delta T_0\frac{1-\lambda}{\lambda}}\ /J_c(T,H) \qquad (8)$$

In these equations C(T) and K_{SC} are the heat capacity and thermal conductivity, respectively, of the superconductor (SC), ρ_{Ag} is the silver stabilizer resistivity, λ is the volume fraction of SC in the composite (herein 0.5) and $\Delta T_0 \equiv J_c/(-dJ_c/dT)$.

The equations can be evaluated using the appropriate cryophysical property data.

Cryophysical Property Data

The temperature dependencies of the relevant thermal and electrical properties of YBCO and copper (for model calculations of the stabilities of YBCO/Cu composites) were previously listed.[5] In what follows we repeat some of the earlier calculations but for the more realistic case of YBCO/Ag, since the following data for Ag has recently become available. In addition, for ΔT_0 and $J_c(T,H)$ we draw on new data from Maley et al.[6] As indicated earlier the $J_c(T,H)$ of melt processed YBCO (T_c = 90 K) is well described by an exponentially decreasing temperature dependence to about 80 K of the form (5.92 x 10^5 A/cm^2)exp(-T/T_s) with T_s = 19.87 K, combined with a Kim-type field dependence quotient of the form $H_0(T)/\{H_0(T)+H\}$ in which $H_0(T) = a\text{-}bT$ (a = 2.504 tesla, b = 2.79x10^{-2} tesla/K). Above about 80 K, J_c drops linearly to zero at T_c. Thus at 4 K, $\Delta T_0 = T_s$ = 19.87 K; while at 77 K, ΔT_0 may be approximated by the usual (T_c-T_b) = 13 K.

Electrical Resistivity of the Silver Stabilizer: Drawn wires of 99.99% Ag and an Ag-0.1%Al alloy were annealed in air for 24h/840°C during which they became charged with oxygen and the alloy internally oxidized to Ag plus Al_2O_3. Their measured resistivities were: **Ag:** ρ_{4K} = 9.27 nΩcm, ρ_{77K} = 290.56 nΩcm; **Ag+Ox:** ρ_{4K} = 247.42 nΩcm, ρ_{77K} = 624.51 nΩcm.

Magnetoresistance of Silver: The magnetoresistivity of Ag over the temperature range 4.2-159 K has been measured by Iwasa et al.[13] Based on their data we have deduced that at 4.2 K a field of 5 T adds to Ag a resistivity of 11.61 nΩcm. In the stability calculations we assume this to be temperature independent and add it to both the 4.2 K and 77 K resistivities to take into account the effect of a 5 T field.

Maximum Filament Diameters for Flux Jump Stability

Based on Eqns. (8) and (9) the maximum filament diameters for adiabatic and dynamic flux jump stability, respectively, are as depicted in Table 1. The table indicates that at 4 K the dynamic criterion applied to the pure-Ag-stabilized composite guarantees the stability of filaments of the size expected in practice (certainly less than 100 μm). Some dynamic stability is lost when oxide-strengthened Ag is employed, in which case the adiabatic and dynamic results are similar. At 77 K both YBCO and YBCO/Ag are "overstable" from both adiabatic and dynamic standpoints; filaments thicker than those that would ever be encountered in practice are immune to flux jumping.

Table 1. Maximum Filament Diameters for Adiabatic and Dynamic Stability

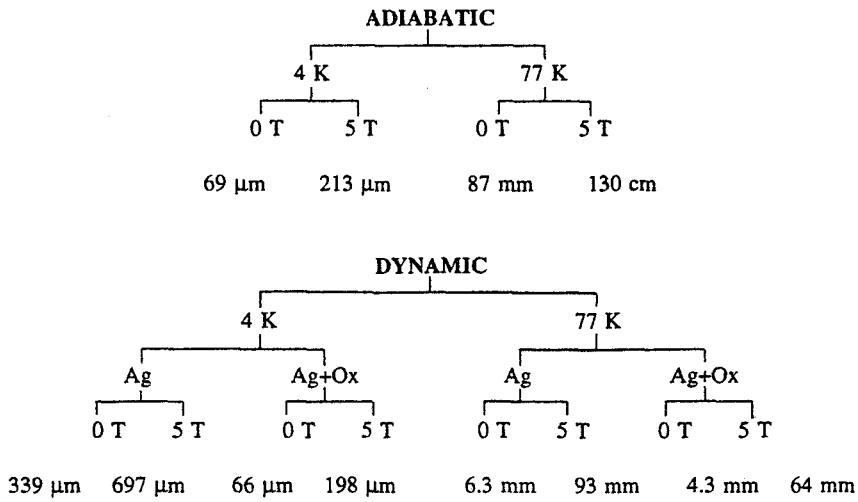

Strand Stability and Cryostability

Other aspects of strand stability, including maximum adiabatic strand diameter and cryostability have been adequately explored in an earlier publication.[5] An important feature of strand cryostability is the possibility of occurrence, as the result of some disturbance, of the "minimum propagating zone" or MPZ, and the rate at which it expands (v_{MPZ}) to quench (and thereby protect) the coil in which it was imbedded. In the reference just cited it is clear that at 77 K the adiabatic v_{MPZ} is so slow that special precautions must be taken to avert hot-spot formation and possible strand burn-out.

AC LOSS

Hysteretic and Eddy Current Loss in HTSC/Ag MF Strands

At low temperatures the attractive characteristic of the HTSC is its high upper critical field. Since advantage would not be taken of this property in an AC application it is doubtful if HTSCs would ever replace LTSCs in such conditions. For this reason we confine our analysis of AC loss to the high temperature regime around 77 K.

According to the Carr's "anisotropic-continuum" representation of a multifilamentary superconductor[14] the AC loss experienced by a superconducting strand in a transverse magnetic field consists of two components -- hysteretic (a property of the irreversible superconductor itself) and eddy current (due to currents circulating around the composite). At low frequencies of the applied magnetic field the hysteretic component in c.g.s practical units is given by

$$\dot{Q}_h = \frac{8x10^{-8}}{3\pi}\lambda J_c d\, H_m f \qquad W/cm^3 \qquad (10)$$

where H_m is the amplitude of a sinusoidal field of frequency f. Again at low frequencies the eddy current component is given by

$$\dot{Q}_e = \frac{10^{-7}}{2}\frac{L_p^2}{\rho_{\perp n\Omega cm}} H_m^2 f^2 \qquad W/cm^3 \qquad (11)$$

where L_p is the twist pitch and $\rho_{\perp n\Omega cm}$ is the transverse resistivity of the strand in nΩcm (which in this case we will take to be the matrix (Ag) resistivity). To provide an estimate of the magnitudes of these quantities to be expected in a typical situation, we imagine fields of amplitudes, H_m, of up to 800 Oe, to be applied to a series of typical MF strands.

Our basic model MF strand is in the form of a central filament surrounded in succession by rings of 6, 12, and 18 filaments. A double-stack strand is composed of a six-around-one bundle of the above, for a total of (1+6+12+18)x7 = 259 filaments. Let strands of 1, 7, 19, 37, and 259 filaments of $J_c(0T) = 1.228 \times 10^4$ A/cm^2 each carry a critical transport current of 10 A. The corresponding filament diameters under these conditions would then be 322, 122, 74, 53, and 20 μm -- a realistic sequence. The H_m-proportional hysteretic power loss would then be as depicted in Fig. 6.

To model the eddy current loss we equate $\rho_\perp$ with the 77 K resistivity of oxidized Ag-0.1%Al, viz. 624.51 nΩcm, and assume twist pitches, L_p, of 1, 0.5, and 0.25 cm. The corresponding eddy current power loss is also depicted in Fig. 6. The maximum possible eddy current loss occurs when the filaments are all fully coupled. In this case Q_e is equivalent to the hysteretic loss of a monocore of critical current density λJ_c equal in diameter, D, to that of the whole filamentary bundle. Obviously the ratio $Q_{coupled}/Q_{monocore}$ is just $Q_{coupled}\sqrt{\lambda}$. Represented by the dashed line in Fig. 6 it places a limit on the magnitude of the low frequency eddy current loss. The possibility of eddy current loss is most serious in strands with very large numbers of fine filaments -- e.g. those intended for LTSC accelerator magnet windings. But even in the present example, for H_m = 800 Oe, the ratio of Q_e(most strongly coupled) to Q_h(finest filaments) is 94.9/4.2 = 22/1.

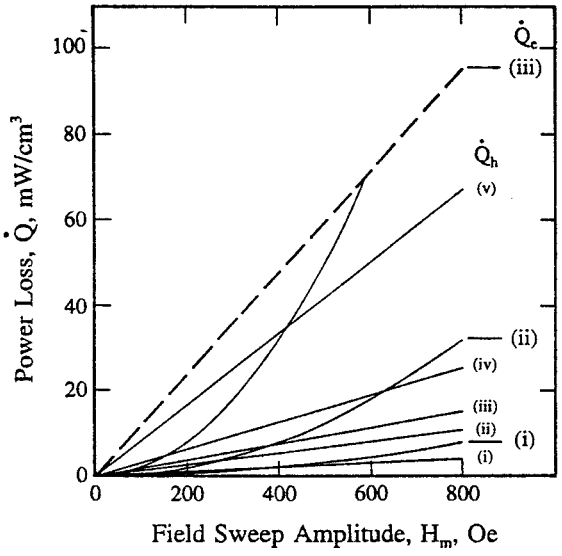

Figure 6. Per-unit-volume AC loss for a series of model MF YBCO/Ag strands of fixed λ (= 0.5) and I_c (= 10 A), hence fixed SC area, but with filament numbers/diameters of: (i) 259/10 μm, (ii) 37/26 μm, (iii) 19/36 μm, (iv) 7/60 μm, and (v) 1/158 μm. Depicted is the hysteretic loss, $\dot{Q}_h$, and the eddy current loss, $\dot{Q}_e$, corresponding to strand twist pitches, L_p, of (i) 0.25, (ii) 0.5, and (iii) 1 cm. Also shown as a dashed line is the limiting eddy current loss, that for a fully coupled strand, equal to $\dot{Q}_{h,monocore}/\sqrt{\lambda}$. The Q_h data are valid for H_m greater than the full penetration fields of: (i) 10, (ii) 26, (iii) 36, (iv) 60, and (v) 158 Oe.

Twist Pitch, Matrix Resistivity, and Filament-Diameter Considerations

Based on the above physical-property data set the ratio Q_e/Q_h is just $0.7681(L_p^2/d_{\mu m})H_m$ which emphasizes the importance of reducing both twist pitch and filament diameter in the minimization of eddy current loss. For equal loss at H_m = 500 Oe, for example, $d_{\mu m}$ = 384 $L_{p,cm}^2$. When d = 24 μm this calls for a twist pitch of 0.25 cm. For the strand diameter D = $d\sqrt{(N/\lambda)}$ = 0.46 mm considered in these examples, this corresponds to a pitch/diameter ratio of 5.5/1 which would be quite tight even for a NbTi/Cu strand. The alternative to reducing L_p is increasing the matrix resistivity.

If sufficient twist or resistivity cannot be introduced, full electrical advantage cannot be taken of multifilamentary subdivision, especially since fine filaments often turn out to be interconnected by "bridges". Nevertheless there are other advantages to be considered: (1) Reduction of filament diameter aids in HTSC grain alignment. (2) The ductile interfilamentary matrix with its crack-stopping potential can be expected to contribute a higher strain tolerance to the finer-filament composite; in which case even bridging may be an advantage.

REFERENCES

1. S.W. Hsu, K. Chen, and W.H. Lee, "Temperature and Field Sweeping Rate Dependence of Flux Jumps in a Melt-Textured $YBa_2Cu_3O_{7-x}$ Superconductor" **75**, 799-803 (1990).
2. K.-H. Müller and C. Andrikidis, "Flux Jumps in Melt-Textured Y-Ba-Cu-O", Phys. Rev. B. **49**, 1294-1306 (1994).
3. R. Hancox, "The Superconductivity of Sintered Nb_3Sn at Temperatures Above 4.2 K", Appl. Phys. Lett. **7**, 138-139 (1965).
4. J. Sosnowski, "Influence of Magnetic History on Flux Jump Fields", J. Appl. Phys. **59**, 4189-4191 (1986).
5. E.W. Collings, "Conductor Design with High-T_c Ceramics: A Review", **Advances in Superconductivity-II**, ed. by T. Ishiguro and K. Kajimura, (Springer-Verlag, 1990) pp. 327-333.
6. P.J. Kung, M.P. Maley, M.E. McHenry, J.O. Willis, J.Y. Coulter, M. Murakami, and S. Tanaka, "Magnetic Hysteresis and Flux Creep of Melt-Powder-Melt-Growth $YBa_2Cu_3O_7$ Superconductors", Phys. Rev. B. **46**, 6427-6434 (1992).
7. M. Chiba, T. Ogasawara, N. Miyazawa, S. Ban, et al, "The Magnetic Stability of Face-Cooled Composite Tape Superconductors", IEEE Trans. Magn. **27**, 1656-1659 (1991).
8. H. Brechna, **Superconducting Magnet Systems**, (Springer Verlag, NY, 1973) pp. 139-142; see also H. Brechna, "Superconducting Magnets", in **Superconducting Machines and Devices, Large Systems Applications**, ed. by S. Foner and B. Schwartz, NATO Advanced Study Series, (Plenum Press, NY, 1974) pp. 162-165.
9. M.N. Wilson, **Superconducting Magnets**, (Oxford, NY, 1983) pp. 41-46.
10. S. Timoshenko and J.N. Goodier, **Theory of Elasticity**, (McGraw Hill, NY, 1951), pp. 69-71.
11. K. Salama, private communication, 1994.
12. E.W. Collings, **Applied Superconductivity, Metallurgy and Physics of Titanium Alloys**, Volume 2, (Plenum Press, NY, 1986).
13. Y. Iwasa, E.J. McNiff, R.H. Bellis, and K. Sato, "Magnetoresistance of Silver over Temperature Range 4.2 - 159 K", Cryogenics **33**, 836-838 (1993).
14. W.J. Carr Jr., **AC Loss and Macroscopic Theory of Superconductors**, (Gordon and Breach, NY, 1983) p. 348.

SINGLE SCAN
5/6-76 313691

Presented at the World Congress on Superconductivity IV, June 27-July 1, '94, Orlando/FL,USA.

342956

ASPECTS OF PASSIVE MAGNETIC LEVITATION BASED ON HIGH-T_c SUPERCONDUCTING YBCO THIN FILMS

P. Schönhuber* and F. C. Moon
Mechanical and Aerospace Engineering, Cornell University,
Ithaca, NY 14853, USA.

Abstract - Passive magnetic levitation systems reported in the past were mostly confined to bulk superconducting materials. Here we present fundamental studies on magnetic levitation employing cylindrical permanent magnets floating above high-T_c superconducting YBCO thin films (thickness about 0.3 μm). Experiments included free floating rotating magnets as well as well-established flexible beam methods. By means of the latter, we investigated levitation and drag force hysteresis as well as magnetic stiffness properties of the superconductor-magnet arrangement. In the case of vertical motion of the magnet, characteristic high symmetry of repulsive (approaching) and attractive (withdrawing) branches of the pronounced force-displacement hysteresis could be detected. Achievable force levels were low as expected but sufficient for levitation of permanent magnets. With regard to magnetic stiffness, thin films proved to show stiffness-force ratios about one order of magnitude higher than bulk materials.

Phenomenological models support the measurements. Regarding the magnetic hysteresis of the superconductor, the Irie-Yamafuji model was used for solving the equation of force balance in cylindrical coordinates allowing for a macroscopic description of the superconductor magnetization. This procedure provided good agreement with experimental levitation force and stiffness data during vertical motion. For the case of (lateral) drag force basic qualitative characteristics could be recovered, too. It is shown, that models based on simple asymmetric magnetization of the superconductor describe well asymptotic transition of drag forces after the change of the magnet motion direction. Virgin curves (starting from equilibrium, i.e. symmetric magnetization) are approximated by a linear approach already reported in literature, only.

This paper shows that basic properties of superconducting thin films allow for their application to magnetic levitation or - without need of levitation forces, e.g. microgravity - magnetic damping devices.

*on leave from Technical University Vienna, Gusshausstr. 27/351, A - 1040 Vienna, Austria.

1. INTRODUCTION

Magnetic levitation and suspension experiments and studies based on either permanent magnets floating above bulk high-T_c superconducting materials or superconducting samples being suspended below magnets, have been reported widely in the past (for a review see [1]). Several basic properties of these arrangements are understood quite well, thus enabling a wide range of possible industrial applications of this new class of materials.

While many efforts are made to further increase important specifications of bulk superconductor-magnet properties, such as maximum force level, long term stability, achievable r.p.m., etc., to our knowledge, no levitation experiments have been reported employing superconducting thin films instead of bulk materials. In this paper we present fundamental studies of such arrangements. These offer new possibilities for applications and devices such as microturbine rotors, micromotors and microgyros, and damping devices in e.g. microgravity environment.

Section 2 gives a short overview of basic properties of superconductor-magnet arrangements. We report on experiments applying typical representatives of bulk materials including sintered as well as melt-quenched samples, describe their characteristic properties and compare the results with those from thin films. In Section 3 we introduce a model of the thin film - permanent magnet interaction which allows for an interpretation of the experimental data. Highly hysteretic force-displacement relations in the case of vertical as well as horizontal magnet motion are explained in terms of a critical-state hysteretic magnetization model of the superconductor. Section 4 deals with force-creep phenomena, which were observed to considerably impair the usable force range. However force-creep is not included in the model presented here.

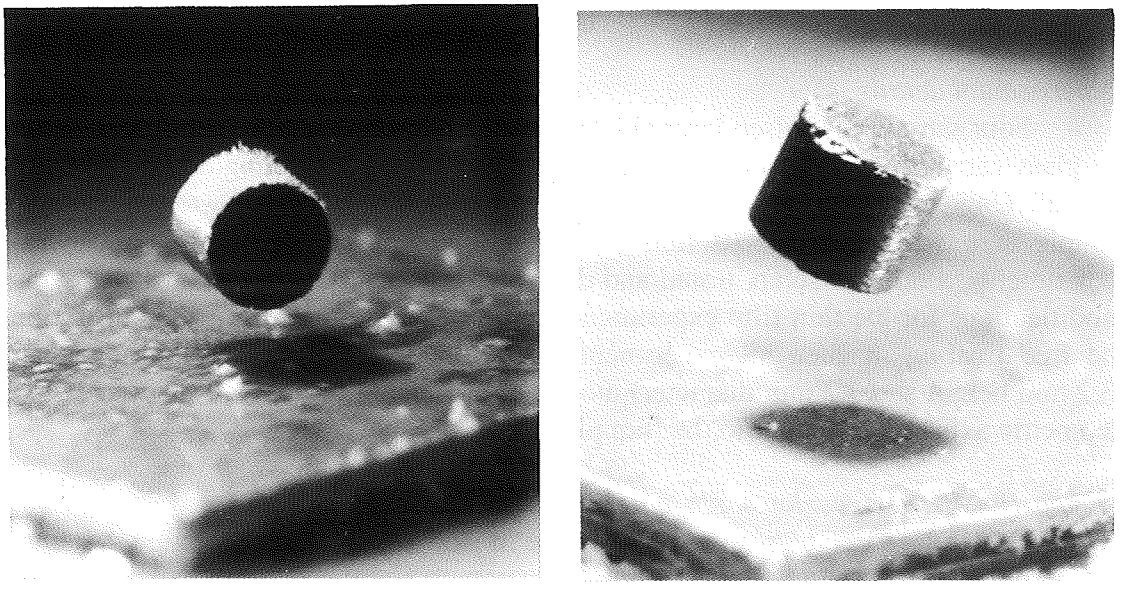

Fig. 1 Cylindrical permanent magnet (diameter 1.2 mm) free floating above a HTSC thin film (10 mm square). Levitation height is about 1 mm.

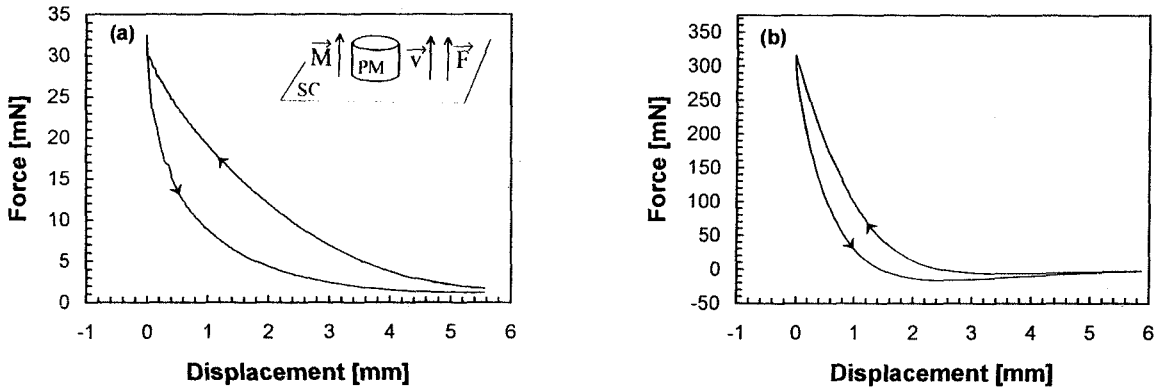

Fig. 2 Typical vertical force vs. magnet height relation for a bulk superconductor (PM ... permanent magnet, SC ... superconductor, **M** ... magnetization, **v** ... magnet velocity, **F** ... vertical force): (a) sintered, (b) melt-quenched sample.

2. SUMMARY OF EXPERIMENTAL DATA AND RESULTS

The free floating permanent magnet

Figure 1 shows a cylindrical permanent magnet free floating above a superconducting YBCO thin film. Although similar pictures from bulk samples are highly familiar to a wide public since 1987 and reported in many journals, it is pointed out, that the experiment shown in Fig. 1 is based on a thin film, the thickness of which is about 0.3 μm, thus at least 4 up to 5 orders of magnitude below that of bulk material. (In fact, the picture primarily shows the glass carrier of the film!) On the other hand, typical values of thin film critical current densities J_c are in the range of 10^6 - 10^7A/cm^2 in comparison to 10^3 - 10^4A/cm^2 in bulk superconductors. The magnet could be placed manually in any arbitrary position within the range of levitation height and resembled a similar behavior as what is known from bulk material and was described by Brandt as "embedded in an invisible heap of sand" [2].

Experimental details

Four samples of pulsed laser ablated YBCO thin films on MgO substrate mounted on glass carriers were provided by the School of Applied and Engineering Physics at Cornell University and one by NASA Lewis Research Laboratory, respectively. The sample size was typically 10 mm square and about 0.3 μm thick. For levitation experiments, a reliable setup, tested and described earlier [3], was used with only minor modifications for the thin film experiments. With the exception of the demonstration of the free floating magnet, all experiments were performed with a cylindrical magnet (3.2 mm height and 3.2 mm diameter) mounted on flexible beams with its magnetic and geometric axis perpendicular to the film plane.

Comparison between various bulk materials and thin films

Hysteretic force-displacement relations in passive magnetic levitation systems are caused by irreversible flux motion within the superconductor and are therefore a common feature in such arrangements. With (weak-pinning) sintered superconducting material, the vertical motion hysteresis loop is typically restricted to repulsive values during the

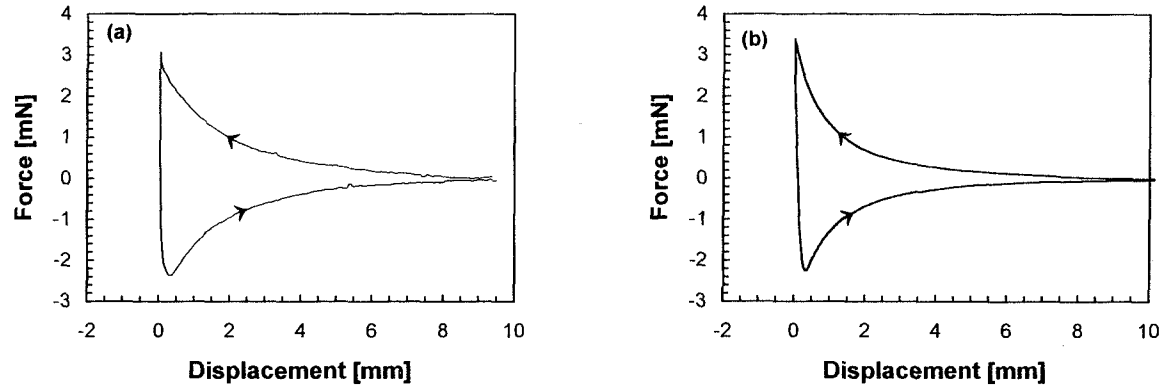

Fig. 3 Vertical force vs. magnet height (= displacement) above thin film sample: (a) measured, (b) calculated.

whole approaching and retreat cycle (Fig. 2a). By introducing modern melt-quenched materials with considerably higher critical current densities, higher force levels can be reached. At the same time, strongly pinned fluxoids cause a transition to attractive forces during the retreat cycle, thus enabling suspension (Fig. 2b). This effect proves to be especially pronounced in the field cooled case. This behavior was predicted on the basis of theoretical considerations [4]. In addition, it was argued, that the amount of the attractive region within the hysteresis depends on the amount of the superconductor volume affected by a sufficiently high magnetic field [5].

The vertical motion hysteresis loop

In the case of the superconducting thin films considered here, the amount of superconducting volume penetrated by a sufficiently high magnetic field is especially high, resulting in pronounced attractive regimes and almost symmetric repulsive and attractive branches of the hysteresis (Fig. 3a). With the 3.2 mm magnet used here, the range of measurable interaction was about 10 mm. Force vs. displacement (i. e. magnet height above thin film) was of exponential type (cf. [1]) with maximum force values of about 4 mN. In contrast to bulk material, the retreat branch exhibited an exponential-type behavior, too. By performing arbitrary back and forth procedures any point within the

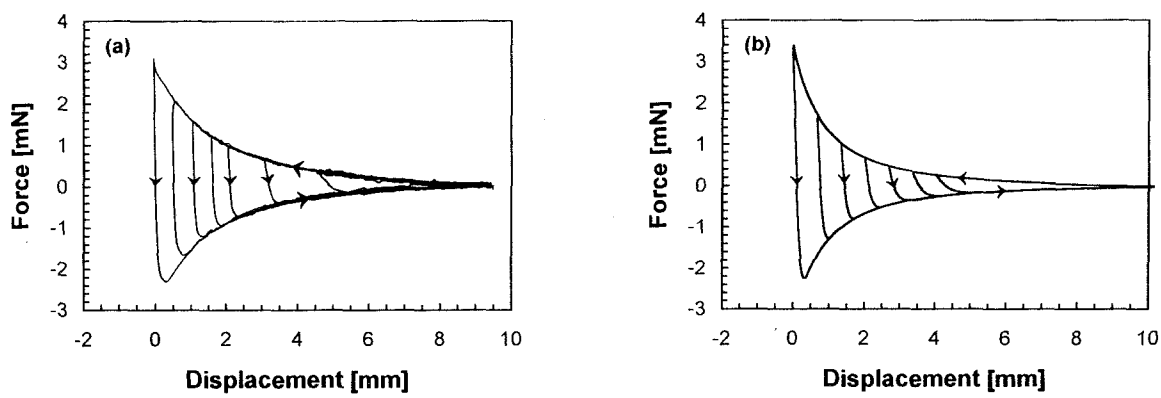

Fig. 4 Set of force-displacement hysteresis loops for a thin film: (a) measured, (b) calculated.

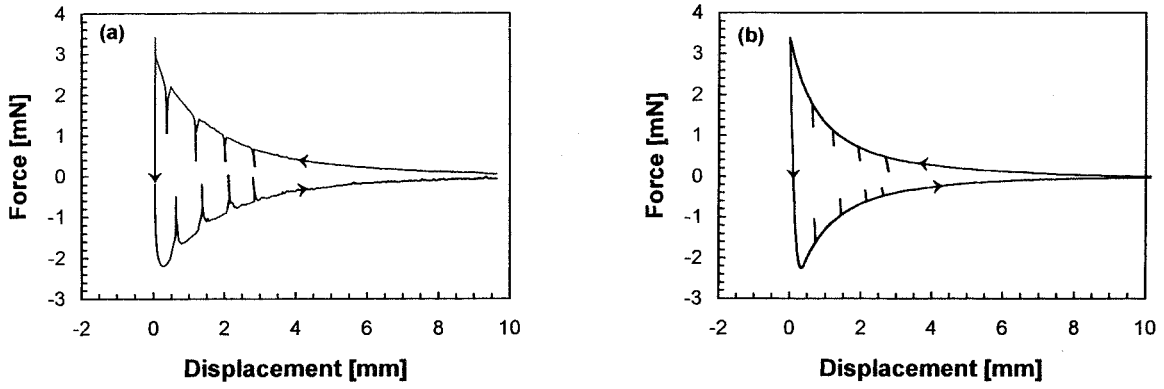

Fig. 5 Set of minor loops for stiffness evaluation: (a) measured, (b) calculated.

hysteresis loop received by a monotonic cycle can be reached. A set of hysteresis loops is shown in Fig. 4a. Here, the reversal point was increased step by step from the film surface. Regarding minor loops, large amplitude reversals were of irreversible hysteretic behavior, while reversible loops of considerably small amplitudes (less than 80 μm, depending on the respective force level) were used for stiffness evaluation (Fig. 5a).

The lateral motion hysteresis loop

For the lateral motion of the magnet, a behavior was found very similar to that known from bulk material. A rather steep linear increase of the drag force opposing the magnet motion direction is followed by a saturating force value. Once the saturation is reached in one direction, rather symmetric branches result from magnet cycling over a sufficient large distance in the mm range. Local reversals of the magnet motion direction yield reversible (or weak hysteretic in the case of high amplitudes, respectively) minor loops, appropriate for stiffness evaluation of the arrangement (Fig. 6, the above mentioned initial curve is not shown in the experimental result, Fig. 6a).

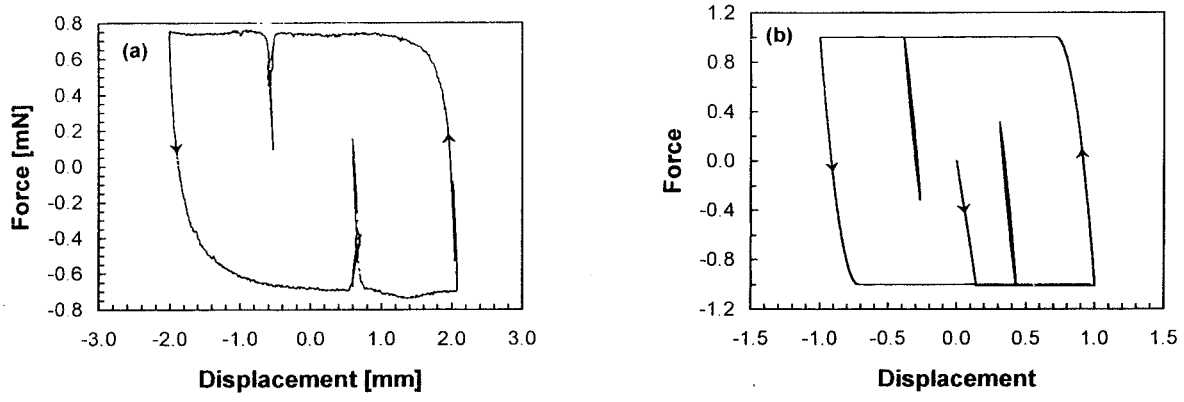

Fig. 6 Lateral force vs. lateral magnet displacement above thin film: (a) measured, (b) model, normalized to maximum force and displacement, respectively.

Vertical and lateral magnetic stiffness

By evaluating the reversible minor loops, thin films were found to have superior stiffness properties than bulk materials. This is especially true for the vertical motion case, where thin films approached an order of magnitude higher values than sintered and melt-quenched bulk samples. This is considered as another consequence of high critical current densities in thin films. In the lateral motion case the effect was not as pronounced but still clearly seen (cf. Fig. 8).

3. MODELING OF THE HYSTERESIS LOOPS

Considerable effort in modeling magnetic levitation forces have been reported (for a review see e. g. [1]). This includes analytical methods to solve the field problem. Here, certain simplifications, such as the image method, cover type I superconductors only. But even more sophisticated methods such as those applied by Z. J. Yang et al. [6] do not take into consideration hysteretic effects. However, keeping in mind that the pronounced magnetic hysteresis of the superconducting material is one of the basic features (maybe the most important one) necessary for self-stabilizing passive magnetic levitation or suspension systems, respectively, we tried to setup a model which is mainly based on the magnetic hysteresis of the superconductor.

Here we follow arguments outlined in the work of Irie and Yamafuji [7] and discussed in more detail in [8]. Solving the balance of force equation (based on the confrontation of Lorentz force and pinning force) formulated for fluxoids yields locally varying flux density and magnetization distributions. By averaging out the sample volume, we get expressions for the superconductor's bulk magnetization [8]. A typical result is shown in Fig. 7 for cycling in an unipolar field including minor loops. (It is realized, that the Bean model, Fig. 7a, is included as a special case of the more general Irie-Yamafuji model, Fig. 7b). With this, the force calculation is performed under the

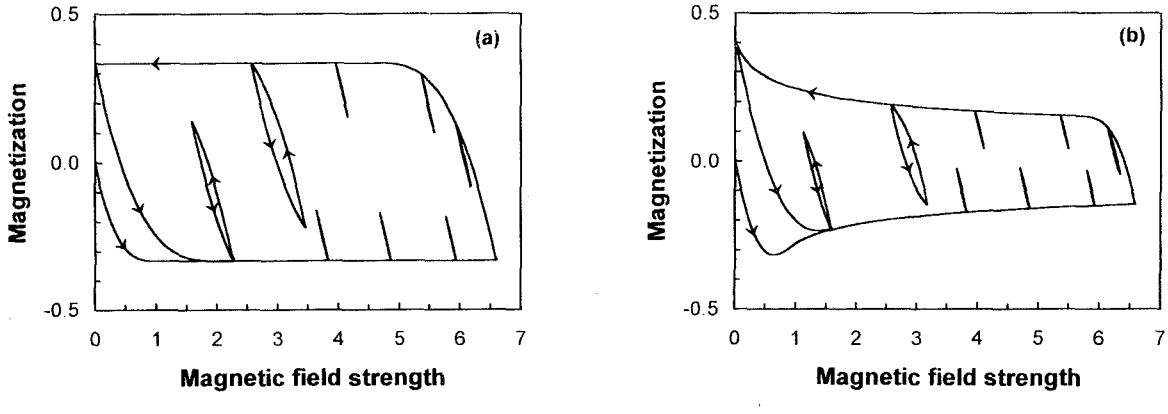

Fig. 7 Calculated magnetic hysteresis of a strong pinning type II superconductor (normalized to penetration field, see [8]): (a) Bean model, (b) Irie-Yamafuji model.

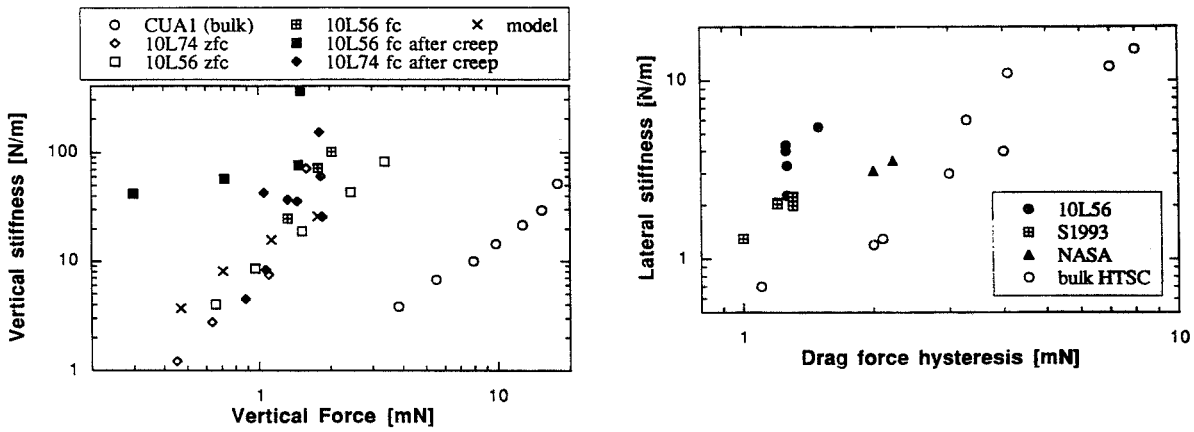

Fig. 8 Magnetic stiffness vs. force for sintered bulk and various thin film samples: (a) vertical, (b) lateral motion.

assumption of a dipole-like magnetic field. Figs. 3b - 5b show respective results of the calculation, simulating similar conditions as in the experiments (Figs. 3a - 5a). Calculated stiffness values taken from minor loops in Fig. 6a proved to be in reasonable accordance to measured results (Fig. 8).

For the case of lateral magnet motion, the modeling process is based on an assumed asymmetric magnetization of the superconductor only. The averaging process over the locally varying magnetization is restricted to each of the two halves, one facing the magnets motion direction and the other averting it. An obvious shortcut is the neglect of the actual field distribution. In spite of the ad-hoc nature of this model, some basic qualitative features can be reproduced in the simulation (Fig. 6).

4. FORCE-CREEP PHENOMENA

In contrast to bulk material, the levitation with thin film specimens showed

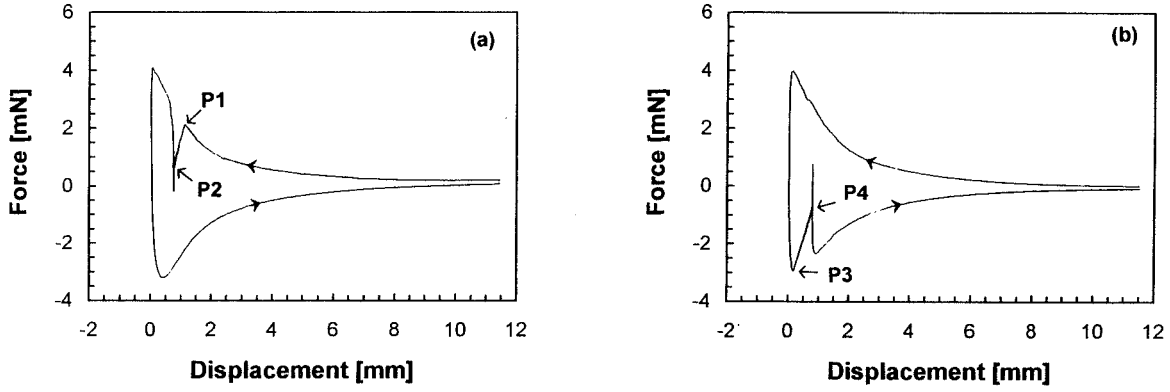

Fig. 9 Force creep during 650 s in maximum force-displacement hysteresis loop in (a) approaching (P1->P2) and (b) retreat (P3->P4) branch.

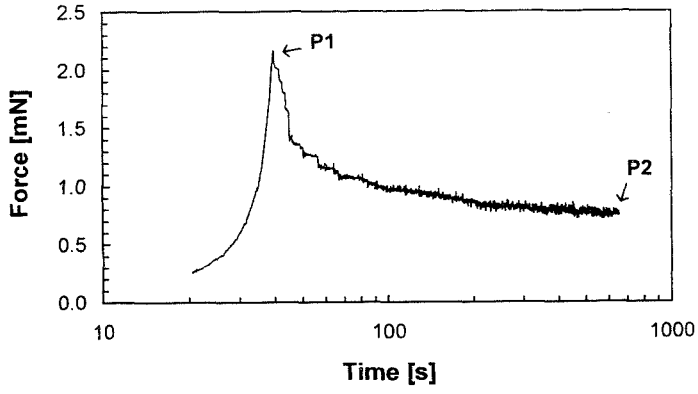

Fig. 10 Force vs. time during creep-phase shown in Fig. 9a.

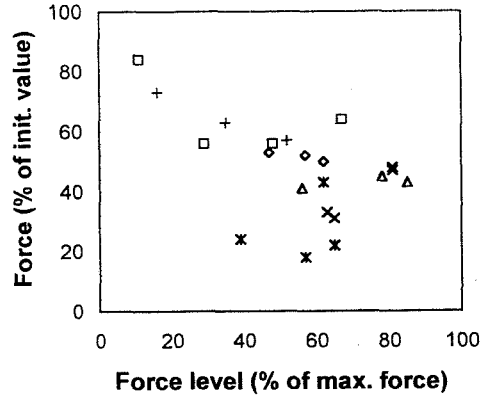

Fig. 11 Percent of remaining force (after creep) vs. initial force level for various film samples.

considerable force-relaxation with time, the amount of which significantly reduced the practical usable force range. As a typical result, Fig. 9 shows the force history after stopping the magnet at a point P1. The linear relation of simultaneously decreasing force and magnet height reflects the beam characteristics and is therefore found to be rather independent of the force level (as long as the force-deflection relation of the beam is linear). A force reduction by about 65% during 650 s lead to a rather stable force level P2 thereafter. By inspection of the course of time of the force (Fig. 10) a strikingly pronounced rather steep initial creep phase followed by several discontinuities and jumps can be observed. As preliminary experiments indicated, such jumps could be produced by external sources such as slightly tapping on the experimental setup. However, although utmost care was taken during the experiments (including the use of a low-stiffness, high-mass table) we could not completely avoid the occurrence of such jumps. They are, therefore, considered to be possibly characteristic for the creep process in the thin films. Fig. 11 shows data concerning the amount of force-creep related to the respective force. From that, a moderate scattering of the amount of creep can be seen.

Improvements of thin film materials such as implementing additional pinning centers may be able to reduce force creep. However possible applications are still to be expected in the low-mass range or where gravity is low e.g., in microgravity environment and magnetic damping is required.

5. CONCLUSIONS

The following conclusions can be drawn from this work:

(a) High-Tc superconducting YBCO thin films can successfully be used for magnetic levitation. This includes free floating cylindrical magnets as well as samples fixed to elastic beams for precise deflection measurements.

(b) Highly symmetric force-displacement hysteresis loops with respect to (repulsive) approaching and (attractive) retreat curves, the latter giving rise to suspension systems, are found to be characteristic for thin film-magnet arrangements described here.

(c) Application of the critical state Irie-Yamafuji-model provides reasonably good simulation data for the force-displacement behavior. Further improvement can be expected from the application of appropriate oblate spherical geometry instead of simple cylindrical one used here.

(d) Simulation of lateral drag force hysteresis, based on asymmetric macroscopic magnetization of the superconductor, exhibits basic features observed experimentally. However more refined models will be necessary for detailed studies including quantitative predictions of achievable force values.

(e) With the thin film samples used in this study, a pronounced force-creep effect was observable, thus considerably reducing the usable force range. Uncertainties arise from a distinct scattering of the amount of creep. However stiffness properties were not affected by the creep phenomenon. Material processing techniques may be possible to minimize this creep effect.

Acknowledgments - Supply of thin film samples by Prof. R. Buhrman, School of Applied and Engineering Physics, Cornell University, and by NASA Lewis Research Laboratory is gratefully acknowledged. One of the authors (P.S.) also acknowledges financial support provided by the Austrian Science Foundation (under contract #J863-TEC) as well as the Bundeskammer der gewerblichen Wirtschaft Österreichs.

REFERENCES

[1] F. C. Moon, *Superconducting Levitation*, J. Wiley & Sons, New York (1994).

[2] E. H. Brandt, "Friction in levitated superconductors," *Appl. Phys. Lett.* **53** (16), 1554, (1988).

[3] F. C. Moon, "Hysteretic levitation forces in superconducting ceramics," *Appl. Phys. Lett.* **52** (18), 1534 (1988).

[4] E. H. Brandt, "Rigid levitation and suspension of high-temperature superconductors by magnets," *Am. J. Phys.* **58** (1), 43 (1990).

[5] J. Hull et al., "Magnetic levitation and stiffness in melt-textured Y-Ba-Cu-O," *J. Appl. Phys.* **72** (5), 2089 (1992).

[6] Z. J. Yang et al., "Lifting forces acting on a cylindrical magnet above a superconducting plane," *Physica C* **197**, 136 (1992).

[7] F. Irie and K. Yamafuji, "Theory of flux motion in non-ideal type-II superconductors," *J. Phys. Soc. Jap.* **23** (2), 255 (1967).

[8] P. Schönhuber and F. C. Moon, "Levitation forces, stiffness and force-creep in YBCO high-T_c superconducting thin films," to appear in *Appl. Supercond.* (1994).

Abstract - World Congress 1994

Hybrid superconductor magnet bearings (HSMBs) utilize high temperature superconductors (HTSs) together with permanent magnets to form a frictionless interface between relatively rotating parts. They are low mass, stable, and do not incur expenditure of energy during normal operation. There is no direct physical contact between rotor and stator, and hence there is no wear and tear. However, just as any other applications of HTSs, it requires a very cold temperature to function. Whereas this might be perceived as a disadvantage on earth, it is of no great concern in space or on the moon. To astronomers, the moon is an excellent site for an observatory, but the cold and dusty vacuum environment on the moon precludes the use of mechanical bearings on the telescope mounts. Furthermore, drive mechanisms with very fine steps, and hence bearings with extremely low friction are needed to track star from the moon, because the moon rotates very slowly. All aspects considered, the HSMB is about the only candidate that fits in naturally. Here, we present a design for one such bearing, capable of supporting a telescope that weighs about 3 lbs on earth.

Author: Wei-Kan Chu
Address: Texas Center for Superconductivity
University of Houston
Houston, Texas 77204-5932
Telephone: (713) 743-8250
Fax: (713) 743-8201
E-mail: WKCHU@UH.EDU

SMALL SCAN
S18-76
313695

Progress in HTS Trapped Field Magnets: J_c, Area, and Applications

Roy Weinstein, Yanru Ren, Jianxiong Liu, Ravi Sawh, Drew Parks, Charles Foster*, Victor Obot**, G. Dickey Arndt***, and Alan Crapo****

Institute for Beam Particle Dynamics and Texas Center for Superconductivity, University of Houston, Houston, TX 77204-5506

*Indiana University Cyclotron Facility, Bloomington, IN 47405

**Dept. of Mathematics, Texas Southern University, Houston, TX 77004

***Johnson Space Center, NASA, Houston, TX 77058

****Emerson Electric Co., St. Louis, MO 63136

Abstract

Progress in trapped field magnets is reported. Single YBCO grains with diameters of 2 cm are made in production quantities, while 3 cm, 4 1/2 cm and 6 cm diameters are being explored. For single grain tiles: $J_c \sim 10{,}000$ A/cm^2 for melt textured grains; $J_c \sim 40{,}000$ A/cm^2 for light ion irradiation; and $J_c \sim 85{,}000$ A/cm^2 for heavy ion irradiation. Using 2 cm diameter tiles bombarded by light ions, we have fabricated a mini-magnet which trapped 2.25 Tesla at 77K, and 5.3 Tesla at 65K. A previous generation of tiles, 1 cm x 1 cm, was used to trap 7.0 Tesla at 55K. Unirradiated 2.0 cm tiles were used to provide 8 magnets for an axial gap generator, in a collaborative experiment with Emerson Electric Co. This generator delivered 100 Watts to a resistive load, at 2265 rpm. In this experiment activation of the TFMs was accomplished by a current pulse of 15 ms duration. Tiles have also been studied for application as a bumper-tether system for the soft docking of spacecraft. A method for optimizing tether forces, and mechanisms of energy dissipation are discussed. A bus bar was constructed by welding three crystals while melt-texturing, such that their a,b planes were parallel and interleaved. The bus bar, of area ~ 2 cm^2, carried a transport current of 1000 amps, the limit of the testing equipment available.

I. Introduction

Our research group has worked to develop trapped field magnets (TFM), made of high temperature superconductor (HTS), since about January of 1988. We will report here progress on TFM since the Third World Congress on Superconductivity in Munich Germany, in 1993 (WCS III)[1]. We will also report progress on certain applications since WCS III. Progress prior to that date is reported in Ref. 1, and in citations therein.

Models of the persistent current flow within a TFM[2-5] show that the maximum trappable field, $B_{t,max}$, is given approximately by

$$B_{t,\max} \propto J_c f(d) \qquad \text{Eq. 1}$$

where J_c is the critical current, d is the diameter of the contiguous current carrying region (a so-called grain, or tile), and f(d) is a complicated monotonically increasing function of d. For example in the present range of interest (but not in general), $f(d) \sim d^{1/2}$. A number of analyses of trapped field magnets in the literature assume incorrect variations of Eq. 1. These lead to disagreements with data, which are then erroneously attributed to TFM properties.

Guided by Eq. 1 our major efforts are directed to: (a) increase J_c; (b) increase d. In addition, we study basic properties of pinning centers to reduce creep. Our studies of creep will be reported elsewhere.

II. Improvements in Grain Diameter

At WCS III we reported a grain diameter of just over 2 cm. This had been achieved in exploratory experiments, not in regular production. In fact, the yield of usable TFMs, per processed ingot of $YBa_2Cu_3O_7$ (Y123), was only circa 15%.

At present two cm grains of Y123 are regularly produced. The yield of usable TFMs of 2 cm size, per processed unit of Y123, is now about 95%. In addition, tiles of 3.0, 4.5 and 6.2 cm have been produced on an exploratory basis. Also, using the same techniques, we produce 6 cm x 2 cm x 2 cm bus bars. These will be discussed in Sec. VI.

The tiles, or grains, reported at WCS III were produced by the melt-texture (MT) process.[6] The larger tiles now produced reliably were achieved by (a) optimization of the MT temperature profile (b) addition of circa 1% Pt, to control the shape of Y_2BaCuO_5 (Y211) inclusions in the Y123 tile, (c) the use of $SmBa_2Cu_3O_7$ (SM123) seeds, to initiate predominantly single grain structure, and (d) the use of Y211 platforms, on which the Y123 rests, which absorb excess Cu-Ba liquid formed during the process.

The single grain structure of the melt-textured tiles can be determined by measuring the trapped magnetic field, e.g., across the face of the tile, and comparing to theory.[4,5] An example of this is shown in Fig. 1. For this type of analysis an automated field scanning device is used.[4]

At the time of WCS III, the trapped field routinely achieved in a single tile, prior to irradiation, was ~1,500 Gauss [1], and was ~5,000 Gauss after irradiation. (The exploratory tile with d~ 2 cm trapped 2,200 G prior to irradiation.) At present, routine 2cm tiles trap 4300-4500 G prior to irradiation, and over 12,000 G after irradiation.

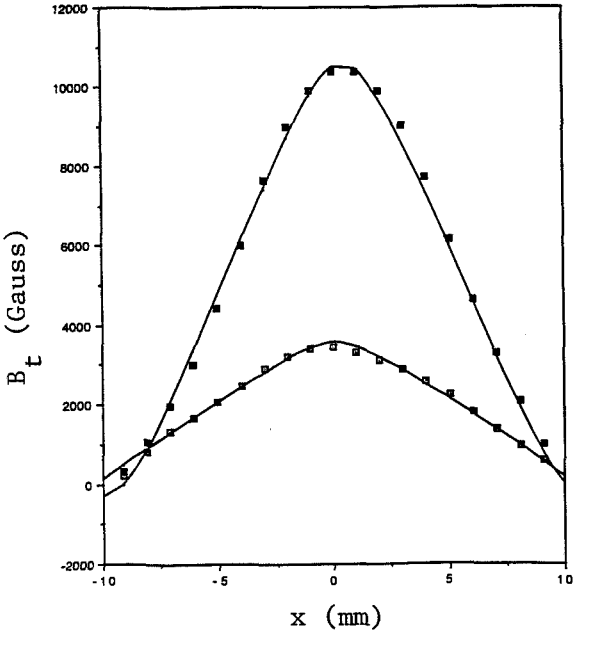

Fig. 1. Trapped field vs. position along the diameter of a single 2 cm grain of Y123. Lower points are before, and upper points are after p^+ bombardment. Solid curves are the theory of Refs. 4,5.

III. Improvement in J_c

J_c is determined in part by the quality of the melt-textured grain, especially by the absence of weak links. For a good MT grain of Y123, J_c = 8-10,000 A/cm^2.

J_c is also dependent upon the presence of pinning centers, which are small diameter regions of poor superconductivity within the tile. We have used Y211, finely divided, to introduce chemical pinning centers, and increase J_c[1]. This showed some success and increased J_c to 10-13,000A/cm^2. We have also used bombardment by light ions (protons and He) to damage the Y123 crystals and increase J_c[7]. This increases J_c markedly, to ~40,000A/cm^2.

We are presently pursuing a technique[7,8] which permits production of columnar pinning centers in MT Y123. There is strong evidence[9] that columnar pinning centers (a) result in higher J_c, particularly at higher temperatures (e.g. 77K); and (b) increase the irreversibility line, thus allowing the production, ultimately, of higher B_{trap}. Increases of J_c by a factor of 3, and irreversibility fields by a factor of 2 have been reported at 77K.[9]

Most methods used to produce columnar pinning centers are unable to produce large scale devices. For example, Ref. 9 utilized 580 MeV Sn ions to cause such defects. However, such ions have a range of only 20μm in Y123.

In order to produce columnar defects in larger scale devices we have developed a method in which the Y123 is seeded with U^{235} and then irradiated with thermal neutrons, n°_t. The n°_t induce fission in the U^{235}

$$n_t^\circ + U^{235} \rightarrow f_1 + f_2 + n^\circ s \qquad \text{Eq. 2}$$

The total energy of the fission fragments is circa 200 MeV, and their range is ~ 20μm. The average Z_f ~ 46, close to the value for tin, for which Z = 50.

The U^{235} seeding can be made uniform over large volumes, and the n°_t penetrates to large distances. Thus a uniform volume distribution of columnar centers can be achieved.

The U^{235} must be dispersed in MT Y123 such that the spacing between U^{235} globules is <20μm. Also, the U^{235} globules themselves must be << 6μm in diameter, so that they do not self absorb the fission fragments. Fig. 2 shows the U distribution actually achieved. Fig. 3 shows results of the first test of this U^{235}/n method. In this experiment J_c = 85,000 A/cm^2 was achieved. This is twice the J_c achieved by our proton or helium bombardments.[1,7]

The U/n method is inhibited by the effect that U addition has on the formation of good quality melt-textured Y123 grains. Addition of U beyond about 0.5% by weight degrades the melt texturing.[7,8] In our initial experiments, depleted U was used, in which only 0.4% of U^{235} remained. The amount of U needed, in order to provide

sufficient U^{235}, prevented us from exploring the maximum J_c achievable by this method. At present we are experimenting instead with 95% enriched U^{235}. Using enriched U^{235} in place of the depleted U, reduces the mass of U needed, at a given fluence, by a factor of over 200. Present experiments seek an optimum for fluence x mass of U^{235}, in order to maximize J_c.

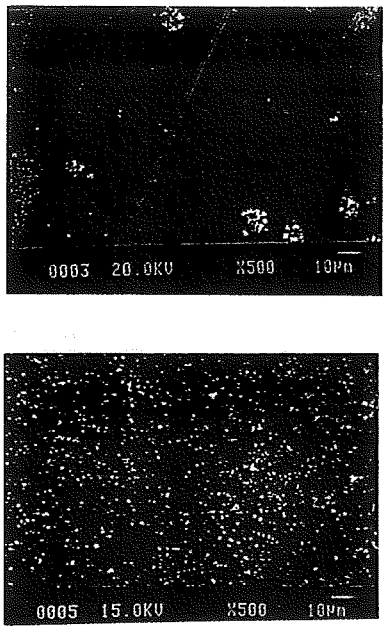

Fig. 2. Top: SEM micrograph of MT Y123 plus 0.6% depleted uranium. Bottom: Same as top after careful U dispersion.

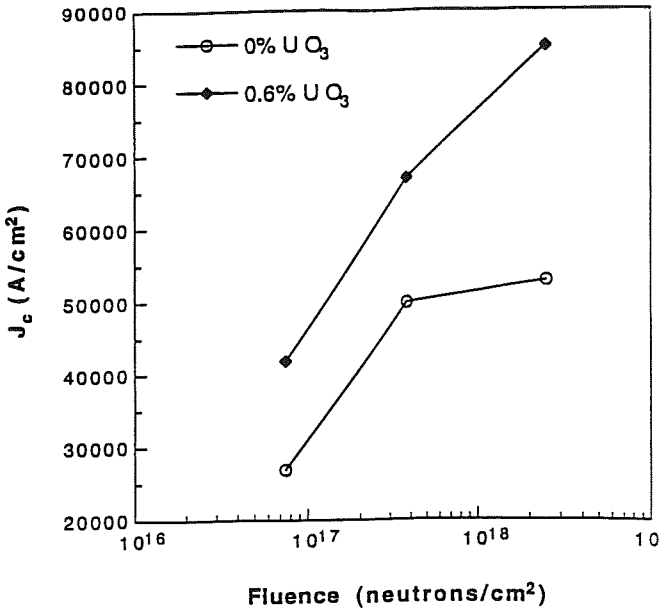

Fig. 3. Top: Effect of $n^{\circ}{}_t$ bombardment of Y123 lus 0.6% depleted uranium. Bottom: control sample.

IV. Temperature Dependence

At the time of WCS III, we had strong evidence of a rapid increase in $B_{t,max}$ as T was decreased.[10,11] Such an increase is expected from Eq. 1 and the fact that J_c generally increases as T decreases. A study of J_c vs. T for unirradiated melt-textured Y123 was done on small samples,[12] utilizing a vibrating sample magnetometer (VSM). Generally VSMs have small activation regions, and cannot analyze samples larger than a few millimeters. For T<65, the result of our tests was an excellent fit to the equation

$$J_c(T) = J_c(65K) \times (T_c - T / T_c - 65)^2 \qquad \text{Eq. 3}$$

Fig. 4 shows these results. A sample produced by Murakami, at ISTEC[13] by the MPMG method is shown for comparison. It exhibits the same $J_c(T)$ dependence, albeit with J_c about a factor of 2 lower. From Eq. 3 and Eq. 1 we conclude that B_t should have

the same temperature dependence as given in Eq. 3, at least for unirradiated Y123. We will consider irradiated Y123 next.

V. Mini-Magnets

We fabricate mini-magnets from a collection of single tiles. Two such magnets were each fabricated from 6 irradiated tiles, ~ 1.2 cm x 1.2 cm x 0.3 cm. In order to test whether Eq. 3 applies to irradiated tiles as well as non-irradiated tiles, these mini-magnets were tested at various temperatures.[8] Fig. 5 shows the results. The solid curve, which fits the data reasonably well, is calculated from Eq. 3. Thus, at least for $T \geq 55K$, Eq. 3 also applies to fabrications made from tiles irradiated by light ions.

Note in Fig. 5 that the trapped field observed is circa 1.5 Tesla at 77K[11], 4.0T at 65K[8] and 7.0T at 55K[8]. The latter two measurements were record trapped fields, eclipsing the record of 2.3T at 4K, set at Stanford in 1977[15]. Fig. 6 shows the activation curve taken at 55K, in which 7T is trapped. Fig. 7 shows more recent results on a mini-magnet made of 2 cm diameter tiles irradiated by protons. Here 2.3 T is achieved at 77K, and 5.3 T at 65K. We expect this generation of tiles to exceed $B_{t,max}$ = 10T at 55K in tests which are in progress.

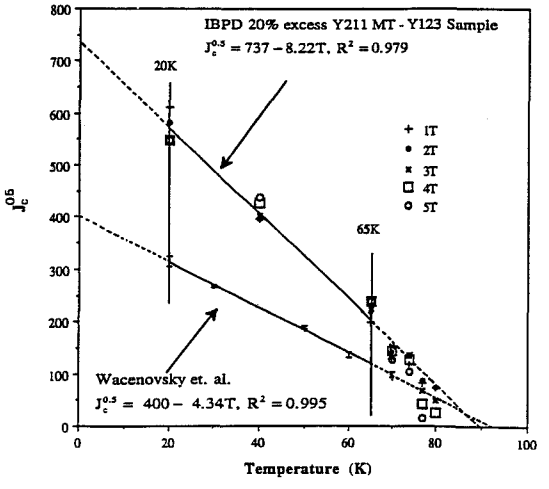

Fig. 4. $J_c^{1/2}$ vs. T, at various fields, measured by VSM on non-irradiated Y123. Top line: IBPD/TCSUH sample. Lower line is ISTEC sample of Ref. 13.

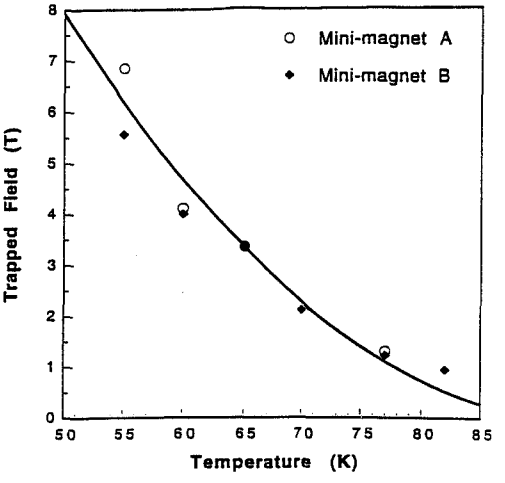

Fig. 5. B_{trap} vs. T for 2 mini-magnets, normalized at 65K. Solid line is from fit of Fig. 4.

VI. Bus Bar

We developed a technique to weld-while-texturing which allows a number of tiles to be welded into a single grain. Using this, we welded 3 tiles together, each 2 x 2 x 1 cm^3. From the trapped field we estimate that this bus bar, 6 cm long, will carry a transport

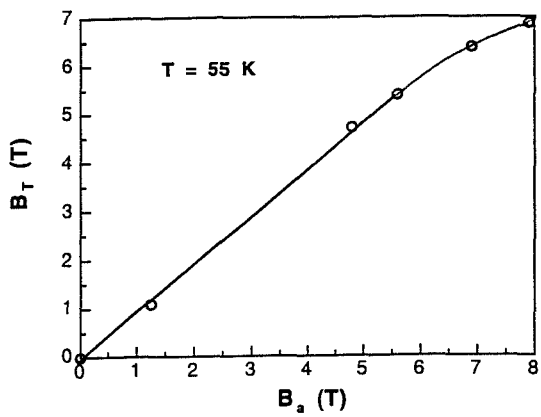

Fig. 6. B_t vs. applied field, Ba, at 55K for 6-tile mini-magnet. At each point the Y123 is field cooled at the value of Ba shown. Tiles have area ~ 1 cm^2.

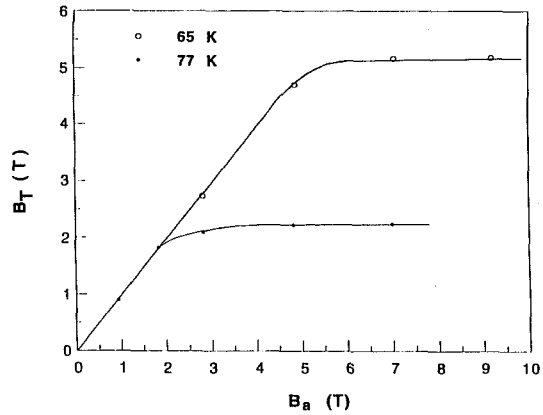

Fig. 7. B_t vs. Ba for 2-tile mini-magnet. Data as in Fig. 6. Tiles have area ~ 3.1cm^2.

current of 2000 A at 77K. In order to experimentally test the transport current in the bus bar, silver leads were epoxied to the Y123, using silver epoxy. The transport current for this device was tested in the laboratory of Kamel Salama[15]. The bar successfully carried 1000A of transport current, which is the maximum for which the lab can test.

In principal this technique will work for bus bars of length up to 40 cm, made with our present equipment.

VII. Generator

Fig. 8 is a schematic of a generator run in collaboration with Emerson Electric Co.[16] The rotor has 8 iron posts on which 8 TFMs were mounted, each 2 cm diameter. The stator of the generator is composed of copper wire, run at 77K. The copper is wound in an 8-pole, 3-phase configuration. The rotor was motor driven, and the generator output went to a three-phase variable resistive load.

In two separate runs the TFMs were (a) field cooled, and (b) zero field cooled. In the first case the TFMs were cooled in an applied field provided by constant current through the stator wires. Current, and therefore fields, were limited by the desire to avoid burning the stator insulation. The TFMs did not limit the field. Activating fields of $\leq$2500 Gauss, limited by armature heating, resulted in TFM fields of ~ 1800 G. In the second case the TFMs were cooled at zero field, and then a 15 ms *pulse* of current was put through the stator. This produced an activating field of ~ 5000 G, which resulted in a trapped field of ~2600 G. This is still less than the 3500-4000 G those particular TFMs could trap. Higher ZFC fields can be obtained with higher pulsed voltage (until inter-wire arcing occurs on the stator).

The generator was run at a large variety of speeds up to 2265 rpm, and supplied up to 100 Watts[16] to the load.

We had previously used the configuration of Fig. 8 as a motor.[1,17] The motor, run with an earlier generation of tiles ~ 1 cm x 1 cm x 0.3 cm, achieved an output of 19 Watts.[17]

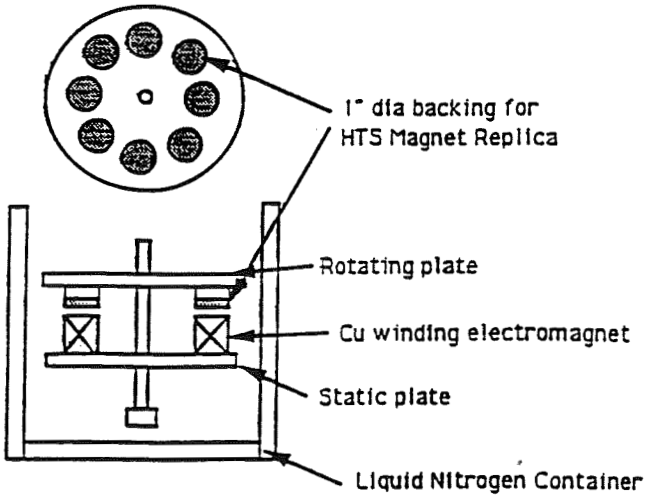

Fig. 8. Schematic of Emerson Electric/ TCSUH motor. Top: view of rotor, with 1" diam. iron rods. Bottom: Side view of rotor, stator and cryostat.

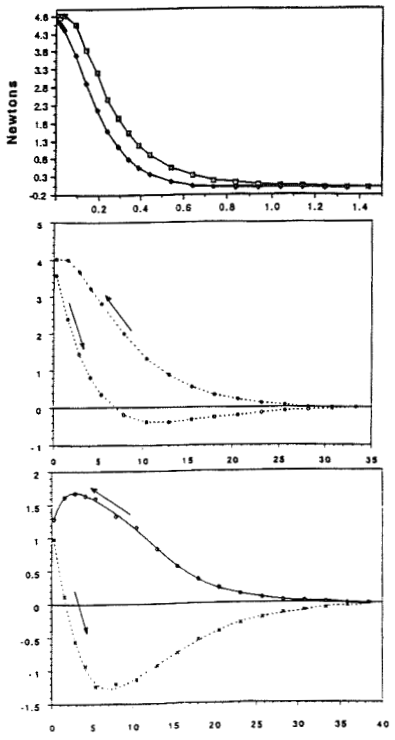

Fig. 9. Force (N) vs. distance (mm) for $Ba/B_{t,max}$ = 0.67 (top); 1.39 (middle; 2.74 bottom.

VIII. Bumper/Tether

Assume a TFM is cooled in zero field and therefore has no trapped field. Assume that a ferromagnet is then brought close to the TFM. As the magnet approaches, the superconductor first acts like a mirror image of the approaching ferromagnet, and repels it. If the approaching ferromagnet has momentum it will continue to approach the superconductor until it is stopped by the repelling force. It then continues to be repelled, and accelerates in the reverse direction. Sig Fig. 9.

The nature of the current is possibly best understood by the Bean model.[2] After such a collision, as the magnet and TFM separate, an attractive force develops at some

distance. This cycle is shown in Fig. 9. The detailed behavior of the repulsion/attraction depends upon the ratio of the ferromagnet field, B_{Fe}, to $B_{t,max}$ of the TFM. Fig. 9 shows three cases, with varying $B_{Fe}/B_{t,max}$. The largest tethering force occurs for $B_{Fe}/B_{t,max} > 2$, after which F_{Tether}/F_{Bumper} ~ constant.

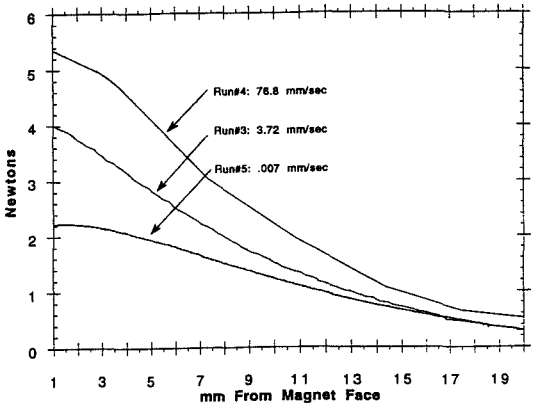

Fig. 10. Velocity dependence of bumper/ tether force over 4 orders of magnitude in v.

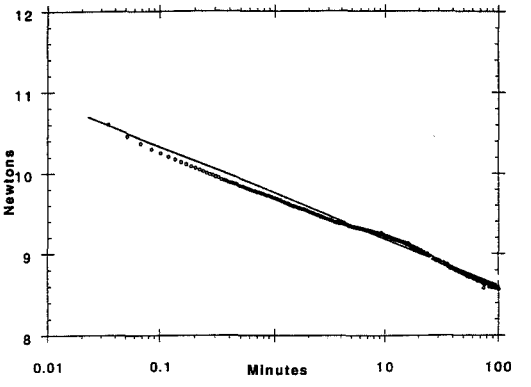

Fig. 11. Decay (creep) of force (circles) following rapid approach.

Because of the force pattern shown in Fig. 9, an array of TFMs can act first as a collision softener and then as a tether. If two spacecraft are approaching, and one has a ferro or electromagnet at the bow, while the other has an array of Y123 TFMs, forces of several tons are achievable for arrays of modest size. We believe that such an array can be a valuable backup to an aerospace docking system.

We have explored such a system to learn its characteristics. One such characteristic is that the repulsive force is velocity dependent. This effect is shown in Fig. 10. The basic source of this velocity dependence is creep. Fig. 11 shows the creep, as it effects the force, following a "sudden" collision (which took place in tenths of a second). The repelling force, as a function of time, is essentially a straight line when plotted vs. log t as is expected for creep. For low velocities, the creep reduces F_{Bumper} in the time it takes for the separation to decrease. The force is thus larger for higher relative velocities, which is desirable.

By studying the energy stored in the magnetic field of the TFM after the collision, and the energy losses to creep, we have thus far accounted for about 85% of the energy of the collision. The time dependence of the conversion of some of this energy to heat is used to place constraints on the cooling system for the TFM in the bumper/tether system.

This test also provides an alternate method to study creep at relatively short times. When creep is studied by using an electromagnet to activate a TFM, it is difficult to study creep at times $t < 1$ min. The collision study described above permits observation of creep to ~0.1 second. Pulsed coils are needed to probe still shorter times. Creep can, of course, also be studied by, e.g., the method of VSM.

This work is supported in part by grants from the Texas, through the Texas Center for Superconductivity at the University of Houston and the Texas Advanced Technology Program, and by grants from NASA, and the Electric Power Research Institute.

References

1. R. Weinstein, Invited Paper, Proc. World Congress on Superconductivity III, Munich, pg. 1145, Pergamon Press (1992)
2. C.P. Bean, Phys. Rev. Lett., 8, 250 (1962); Rev. Mod. Phys., 36, 31 (1964)
3. Y.B. Kim, C.F. Hempstead, A.R. Strand, Phys. Rev., 129, 528 (1963)
4. I.G. Chen, J. Liu, R. Weinstein, K. Lau, Jour. Appl. Phys., 72, 1013 (1992)
5. J. Liu, I.G. Chen, R. Weinstein, J. Xu, Jour. Appl. Phys., 73, 6530 (1993)
6. V. Selvamanickam, L. Gao, K. Sun, K. Salama, Appl. Phys. Lett., 54, 2352 (1989)
7. R. Weinstein, et al, Invited Paper, Proc. International Workshop on Superconductivity, Kyoto, Japan (June 1994)
8. R. Weinstein, Y. Ren, J. Liu, I.G. Chen, R. Sawh, C. Foster, and V. Obot, Proc. Int. Sympo. on Superconductivity, Hiroshima, Springer Verlag, in press (1993)
9. L. Civale, A.D. Marwick, T.K. Worthington, M.A. Kirk, J.R. Thompson, L. Krusin-Elbaum, Y. Sun, J.R. Clem, F. Holtzberg, Phys. Rev. Lett., 67, 648 (1991)
10. R. Weinstein, I.G. Chen, J. Liu, and K. Lau, Jour. Appl. Phys. 70, 6501 (1991)
11. R. Weinstein, I.G. Chen, J. Liu, and J. Xu, Joun. Appl. Phys., 73, 6533 (1993)
12. I.G. Chen, J. Liu, Y. Ren, R. Weinstein, G. Kozlowski, and C. Oberly, Appl. Phys. Lett., 62, 3366 (1993)
13. M. Wacenovsky, R. Miletich, H. Weber and M. Murakami, Supercond. Sci. Technol. 5, S184 (1992)
14. M. Rabinowitz, H. Arrowsmith, S. Dahlgren, Appl. Phys. Lett., 30, (11), 607 (1977)
15. K. Salama, ME Dept., and TCSUH, Univ of Houston, Houston, TX 77204
16. R. Weinstein, A. Crapo and R.P. Sawh, contributed paper to Applied Supercond. Conf., Boston (Oct 1994)
17. C. Gillespie, Editor, Superconductor Industry, Pg. 31, Spring Issue (1993)

THE SUPERCONDUCTING MHD-PROPELLED SHIP YAMATO-1

YOHEI SASAKAWA, Chairman, YAMATO Project Committee, Ship & Ocean Foundation
SETSUO TAKEZAWA, Ship & Ocean Foundation
YOSHINORI SUGAWARA, Ship & Ocean Foundation
YOSHIHIRO KYOTANI, Ship & Ocean Foundation

519-76
31370/
IOP.
342975

YAMATO-1 running in the harbor of Kobe

1. Introduction

In 1985 the Ship & Ocean Foundation (SOF) created a committee under the chairmanship of Mr. Yohei Sasakawa, Former President of the Ship & Ocean Foundation, and began researches into superconducting magnetohydrodynamic (MHD) ship propulsion. In 1989 SOF set to construction of a experimental ship on the basis of theoretical and experimental researches pursued until then. The experimental ship named YAMATO-1 became the world's first superconducting MHD-propelled ship on her trial runs in June 1992.

This paper describes the outline of the YAMATO-1 and sea trial test results.

2. The YAMATO-1 project

In the first year of the project (1985), we gathered information on superconducting magnets and cryogenic technology to gain a clear picture of superconductivity applications, and worked out an action plan. Model ship thrusters were designed to incorporate saddle-shaped superconducting coils made of NbTi wire. In 1986 the best people from industry joined us to work on this project. At the Tsukuba Institute, researchers performed tests and experiments by use of model thrusters having the basic structure shown in Fig. 1, to look into MHD thruster's performance and characteristics as a hydraulic device, and pressure increase of seawater in the thruster ducts; propulsion characteristics and the interaction between the hull and thrusters were examined by using model ships.

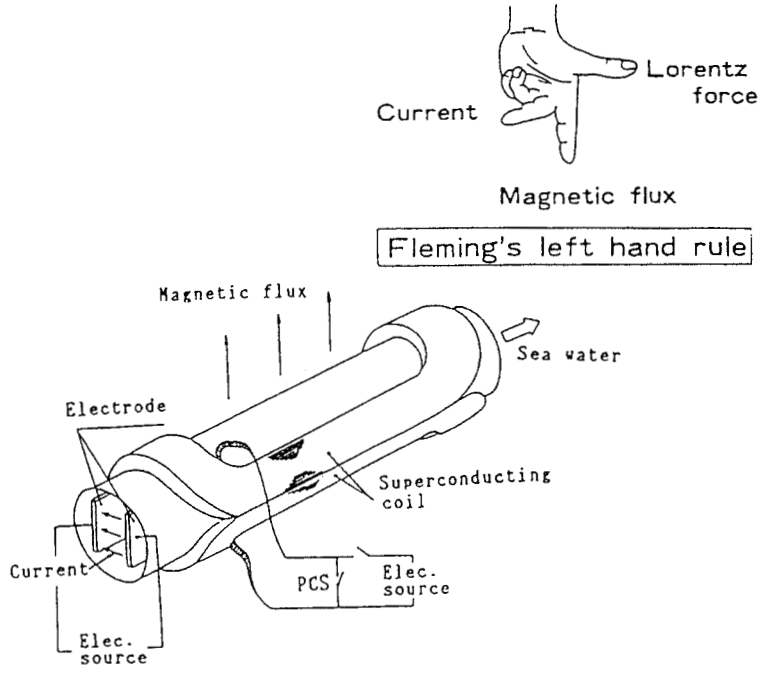

Fig.1 Principle and Basic structure of MHD thruster

In 1988 the experimental ship thruster was designed according to the particulars shown in Table 1 so as to have a shielding-free structure which can minimize magnetic leakage by accommodating six superconducting coil units in a single cryostat (Fig. 2). Construction of a experimental ship featuring a streamlined hullform (Fig. 3) began in the wake of the manufacture of twin thrusters, and the experimental ship YAMATO-1 was completed at the end of 1991. Table 2 summarizes the YAMATO-1 project in chronological order. Photo 1 is the YAMATO-1 under fitting work.

Table 1 Basic particulars of the MHD thruster

·Compound magnetic flux density at center	4 Tesla
·Electrode current(normal)	2,000 A
·Lorentz force	8,000 N/set
·Thrust	4,000 N/set
·Weight	18 Ton/set

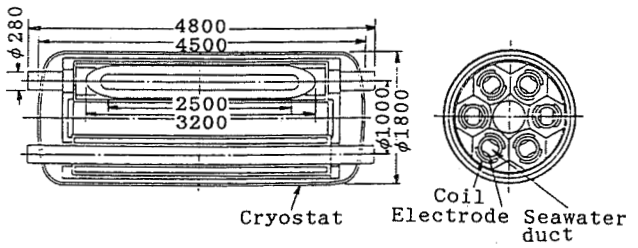

Fig.2 Basic structure of MHD thruster

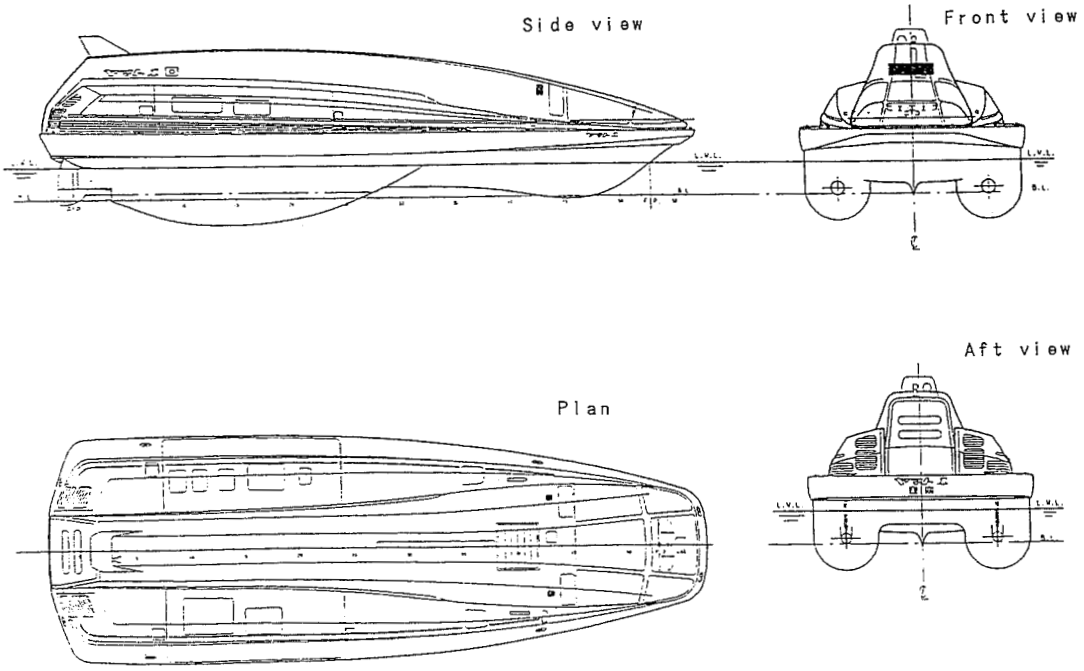

Fig.3 Hull form for YAMATO-1

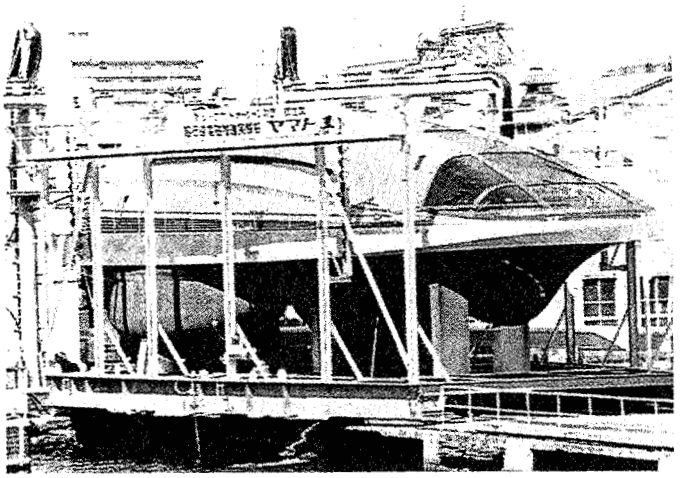

Photo 1 YAMATO-1 under outfitting wark

Table 2 The YAMATO-1 project

1985	·Study on the present state of cryogenenic technology ·Researches into MHD thrusters to work out the basic plan	Researches and experiments		
1986	·Researches into hull forms and MHD propulsion systems ·Manufature of superconducting MHD thruster for experimetal purposes			
1987	·Self-Propulsion experiments by use of an internal magnetic fieled type model ship ·Manufacture of a large-sized superconducting MHD thruster and characteristic tests ·Designning of superconducting MHD thrusters for use in the experimental ship		Designning	
1988	·Designning of the exp. ship ·Manufature of superconducting MHD thrusters for use in the experimental ship	experimental ship		
1989	·Construction of the hull of experimental ship ·Assembly of superconducting MHD thrusters		Manufacture and adjustment	
1990	·Christening of YAMATO-1 ·Assembly of superconducting MHD thrusters and performance tests on land			
1991	·Manufacture of ancillary equipment ·Installation of the thrusters and ancillary equipment			
1992	·Adjustment of inboard equipment and appararus ·Sea trials and evaluation tests		Trials	

Table 3 Principal particlars of YAMATO-1

·Length overall	30m
·Length between perpendiculars	26.4m
·Breadth(moulded)	10.39m
·Depth(max.)	3.69m
·Draft(max.)	2.69m
·Displacement (including water in the ducts)	185ton
·Speed (at Lorentz force 16,000N)	abt. 8kts
·Material of the hull	Aluminium
·Number of person	10 including 3 crew

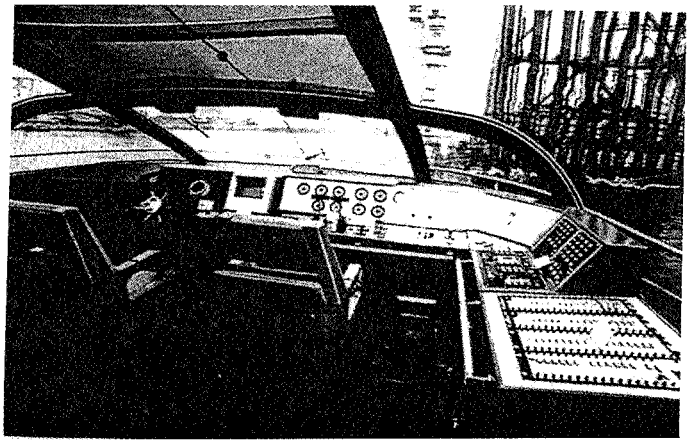

Photo 2 Wheel house equipment of YAMATO-1

3. The YAMATO-1

3-1. Hull

The unique hullform accounts for the experimental ship's remarkable sea keeping ability and course keeping ability --- a monohull having a pod on each side of the afterbody to accommodate a thruster. The ship's principal particulars and the arrangement of main equipment are shown in Table 3 and Fig. 4, respectively.

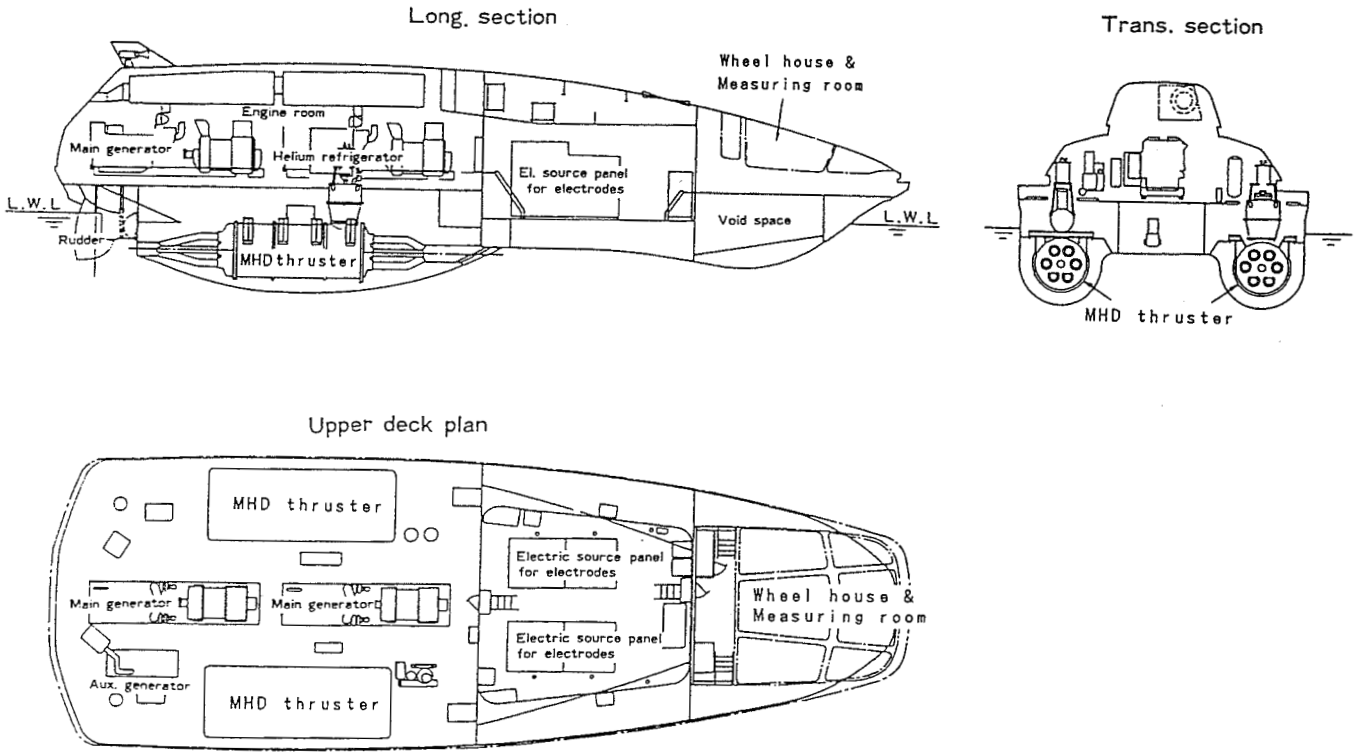

Fig.4 The general arrangement of YAMATO-1

The YAMATO-1 consists of a wheelhouse and a power-supply room and a machinery room, which are partitioned from one another by bulkheads. In the wheelhouse are steering equipment and space for ten persons including crew. Among the wheelhouse equipment are a steering console in front and a control/surveillance console on the starboard side (Photo 2). Two electrode power supply units to electrify the thrusters are housed in the power-supply room where measuring instruments are stored in racks on the port side. Main generators, two in number, are installed in the middle of the machinery room where there are an auxiliary generator and a compressor on the starboard side, whilst ancillary equipment for the main generators on the port side. The thrusters are accommodated in the pods below water line. The hull is made of anticorrosive aluminum alloy to make the ship light in weight and magnetic-resistant.

3-2. Superconducting MHD thrusters

The superconducting MHD propulsion system for use in the YAMATO-1 consists of :

a. Superconducting MHD thrusters (superconducting coils, cryostats, electrodes, etc.)
b. Cooling/refrigerating equipment
c. Land-based energizing power-supply units
d. Onboard electrode power-supply units

Refrigerators to reliquefy helium evaporated on account of heat intrusion are mounted on board, whilst a large-sized cooling equipment for initial cooling of superconducting coils is installed on shore to reduce the ship weight and to make the thrusters compact. Once energized, superconducting magnets can be used in permanent current mode; therefore, the energizing power-supply units need not be carried aboard either. Fig. 5 is the conceptual diagram of the YAMATO-1's propulsion system.

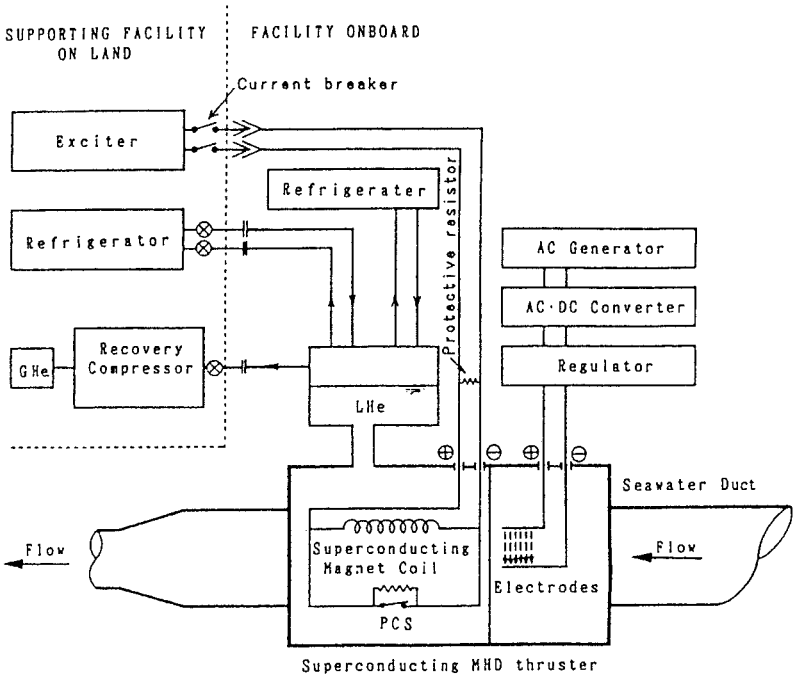

Fig.5 A schematic diagram of the total system of the YAMATO-1

NbTi wire is wound into a superconducting coil, which is of double-layered structure and cooled by being immersed in liquid helium; coil collars and vacuum vessels are made of aluminum alloy for the purpose of weight reduction; helium containers to accommodate superconducting coils are made of stainless steel which is widely adopted as a cryogenic material. Table 4 shows the specifications of the thruster, and Fig. 6 its dimensions. Fig. 7 is a cut-away view of the thruster, and Photo 3 the completed thruster.

The YAMATO's duct system per thruster consists of: an intake, a manifold or the portion branched into six tubes; the thruster tube, and another manifold or the portion where the six tubes are integrated into a single duct, which ends in a jet nozzle (Fig. 8).

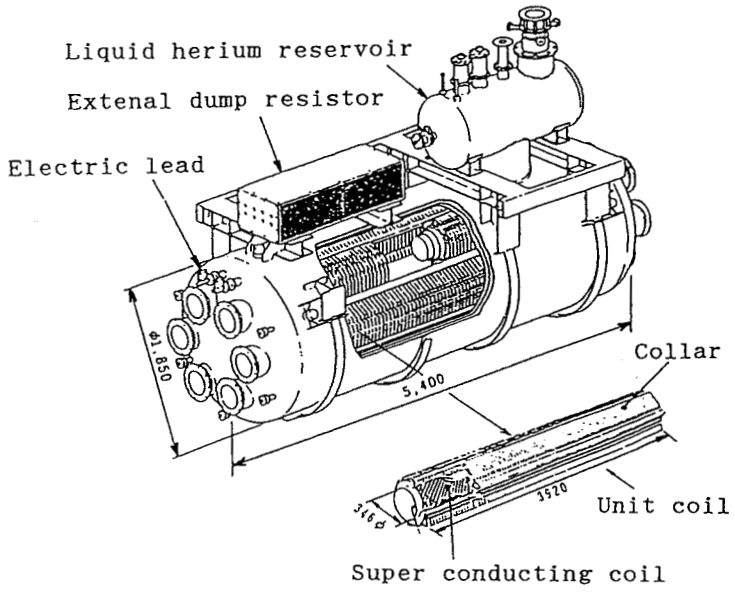

Fig.7 Cataway view of the MHD thruster

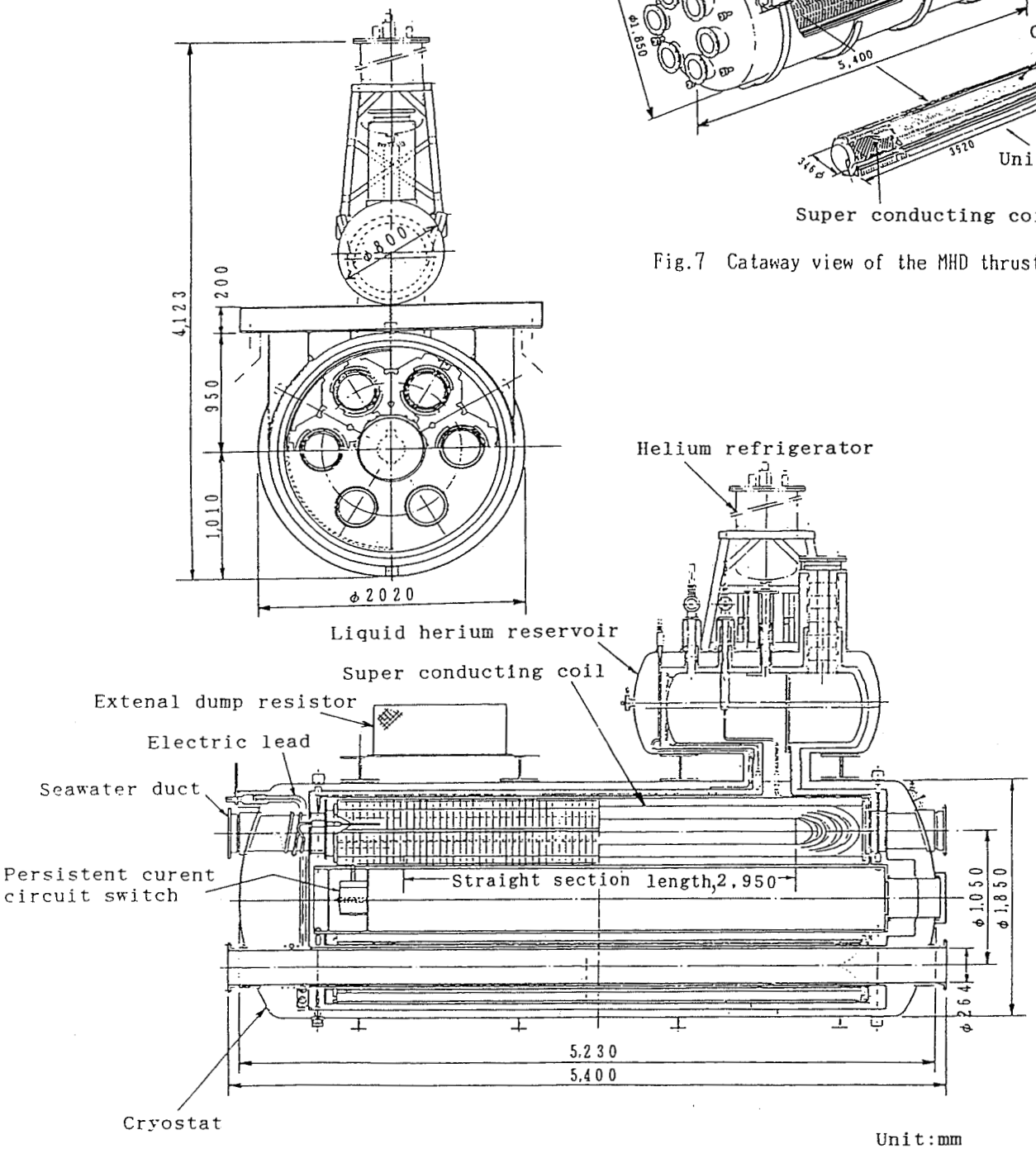

Fig.6 Principal dimensions of the MHD thruster

Table 4 Principal particlars of MHD thruster

		Magnet I (port)		Magnet II (starboard)	
Coil(unit)					
·Coil shape		Double shell type dipole			
·Cable material		Nb·Ti			
·Copper ratio		1.3		1.0	
·Dia.of winding	inner dia.	360 mmϕ			
	outer dia.	405 mmϕ		401 mmϕ	
·Straight section length		3,000 mm		2,950 mm	
Coil(Fully assembled six coils)					
·Assembly circle dia.		1,050 mm			
·Inductance		3.3 H		3.7 H	
·Stored energy		23.0 MJ		20.0 MJ	
		unit	six coil	unit	six coil
·Field strength at bore center		3.5 T	4.0 T	3.5 T	4.0 T
·Maximum field on superconductor		5.5 T		5.9 T	
·Operation current		4,580 A	3,770 A	3,960 A	3,210 A
·Weight(with cryostat)		18.0 ton		15.8 ton	

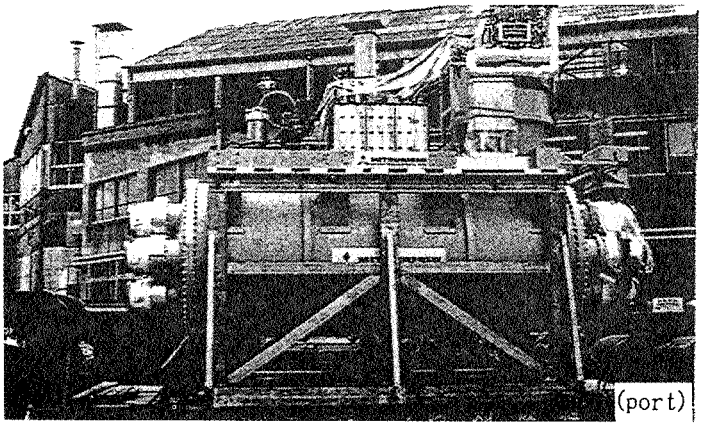

Photo 3 a Outside view of the MHD thruster

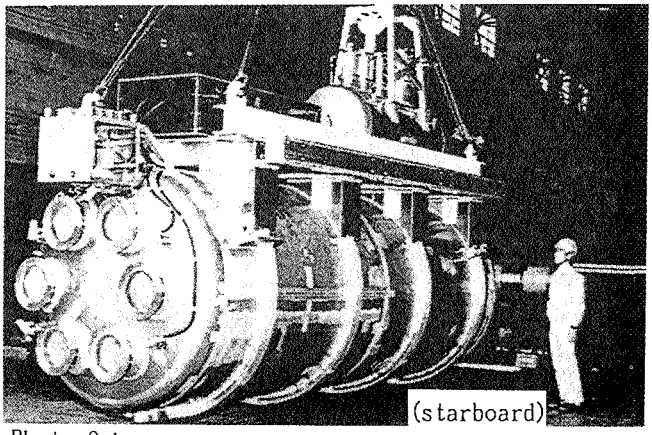

Photo 3 b Outside view of the MHD thruster

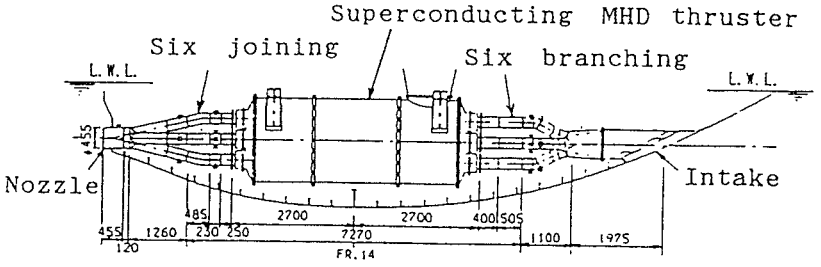

Fig.8 Configuration of the duct system

4. The results of sea trials

On January 27, 1991, the YAMATO-1 was put into the water. The YAMATO-1 underwent mooring tests and bollard-pull tests in preparation for sea running tests. In bollard-pull tests, the ship was moored to a bollard by use of rope furnished with a tension meter (Fig. 9); generated thrust was calculated from measurements of towing force and pressure inside the ducts. Fig. 10 shows the measurements. At a constant magnetic field density, towing force increases in proportion to electrode current. Towing force is larger than thrust. This is due to pressure distribution around the hull, which is different from that in case of navigation: a phenomenon recognized likewise for tugboats at work. Photo 4 is the YAMATO-1 under bollard-pull tests.

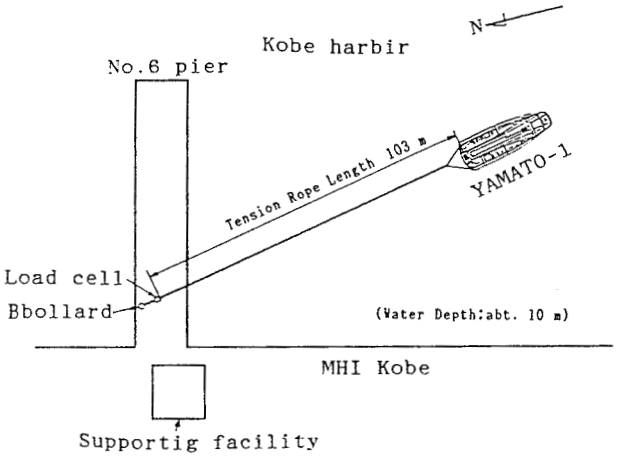

Fig.9 Bollared pull test arrangement

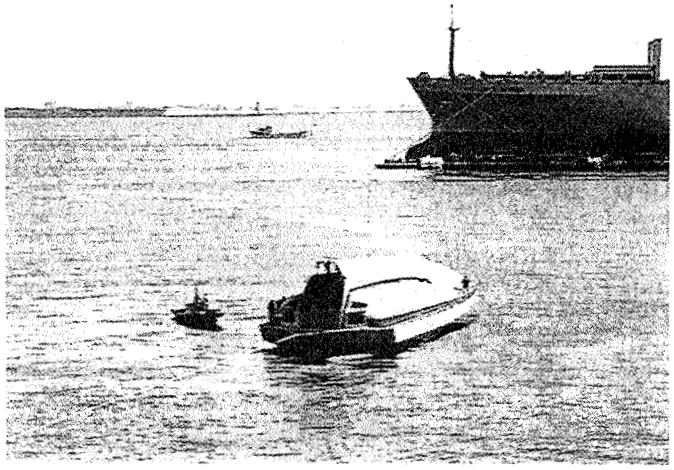

Photo 4 YAMATO-1 at the bollared pull test

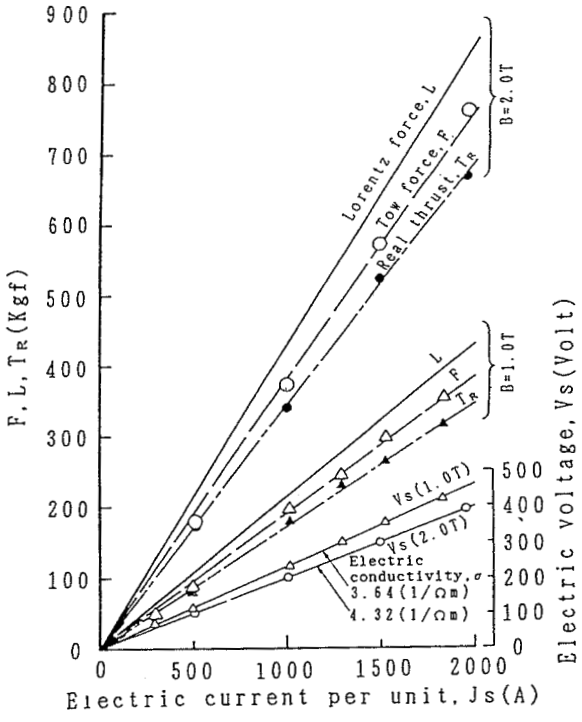

Fig.10 Result of the bollared pull test

Sea running tests started from June 16, 1992. Fig. 11 shows the ship's speed at a magnetic flux density of 1.0 Tesla, 1.5 Tesla, and 2.0 Tesla, respectively. Fig. 12 shows ship's speed at magnetic flux density of 1 through 4 Tesla and electrode current 2,000 A. Speed trial was performed at magnetic flux density of up to 2 Tesla, while mooring test at magnetic flux density of up to 3 Tesla; ship's speed at 4 Tesla was extrapolated to be some 7.5 knots from measurements at 1 to 3 Tesla; ship's speed of 5.3 knots in case of 2 Tesla. Photo 5 shows the YAMATO-1's sea running test in the harbor of Kobe.

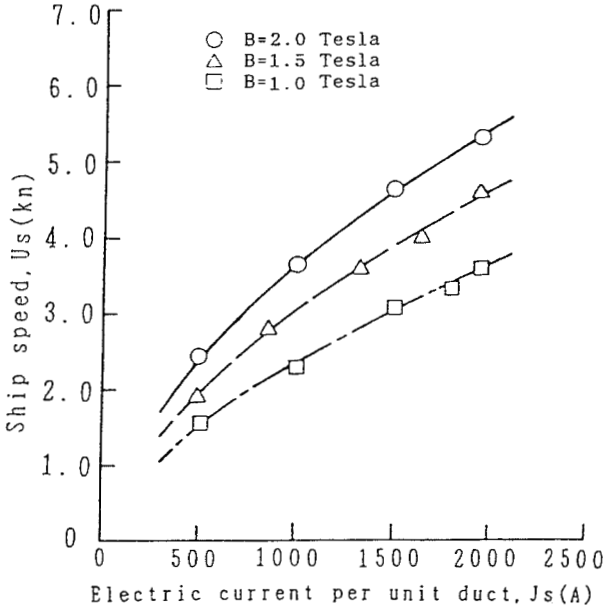

Fig.11 Result of speed trials(1)

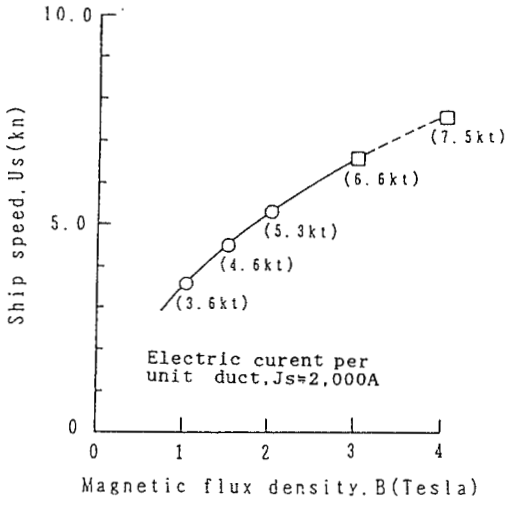

Fig.12 Result of speed trials(2)

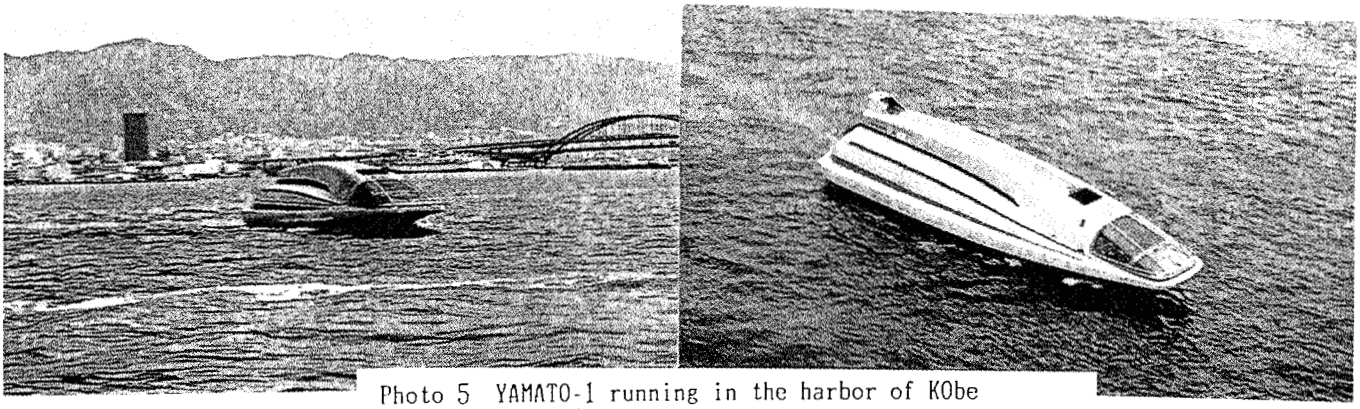

Photo 5 YAMATO-1 running in the harbor of KObe

5. Conclusion

Superconducting MHD ship propulsion has just come out of laboratory, unable to vie in propulsion efficiency with ships using conventional modes of propulsion. Further R&D efforts are required to put the innovative propulsion system to practical use. Nonetheless, the YAMATO has proved that superconducting MHD ship propulsion, which was long considered impossible on account of structural problems involved and enormous weight of superconducting coils, could be practicable.

SHIT THIS
PAGE

THIS PAGE INTENTIONALLY LEFT BLANK

Page intentionally left blank

Performance Characterization

Session 1 Chair: Dr. R. K. Pandey
Co-Chair: Dr. U. Varshney

OMIT THIS PAGE

ELECTRIC FIELD EFFECT IN SUPERCONDUCTOR-FERROELECTRIC STRUCTURES

V.V.Lemanov

A.F.Ioffe Physical-Technical Institute,
26 Polytechnicheskaya st.,194021 St.Petersburg,Russia

Electric field effect (the E-effect) in superconductors has been studied since 1960 when Glover and Sherill [1] published their results on a shift of the critical temperature Tc about 0.1mK in Sn and In thin films under the action of the field E=300 kV/cm.
Stadler [2] was the first to study the effect of spontaneous polarization of ferroelectric substrate on the electric properties of superconductors.He observed that the reversal of polarization of TGS substrate under action of external electric field in Sn-TGS structures induced the Tc shift in Sn about 1.3 mK. Since in this case the effect is determined not by the electric field but by the spontaneous polarization,we may call this effect the P-effect.

High-Tc superconductors opened the new possibilities to study the E- and P-effects due to low charge carrier density,as compared to conventional superconductors,and to anomalously small coherence length.Experiments in this field began in many laboratories (see Refs.3 and 4 and the references cited therein) but a breakthrough was made in Ref.5 where a shift in Tc by 50 mK was observed in YBCO thin films.Much higher effects were observed in subsequent studies [3,4].The first experiments on the P-effect in high-Tc superconductors were reported in Refs.6,7.

In this report we shall give a short description of study on the P-effect in high-Tc superconductors.

In Fig.1 a typical structure for study of the P-effect is shown.

There is a number of advantages of the P-effect as compared to the E-effect [7],in particular,the surface charge density due to the spontaneous polarization in ferroelectrics can be significantly larger than the charge density induced by the electric field in ordinary dielectrics.In the case of superconductor-dielectric structure with capacitance C the density of surface charge induced by the gate voltage Vg is given by

$$Q^{(E)} = CV_G = \varepsilon_d V_G/4\pi l_d = \varepsilon_d E/4\pi \qquad (1)$$

and the change of the sheet density of charge carriers is

$$\Delta n_{sh}^{(E)} = Q^{(E)}/e = \varepsilon_d E/4\pi e \qquad (2)$$

Here ε_d and l_d are dielectric constant and thickness of dielectric layer,respectively.

In the case of ferroelectric layer with polarization P one has

$$Q^{(P)} = P \ , \ \Delta n_{sh}^{(P)} = P/e \qquad (3)$$

One can rewrite Eqs.2 and 3 in the more convenient form

$$\Delta n_{sh}^{(E)} = 5.5\ 10^{5}\ \varepsilon_d E \qquad (2a)$$

$$\Delta n_{sh}^{(P)} = 6.2\ 10^{18} P \qquad (3a)$$

where Δn_{sh} is in cm^{-2}, E is in V/cm and P is in C/cm^2.

For the ratio of carriers sheet density cange in the P- and E-effects we have

$$\Delta n_{sh}^{(P)}/\Delta n_{sh}^{(E)} = 4\pi P/\varepsilon_d E = 1.1\ 10^{13}\ (P/\varepsilon_d E) \qquad (4)$$

If we take the spontaneous polarization for ferroelectric perovskite $P = 10^{-4}$ C/cm^2 (which seems to be the maximum experimentally observed value) and suppose that dielectric layer has dielectric constant $\varepsilon_d = 100$, then the E-effect will be equal to the P-effect only in the electric field $E = 1.1\ 10^{7}$ V/cm. This value is far beyond the breakdown field values for dielectric layers.

The other characteristic, very important in the study of the E-and P-effects, is the Thomas-Fermi screening length which describes the screening of the electric field or polarization by charge carriers in metals or degenerate semiconductors. The screening length is given by

$$l_{T.F.} = (\varepsilon E_F/6\pi ne^2)^{1/2} \qquad (5)$$

or

$$l_{T.F.} = 6.1\ 10^{2}\ (\varepsilon E_F/n)^{1/2} \qquad (5a)$$

where ε is the dielectric constant of a superconductor, E_F is the Fermi energy, and n is the volume carrier density. In Eq.5a $l_{T.F.}$ is in cm, E_F is in eV, and n is in cm^{-3}.

For YBCO using Eq.5a and the appropriate values of parameters we have as an upper limit $l_{T.F.} = 1$ nm.

The change of sheet density in a superconductor under action of electric field or polarization is distributed along this length and for the total relative change of volume carrier density in the superconductor thin film of thickness $l_{T.F.}$ we have

$$\Delta n/n = \Delta n_{sh}/l_{T.F.} n \qquad (6)$$

For the film thickness l_s larger than $l_{T.F.}$ the change of sheet density should be referred to the thickness l_s. If the film resistance is completely determined by the carrier density then one obtains

$$\Delta R/R = \Delta n_{sh}/l_s n \qquad (7)$$

If we take l_s= 100 nm , n= 4 10^{21} cm^{-3} and P= 7 10^{-5} C/cm^2 then we have $\Delta R/R = 10^{-2}$,that is the switching of polarization in a ferroelectric from +P to -P should give the change in resistance in an adjacent superconductor film about 2% .If the critical temperature Tc of the superconductor is also proportional to the carrier density,then one should observe the Tc shift also by 2% .

The change of charge carrier density should also influence the resistance of superconductor in the mixed state though the mechanism of this effect may be different as compared to the normal state.

In Fig.2a the resistance change in the mixed state of YBCO film with thickness l_s 200 nm is shown as a function of electric field applied to BaTiO3 substrate.Fig.2b shows the polarization hysteresis loop in the same substrate at the same temperature.The YBCO film is deposited on (001) plane of BaTiO3,the thickness of the substrate is about 0.5 mm.From Fig.2 it follows that there is a distinct correlation between the resistance and polarization changes. The Tc shift in the same structure determined from temperature dependence of resistance is 0.5 K or 0.5 % which is near to the estimation from Eq.7.

In Fig.3 the resistance temperature dependences of YBCO films deposited on $LiNbO_3$ substrate are shown.The spontaneous polarization of LiNbO3 is 7 10^{-5} C/cm^2 , however the polarization in this crystal cannot be reversed at low temperatures due to very high coercive field.Therefore to observe the P-effect YBCO films were deposited on the opposite sides (+P and -P) of two single-domain LiNbO3 plates in one experiment in the identical conditions.One can see that there is a considerable shift of the Tc at R =0 by about 40 K.This shift is much larger than predicted by Eq.7 for the film with thickness about 100 nm.

For the possible application it is important to study the P-effect in superconductor-ferroelectric layered structure where both superconductor and ferroelectric are deposited as thin films.An example of such a structure is shown in Fig.4 [8].YBCO film 400 nm thick is deposited on NdGaO3 by laser ablation method.Onto the YBCO film BaSrTiO3 film with thickness 1500 nm is deposited by rf magnetron sputtering technique.Using BaSrTiO3 solid solutions gives the possibility to change the ferroelectric Curie temperature which can vary from liquid Helium region up to 400 K.This possibility may be useful to optimize the conditions for the E- and P-effects.Some characteristics of YBCO-BST structure are presented in Fig.5.

Along with the true E- and P-effects the elastic strain effect (the S-effect) should also exist.Indeed,under the action of electric field we have electrostrictive (any solids) and piezoelectric (crystals without inversion symmetry) strains in dielectric (ferroelectric) layers and there will be consequently elastic strains in superconductor film.These strains can change the superconductor electric properties.It was shown [9] that the elastic strains in BaSrTiO3 ceramic substrates resulted in the shift of the superconductor critical temperature Tc by 0.03 K in the electric field about 10 kV/cm.

The experimental results on the P-effect presented in Figs.2 and

3 have been obtained for YBCO films with thickness about 100 nm that is much larger than the Thomas-Fermi screening length.To increase the P-effect it is necessary to use ultrathin YBCO films comparable to the Thomas-Fermi screening length [10].Let us estimate the value of polarization of a ferroelectric layer which could switch ultrathin YBCO film from the N-state to the S-state,and vice versa,due to the P-effect.We shall discuss three-layered structure shown in Fig.6. Using Eqs.3 and 7 and assuming that $\Delta R/R = 1$ we have $P\ (C/cm^2) = (l_s n/6.2)\ 10^{-18}$,where l_s is in cm and n is in cm^{-3}. Then for l_s=2.5 nm and $n = 5\ 10^{21} cm^{-3}$ one obtains $P=2\ 10^{-4} C/cm^2$. This value sould be divided over 4 due to the P reversal from +P to -P and due to the double ferroelectric layers in Fig.6. So, finally we have $P= 5\ 10^{-5}\ C/cm^2$,more or less ordinary value for a number of ''strong'' ferroelectric crystals.

Another approach to this problem may also be used.If we assume that the resistance of the ultrathin film is of the order of the quantum unit $R_q = h/4e^2 = 6.45\ k\Omega$ [11],and the change of the resistance under action of polarization,for transition from the N-state to the S-state,has the same value,then we obtain $P = 1/\mu R_q = 4e^2/\mu h$ or $P\ (C/cm^2) = 1.55\ 10^{-4}/\mu$,where μ is mobility in $cm^2/V\ s$. For the mobility of the order of 1 $cm^2/V\ s$ the polarization P has the same value as in the first estimation.

Thus,for ultrathin superconductor film it is possible to switch the film from the N-state to S-state by switching the polarization in ferroelectric layers under action of the electric field (Fig.6).

It should be noted that ferroelectric layers in superconductor-ferroelectric structures may have ferroelectric domain structure which can be used to form some weak links and N-S junctions in adjacent superconductor layers [12].

The P-effect in superconductors,as well as the E-effect,can in principle find many technical applications [4] :superconducting field effect transistors (SuFET),electrocryotrons,mixers,adjustable filters,etc.The advantage of the P-effect is the possibility to have devices with long-term memory.

REFERENCES

1.R.E.Glover and M.D.Sherill, Phys.Rev.Lett.5,248,1960.
2.H.L.Stadler,Phys.Rev.Lett.14,979,1965.
3.J.Mannhart,Mod.Phys.Lett.B6,555,1992.
4.V.V.Lemanov and A.L.Kholkin,Fiz.Tverd.Tela 36,1537,1994.
5.J.Mannhart,D.G.Schlom,J.G.Bednorz,and K.A.Müller,
Phys.Rev.Lett.67,2099,1991.
6.V.V.Lemanov,A.L.Kholkin,and A.B.Sherman,JETP Lett.56,562,1992.
7.V.V.Lemanov,A.L.Kholkin,and A.B.Sherman,
Supercond.Sci.Technol.6,814,1993.
8.B.M.Goltsman,V.V.Lemanov,A.L.Kholkin,and S.G.Shulman,
Tech.Phys.Lett.19,639,1993.
9.V.V.Lemanov,V.V.Makarov,and A.B.Sherman,Fiz.Tverd.Tela 36,N8,1994.
10.X.X.Xi,C.Doughty,A.Walkenhorst,C.Kwon,Q.Li,and T.Venkatesan,
Phys.Rev.Lett.68,1240,1992.
11.D.B.Haviland,Y.Liu,and A.M.Goldman,Phys.Rev.Lett.62,2180,1989.
12.V.V.Lemanov,Tech.Phys.Lett.19,714,1993.

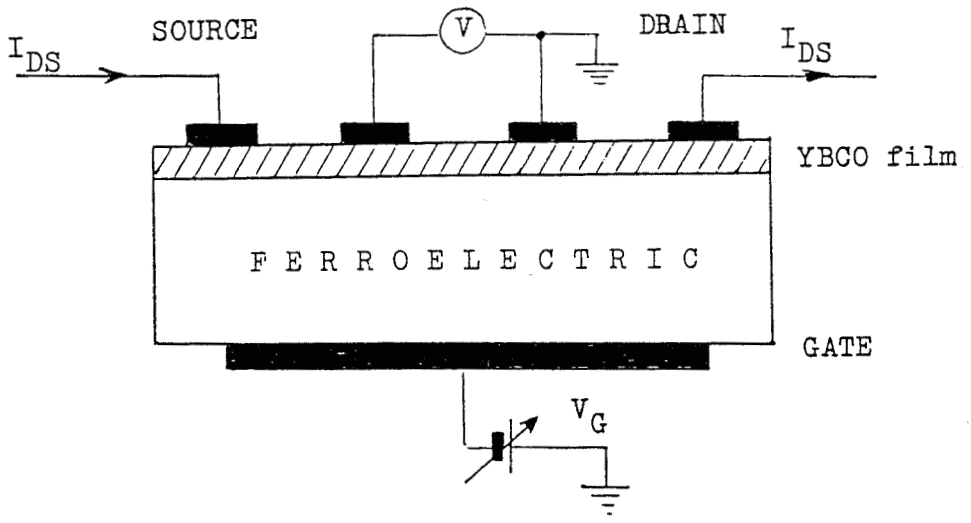

Figure 1.- Typical structure for study of the P-effect.

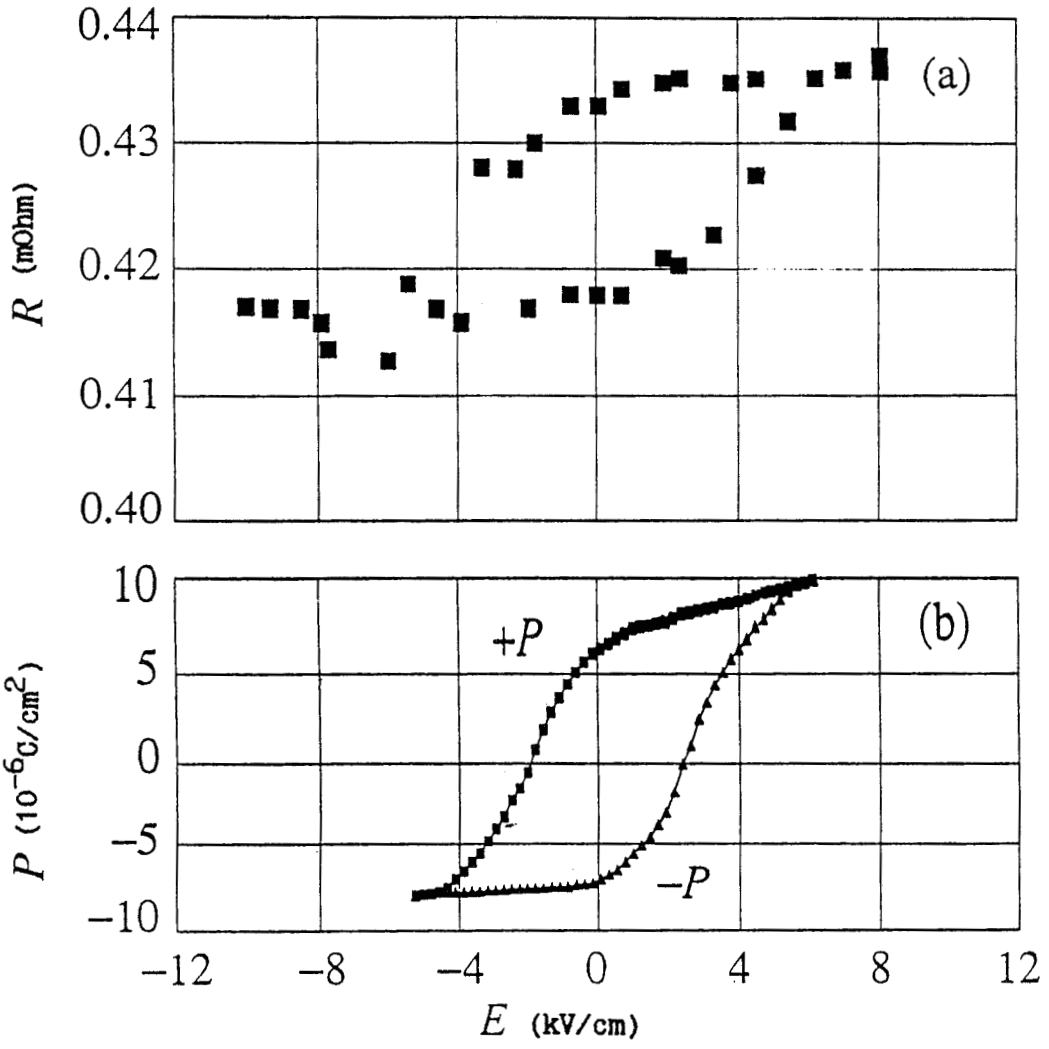

Figure 2.- Resistance change in the mixed state of YBCO film on BaTiO3 substrate (a) and polarization hysteresis loop for the substrate (b) at 77 K.

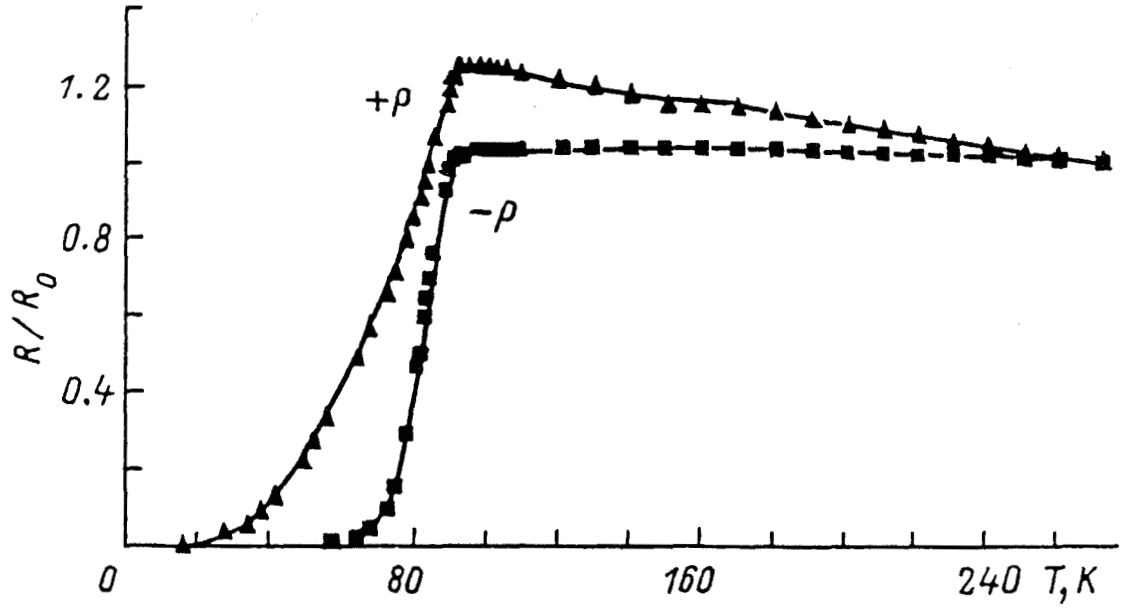

Figure 3.- Temperature dependence of resistance of YBCO films deposited on the opposite sides (+P and -P) of LiNb03 substrates (+P :polarization directed toward the film, -P :polarization directed away from the film).

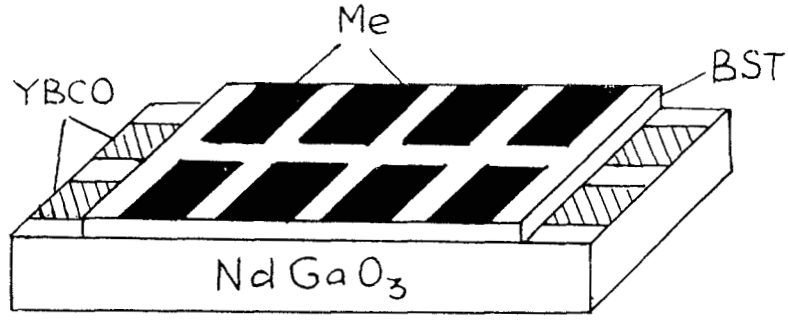

Figure 4.- YBCO-BasrTi03 (BST) - Metal structure.

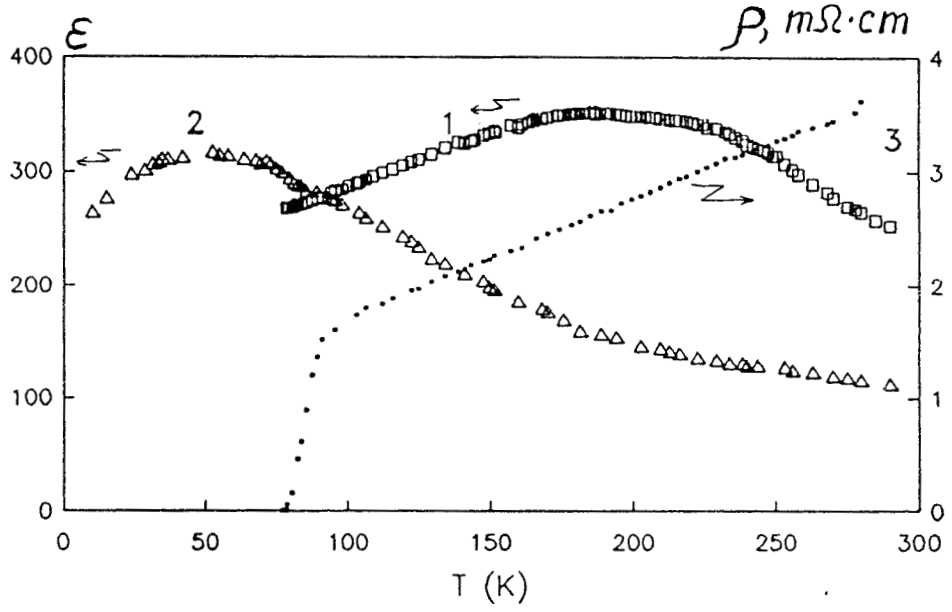

Figure 5.- Temperature dependencies of the dielectric constant of $Ba_xSr_{1-x}TiO_3$ films with x-0.5 (1) and x=0.21 (2) and the resistivity of YBCO film (3) in the YBCO/BST/Au structure shown in Figure 4. The X values refer to the target.

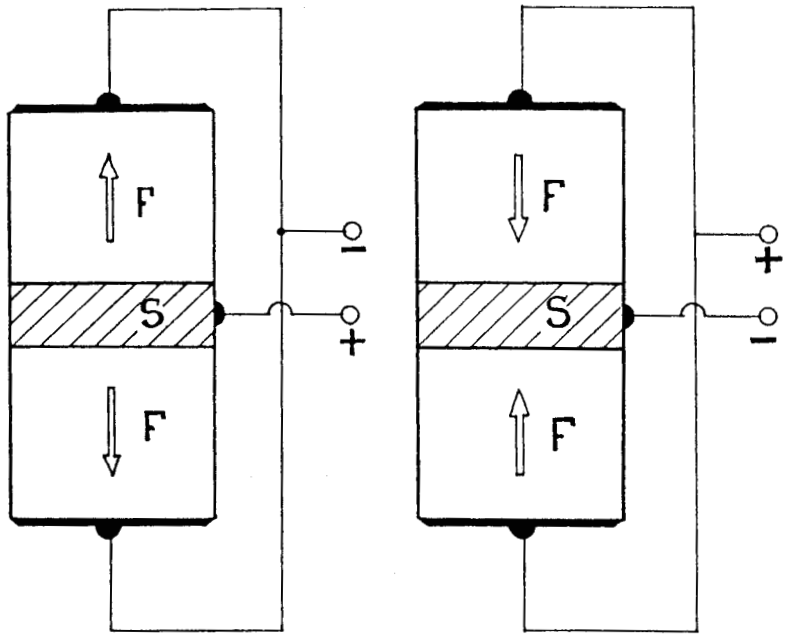

Figure 6.- Superconductor(S)-Ferroelectric (F) three-layered structure. The switching of polarization of the ferroelectric layers from the -P state to the +P state may induce transition of the superconductor layer from the S-state to the N-state.

SINGLE SCAN
521-76
313741

OXIDE PEROVSKITE CRYSTALS FOR HTSC FILM SUBSTRATES MICROWAVE APPLICATIONS

A.S. BHALLA AND RUYAN GUO
Materials Research Laboratory, The Pennsylvania State University
University Park, PA 16802

ABSTRACT

The research focused upon generating new substrate materials for the deposition of superconducting yttrium barium cuprate (YBCO) has yielded several new hosts in complex perovskites, modified perovskites, and other structure families. New substrate candidates such as. $Sr(Al_{1/2}Ta_{1/2})O_3$ and $Sr(Al_{1/2}Nb_{1/2})O_3$, $Ba(Mg_{1/3}Ta_{2/3})O_3$ in complex oxide perovskite structure family and their solid solutions with ternary perovskite $LaAlO_3$ and $NdGaO_3$ are reported. Conventional ceramic processing techniques were used to fabricate dense ceramic samples. A laser heated molten zone growth system was utilized for the test-growth of these candidate materials in single crystal fiber form to determine crystallographic structure, melting point, thermal, and dielectric properties as well as to make positive identification of twin free systems. Some of those candidate materials present an excellent combination of properties suitable for microwave HTSC substrate applications.

INTRODUCTION

There is great interest worldwide in the deposition of high quality thin films of high Tc superconductors (HTSC), using a whole variety of available deposition techniques. The selection of useful substrate materials is of first importance and is subjected to a number of constrains such as: thermal and chemical stability under the conditions used in the film processing and operating; suitable lattice parameter and ionic structure matching; thermal compatibility in terms of thermal expansion matching over the temperature range of film processing and operating; physical properties suitable for specific use (for instance the dielectric constant and loss for electronic devices and high thermal conductivity for high-power-density applications); commercial availability and if possible, low cost.

In addition to satisfy the general requirements, substrates to be used in microwave devices must be twin-free single crystals with potential to be grown in large size (2-4" wafer). Congruent melting compositions with modest melting temperatures are therefore favorable. The dielectric constant influences the propagation speed and the package dimensions therefore a moderately low dielectric constant (<25) is required. Because the conductor loss of the superconductor is diminished, the role of the dielectric loss becomes critically important. Very low dielectric loss ($<10^{-4}$) is therefore demanded.

The potential application of YBCO superconductor to the development of ultra high density interconnect systems for a new generation of high speed high density multichip

modules dictates new requirements for the substrate design. An essential feature is the geometry of the X and Y layers of HTSC lines that must have geometries in cross section of order 2 x 1 μ meters thus necessitating a current carrying capability for the HTSC of ~10^6 A/cm^2. For this current capability clearly the YBCO must be highly grain oriented very near to single crystal, so that the whole multilayer structure is in the form of highly oriented overgrowths on a single crystal substrate. Impedance characteristics for the interconnect structure dictate that the dielectrics used must be of low permittivity (ideally <10) if the geometry is to be preserved. Highly oriented thin films (2 μm or above) will be needed for the separation of strip lines and ground plane structures. Dielectric loss requirements are a little less stringent than those required for the microwave applications; however, tanδ < 0.001 is highly desirable at the 77K working temperature.

A family of substrates with the perovskite structure is most important as those materials are among the most obvious candidates for epitaxial growth of YBCO films. Substrates of perovskite structure usually have the ideal cubic (such as $SrTiO_3$), double cell cubic (such as Ba_2YSbO_6), hexagonal distorted pseudo cubic (such as $LaAlO_3$) or other pseudo cubic cells (such as $NdGaO_3$ that has the [$GdFeO_3$] structure with orthorhombic symmetry). $SrTiO_3$ crystals of high quality and large sizes, though are readily available and yield the best epitaxial quality thin films (primarily due to their close interatomic structure matching to the HTSC), have high dielectric constant (>300) arising from the phase transition near the working temperature (~110K). Another probably the most used substrate currently, $LaAlO_3$, though good in lattice matching and of reasonable dielectric properties, is heavily twinned and goes through a ferroelastic phase transition at ~435°C.[1] These macroscopic defects in the crystals are not tolerable in substrates used for complex microcircuits.

In our ongoing search for substrates suitable for microwave device and integrated circuit applications, the focus has been upon developing and identifying new substrate materials primarily with perovskite structures for the deposition of superconducting yttrium barium cuprate (YBCO) films. It became increasingly clear to us that the demand on the substrates to have a close "lattice match" was in many cases less appropriate.[2] Similarity in structure is a higher order criterion than simply lattice parameter matching though they are not independent.[3] A wide range search for new low permittivity candidate materials using the predictive capability of the phenomenological ionic polarizability arguments is currently undertaking.[4] The unique capabilities of a laser heated molten zone (LHMZ) growth system have been utilized for test-growth of candidate materials in single crystal fiber form to determine structure, thermal, and dielectric properties and make positive identification of twin free systems. This paper reports the combination of experimental and theoretical approaches in this field with focus on the complex oxide perovskites and related solid solutions.

CRYSTALS OF COMPLEX OXIDE PEROVSKITE COMPOUNDS

Ceramic samples were prepared by solid state reaction, using conventional techniques. X-ray diffraction technique was used extensively to characterize the crystallographic

phases and to adjust the processing conditions. The laser heated molten zone growth method has been shown to be a powerful method for rapidly growing small diameter single crystals, particularly oxides of high melting temperature, for both property studies and fiber devices.[5,6,7] The LHMZ equipment used in this investigation consisted of a power source (water cooled, tunable flowing gas CO_2 55W laser), an optical layout, and a growth section. The molten zone temperature during a stable growth was monitored using an optical pyrometer.

Radio frequency dielectric constants and the loss tangent were measured using a General Radio 1621 Capacitance Measurement System. Dielectric properties at microwave frequency were measured using resonance techniques equipped with an HP8510A network analyzer. Post resonance technique (the Hakki and Coleman technique) was used to measure the dielectric constants of the ceramic samples. Cavity perturbation technique was used for the measurements on samples of thin rod (e.g., single crystal fiber samples) or bar-shaped. The Q factors (of microwave frequency) at liquid nitrogen temperature were measured by a transmission resonance technique.

$Ba(Mg_{1/3}Ta_{2/3})O_3$ (BMT)

Ceramics of complex perovskite oxides $A(B1_{1/3}B2_{2/3})O_3$ type have been explored previously as the candidate materials with excellent microwave dielectric properties.[8] $Ba(Mg_{1/3}Ta_{2/3})O_3$ (BMT), in particular, was reported to have a dielectric constant κ~25 and dielectric Q~16,800 (one of the highest in the oxide family) at 10.5 GHz, in samples with 1 mol% Mn additive as a sintering aid.[9] BMT compound is one of the most refractory oxides known thus the growth of single crystals is difficult. A single crystal of BMT was grown from a BaF_2 flux. It yielded a significantly higher dielectric constant (~200),[10] presumably attributable to the flux contamination.

BMT single crystal fibers were grown successfully using our LHMZ technique. It grows congruently from the melt in the temperature range of 2900-3100°C. A high temperature phase of simple cubic perovskite was obtained at room temperature, in comparison to the hexagonal ordered perovskite structure usually obtained in ceramics (see Fig. 1). Dielectric properties of both the ceramic and the single crystal BMT were studied. BMT ceramic samples have ultra low dielectric loss ($<1x10^{-5}$ at 90K and 10kHz) and good thermal compatibility ($\alpha \sim 9.0x10^{-6}$/°C) with the YBCO superconductors. The single crystal BMT has a cubic lattice parameter a=4.0877Å. The dielectric constant increases and saturates as the bulk density approaches the theoretical density. Dielectric loss reduces with the enhancement of the ordering of the B-site. Single crystals of high temperature disordered cubic form preserve a moderate dielectric constant (26.0 at 10GHz) and low dielectric loss tanδ ($2.78x10^{-4}$ at room temperature and 10kHz and $<10^{-5}$ at 90K) that make this material unique for microwave device applications.

The BMT lattice parameter of a=4.0877Å, represents a lattice mismatch of 5.3% to the b-axis of YBCO (b=3.883Å); this seems less ideal as a substrate for YBCO. However, there has been no clear cut-off for lattice parameter matches for "epitaxial" (or highly oriented) film deposition of YBCO. "Epitaxial" YBCO thin films on MgO single crystals (with mismatch of 8.5%) have been reported.[11] A BMT single crystal has a twin-

free cubic perovskite structure that is advantageous as a substrate compared to some of the heavily twinned substrates, e.g., $LaAlO_3$ and $NdAlO_3$. High temperature BMT single crystal grown by LHMZ is twin free, of moderate dielectric constant, low dielectric loss, and good thermal expansion matching and is therefore identified to be a potentially suitable substrate for the HTSC thin film deposition.

The application of BMT as a substrate, beside its fiber crystals' applications for microwave antenna, may be restricted by the fact that single crystals are difficult to grow. Skull melting growth techniques,[12] could presumably be used to grow BMT crystals of adequate sizes. The high melting temperature of BMT will not be a crucial issue, when the material is used as an insulating layer between the YBCO films in a multichip-module type of integrated structure, because vapor phase deposition techniques (e.g., laser ablation and metal-organic chemical vapor deposition) rather than liquid phase growth methods will be utilized.

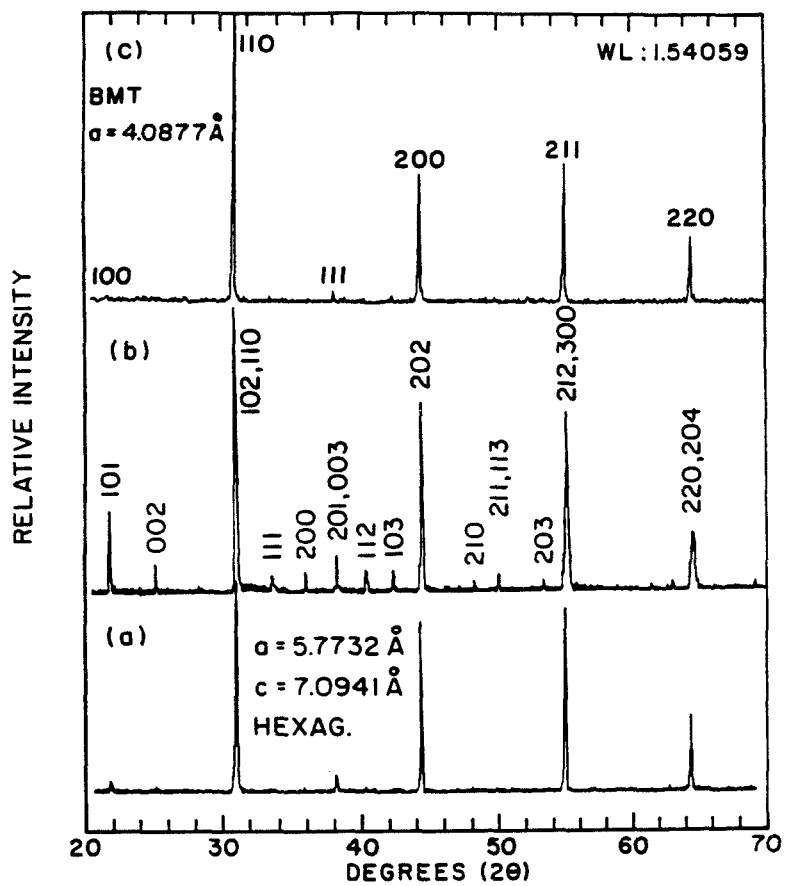

Fig. 1. Typical x-ray diffraction pattern of $Ba(Mg_{1/3}Ta_{2/3})O_3$: (a) ceramic powder calcined at 1500 °C for 3 h showing weak ordering; (b) ceramic sintered at 1655 °C for 5 h showing strong B-site ordering; and (c) single crystal (powder) grown by LHMZ showing an ideal simple cubic perovskite structure with a=4.0877 Å. BMT ceramic XRD patterns are indexed as a hexagonal perovskite structure with a=5.7731(6) Å and c=7.0941(2) Å.

$Sr(Al_{1/2}Ta_{1/2})O_3$ (SAT) and $Sr(Al_{1/2}Nb_{1/2})O_3$ (SAN)

The compounds of $Sr(Al_{1/2}Ta_{1/2})O_3$ (SAT) and $Sr(Al_{1/2}Nb_{1/2})O_3$ (SAN) were first prepared and tested to learn their crystallographic phases and melting behavior by the group at the AT & T Bell Labs.[13] Ceramic samples were identified to have double cell cubic perovskite structure with a=7.795Å and melting temperatures of 1900°C and 1790° C for SAT and SAN, respectively. On the basis of our understandings of the crystal chemistry-dielectric property relation of various oxide perovskites, and the reports by the Bell Labs group that showed both the SAN and SAT melt congruently and produce a single phase of the perovskite structure after melting, we selected the SAT and SAN as primary candidates in the $A(B1_{1/2}B2_{1/2})O_3$ complex oxide perovskite family for crystal growth and to investigate their properties in relation to substrate applications.

$Sr(Al_{1/2}Ta_{1/2})O_3$ (SAT) and $Sr(Al_{1/2}Nb_{1/2})O_3$ (SAN) are grown using the LHMZ growth technique. Their crystallographic structures are found to be simple cubic perovskite with lattice parameters a=3.8952Å (SAT) and a=3.8995Å (SAN) that are of close lattice matching to the YBCO superconductors. No structural phase transitions or twins have been found and the average coefficients of the thermal expansion are in good matching with the YBCO superconductor materials. SAT currently represents one of the best potential HTSC substrate materials for microwave applications. The unique feature of this material is that it has desired dielectric properties (dielectric κ~12, loss factor $\tan\delta<10^{-4}$) at the microwave frequencies with twin-free lattice and good thermal expansion matching along with chemical compatibility with the YBCO superconductors. Dielectric constants in RF region as measured on the dense ceramic samples of SAT and SAN at 23°C are shown in Fig.2.

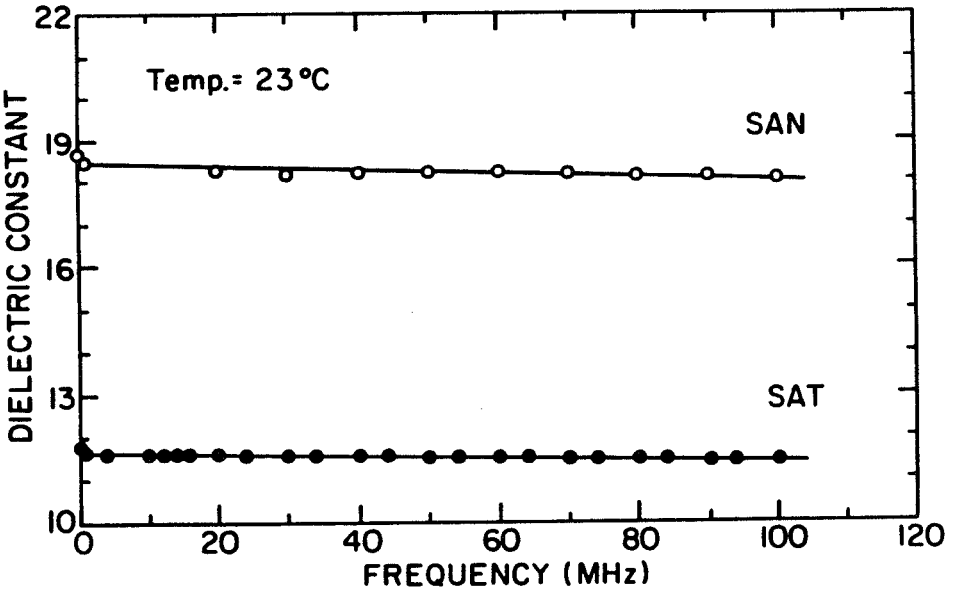

Fig. 2. Dielectric constants of SAT and SAN ceramics as functions of frequency at room temperature.

Our experimental results on the SAT composition along with the earlier report on the congruent melting nature of the SAT and SAN compounds, have stimulated research works in the thin film area. MOCVD-derived SAT films grown at 850°C on $LaAlO_3$ were found to have exclusively (001) growth with in-plane orientation.[14] Using SAT polycrystalline materials as targets in a pulsed laser deposition process, Findikoglu *et al.*[15,16] have reported high quality epitaxial (c-axis orientation) growth of thin films of SAT and multilayers of YBCO/SAT on (001) $LaAlO_3$ and MgO substrates. Dielectric constants of the SAT films (~100-390nm thick), however, were reported to be ~23-30, notably higher than the value (κ~12) found in bulk ceramic materials. The deviations from perfect cation stoichiometry in films may be one of the causes for the discrepancy in value of the dielectric constants as the Al/Ta ratio in SAT films was found to be ~0.8 rather than the stoichiometric ratio of unity.[12,13] No dielectric loss data has been reported for the SAT films therefore direct comparison between the dielectric constants of the film and that of the bulk SAT sample is not intended.

SOLID SOLUTION OF TERNARY AND COMPLEX PEROVSKITE OXIDES

Further modification of the SAN and SAT compositions has been carried out to fine tune their properties, particularly reducing their melting temperatures (SAT: 1900~(1908±25)[13], and SAN:1790~(1739±10)[13])[17] for easier fabrication of the crystals and better control of the reduction problem of the Nb^{5+} and Ta^{5+}. This modification was also an attempt to overcome the twinning problem and to stabilize the cubic phase at room temperature in $LaAlO_3$ crystals.

$LaAlO_3$ has a rhombohedrally distorted perovskite ($A^{3+}B^{3+}O_3$ type) structure. Although the La^{3+} ion generally prefers the 12-coordination-site, it has a tendency for 9-coordination. The distortion in the LaO_{12} polyhedron is brought about by a slight displacement of the oxygen atoms away from the ideal positions of the cubic perovskite form, that is more clearly shown in other [rear-earth]$^{3+}AlO_3$ family members when the A-site cation radii become even smaller, e.g., in the case of $PrAlO_3$.[18,19]. Fig. 3 presents a classification of $[A]^{3+}[B]^{3+}O_3$ type compounds according to the constituent ionic radii (8-coordination cation radii were used for A-site cations) focusing on the perovskite region. In fact, no ideal cubic perovskite structure but the rhombohedral [$LaAlO_3$] and the orthorhombic [$GdFeO_3$] structure have been reported in ternary compounds of the $[A]^{3+}[B]^{3+}O_3$ type.[20] For aluminate compounds, rhombohedral symmetry is found when A-site is occupied by the largest A^{3+} cation, La^{3+}, and other $[A]^{3+}[Al]^{3+}O_3$ compounds have even lower symmetry

Our approach following this direction was to introduce "balanced" cation substitution simultaneously in the A- and B-sites to increase the average cation size at the A-site, hence to stabilize the 12-coordination of that position and consequently the cubic perovskite structure. The solid solution of ternary $LaAlO_3$ and complex oxides of $Sr(Al_{1/2}Ta_{1/2})O_3$ or $Sr(Al_{1/2}Nb_{1/2})O_3$ was chosen for investigation.

By forming crystalline solutions with compounds of low melting temperatures, it was expected that the crystalline solution would result in lower melting temperature and consequently avoid the reduction problem and permit growth in platinum crucibles.

$NdGaO_3$ was found to have a melting temperature of ~1484±24°C, and it was therefore selected as an end member of the crystalline solution series with SAT and/or SAN for the present studies. $NdGaO_3$ has the [$GdFeO_3$] structure with orthorhombic symmetry. No twinning problems are reported in this material. YBCO thin films deposited on $NdGaO_3$ were of better quality compared to those deposited on $LaAlO_3$ substrates. However, the high dielectric loss in the $NdGaO_3$ is a limiting factor for the YBCO film applications in microwave devices.

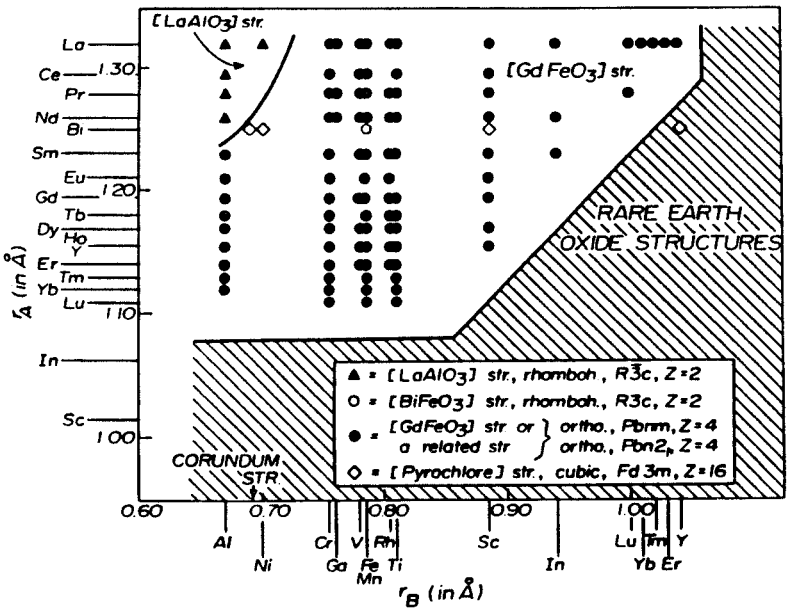

Fig. 3. Structure field map for $[A]^{3+}[B]^{3+}O_3$ type compounds (ref. 19).

Single crystal fibers of modified strontium aluminum tantalum oxide $(1-x)Sr(Al_{1/2}Ta_{1/2})O_3$:$xLaAlO_3$ (SAT:LA) and $(1-x)Sr(Al_{1/2}Ta_{1/2})O_3$:$xNdGaO_3$ (SAT:NG), and modified strontium aluminum niobium oxide $(1-x)Sr(Al_{1/2}Nb_{1/2})O_3$:$xNdGaO_3$ (SAN:NG) and $(1-x)Sr(Al_{1/2}Nb_{1/2})O_3$:$xLaAlO_3$ (SAN:LA) were grown using a laser heated molten zone growth technique.[21] 0.7SAT:0.3LA grows congruently and remains twin free simple cubic perovskite structure (as the SAT) when cooled down to room temperature. 0.7SAT:0.3LA crystals have moderate dielectric constant (κ=21.7) and low dielectric loss ($\tan\delta=7.5\times10^{-5}$) at 10 kHz and 90K. The reduction problem of Ta^{5+} is eliminated (which is common in the case of SAT growth). 0.7SAT:0.3NG and 0.7SAN:0.3NG have lower melting temperatures and crystal growth is easier. $NdGaO_3$ addition to the SAT and SAN enhances the potential of SAT and SAN as large area substrates for HTSC growth. However, the dielectric constants increased from κ~12 to κ~16 (0.7SAT:0.3NG) and from κ~18 to κ~23 (0.7SAN:0.3NG) as a result of $NdGaO_3$ incorporation.

Our results further confirmed the report of Mateika *et al.*[22,23] that the ideal cubic phase can be formed in $(La,Sr)(Al,Ta)O_3$ compounds. It is interesting to notice that similar substitutions using [Ca,Ta] instead of [Sr,Ta] did not produce a compound with cubic structure. The average A-site cation radii of the [Ca,Ta] substitution is smaller than that of $LaAlO_3$ (ionic radii of Ca^{2+}, La^{3+}, and Sr^{2+} are 1.14, 1.185, and 1.27Å, respectively),[24] therefore, no stabilization effect on 12-coordination A-site is expected.

The cubic symmetry for the compound of SAT-NG and SAN-NG may be due to the fact that Ga^{3+} is almost of the same cation size as Ta^{5+}/Nb^{5+}. Slight reduction in the A-site cation size is accompanied by the slight increase of the B-site cation size and thus the cubic structure of SAN or SAT stays intact.

The ideal cubic perovskite structure can be stabilized in the case of ternary $LaAlO_3$ by forming a crystalline solution composition with cubic $Sr(Al_{1/2}Ta_{1/2})O_3$ and $Sr(Al_{1/2}Nb_{1/2})O_3$. The mechanism of this type of stabilization is through introducing the compensated cation substitution in the form of $[2La^{3+}]+[Al^{3+}] \rightarrow [2A^{2+}]+[B^{5+}]$ with the A^{2+} cation having a radius larger than that of La^{3+} and therefore stabilizing the 12-coordinated A-site. Crystalline solutions of SAT-LA maintained or improved most of the dielectric and thermal properties of $LaAlO_3$ and gained the advantage of forming a twin-free simple cubic structure and improved lattice compatibility. $NdGaO_3$ is shown to be an effective end member to decrease the melting temperature of SAN and SAT without disturbing their simple cubic (twin-free) crystal structure. Dielectric constants of SAN and SAT with addition of the $NdGaO_3$ were increased; however, the dielectric loss factor still remained less than $5x10^{-4}$. The results suggesting that SAT-LA and SAN-LA are better candidates as substrate materials than $LaAlO_3$ because the latter is intrinsically twinned. The growth of SAT-NG and SAN-NG are comparatively convenient as they have relatively low melting temperatures together with the relatively lower dielectric constants and the ideal lattice constants and thermal compatibility with the YBCO superconducting materials.

Other substrate candidates such as $La(Mg_{2/3}Ta_{1/3})O_3$,[25] $La(Mg_{1/2}Ti_{1/2})O_3$,[26] $(Ca,Sr)(Ga,Nb)O_3$[27] and a family of materials of the magnetoplumbite structures[28] have also been fabricated and their dielectric properties studied. These crystals and their associated solid solutions provide several new options for ultra low loss, low permittivity, twin free oxides with low congruent melting temperature, matching thermal expansion and excellent chemical compatibility.

SUMMARY

Oxide crystals with the perovskite structure are major candidates for YBCO film epitaxial deposition particularly if large size cubic, twin free crystals become available. SAT has already shown promise in high quality epitaxial YBCO film growth. With improved growth capability, the SAT and particularly its modified solid solutions may be more useful than the intrinsically twinned $LaAlO_3$. Solid solutions between the known complex perovskite oxide and ternary end members, especially gallates, will provide large number of options to tailor the material for specific device applications. The property

parameters of the newly proposed substrate materials of oxide perovskite family are summarized in Table I. $LaAlO_3$ and $NdGaO_3$ are also listed for comparison.

TABLE I. Properties of Some Newly Proposed Oxide Perovskite Substrate Materials

Composition	symmetry	Lattice Constant (Å)	κ 10kHz 90K	tanδ 10kHz 90K	α ($x10^{-6}$/°C) (@~300K)	Melting Point (°C) *
BMT (crystal)	Cubic	4.0877	25.9	$<10^{-5}$	9.0	(>2800)
SAT	Cubic	3.8952	11.8	$4.2x10^{-5}$	9.7	1908±25
SAN	Cubic	3.8995	18.7	$2.2x10^{-4}$	8.5	1739±10
SAT-LA	Cubic	3.8727	21.7	$7.5x10^{-5}$	7.7	1830±22
SAN-LA	Cubic	3.8634	25.7	$2.8x10^{-4}$	9.5	1705+20
SAT-NG	Cubic	3.8866	16.0	$4.3x10^{-4}$	8.8	1767±31
SAN-NG	Cubic	3.8790	23.0	$5.2x10^{-4}$	10.8	1582±20
$LaAlO_3$ (crystal)	Rhomb.	a=3.789 a=90.12°	23	$7.5x10^{-5}$	8.2//[1$\bar{1}$0] 6.4//[001]	2040±9
$NdGaO_3$ (crystal)	Ortho.	a=5.426 b=5.502 c=7.706	23 (77K,10GHz)	$3.2x10^{-4}$		1484±24

*The melting point was determined rather simply using a strip furnace, with two operators using two separate optical pyrometers and averaging several readings per sample.

ACKNOWLEDGMENT

This work was supported by the Defense Advanced Research Projects Agency (DARPA) under the contract No. DN 00014-90-J-4140.

REFERENCES

1 E.A. Wood, *Amer. Min.* **36** 768 (1951).
2 R. Roy, Ruyan Guo, A. S. Bhalla, and L.E. Cross, *J. Vac. Sci. Technol. A.* **12**(2) 269 (1994).
3 Ruyan Guo, A.S. Bhalla, L.E. Cross, and R. Roy, *J. Mat. Res.* **9**(7), 1644 (1994).
4 Ruyan Guo, A.S. Bhalla, R. Roy, and L.E. Cross, *Ferroelectrics* **155**(1-4) 43 (1994).
5 J.S. Haggerty, W.P. Menashi and J.F. Wenckus, U.S. Patent No. 3 944 640 (16 March 1976); U.S. Patent No. 4 012 213 (15 March 1977).

[6] R.S. Feigelson, *MRS Bull.* **13** 47 (1988).
[7] J. Yamamoto and A.S. Bhalla, *Mat. Res. Bull.* **24** 761 (1989).
[8] K. Wakino, *Ferroelectrics* **91** 69 (1989).
[9] S. Nomura, K. Toyama, and K. Kaneta, *Jpn. J. Appl. Phys.* **21**(10) L624 (1982).
[10] F. Galasso and J. Pinto, *Nature* vol. **207** No. 4992, 70 (1965).
[11] e.g., T. Terashima, K. Iijima, K. Yamamoto, K. Irata, Y. Bando, and T. Takada, *Jpn. J. Appl. Phys.* **28**, L987 (1989).
[12] H.R. Harrison and J.M. Honig, *Bull. Mater. Sci.* **3**(3), 247 (1981).
[13] C.D. Brandle and V.J. Fratello, *J. Mater. Res.* **5**(10), 2160 (1990).
[14] B. Han, D. A. Neumayer, B.H. Goodreau, T. J. Marks, H. Zhang, and V.P. Dravid, *Chem. Mater.* (in press).
[15] A.T. Findikoglu, C. Doughty, S. Bhattacharya, Qi Li, X.X. Xi, T. Venkatesan, R.E. Fahey, A.J. Strauss, and J. M. Phillips, *Appl. Phys. Lett.* **61** 1718 (1992).
[16] A.T. Findikoglu, S. Bhattacharya, C. Doughty, M.S. Pambianchi, Qi Li, X.X. Xi, S.M. Anlage, R.E. Fahey, A.J. Strauss, J.M. Phillips, and T. Venkatesan, *IEEE Trans. Appl. Superconductivity*, **3**(1) 1425 (1993).
[17] R. Guo, A.S. Bhalla, J. Sheen, F. Ainger, E.C. Subbarao, S. Erdei, and L.E. Cross, *J. Mat. Res.* (in press, 1994).
[18] R.D. Burbank, *J. Appl. Cryst.* **3** 112 (1970).
[19] O. Muller and R. Roy, in "*The major ternary structural families*" (Springer-Verlag, Berlin, Heidelberg, New York 1974) p.215.
[20] F.S. Galasso, in "*Structure, properties and preparation of perovskite-type compounds*" (Pergamon Press, Oxford, London, Edinburgh, Now York, Toronto, Sydney, Paris, Braunschweig 1969) p.10.
[21] R. Guo, P. Ravindranathan, U. Selvaraj, A.S. Bhalla, L.E. Cross, and R. Roy, *J. Mater. Sci.* (in press, 1994).
[22] S. Haussühl and D. Mateika, *Crystal. Res. Technol.* **26**(4) 481 (1991).
[23] D. Mateika, H. Kohler, H. Laudan and E. Völkel, *J. Cryst. Growth* **109** 447 (1991).
[24] R.D. Shannon and C.T. Prewitt, *Acta Cryst.* **B25** (1969) 925; *Acta Cryst.* **B26** 1046 (1970).
[25] P. Ravindranathan and A.S. Bhalla *et al.* (to be published).
[26] G. Harshe, A.S. Bhalla, and L.E. Cross, *Materials Letters* **18**(4), 173 (1994).
[27] S. Erdei, L.E. Cross, F.W. Ainger, and A.S. Bhalla, *J. Cryst. Growth* **139**, 54 (1994).
[28] R. Guo and A.S. Bhalla (to be published).

Space Sci
522-76
313779

Texturing of High T_c Superconducting Polycrystalline Fibers/Wires by Laser-Driven Directional Solidification in a Thermal Gradient

Usha Varshney and B. Davis Eichelberger, III
American Research Corporation of Virginia
1509 Fourth Street, P. O. Box 3406
Radford, Virginia 24143

ABSTRACT

This paper summarizes the technique of laser-driven directional solidification in a controlled thermal gradient of yttria stabilized zirconia core coated Y-Ba-Cu-O materials to produce textured high T_c superconducting polycrystalline fibers/wires with improved critical current densities in the extended range of magnetic fields at temperatures greater than 77K. The approach involves laser heating to minimize phase segregation by heating very rapidly through the two-phase incongruent melt region to the single phase melt region and directionally solidifying in a controlled thermal gradient to achieve highly textured grains in the fiber axis direction. The technique offers a higher grain growth rate and a lower thermal budget compared with a conventional thermal gradient and is amenable as a continuous process for improving the J_c of high T_c superconducting polycrystalline fibers/wires. The technique has the advantage of suppressing weak-link behavior by orientation of crystals, formation of dense structures with enhanced connectivity, formation of fewer and cleaner grain boundaries, and minimization of phase segregation in the incongruent melt region.

I. INTRODUCTION

Progress in the application of high critical temperature (T_c) ceramic superconducting polycrystalline fibers/wires (with zero resistance above liquid nitrogen temperature at 77K) for very high speed system interconnects, integrated optical components and passive microwave devices for microelectronics and instrumentation applications is currently limited by the lack of formability, strength, toughness and low transport current properties. The low critical current densities (J_c) are associated with extremely small coherence length, causing grain boundaries to act as Josephson junctions such that tunneling currents are highly field dependent; a high degree of superconductivity anisotropy, severely suppressing tunneling currents at high-angle grain boundaries; grain boundary segregated phases; and anisotropic thermal contraction and microcracking at the grain boundaries. The causes of the weak link behavior can be greatly diminished by development of a process method which will yield formation of dense structures with enhanced connectivity, crystallographic texturing of the grains, formation of cleaner and fewer grain boundaries parallel to the conduction direction, and minimization of phase segregation in the incongruent melt zone. One method of forming textured microstructures is directional solidification from the melt in a thermal gradient. However, in the Y-Ba-Cu-O system, the $Y_1Ba_2Cu_3O_7$ or 123 phase could not be obtained congruently from the melt of the 123 composition because of its incongruent

crystallization under the equilibrium phase transformation. The 123 phase is formed by the peritectic reaction through the Y_2BaCuO_5 (211) phase and the liquid phase. If the crystal-growth under the metastable state is realized, the peritectic reaction can be suppressed by rapid solidification with very high growth rate due to high interface undercooling and the 123 phase could be crystallized congruently resulting in highly oriented fibers with improved grain boundaries and high J_c. In the 123 phase the critical current density is one order of magnitude higher along the a-b plane than along the c-axis direction.

Research efforts have been directed toward increasing the J_c of high T_c superconducting materials by texturing the grains using different techniques such as melt textured growth, liquid phase processing and directional solidification, quench and melt growth processes, and zone melting and laser float zone melting. All these techniques have resulted in highly textured microstructures [1]. The significance of the technique of laser-driven directional solidification in a controlled thermal gradient lies in its adaptability as a continuous process for improving the critical current densities of high T_c superconducting polycrystalline fibers/wires. The technical approach involves laser heating to minimize phase segregation by heating very rapidly through the two-phase incongruent melt region (1010-1258°C) to the single phase melt region (> 1258°C) and directionally solidifying in a controlled thermal gradient to achieve highly textured grains in the fiber axis direction.

II. EXPERIMENTAL TECHNIQUES

Texturing of extruded Y-Ba-Cu-O fiber, Duranickel 301 (95%Ni • 4.4%Al • 0.6%Ti) core coated Dy-Ba-Cu-O and yttria stabilized zirconia (YSZ) core coated Y-Ba-Cu-O high T_c superconducting polycrystalline fibers/wires was investigated. Five cm long fiber segments were mounted on an alumina tube with the help of alumina paste to hold the fiber and translated in a laser-driven directional solidification thermal gradient (LDT) furnace as shown in Figure 1. The computer controlled LDT furnace is comprised of a multiple heater array, a fiber translation mechanism capable of translating at rates of 0.5 to 200cm/hr, a fiber feed and fiber take-up system for feeding the fiber preforms and removing the processed fibers, and a laser beam delivery system consisting of laser optics to homogeneously melt the fiber from four directions to the single phase melt zone. The LDT furnace consists of two split tube furnaces having 6.4cm internal diameter and eight independently computer controlled resistively heated zones. The upper split tube furnace consists of two heating zones, a 6.4cm long binder burnout zone and a 10.2cm long preheat zone. The lower split furnace consists of six heating zones, four 6.4cm long thermal gradient zones and two 10.2cm long annealing zones. Each zone is installed with a temperature sensor to provide flexibility in varying the temperature profile in the thermal gradient. The furnaces are controlled by a closed loop computer based system. A 386-25MHz computer contains two data acquisition and control boards to provide sixteen channels of differential analog input and cold junction compensation for thermocouple signals. An Inconel sheathed type-K thermocouple is

installed in the center of each furnace zone and connected to one channel of the expansion system. The DT2815 data translation board provides eight 4-20mA output channels to control each thermal gradient zone using an Omega PCM1 4-20mA driver. Labtech Notebook software controls the furnace zones using a PID control algorithm. Each thermocouple is sampled at a rate of 10Hz. Labtech Notebook also samples a ninth thermocouple at a slower rate and writes the temperature to a data file. By translating this thermocouple through the furnaces, an exact profile of the gradient can be recorded.

The thermal gradient furnace assembly consists of a fiber translation system which includes a friction drive system to feed the fiber into the gradient and to remove the processed fiber [2-3]. The LDT furnace is installed with a laser beam delivery system consisting of laser optics to homogeneously melt the fiber from all directions to the single phase melt zone. This is accomplished using an 18 Watt CW Nd:YAG laser beam (λ = 1.06μm) which is evenly divided into 4 x 4.5 Watts, using beam splitters, mirrors and lenses arrangement as shown in Figure 2. The optics are mounted using an adjustable height post system. Each post is fastened to a micro optical rail to maintain alignment between the components. The rails are mounted on an aluminum plate installed surrounding the furnace. A He-Ne laser and four pinhole apertures were used to align each rail so as to focus the 4 x 4.5 Watt laser beam at the center of the laser zone, between the two split furnaces as shown in Figure 1, where the fiber is coaxially translating. All the components are housed in a frame constructed from slotted steel angle iron and aluminum plates as shown in Figure 1. Labtech Notebook software has been configured for controlling the multiple heater array, fiber translation mechanism, fiber feed and fiber take-up mechanism. The fibers were laser impacted with a laser beam diameter of 2.5mm while translating through the laser melt zone. The processed fibers were characterized at the surface, as well as at the cross-section, using secondary electron images on a Phillips Model 505 SEM. The elemental distribution and interdiffusion were determined using Philips Model PV 99W EDS energy dispersive X-ray analyzer. The fibers were tested for critical temperature using flux exclusion technique and critical current densities using a four probe technique.

III. RESULTS AND DISCUSSION

Initially, extruded fibers of 123 materials were investigated [1]. The fragile characteristic of the processed fiber resulted in handling difficulty, therefore, core coated high T_c superconducting fibers were identified as a more promising candidate for LDT process. Duranickel 301 (95%Ni • 4.4%Al • 0.6%Ti) core coated high T_c superconducting Dy-Ba-Cu-O fibers obtained from Pacific Superconductors were translated in the thermal gradient. Work was discontinued on the Duranickel 301 core coated high T_c superconducting Dy-Ba-Cu-O fibers due to the interdiffusion of copper (Cu) and nickel (Ni) between the coating and the core at 800°C, which is below the peritectic melting temperature of high T_c superconducting Y-Ba-Cu-O materials, thereby resulting in destroying the superconducting property of the fiber [2-4].

Work was performed on yttria stabilized zirconia core coated high T_c superconducting Y-Ba-Cu-O fibers obtained from ICI superconductors. Figure 3 shows the secondary electron image surface morphology of the yttria stabilized zirconia core coated high T_c superconducting Y-Ba-Cu-O fibers along the fiber-axis direction. Figure 3(a) shows the surface morphology of an unprocessed fiber. Figure 3(b) shows the surface morphology of a fiber translated in the thermal gradient at a rate of 1.7cm/hr, in the presence of 42.6ml/min flowing oxygen, with the laser melt zone temperature at 1080°C. As seen from the micrograph elongated textured grains greater than 10x60μm dimensions were observed to extend in the direction of translation which is along the axis of the fiber. A high degree of crystal continuity and alignment was observed at the boundary region. Figure 4 shows the cross-sectional view of the yttria stabilized zirconia core coated high T_c superconducting Y-Ba-Cu-O fiber. Figure 4(a) shows the secondary electron image of an unprocessed fiber. The core diameter is observed to be 810μm, whereas the coating thickness is observed to be 50μm. Figure 4(b) and 4(c) shows the typical energy dispersive X-ray (EDX) map of the elemental distribution of barium (Ba) and yttria (Y) over the fiber cross-section when processed under the parameters of Figure 3(b). No elemental interdiffusion was observed between the coating and the core for all the elements under consideration.

Figure 5 shows the secondary electron image surface morphology along the fiber axis direction of the yttria stabilized zirconia core coated high T_c superconducting Y-Ba-Cu-O fibers translating at a rate of 1.7cm/hr in the thermal gradient, in the presence of 42.6 ml/min flowing oxygen, with the laser melt zone temperature at 1020°C. Figure 5(a) shows the microstructure of a non-laser impacted zone of the fiber translated in the thermal gradient, whereas Figure 5(b) shows the surface morphology of the fiber impacted with a laser radiance of 49W/cm^2 while translating at a rate of 1.7 cm/hr in the thermal gradient with the laser melt zone temperature at 1020°C. By comparing Figure 3(b) and 5(b) it can be observed that the laser-driven directional solidification in a controlled thermal gradient has a higher growth rate and a lower thermal budget than the conventional thermal gradient processing. Textured elongated grains in the fiber axis direction can be observed at 1020°C as compared to 1080°C in the conventional thermal gradient. Besides having higher growth rates the significance of laser heating is that complete melting to the single phase melt occurs in 53sec, as compared to 10 hours by resistively heating, a time scale too short to allow significant segregation under the driving force of the peritectic reaction. Figure 6 shows the final thermal profiles developed from the results obtained and are compared between resistively heated and laser heated to the single phase melt zone. Further considering the 53sec time scale in the incongruent melt region the intra-grain inclusions of Y_2BaCuO_5 will also be smaller so as to be beneficial for flux pinning thereby improving the critical current properties of the high T_c superconducting polycrystalline fibers/wires for device applications. A superconducting critical temperature was observed to be 80K in the processed fiber as compared with 95K in the unprocessed yttria stabilized zirconia core coated high T_c superconducting Y-Ba-Cu-O fibers. A critical current density of 1.8x10^2 Amps/cm^2 at 77K, 0.6T was observed in

the processed fiber as compared to $2.8x10^2$Amps/cm^2 in the unprocessed fibers as shown in Figure 7. The results indicate that careful control of the specimen processing can lead to the formation of optimized samples which are highly densified and textured due to recrystallization following melting of the material in the single phase melt region. Work is in progress to further optimize the process parameters in order to improve the critical current density of the processed fiber.

IV. CONCLUSIONS

Based on the analytical discussion and experimental results, it can be concluded that the laser-driven directional solidification in a thermal gradient technique is highly feasible for development as a continuous process for improving the critical current densities of high T_c superconducting polycrystalline fibers/wires with elongated textured grains. The time spent in the incongruent melt region, on the order of 53sec, is too short as compared to 10 hours in a conventional thermal gradient to allow significant segregation under the driving force of the peritectic reaction. Also the possibility of Y_2BaCuO_5 inclusions is much smaller, which is beneficial for flux pinning. The technique has a significant advantage of yielding higher growth rates and lowering the thermal budget as compared to the conventional thermal gradient, and further suppressing weak-link behavior by orientation of crystals, formation of dense structures with enhanced connectivity, formation of fewer and cleaner grain boundaries and minimization of phase segregation in the incongruent melt region, thereby enhancing J_c in the high T_c superconducting polycrystalline fibers/wires. The technique is capable of fabricating polycrystalline fibers with high density, mechanical strength and critical current density and is amenable to scale up.

ACKNOWLEDGMENTS

The work has been supported by the National Science Foundation under Grant No. ISI-9101565. The authors wish to acknowledge the helpful technical discussions with Dr. Angus I. Kingon of North Carolina State University and Dr. M. A. Subramanian from Du Pont, Central Research & Development Experimental Station, Wilmington for his assistance in testing the critical current temperature and densities of the fibers.

REFERENCES

1. Usha Varshney, R.J. Churchill, J.M. Glass and A.I. Kingon, Proceedings of the 1991 NSF Design and Manufacturing Systems Conference, Austin, Texas, pp. 385-388, (1991).
2. Usha Varshney, Phase II Final Report, National Science Foundation, Contract No. ISI-9101565, (1994).
3. Usha Varshney, Proceedings of the 1993 NSF Design and Manufacturing Systems Conference, Charlotte, North Carolina, pp. 367-372, (1993).
4. Usha Varshney, Proceedings of the 1994 NSF Design and Manufacturing Systems Conference, Cambridge, Massachusetts, pp. 657-658, (1994).

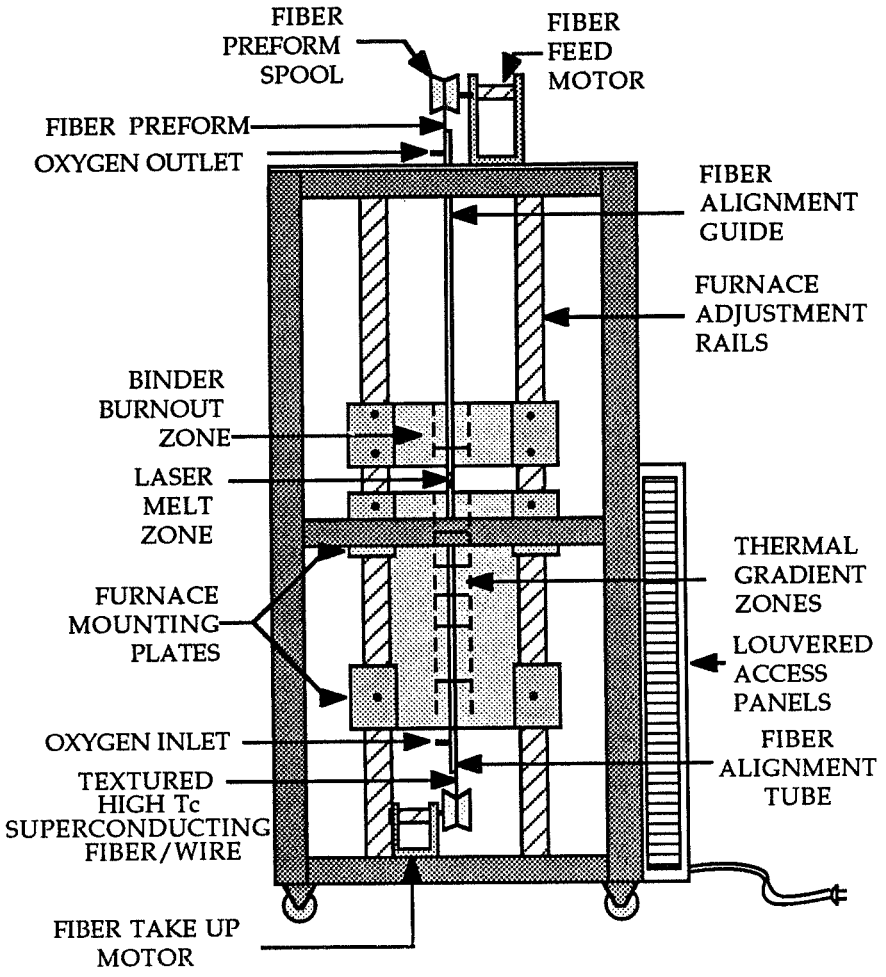

Figure 1. Thermal gradient furnace comprised of a multiple heater array.

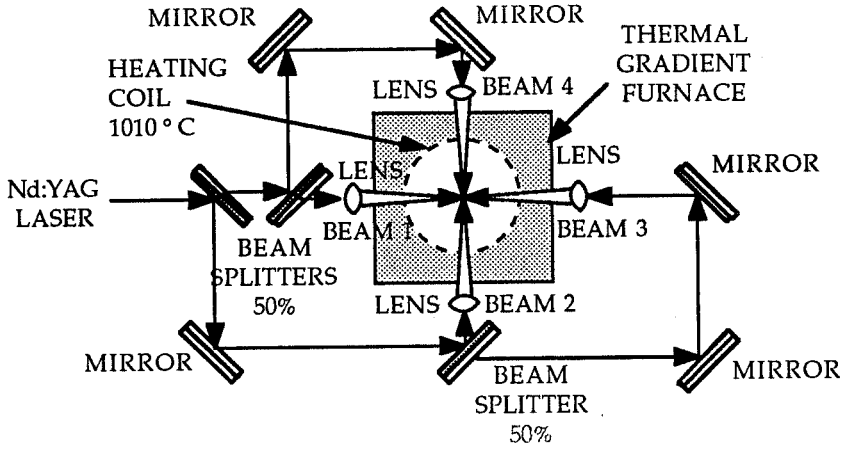

Figure 2. Top view of the laser optics in the laser melt zone of the thermal gradient furnace.

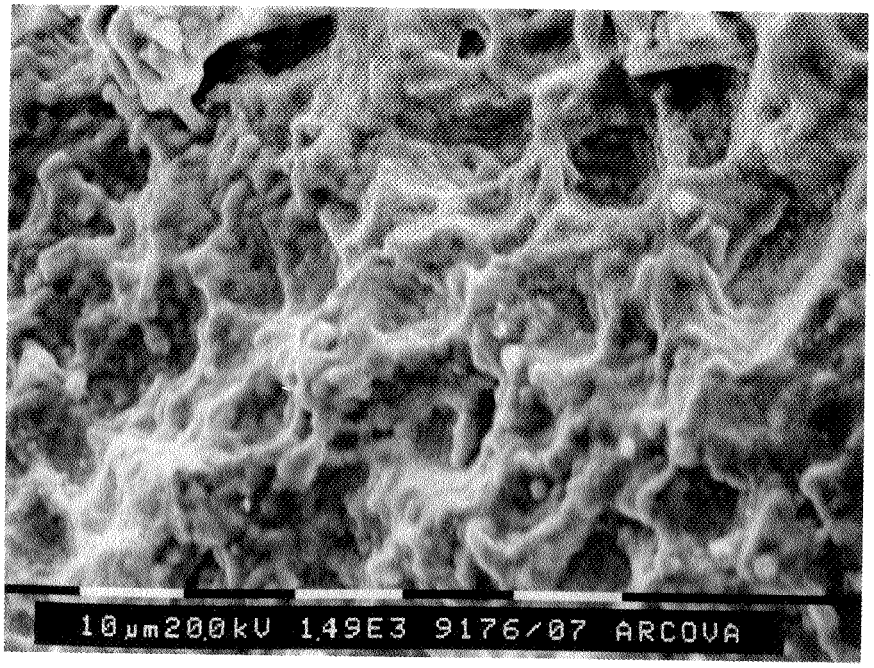

(a) Unprocessed

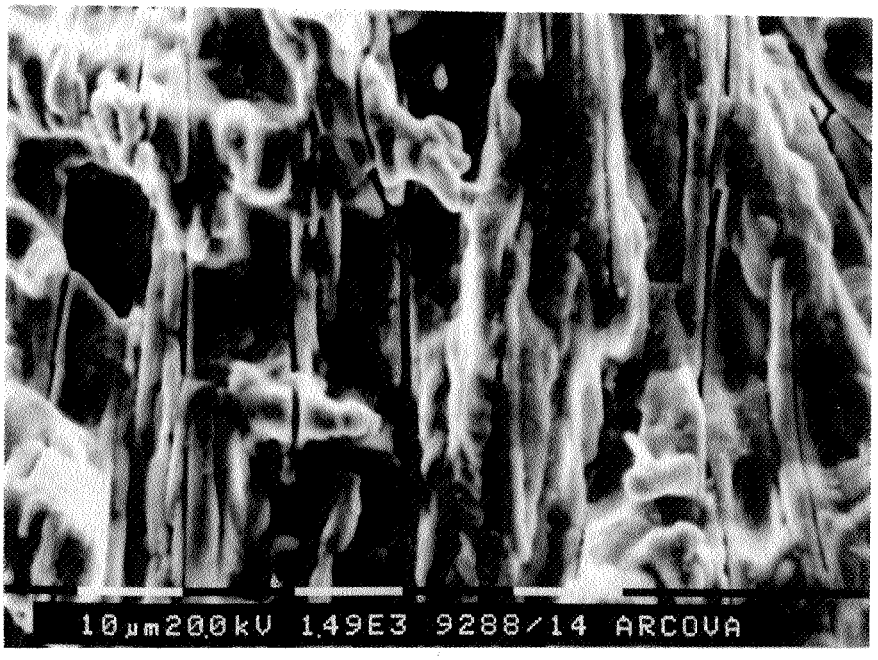

(b) Translated in the Thermal Gradient at a Rate of 1.7 cm/hr, in the Presence of 42.6 ml/min Flowing Oxygen, with theLaser Melt Zone Temperature at 1080°C.

Figure 3. Secondary electron image surface morphology along the fiber axis direction of the yttria stabilized zirconia core coated high T_c superconducting Y-Ba-Cu-O fibers.

(a) Secondary Electron Image of an Unprocessed Fiber

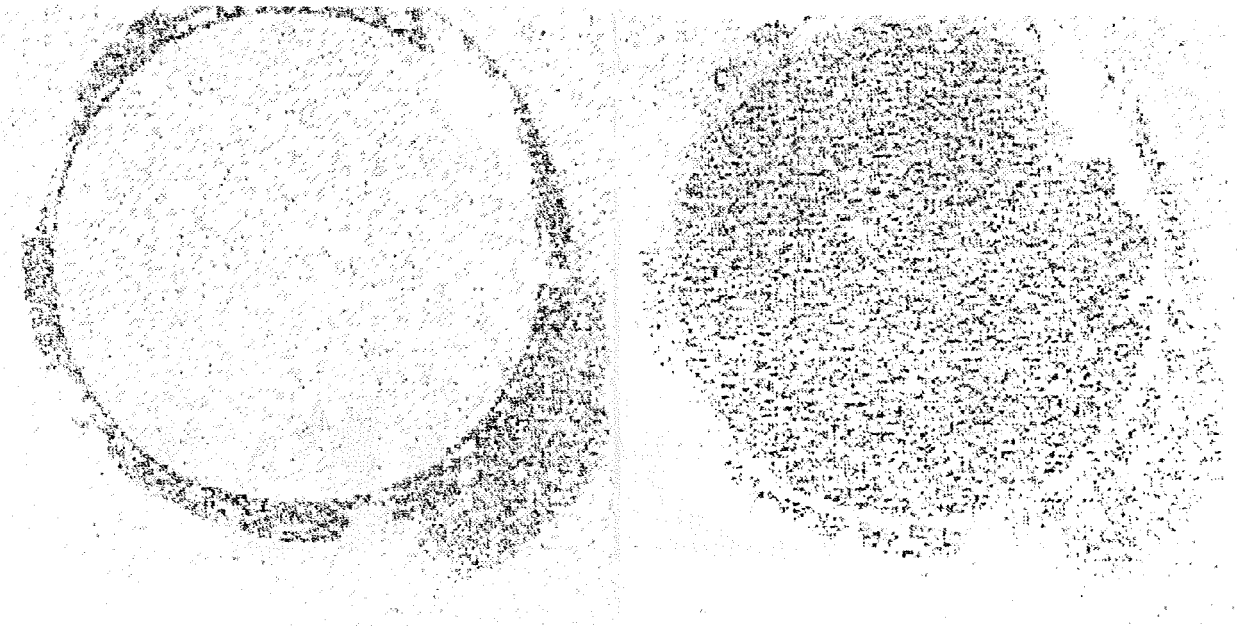

(b) X-ray Map of Ba in the Processed Fiber (c) X-ray Map of Y in the Processed Fiber

Figure 4. Cross-sectional view of the yttria stabilized zirconia core coated high T_c superconducting Y-Ba-Cu-O fibers.

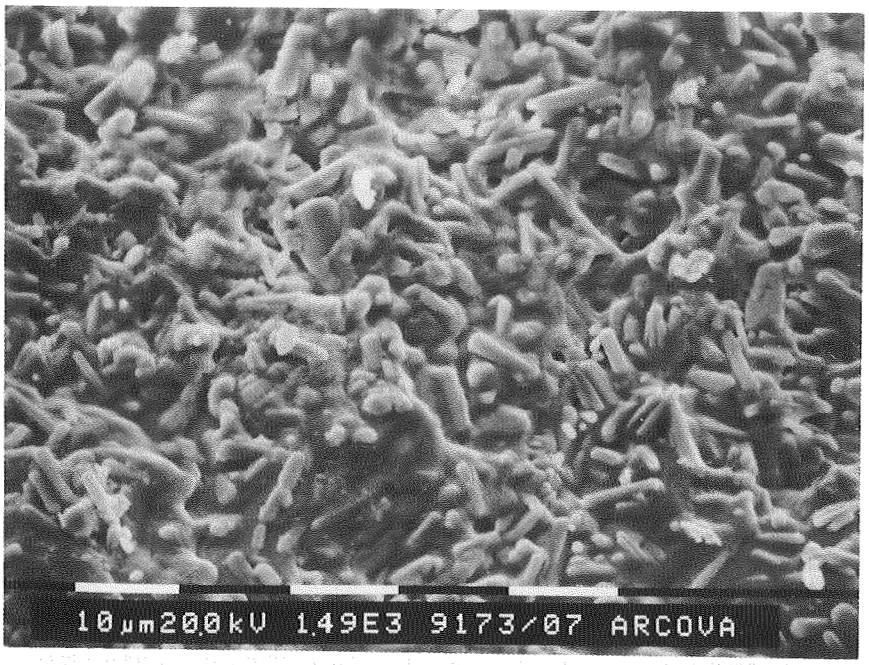

(a) Non-Laser Impacted

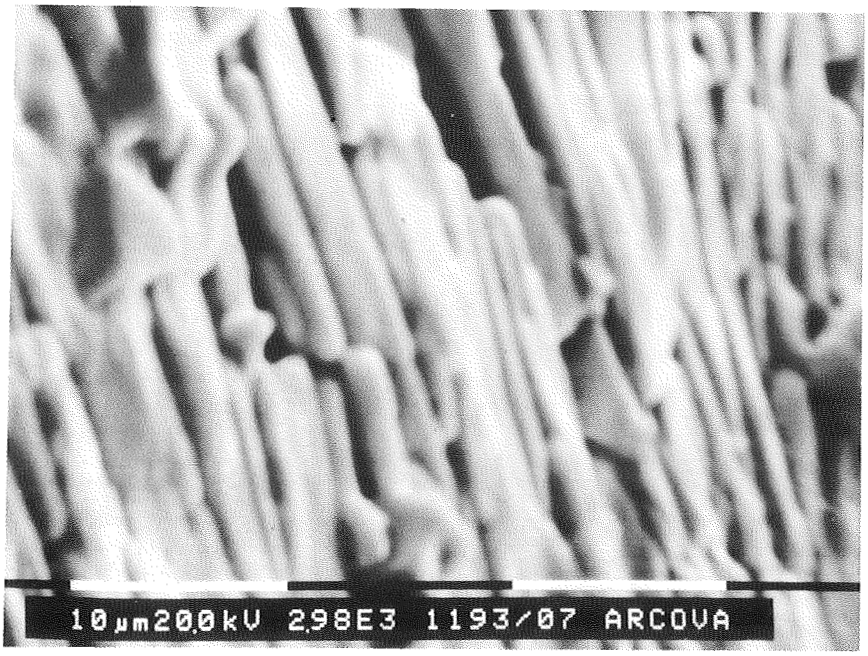

(b) Laser Impacted with 49 W/cm^2 Radiance while Translating

Figure 5. Secondary electron image surface morphology along the fiber axis direction of the yttria stabilized zirconia core coated high T_c superconducting Y-Ba-Cu-O fibers translating at a rate of 1.7cm/hr in the thermal gradient, with the laser melt zone temperature at 1020°C.

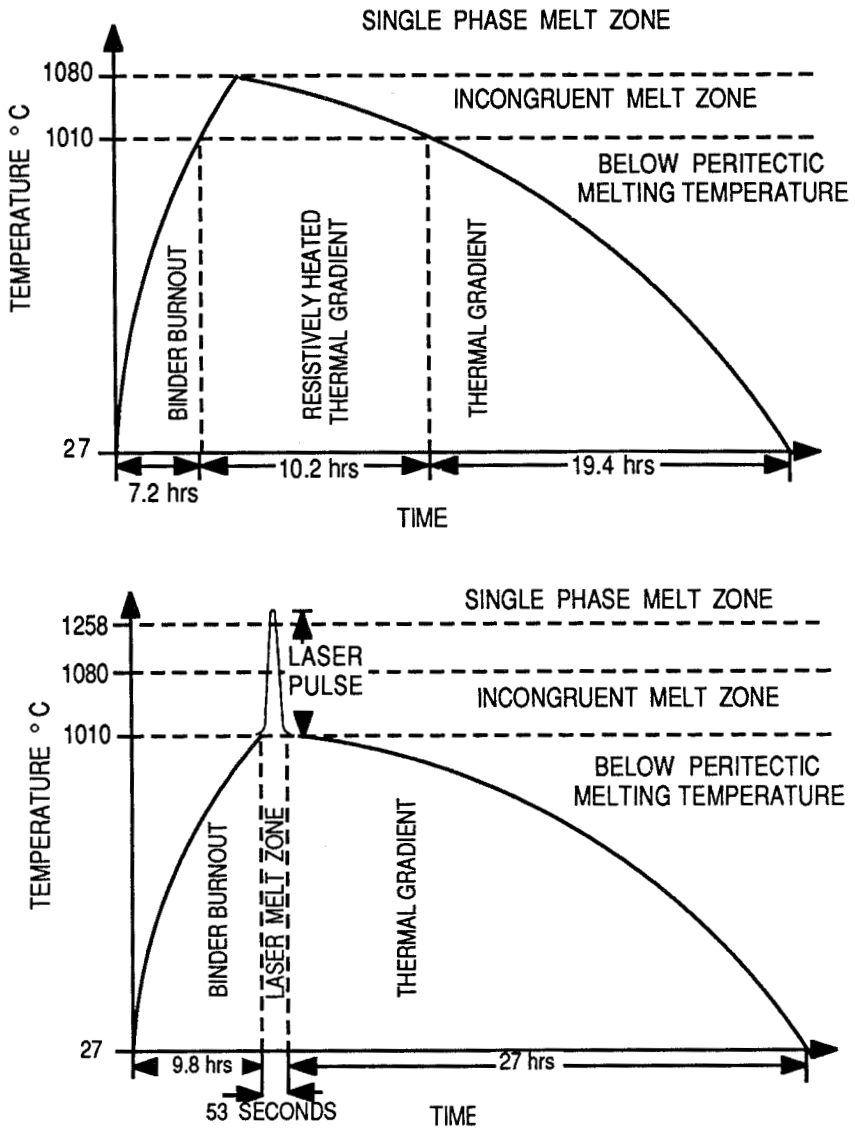

Figure 6. Thermal profiles of fibers heated to a single phase melt zone and translated in a thermal gradient for continuous processing (not to scale).

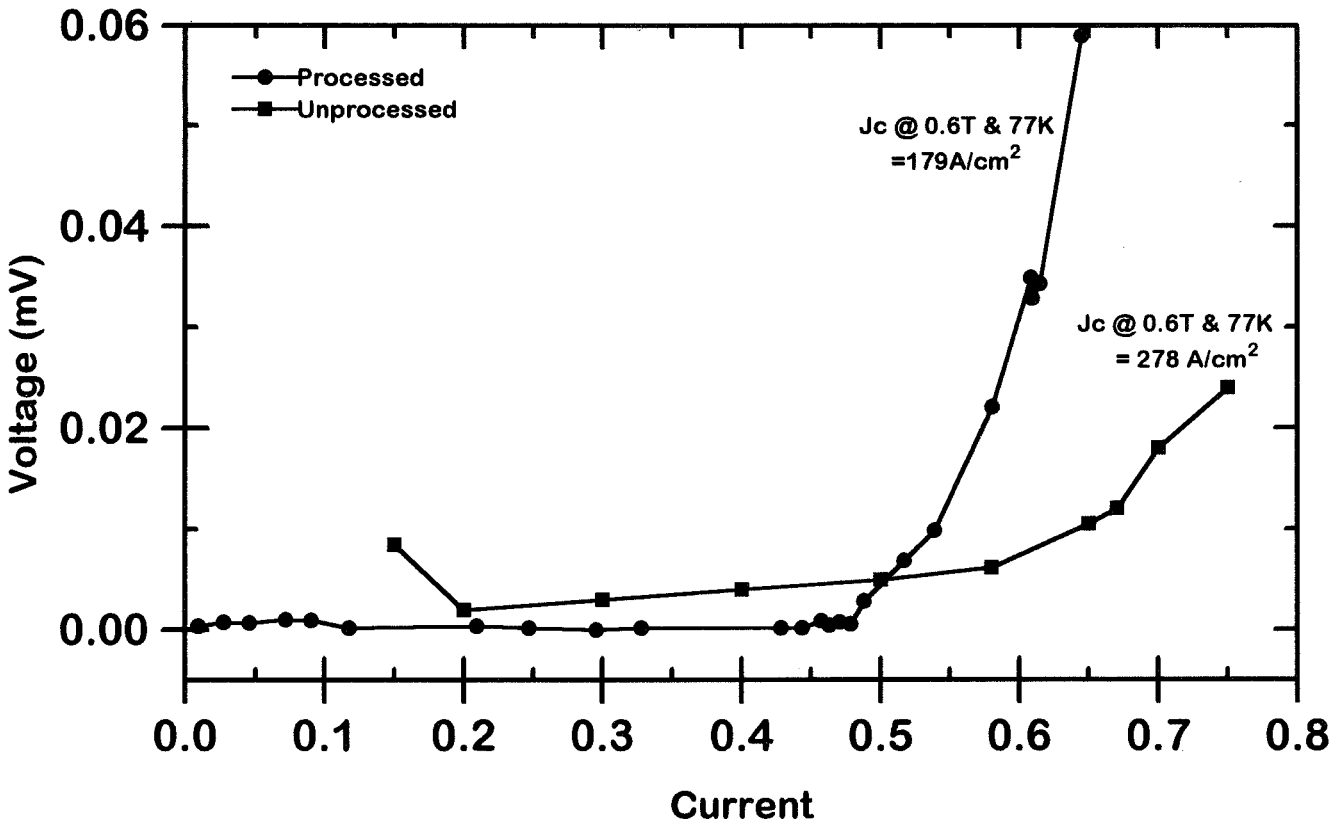

Figure 7. Critical current densities of the yttria stabilized zirconia core coated high Tc superconducting Y-Ba-Cu-O fibers.

S23-72

HEAVY FERMION BEHAVIOUR EXPLAINED BY BOSONS

A. Kallio, S. Pöykkö and V. Apaja
University of Oulu, Department of Theoretical Physics, Linnanmaa, SF-90570 Oulu, Finland
(May 27, 1994)

3Y298b
10⁻

Abstract

Conventional heavy fermion theories require existence of massive fermions. We show that heavy fermion phenomena can also be simply explained by existence of bosons with moderate mass but temperature dependent concentration below the formation temperature T_B, which in turn is close to room temperature. The bosons B^{++} are proposed to be in chemical equilibrium with a system of holes h^+: $B^{++} \rightleftharpoons h^+ + h^+$. This equilibrium is governed by a boson breaking function $f(T)$, which determines the decreasing boson density and the increasing fermion density with increasing temperature. Since HF-compounds are hybridized from minimum two elements, we assume in addition existence of another fermion component h_s^+ with temperature independent density. This spectator component is thought to be the main agent in binding the bosons in analogy with electronic or muonic molecules. Using a linear boson breaking function we can explain temperature dependence of the giant linear specific heat coefficient $\gamma(T)$ coming essentially from bosons. The maxima in resistivity, Hall coefficient and susceptibility are explained by boson localization effects due to the Wigner crystallization. The antiferromagnetic transitions in turn are explained by similar localization of the pairing fermion system when their density $n_h(T_{FL})$ becomes lower than n_{WC}, the critical density of Wigner crystallization. The model applies irrespective whether a compound is superconducting or not. The same model explains the occurrence of low temperature antiferromagnetism also in high-T_c superconductors. The double transition in UPt_3 is proposed to be due to the transition of the pairing fermion liquid from spin polarized to unpolarized state.

I. INTRODUCTION

Despite of the great efforts to understand heavy fermion (HF) properties [1–3] in terms of conventional Fermi liquid theories [4–6], the Kondo model [7] or unconventional order parameter models [8,9], the theories have not provided a clear overall picture of the most dramatic properties: the large value and the temperature dependence of specific heat coefficient $\gamma(T)$, the resistance maximum at low temperatures, the Hall coefficient and the susceptibility maxima near the same temperature. Likewise the superconducting states exhibit power law behaviors of several quantities such as the specific heat near $T = 0$ and an additional linear term in the specific heat. From the above reviews the following picture emerges: In the HF-compounds the f-electrons show localized behaviour at high temperatures and become delocalized at low temperatures. The point of division for the two behaviours is the Kondo temperature T_K.

The purpose here is to show that the spectator fermion superfluid model (SFS), originally proposed for high-T_c compounds [10,11] and the superfluid states of heavy fermions [12,13], also provides a global picture which connects the superfluid state with the normal state and, at the same time, explains the properties of non-superconducting HF-compounds within the same framework with bosons decaying into pairing fermions, the holes. Since the boson density for $T \gg T_c$ and the pairing fermion density for $T \ll T_c$ both become small, they get localized due to Wigner crystallization [11,14]. In what follows we intend to show that the boson localization temperature $T_{BL} < T_B$ is in fact the coherence temperature corresponding to maxima of Hall coefficient and susceptibility. Similarly the pairing fermion Wigner crystallization

temperature is $T_{FL} = T_N$, the Néel temperature, since the fermion spins are antiferromagnetically ordered for $T < T_{FL}$. Both temperatures T_{BL} and T_{FL} are logical consequences of the SFS-model, not an extra input. In the case of high-T_c compounds of the type $RBa_2Cu_3O_{7-x}$, 3D-antiferromagnetism is known to exist together with superconductivity [15,16], with the Néel temperatures in the range 0.5 K< T_N <2.2 K. For HF-compound UPt_3 the low temperature peak at $T_{FL} \approx 20$ mK observed by Schuberth *et al.* [17] is here proposed to be also an example of Wigner crystallization of the pairing holes. Immediately above T_{FL} the holes are proposed to be polarized up to the lower temperature T_c^- of the double peak of UPt_3 as a consequence of the ordering of the pairing hole liquid, rather than having unconventional order parameter for the superfluid. The sequence of temperatures $T_{FL} = T_N$, T_c^- and T_c^+ is in agreement with MC-calculations by Ceperley *et al.* [18,19].

The plan of the paper is as follows. In chapter II we propose that the giant linear specific heat coefficient $\gamma(T)$ is a consequence of the bosons as charge carriers in these compounds. In chapter III we show how the maxima in Hall coefficient and susceptibility follow from the boson localization. Knowing the boson localization temperature $T_{BL} > T_c$, one can estimate the pairing fermion localization temperature $T_{FL} = T_N$, which is discussed in chapter IV. The Wigner crystal has two transverse electronic sound modes, and in the fermion localization case also spin waves with a gap. The longitudinal plasmon of fermion Wigner crystal gives a spectrum with temperature dependent gap below T_N, similar to the spin wave spectrum.

II. THE NORMAL STATE SPECIFIC HEAT

We follow closely the discussion of SFS carried recently [14] through in details for the high-T_c compound $YBa_2Cu_{3-x}M_xO_{7-\delta}$ and proceed to show that the same model can explain also many of the heavy fermion features mentioned above. We adopt here the same simple principle proved successful in the case of 123-compounds: The temperature dependence of an experimental quantity is simply determined by the concentration dependence of that same quantity, since carrier densities are temperature dependent according to the charge conservation in the chemical equilibrium

$$\begin{aligned} n_B(T) &= n_0 f(T) \\ n_h(T) &= 2n_0[1 - f(T)] \\ n_s(T) &= \text{constant}, \end{aligned} \tag{1}$$

with $f(0) = 1$ and $f(T_B) = 0$. These equations are quite general and form a cornerstone for SFS. In particular we don't need to assume statistical mechanics of non-interacting particles to their validity. The holes with temperature dependent density $n_h(T)$ are treated in the superfluid and normal states like conventional charge carriers. Their density of states can in principle be calculated from the two-fluid formalism [14]. The fact that their density of states is temperature dependent can be looked upon as coming from the existence of bosons. With the concentration rule we may proceed to connect various experiments without knowing the exact band structure and the binding mechanism of the bosons [11,14]. In the normal states we use a simple linear function $f(T) = 1 - T/T_B$. Since T_c's are zero or very small in comparison with the boson formation temperature T_B we can take $f(T_c) \approx f(0) = 1$, as a first approximation. These features come out of an explicit fit of the model parameters to experiments in the case of UPt_3 and URu_2Si_2, to be discussed later in more detail. We assume the existence of bosons also in the non-superconducting cases. The picture proposed here is very close to ionization of atoms in gas. There the fraction of non-ionized atoms is given [20] by $f(T) = 1 - [1 + (P/P_0)(T_0/T)^{5/2} e^{2\Delta/k_B T}]^{-1/2}$, which is linear in a range of temperatures.

Following the concentration rule, the internal energy is taken to be a sum of a boson contribution and the pairing and the spectator fermion contributions

$$u(T) = \frac{3}{2} k_B n_0 T f(T) + \frac{1}{2}\gamma_h T^2[1 - f(T)] + \frac{1}{2}\gamma_s T^2, \tag{2}$$

where γ_h and γ_s are linear specific heat coefficients at $T = 0$ for the two fermion components. We will use the expression for noninteracting bosons, and therefore Eq. (2) represents the simplest

approximation one can think of. For $f = 0$ this reduces to the conventional two fermion result and for $f = 1$ we obtain the free boson and the spectator contributions. In the normal state this expression is supposed to be valid only down to finite temperatures near T_c where the superfluid fluctuations become important. In the superconducting state one may use the expression (2), except that the boson part is replaced by the acoustic plasmon contribution to be discussed later. In the BCS-like situation ($T_B = T_c$, no plasmon sound) we have $f(T) = n_s(T)$, where the superfluid fraction behaves exponentially, $n_s \approx 1 - e^{\kappa(1-1/t)}$, with $t = T/T_c$, Eq.(2) reproduces the typical BCS result with a step in the specific heat at T_c. The expression (2) is therefore reasonable in the three special cases $f = 1$, $f = 0$ and $f = n_s$. We anticipate that the calculation of boson breaking function $f(T)$ is in principle possible once we know the details of the boson binding, the band structure and the chemical lattice. So far we are content to assume that the spectators play an essential role in the binding [14]. In view of the fact that the compounds we are working with are rather complicated, we therefore should use a formalism, simple enough, to enable one to relate various experiments with a reasonable accuracy as was done in Ref. [14] for the 123-case. In what follows we intend to show that also the heavy fermions can be treated in this spirit and the results turn out to be equally good.

Eq.(2) gives for the normal state the specific heat coefficient

$$\gamma(T) = \frac{c(T)}{T} = \frac{3}{2}\frac{k_B n_0}{T}(1 - 2\frac{T}{T_B}) + \gamma_s + \frac{3}{2}\gamma_h\frac{T}{T_B}, \tag{3}$$

using the simple linear function for $f(T)$. At low temperatures the boson contribution dominates, since $T_B \approx 300 - 500$ K, and at low temperatures ($T < 20$ K) we obtain

$$\gamma(T) = \gamma_s + \frac{A}{T}. \tag{4}$$

This also shows, how the spectators give the linear term in the specific heat in the superconducting state at $T = 0$. At the temperature T_B the linear term reads

$$\gamma(T) = \gamma_s + \frac{3}{2}\gamma_h. \tag{5}$$

Above T_B we obtain the normal metallic behaviour $\gamma(T) = \gamma_s + \gamma_h$. Immediately below T_B we obtain linear behaviour and a step at T_B. We anticipate that $m_h^* >> m_s^*$, therefore the contribution from the pairing fermions γ_h should dominate at room temperature. On the other hand, already at much lower temperature the boson contribution gets small as compared with fermion parts, therefore one may be able to separate the contributions from γ_h and γ_s, since the latter one can be obtained at least in the superconducting situation from the measurements near $T = 0$. Near the localization temperatures T_{BL} and T_{FL} these expressions have to be modified in a way to be discussed later. In particular the boson term cannot continue down to zero temperature but is intruded by the superconducting or the antiferromagnetic transition. Since these are ordered states, the boson contribution is replaced below the ordering temperature by the plasmon sound or spin wave contributions, which will give finite entropy.

We have compared the electronic specific heat coefficient $\gamma(T)$ from Eq. (4) with experiments in Fig. 1 a) for UBe_{13} and $CeCu_2Si_2$ and in Fig. 1 b) for $CeAl_3$ and $CeCu_6$. These figures are based on figures (6) and (16) of Stewart [2]. It is seen that this simple theory gives a satisfactory explanation for the observed behaviour of $\gamma(T)$ in these four cases. The coefficients A come out to be nearly the same $A \approx 1400$ mJ/Kmol corresponding to boson densities of the order 10^{21}cm^{-3}. One obtains this order of magnitude also from the the analysis of the Hall-data, as we shall see. The model therefore proposes that the large size of $\gamma(T)$ is due to the bosons rather than fermions. This means also that the fermions need not be excessively heavy, which is desirable, since band structure calculations do not produce excessively narrow bands required by the conventional heavy fermion theories (see Ref. [4], p. 121). In fact the bandwidths obtained from band calculation are two orders of magnitude larger.

The compounds in Fig. 1 a) become superconducting at very low temperatures, but those in Fig. 1 b) do not. This simple theory should apply to both types. As we shall see the present model predicts a glassy antiferromagnetic transition at very low temperatures so that $\gamma(T)$ is cut off. For $CeAl_3$ this is clearly visible (see Ref. [2], Fig. 15) but for $CeCu_6$ less so. At

present we are not able to determine the fermion effective masses very accurately. There is some uncertainty associated with the possible non-linearities in $f(T)$ which no doubt can be estimated easily, but goes beyond the scope of this paper. Clearly Eqs. (2)-(5) cannot be valid down to zero temperature, as mentioned above. For superconducting compounds $\gamma(T)$ near T_c is modified by superconducting fluctuations and below T_c the plasmonic contribution replaces the free boson part. For non-superconducting compounds the superconducting fluctuations may exist near $T = 0$. The ordered transitions at T_c or $T_{FL} = T_N$ seem to offer a natural cut off for most HF-compounds.

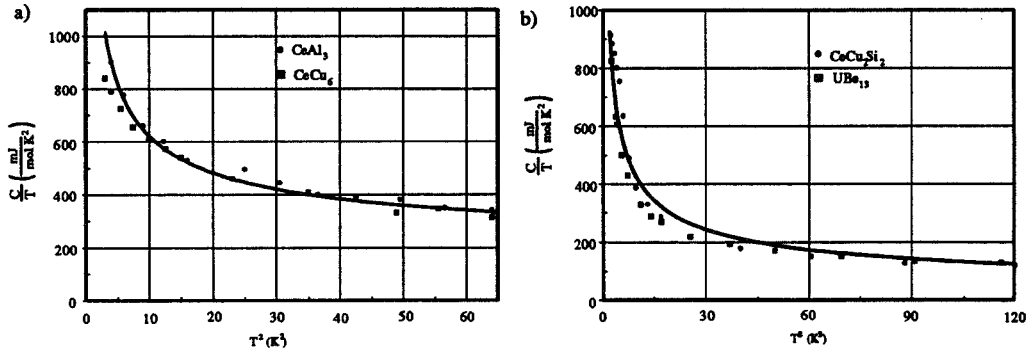

FIG. 1. The electronic specific heat coefficient $\gamma(T)$ for a) UBe_{13} and $CeCu_2Si_2$ and b) $CeAl_3$ and $CeCu_6$. Solid lines presents our theoretical result from Eq. (4) with parameters: a) $A = 1300$mJ/molK and $\gamma_s \cong 5$mJ/molK^2 and b) $A = 1500$mJ/molK and $\gamma_s \cong 140$mJ/molK^2. Experimental points are from Figs. 6 and 16 in Ref. [2].

III. BOSON LOCALIZATION

A logical consequence of the SFS model is the Wigner crystallization (WC) of bosons, because at a certain temperature T_{BL}, which lies in between T_c and T_B, their density diminishes below the critical value corresponding to $r_s = 170$ [19]. The localization temperature T_{BL} can be estimated from the condition for the critical density,

$$n_{WC} = n_0 f(T_{BL}) \approx n_0(1 - T_{BL}/T_B) \approx 0.16 \cdot 10^{21} \left(\frac{m_h}{m}\right)^3 \text{ cm}^{-3}, \tag{6}$$

where m is the electron mass and the boson mass $m_B = 2m_h$. This order of magnitude estimate corresponds to a jellium background and may be inaccurate for backgrounds prevalent in the heavy fermions with spectators and the chemical lattice. Most likely, however, such a transition does take place, and the main consequence is that the bosons become gradually delocalized below T_{BL}. The measured carrier densities in HF-compounds are of the order of magnitude 10^{21}cm^{-3} [6], close to those required by Eq. (6). Above T_{BL} the bosons cease to be active charge carriers.

A fully consistent thermodynamical description of the localization is not attempted here for the following reasons: Above T_{BL} the bosons continue to decay into holes with approximately linear temperature dependence, as deduced from Hall-measurements. Because of this decay, the Wigner crystal is never complete. Since the boson localization phenomena occur at moderately low temperatures, the Wigner crystal is never in thermal equilibrium, and one expects a glassy behaviour. The situation is further complicated by the lattice which can cause partial localization of the bosons even below T_{BL}. This is presently the main uncertainty which clearly affects our calculation of the coefficient A in Eq. (4) with density n_0 deduced from the Hall-measurements.

The Monte-Carlo-calculations by Ceperley *et al.* [18,19] indicate, that the energy densities of Coulomb liquid and crystal states are not very different, therefore the associated specific heat jump may be small at elevated temperatures. For these reasons the liquid-crystal transition is very rounded and shows up most clearly in the Hall density which well above T_{BL} is determined solely by the holes. This explains the near linearity of $n_H(T)$ observed in virtually all compounds

above the coherence temperature, which we associate here with T_{BL}. We actually do not exactly know what $f(T)$ to use between T_c and T_{BL}, therefore we have used the following purely phenomenological description: Divide the density of bosons below T_{BL} into localized and delocalized portions with a phenomenological function $\xi(T)$ such that the density of mobile bosons is

$$n_{BDL}(T) = n_0 f(T)\xi(T) \approx n_0(1 - T/T_B)\,\xi(T), \tag{7}$$

where $\xi = \alpha \leq 1$ for $T << T_{BL}$ and $\xi = 0$ for $T >> T_{BL}$. Here $\alpha < 1$ means that a fraction $(1-\alpha)$ of the bosons remain localized for $T << T_{BL}$. Localized bosons continue to produce holes with linear rate $f(T)$. This was previously [14] used successfully to explain the Hall effect in the high-T_c case. The existence of bosons in the normal state was also used to explain the "reservoir" effect for 123-compounds.

The function $\xi(T)$ can be obtained from the experimental Hall coefficient $R_{ab} \propto n_h(T)^{-1}$. The effective Hall density (in the ab-plane) reads

$$n_H = \begin{cases} 2n_0(1 - f(T)) \cong 2n_0\frac{T}{T_B}, & \text{for } T \gg T_{BL} \\ 2n_0(1 - f(T)) + 2n_0 f(T)\xi(T) \cong 2n_0\frac{T}{T_B} + 2n_0(1 - T/T_B)\xi(T), & \text{for } T \leq T_{BL}. \end{cases} \tag{8}$$

These equations together with the Hall-measurements can be used to fix T_B as well. The localization explains the minimum in n_H, a feature which seems to be as common for heavy fermions as it is for high-T_c superconductors [14]. We have shown for 123 compounds [14] that $f(T)$ is a universal function.

The Hall density in the normal state together with the experimental data of Lapierre *et al.* [21] and Schoenes *et al.* [22] is shown in Figs. 2 a) and 2 b). The theoretical curve in Fig. 2 a) for UPt_3 was calculated using Eqs. (8) with the phenomenological boson localization factor of the type

$$\xi(T) = \exp\left[3.5\left(\frac{T - 6\text{ K}}{T - 50\text{ K}}\right)\right] \quad ,6\text{ K} < T < 50\text{ K}. \tag{9}$$

Similar function was used also for URu_2Si_2 in Fig. 2 b).

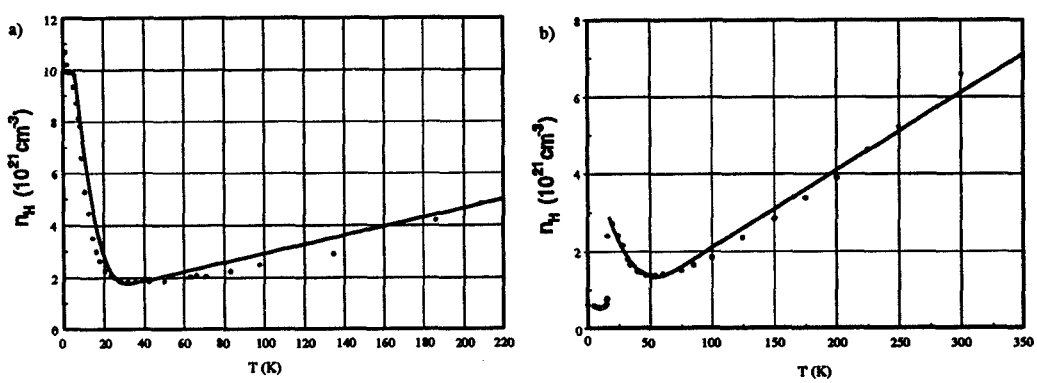

FIG. 2. a) The Hall density in the normal state for UPt_3 from Eq. (8) together with the experimental data of Lapierre *et al.* [21]. Theoretical result is obtained by using parameters: $T_B = 500$ K, $f_c = .88$, $n_0 = 4.95 \cdot 10^{21}\text{cm}^{-3}$ and $\alpha = 1$. b) The Hall density in the normal state for URu_2Si_2 from Eq. (8) together with the experimental data of Schoenes *et al.* [22]. Theoretical result is obtained by using parameters: $T_B = 350$ K, $f_c = .98$ and $n_0 = 5.7 \cdot 10^{21}\text{cm}^{-3}$ and boson localization factor $\xi(T) = .36 \cdot \exp\left[4\left(\frac{T-18\text{ K}}{T-110\text{ K}}\right)\right]$ for 18 K $< T <$ 110 K.

We overlook the further complication, that the spectators could bring in a more complicated two-band Hall behaviour. The fact that, Hall coefficient with $\mathbf{H} \perp \hat{c}$ is nearly constant whereas the one with $\mathbf{H} \parallel \hat{c}$ changes with temperature above T_{BL} [23], gives evidence that band mixing is small, therefore this point is not fully understood at present. The outcome of Eq. (8) for

two compounds, UPt_3 in Fig. 2 a) and URu_2Si_2 in Fig. 2 b) gives us their T_B-values and the localization temperatures. The reason for selecting these two HF-compounds is that they represent the two main cases with respect to fermion localization: In UPt_3 the antiferromagnetic transition turns out to occur in the superconducting state and for URu_2Si_2 in the normal state. In both cases n_H-curves show slight upwards bending for $T > T_{BL}$ and the T_B-values are of the order 300-500 K. The localization temperatures are $T_{BL} \approx 30$ K for UPt_3 and approximately 50 K for URu_2Si_2.

Also the experimental specific heats show structure associated with T_{BL} and T_B. The approximate separation of the electronic part ΔC by Renker *et al.* [24] shows a broad maximum for UPt_3 near 30-40 K and a peak near 300-500 K. We expect that the pairing fermion band and the spectator band rearrange themselves near T_B, which could also show up in the electronic specific heat. The broad maximum at 30-40 K can be interpreted in terms of Bose glass transition associated with boson localization. A qualitatively correct behaviour is obtained by taking a linear superposition of the Bose liquid and the crystal internal energies $\frac{3}{2}n_B(T)k_BT$ and $3n_B(T)k_BT$ for the boson liquid and solid, respectively, hence

$$\Delta C = \begin{cases} \frac{3}{2}n_0 k_B \frac{d}{dT}\left[Tf(T)(2-\xi(T))\right] + \gamma_s T + \frac{3}{2}\gamma_h\left[1-f(T)\right]T & \text{, for } T \le T_B \\ (\gamma_s+\gamma_h)T & \text{, for } T > T_B \end{cases} . \qquad (10)$$

The total electronic specific heat from Eqs. (10) is compared with the data of Renker *et al.* [24] in Fig. 3 for UPt_3. The agreement is rather striking. In particular the boson formation temperature T_B shows up clearly in both compounds as a peak with quadratic temperature dependence near T_B. Just above T_B we predict a jump by amount $\frac{1}{2}\gamma_h T_B$ in the specific heat. Unfortunately the data do not go high enough in temperature to show the jump. In the case of URu_2Si_2 one obtains from Renker *et al.* [24] similar picture except for the peak near the antiferromagnetic transition at $T_N = 18$ K, which will be discussed later. In the latter case the jump at T_B shows up.

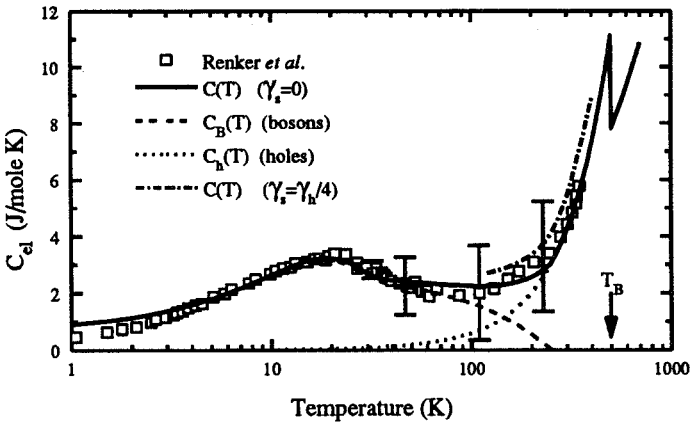

FIG. 3. The electronic specific heat for UPt_3 after Renker *et al.* [24]. Solid line is our result from Eq. (10 with parameters: $\gamma_s = 0$ and $\gamma_h = 16\text{mJ/molK}^2$. Dash-dotted line is the result with $\gamma_s = 4\text{mJ/molK}^2$ and $\gamma_h = 16\text{mJ/molK}^2$.

The boson localization temperature T_{BL} limits the attainable transition temperature T_c, since $T_{BL} > T_c$. By Eq. (6) one should make the effective mass m_h small to increase T_{BL} and thereby the T_c. At the same time the background can also have a decisive effect. In Ref. [14] we found effective mass $m_h \sim m_e$ and the estimate for UPt_3 is 5-20 electron masses.

IV. FERMION LOCALIZATION AND THE ANTIFERROMAGNETISM

Since the Wigner crystallization takes place independent of the statistics, also the pairing holes must become localized at some temperature $T_{FL} < T_{BL}$, since their density vanishes at $T = 0$. Assuming that T_{BL} is known, we can actually calculate T_{FL} from Eqs. (1) since the

bosons have double charge and mass. The crystallization densities of holes and bosons are therefore related by

$$2n_0[1 - f(T_{FL})] = \frac{n_0 f(T_{BL})}{64} Q. \tag{11}$$

The factor Q takes into account the fact that the background here is not jellium, which would correspond to $Q = 1$ and $r_s = 170$. For the superconducting compounds we have to make distinction between the two cases $T_{FL} < T_c$ and $T_{FL} > T_c$. It is well known that for fermions the spins are in antiferromagnetic arrangement in the Wigner crystal phase for jellium background. In this connection one should remember that for somewhat higher densities, hence here above T_{FL}, the holes may form a spin polarized liquid. The direction of spins may be strongly influenced by non-jellium background effects, but WC-localization offers a natural explanation for occurrence of antiferromagnetism in the HF-compounds. If the antiferromagnetic transition takes pla e above T_c we obtain from Eq. (11), by using the linear approximation for $f(T)$,

$$T_{FL} = \frac{T_B}{128}(1 - \frac{T_{BL}}{T_B})Q \approx \frac{T_B}{128} Q. \tag{12}$$

Depending upon the values of T_B and Q this gives $T_{FL} > 1$ K. The main source of inaccuracy in Eq. (11) is the factor Q and the sensitivity of the left hand side to possible non-linearities in $f(T)$, which show up in the experiments for the Hall densities illustrated in Figs. 2 a) and 2 b).

The fermion localization at $T_N = 18$ K explains also the sudden drop in n_H for URu_2Si_2 apparent in Fig. 2 b). The amount of the drop is larger than we would expect. This we believe is coming from spectators and for a quantitative calculation of the drop one should use a two-band formula. The main point we want to make is that the strange behaviour of URu_2Si_2 Hall coefficient is understood with the boson and fermion localizations. This includes also the different behaviour for UPt_3. Conversely the Hall density n_H is like a map where the localization effects can be read out.

To carry out a calculation of T_{FL} one must first determine $f(T)$ from experimental data on Hall effect, specific heat etc.. As an example we show how to calculate T_{FL} for UPt_3, where the antiferromagnetic transition supposedly occurs in the superfluid state. Another example we have been able to carry through with reasonable accuracy is the superconductor URu_2Si_2, where $T_N = T_{FL} \approx 18$ K in the normal state. We start the discussion with UPt_3. Using the Hall data, the specific heat data and the exponent relations derived by Kallio *et al.* [12] we have determined the boson breaking function $f(T)$ and the superfluid fraction $n_s(T)$ using the functional form ($t = T/T_c$)

$$\begin{aligned} f(t) &= n_s(t) + f(T_c)t^{4-5\gamma/3} \\ n_s(t) &= 1 - at^\gamma - (1-a)e^{\kappa(1-1/t)}. \end{aligned} \tag{13}$$

The philosophy behind these terms is of course that the functions $f(t)$ and $n_S(t)$ have direct connection with experiments and the exponent γ is limited by the two-fluid model to the range $0 \leq \gamma \leq 1.5$. For UPt_3 we use the specific heat data of Midgley *et al.* [25] and Hall density data of Lapierre *et al.* [21] to obtain for the parameters the values $\gamma = 1.42$, $f(T) = .88$, $a = .91$, and $\kappa = 3.5$. In the normal state we therefore obtain

$$f(T) = .88(1 - T/T_B) \qquad , T_B \cong 500 \text{ K}. \tag{14}$$

In calculating the specific heat we used Eq. (2) with the boson contribution replaced by the plasmon term [14]

$$U_{pl} = \frac{\pi^2}{30} \frac{(k_B T)^4}{[\hbar u_1(T)]^3}, \tag{15}$$

where $u_1(T)$ is the plasmon sound velocity (see Eqs. (16) and (17)). The data for UPt_3 are extremely well fitted with these functions. As an example we show the specific heat in the superfluid state in Fig. 4 a). Because of the low value of T_c, $f(T_c)$ is nearly unity justifying our approximation $f(T) = 1 - T/T_B$ in Eq. (3). The value of exponent $\gamma = 1.42$ in Eq. (13) is close

to the one obtained for 123 in Ref. [14] ($\gamma = 1.3$) as well as the gap parameter $\kappa = 3.5$ instead of 3. The small coefficient .09 in front of the gap term makes $n_s(t)$ to have nearly power-law behaviour. The most dramatic difference between the HF- and high-T_c compounds is the pair breaking at T_c which gives $f_c \approx 1$ for former and $f_c \approx .6$ for the latter. For URu_2Si_2 it comes out close $f_c \cong .98$. The physical explanation for this is the low value of T_c for HF-compounds. The heavy fermions are therefore further away from the BCS than the high-T_c superconductors, in view of the fact that within the present framework $f_c = 0$ for BCS. Since the boson densities are not very different for the high-T_c and HF-compounds, simple Bose-Einstein model for heavy fermions would give, with moderate boson mass $m_B < 10m_e$, right order of magnitude for T_c [14,26]. Without boson breaking this model would, however, have difficulties in explaining the localization phenomena discussed here.

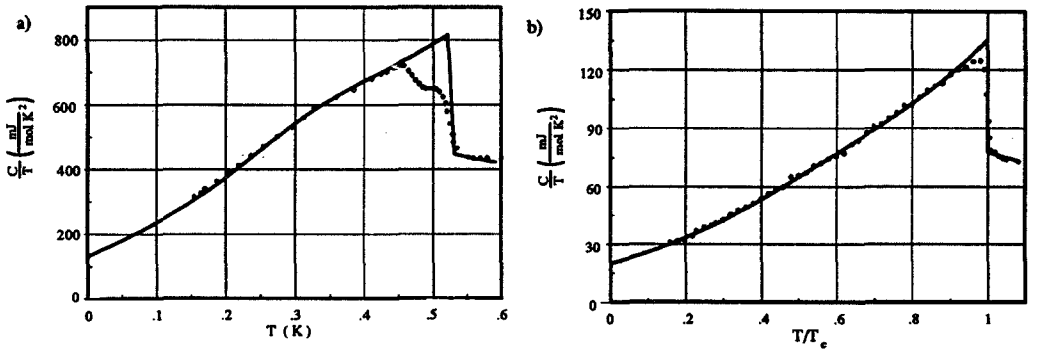

FIG. 4. a) The experimental specific heat for UPt_3 from Ref. [25] together with our theoretical result. For $f(t)$ we have used parameters: $f_c = .88$, $\gamma = 1.42$, $a = .91$ and $\kappa = 3.5$. The used spectator contribution $\gamma_s = 130\text{mJ/molK}^2$ is much larger than the one obtained from Fig. 3. b) The experimental specific heat for URu_2Si_2 from Ref. [30] together with our theoretical result. For $f(t)$ we have used parameters: $f_c = .98$, $\gamma = 2.16$, $a = .987$ and $\kappa = 3.6$. The spectator contribution comes out to be $\gamma_s = 23\text{mJ/molK}^2$.

Knowing the boson breaking function $f(T)$ for UPt_3 we can now calculate the Wigner crystallization temperature T_{FL} for the holes to be about 20 mK, close to the experimental value 18 mK found for the extra peak by Schuberth *et al.* [17]. Our result is obtained from Eq. (11) with $Q = 1$. Since in the Wigner crystal for the holes the spins are in the antiferromagnetic arrangement, we propose that $T_{FL} = T_N$, the Néel temperature.

Although the properties of the antiferromagnetic transition may be affected by the chemical lattice, we may explain some properties, like the specific heat peak, by the Wigner crystal model below T_N. Since the transition takes place at low temperatures, we may use the sound mode approximation for the WC specific heat. The excitation modes of WC have been studied theoretically by Carr [27]. According to his calculations the Wigner crystal has two transversal sound modes, with the density dependent sound velocities $u_\perp \propto r_s^{-1/2}$. In the present case this translates into the temperature dependence [14]

$$u_\perp(T) = u_\perp(T_{FL}) \left[\frac{1 - f(T)}{1 - f(T_{FL})}\right]^{1/6} . \tag{16}$$

In the case of pairing fermions forming a liquid, the longitudinal sound velocity $u_1(T)$ was determined by the relation

$$u_1(T) = u_1(T_c) \left[\frac{1 - f(T)}{1 - f(T_c)}\right]^{1/3} . \tag{17}$$

Despite of the pairing fermion localization the two-fluid philosophy remains the same: The normal liquid density in the superfluid system consisting of bosons and holes, is obtained from the bosonic (sound modes, spin waves) and fermionic excitations (boson breaking). The latter ones are determined by $[1 - f(T)]$ which should be determined by the chemical equilibrium, but

we choose to follow the philosophy of Ref. [14] and try to determine $f(T)$ from experiments, if possible. One uncertainty remains: Are the sound mode or the spin waves the dominating feature in the bosonic excitations, which determine the specific heat in the superfluid state? The data on UPt_3 is insufficient to give an answer, because T_{FL} is so low. If the transition takes place in the normal state, we believe that immediately below T_{FL} the boson part in the specific heat will be dominated by the spin waves as compared with plasmonic contributions. This will be apparent in URu_2Si_2, to be discussed later. Much below T_{FL} the spin wave dominated specific heat would go to zero exponentially when $T \to 0$ since there is the gap, which experimentally turns out to be rather large. We expect this to be true also for non-superconducting compounds: The giant bosonic specific heat coefficient is cut off at $T_{FL} = T_N$, because in the antiferromagnetic state the bosonic coefficient has to be replaced by the plasmonic contribution. We of course do realize, that some of the HF-compounds, so far, show no order whatsoever, below the lowest temperatures measured. One such example is $CeAl_3$, with $\gamma(0) \approx 18.5\ \mathrm{mJK^{-2}cm^{-3}}$. However, below 0.32 K for this compound the specific heat coefficient $\gamma(T)$ starts reducing, which can be interpreted as coming from a glassy antiferromagnetic transition (See Ref. [2], Fig. 15). One should also beware of that some of the antiferromagnetic transitions can have a different origin.

The antiferromagnetic Wigner crystal made of the holes is also never in equilibrium because their number density is changing with temperature and one has vacancies and/or the full WC-order can never be extended in practice. For this reason one should expect also here spin glass behaviour. In the high-T_c case the situation should be similar: The antiferromagnetic transition of holes should take place at about 1-2 K, if one uses Eq. (12) and the $f(T)$ determined in Ref. [14]. This is born out in the experiments on $Bi_2Sr_2CaCu_2O_8$ by Caspary *et al.* [28], who separated out the electronic specific heat in this temperature range and found broad maxima of $\gamma(T)$ at different magnetic fields. These maxima were interpreted as spin glass behaviour by Caspary *et al.*, for different reasons though. Several other high-T_c compounds show antiferromagnetic transitions at low temperatures below T_c.

A further feature easily understood within the present model is that the antiferromagnetic specific heat peak should exist even in magnetic fields higher than H_{c2}, because the bosons still exist, and hence their decay into holes occurs independent of superconductivity. This was indeed observed in UPt_3 by Schuberth *et al.* [29].

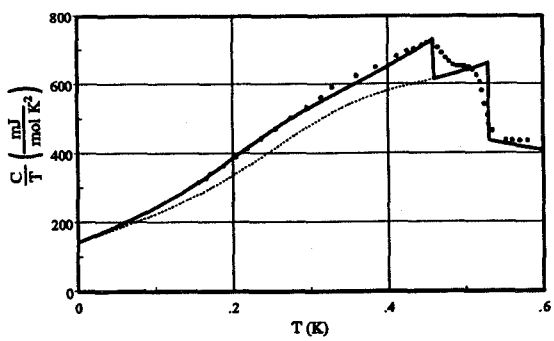

FIG. 5. The experimental specific heat for UPt_3 from Ref. [25] together with our theoretical result, with double peak at T_c. For spin polarized liquid we have used parameters: $T_c^- = .47$ K, which corresponds $T_c^- = .904 \cdot T_c^+$ and $\kappa^- = 3.5$. For unpolarized liquid: $T_c^+ = .52$ K, $\kappa^+ = 4.3$. Exponent $\gamma = 1.41$ and coefficient $a = .91$ are the same for both liquids. The gray line shows our result for unpolarized liquid below T_c^-.

In the Monte Carlo calculations of Ceperley *et al.* [18,19] it was found that for $r_s < 100 - 170$ (hence $T > T_{FL}$ in our case) one obtains a spin polarized liquid and below $r_s = 60 - 75$ unpolarized liquid. Since the energy difference between the two liquids is very small and in UPt_3 we have chemical lattice different from jellium, the possibility exists that the double peak near $T_c \approx .5$ K is explained by the phase transition between the two types of pairing fermion liquids. In fact, if one makes use of $f(T)$ deduced from experiments and assigns for $T_{FL} = .02$ K the value $r_s = 170$, we obtain at T_c the value $r_s = 60$, which is close to the value 75 obtained by Ceperley *et al.* for the crossing of the polarized and unpolarized liquid

energies. This interpretation of the double peak would be in agreement with the domain structure found by Midgley *et al.* [25], since the energies for the two structures are close. The associated domain structure could also be a reason for the metamagnetism observed in several compounds. Since the T_c's are low it would also occur in the normal states. We stress that the present interpretation preserves $^1S_0$-order parameter for the superfluid. Actually the r_s-limits for Wigner crystal of fermions are numerically uncertain even for jellium background due to the fact that the GMC-method is strictly speaking "exact" only for Bose systems, as discussed by Ceperley *et al.* Since we have a different background, the right hand sides of Eqs. (11) and (12) can have sizable Q-factors, which can only be determined experimentally, owing to the complicated background and the glassy nature of the Wigner crystal transitions. We believe, however, that the order of the two localization temperatures remains always the same, i.e., $T_{BL} > T_N$.

V. CONCLUSIONS

If we identify the pairing holes belonging to f-band in the SFS case the following picture emerges: The f-electrons combine into bosons at high temperatures $T < T_B$ which remain localized down to temperature T_{BL}. In the temperature range $T_{BL} < T < T_B$ the chemical equilibrium requires existence of mobile f-holes with density $n_h \sim 1 - f(T) \approx T/T_B$, where $f(T)$ is a universal function. At very low temperatures the pairing fermions suffer a glassy antiferromagnetic transition at T_N. This explains the existence of superheavy quasiparticles in dHvA-experiments, which then, near T_N, measure the distribution of masses near a localization transition.

[1] H. R. Ott, and Z. Fisk in *Handbook on the Physics and Chemistry*, Eds. A.J. Freeman and G.H. Lander (Elsevier, 1987) 85.
[2] G.R. Stewart, Rev. Mod. Phys. **56** (1984) 755.
[3] A. de Visser, A. Menovsky, and J.J.M. Franse, Physica **147B** (1987) 81.
[4] P. Fulde, J. Keller and G. Zwicknagl, Solid State Phys. **41** (1988) 1.
[5] P. A. Lee *et al.*, Comments Cond. Mat. Phys. **12** (Gordon and Breach, 1986) 99.
[6] Z. Fisk *et al.*, Science, **239** (1988) 33.
[7] J. Kondo, Progr. Theor. Phys. **32** (1964) 37.
[8] S. Schmitt-Rink, K. Miyake and C. M. Varma, Phys. Rev. Lett. **57** (1986) 2575.
[9] C. H. Choi and J. A. Sauls, Phys. Rev. Lett. **66** (1991) 484.
[10] A. Kallio, and X. Xiong, Phys. Rev. **B41** (1990) 2530.
[11] V. Apaja, and A. Kallio, Physica **C208** (1993) 519.
[12] A. Kallio, V. Apaja, and X. Xiong, Physica **C191** (1992) 23.
[13] A. Kallio, and X. Xiong, Physica **C199** (1992) 340.
[14] A. Kallio, V. Apaja, X. Xiong, and S. Pöykkö, Physica **C219** (1994) 340.
[15] B.W. Lee *et al.*, Phys. Rev. **B37** (1988) 2368.
[16] D. McK. Paul *et al.*, Phys. Rev. **B37** (1988) 2341.
[17] E. A. Schuberth *et al.*, Physica **C185-189** (1991) 2645; Phys. Rev. Lett. **68** (1992) 117.
[18] D. Ceperley, Phys. Rev. **B18** (1978) 3126.
[19] D. M. Ceperley and B. J. Alder, Phys. Rev. Lett. **45** (1980) 566.
[20] L.D. Landau and E.M. Lifshits, Statistical Physics (Pergamon, 1959) p.322.
[21] F. Lapierre *et al.*, J. Magn. Magn. Mat. **63-64** (1987) 338.
[22] J. Schoenes *et al.*, Phys. Rev. **B35** (1987) 5375.
[23] J. Schoenes, F. Troisi, E. Brück and A. A. Menovsky, J. Magn. Magn. Mat. **108** (1992) 40.
[24] B. Renker *et al.*, Physica **148B** (1987) 41.
[25] P. A. Midgley *et al.*, Phys. Rev. Lett. **70** (1993) 678.
[26] C. P. Enz and Z. M. Galasiewicz, Physica **C214** (1993) 239.
[27] W. J. Carr, Jr., Phys. Rev. **122** (1961) 1437.
[28] R. Caspary *et al.*, Europhys. Lett. **8** (1989) 639.
[29] E. A. Schuberth and M. Fischer, Physica C **194-196** (1994) 1983.
[30] K. Hasselbach, P. Lejay and J. Flouquet, Phys. Lett. **A 156** (1991) 313.

OMIT THIS PAGE

THIS PAGE INTENTIONALLY LEFT BLANK

Page intentionally left blank

Performance Characterization

Session 2 Chair: Dr. R. K. Pandey
Co-Chair: Dr. U. Varshney

OMIT THIS PAGE

SINGLE SCAN
524-76
313905
10
342988

An Electron Tunneling Study of Superconductivity in Amorphous $Sn_{1-x}Cu_x$ Thin Films

D. G. Naugle, P. W. Watson III and K. D. D. Rathnayaka
Physics Department, Texas A&M University, College Station, TX 77843-4242

The amorphous phase of Sn would have a superconducting transition temperature near 8 K, much higher than that of crystalline Sn with $T_c = 3.5$ K. To obtain the amorphous phase, however, it is necessary to use a Sn alloy, usually Cu, and quench condense the alloy films onto a liquid He temperature substrate. Alloying with Cu reduces the superconducting transition temperature almost linearly with Cu concentration with an extrapolation of T_c to zero for $x = 0.85$. Analysis of the tunneling characteristics between a normal metal electrode with an insulating barrier and superconducting amorphous Sn-Cu films provides detailed information on the changes in the electron-phonon coupling which determines T_c in these alloys. The change from very strong electron-phonon coupling to weak-coupling with the increase in Cu content of amorphous Sn-Cu alloys for the range $0.08 \leq x \leq 0.41$ is presented and discussed in terms of theories of the electron-phonon coupling in disordered metals.

I. INTRODUCTION

It has been shown by many researchers that amorphous metals have dramatically different superconducting characteristics from their crystalline counterparts.[1–3] Knorr and Barth[4] found that the transition temperature, T_c, of an amorphous $Sn_{0.9}Cu_{0.1}$ alloy was almost 7 K, as opposed to 3.6 K for crystalline Sn. Their tunneling measurements also showed that it is a strong-coupling superconductor. Leitz[5] and Dutzi and Buckel[6] reported that the T_c of amorphous SnCu alloys decreased linearly with the Cu concentration. Heat capacity measurements of amorphous $Sn_{1-x}Cu_x$ films ($0.47 < x < 0.75$) determined that θ_D increases with increasing copper concentration.[6] The results were interpreted in terms of the McMillan[7] expression for T_c,

$$T_c = \frac{\theta_D}{1.45} \exp\left[- \frac{1.04(1+\lambda)}{\lambda - \mu^*(1+0.62\lambda)} \right] \tag{1}$$

where λ is the electron-phonon coupling constant, μ^* is the repulsive Coulomb electron-electron interaction, and θ_D is the Debye temperature. With the assumption of a constant value for μ^*, they concluded that while θ_D was increasing, evidently λ was changing in such a way as to cause a linear decrease in T_c. Dynes[8] has developed a better approximation for the transition temperature,

$$T_c = \frac{\langle\omega\rangle}{1.20} \exp\left[- \frac{1.04(1+\lambda)}{\lambda - \mu^*(1+0.62\lambda)} \right] \tag{2}$$

where $\langle\omega\rangle$ is the average phonon energy, in which $\langle\omega\rangle$ doesn't necessarily scale with θ_D. To identify the parameters responsible for the linear decrease of T_c with the copper concentration for this strong-coupling simple metal amorphous superconducting alloy, and investigate in detail the expected change from very strong-coupling to weak-coupling behavior in an amorphous metal alloy, we present tunneling measurements which have been analyzed to provide $\langle\omega\rangle$, λ, $\mu^*$and the frequency dependence of $\alpha^2F(\omega)$ for $0.08 \leq x \leq 0.41$.

II. EXPERIMENTAL DETAILS

The UHV deposition system and cryostat have been described previously[9], but the liquid-helium thermal shield has been modified to include a movable mask consisting of the horizontal and vertical slits needed to form the tunnel junctions. This allowed the entire junction to be fabricated in the UHV system and oxidation of the counterelectrode in pure O_2 at an elevated temperature instead of

in ambient room air. This *in situ* fabrication technique was essential to preparation of high quality junctions with reproducible junction resistance and low leakage characteristics.

The tunneling base electrode was made by evaporating aluminum through the horizontal slit in the liquid-helium shutter. The resulting film, 0.25 mm wide and typically 1300Å thick, was then oxidized in 1 atmosphere of dry oxygen at ~85°C for about 14 hours, resulting in a barrier oxide layer about 23Å thick. The system was then pumped overnight to a pressure of approximately 10^{-9} Torr after which the substrate was heated to ~60°C for two hours and then immediately cooled to liquid He temperature. Four SnCu films were e-beam evaporated sequentially, each deposition from an alloy ingot. The resulting films were 1 mm wide and typically 400Å thick. The base pressure before evaporation was less than 2×10^{-10} Torr with the pressure during evaporation in the mid 10^{-9} Torr range. Heating the substrate just before cooling to liquid He temperature was essential to prevent a zero-bias anomaly in the tunneling data that exhibited a $-\ln T$ dependence similar to that produced by sub-monolayers of molecular oxygen deliberately deposited on the counter electrode prior to junction formation in studies by Bermon and So.[10]

The electronics and experimental apparatus are described in more detail elsewhere.[11]

III. DATA MEASUREMENT

A. Energy Gap Determination

The input parameters to the McMillan-Rowell inversion program are the energy gap, Δ_0, and the deviation from a BCS-like superconductor. The deviation is calculated using the measured Δ_0 and the normalized tunneling density of states obtained from the raw data. Since the deviation strongly depends on Δ_0 in the low bias voltage region where the BCS density of states is changing rapidly, an incorrect determination of Δ_0 can have a large effect on the deviation. This, in turn, can cause large differences in $\alpha^2F(\omega)$ and μ^* calculated by the inversion program. Thus, an accurate determination of Δ_0 is essential in order to obtain meaningful results from the inversion program.

The determination of the energy gap is straightforward, involving the measurement of the leakage conductance and the superconducting state first derivative in the region of the gap, and was usually measured immediately after the normal state derivative. The substrate was cooled to the lowest temperature possible, ~1.5 Kelvin, while the resistance of the aluminum counterelectrode was monitored to make sure it showed no signs of superconductivity.

The leakage conductance was measured by balancing the bridge at zero bias using the smallest AC signal possible, typically less than 0.5μV. This gives R_{max}, which is directly related to the leakage conductance since it should be infinite. For "good" junctions, the leakage conductance was usually less than 4% of the normal state. Zero bias was achieved by disconnecting the current sweep generator. Also, the filters were disconnected since the junction resistance was an appreciable fraction of the filters' reactance.

The superconducting state first derivative was measured with a lock-in amplifier with an AC signal typically less than 5μV and a 300 msec time constant. A very rough estimate of the gap Δ_0 was obtained by determining the voltage at which the resistance matched the high bias resistance. The bias voltage was swept starting at about $-3\Delta_0$, through zero, to about $3\Delta_0$, taking typically 20 to 30 minutes with data points about every 2μV. The sensitivity of the lock-in amplifier was set such that the lock-in didn't go off scale until the absolute value of the bias voltage was less than Δ_0. The normal and superconducting first derivative data were then smoothed and interpolated with an increment of 5μV. Data where the lock-in was off scale was not used.

The energy gap was basically determined from fitting the tunneling density of states, N_T, to the BCS density of states. This, however, is complicated by three factors: 1) the tunneling density of states is shifted slightly with respect to bias voltage due to the time constant of the lock-in amplifier; 2) the normal state first derivative data is shifted vertically from that of the superconducting state because the resistance of the film over the oxide layer is not negligible compared to the junction resistance; 3) there is a small leakage conductance. The leakage conductance is easily accounted

for by subtracting it from both the superconducting and normal state data. In terms of what is measured,

$$N_T = \frac{\sigma_S - \sigma_L}{\sigma_N - \sigma_L} = \frac{\frac{R_N}{R_S} - \frac{R_N}{R_{max}}}{1 - \frac{R_N}{R_{max}}} \tag{3}$$

where $R_N(R_S)$ is the first derivative in the normal (superconducting) state. The vertical shift in the normal state data is easily accounted for by introduction of a variable parameter, y_{offset}, and a change of variable, $R'_N = R_N + y_{\text{offset}}$.

The temperature dependent tunneling density of states in the BCS approximation is given by

$$\begin{aligned} N_T(eV,T) = \frac{dI_{sn}/dV}{dI_{nn}/dV} &= \int_{-\infty}^{\infty} dE \, \frac{N_1(E)}{N_1(0)} \frac{df(E-eV)}{dV} \\ &= \beta \int_{-\infty}^{\infty} dE \, N_{\text{BCS}}(E) \frac{e^{\beta(E-eV)}}{(1+e^{\beta(E-eV)})^2} \end{aligned} \tag{4}$$

where $N_{\text{BCS}}(E) = |E|/(E^2 - \Delta_0^2)^{1/2}$, and $\beta = (0.08617T)^{-1}$ in units of meV^{-1}. The shift in the density of states with bias voltage is accounted for by introduction of another variable parameter, x_{offset}, and a change of variable, $E' = E + x_{\text{offset}}$. The variables Δ_0, y_{offset}, and x_{offset} were varied to give the best least squares fit between equations (3) and (4). This procedure is repeated for at least three different sets of data and the resulting Δ_0's compared for consistency.

B. First Derivative Measurement

The tunneling density of states involves the measurement of the first derivatives in the normal and the superconducting states over the phonon frequency range. This is similar to the measurements needed to determine the energy gap, and in fact, the normal state first derivative had to be measured prior to actually determining the energy gap. Figure 1 is an example of the raw data for $Sn_{0.78}Cu_{0.22}$. At this stage, the AC signal was typically about 100μV so that thermal smearing was the dominant factor in the resolution of the data. Again, a 300 msec time constant on the lock-in amplifier was used, and the data was swept as slowly as possible, taking almost an hour to sweep from 0 to 50mV. Initially, data was taken with the SnCu film biased both negatively and positively. However, the junctions are not symmetric about zero bias[12], as can easily be seen in Figure 2, which is a plot of

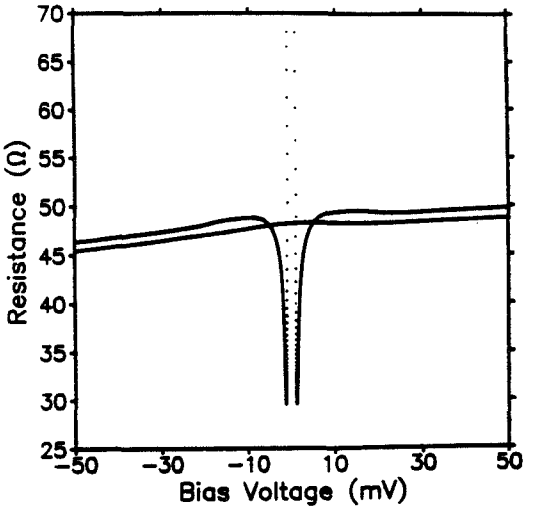

FIG. 1. Raw data for the normal state and superconducting state first derivative.

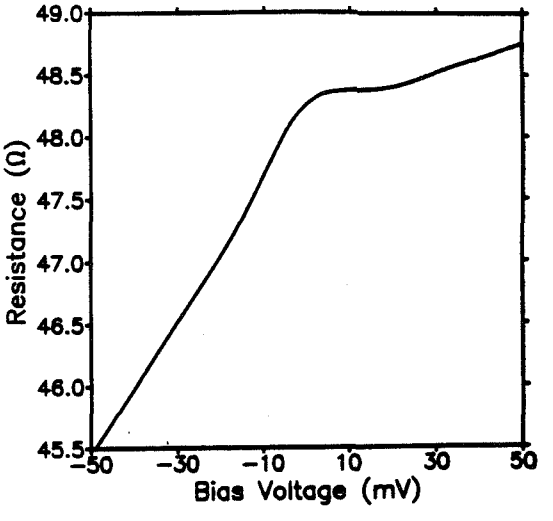

FIG. 2. The normal state first derivative raw data.

the normal state raw data. Because the junction resistance changes much more rapidly with the SnCu film biased negatively, the signal-to-noise ratio for this polarity is lower. Thus, since each polarity contained identical information, only the positively biased data was used.

The normal state first derivative was obtained by heating the substrate above the transition temperature. Since the SnCu film has a resistance in this state, this causes a small displacement of the measured first derivative above or below that measured for the superconducting state, depending on the resistivity of the film as compared to the junction resistance. Consequently, one must manually shift the data so that it matches the superconducting state at high bias voltages. Therefore, data was taken up to a bias voltage much higher than the maximum phonon energy. Thus, both the normal and superconducting state data were smoothed and interpolated with an increment of 0.05mV. The average difference was then calculated from 40mV to 50mV, and the result used to adjust the normal state data. The tunneling density of states is then given by equation (3).

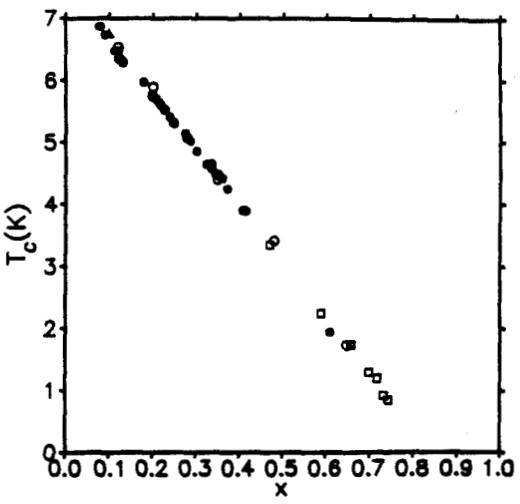

FIG. 3. Transition temperature as a function of copper concentration. The filled circles are from this study, the triangle is from Knorr and Barth[4], the open circles are from Leitz[5], and the squares are from Dutzi and Buckel[6].

IV. RESULTS AND DISCUSSION

Measurement of the superconducting transition temperature agree very well with that of others, as seen in Figure 3. Thus, the linear dependence of T_c on the copper concentration is confirmed.

Table I shows the results of the tunneling analysis, where

$$\lambda = 2\int_0^\infty \alpha^2(\omega)F(\omega)\omega^{-1}\,d\omega \tag{5}$$

$$\langle f(\omega)\rangle = \frac{2}{\lambda}\int_0^\infty \alpha^2(\omega)F(\omega)f(\omega)\omega^{-1}\,d\omega$$

$$\omega_{\log} = \exp\langle \ln\omega\rangle$$

$\omega_{\min}$ is the minimum frequency for which there is useful tunneling data. Also, the value of μ^* obtained from the inversion program is scaled to the arbitrary integration cutoff frequency ω_{co}, but $\mu^*(\omega_{ph})$ is the parameter appropriate for calculating T_c.[13] It has been rescaled to the phonon cutoff frequency ω_{ph} by

$$\frac{1}{\mu^*(\omega_{ph})} = \frac{1}{\mu^*(\omega_{co})} + \ln\left(\frac{\omega_{co}}{\omega_{ph}}\right) \tag{6}$$

Therefore, all values reported will be $\mu^*(\omega_{ph})$.

In Figure 4, $2\Delta_0/k_BT_c$ and λ are plotted as a function of copper concentration. Both $2\Delta_0/k_BT_c$ and Δ_0 decrease linearly with increasing copper concentration. Even at 41 at.% copper, the value of $2\Delta_0/k_BT_c$ is still well above the weak-coupling BCS value of 3.52. The variables in Dynes' equation for T_c are λ, μ^*, and $\langle\omega\rangle$. Values of λ determined from the tunneling measurements decrease with Cu concentration, while μ^* appears to be relatively constant (Table I) at about 0.10, which is quite different from the value of 0.04 found by Knorr and Barth[4]. $\langle\omega\rangle$ increases with increasing copper concentration, which could be expected since the average mass per atom is decreasing. Values of λ at higher Cu concentrations deduced from values of T_c and θ_D with the McMillan equation also decrease with Cu concentration,[6] but the concentration dependence is much weaker than that determined from tunneling measurements on the lower Cu concentration alloys, and there is a large discrepancy in the magnitude of λ determined in the tunneling measurements and that inferred from θ_D and T_c in the one region where the Cu concentrations are similar. This illustrates the now well known fact

TABLE I. Tunneling results. R_j is the junction resistance at 20meV. ω_{min} is the minimum energy for which there is useful tunneling data. The other quantities are defined in the text. The parameters ω_{min}, ω_{ph} and ω_{co} are given with respect to the energy gap edge, Δ_0.

Sample	SnCu#34-1	SnCu#33-4	SnCu#35-3	SnCu#35-4	SnCu#28-4	SnCu#40-3	SnCu#42-3
Concentration	$Sn_{0.92}Cu_{0.08}$	$Sn_{0.88}Cu_{0.12}$	$Sn_{0.87}Cu_{0.13}$	$Sn_{0.87}Cu_{0.13}$	$Sn_{0.78}Cu_{0.22}$	$Sn_{0.72}Cu_{0.28}$	$Sn_{0.59}Cu_{0.41}$
T_c (K)	6.865	6.332	6.302	6.283	5.585	5.068	3.905
R_j (Ω)	50	117	57	65	50	168	28
Δ_0(meV)	1.348	1.216	1.200	1.205	1.03	0.906	0.670
$2\Delta_0/k_BT_c$	4.557	4.457	4.437	4.432	4.280	4.149	3.982
Leakage (%)	1.4	1.2	0.9	0.9	4.0	4.5	4.0
ω_{min} (meV)	1.40	1.70	1.20	1.60	1.25	1.90	1.90
ω_{ph} (meV)	21	23	24	24	23	24	24
ω_{co} (meV)	110	110	110	220	110	110	110
λ	1.80	1.72	1.78	1.73	1.35	1.33	1.01
$\mu^*(\omega_{ph})$	0.089	0.114	0.118	0.116	0.079	0.113	0.090
$\langle\omega\rangle$(meV)	4.656	4.965	4.809	4.925	5.215	5.504	5.980
$\langle\omega^2\rangle^{1/2}$ (meV)	6.296	6.667	6.519	6.624	6.861	7.193	7.700
ω_{log} (meV)	2.750	2.993	2.838	2.961	3.222	3.456	3.872

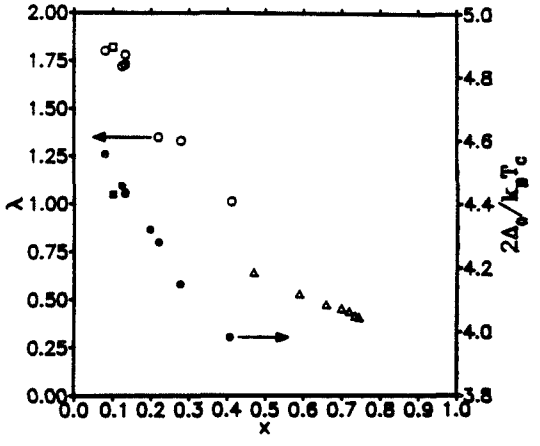

FIG. 4. λ and $2\Delta_0/k_BT_c$ as a function of copper concentration. The circles are from this study, the squares are from Knorr and Barth[4], and the triangles are values of λ from Dutzi and Buckel[6] using McMillan's T_c formula.

that the McMillan equation does not provide accurate values of λ.

Allen and Dynes[13], however, point out that equation (2) was derived with only one shape for $\alpha^2F(\omega)$. They investigated the dependence on the shape of $\alpha^2F(\omega)$ and found that the equation should be modified to be

$$T_c = \frac{f_1 f_2 \omega_{log}}{1.20} \exp\left[-\frac{1.04(1+\lambda)}{\lambda - \mu^*(1+0.62\lambda)}\right] \quad (7)$$

where

$$f_1 = \left[1 + (\lambda/\Lambda_1)^{3/2}\right]^{1/3},$$
$$f_2 = 1 + \frac{(\overline{\omega}_2/\omega_{log} - 1)\lambda^2}{\lambda^2 + \Lambda_2^2},$$
$$\Lambda_1 = 2.46(1 + 3.8\mu^*),$$
$$\Lambda_2 = 1.82(1 + 6.3\mu^*)(\overline{\omega}_2/\omega_{log}),$$
$$\overline{\omega}_2 = \langle\omega^2\rangle^{1/2}$$

The functions f_1 and f_2 are fairly close to unity for the case of SnCu, so this essentially changes the prefactor to involve ω_{log} instead of $\langle\omega\rangle$. However, ω_{log} has a dependence on copper concentration similar to that of $\langle\omega\rangle$.

Figure 5 shows the prediction of the T_c using both equation (2) and equation (7). Neither equation gives very accurate results. Equation (2) consistently overestimates T_c by as much as 20%, whereas equation (7) consistently underestimates it. Thus, caution also should be used in routinely relying on these equations to find the microscopic parameters of a superconductor given its T_c.

Figure 6 shows plots of the $\alpha^2F(\omega)$ data found for the amorphous SnCu films in this study. As can be seen, $\alpha^2F(\omega)$ is smeared out with increasing copper concentration. There is definitely a shift to higher energies of the low energy structure, as well as an overall decrease in amplitude. The peak at ~13meV also disappears. Whether this is due to a shift to lower energies, or only to a broadening and decrease in amplitude, cannot be determined.

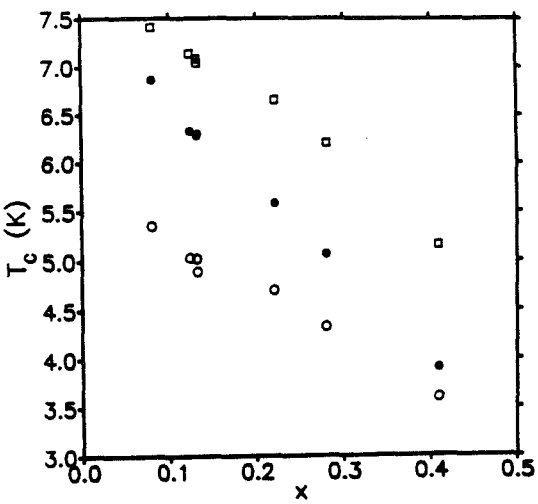

FIG. 5. Comparison between experimental and calculated values for T_c. The filled circles are experimental values from this study. The open circles are calculated using equation (7), and the open squares are calculated using equation (2).

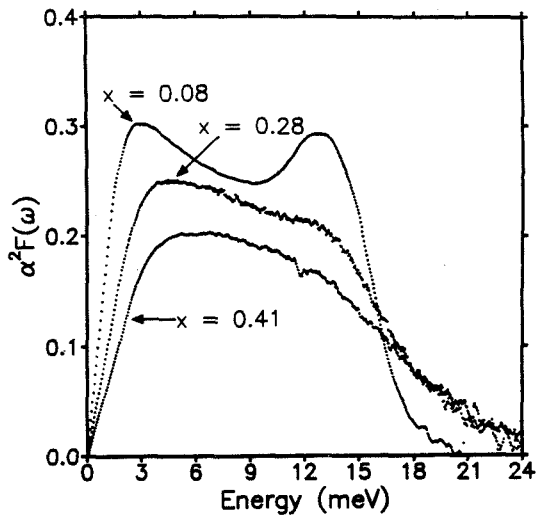

FIG. 6. $\alpha^2F(\omega)$ as a function of energy showing the data for copper concentration $x = 0.08$, 0.28, 0.41.

As mentioned previously there is a minimum energy, $\omega_{\min}$, above the gap edge up to which the experimental tunneling data is not useful. One cause of this is the effect of a non-zero temperature. The inversion program uses the $T = 0$ equations to obtain its results. Thus, temperature broadening, and especially taking the superconducting data at a temperature that is an appreciable fraction of the transition temperature, is not taken into account by the program. This will have the greatest effect near the gap as the data is changing rapidly there. The other major cause is the difficulty in taking data near the gap. The data was taken as a function of bias voltage by sweeping a DC current through the junction. Thus, there is a constantly changing bias voltage. This, coupled with the use of a lock-in amplifier, always results in a small offset and smearing of the data no matter how slowly the data is taken. In this respect, it would be better to use a computer-controlled voltage source that was sufficiently free of noise. Again, since the data is changing very rapidly near the gap edge, the largest effect would be seen there. Since it is not really possible to say at what point the data is good, the parameter $\omega_{\min}$ is somewhat arbitrary. Generally, it is set to the maximum energy that still gives a smooth $\alpha^2F(\omega)$ and doesn't add any extraneous structure. Again, this is somewhat arbitrary, so the additional condition that it maximizes the fit to the tunneling data was used.

Because the tunneling data is not used up to $\omega_{\min}$, a functional form for $\alpha^2F(\omega)$ must be used for this region. For most materials, this form is ω^2 and comes from the Debye theory for $F(\omega)$, assuming that $\alpha^2(\omega)$ is constant. This is usually a good approximation; however, for the SnCu films of this study, it was necessary to use $\alpha^2F(\omega) \propto \omega$ to fit the tunneling data. Knorr and Barth[4] also needed a linear dependence on ω for $\alpha^2F(\omega)$ at low energies for amorphous $Sn_{0.9}Cu_{0.1}$. Their results prompted theoretical studies for amorphous s–p superconductors[14–16] which resulted in the following theoretical expression for $\alpha^2F(\omega)$ at low frequency,

$$\alpha^2F(\omega) = \left[\frac{e^2E_F k_F^2 N(0)\rho}{3\pi^3\langle v^3\rangle mM}\right]\omega \equiv A\omega \tag{8}$$

where $N(0)$ is the electronic density of states at the Fermi energy in states/eV-atom-spin, ρ is the resistivity, M is the atomic weight, m is the electronic mass, and v is the speed of sound. The assumption of small q such that $\omega = vq$ for the phonons has been made, and

$$\frac{1}{\langle v^3 \rangle} = \frac{1}{3}\left(\frac{1}{v_l^3} + \frac{2}{v_t^3}\right)$$

where v_l and v_t are the longitudinal and transverse sound velocities, respectively. Following the approximations made by Poon and Geballe[15], the free electron model is used to obtain

$$E_F = \frac{\hbar^2 k_F^2}{2m}$$
$$N(0) = \frac{m k_F}{\pi^2 \hbar^2} \frac{M}{\rho_m A_o}$$

with ρ_m being the mass density of the alloy, and A_o is Avogadro's number. Also, $\langle v^3 \rangle \propto M\theta_D^3/\rho_m$; thus,

$$A \propto \frac{\hbar^3 k_F^5 \rho A_o}{6\pi^5 m M \theta_D^3} \tag{9}$$

Poon and Geballe[15] then determined the constant of proportionality for PbBi with known values of θ_D and $\langle v^3 \rangle$ which they assumed was the same for amorphous SnCu, 11.56. This can then be written in terms of $\langle \omega \rangle$ using McMillan's T_c equation by $\theta_D = 1.45\langle \omega \rangle / 1.20$. Thus,

$$A = \frac{11.56\hbar^3 k_F^5 \rho A_o}{6\pi^5 m M \langle \omega \rangle^3} \left(\frac{1.20}{1.45}\right)^3 \tag{10}$$

The Fermi wavevector, k_F is given by

$$k_F = \sqrt[3]{3\pi^2 \overline{Z}\, \overline{\eta}_o}$$
$$\overline{Z} = (1-x) Z_{\mathrm{Sn}} + x\, Z_{\mathrm{Cu}}$$

where Z_{Sn} and Z_{Cu} are the valences of the pure elements counting s– and p– states only, one for copper and four for tin. The mean number of atoms per unit volume is η_o and is given by

$$\eta_o^{-1} = (1-x)\frac{M_{\mathrm{Sn}}}{A_o \rho_{\mathrm{Sn}}} + x \frac{M_{\mathrm{Cu}}}{A_o \rho_{\mathrm{Cu}}}$$

where M_i and ρ_i are the atomic weights and the mass densities of the pure elements.

This allows calculation of the slope of $\alpha^2 F(\omega)$ to be made. Figure 7 shows a comparison between these calculations (open circles) and experimental data (closed circles) from this study. The agreement is surprisingly good considering the number of approximations made. However, this agreement is probably fortuitous, since use of values for θ_D from recent heat capacity measurements[17] in equation (9) gives very poor agreement (the open squares of Figure 7). Figure 8 shows θ_D data from the heat capacity measurements by Dutzi and Buckel[6] and Sohn[17] and $\langle \omega \rangle$ converted to θ_D using the ratios of equations (1) and (2), i.e. $\theta_D = 1.45\langle \omega \rangle / 1.20$.As seen in the figure, this commonly used relation is not valid for the amorphous SnCu system.

More fundamental than the question of what parameters to use in the calculation of A from equations (8) or (9) is the question of whether $\alpha^2 F(\omega)$ is really linear in ω at low frequency. Belitz[18] has pointed out that the derivation of equation (8) is based on incorrect assumptions and has derived the following expressions for $\alpha^2 F(\omega)$ at low frequency,

$$\alpha^2 F(\omega) = h_l^2 4k_F^3 / q_D^3 (\omega / E_F) \left[1 - \widehat{\rho}\frac{9}{\pi^2}\frac{4k_F}{q_D} F + O(\widehat{\rho}^2)\right], (\omega/\omega_D \ll \eta),$$

where

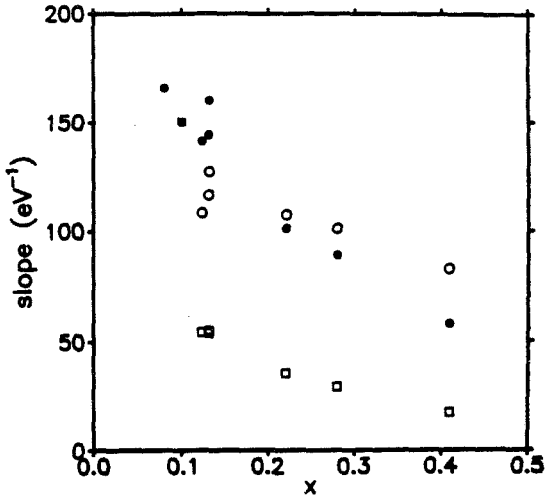

FIG. 7. Slope of $\alpha^2F(\omega)$ as a function of copper concentration. The filled circles are experimental values from this study, the filled square is from Knorr and Barth[4], the open circles are calculated values using equation (10), and the open squares are calculated values using equation (9).

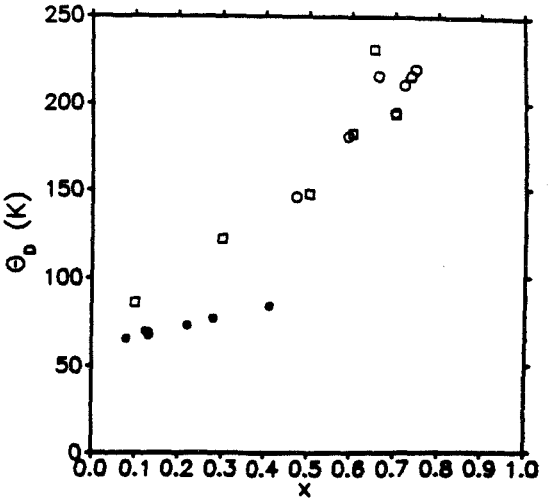

FIG. 8. θ_D as a function of copper concentration. The open circles are from Dutzi and Buckel[6], the squares are from Sohn[17], and the filled circles are from this study using $1.45\langle\omega\rangle/1.20$.

$$F = \int_0^\infty dx[\pi^2/36 - f_l^2(x)/x^2 - (v_l/v_t)^4 f_t^2(x)/x^2]$$

$$f_l(x) = \frac{1}{3}\frac{x^2 \arctan x}{x - \arctan x} - 1$$

$$f_t(x) = \frac{1}{2x^3}[2x^3 + 3x - 3(x^2+1)\arctan x];$$

$$\alpha^2F(\omega) = h_l \frac{q_D/k_F}{5\pi}\frac{8}{\hat{\rho}}(1 + \frac{3}{2}v_l^5/v_t^5)(\omega/\omega_D)^3, \qquad (\eta \ll \omega/\omega_D \ll \hat{\rho}\, k_F/q_D),$$

$$\alpha^2F(\omega) = h_l\left[(\omega/\omega_D)^2 + \frac{k_F/q_D}{\pi}\left[12v_l^3/v_t^3 - (8-\pi^2/2)\right]\hat{\rho}\omega/\omega_D\right], (\hat{\rho}\, k_F/q_D \ll \omega/\omega_D \ll \hat{\rho}\, 2E_F/\omega_D)$$

where $\eta = k_F^4/9\rho_m v$, $h_l = \hbar^4 k_F^2 q_D^2 N(0)/36m^2\rho_m v_l^2$, $\hat{\rho} = 1/k_F l$. Thus, $\alpha^2F(\omega)$ is essentially linear with ω except for the range $(\eta \ll \omega/\omega_D \ll \hat{\rho}\, k_F/q_D)$ for which it goes as ω^3. For the SnCu films in this study, $\eta \sim 0.057$ and $\hat{\rho}\, k_F/q_D \sim 0.080$. Thus, for $\omega_D \sim 6$meV, $\eta \sim 0.34$meV and $\hat{\rho}\, k_F/q_D \sim 0.48$meV. Unfortunately, this range is smaller than the minimum energy for which the data of this study is reliable; so, the ω^3 region cannot be directly observed. This theory also involves v_l, v_t and θ_D which are unknown for the amorphous SnCu films of this study. An attempt was made to set $\alpha^2F(\omega)$ proportional to ω^3 up to 0.5meV and then proportional to ω up to $\omega_{\min}$ when doing the tunneling analysis. This invariably lead to an $\alpha^2F(\omega)$ and μ^* which didn't reproduce the tunneling data, as demonstrated in Figures 9 and 10 for $Sn_{0.87}Cu_{0.13}$. Figure 9 shows the resulting $\alpha^2F(\omega)$. In Figure 10 curve (a) shows the difference between the experimental tunneling density of states and the calculated density of states. There is a large difference, whereas when $\alpha^2F(\omega)$ is assumed to be proportional to ω up to $\omega_{\min}$, the difference is about 1×10^{-5}, as shown in curve (b). Also, $\mu^*(\omega_{ph})$ and λ are 0.07 and 1.46, respectively, compared with the previous results of 0.116 and

1.73. Consequently, this tunneling data is best fit by a purely linear ω dependence for $\alpha^2F(\omega)$ at low frequency in these alloys.

A material for which the range of the predicted $\alpha^2F(\omega) \propto \omega^3$ is large and at high enough energies that very accurate data can be measured would allow direct observation of the low frequency $\alpha^2F(\omega)$ spectrum to see if an ω^3 dependence exists. We are unaware of such a material. Efforts to incorporate the predicted ω^3 dependence to fit the present tunneling data were totally unsuccessful. However, it should be pointed out that Belitz's theory may be correct within the framework in which it is derived, and that this study is perhaps seeing a breakdown in the fundamental assumptions upon which this theory is based. One speculation is that perhaps the adiabatic approximation breaks down at this level of detailed measurement in such strong-coupling metals.

V. SUMMARY AND CONCLUSIONS

Amorphous $Sn_{1-x}Cu_x$ thin films ($0.08 \leq x \leq 0.41$) were prepared by e-beam deposition in an ultra-high vacuum system, forming high quality aluminum – aluminum oxide – superconductor tunnel junctions. Measurements of the transition temperature, T_c, were in excellent agreement with work done by others, confirming the linear decrease in T_c with increasing x. The superconducting energy gap, Δ_0, and $2\Delta_0/k_BT_c$ show a linear decrease with increasing x; however, $2\Delta_0/k_BT_c$ was 3.982, well above the BCS prediction of 3.52, and λ was 1.01 for $x = 0.41$, suggesting that this alloy composition is still a strong-coupling to intermediate-coupling superconductor.

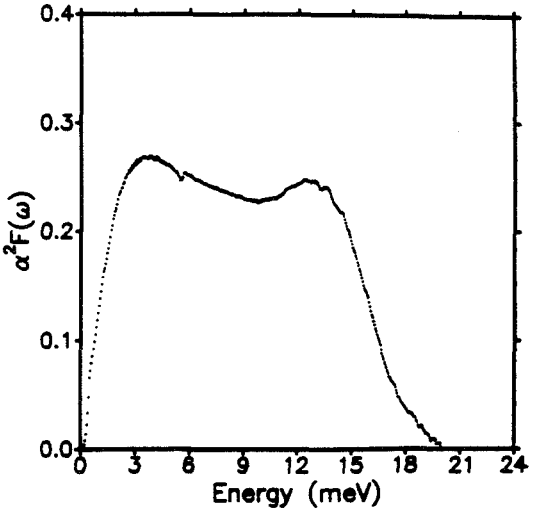

FIG. 9. $\alpha^2F(\omega)$ as a function of energy for sample SnCu#35–4 ($Sn_{0.87}Cu_{0.13}$). $\alpha^2F(\omega)$ was assumed to be proportional to ω^3 up to 0.5meV and then proportional to ω up to ω_{min}.

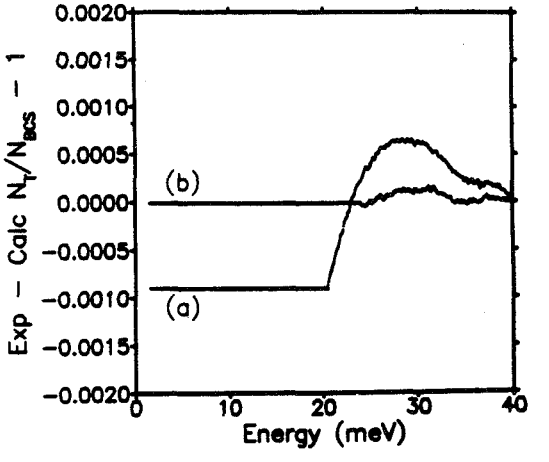

FIG. 10. Difference between the experimental and calculated tunneling density of states as a function of energy when $\alpha^2F(\omega)$ was assumed to be (a) proportional to ω^3 up to 0.5meV and then proportional to ω up to ω_{min}, and (b) linear up to ω_{min}.

The Coulomb pseudopotential is approximately independent of x, $\mu^*(\omega_{ph}) = 0.10 \pm 0.02$; λ decreases while $\langle\omega\rangle$ increases with x, indicating that λ is the cause for the decrease in transition temperature with x. The experimental values for T_c were compared to the theories of Dynes[8] and Allen and Dynes[13]. Neither formula provided quantitative agreement, suggesting that these formulae should not be routinely used to extract the microscopic parameters of a superconductor given its T_c.

A linear dependence on ω for $\alpha^2F(\omega)$ at small ω was needed to reproduce the experimental tunneling spectra in contrast to the most recent predictions which require a small region proportional

to ω^3. The shape of $\alpha^2F(\omega)$ changed from two distinct peaks at low x, to one smeared peak at $x = 0.41$. The reason for this qualitative change in the shape of $\alpha^2F(\omega)$ has not been determined.

Future work needs to be done to explore better the change from strong-coupling to weak-coupling behavior in more copper rich alloys and to better test the theories of the behavior of $\alpha^2F(\omega)$ at low frequency. This could be useful in resolving the disagreement between the theory of Belitz[18] and present data on amorphous alloys. To date there is no experimental confirmation of the detailed predictions for the low frequency behavior of $\alpha^2F(\omega)$ for strong-coupling superconductors given by this state of the art theory. A clear test will require much more accurate tunneling data near the energy gap and a strong-coupling superconductor with a broader region for the predicted ω^3 behavior.

ACKNOWLEDGMENTS

This work was supported by the Robert A. Welch Foundation, Grant No. A-0514 and the National Science Foundation, DMR-9104194. The authors acknowledge helpful discussions with D. Belitz, R. C. Dynes, G. Arnold, and E. L. Wolf. Also we thank G. Arnold for supplying a copy of the data analysis programs, and M. Sohn for providing values of his heat capacity data prior to publication.

---

[1] M. M. Collver and R. H. Hammond *Phys. Rev. Lett.* **30**, 92 (1973)
[2] G. Bergmann *Phys. Reports* **27C**, 161 (1976)
[3] W. L. Johnson and M. Tenhover, in *Glassy Metals: Magnetic, Chemical and Structural Properties,* edited by R. Hasegawa (CRC Press, Florida, 1983), p. 65.
[4] K. Knorr and N. Barth *J. Low Temp. Phys.* **4**, 469 (1971)
[5] H. Leitz *Z. Physik* B **40**, 65 (1980)
[6] J. Dutzi and W. Buckel *Z. Physik* B **55**, 99 (1984)
[7] W. L. McMillan *Phys. Rev.* **167**, 331 (1968)
[8] R. C. Dynes *Solid State Comm.* **10**, 615 (1972)
[9] D. G. Naugle, B. Bandyopadhyay, Yin Bo, V. M. Nicoli, F.-C. Wang, and D. Rathnayaka *Rev. Sci. Instrum.* **58**, 1271 (1987)
[10] S. Bermon and C. K. So *Solid State Comm.* **27**, 723 (1978)
[11] P. W. Watson III Dissertation, Texas A&M University (1993)
[12] W. F. Brinkman, R. C. Dynes and J. M. Rowell *J. of Appl. Phys.* **41**, 1915 (1970)
[13] P. B. Allen and R. C. Dynes *Phys. Rev.* B **12**, 905 (1975)
[14] G. Bergmann *Phys. Rev.* B **3**, 3797 (1971)
[15] S. J. Poon and T. H. Geballe *Phys. Rev.* B **18**, 233 (1978)
[16] L. V. Meisel and P. J. Cote *Phys. Rev.* B **23**, 5834 (1981)
[17] M. Sohn, private communication
[18] D. Belitz *Phys. Rev.* B **36**, 2513 (1987)

CHANGES IN THE SUPERCONDUCTING PROPERTIES OF HIGH-Tc CERAMICS PRODUCED BY APPLIED ELECTRIC FIELDS.

B.I.Smirnov, T.S.Orlova, H.-J.Kaufmann
A.F.Ioffe Physico-Technical Institute, Russian Academy of Sciences, St.Petersburg 194021, Russia

Abstract
Effect of an electrostatic field in the electrode-insulator-superconductor system on the current-voltage characteristics of high-Tc ceramics with various composition and different preparation technology has been studied at 77K. Ceramics of Y-Ba-Cu-O (123) and Bi-Pb-Sr-Ca-Cu-O (2223) systems and also ones doped by Ag have been used. Electric field strength has been up to 140 MV/m.
It has been shown that there are reversible changes in the critical current Ic and in the conductivity in electric field at the currents somewhat more than Ic at T<Tc, while at T>Tc the noticeable electric field effect has not been found. These effects are qualitatively similar in both ceramic systems. High negative and positive gate voltages result in an increase of the conductivity. The electric field effect is modified by magnetic field H. The field effect decreases with increasing magnetic field and disappears at H>30 Oe. In Y-Ba-Cu-O/Ag (10 wt.%) ceramics the field effect is practically absent.
It may be supposed that in the ceramics the field-induced effect is consistent with weak links at grain boundaries.

1. Introduction

Problem of an electric field effect on the conductivity of superconductors has attracted attention for more than 30 years [1-3]. The first experimental paper [1] reported that indium and tin films d≈70Å thick subjected to fields E=30 MV/m exhibited a change in the conductivity and a shift in critical temperature Tc by $\Delta Tc \approx 10^{-4}$K.

After the discovery of high-Tc superconductors similar studies were stimulated, especially during last four years [4-9]. In most cases thin films were objects of these investigations because it is usually believed that the field effect is attributed to a change of the carrier concentration in very thin surface layer of about 5Å thickness [6]. Considerable modulation of Tc and the current-voltage characteristics under applied electric field were reported [7-9].

At the same time there are data on the electric field effect in quite thick low-Tc superconductors. The 0.6K shift in Tc for $Ba(PbBi)O_3$ single crystals of 0.6 mm thickness was reported in [10]. In the case of high-Tc superconductors the field effect can occur also in less perfect samples of quite large thickness [11-14].

In the present paper we demonstrate the experimental evidence for considerable reversible effect of an applied electric field on the conductivity of high-Tc ceramics.

The following questions will be presented and discussed in the paper:

1. Reversible effect of an applied electric field on the current-voltage characteristics of high-Tc ceramics at T<Tc.
2. Influence of the electric field polarity on the effect.
3. The electric field effect in the presence of magnetic field.

4. Influence of silver addition to the ceramics on the effect.

2. Experimental

Main results have been obtained on yttrium ceramics of the 123 system. Some tests have been made on similar ceramics doped by silver and also on Bi-based compound of the 2223 system.

Samples of rectangular shape were prepared by standard powder sintering method and had dimensions of about 1.5x2x4 mm. By varying the anneal temperature and time, and the rate of the cooling, it was possible to obtain $YBa_2Cu_3O_{7-x}$ (YBCO) ceramics with various superconducting transition properties, the value of Tc remaining almost the same ($90K \leq Tc \leq 93K$) but the critical current density jc varying much more ($1A/cm^2 \leq jc \leq 120A/cm^2$) [15].

To obtain samples containing silver, the finished pure $YBa_2Cu_3O_{7-x}$ ($x \approx 0.07$) pellets were again crushed, and silver powder was added. Samples of this mixture were compacted and then twice annealed in oxygen at 930^oC for 6 h, with crushing and compacting between the anneals. To verify the effect of silver on the ceramic properties, control samples were also prepared, and treated like the others except that no silver was added.

Investigations of field-induced effect were carried out in the metal-insulator-superconductor system shown in Fig.1. Teflon film of thickness $l=50$ μm was used as the insulator. Such a configuration allows us to apply considerable positive (or negative) gate voltage U up to 7 kV between the gate electrode and a superconductor.

Current-voltage (I-V) characteristics were taken with a standard four-probe technique, and Ic, the experimental critical current, was determined by a 1 μV/mm criterion.

It should be noted that the leakage current in the electrode-insulator-superconductor system did not exceed 3 nA at the maximum voltage U=7kV, whereas the transport current could reach a few amperes.

We studied effect of an electric field on the I-V characteristics of the ceramics. The experiment was carried out in the following way. At first I-V curve without electric field was measured. Then at some chosen point of this curve (Io-Vo) a gate voltage U was applied and drain-source voltage change ($\Delta V = V - Vo$) at a constant transport current was determined. Electric field ($E = U/l$) can be changed smoothly from 0 to 140 MV/m or some electric field Eo was switched sharply on or off. The similar measurements were made for various drain-source voltages Vo, i.e. for different transport currents. Also it was possible to measure and compare values of Ic and I-V characteristics without and with an electric field [16,17]. In addition, all the above mentioned experiments could be performed in a magnetic field H generated by an energized coil and directed parallel to the electric field [17].

3. Results and discussion

In the superconducting state, the I-V characteristics can be significantly affected by the gate voltage U (see Fig.2). Strong electric field shifts the I-V curve to the right, i.e. enhances the critical current and reduces the sample resistance R at $I > Ic$ no matter what the polarity of the field.

Fig.3 shows change of drain-source voltage due to the switching of strong electric field on and off at 77 K. It is seen that vol-

tage decreases at the moment when the field is switched on. The opposite effect is observed when the field is switched off. Strangely enough, we obtained qualitatively similar result also in the case when a metal foil 15 μm thick was placed between the insulator and a superconducting sample [18].

Thus, we can conclude that in the ceramic samples at temperature below Tc the field effect also exists. The value of drain-source voltage is restored after removing the field, i.e. the field effect has reversible character.

The following Fig.4 demonstrates characteristic experimental dependence drain-source voltage versus electric field for the cases of positive and negative gate voltages at 77K. As seen, the character of this relationship V(E) can depend on the field polarity. Applying a positive gate voltage to a fresh sample usually results in decrease of V ($\Delta V<0$). In the case of a negative gate voltage the value of V first rises with E ($\Delta V>0$) but then gradually decreases having a maximum at electric field E≈40 MV/m. After the electric field has reached E≈60-70 MV/m the value of ΔV changes its sign so that we have an decrease of the resistance. It is of interest that after the prolonged testing a sample the relationships V(E) can change essentially, including the appearance of maximum on the curve V(E) also for a positive gate voltage [19].

A qualitatively similar result was obtained for high Tc ceramic $Bi_{1.85}Pb_{0.35}Sr_{1.9}Ca_{2.1}Cu_{3.1}O_y$ (Tc≈95K) [16].

It should be also noted that in the above both cases the electric field effect exists only at T<Tc. At T>Tc the noticeable field effect was not observed [16].

Our further interest was in the elucidation of the electric field effect peculiarities arising from the application of a magnetic field. Fig.5 shows the influence of strong electric field E=-120 MV/m on the I-V characteristics of YBCO ceramic in various magnetic fields H. It is seen that the shift of the I-V curves under an electric field depends on the value of H. So, at H=0 the field effect is sufficiently large ($\Delta R/R=\Delta V/V$ can reach 100% for low V and about 40% for high V). However, it falls off with increasing H and practically disappears at H≥30 Oe.

Fig.6 presents the results on the influence of an electric and a magnetic fields on the critical current. At H=0, the critical current Ic is seen to grow with increasing E (see inset of Fig.6), the change reaching $\Delta Ic/Ic\approx 10\%$ at E=-120 MV/m. After the magnetic field is switched on, the electric field effect falls off rapidly, to practically disappear at H≥30 Oe. Thus, the electric field effect on the I-V curves is observed only at low magnetic fields.

Next we will consider the field effect in $YBa_2Cu_3O_{7-x}$ /Ag (10 wt.%) ceramics (YBCO/Ag). Fig.7 displays the comparison of the experimental results obtained for the pure YBCO and YBCO/Ag ceramic samples. As seen doping with silver suppresses the field effect practically completely.

Thus, the results obtained show that an applied electric field affects the current-voltage characteristics of high-Tc ceramics at T<Tc and can modify the value of the critical current Ic. The field effect is reversible. It should be stressed that the field effect observed in high-Tc ceramics is qualitatively different from the effect in the high-Tc films.

The question of what is the possible mechanism behind the observed field effect arises. Unfortunately, the nature of this

effect has not been clear for us. It may be only supposed that in the ceramics the field-induced effect is consistent with change of weak link states at grain boundaries [16]. This is supported in particular by those facts that both magnetic field and doping with silver greatly suppress the electric field effect. In the latter case the marked reduction of the field effect can be explained replacing the weak links of superconductor-insulator-superconductor type (S/I/S) by the weak links of superconductor-normal metal-superconductor type (S/N/S) [20]. Further studies are required to gain a better understanding of the nature of the field effect observed.

4. Conclusions

In summary, the present study allows the following conclusions:

1. An applied electric field affects the I-V characteristics of high Tc ceramics at $T<Tc$ and can modify the value of the critical current Ic.

2. In ceramic samples at $T>Tc$ the noticeable field-induced effect was not found.

3. The effect has reversible character. Strong positive and negative gate voltages lead to enhancement of the conductivity.

4. Magnetic field and adding silver to the ceramics result in the suppression of the electric field effect.

5. It may be supposed that in ceramics the field-induced effect is consistent with weak links at grain boundaries.

References

1. Glover R.E. and Sherrill M.D. Phys. Rev. Lett. **5**, 248 (1960)
2. Sandomirskii V.B. Pis'ma Zh. Exp. Teor. Fiz. **2**, 396 (1965)
3. Meissner H. Phys. Rev. **154**, 422 (1967)
4. Mannhart J., Bednorz J.G., Müller K.A. and Schlom D.G. Z. Phys. B **83**, 307 (1991)
5. Mannhart J., Schlom D.G., Bednorz J.G., and Müller K.A. Phys. Rev. Lett. **67**, 2099 (1991)
6. Xi X.X., Doughty C, Walkenhorst A., Kwon C., Li Q. and Venkatesan T. Phys. Rev. Lett. **69**, 1240 (1992)
7. Mannhart J. Modern Phys. Lett. B **6**, 555 (1992)
8. Xi X.X. and Venkatesan T. Phys. News in 1992, Ed. Schewe P.F., American Inst. of Phys. 44 (1993)
9. Lemanov V.V. and Kholkin A.L. Fiz. Tverd. Tela **36**, 1537 (1994)
10. Bogatko V.V. and Venevzev Yu.N. Fiz. Tverd. Tela **29**, 2872 (1987)
11. Gomenyuk Yu.V., Lozovskii V.Z., Lysenko V.S., Pokhodnya K.N., Snitko O.V., Sytenko T.N. and Tyagul'skii I.P. Dokl. Akad. Nauk Ukr.SSR, ser. A, № 11, 49 (1989)
12. Gomenyuk Yu.V., Klyui N.I., Lozovskii V.Z., Lysenko V.S., Prokof'ev A.Yu., Romanyuk B.N., Sytenko T.N. and Tyagul'skii I.P. Sverkhprovodimost': Fizika, Khimija, Tekhnika **4**, 762 (1991)
13. Smirnov B.I., Krishtopov S.V. and Orlova T.S. Fiz. Tverd. Tela **34**, 2482 (1992)
14. Lemanov V.V., Kholkin A.L. and Sherman A.B. Pis'ma Zh. Eksp. Teor. Fiz. **56**, 580 (1992)
15. Orlova T.S., Smirnov B.I., Shpeizman V.V., Stepanov Yu. P. and Chernova S.P. Fiz. Tverd. Tela **32**, 1031 (1990)
16. Smirnov B.I., Orlova T.S. and Krishtopov S.V. Fiz. Tverd. Tela **35**, 2250 (1993)
17. Smirnov B.I., Orlova T.S. and Kudymov A.N. Fiz. Tverd. Tela **36**, 1529 (1994)
18. Smirnov B.I., Orlova T.S. and Kaufmann H.-J. Fiz. Tverd. Tela **36**, 460, (1994)
19. Orlova T.S., Smirnov B.I. Supercond. Sci. Technol.(to be published)
20. Jung J., Isaac I. and Mohamed M.A-K. Phys. Rev. B **48**, 7526 (1993)

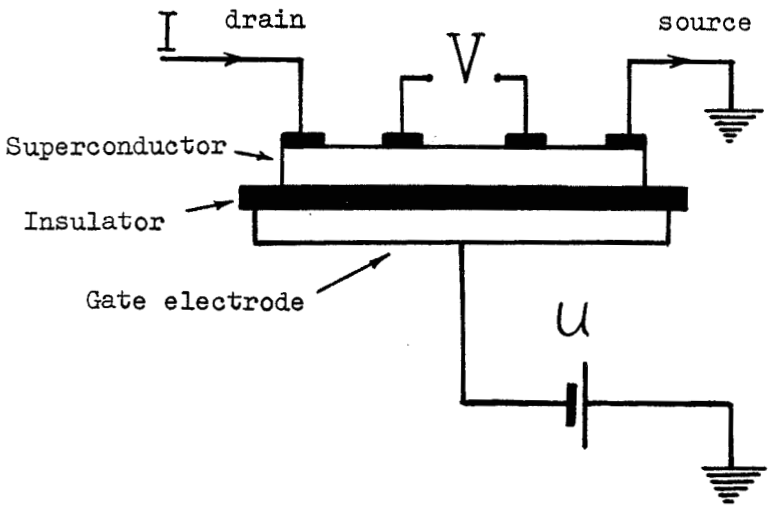

Figure 1.- Configuration used for the study of electric field effect.

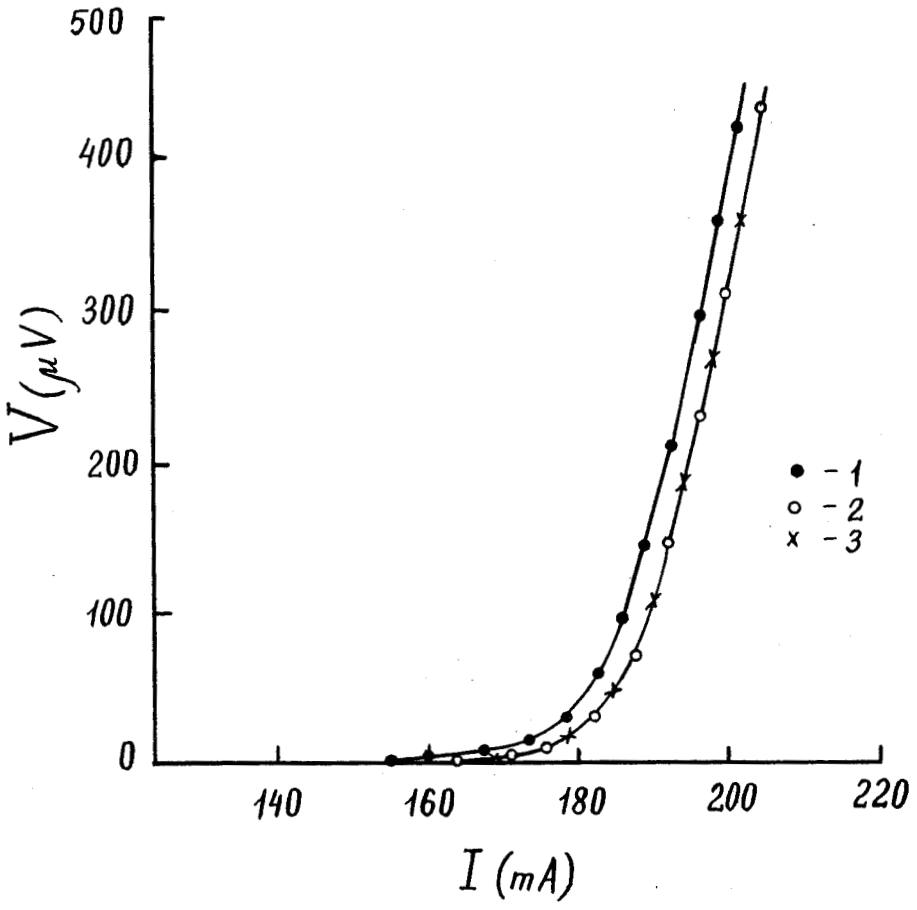

Figure 2.- Current-voltage characteristics of the YBCO ceramic with low jc≈5 A/cm^2 for electric field E(MV/m): 0 (1), -120 (2), and 120 (3). T=77K.

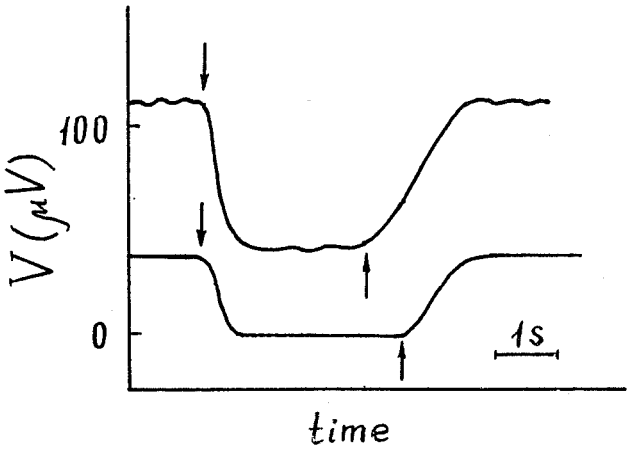

Figure 3.- Change in drain-source voltage V as a result of the switching of an electric field E=-120 MV/m on and off. T=77K. I=const in each experiment. The arrows show the times which the field was switched on (⇑) and off (⇓).

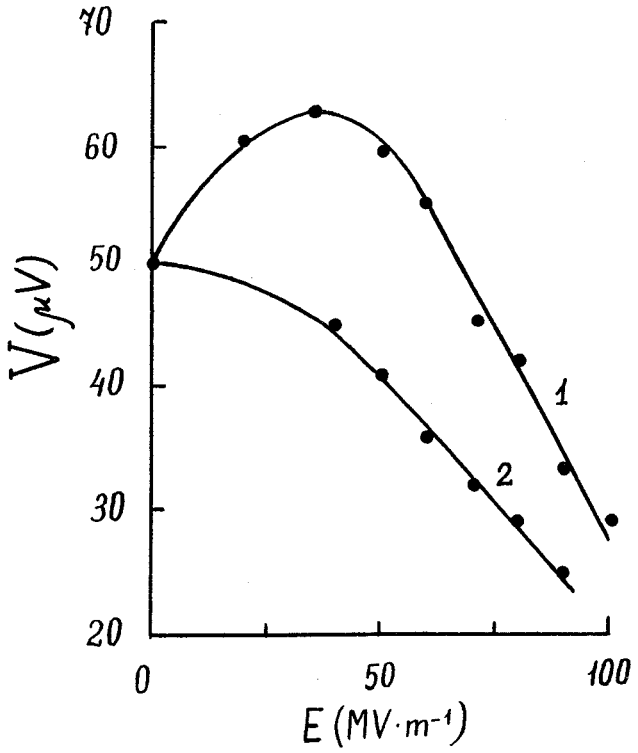

Figure 4.- Typical V (E) plots for the YBCO ceramic with negatively and positively biased gate electrode at 77K.

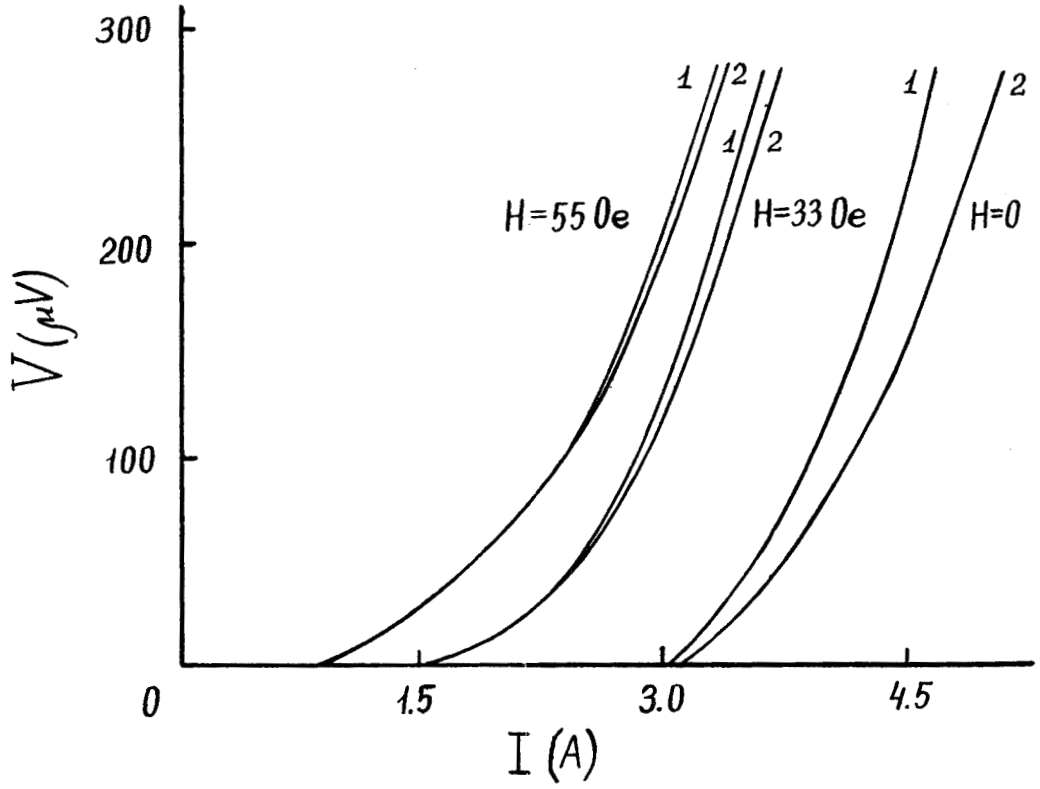

Figure 5.- Current-voltage characteristics of the YBCO ceramic with jc≈100 A/cm^2 on magnetic field H for the YBCO ceramic when E(MV/m): 0 (1), and -120 (2).

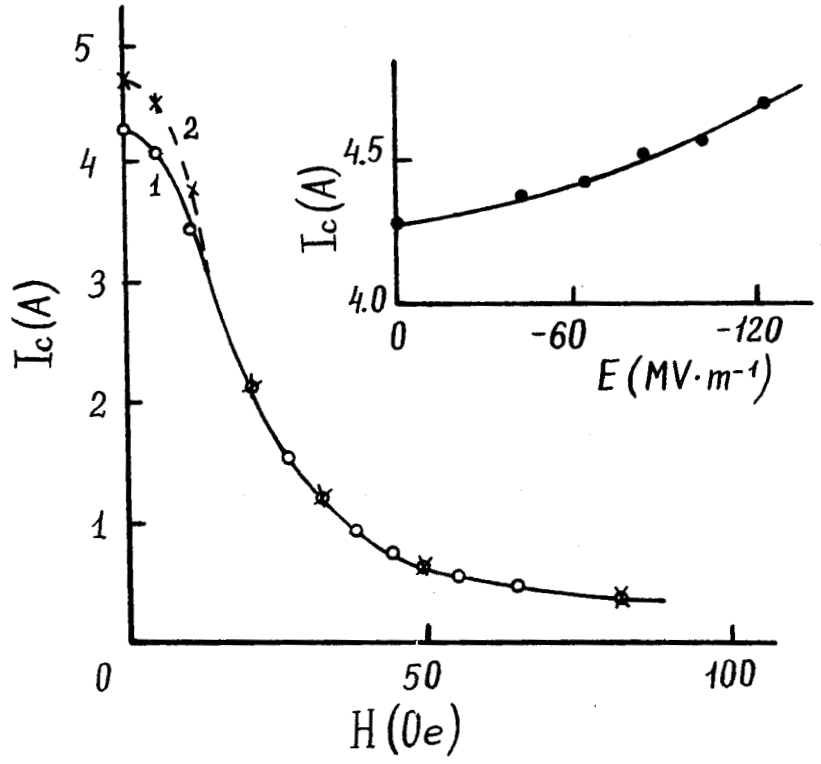

Figure 6.- Ic as a function of magnetic field H for the YBCO ceramic when E(MV/m): 0 (1), and -120 (2). Inset: Ic(E) dependence at H=0.

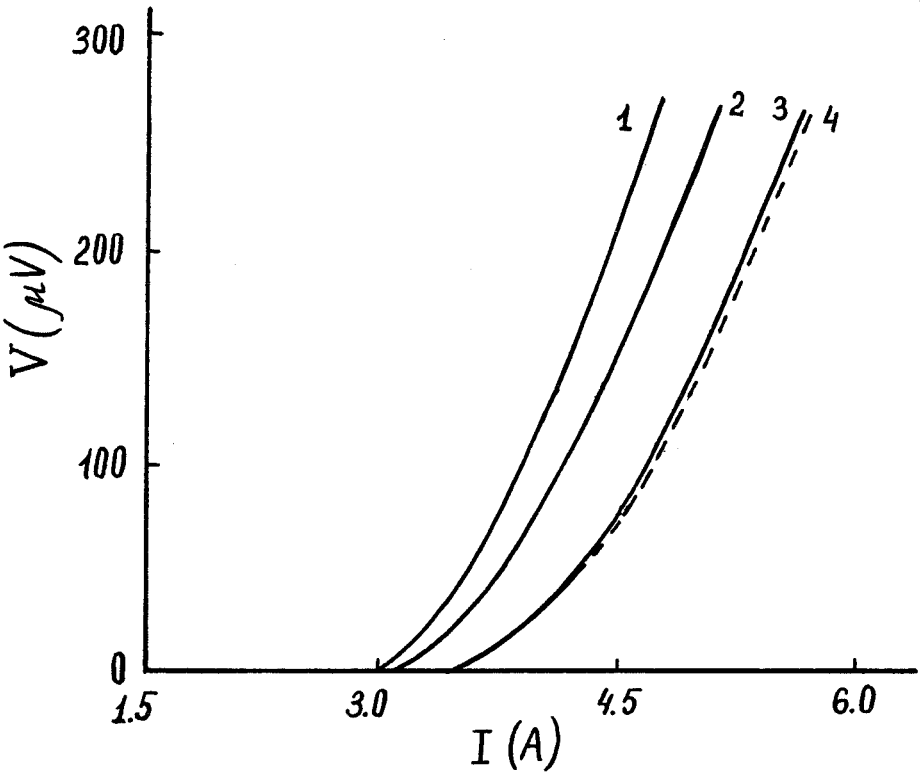

Figure 7.- Current-voltage characteristics of pure YBCO (1,2) and YBCO/Ag (10 wt.%) (3,4) ceramics for E(MV/m): 0 (1,3), and -120 (2,4).

EFFECT OF Nb_2O_5 AND V_2O_5 ADDITION ON THE SUPERCONDUCTING PROPERTIES OF $YBa_2Cu_3O_Y$ THIN FILMS

S.SRINIVAS AND A.K.BHATNAGAR
SCHOOL OF PHYSICS,UNIV.OF HYDERABAD,HYDERABAD 500134, INDIA
AND
R.PINTO, S.P.PAI, P.R.APTE, S.C.PURANDARE AND C.P.D.SOUZA
SOLID STATE ELECTRONICS GROUP, T.I.F.R., BOMBAY, INDIA

ABSTRACT

The effect of Nb_2O_5 and V_2O_5 addition on the superconducting properties and microstructure of $YBa_2Cu_3O_y$ has been studied in thin films. Polycrystalline targets for laser ablation were prepared by mixing high purity V_2O_5 or Nb_2O_5 powders with a well characterized $YBa_2Cu_3O_y$ powder in the range 0 to 4 wt% by solid state reaction method. Thin films (≈1500 A thickness) of the above targets were grown on <100> $SrTiO_3$ (STO) and <100> $LaAlO_3$ (LAO) substrates at 700°C temperature by Pulsed Laser Deposition (PLD) technique. In the case of Nb_2O_5 addition we have noticed an increase in J_c upto 0.5 wt% and higher additive concentration (greater than 0.5 wt%) have degraded the superconducting properties. However, in the case of V_2O_5 addition, there is an improvement in current density and microstructural properties up to 1 wt% and the superconducting properties degrade for concentrations greater than 1 wt%. The best J_c for 0.5 wt% of Nb_2O_5 added YBCO thin film is 1.6×10^6 A/cm^2 and for that of V_2O_5 added sample is 3.4×10^6 A/cm^2 at 77K as compared to the pure $YBa_2Cu_3O_y$ (YBCO) film J_c (1.2×10^6 A/cm^2) observed on STO substates. The reason for improvement in J_c and microstructural properties in the case of V_2O_5 addition could be due to the low melting of V_2O_5 (690°C) which can act as a very good surfactant during deposition. Over all, we have realized that Nb_2O_5 addition or V_2O_5 addition to YBCO have shown significant improvement over the undoped $YBa_2Cu_3O_{7-x}$ films grown under identical conditions

1. INTRODUCTION

Research in high temperature superconductivity (HTSC) has made significant progress towards improving the microstructural and crystallographic quality of thin films during the last four years [1-3]. Effect of addition or substitution of transition metal elements in YBCO compound has been investigated and it is well established that superconducting properties will be suppressed by substitution at the Copper site by elements like Al, Ag, V, Nb, Ta and more severely suppressed by the substitution of Fe, Co, Ni & Zn [4,5,9]. Also, addition of transition metal elements to YBCO has resulted in similar effects above a certain concentration of additive [6]. Evidences confirm that Nb_2O_5 addition upto 0.5% has resulted in improvement of mechanical, microstructural and superconducting properties of YBCO compound in bulk form [7-8]. It has been stated that Silver plays an important role in improving the microstructural and transport properties [10-11] due to dissociation of Ag_2O on the substrate and the increased mobility of Ag atoms segregating out of the YBCO grains is responsible for the enlargement and alignment of grains in Ag-doped YBCO films. This result has motivated us to study the doping of some oxides which can melt on the substrate at low temperatures to aid the grain growth. In the present study we report the addition effect of V_2O_5 and Nb_2O_5 to YBCO on its superconducting properties.

2. EXPERIMENTAL

Targets for the Laser deposition were prepared by mixing 3N pure V_2O_5 and Nb_2O_5 powders with a well characterized $YBa_2Cu_3O_y$ (YBCO, 99.99% pure) in the concentration range of 0.0 to 4 wt% by solid state reaction method. Thin films of above samples were made using an excimer laser (Lambda Physik 301:KrF,248 nm and 300mm focal length quartz lens for laser beam focussing) [12]. The substrate to target distance was 4.5cm and growth pressure was

200 mTorr oxygen at 700°C substrate temperature and films were deposited in the thickness range 1500-2000 Angstroms. Structural characterization was done using JEOL 8030 XRD powder diffractometer and surface morphology of the films were studied by JEOL 840 scanning electron microscopy (SEM). DC electrical resistivity was measured by using standard linear four probe technique. Critical current density measurements were carried out using laser patterned 40-20 μm wide and 1mm long microbridges. The standard voltage criterion of 1μV/mm was used for determining J_c.

3. RESULTS AND DISCUSSION

a) V_2O_5 DOPED YBCO THIN FILMS :

XRD data has shown c-axis oriented films for 0.5 to 1 wt% V_2O_5 added YBCO thin films. An addition 4 wt% of V_2O_5 has yielded poor quality superconducting thin films (fig. 3) compared to undoped YBCO thin film. Undoped YBCO thin film made under identical conditions has relatively lower T_c(≈89K) and J_c (≈1.2x10^{6}A/cm^2 at 77K) values. The best results for V_2O_5 doped YBCO thin films were observed for 0.5 wt% addition ($T_{c,o}$ ≈ 89.5K and J_c≈ 3.6x10^{6}A/cm^2 at 77K). Such high Jc values in the case of undoped YBCO thin films could be realized only at higher deposition temparatures (800°C) on STO<100> substrate [9]. The V_2O_5 doped YBCO thin films deposited on LAO substrate have yielded relatively inferior quality superconducting flims when compared to that deposited on $SiTiO_3$ <100> substrate. The reason for this could be a good lattice match of $SiTiO_3$ with YBCO. We couldn't get any information from scanning electron micrographs as they are featureless which may be due to perfect orientation of grains. It is evident from fig. 3, the slope of the T_c-T vs $\sqrt{J_c}$ plot of V_2O_5 doped films is larger compared to that of undoped YBCO film, indicating grain enlargement and reduction of weak links.

b) Nb_2O_5 DOPED YBCO THIN FILMS :

Our results show that Nb_2O_5 addition upto 0.5 wt% in

bulk has improved the superconducting properties of YBCO compound, however, no substantial improvement in the case of thin films deposited even on $SrTiO_3$<100> substrates has been noticed. X-ray diffraction patterns have showed (fig. 1) that films are c- axis oriented YBCO along with growth of <hoo> oriented a secondary phase YBa_2NbO_6 with the increase of $Nb_2O_5 \geq$ 1wt%. However, the $T_c \approx 89.1$ and $J_c = 1.6 \times 10^6$ A/cm^2 for Nb = 0.5 wt% doped YBCO thin films have been recorded, degradation of superconducting properties has been noticed with increase in Nb_2O_5 concentration ($\geq$ 1wt%). The slope of $T_c - T$ vs $\sqrt{J_c}$ plot is slightly larger than the undoped YBCO film but smaller than V_2O_5 doped YBCO thin film which indicates that the grain size has not substantially improved when compared with that of V_2O_5 added film.

c) POSSIBLE EXPLANATION :

From the above results it is clear that V_2O_5 addition has improved the quality of YBCO superconducting thin films compared to that of Nb_2O_5 added YBCO thin films on $SrTiO_3$ substrate. Films deposited on $LaAlO_3$ substrates have resulted in poor quality due to the lattice mismatch between substrate and film. However, there is an improvement in J_c of 0.5 wt % V_2O_5 added film compared to that of Nb_2O_5 added and undoped YBCO film. Due to its low melting point, V_2O_5 during growth process may act as a surfactant and aids in better coalition of the individual grain which leads to increase in grain size of YBCO, where as in the case of Nb_2O_5 addition since the melting point is very high such a process does not take place. This is clearly evidenced in the improvement in J_c in the former case. De Gennes [13] and Clarke [14] have predicted a mechanism that near T_c the critical current density of S-N-S junctions can be expressed as

$$J_c(T) \alpha (T_c - T)^2 \exp (-d/\xi_n)$$

Where d is the thickness of the the grain boundary layer and ξ_n is the coherence length. From this equation the nature of grain boundaries in doped and undoped YBCO thin films can be studied by plotting $T_c - T$ vs $\sqrt{J_c}$ and the slope of this plot will

decide the grain boundary domain thickness which in turn reflects on the nature of weak links. We have plotted T_c-T vs $\sqrt{J_c}$ values upto 77K for the sake of comparison in the cases of 0.5 wt % added V_2O_5 and Nb_2O_5 and undoped YBCO film. From fig.2, it is evident that V_2O_5 addition yields a larger slope value compared to Nb_2O_5 doped and undoped YBCO thin films, which is indicative of improvement in grain structure.

CONCLUSIONS

The effect of V_2O_5 and Nb_2O_5 addition on the superconducting properties of YBCO thin films is studied. It has been realized that V_2O_5 can act as a very good surfactant than Nb_2O_5 because of its low melting point. Also, it is found that there is an improvement in the J_c of the 0.5 wt% V_2O_5 doped YBCO thin film compared to that of Nb_2O_5 (0.5 wt %) doped and undoped YBCO thin films. This could be due to the surfactant effect of V_2O_5 which melts at relatively low temperature and improves the grain structure. On the other hand, the addition of Nb_2O_5 (which has high melting point) does not show such improvement.

ACKNOWLEDGEMENTS:

One of the authors (SS) would like to thank University Grants Commission, INDIA for financial support and (A.K.B) is thankful to Council of Scientific and Industrial Research (CSIR) for HTSC research support .

REFERENCES:

1. J. Z. Sun, M. J. Scharen, L.C. Bourne. J.R Schrieffer : Phys. Rev. B.44(1991) 5275.
2. B. Roas, L. Schultz, G. Saemann and Ischenko : Phys. Rev. Lett. 64(1990) 479.
3. S.Tahara S.M.Anlage, J. Halbritten, C.B.Eom, D.K. Fork, T.H.Geballe and M.R. Beasley : Phys. Rev. B 41(1990) 11203.
4. Y.Maeno T. Tomita M.Kyogoku, S.Awaji, Y.A. Oki, K.Hoshimo, A. Mimanit,T. Fujita,: Nature328(1987) 512.
5. G.Xiao, M.Z.Leeplak, A.Gavnm, F.H.Steitz, A.Bakshai and C.L.

Chein Phys. Rev. Lett.60(1988) 1446.

6. C.W. Kammlott, T.H. Tiefel and S.Jin, Appl. Phys. Lett 56(1990) 2459.
7. Yasuo Hikichi, T.Maruta S.Suziki, M.Miyamoto, S.Okada and K.Kudou. Jpn. J. Appl. Phys. 31(1992) L1232.
8. K.V.Paulouse, J.Koshy, A.D.Damodaran Jpn.J. of App. Phys.31(1992) L1232.
9. V.P.N Padmanabhan and K.Shahi Physica C 208(1993) 263.
10. R.Pinto et.al, Physica C 207(1993) 13.
11. D.Kumar et.al, Appl.Phys.Lett.62(1993) 3572.
12. R.Pinto et.al, Physica C 196(1992) 264.
13. P.G.DeGennes, Rev Mod Phys 36(1964) 225.
14. J. Clarke, Proc R.Soc. London A 308(1969) 447.

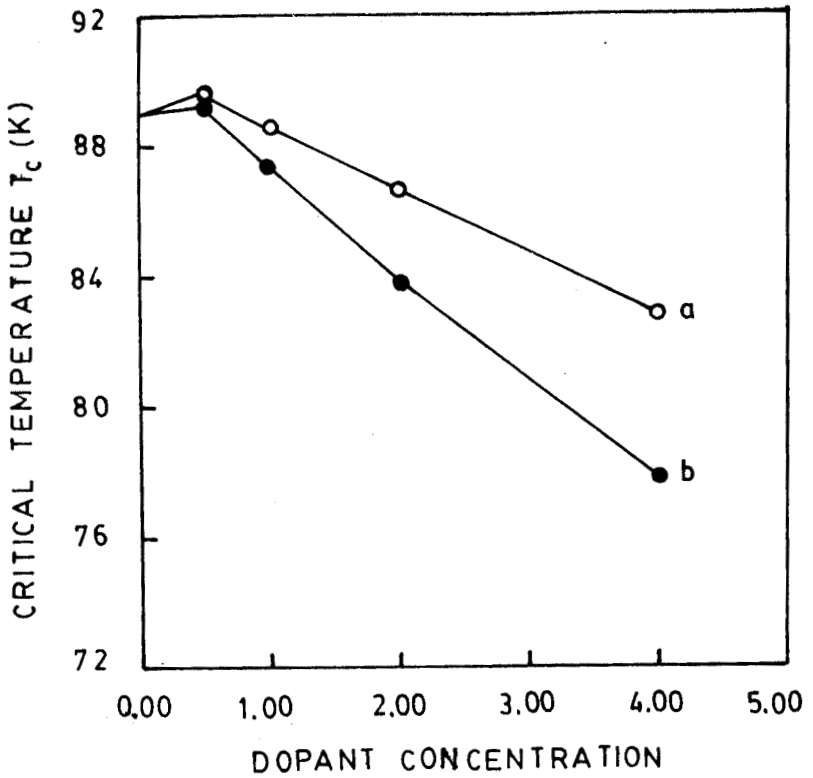

Fig.1. Dopant conc. vs. T_c plots for
(a) V_2O_5 doped YBCO thin film
(b) Nb_2O_5 doped YBCO thin film

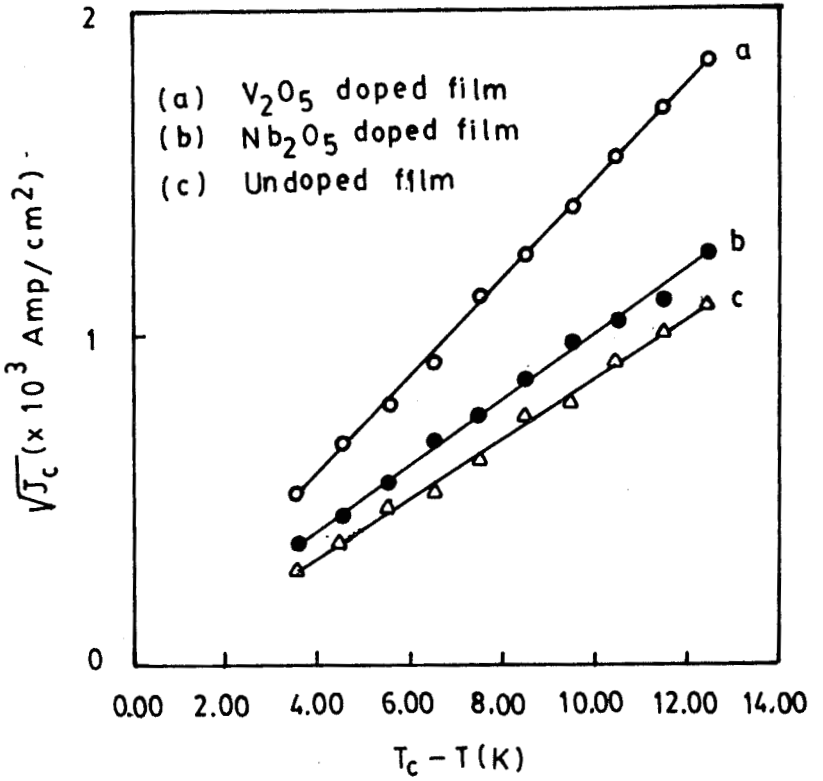

Fig.2. $\sqrt{J_c}$ vs $(T_c - T)$ plots for undoped, V_2O_5 doped and Nb_2O_5 doped YBCO films grown at 700°C on $SrTiO_3$ <100> Substrate.

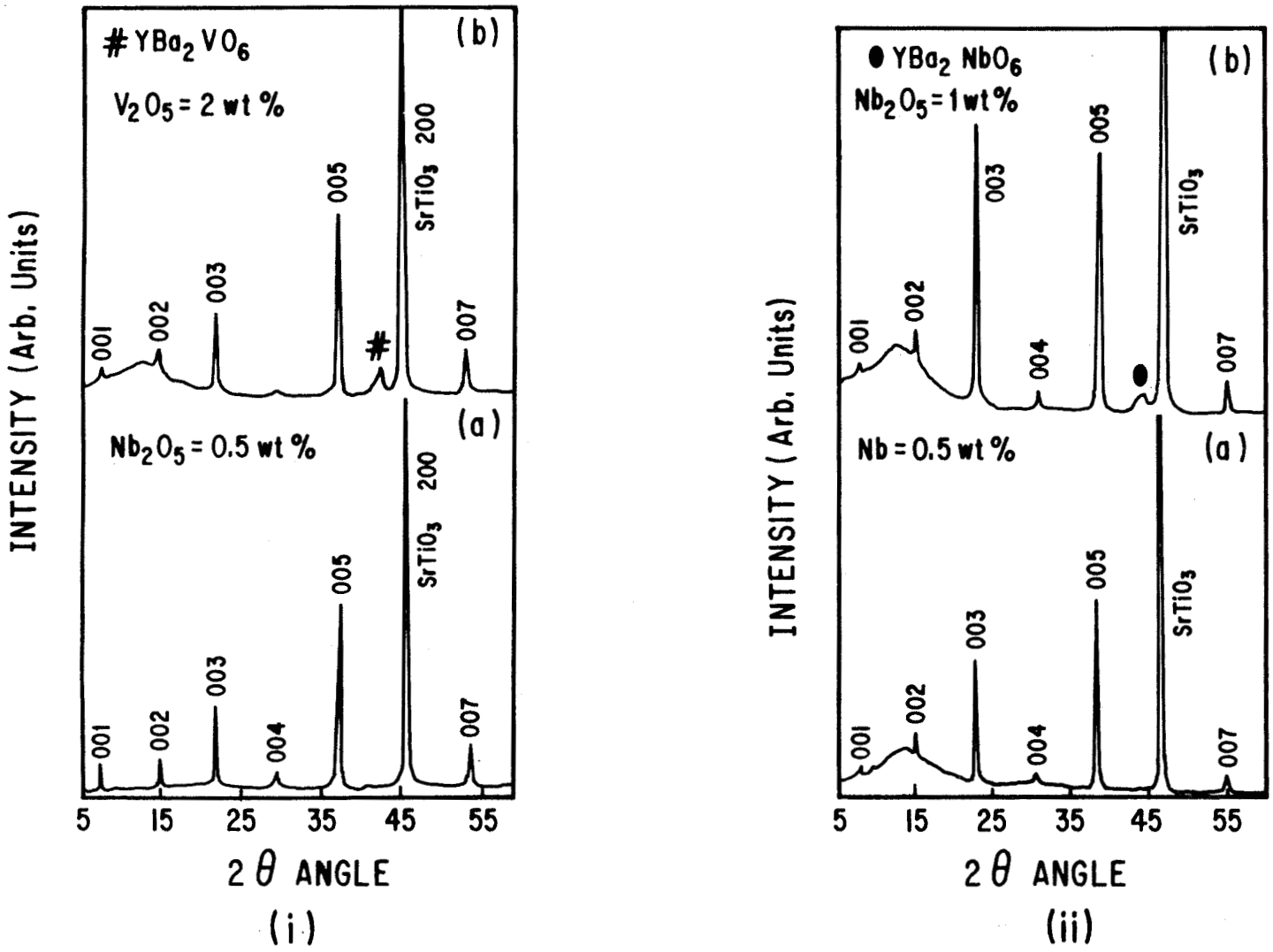

Fig. 3. Xrd Patterns of (i) V_2O_5 (ii) Nb_2O_5 added YBCO Thinfilms.

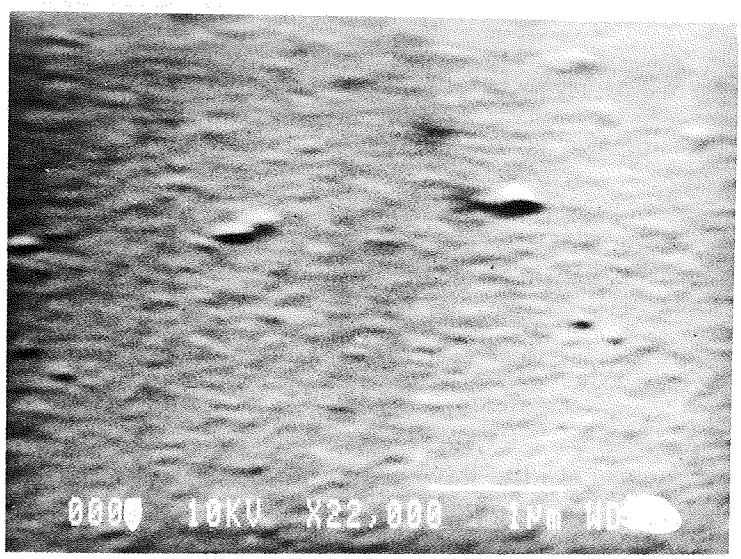

(A)

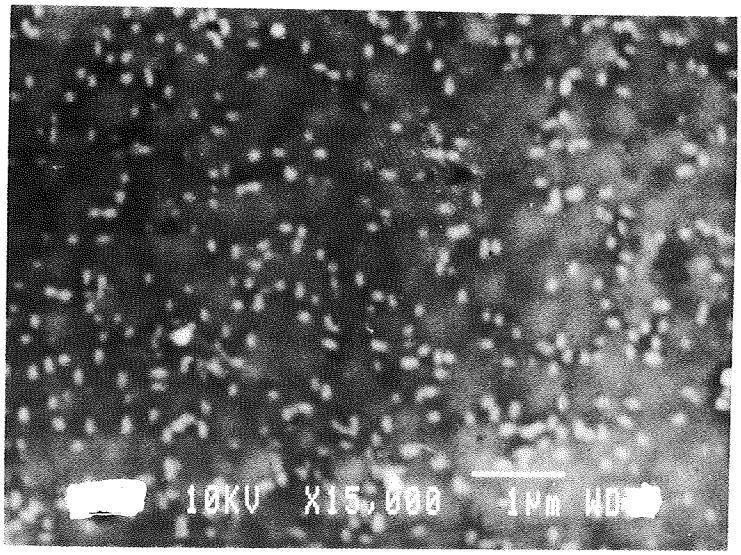

(B)

Figure 4.- Scanning Electron Micrograph for (A) V_2O_5 and (B) Nb_2O_5 doped YBCO thin film.

SINGLE SCAN
S27-76 314017
10P.
343.59

Transparent Magnetic State in Single Crystal $Nd_{1.85}Ce_{0.15}CuO_{4-y}$ Superconductors

F. Zuo
Physics Department, University of Miami
Coral Gables, FL 33124

Several experimental studies have been reported as evidence of Josephson coupling between the superconducting layers in the highly anisotropic oxide such as the $Bi_2Sr_2CaCu_2O_8$ and $Tl_2Ba_2CuO_6$ systems[1-8]. These include the large penetration depth of 100 μm measured[1], ac and dc Josephson effects[3]. Recently two critical temperatures corresponding to Josephson coupling in between the layers and the Berezinskii-Kosterlitz-Thouless transition in the ab-plane have been directly observed in the transport measurements[7]. If the field is applied parallel to the superconducting layers, the magnetic excitation is not the conventional Abrikosov vortices, but the Josephson vortices which extend λ_{ab} in the c-axis direction and $\lambda_J = \gamma s$ in the plane (s is the interlayer distance, γ is the anisotropy constant). Because of the weak screening effect associated with the Josephson vortices, there have been predictions of magnetic transparent states at magnetic field above a characteristic field H_J, a behavior distinctively different from that of the type-II superconductors.

In this paper, we report an experimental result which illustrates a transition from the Meissner state to the magnetic transparent state in single crystal of $Nd_{1.85}Ce_{0.15}CuO_{4-y}$. Magnetization has been measured as a function of temperature and field in the magnetic field parallel or close to ab-plane geometry. For a fixed magnetic field, the magnetization shows a two-step transition in M(T); for a fixed temperature, the magnetization shows an abrupt change to almost zero value above a characteristic field H_J, an indication of magnetic transparent state. The data of magnetization as a function of field clearly deviates from the behavior predicted by the Abrikosov theory for type-II superconductors. Instead, the data fit well into the picture of Josephson decoupling between the CuO_2 layers[8].

Single crystals of $Nd_{1.85}Ce_{0.15}CuO_{4-y}$ are grown using a directional solidification technique[9]. Four crystals are used in the measurement with average dimensions

of 1×1×0.02mm. Extensive measurements were made on two samples A and B with T_c of 22.5K and 21K, respectively. Typical magnetic transition widths measured at 1G with zero-field cooling are about 1–2K. Measurements are performed using a Quantum Design magnetometer with low field options. After degaussing and magnet resetting (quenching) the remanent field is typically 5–10mG. All measurements were done with the sample zero-field cooled to a temperature below T_c. Magnetizations in both directions H || ab and H⊥ ab were measured. For samples with ab-plane aligned parallel to the field, misalignment of a few degrees were often observed.

Shown in Figure 1(a) and (b) are plots of magnetization of sample A as a function of temperature in field parallel to c-axis and ab-plane, respectively. In Figure 1(a), the transition temperature T_c is about 22.5K and M(T) is almost flat for T below 20K. The transition width is less than 2K in the applied field of 1G, an indication of high crystal quality. The magnetization in the field close to ab-plane direction is clearly different from that of field parallel to c-axis direction. For an applied field of 10G, there are two apparent transitions. The high temperature transition corresponds to the same T_c as from Figure 1(a), the lower transition starts around 12K and magnetization saturates above 16K.

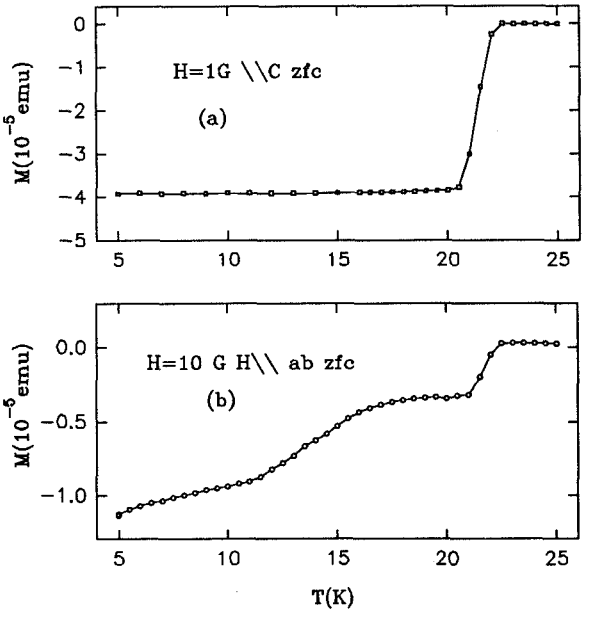

Fig. 1 Temperature dependence of magnetization in field parallel to c-axis (a) and ab-plane (b).

Shown in Figure 2 is an overlay of magnetization as a function of temperature of sample A at different applied field H=30G, 40G, 50G and 60G. Again, two

regimes are clearly distinguishable. In the low temperature regime, the magnetization is nonlinear with the applied field. At the lowest temperature measured (5-6K), magnetization increases in magnitude from 30G to 40G, then decreases at 50G and followed by further increase at H=60G. The magnetization of H=50G and 60G crossover at higher temperature ($\sim$ 8K). In the high temperature regime, the magnetization is relatively flat with respect to temperature. The magnitude of M is quasi-linear with field H. With further increases in temperature the sample becomes normal with paramagnetic susceptibility above T_c. The transition width increases with increasing field.

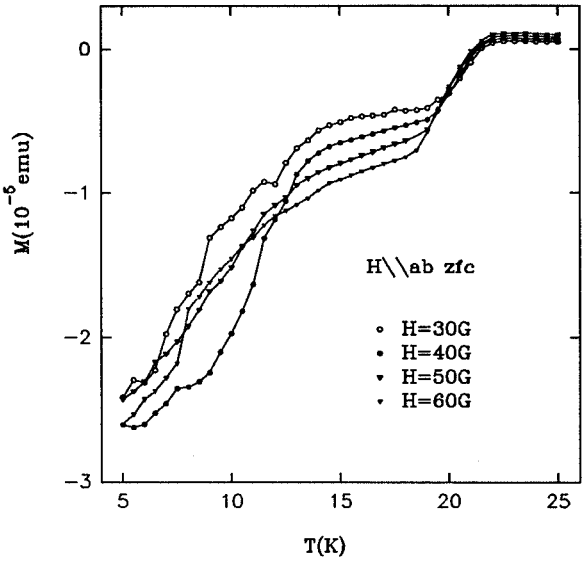

Fig. 2 Temperature dependence of magnetization at different fields H=30G, 40G, 50G and 60G with the field parallel to ab-plane.

The nonlinear field dependence of M observed at low temperature is in contrast with magnetization in the c-axis direction. To understand this anomalous behavior, we have performed detailed magnetization as a function of field at fixed temperatures. For these measurements, the sample is zero-field cooled to a set temperature and M is measured with the magnet set in the non-overshot, persistent mode. Plotted in Figure 3 is a typical magnetization as a function of field for a second sample B of T_c=21K.

Two linear regimes are observed. In the first regime, M is linear in H (<65G), then followed by an abrupt increase in M at a critical field (H_J=65G); in the second regime (H>100G) M is again linear in H. For intermediate field $65G < H < 100G$, additional, smaller jumps are typically observed. In the H-descending direction, M is

linear all the way to zero field with the same slope defined in the second regime. This characteristic dependence has been observed in $Bi_2Sr_2CaCu_2O_8$ single crystal[6] where detailed angular dependence were performed to confirm the fact that the M(H) in the second regime is the contribution of $M_\perp$ (parallel to c-axis) due to misalignment. We have also checked it by varying the sample orientation slightly, and we found the slope of M(H) changes accordingly in the second regime. Typical misalignment is about 2-6 degrees.

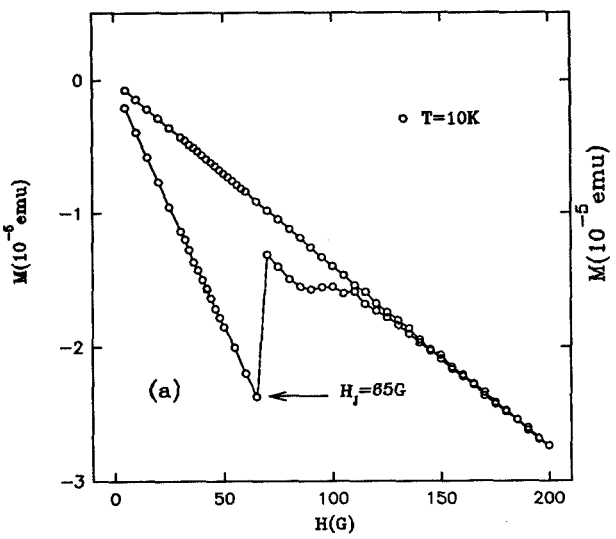

Fig. 3 Magnetization as a function of applied field at T=10K for sample B.

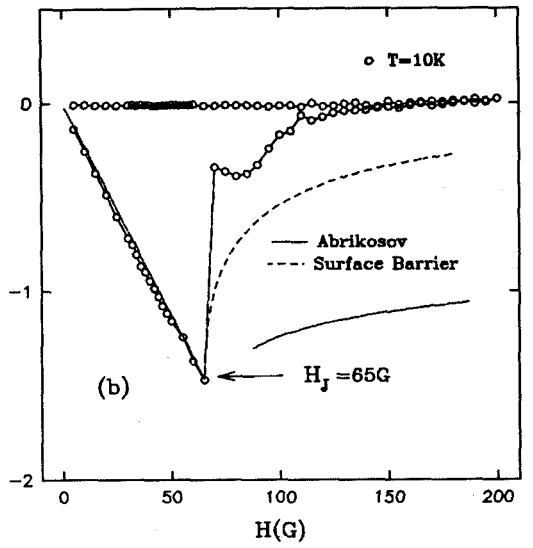

Fig. 4 The corrected magnetization as a function of applied field. The dashed and dotted line are theoretical fits.

The measured magnetic moment M can be written as $M = M_{||}\cos\theta + M_\perp \sin\theta)$ with $M_{||} = (VH\cos\theta/4\pi)/(1-N_{ab})$ and $M_\perp = (VH\sin\theta/4\pi)/(1-N_c)$, where V is the volume of the sample, θ is the angle between the ab-plane and the applied field, and N_{ab} and N_c are the demagnetization factors for field along the ab-plane and c-axis, respectively. For sample B, we obtained $1/(1-N_c) \sim 110$ using the susceptibilities measured on both directions. Shown in Figure 4 is a plot of magnetization along the ab-plane after subtracting the contribution of $M_\perp$. The $M_\perp$ contribution is obtained by measuring the slope χ_2 of the second linear regime or the slope of the descending branch. The corrected magnetization is given by $M = M - \chi_2 H$. From the corrected magnetization and χ_2 one can calculate the misalignment angle to be around 3.3 degrees. The corrected magnetization, again, shows a sharp transition in M at H=65G, followed by a plateau and then M goes to zero quickly starting at about H=85G. The jump in M at H_J at T=10K is about 80% of full Meissner value. The dashed and dotted lines are models to be discussed later. On the descending branch

of the magnetization, M is essentially zero, independent of the field value.

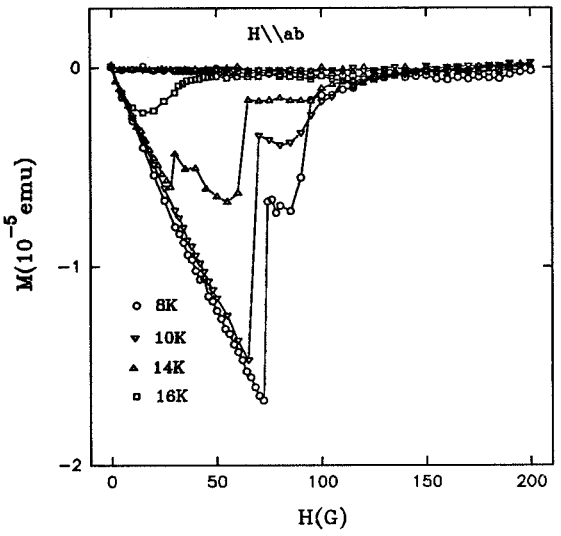

Fig. 5 An overlay of magnetization as a function of field at different temperatures T=8K, 10K, 14K and 16K.

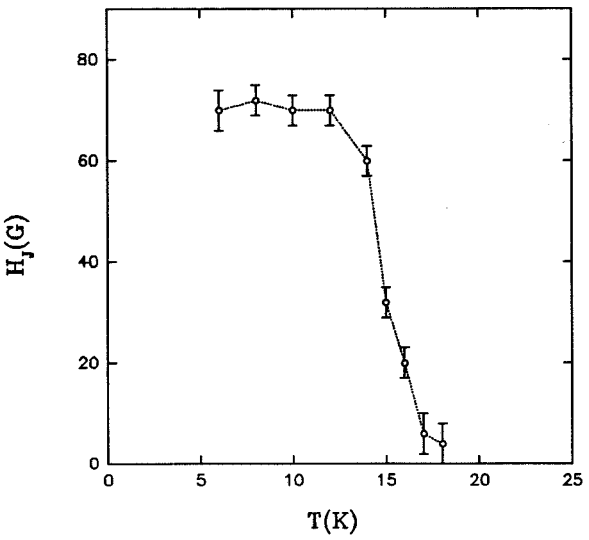

Fig. 6 The first critical field as a function of temperature.

Plotted in Figure 5 is an overlay of magnetization (after subtraction) as a function of field at T = 8, 10, 14, and 16K. The overall features of M at different T are similar, but some differences are observed. For T=8K, the first transition occurs at H=70G, followed by a second transition at about H=82G. The plateau seen in M at T = 10K clearly becomes a sharp transition. At T=14K, there are three transitions in M(H), with the largest jump in M occurring at the second transition. The transition is continuous at T=16K. We define the critical field H_J to be field value at the first jump. As is clear from the data, the critical field decreases with increasing temperatures, and the increase in M at H_J becomes more gradual. For T>15K, no abrupt changes are observed, the shapes of M(H) are similar to the reported data on $Bi_2Sr_2CaCu_2O_8$.

Figure 6 is a plot of the first critical field as a function of temperature. For temperature below 12K, the critical field H_J is almost constant around 70G, while H_J decreases sharply for T greater than 12K.

To study the effect of transition temperature on the critical field H_J, we have performed similar measurements on several $Nd_{1.85}Ce_{0.15}CuO_{4-y}$ crystals. Shown in Figure 7 is an overlay of magnetization as a function of field at different temperatures for sample A. Again the abrupt changes are observed in the M(H) at the critical field.

At T=5K, several steps are in fact observed with the first critical field around 35G. At higher temperatures, the similar features to that of Figure 5 are observed, except the critical field is much smaller than that of sample B. The magnetization in descending branch of the hysteresis loop is also zero after correction.

The direct measurement of M(H) is consistent with the results of magnetization as a function of temperature. In Figure 2, the nonlinear field dependence of M seen at low temperature is a direct reflection of abrupt change in M at $H_J \sim 35G$. The crossover between the 50G and 60G data at low temperature indicates the relative contributions due to the jump and $M_\perp$. The quasi-linear M on H demonstrates the fact that at high temperatures the main contribution is from $M_\perp$ when the sample is misaligned.

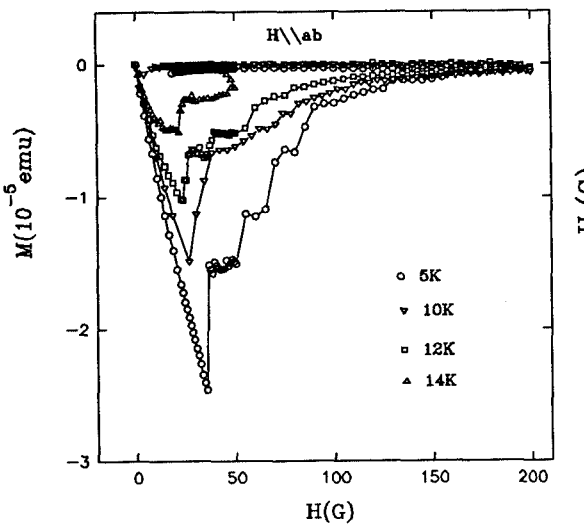

Fig. 7 An overlay of corrected magnetization as a function of temperatures T=5K, 10K, 12K,and 14K for sample A.

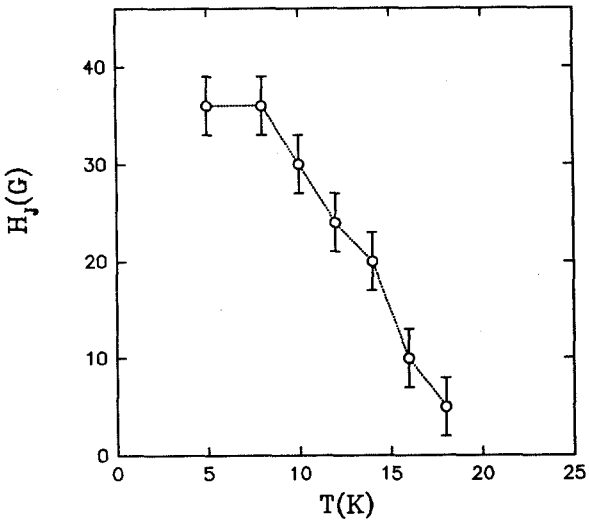

Fig. 8 The first critical field as a function of temperature for sample A.

Plotted in Figure 8 is the temperature dependence of the first critical field. The temperature dependence is also similar to that of sample B, i.e. H_J saturates at low T and decreases sharply at high T. Notice the saturation value of H_J is considerably smaller than that of sample B.

The abrupt change in the magnetization at the critical field is clearly different from that of conventional type-II superconductors. The magnetization of conventional type-II superconductors can be well described by the Abrikosov's theory[10]. At field

slightly larger than the lower critical field H_{c1}, the magnetization is obtained by neglecting interaction between vortex lines $4\pi M = \frac{2\phi_o}{\sqrt{3}\lambda^2}\{\ln[\frac{3\phi_o}{4\pi\lambda^2(H-H_{c1})}]\}^{-2} - H$. In the case of high T_c cuprate, the very large value of the Ginzburg-Landau parameter κ renders the use of this result to magnetic field very close to H_{c1} ($H_{c1} < H < H_{c1}+10G$). For intermediate fields, the magnetization is given by $4\pi M = -H_{c1}\frac{\ln(\beta' l/\xi)}{\ln(\lambda/\xi)}$ where β'=0.231, and l is the lattice constant given by $B = 2\phi_o/\sqrt{3}l^2$ for a triangular lattice[10]. Assuming $\kappa = \lambda/\xi \sim 20$ and H_{c1}=65G, the equilibrium magnetization can be calculated numerically as a function of field. The result is shown as the dotted line in Figure 4. The jump in M(H) clearly rejects the use of this model.

As suggested by the zero magnetization in the descending branch of the hysteresis loop, the entrance field is determined by Bean-Livingston surface barriers[11]. In the presence of surface barriers, the penetration field is not the lower critical field H_{c1}, but comparable to the thermodynamic critical field H_c. The surface barrier is a result of attractive interaction between an image vortex with the entering vortex. Strong evidence has been found in the field parallel to the c-axis direction in high quality single crystal materials[12, 13, 14] The magnetization for field greater than the penetration field H_p and assuming no bulk pinning, has been discussed in several recent articles[12, 15]. By modeling an Abrikosov lattice in the bulk of the sample and vortex-free zone near the surface due to surface barriers, the magnetization is derived and given by $-4\pi M = H - \sqrt{H^2 - H_p^2}$. The result is plotted as the dashed line in Figure 4. Again, the model deviates from the magnetization data. It is to be noted that the expression above is derived for conventional type-II superconductors, where the flux lattice is the Abrikosov lattice.

The abrupt change occurred at H_J strongly indicates the inadequacy of the use of Abrikosov's theory in the magnetization of $Nd_{1.85}Ce_{0.15}CuO_{4-y}$ crystals in the H $\parallel$ ab direction. Since the $M_\perp$(H) clearly exhibits the Meissner effect in the perpendicular direction, the jump in $M_{\parallel}(H)$ shows directly magnetic decoupling between superconducting layers at the critical field H_J.

For weakly Josephson coupled layered superconductors, the critical current in the c-axis direction, which provides magnetic screening when field is in the ab-plane, is determined by the coupling strength. For small applied field, complete screening of external field is possible. At the critical field, the Josephson coupling breaks down, magnetic field penetrates into the sample. If the layers are effectively decoupled, a transparent magnetic state is expected, due to the fact that the 2D superconducting layers can not support screening current by themselves.

The jump in $M_{\parallel}(H)$ can also be qualitatively understood from the field dependence of critical current of a single Josephson junction: $J_c(H) = J_o \sin(\frac{\pi\phi}{\phi_o})/(\frac{\pi\phi}{\phi_o})$

where $J_c(H)$ is the field dependent critical current, J_o is the maximum zero field critical current, and ϕ is the magnetic flux through the junction. The critical current is almost zero when there is a finite number of Josephson vortices threading through the junction. Assume the magnetization is proportional to the critical current, M should become zero as Josephson vortices penetrate into the junction. For stacked layers with Josephson coupling, the field dependence of J_c should not be the same as that of single Josephson junction, rather one expects a stronger reduction in $J_c(H)$ with increasing H. In this picture, the experimentally observed smaller jumps in the magnetization data thus would indicate the presence of superconducting layers with different Josephson couplings.

To describe the vortex state of the Josephson coupled superconducting stacks quantitatively, one has to solve the coupled Lawrence-Doniach equations[16]. In the case where the applied field is tilted to the superconducting layers, several theoretical models are proposed. Recently it has been shown that there are two distinct vortex structures depending on the anisotropy constant $\gamma = \lambda_J/s$, where λ_J is the Josephson penetration depth and s is the separation between the superconducting layers. If $\lambda_J < \lambda_{ab}$, the theory suggests a tilted vortex line structure, where different segments of vortex lines parallel to the ab-planes are connected by pancakes residing in the ab-planes[17, 18]. If $\lambda_J > \lambda_{ab}$, the model predicts that coexisting sets of perpendicular and parallel vortices should exist when the field is applied close to the ab-plane. The Abrikosov vortices are due to $H_\perp$, and Josephson vortices are due to $H_{||}$. The vortices due to $H_{||}$ and $H_\perp$ act independently of each other. The complete Meissner effect is possible only if $H_{||} < H_{c1}^{||}$ and $H_\perp < H_{c1}^{\perp}$. For $H_{||} > H_{c1}^{||}$, $H_{||}$ penetrates into the layers between the CuO_2 planes almost completely, creating the so called magnetic transparent state[18, 19, 20].

The experimental results clearly demonstrate the complete Meissner state for $H < H_J$. The linear field dependence of M in the descending branch and the overlapping M(H) at high field indicate $H_\perp < H_{c1}^{\perp}$. For $H > H_J$, there are only Josephson vortices parallel to the ab-plane and $M_\perp$ is still in the Meissner state. The jump in M(H) for $H > H_J$ indicates the transition to the magnetic transparent state in Josephson coupled layered superconductors.

The difference in magnetic transition around the critical field between the $Nd_{1.85}Ce_{0.15}CuO_{4-y}$ and the $Bi_2Sr_2CaCu_2O_8$, $Tl_2Ba_2CuO_6$ crystals is not clear. One possibility is that the $Bi_2Sr_2CaCu_2O_8$, $Tl_2Ba_2CuO_6$ crystals studied are very thick[6, 21]. A broad distribution in the coupling strength will smear out the transition. This picture is supported by a recent report which shows a similar abrupt change in M(H) in another $Tl_2Ba_2CuO_6$ crystal[22].

In summary, we have presented an experimental measurement of an abrupt

Josephson decoupling between the CuO_2 planes at the critical field H_J parallel to ab-planes. The abrupt increase in M(H) at H_J is incompatible with the conventional Abrikosov theory. For field $H_{||} > H_J$, the magnetic field has a complete penetration in between the superconducting layers–a magnetic transparent state. A more detailed study of H_J as a function of T_c will help to elucidate the mechanism of superconductivity in the layered superconductors.

References

[1] J. R. Cooper, L. Forro, and B. Keszei, *Nature* (London) **343**, 444 (1990).

[2] J. C. Martinez et al. *Phys. Rev. Lett.* **69**, 2276 (1992).

[3] R. Kleiner, F. Steinmyer, G. Kunkel, and P. Muller, *Phys. Rev. Lett.* **68**, 2394 (1992).

[4] R. Fastampa, M. Giura, R. Marcon, and E. Silva, *Phys. Rev. Lett.* **67**, 1795 (1992).

[5] A. Schilling, R. Jin, J. D. Guo, and H. R. Ott, *Phys. Rev. Lett.* **71**, 1899 (1993).

[6] N. Nakamura, G. D. Gu, and N. Koshizuka, *Phys. Rev. Lett.* **71**, 915 (1993).

[7] Y. M. Wan, S. E. Hebboul, D. C. Harris, and J. C. Garland, *Phys. Rev. Lett.* **71**, 157 (1993).

[8] F. Zuo, S. Khizroev, Xiuguang Jiang, J. L. Peng and R. L. Greene, *Phys. Rev. Lett.* **72**, 1746 (1994).

[9] J. L. Peng, Z. Y. Li, and R. L. Greene, *Physica C*, **177**, 79 (1991).

[10] P. G. de Gennes, *Superconductivity of Metals and Alloys* (Benjamin, New York, 1966).

[11] C. P. Bean and J. D. Livingston, *Phys. Rev. Lett.* **12**, 14 (1964).

[12] L. Burlachkov, Y. Yeshurun, M. Konczykowski, and F. Holtzberg, *Phys. Rev. B* **45**, 8193 (1992); L. Burlachkov, *Phys. Rev. B* **47**, 8056 (1993).

[13] Ming xu et al. *Phys. Rev. B* 48, 10630 (1993).

[14] F. Zuo, S. Khizroev, Xiuguang Jiang, J. L. Peng and R. L. Greene, *Phys. Rev. B* **49**, 12326 (1994).

[15] J. R. Clem, *Proc. of Low Temp. Phys.–LT 13*, ed. Timmerhaus et al. (Plenum, NY, 1974), Vol.3, P.102.

[16] W. Lawrence and S. Doniach, in *Proceedings of Twelfth International Conference on Low Temperature Physics*, edited by Eizo Kanda (Acedemi, Kyoto, 1971), P.361.

[17] D. Feinberg, and C. Villard, *Phys. Rev. Lett.* **65**, 919 (1990).

[18] L. N. Bulaevskii, *Sov. Phys. JETP* **37**, 1133, 1973; and L. N. Bulaevskii, M. Ledvij, and V. G. Kogan, *Phys. Rev. B* **46**, 366 (1992); L. N. Bulaevskii and J. R. Clem, *Phys. Rev. B* **44**, 10234 (1991).

[19] P. H. Kes, J. Aarts, V. M. Vinokur, C. J. van der Beek, *Phys. Rev. Lett.* **64**, 1063 (1990).

[20] S. Theodorakis, *Phys. Rev. B* **42**, 10172 (1990).

[21] F. Zuo, S. Khizroev, S. Voss and A. M. Hermann, *Phys. Rev. B* **49**, 9252 (1994).

[22] N. E. Hussey, A. Carrington, J. R. Copper and D. C. Sinclair (to be published).

SINGLE SCAN
528-26
314063
pp. 3-13 159

Processing and Property Evaluation of Metal Matrix Superconducting Materials

Appajosula S. Rao

Naval Surface Warfare Center
Annaplois, MD 21402

ABSTRACT

Metal - superconductor (YBCO) systems have been prepared and characterized by resistivity, ac susceptibility and dc SQUID magnetic moment measurements. The silver composites showed superconducting transition for all the composites processed and the superconducting transition temperature tends to depend upon the concentration of the silver in the composite. Aluminum composites showed an unusual resistivity results with two transitions around 90 K and 120 K. The superconducting property of silver composites can be explained qualitatively in terms of the proximity theory that has been suggested for the low temperature superconductors.

Key Words : Processing, superconductivity, silver , aluminum / YBCO composites

INTRODUCTION

The present day technology of superconducting electrical systems requires cryogenic systems that are operational at liquid helium temperatures (temperature ~ 4 K). The new generation of ceramic superconductors that can superconduct at liquid nitrogen temperatures (temperature ~ 77 K) offer a potential and logistical advantage for both the system reliability and operational cost. Although, few superconducting component systems that can operate at liquid nitrogen temperatures were demonstrated, the full potential of these materials has not been exploited to date. This is essentially due to the fact that the materials are very hard brittle and difficult to form into net shaped components. In the open literature, many attempts were reported to improve the ductility of the high temperature superconducting materials by composting them with silver or gold [1-2]. However, the phenomenology of the superconductivity in the metal - superconductor composite system has yet to be established. This project was undertaken in an attempt to develop a processing methodology for producing flexible superconducting wires / tapes with different metallic species and to model the mechanism of the superconductivity of these composite systems. In this paper, the experimental results obtained on 0 - 72 wt.% silver or aluminum composites and a possible model to explain the superconducting behavior of the composites is being presented.

EXPERIMENTAL PROCEDURE

The basic superconducting ceramic powder, $YBa_2Cu_3O_{6+x}$, was prepared by solid state chemical reaction and the details of the powder synthesis were given elsewhere [3]. Although pure $YBa_2Cu_3O_{6+x}$ powder has good superconducting properties, we found that the presence of excess copper oxide will improve the final composite properties. . Therefore, during the synthesis of the superconducting $YBa_2Cu_3O_{6+x}$ powder, nearly 5 moles of excess copper oxide were added to the precursors. It should be pointed out that any reference in this paper for $YBa_2Cu_3O_{6+x}$ represent the YBCO with 5 moles of excess CuO. From the micro structural characterization and chemical compositional analysis, it was found that the excess (5 moles) copper oxide remained unreacted with the

final $YBa_2Cu_3O_{6+x}$ compound. However, a small amount of the excess CuO was reduced to metallic copper.

The as-synthesized $YBa_2Cu_3O_{6+x}$ powder and commercial silver or aluminum powder were mixed thoroughly in dry state in a ball mill using zirconia balls for one hour. The powder mixture (silver or aluminum powder and $YBa_2Cu_3O_{6+x}$ powder) was dry pressed into small 2.5 cm diameter discs under an applied pressure of 25,000 psi. The cold pressed discs were placed between two thick silver or aluminum plates and were sintered at 880°C (in the case of silver) and at 400°C (in the case of aluminum) for 30 minutes. During sintering the composite sample was also subjected to a constant axial load of 10,000 psi. The sintered discs were cooled in nitrogen and were cut into small 2 X 2 X 25 mm bars.

The micro structure of all samples was examined under both optical, scanning and transmission electron microscopes. The structural characterization of the superconducting $YBa_2Cu_3O_{6+x}$ particles was carried out using x-ray diffraction. The electrical resistance of all samples was measured as a function of temperature using a dc four probe resistivity measurement unit, ac susceptibility apparatus and dc SQUID magnetometer.

RESULTS

The as-synthesized $YBa_2Cu_3O_{6+x}$ powder has an average particle size of ~ 10 microns. The morphology of the particles resemble that of small pebbles or rocks. The density of the powder was found to be ~ 6.0 $gmcm^{-3}$. Upon sintering the $YBa_2Cu_3O_{6+x}$ particles tend to sinter to form long elongated rods or plates. The sintered samples show a zero resistance (superconducting) transition and diamagnetic magnetic moment around 86 $\pm$ 4 K and has a crystal structure that represents the orthorhombic structure of $YBa_2Cu_3O_{6+x}$ and the detailed analysis of the results are given else where [4-6].

Silver/$YBa_2Cu_3O_{6+x}$ Composite System

Figure 1 shows typical electrical resistance versus temperature plots of pure silver and silver/$YBa_2Cu_3O_{6+x}$ composites. The zero resistance temperature versus silver concentration in the composites was determined from a number of resistance versus temperature plots similar to those shown in Figure 1 and the results are shown in Table 1. The results indicate that the silver composites show superconducting behavior throughout the entire concentration range investigated (0 - 72 wt.% silver). However, the zero resistance temperature (T_c) tends to decrease with an increase in the concentration of silver in the range 0 - 10 wt.% and 40 - 72 wt.%. The T_c remains nearly independent of silver concentration in the range 10 - 40 wt.%. In addition, the results also suggest that the normal state resistance of the composites decreases with an increase in the silver concentration.

The typical micro structure of silver composites obtained from polished sample surfaces is shown as a function of silver concentration in Figure 2. The results suggest that the distribution of $YBa_2Cu_3O_{6+x}$ in silver matrix is very uniform and the degree of uniformity increases with an increase in the concentration of silver in the composites. In order to model the superconducting property of the composites in terms of the separation distance between two $YBa_2Cu_3O_{6+x}$ particles, a number of optical photomicrographs representing the micro structure of all composites were obtained. From the micro graphs the average particle size was estimated and the results are given in Table 1. Assuming that the particles are spherical, and are not connected in a 3 dimensional network, the $YBa_2Cu_3O_{6+x}$ particle - particle separation distance was estimated as a function of silver concentration and the results are also shown in Table 1 . The results suggest that the particle size of $YBa_2Cu_3O_{6+x}$ increases with an increase in the silver concentration initially in the range 0 - 10 wt.%. For the silver concentration above 10 wt.% this trend is reversed. The results also indicate that the separation distance increases with an increase in the silver concentration.

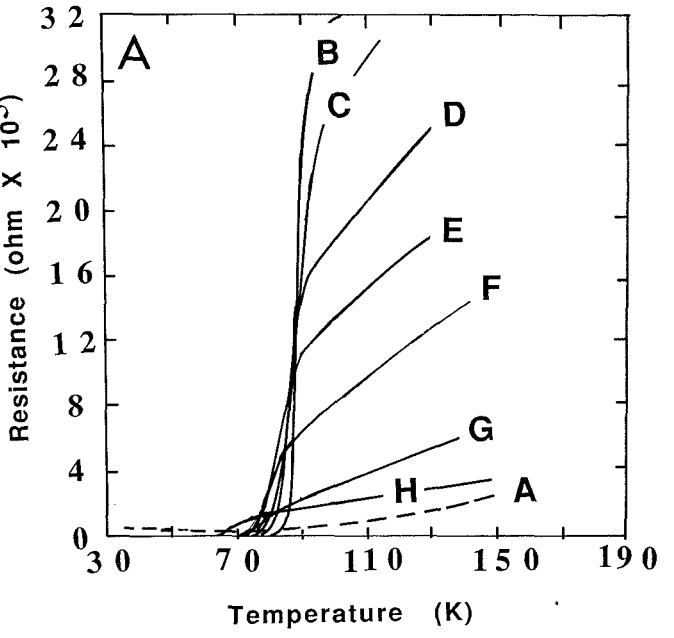

Figure 1. Electrical resistance versus temperature profiles of commercial silver / $YBa_2Cu_3O_{6+x}$ composites. Silver concentration (A) 100, (B) 10, (C) 20, (D) 30, (E) 40, (F) 50, (G) 60 and (H) 63.6 wt.%. The actual applied current 20 milli amp.

Table 1. The superconducting transition temperature (T_c), the normal state resistance measured at 100 K (R_{100K}), the average $YBa_2Cu_3O_{6+x}$ particle size and the particle - particle separation distance measured for sintered silver / $YBa_2Cu_3O_{6+x}$ composites as a function of silver concentration of the composite.

Silver conc. (wt. %)	T_c (K)	R_{100K} (ohm X 10-5	particle size (micron)	separation distance (micron)
0	86 ± 4	2000	35 ± 4	
2	88 ± 4	800	35 ± 4	0.2
5	90 ± 2	300	40 ± 4	0.5
10	82 ± 2	30	45 ± 4	1.0
20	80 ± 2	25	40 ± 4	4.0
30	80 ± 2	16	37 ± 4	8.0
40	82 ± 2	12	25 ± 2	15.0
50	76 ± 2	6	23 ± 2	22.0
55	70 ± 2	4	20 ± 2	26.0
60	68 ± 2	3	18 ± 2	30.0
63.6	62 ± 2	2	16 ± 2	32.0
72.2	62 ± 2	1	14 ± 2	37.0

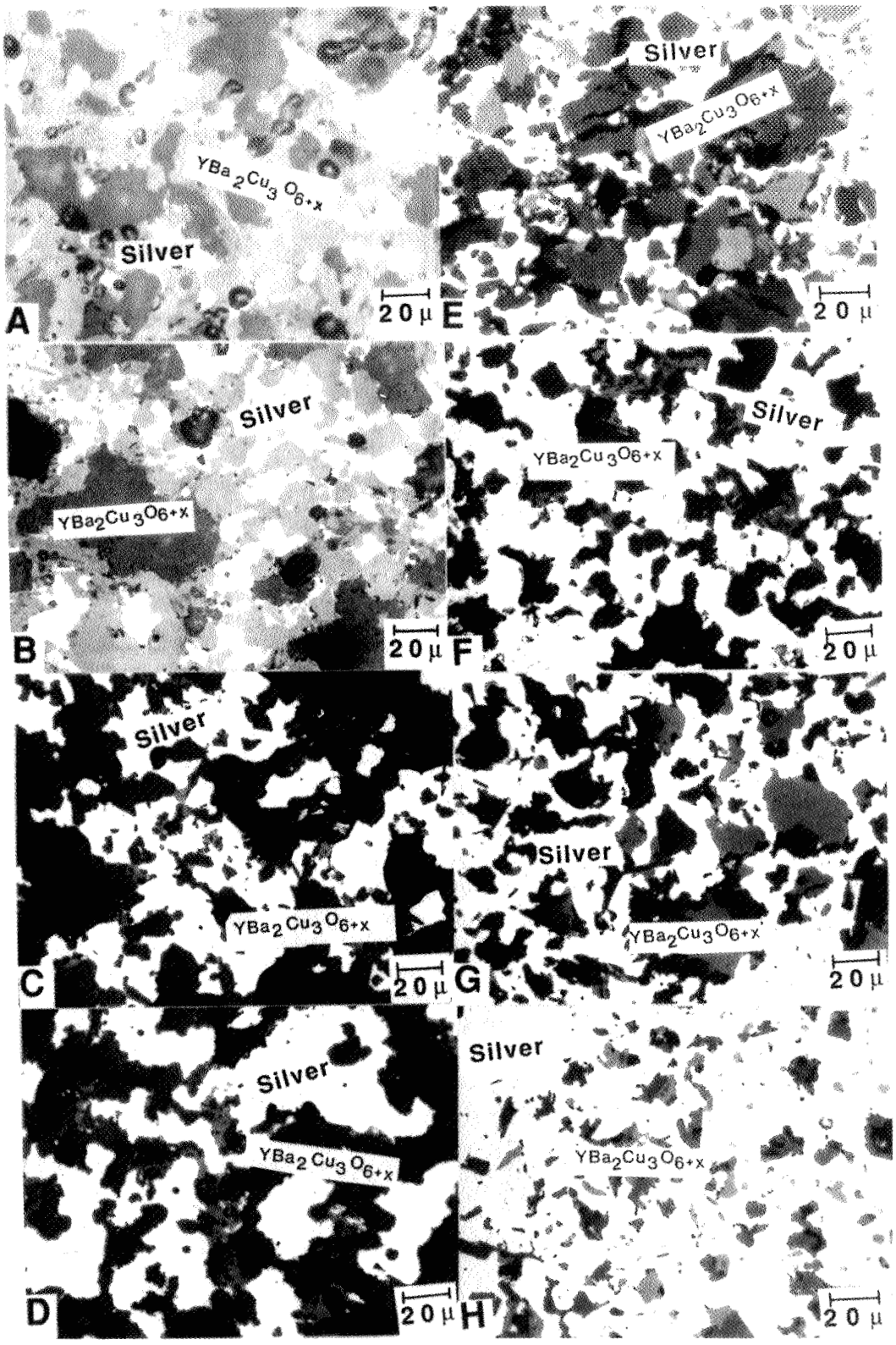

Figure 2. Typical micro structure of polished silver / $YBa_2Cu_3O_{6+x}$ composites. Silver concentration (A) 10, (B) 20, (C) 30, (D) 40, (E) 50 (F) 60 (G) 63.6 and (H) 72 wt.%.

In order to understand the mechanism of the superconducting behavior of the silver composites, the proximity theory was applied. According to the classical proximity theory of low temperature superconductors, the extrapolated length for the diffusion of "Cooper pairs" from superconductor to the non superconducting metallic conductor is ~ 0.1 microns. However, the measured separation distance for the silver superconductors range from 1 - 37 microns. It is therefore, evident from the measured separation distance data that the proximity theory of low temperature superconductors is not applicable to the high temperature superconducting silver composite system. However, an effort was made to estimate the extrapolated length of diffusion of the superconducting electrons into the silver matrix using the Deutscher and de Gennes model that was suggested for low temperature superconducting materials [7].

Although the high temperature superconducting materials have been established during the past five years, the actual mechanism of the superconducting behavior of these materials, in particular in composite systems, has not been understood. The behavior of composites in low temperature superconductors has been explained in terms of the diffusion of "Cooper pairs" from superconducting material into the non superconducting metallic conductor.

In general it has been suggested by Deutscher and de Gennes that the superconducting transition temperature of the composite system (T_{cc}) can be related to the T_{cs} of the pure superconductor and the extrapolated length of diffusion of superconductivity from superconductor to the metal as

$$T_{cc} = T_{cs} - A\,(1/D_s+B)^2 \qquad \text{.....(1)}$$

where A is a constant, D_s is the thickness of the superconducting layer and B is the extrapolation length for the diffusion of superconductivity from a superconductor to the metal.

As a first attempt to explain the superconductivity of the metal matrix composite system, we assumed that the process of the diffusion of superconducting electrons from the superconductor through the non-superconducting metal matrix is similar to that of the diffusion of the electric charge from a polarized oxide surface into the liquid phase and form an electrical double layer at a solid - liquid interface. To analytically model the superconducting behavior, we also assumed that the penetration of the superconducting electrons into the non-superconducting metal matrix constitutes two different regions. In the first region, the electrons form a fixed boundary which is formed due to the leakage of the "Cooper Pairs", a process similar to that of the diffusion in low temperature superconductors (typical distance ~ 0.1 micron). The second region constitutes the superconducting electron diffusion into the metal. Assuming that the electron distribution in the diffused boundary follows Poisson - Boltzmann equation, the superconductivity of the composite can be represented as a function of concentration of the superconducting phase and the extrapolation length for the diffusion of the superconductivity in the simplified final form as

$$(T_{cc} / T_{cs}) = A \exp(-CB) \qquad \text{.....(2)}$$

where A is a constant that represents the "Cooper Pair" leakage distance into the non-superconducting metal
$C = ((1 - f_v) / f_v)$ where
f_v is the volume fraction of the superconducting phase, $(1-f_v)$ is the volume fraction of the non superconducting phase and
B is the diffusional distance for the superconducting electrons into the metal.

The above expressions not only can be applied to test the validity of the proximity theory of low temperature superconductors for high superconducting metal matrix composites, but also can be used for the determination of the extrapolated length of the diffusion of superconductivity from the superconductor

to the metal matrix from the information of the superconducting transition temperature of a composite (T_{cc}) measured as a function of composite composition.

The results of the modeling indicated that the present "T_c versus Silver concentration" data on silver composites can be normalized on the Deutscher and de Gennes's expression (equation 1), over the entire concentration range investigated (i.e. silver concentration range 10 - 72 wt.%). However, the model predicts that the maximum distance that the superconducting electrons can penetrate into the matrix will be ~ 6 microns. A similar analytical treatment of the measured data with the our model reveal that the over all behavior of the silver composites (over the concentration range 10 - 72 wt.%) cannot be normalized into one generalized expression. However, the observed superconducting behavior of silver composites fall into two categories (viz. composites containing 10 - 40 wt.% silver; and $T_c \geq 60$ K) and composites containing 40 - 72 wt.% silver; and $T_c \leq 60$ K). In addition, the present model predicted the diffusional depth for superconducting electrons to range from 0.28 - 2 microns. These results indicate that the predicted extrapolated lengths for the diffusion of superconductivity are too low compared to the measured separation distance (range 1 - 37 micron).

The above disagreement may arise due to several factors. For example, (1) the above models assume that the superconducting phenomena in these materials is similar to that of low temperature (liquid helium temperature) superconductors; (2) the separation distances were estimated taking into consideration only the large superconducting $YBa_2Cu_3O_{6+x}$ particles that were accessible for the estimation of particle size (it is possible that a large fraction of very fine (<0.1 micron) size particles that are often distributed throughout the matrix may account for smaller separation distance between any two adjacent superconducting $YBa_2Cu_3O_{6+x}$ particles); and (3) the model does not take into account the three dimensional effect of the particle - particle separation.

Aluminum/$YBa_2Cu_3O_{6+x}$ Composite System

The typical electrical resistance versus temperature plots of pure aluminum and aluminum / $YBa_2Cu_3O_{6+x}$ composites indicate that all aluminum composites show typical metallic behavior . However, if the concentration of the aluminum in the composites is ~ 60 wt.%, the composite system shows two transitions of the electrical resistance [4]. Figure 3 shows a typical plot of the electrical resistivity of 60 wt.% aluminum composite represented as a function of temperature. The magnetic moment versus temperature profiles of the same sample measured using dc SQUID magnetometer and ac susceptibility method are given in Figures 4 and 5 respectively. The results suggest that the composite shows two transitions around 90 and 120 K respectively. In addition the results also suggest that the composites behave as diamagnetic below 86-88 K. Although, the magnetic moment data does not suggest the presence of diamagnetism above 88 K, it provides ample evidence that the paramagnetic component of the aluminum matrix is being opposed. Such a lowering of the paramagnetic component of the matrix (aluminum) leads to the speculation that a new and higher temperature superconducting phase may be present in these composites. From micro structural characterization of the composites using high resolution electron microscopy, we found that a thin (thickness 10 - 20 nm) layer of new phase is present at the interface between the aluminum matrix and $YBa_2Cu_3O_{6+x}$. No such interfacial film formation and or growth was observed in the silver composites. The detailed analysis, stoichiometric composition and the structure of this new interfacial phase will be reported in the future.

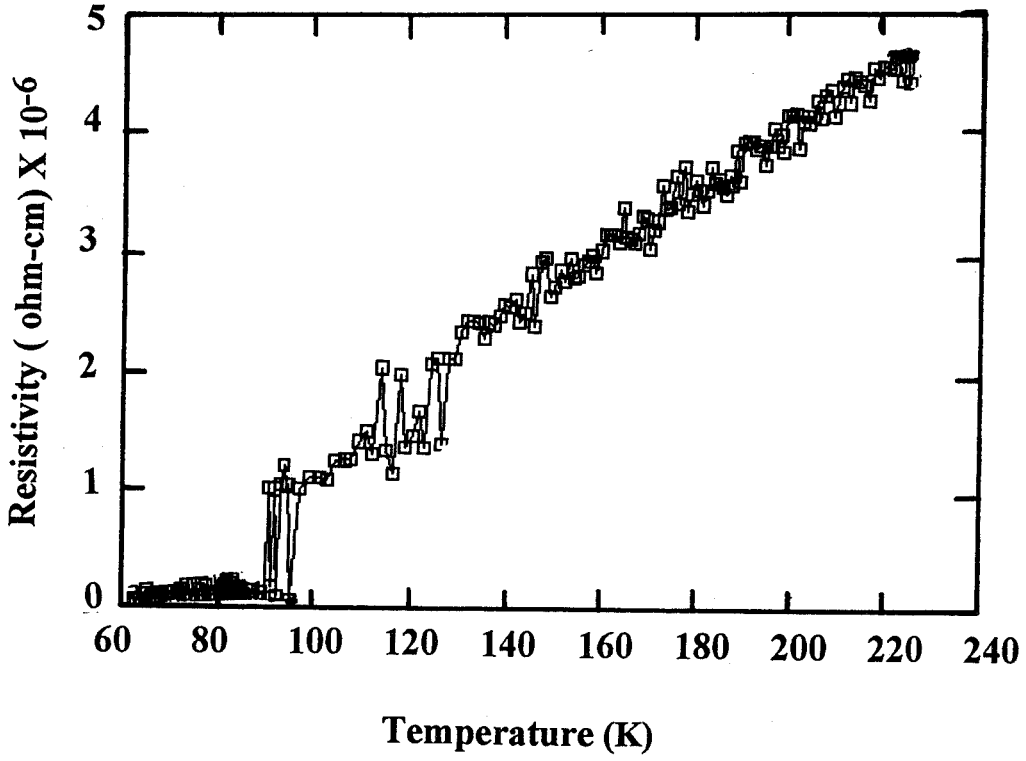

Figure 3. Electrical resistivity versus temperature plot obtained from 60 wt.% aluminum / 40 wt.% $YBa_2Cu_3O_{6+x}$ composite. Actual applied current 20 milli amp.

DISCUSSION

The high temperature superconducting ceramic materials are expected to provide a suitable and cost effective alternative to the presently used metallic superconductors, such as NbTi and Nb_3Sn that are being operated at liquid helium temperatures (~4 K). However, for the large scale processing of the ceramic materials into ductile forms remains unresolved. Although, processing via composite fabrication is the possible practical solution to overcome the brittle nature of the ceramic superconductors, both the superconducting transition temperature (T_c) and the critical current capacity of the ceramic superconductor (J_c) has to maintained. In addition, the added metallic species should not alter the stoichiometry of the superconducting $YBa_2Cu_3O_{6+x}$ ceramic material. Both silver and gold may satisfy all the above requirement, however, based on the economical criteria for large scale manufacturing the noble metal based composite systems are not very practical. Aluminum is a better substitute for the noble metals. It is because (i) the aluminum is readily available and is very cost effective; (ii) from the present investigation it has demonstrated that the aluminum based YBCO composites also behave as superconductors at liquid nitrogen temperature. However, it has to be recognized from the present investigation, aluminum based superconducting composite material technology requires further refinement of the processing as well as a better understanding of both the macro- and micro- structural properties of the composites.

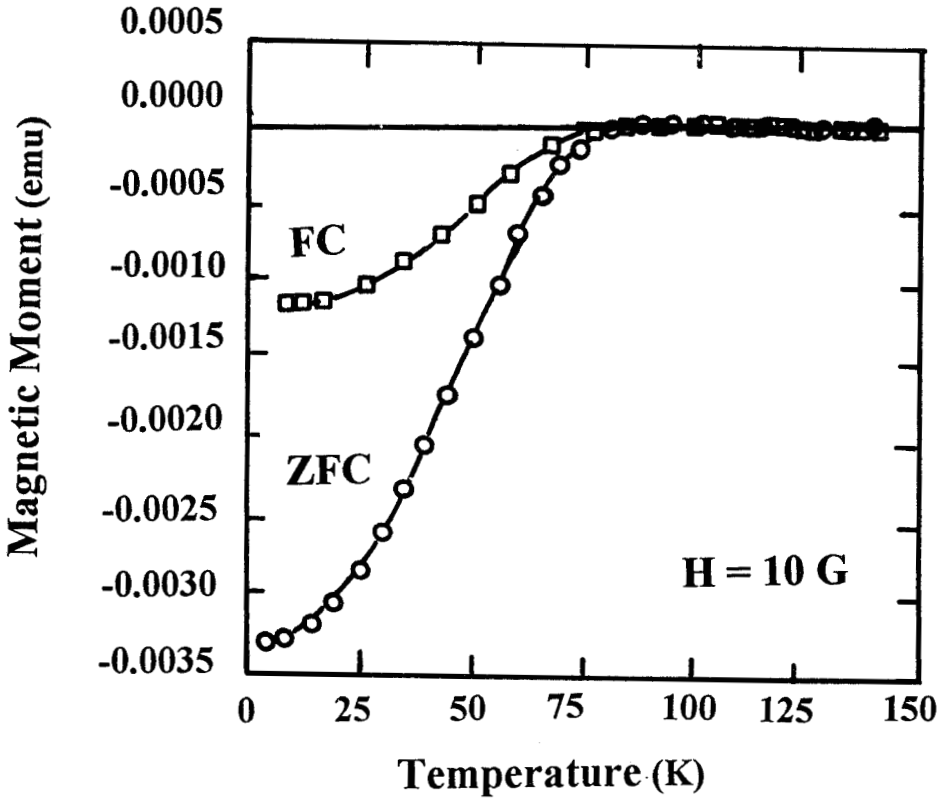

Figure 4. Magnetic moment versus sample temperature profiles of 60 wt.% aluminum / 40 wt.% $YBa_2Cu_3O_{6+x}$ composites measured using SQUID. FC Field cooling and ZFC zero field cooling.

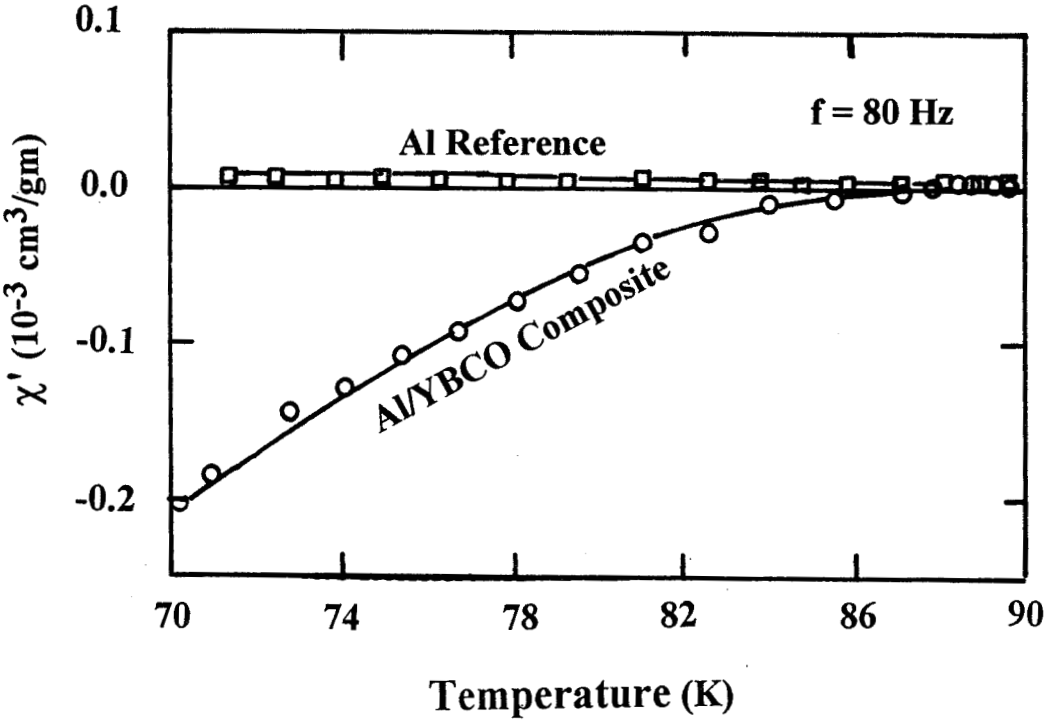

Figure 5. Magnetic moment versus sample temperature profiles of pure aluminum and 60 wt.% aluminum / 40 wt.% $YBa_2Cu_3O_{6+x}$ composites measured using ac susceptibility apparatus..

CONCLUSION

From the present investigation the following conclusions can be derived :

1. The addition of silver to the $YBa_2Cu_3O_{6+x}$ does not affect the superconducting behavior of $YBa_2Cu_3O_{6+x}$ over the entire concentration range of 10 - 72 wt.% silver. However the T_c decreases from T_c 77 K to 60 K with an increase in the concentration of silver above 40 wt.% to 72 wt.%.

2. Although, the theoretical models based on classical proximity theory of low temperature superconductors can predict the lowering of T_c with the increase in the concentration of silver in the composites, the extrapolated length for the diffusion of superconductivity from $YBa_2Cu_3O_{6+x}$ into silver matrix predicted from the theory are not agreeable with the experimentally determined superconducting $YBa_2Cu_3O_{6+x}$ particle - particle separation distance.

3. 60 wt. % Aluminum/$YBa_2Cu_3O_{6+x}$ composites behave as superconductors and these composites show two transitions around 90 and 120 K respectively.

ACKNOWLEDGMENT : The author would like to thank Drs. O. P. Arora, L. F. Aprigliano, A. Purohit (ANL) and C. S. Pande (NRL) for their valuable suggestions and useful discussions, and Dr. B. Douglas, Director of Research, CDNSWC for funding this project under ONR sponsored ILIR Program.

REFERENCES

1. Hepp, A. F., Gaier, J. R., Hambourger, P. D. and Pouch, J. J., "Interaction of Au, Ag, and Bi Ions with $YBa_2Cu_3O_{7-y}$: Implications for Superconductor Applications," Processing and Applications of High T_c Superconductors, edt. W. E. Mayo, Pub. The Metallurgical Society, 213 (1988).
2. Sen, S., In-Gann Chen, Chen, C. H. and Stefanescu, D. M., "Fabrication of Stable Superconductive Wires with $YBa_2Cu_3O_{6+x}$ /Ag_2O Composite Core," Appl. Phys. Letts., 54(8), 766 (1989).
3. Rao, A. S., Aprigliano, L. F. and Arora, O. P., "Effect of the Additives on Morphology and Superconductivity of $YBa_2Cu_3O_{6+x}$ Ceramic materials," Bull. Mater. Sci., 14(2), 269 (1991)
4. Rao, A. S. " Processing and Property Evaluation of $YBa_2Cu_3O_{6+x}$ / Aluminum Composites," Applied Superconductivity, 1[3-6], 725 (1993).
5. Rao, A. S. " Properties of Superconducting $YBa_2Cu_3O_{6+x}$ Ceramic Materials : Effect of Processing Parameters," Applied Superconductivity, 1[3-6], 607 (1993).
6. Rao, A. S., Arora, O. P. and Pande, C. S., " Superconductivity in YBCO / Al Composite System," Physica C, 224, 221 (1994).
7. Deutscher, G., and de Gennes, P. G.., "Proximity Effects," in Superconductivity, edt. Parks, R.D., Pub. Macel Dekker, Inc., New York, NY, 2, 1005 (1969).

OMIT THIS PAGE

THIS PAGE INTENTIONALLY LEFT BLANK

Page intentionally left blank

Physical Properties

Session PP-1 Chair: **Prof. Valeri Ozhogin**
Co-Chair: **Prof Evgenii Z. Meilikhov**

Page intentionally left blank

S29-76
3/4/03
10 P.

ELECTRONIC PROPERTIES OF Y-Ba-Cu-O SUPERCONDUCTORS AS SEEN BY Cu and O NMR/NQR

3Y3 323

D. Brinkmann
Physik-Institut, University of Zürich
Winterthurerstrasse 190, 8057 Zürich, Switzerland

Abstract Nuclear Magnetic Resonance (NMR) and Nuclear Quadrupole Resonance (NQR) allow the investigation of electronic properties at the atomic level. We will report on such studies of typical members of the the Y-Ba-Cu-O family such as $YBa_2Cu_3O_{6+x}$ (1-2-3-(6+x)), $YBa_2Cu_4O_8$ (1-2-4) and $Y_2Ba_4Cu_7O_{15}$ (2-4-7) with many examples of recent work performed in our laboratory. In particular, we will deal with Knight shift and relaxation studies of copper and oxygen. We will discuss important issues of current studies such as: (1) Existence of a common electronic spin-susceptibility in the planes (and perhaps in the chains) of 1-2-4. (2) Strong evidence for the existence of a pseudo spin-gap of the antiferromagnetic fluctuations in 1-2-4 and 2-4-7. (3) Evidence for *d*-wave pairing in 1-2-4. (4) Strong coupling of inequivalent Cu-O planes in 2-4-7 and possible origin for the high T_c value of this compound. (5) The possibility to describe NMR data in the framework of a charge-excitation picture.

1. Introduction

While there is not yet a generally accepted theory of the mechanism of high-temperature superconductivity (HTSC) experiments have provided a wealth of sound data and relevant information which wait for proper and adequate interpretation. Among the techniques which probe properties on the *atomic* scale, are Nuclear Magnetic Resonance (NMR) and Nuclear Quadrupole Resonance (NQR). How these disciplines obtain their informations and what the results and issues are, at least for the Y-Ba-Cu-O and the La-Sr-Cu-O families of HTSC, has been reviewed recently [1]. A collection of articles on NMR/NQR applications in HTSC from many leading groups in the field may be found in a special issue of Applied Magnetic Resonance [2]. Recent short reviews of our work emphasizing Y-Ba-Cu-O compounds deal with either crystallographic and materials science aspects [3] or relaxation [4].

In this paper we review some of the results gathered in our laboratory. They are concerned with several issues presently under debate in the HTSC community: (i) the existence of a single-spin fluid in the Cu-O planes and chains; (ii) the spin-gap effect; (iii) the orbital symmetry of the pair-wave function; (iv) the coupling between CuO_2 planes; (v) the possibility to describe NMR data within the framework of a charge-excitation picture. Our answers are based on new Knight shift and NMR/NQR spin-lattice and spin-spin relaxation data for $YBa_2Cu_4O_8$ and $Y_2Ba_4Cu_7O_{15}$.

2. The single-spin fluid model

Many properties of the cuprates are intimately connected with the fact that the parent structure of these compounds is an anti-ferromagnet, namely $YBa_2Cu_3O_{6+x}$ which has a Néel temperature of $T_N = 415$ K for x = 0. Introducing oxygen destroys the long-range anti-ferromagnetic (AF) order. However, the Cu electron spins still exhibit short-range AF spin fluctuations which give rise to a frequency (ω) and wave-vector ($\vec{q}$) dependent dynamic electronic susceptibility $\chi(\vec{q},\omega)$.

The question arises whether the susceptibilities associated with the Cu spin and the oxygen hole are independent of each other or not. This can be answered by Knight shift measurements. The NMR line shift due to magnetic interactions is expressed by the *magnetic shift tensor* K, whose components (in a reference frame $\alpha = x, y, z$), can be decomposed into a spin, an orbital and a diamagnetic part:

$$K_{\alpha\alpha}(T) = K_{\alpha\alpha}^{spin}(T) + K_{\alpha\alpha}^{orb} + K_{\alpha\alpha}^{dia} \ .$$

In HTSC compounds, K^{orb} is predominantly temperature independent, whereas the temperature dependent K^{spin} is expected to vanish in the superconducting state due to singlet spin pairing. K^{dia} is small and can be neglected quite often.

Each tensor can be expressed by the respective hyperfine interaction tensor and the *static* electronic susceptibility (*i.e.* at zero wave vector and zero frequency) as:

$$K_{\alpha\alpha}^{spin} = \frac{1}{g\mu_B} \sum_j (A_j)_{\alpha\alpha} (\chi_j)_{\alpha\alpha}$$

For the analysis of the data, we introduce the following notations. K_{cc} denotes the tensor component perpendicular to the CuO_2 planes ($B_0 \parallel c$), while the in-plane components of the shift are given by $K_{\parallel}$ and $K_{\perp}$, where B_0 is parallel and perpendicular to the CuO–bond axis, respectively. We define the axial spin part of K as $K_{ax}^{spin} = (1/3)(K_{\parallel}^{spin} - K_{\perp}^{spin})$. The equivalent definition for the isotropic spin part of K is $K_{iso}^{spin} = (1/3)(K_{\parallel}^{spin} + K_{\perp}^{spin} + K_c^{spin})$.

The new measurements of the planar Cu and O Knight shifts [5] enlarge and improve our previous data [6,1]. Various Cu and O shift components can be calculated from the data, the result is shown in Fig. 1. While in a "classical" superconductor like aluminum the Knight shift stays constant in the normal state and starts to decline at T_c, the Knight shift components of $YBa_2Cu_4O_8$ begin to decrease already well above T_c. This behavior is typical for under-doped HTSC [1], *i.e.* for compounds whose doping level is below the value that corresponds to a maximum T_c. In addition, all components exhibit the same temperature dependence. These facts support the "single-spin fluid" model which states that the Cu-d holes and the doped holes (which mainly go into O-2p states) have one spin degree of freedom.

Our $YBa_2Cu_4O_8$ shift data resemble very much those for $YBa_2Cu_3O_{6.63}$ [7] thus demonstrating again that both compounds are under-doped. Similar ^{17}O

shift data for $YBa_2Cu_4O_8$ were reported by Machi *et al.* [8] and similar Cu Knight shift data were obtained in $Bi_2Sr_2CaCu_2O_8$ [9]. The existence of a planar single-spin fluid had also been deduced from Y and Tl NMR [1]. The concept is now well established.

A single-spin fluid seems to exist also in the chains of $YBa_2Cu_4O_8$ [5]. The components of both the Cu1 and O1 Knight shift decrease below T_c although this is less pronounced for the K_a component. All K components of Cu1 are proportional to the respective component of O1, which again points to the existence of a single-spin fluid. However, the susceptibilities of planes and chains are different.

3. The spin-gap effect

The study of spin-lattice (and spin-spin) relaxation in HTSC is intimately connected with the question about the origin of superconductivity in these materials, although not in a simple straightforward manner. For instance, some groups have proposed that superconductivity is induced by electron spin fluctuations [10]. The relevance of these fluctuations in neutron scattering and NMR relaxation experiments is well established [1]. Nearly all mechanisms which are responsible for spin-lattice relaxation in HTSC are based on electron-nuclear interactions. The only exception seems to be the Ba relaxation in $YBa_2Cu_4O_8$ [1,11] which is due to the two-phonon Raman process, *i.e.* a coupling between phonons and the Ba quadrupole moment.

Thus, for Cu, O and Y the relaxation is described by the Moriya formula which relates the relaxation rate to the hyperfine fields and the dynamical electron susceptibility:

$$^i(\frac{1}{T_1})_\alpha = \frac{\gamma_i^2 k_B T}{2\mu_B^2} \sum_{\vec{q},\alpha\neq\alpha'} |^iA_{\alpha'}(\vec{q})|^2 \frac{\chi''_{\alpha'\alpha'}(\vec{q},\omega_i)}{\omega_i} \qquad (1)$$

Here, i denotes the nuclear species and ω_i is its NMR frequency. The magnetic field B_0 is oriented along the α direction which coincides with one of the crystallographic axes (a,b,c). $\chi''_{\alpha'\alpha'}(\vec{q},\omega_i)$ is the imaginary (dissipative) part of χ. $A_{\alpha'}(\vec{q})$ are formfactors related to the hyperfine fields. Eq.(1) demonstrates that the spin-lattice relaxation provides a tool to probe the average over the *q-dependent* electron susceptibility.

As an example, Fig. 2 shows the temperature dependence of the relaxation rate per Kelvin for the planar Cu and O nuclei in $YBa_2Cu_4O_8$ [5]. $^{63}(T_1T)^{-1}$ reaches a maximum around 130 K and rapidly decreases towards lower temperatures. On the other side, $^{17}(T_1T)^{-1}$ displays a monotonous decrease with lowering temperature. These are typical behaviors found in oxygen-deficient $YBa_2Cu_3O_{6+x}$ and, thus, may be taken as signature of under-doped material.

A good starting point for explaining these data is the the phenomenological Millis-Monien-Pines model [12,1]. It is assumed that there is a direct hyperfine interaction between the Cu2 nuclei and an electron of the on-site $3d_{x^2-y^2}$ orbital

and a transferred interaction with electrons of the $3d_{x^2-y^2}$ orbitals of the four neighboring copper ions. For the planar oxygen nuclei, there exists a transferred hyperfine coupling. The electron spins themselves interact anti-ferromagnetically. The electronic spin fluctuations peak near $\vec{Q} = (\pi/a, \pi/a)$ which is the AF ordering point in $\vec{q}$-space. Since the O and Y formfactors entering into Eq.(1) vanish at $q = Q$, the different behavior of Cu, O and Y relaxation rates can be explained.

Further progress in understanding the Cu relaxation behavior was triggered in two ways. First, Millis and Monien [13] suggested that the spectral weight in the spin fluctuations decreases as the temperature is lowered. This missing spectral weight must reappear at a higher energy in the form of a transition over a "spin pseudo-gap", Δ. While the AF fluctuations increase with falling temperature and hence increase $1/T_1T$, there will be a temperature where the spin gap effect wins and $1/T_1T$ will decrease; this explains the maximum of $1/T_1T$ for Cu. Secondly, Rossat-Mignod *et al.* [14] were the first to discover the spin-gap effect in $YBa_2Cu_3O_{6+x}$ by neutron scattering where the results for $\chi''(\vec{Q}, \omega)$ resemble very much the $1/T_1T$ data.

When describing the spin-lattice relaxation rate in terms of the spin-gap effect it became customary [1,15,16] to use the following *ad hoc* formula:

$$\frac{1}{T_1T} = \left(\frac{A_0}{T}\right)^{\alpha} \left[1 - \tanh^2\left(\frac{\Delta_{AF}}{2T}\right)\right] \tag{2}$$

Here, A_0 is a constant. Δ_{AF} denotes the spin-gap energy at Q. The factor $T^{-\alpha}$ is introduced to assure a reasonable description of the high-temperature behavior.

We have fitted Eq.(2) to the planar Cu relaxation data of both the $YBa_2Cu_4O_8$ [5] and the $Y_2Ba_4Cu_7O_{15}$ [1,16] structure, the latter case is shown in Fig. 3. The fit parameters for both Cu sites, Cu2 and Cu3, are $\Delta = 240 \pm 20$ K and $\alpha = 1.25$ and thus agree within the error limits with $\Delta = 260 \pm 10$ K and $\alpha = 1.25$ we obtained for the fit to the Cu2 data in $YBa_2Cu_4O_8$. We will return to this point later.

The Knight shift data have also been fitted by a spin-gap formula, similar to Eq.(2), namely by

$$K = K_0 \left[1 - \tanh^2\left(\frac{\Delta_0}{2T}\right)\right] \tag{3}$$

where Δ_0 refers to the gap at zero wave vector. Our fit to the $YBa_2Cu_4O_8$ data yields $\Delta_0 = 180$ K which is in good agreement with the neutron scattering result. If the temperature variation of the Knight shift is really due to the opening of a spin-gap and Eq.(3) is appropriate for analyzing the data, the result implies that a spin-gap opens also at $q = 0$ and that this values is different from the Δ_{AF} value.

4. The symmetry of the pair-wave function

Whether the spatial symmetry of the pairing state is a *s*-wave or *d*-wave is a controversial topic. This is not the place to deal with all the aspects of this

problem, we just focus on various possibilities NMR/NQR offer to check this symmetry, in particular in $YBa_2Cu_3O_7$ and $YBa_2Cu_4O_8$.

One way is to study the anisotropy of the relaxation rate, that is the ratio $r = {}^{63}T_1^c/{}^{63}T_1^{ab}$ of the Cu relaxation rate in the superconducting state where c and ab specify the orientation of the applied magnetic field, B_0. Detailed theoretical analyses of the relaxation data for $YBa_2Cu_3O_7$ [17,18] revealed that the temperature variation of r is not compatible with s-wave pairing and favors d-wave symmetry. Our $YBa_2Cu_4O_8$ data [19] are in qualitative agreement with the $YBa_2Cu_3O_7$ data and thus also favor d-wave symmetry.

A very promising check of the pairing state symmetry is the measurement of the copper and oxygen relaxation rates at very low temperatures. Both rates display a power-law behavior, *i.e.* $1/T_1 \propto T^n$ with n between 2.5 and 3 as recently observed for $YBa_2Cu_3O_7$ [20] and $YBa_2Cu_4O_8$ [5]. This points to the existence of nodes in the superconducting gap as one expects, for instance, for d-wave pairing superconductivity [21].

Last but not least, the Knight shift may reveal the pairing state symmetry provided the data are accurate enough. For instance, the chain Cu1 Knight shift data in $YBa_2Cu_3O_7$ [22] and $YBa_2Cu_4O_8$ [5] can not satisfactorily be fitted by an s-wave expression while an d-wave fit is perfect for the $YBa_2Cu_3O_7$ data. Although the theoretical expression for $YBa_2Cu_4O_8$ has not yet been calculated the similarity between data of both structures suggests that in both cases the d-wave expression provides the better fit. Thus, one may conclude that NMR/NQR data favor d-wave symmetry at least in the $YBa_2Cu_3O_7$ and $YBa_2Cu_4O_8$ structures of the Y-Ba-Cu-O family.

5. Inter-plane coupling

One of the key issues in understanding HTSC is the question whether a coupling between CuO_2 planes favors or impedes superconductivity. Before speculating in one or the other direction, it is necessary to prove that an inter-plane coupling exists. As far as NMR/NQR is concerned, the multi-layer structure $Y_2Ba_4Cu_7O_{15}$ with its alternating 1-2-3 and 1-2-4 blocks offers the unique possibility to study the coupling between *inequivalent* CuO_2 planes.

We have studied the relaxation rates and the Knight shifts of the Cu2 and Cu3 sites in the 1-2-3 and 1-2-4 block, respectively, of the $Y_2Ba_4Cu_7O_{15}$ compound [1,16]. It turned out that the ratios of these quantities are constant above T_c. Thus, both the static and the dynamic electron spin susceptibilities of the individual planes of a double-plane are governed by the *same* temperature dependence. This implies the existence of common spin dynamics in both planes, and hence these planes must be strongly coupled. Despite their coupling, their spin susceptibilities retain a distinct q dependence. The presence of the coupling has also been demonstrated by performing SEDOR (spin-echo double resonance) experiments on the Cu2 and Cu3 nuclei [23].

Below T_c, the common temperature dependence is lost, which could arise from the opening of two superconducting energy gaps that differ in the individual planes, thus revealing the different plane charge carrier densities of the 1-2-3 and 1-2-4 block. This difference in doping levels had also been inferred from the temperature dependence of the Cu2 and Cu3 NQR frequencies. We found that the 1-2-3 block is less doped than the pure $YBa_2Cu_3O_7$ compound, hence the doping level of the 1-2-3 block is closer to optimal doping. If one simply assumes that the block with the highest T_c "wins", then this would explain the high T_c, namely 93 K, of the $Y_2Ba_4Cu_7O_{15}$ compound.

As mentioned above and shown in Fig. 3, the Cu2 and Cu3 relaxation rates in $Y_2Ba_4Cu_7O_{15}$ could be fitted by the spin-gap formula Eq.(2) with the same parameters for both data sets. The fact that these values are the same as those used for the fit of the $YBa_2Cu_4O_8$ relaxation data, demonstrates the very similar spin dynamics in $YBa_2Cu_4O_8$ and $Y_2Ba_4Cu_7O_{15}$ and that the doping level of the blocks in $Y_2Ba_4Cu_7O_{15}$ are close to optimal doping.

6. Hubbard model with magnetic exchange

The excellent fit of the spin-gap expression to the planar Cu relaxation data in $YBa_2Cu_4O_8$ and $Y_2Ba_4Cu_7O_{15}$ certainly cannot "prove" that the relaxation arises from the spin-gap effect. Other physical phenomena in HTSC need to be explained by this effect. As an alternative to explain Knight shift and relaxation data we conclude our survey by drawing the attention to an approach which is a variant of the Hubbard model comprising magnetic exchange in second order between copper and oxygen holes [24]. The exchange gives rise to a new singlet correlated band separated from the oxygen band. The energy spectrum has been calculated. The low energy physics is determined by a high density of charge excitations in the singlet impurity band together with spin excitations in the lower Hubbard band. Taking an idealized density of states, an analytical form is obtained for the temperature dependent susceptibility:

$$\chi'' \propto \frac{1}{T}\left[1 - \tanh^2\left(\frac{\mu_0 - \alpha T}{k_B T}\right)\right]$$

where the factor $\alpha = 0.4 \times 10^{-4}$ eV/K of the chemical potential is *not* a fit parameter. This expression perfectly describes the Cu2 relaxation rate in $YBa_2Cu_4O_8$ from T_c up to 600 K.

These examples clearly show that the debate about the proper description of spin-lattice relaxation in HTSC, at least of the Y-Ba-Cu-O type, is not yet closed.

References

[1] Brinkmann D., Mali M.: NMR Basic Principles and Progress **31**, 171 (1994)
[2] Appl. Magn. Reson. **3**, 383 - 750 (1992)
[3] Brinkmann D. in: Proc. of the 20th Intern. School of Crystallography (Kaldis E., ed.), Kluwer Academic Publ., 225 (1994)
[4] Brinkmann D. in: Proc. of 2nd Internat. Discussion Meeting on Relaxation in Complex Systems (Ngai K., ed.), Alicante (Spain), 1993, J. Non-Crystalline Solids, in press
[5] Bankay M., Mali M., Roos J., Brinkmann D.: Phys. Rev. B, in press
[6] Mangelschots I., Mali M., Roos J., Brinkmann D., Rusiecki S., Karpinski J., Kaldis E.: Physica C **194**, 277 (1992)
[7] Takigawa M., Reyes A.P., Hammel P.C., Thompson J.D., Heffner R.H., Fisk Z., Ott K.C.: Phys. Rev. **B 43**, 247 (1991)
[8] Machi T., Tomeno I., Miyatake T., Koshizuka N., Tanaka S., Imai T., Yasuoka H.: Physica C **173**, 32 (1990)
[9] Walstedt R.E., Bell R.F., Mitzi D.B.: Phys. Rev. B **44**, 7760 (1991)
[10] Monthoux P., Pines D.: Phys. Rev. Lett. **69**, 961 (1992)
[11] Lombardi A., Mali M., Roos J., Brinkmann D., Yakubovskii A.: Submitted to 4th Intern. Conference on Materials and Mechanisms of Superconductivity High-Temperature Superconductors (M^2S-HTSC-IV), Grenoble (July 1994)
[12] Millis A.J., Monien H., Pines D.: Phys. Rev. B **42**, 167 (1990)
[13] Millis A.J., Monien H.: Phys. Rev. B **45**, 3059 (1992)
[14] Rossat-Mignod J., Regnault L.P., Vettier C., Burlet P., Henry J.Y., Lapertod G.:, Physica B **169**, 58 (1991)
[15] Mehring M.: Appl. Magn. Reson. **3**, 383 (1992)
[16] Stern R., Mali M., Mangelschots I., Roos J., Brinkmann D., Genoud J.-Y., Graf T., Muller J.: Phys. Rev. B (1 July 1994)
[17] Martindale J.A., Barrett S.E., Klug C.A., O'Hara K.E., DeSoto S.M., Slichter C.P., Friedmann T.A., Ginsberg D.M.: Phys. Rev. Lett. **68**, 702 (1992)
[18] Takigawa M., Smith J.L., Hulst W.L.: Phys. Rev. B **44**, 7764 (1991)
[19] Bankay M., Mali M., Roos J., Mangelschots I., Brinkmann D.: Phys. Rev. B **46**, 11228 (1992)
[20] Martindale J.A., Barrett S.E., O'Hara K.E., Slichter C.P., Lee W.C., Ginsberg D.M.: Phys. Rev. B **47**, 9155 (1993)
[21] Bulut N., Scalapino D.J.: Phys. Rev. Lett. **68**, 706 (1992)
[22] Slichter C.P., Barrett S.E., Martindale J.A., Durand D.J., Pennington C.H., Klug C.A., O'Hara K.E., DeSoto S.M., Imai T., Rice J.P., Friedmann T.A., Ginsberg D.M.: Appl. Magn. Reson. **3**, 423 (1992)
[23] Mali M., Roos J., Stern R., Brinkmann D., to be submitted to Phys. Rev. Lett.
[24] Eremin M.V., Varlamov S.V., Solovjanov S.G., Brinkmann D., Mali M., Markendorf R., Roos J.: Submitted to 4th Intern. Conference on Materials and Mechanisms of Superconductivity High-Temperature Superconductors (M^2S-HTSC-IV), Grenoble (July 1994)

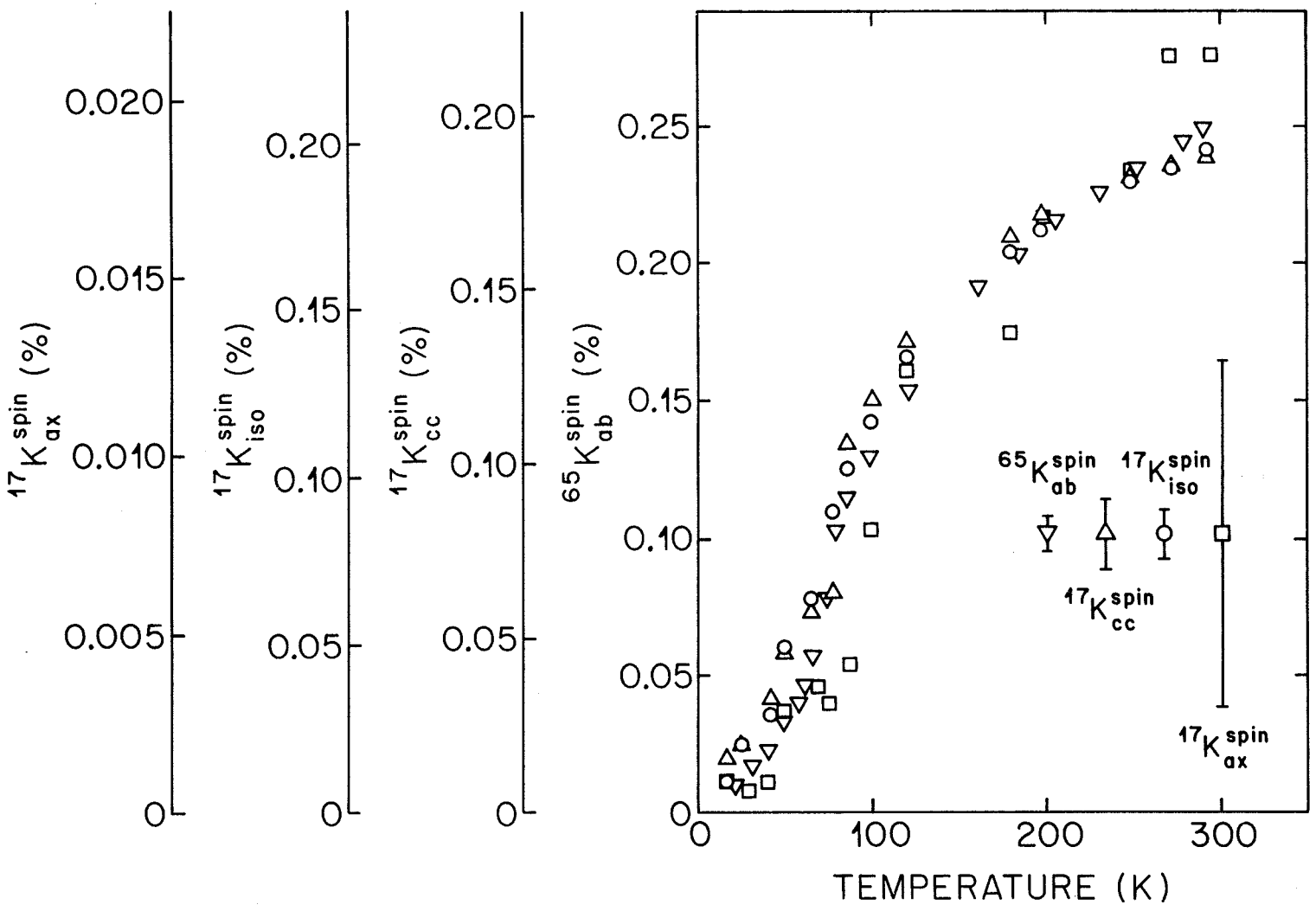

Figure 1.- Various Knight shift components of planar copper and oxygen nuclei in $YBa_2Cu_4O_8$ are plotted vs temperature (with different vertical scales). From Ref. [5].

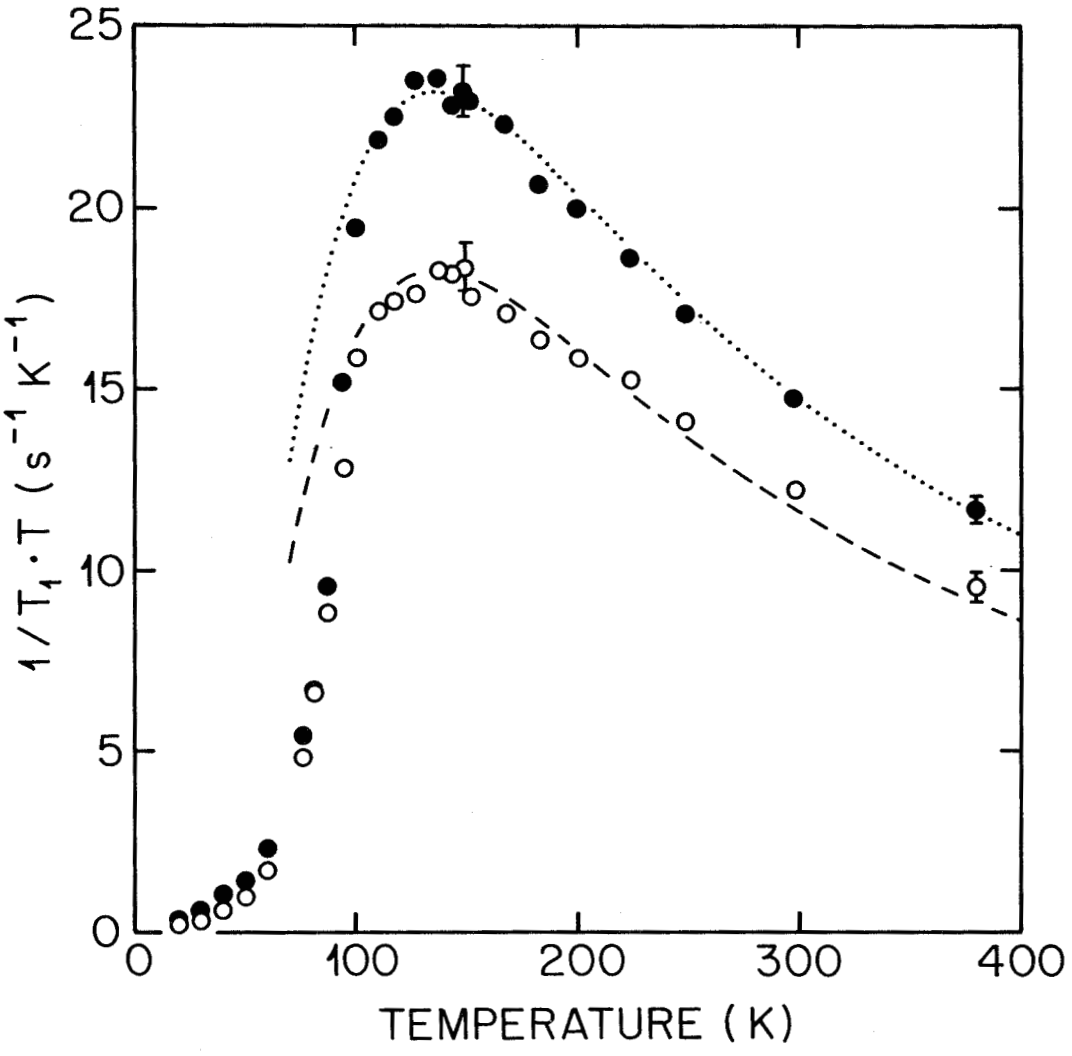

Figure 2.- The temperature dependence of the relaxation rate per Kelvin for the planar Cu and O nuclei in $YBa_2Cu_4O_8$. From Ref. [5].

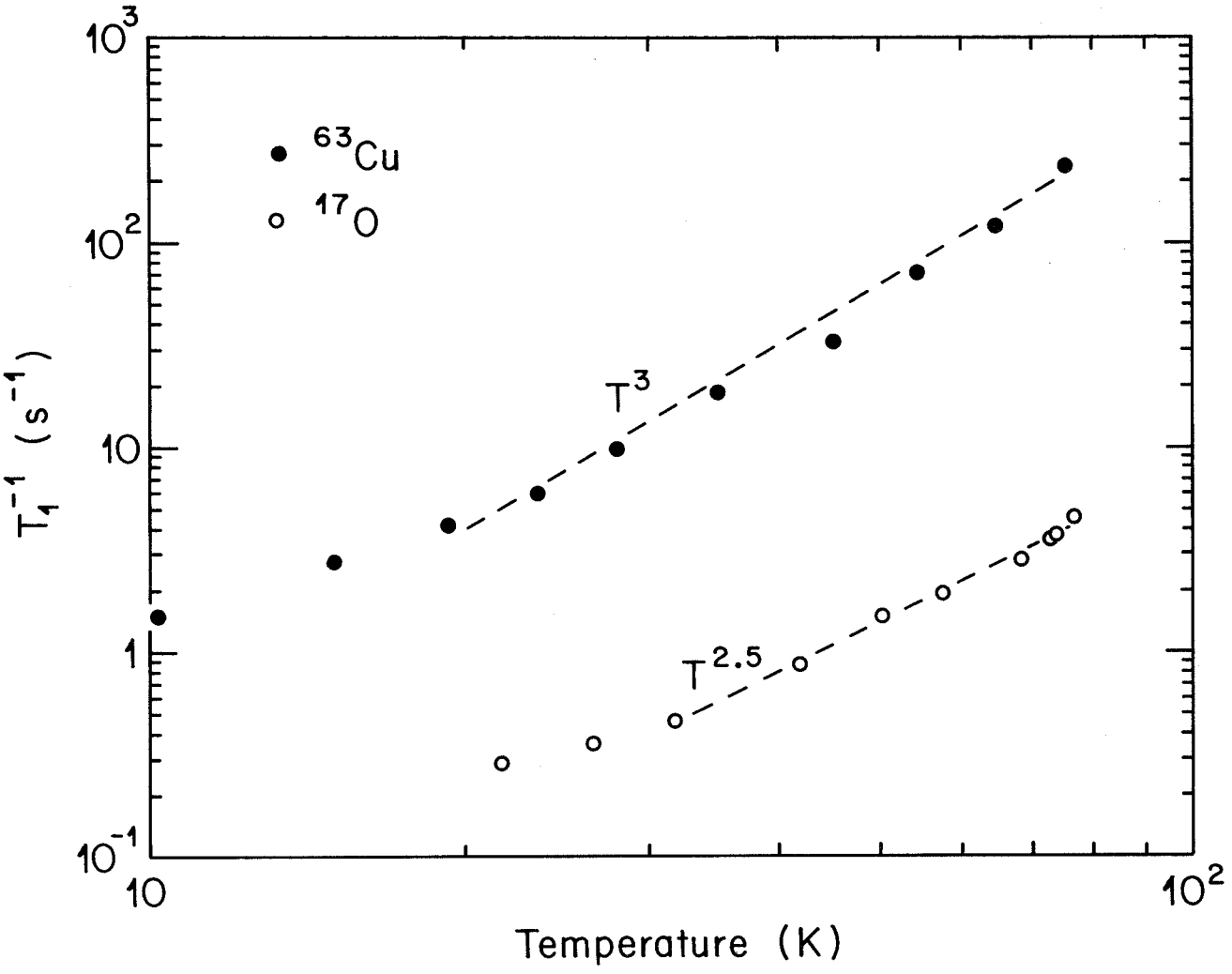

Figure 3.- Fit of Eq.(2) to the relaxation data of the two planar Cu Nuclei in $Y_2Ba_4Cu_7O_{15}$. From Ref. [16].

Quaternary Borocarbides - New Class of Intermetallic Superconductors

R. Nagarajan[1], L.C. Gupta[1], S.K. Dhar[1], Chandan Mazumdar[2], Zakir Hossain[1], C. Godart[3], C. Levy-Clement[4], B.D. Padalia[2] and R. Vijayaraghavan[1]

[1]Tata Institute of Fundamental Research, Bombay - 400 005, India.
[2]Department of Physics, Indian Institute of Technology, Bombay 400 076, India.
[3]UPR-209, C.N.R.S., Meudon Cedex, 92195, France.
[4]Laboratoire Physique Solides, C.N.R.S., Meudon Cedex, 92195 France.

30-76
314149
15 P.
3Y33 3V

Abstract

Our recent discovery of superconductivity (SC) in the four-element multiphase Y-Ni-B-C system at an elevated temperature (T_c~12K) has opened up great possibilities of identifying new superconducting materials and generating new physics. Superconductivity with T_c (> 20 K) higher than that known so far in bulk intermetallics has been observed in multiphase Y-Pd-B-C and Th-Pd-B-C systems and a family of single phase materials $RENi_2B_2C$ (RE= Y, rare earth) have been found. Our investigations show YNi_2B_2C to be a strong coupling hard type-II SC. $H_{c2}(T)$ exhibits an unconventional temperature dependence. Specific heat and magnetization studies reveal coexistence of SC and magnetism in RNi_2B_2C (R = Ho, Er, Tm) with magnetic ordering temperatures (T_c ~8 K, 10.5 K, 11 K and T_m ~5 K, ~7 K, ~4 K respectively) that are remarkably higher than those in known magnetic superconductors . μ-SR studies suggest the possibility of Ni atoms carrying a moment in $TmNi_2B_2C$. Resistivity results suggests a *double re-entrant* transition (SC-normal-SC) in $HoNi_2B_2C$. $RENi_2B_2C$ (RE = Ce, Nd, Gd) do not show SC down to 4.2K. The Nd- and Gd- compounds order magnetically at ~4.5 K and ~19.5 K, respectively. Two SC transitions are observed in Y-Pd-B-C (T_c ~22 K, ~10 K) and in Th-Pd-B-C (T_c ~20 K, ~14 K) systems, which indicate that there are at least two structures which support SC in these borocarbides. In our multiphase $ThNi_2B_2C$ we observe SC at ~6 K. No SC was seen in multiphase UNi_2B_2C, UPd_2B_2C, UOs_2Ge_2C and $UPd_5B_3C_{0.35}$ down to 4.2K. T_c in YNi_2B_2C is depressed by substitutions (Gd, Th and U at Y- sites and Fe, Co at Ni-sites).

1. Introduction.

Our recent discovery of superconductivity in Y-Ni-B-C [1-4], with T_c ~12 K to 15 K, which is relatively high superconducting critical temperature for intermetallics, has triggered an intense activity in the areas of superconductivity and magnetism. This discovery came about as a result of our on going investigations in Ni-based systems [5, 6]. An extension of Y-Ni-B-C system - going from a 3d- to 4d- element - led to the observation of record T_c (~23K [7], 22K [8]) in multiphase Y-Pd-B-C system. It may not be out of place to remark that a similar situation occurred during the initial phase of the discovery of high-T_c superconductivity. Superconductivity was observed in a multiphase material La-Ba-Cu-O with a relatively low T_c (~30K) [9] and later, superconductivity was reported in a multiphase material Y-Ba-Cu-O with a much higher T_c (~93 K) [10].

We have been investigating Ni-based intermetallics for more than a decade in search of new valence fluctuation (VF) systems, besides our being interested in their magnetic and transport properties. We succeeded in identifying a number of new Ni-based VF systems such as $EuNi_2P_2$ [11], $EuNiSi_2$ [12], $Eu_2Ni_3Si_5$ [13], $Ce_2Ni_3Si_5$ [14]. Discovery of the above Eu-based VF compounds is particularly significant, as not many stoichiometric Eu-compounds exhibiting VF are known even today. After the discovery of high-T_c superconductors, Ni-based materials acquired additional significance. All high-T_c oxide superconductors, except $Ba_{1-x}K_xBiO_3$ [15], contain Cu as an essential component. As is well known, Ni-based oxides such as NiO and La_2NiO_4 are Mott-Hubbard insulators (just as CuO and La_2CuO_4 are), and attempts to induce SC in the nickel oxides failed. Moreover, partial Ni-substitution in cuprate superconductors suppressed T_c. Thus, nickel did not seem to favour superconductivity in oxides. On the other hand, in most Ni-based intermetal-

lics, Ni-moment is quenched and, therefore, they are potential candidates for superconductivity.

Ni-containing boride series RNi_4B (R=rare earth) was taken up by us for investigation, as many ternary rare earth-transition metal borides were known to support SC. Some of them are even magnetic superconductors, exhibiting coexistence of SC and magnetism. RNi_4B series turned out to be remarkable as we observed various phenomena in the same series, viz., VF in $CeNi_4B$ [16], anomalously high ferromagnetic ordering temperature (= 39K) in $SmNi_4B$ [5, 6, 17] as compared to that of $GdNi_4B$ (= 36 K) [5, 6, 17] and weak signals of superconductivity in our samples of YNi_4B [1]. Our further work showed that superconductivity in YNi_4B originated due to the presence of carbon which stabilizes a SC phase in the material. We present below further details of our discovery of superconductivity in Y-Ni-B-C system and some of our recent results on the borocarbide superconductors.

2. Discovery of Superconductivity in Y-Ni-B-C System.

YNi_4B crystallizes in the hexagonal $CeCo_4B$ type structure (space group *P6/mmm*) [18] and is also reported to have a superstructure ($a' = 3a_0$; $c = c_0$) in its lattice [19]. We synthesized YNi_4B by standard arc melting technique. Powder x-ray diffraction (XRD) pattern of the material confirmed the formation of the material in single phase belonging to the above mentioned structure. The lattice constants obtained from Rietveld analysis, including a superstructure, of our XRD pattern yielded lattice parameters as: a = 14.96(5) Å, c= 6.95(2) Å [1], which agree well with the published values [19].

Magnetic susceptibility of our sample of YNi_4B, measured as a function of temperature in a field of 4000 G, showed a sharp drop near 12 K [1, 6] (Fig. 1). This drop is not that of a typical antiferromagnet because, the drop is rather sharp and susceptibility increases on further cooling of the sample. Resistivity of our sample as a function of temperature (Fig. 1) also shows a sharp drop (but does not go to zero) around 12 K, the same temperature where the drop in susceptibility is seen [1]. The two observations together indicated the possibility of occurrence of superconductivity in this sample. M Vs H measurements clearly showed diamagnetism at low field, confirming occurrence of superconductivity. Reproducibility of drop in resistivity was confirmed by studying many independent batches (for one of them, the starting materials were obtained from a different source) of YNi_4B [1].

M Vs. T measurements (Fig. 3) at 65 G on a single piece of $YNi_4BC_{0.2}$ showed shielding and the Meissner fractions to be 4% and 1% respectively. Powdered material also showed diamagnetic response and Meissner effect. Annealing of the sample, though decreased the shielding fraction, improved Meissner fraction and T_c (~15 K) (Fig. 2). As the SC fraction was small, the sample was examined for impurity phases by energy dispersive analysis of x-rays (EDAX) and electron microprobe analysis. The sample was essentially homogeneous except for some small inclusions which appeared to be Y_2O_3 and YNi_5 (both are non superconducting). No binary or ternary alloys of Y, Ni, B are known to be superconducting with such a high T_c. Thus, observation of superconductivity at 12 K was a new and surprising result.

Low volume fraction of superconductivity implied that the entire sample was not superconducting and it was necessary to understand the origin of observed superconductivity. We considered the possibility of crystallographic superstructure [1] being responsible for this behaviour. However, we also considered the possibility of the origin of SC being due to a minority phase stabilized by the presence of a fourth element. Carbon was considered to be one possible fourth element which got introduced in the system unintentionally. In order to check this, 0.2 atom fraction of carbon was deliberately added to YNi_4B, remelted and the material was studied. On addition of carbon, resistance dropped to zero around 12 K (Fig. 3) and the superconducting shielding fraction dramatically enhanced to nearly 80% of perfect SC [4]. These results were confirmed on many independently prepared batches. It became clear that carbon plays the crucial role in the observed superconductivity. Presence of carbon introduces structural changes as well; XRD pattern of $YNi_4BC_{0.2}$ indicated that superstructure of YNi_4B gets suppressed as carbon is introduced in the material [4]. Thus, one could argue that carbon does not play any chemical role, it brings in structural changes that in turn are responsible for the observed superconductivity. The observed SC being due to possible formation of Y_2C_3, which is a known superconductor [20], was ruled out on the basis of EDAX analysis of the material and on other considerations [4].

Encouraged by this observation, carbon was also added to many other compositions $Y_xNi_yB_z$. Of all these materials, the material with the nominal composition $YNi_2B_3C_{0.2}$ (multiphase) exhibited superconductivity at ~13.5 K with large specific heat anomaly across T_c (Fig. 4) [4]. The material showed large Meissner fraction (~15%) even in the powdered condition (Fig. 5). From these results we concluded that *Y-Ni-B-C system has a bulk superconducting phase with an elevated transition temperature (~12 K)* [4]. We presented these results at the two International Conferences, LT20, Eugene, U.S.A., Aug. 1993 [2] and SCES'93, San Diego, U.S.A., Aug. 1993 [3] and also communicated for publication [4].

3. Superconductivity and magnetism in $RENi_2B_2C$ (RE = Y, Er, Ho, Tm).

3.1 YNi_2B_2C

EDAX analysis of multiphase $YNi_2B_3C_{0.2}$ indicated that majority phase in the material has Y:Ni ratio as 1:2 [4]. It was difficult to ascertain boron and carbon contents by EDAX analysis as these are low Z elements. While our efforts to isolate the SC phase by varying concentration of B and C were in progress, Cava et al. [21] reported SC in single phase materials, $RENi_2B_2C$ (RE = Y, Ho, Er, Tm and Lu, T_c = 15.6 K, 8 K, 10.5 K, 11 K, 16.6 K respectively), and Siegrist et al. [22] reported crystal structure of $LuNi_2B_2C$. Thus, the concentration of B:C in the SC phase turned out to be 2:1. We have prepared $RENi_2B_2C$ (RE = Y, Ho, Er, Tm) and studied in detail their superconducting and magnetic behaviour. Our preliminary results were reported earlier [23]. Some of the results are given below.

We carried out detailed structural studies of YNi_2B_2C, using electron diffraction and x-ray diffraction on single crystals picked up from the arc-melted button of one of our samples [24]. Results of the analysis of the data were in agreement with those reported by Siegrist et al. [22]. Figure 6 shows a unit cell of the structure of YNi_2B_2C. The tetragonal structure belongs to the centro-symmetric space group *I4/mmm* and is a 'filled-in' version of the well known $ThCr_2Si_2$-type structure. We shall refer to this structure as 1221-structure in the rest of this paper. Carbon atoms are located in the Y(Th)-planes. Remarkable features of this structure are: rather short B-C distance, nearly ideal Ni-B4 tetrahedra and Ni-Ni bond length shorter than that in Ni-metal, implying that Ni-Ni bonds are strong. The c/a ratio (a = 3.524(1) Å and c = 10.545(5) Å) is 2.99, suggesting that the structure is highly anisotropic. The results further showed that (i) there is no superstructure in YNi_2B_2C (ii) free parameter z of boron atoms is 0.358 (iii) C-atoms have a rather large amplitude of thermal vibration, especially in the Y-C plane [24]. Our XRD studies did not show any crystallographic phase transition down to 50 K. Further, lattice constants at 50 K are almost unchanged (a = 3.521 A and c = 10.549 A).

Magnitude of the room temperature resistivity, R(T), of our sample of YNi_2B_2C is large (> 100 μohm cm) [24] for a metallic system. This implies that the electron-phonon interaction may be large. Superconductivity occurs at 15.3 K with a width δT_c (90% - 10%) of the resistive transition of about 0.5 K. R(T) is linear in temperature down to 40 K. High-T_c cuprates also exhibit R(T) proportional to T behaviour in the normal state. Scattering of the carriers from 2D-antiferromagnetic fluctuations of Cu-spins has been suggested to be one possible mechanism of this behaviour [25]. In this context, it may be mentioned that evidence of antiferromagnetic spin fluctuations in YNi_2B_2C has been found in the anomalous nuclear spin relaxation rate of boron ($1/T_1$ increases with decrease of temperature) [26, 27]. Considering the highly anisotropic structure of YNi_2B_2C, it is conceivable that these fluctuations could also be anisotropic. Also possibility of Ni-atoms carrying a moment has been indicated in μ-SR measurements in, e.g., $TmNi_2B_2C$ [28]. To what extent these fluctuations influence the R(T) of the material is worth investigating, preferably on single crystals.

In the normal state, susceptibility of our sample of YNi_2B_2C exhibits paramagnetic behaviour over the temperature range 15-300K. From a Curie-Weiss fit to the data and assuming that paramagnetic behaviour arises due to moments on Ni ions only (as there are no other magnetic ions), we get a value of 0.18 μ_B/Ni ion. However, caution is to be exercised in this conclusion as susceptibility from minority impurity phases may influence this value.

Diamagnetic response of our sample (bulk, as well as powder) below T_c, both in field cooled (FC) and zero field cooled (ZFC) conditions, is shown in Fig. 7. Both bulk (annealed and as-cast) and powder samples exhibit nearly 100% shielding signal (ZFC). The Meissner fraction (FC) of the as-cast material is

about 10%. In the annealed bulk sample, the Meissner fraction is even smaller (5%). However, in the powdered sample of the annealed material (after powdering, this sample was not annealed), we observe a Meissner fraction of 50%.

We measured molar heat capacity C_p of annealed and unannealed samples of YNi_2B_2C in the temperature range $5K < T < 22K$. In the annealed sample, anomaly in C_p, observed in going through the superconducting transition, is narrower, and occurs at a higher temperature, suggesting that the quality of the sample improves on annealing. This is reflected in the x-ray diffraction pattern of the material as well and also in its diamagnetic response. From the analysis of the data we obtain $\Gamma = 8.9$ mJ/mole K^2 and $\beta = 0.163$ mJ/mole K^4, where Γ and β are the temperature coefficients of the electronic and the lattice specific heat capacities respectively. The ratio $\delta C_p/(\Gamma T_c)$ is calculated to be 3.6 which is much higher than 1.43, the BCS value for the weak-coupling limit. It is, however, to be emphasized that considering that the observed transition is broad, this figure may be taken to suggest the trend. In fact, recent specific heat measurements on a single crystal sample [29] yield this number to be ~1.8 which still implies strong-coupling in YNi_2B_2C. From the value of β, Debye temperature (T_D) is estimated to be 415 K. Large value of the ratio T_c/T_D also is consistent with this conclusion.

C_p/T Vs. T^2 in YNi_2B_2C, below the SC transition down to 5 K, follows a linear relationship. It should be interesting to extend these measurements, below 5 K, to check and confirm this temperature dependence of C_p. It may be pointed out that the power-law behaviour of the heat capacity in the SC state of heavy fermion systems has been taken as an indication of unconventional superconductivity where the symmetry of the superconducting energy gap is lower than the symmetry of the Fermi surface. More detailed studies are needed to investigate such possibilities in borocarbide quaternary superconducting materials.

Magnetization M(H) measurements of YNi_2B_2C at 5K, as function of applied field, H, show the material to be a hard type-II superconductor. The temperature of dependence of $H_{c2}(T)$, determined from the studies of R(H,T) under applied field [30], is unconventional [24]. The slope, $dH_{c2}(T)/dT$ is close to zero at T_c and increases with decrease of temperature below T_c [24] whereas, in a conventional type-II superconductor, $dH_{c2}(T)/dT$ is non zero at T_c and is nearly constant for a considerable range of temperature below T_c [31]. It would be of interest to investigate this unconventional behaviour of $H_c(T)$ in YNi_2B_2C. From $H_{c2}(T)$ measurements we estimate the coherence length in this material to be ~ 80 Å at 5 K.

Magnetic history effects in YNi_2B_2C [32] also confirm the material to be a hard type-II superconductor [32]. Temperature dependence of M_{rem}, M_{zfc} and M_{fc} (symbols have their usual meaning [32]) at 50 G were measured over the temperature $5K < T < T_c$. These magnetizations do not satisfy the relation $M_{rem}(H,T) = M_{fc}(H,T) - M_{zfc}(H,T)$ even at 5 K and 50 G. We have $M_{rem}(H,T) < \{M_{fc}(H,T) - M_{zfc}(H,T)\}$. This implies that H_{c1} at 5 K is less than 50 G [32].

The value of lower critical field H_{c1} of YNi_2B_2C estimated from magnetic-field-modulated low-field microwave absorption measurements is ~20G at 10K [33]. An interesting aspect of our preliminary results of direct microwave absorption (with no field modulation) measured as a function of temperature at 9.3 GHz is that it exhibits a drop at ~23 K in addition to the expected drop due to SC at ~15K [33]. Though one may associate the drop near 23 K to onset of SC, the exact origin of this is not clear at present.

^{11}B Nuclear magnetic resonance (NMR) experiments on YNi_2B_2C [26, 27] show that the relaxation rate ($1/T_1$) increases with decrease of temperature, unlike in a metal where 1/T1 is proportional to T. Antiferromagnetic fluctuations on Ni-atoms may be responsible for this behaviour as there are no other magnetic atoms. An interesting feature of the NMR results is that below T_c, instead of one line (there is only one crystallographic B- site in the unit cell), two lines are observed [26]. Observation of the second line implies that there are normal regions in the material, even below T_c. We believe that variation of stoichiometry at microscopic level, could be the cause of the normal state regions below T_c. Such aspects are being looked into in our NMR investigations.

3.2 $ErNi_2B_2C$

Our sample of $ErNi_2B_2C$ shows a sharp superconducting resistive transition (δT of transition (90%

- 10% resistivity) is 0.5 K) at T_c = 10.3K [24]. Resistivity of $ErNi_2B_2C$ is higher than that in YNi_2B_2C which we attribute to magnetic scattering of the carriers from Er-spins. In the normal state, magnetic susceptibility of $ErNi_2B_2C$ follows a Curie-Weiss behaviour with μ_{eff} = 9.32 μ_B per formula unit and paramagnetic Curie temperature (Θ_p) ~-2 K [24]; The value of μ_{eff} is less than that of Er^{3+} free-ion (9.59 μ_B). One possibility of the reduced magnetic moment is that Er- and Ni- moments are antiferromagnetically correlated even in the paramagnetic state. It should be of interest to investigate these and other related aspects by neutron diffraction measurements.

In the ZFC-configuration, bulk and powder samples of $ErNi_2B_2C$ exhibit shielding signals that are nearly 100% and 50%, respectively, of the perfect diamagnetism. However, noteworthy is the fact that in both cases, in the FC-configuration, the material exhibits paramagnetic response down to the lowest temperature. This is an indication of sufficient field penetration and field trapping, even at a field as low as 30 G. Paramagnetic contribution from Er-spins in the flux-lines in the interior of the material masks the superconducting diamagnetic response.

Specific heat of $ErNi_2B_2C$ shows a large anomaly around 5.8 K (Fig. 8) which we interpret as due to the magnetic ordering of Er-spins. Since the resistivity does not show any re-entrant behaviour below this temperature, and the material continues to exhibit diamagnetic response down to ~5 K, we conclude that SC and magnetic ordering coexist in this system.

Coexistence of SC and magnetic ordering occurs, for example, in ternary rare earth rhodium boride and molybdenum chalcogenide superconductors. In the ternary system $ErRh_4B_4$ (T_c = 8.2K), a reentrant transition to the normal state is observed below the magnetic ordering temperature (~1.2 K). This is because in $ErRh_4B_4$, Er-spins undergo a ferromagnetic ordering and superconductivity is destroyed below the magnetic ordering temperature. On the other hand, in cases like $TmRh_4B_4$, where Tm ions are known to order antiferromagnetically, superconductivity is not destroyed due to magnetic ordering. These results suggest that it is very likely that Er-spins in $ErNi_2B_2C$ order antiferromagnetically. Preliminary results of neutron investigations [34] confirm magnetic ordering below 7 K. To investigate the magnetic interactions at the microscopic level, we plan to carry out Er-Mossbauer measurements in $ErNi_2B_2C$.

3.2 $HoNi_2B_2C$ and $TmNi_2B_2C$

In the case of $HoNi_2B_2C$ and $TmNi_2B_2C$ also, coexistence of superconductivity and magnetism has been observed [23]. Resistivity and diamagnetic response show that superconductivity occurs in both the materials (T_c ~ 8 K and 11 K respectively). Heat capacity measurements show a large anomaly around 4.5K and 4 K in $HoNi_2B_2C$ (Fig. 8) and $TmNi_2B_2C$, respectively, originating from the magnetic ordering of Ho and Tm ions. μ-SR measurements suggest magnetic ordering of Tm- moments taking place at ~2.5 K [28]. In our sample of $HoNi_2B_2C$, we see two SC transitions (Fig. 9) [30]. The resistivity starts dropping around 9 K (T_{c1}), and continues to drop till 7 K but does not go to zero. On further cooling it starts rising. This is similar to reentrant behaviour seen, for example in $ErRh_4B_4$. The unique feature of this material is that resistivity starts dropping again below 5.5 K (T_{c2}) signaling a second SC transition. This is the first material which exhibits such a *double reentrant*, superconducting-normal-superconducting, behaviour. The observed feature is seen even at applied fields up to 1 KG (Fig. 9) [30]. The magnetic response of the material measured at 20 G is primarily paramagnetic. It does show a reduction near 8 K, which is due to the onset of superconductivity. The Meissner fraction however is poor. It is possible that H_{c1} for this material is very small. Therefore, it may be necessary to study the magnetic response in rather low applied magnetic fields. Even after annealing, the material did not show zero resistance, though, the XRD pattern showed some improvement. Coexistence of SC and magnetism in these materials have also been reported by Eisaki et al. [35].

4. Non-superconducting materials - $RENi_2B_2C$ (RE = Ce, Nd, Gd).

Cava et al. [21] have reported the formation of other $RENi_2B_2C$ materials (RE = La, Ce, Sm, Tb, Dy) also which do not show SC down to 4.2K. From the lattice parameters, it was concluded that $CeNi_2B_2C$ is a mixed valence material [22]. We have synthesized and investigated the magnetic properties of $RENi_2B_2C$ (RE = Ce, Nd and Gd). We find that $NdNi_2B_2C$ and $GdNi_2B_2C$ also crystallize in the 1221-type structure. The lattice parameters of Ce-, Nd- and Gd- compounds, respectively, are: a: = 3.634 Å, 3.686 Å, 3.583 Å; c: =

10.232 Å, 10.103 Å and 10.381 Å. Lattice parameters of $CeNi_2B_2C$ are in agreement with those reported by Siegrist et al. [22]. Our magnetic studies show that none of these compounds is superconducting down to 4.2 K. The $NdNi_2B_2C$ orders antiferromagnetically at ~4.5 K. Susceptibility of $GdNi_2B_2C$ exhibits a peak at ~19.5 K, but on further cooling the susceptibility drops slightly and saturates. At present we do not know if the magnetic order in this material is ferromagnetic or antiferromagnetic. No magnetic ordering is observed in $CeNi_2B_2C$ down to 4.2 K. Low value of room temperature susceptibility (~$7x10^{-4}$ emu/mol.) suggests loss of magnetic moment of Ce- atoms. L_{III} edge measurements are planned to investigate the valence of Ce in this material. Details of results on these materials will be published elsewhere.

5. Superconductivity in Y-Pd-B-C, Lu-Pd-B-C and Sc-Pd-B-C.

An extension of our work on $YNi_4BC_{0.2}$, namely, replacing 3d- element by 4d- element, we synthesized and studied the materials of nominal composition $YPd_4BC_{0.2}$ and $YPd_4BC_{0.5}$. Both of them turned out to be multiphase samples but exhibited SC [8].

Resistance R(T) of both the samples is only weakly temperature dependent over the temperature interval 25K < T < 300K. This is a typical behaviour of the materials having considerable chemical/structural disorder. Sample of the composition $YPd_4BC_{0.2}$ prepared from pieces of the constituents (sample of batch 1) exhibits a drop in resistance at 21 K. Within a width of ~4K, resistance drops by about 50%. The material also exhibits a diamagnetic transition at ~22 K, measured both in the field cooled and zero field cooled conditions in an applied field of 20 G. We should, however, point out that the shielding signal is ~2% of that expected for perfect diamagnetism. The strength of the Meissner signal is nearly half of that of the shielding signal. These results indicate that the material has a superconducting phase with T_c ~22 K. Another sample of $YPd_4BC_{0.2}$ (batch 2) prepared by melting a pellet of powders of the elements shows a superconducting transition at ~10 K only. Magnitude of magnetic response of this sample is about one third of that of the sample of batch 1. Thus, it appears that physical properties of the end-products depend on whether the starting components were taken as powders or pieces.

Sample of the composition $YPd_4BC_{0.5}$ exhibits *two* superconducting transitions, one near 22 K and the other near 9 K (Fig. 10) [8]. It is clear from these measurements that the Y-Pd-B-C system has at least two superconducting phases. Relative proportions of the two phases depend upon not only whether the elements are taken as powders or small pieces but also on the amount of carbon in the system. Cava et al., reported superconductivity at T_c ~ 23 K, in a multiphase material $YPd_5B_3C_x$ ($0.3 < x < 0.4$) [7].

To study the effect of rare earth substitution on the superconducting properties of $YPd_4BC_{0.2}$, we have studied superconducting behaviour of $LuPd_4BC_{0.2}$ and $ScPd_4BC_{0.2}$ [8]. Both the materials exhibit superconductivity at ~9 K although the strength of the superconducting signals is much weaker than in $YPd_4BC_{0.2}$.

We also synthesized the materials YT_2B_2C (T = Ir, Rh, Os, Co). All of them were multiphase. However, in the XRD pattern of YCo_2B_2C, a set of lines could be indexed on the basis of 1221-type phase (a = 3.513Å, c = 10.581Å). None of these was found to be SC down to 4.2 K. It is interesting to point out that YCo_2B_2 forms in $ThCr_2Si_2$ structure [36] and carbon can be incorporated in the lattice to form YCo_2B_2C but does not exhibit SC down to 4.2 K. On the other hand, YNi_2B_2 does not form [24], but YNi_2B_2C forms and superconducts. Crystal chemistry aspects of this are being looked into.

6. A-M-B-C (A = Th and U; M = transition elements).

We also investigated the existence of SC in various Th- and U-, the 5f- element based borocarbide materials. We observe SC in Th-Pd-B-C and Th-Ni-B-C systems [37]. Sarrao et al. have also reported SC in these materials [38].

We observe two superconducting transitions (T_c ~17 K and 12 K) in our resistance and magnetic measurements of multiphase $ThPd_4BC$. Resistance of the sample does not go to zero even below the lower transition temperature ~12 K. Shielding signal, measured at 20 G, is low (~10%); however, one does see a Meissner signal (~1%). The superconducting phases are minority phases in this multiphase material. A

number of samples of the composition $ThPd_2B_2C$ were synthesized and studied. These samples were also multiphase. Our results show that there are two superconducting transitions in this composition as well (T_c ~20 K, 14 K) (Fig. 11). Zero resistnce is acheived below 14 K (Fig. 11). The strength of the shielding signal and the Meissner signal are sample dependent. These results show that the system Th-Pd-B-C also has at least two superconducting phases just as the system Y-Pd-B-C has.

Our samples of $ThNi_2B_2C$ are multiphase but do contain the 1221-type phase (a = 3.699Å, c = 10.192Å). Resistance of this sample goes to zero below 6 K. Diamagnetic shielding signal at 4.2 K is close to what one expects for perfect diamagnetism. Thus there is a superconducting phase in the sample with T_c ~ 6 K. Magnetic response in the field cooled condition, however, is positive below ~6 K.

If in our multiphase $ThNi_2B_2C$, 1221-type phase is the SC phase, then it is interesting to compare the reduced T_c in $ThNi_2B_2C$ (in relation to YNi_2B_2C) with that in $ThRh_4B_4$ (in relation to YRh_4B_4). $ThRh_4B_4$ has T_c ~4.5 K which is much lower than T_c of YRh_4B_4 (~10.5 K) [39]. In the case of $ThRh_4B_4$, this drop in T_c has been explained as a consequence of change of the electron/atom ratio on replacing trivalent Y by tetravalent Th. Subtle changes in the density of states at the Fermi level, which can occur due to the concomitant variation in the cell constants, also may be responsible, at least partly, for this large change of T_c [39, 40].

We synthesized ThM_2B_2C (M = Co, Ir, Os) and also several compositions of U-based materials, such as, UNi_2B_2C, UPd_2B_2C, UOs_2Ge_2C and $UPd_5B_3C_{0.35}$. All these samples were multiphase. a.c. susceptibility investigations of these materials did not show SC down to 4.2K.

7. Dilute substitution studies: $Y_{1-x}A_xNi_{2-y}M_yC$ (A = U, Th, Gd; M = Co, Fe; x = 0 and y = 0.1; x = 0.1 and y = 0).

In order to get an insight into the mechanism of SC in these borocarbides, we investigated the effect of partial substitution at the Y-site and the Ni-site on superconducting properties of YNi_2B_2C.

In $Y_{0.9}Th_{0.1}Ni_2B_2C$, $Y_{0.9}Gd_{0.1}Ni_2B_2C$ and $Y_{0.9}Ce_{0.1}Ni_2B_2C$ which are essentially single phase, resistance and susceptibility results show that T_c is depressed by about ~5 K in all the cases (Fig. 12), even though Th-ions are non-magnetic, Gd-ions are magnetic and Ce-ions are mixed valent and are weakly magnetic. This is an interesting result, if effects such as variation in cell constants or difference in valence state (Th is tetravalent and Gd is trivalent) do not play an important role in the depression of T_c. It implies that pair-breaking is not influenced much by the magnetic state of the impurity ions. Similar effects have been observed in heavy fermion superconductors [41]. This has certain implications with respect to the nature of pairing (*s*- vs non-*s*). Further work on this aspect is desirable. We have also observed that substitution of 0.05 atomic fraction of Y by U depresses T_c (onset) by 3 K, but major drop in resistance occurs at ~5 K and T_c(zero) is depressed by ~10 K. It would be interesting to ascertain if U-atoms have magnetic moment in this dilute limit.

In single phase $YNi_{1.9}Fe_{0.1}B_2C$ and $YNi_{0.9}Co_{0.1}B_2C$, resistance and a.c. susceptibility results show that T_c is depressed by about ~5 K in Co- and ~7 K in Fe- cases, respctively. It would be interesting to examine the magnetic state of Fe and Co in dilute limits in borocarbides.

8. Conclusions.

Weak signal of superconductivity at an elevated temperature, T_c ~12 K - 15 K, that we observed in YNi_4B led us to the discovery of bulk superconductivity in multiphase four-element borocarbide system Y-Ni-B-C. This discovery laid the foundation of new field of superconductivity and magnetism in quaternary borocarbides. Y-Pd-B-C and Th-Pd-B-C systems have a phase with T_c's (> 20 K) higher than that observed in bulk intermetallics known so far. Further, in these two systems there are at least two phases that support superconductivity. The borocarbide $RENi_2B_2C$ series, besides having superconducting members, also has members which are not superconducting. They exhibit a variety of magnetic behaviour.

Our structural investigations on single phase superconductor YNi_2B_2C suggest that carbon atoms have large and highly anisotropic thermal vibrations and that there is no structural change down to 50 K. From our specific heat and magnetization studies, we conclude that this material is a strong-coupling superconductor and the temperature dependence of $H_{c2}(T)$ is rather unusual. Our ^{11}B nuclear relaxation measurements suggest short lived moments on Ni-ions in the normal state of YNi_2B_2C. Microwave absorption measurements in YNi_2B_2C indicate H_{c1} to be ~20 G at 10 K and exhibit a change in slope at ~23K, origin of which is not clear at present.

Single phase materials, $RENi_2B_2C$ (RE = Ho, Er, Tm), exhibit coexistence of superconductivity and magnetism. *double reentrant* transition $HoNi_2B_2C$, anomalously high magnetic ordering temperatures, possibility of moment on transition metal ions are some of the phenomenon that distinguish these magnetic superconductors from all other known magnetic superconductors, including high-T_c cuprates.

Thus, borocarbides are not only new superconductors, but they have also provided hopes for new physics and higher T_c's in intermetallics. It is evident that this discovery will motivate efforts not only to identify quaternary systems with other elements such as Al, N, Si and Ge etc. but also multicomponent intermetallic superconductors with still higher number of elements. Our own efforts in this direction are in progress.

Acknowledgment: Part of this work was carried under Project 509-1 of Indo-French Centre for Promotion of Advanced Research, New Delhi. We wish to express our thanks to K.V. Gopalakrishnan for assistance in SQUID measurements, S.V. Purandare for assistance in EDAX analysis and S.K. Paghdar for assistance in other experiments.

References.

1. Chandan Mazumdar, R. Nagarajan, C. Godart, L.C. Gupta, M. Latroche, S.K. Dhar, C. Levy-Clement, B.D. Padalia, and R. Vijayaraghavan, Solid State Comm. **87**, 413 (1993).
2. Chandan Mazumdar, R. Nagarajan, C. Godart, L.C. Gupta, M. Latroche, S. K. Dhar, C. Levy-Clement, B.D. Padalia, and R. Vijayaraghavan, Oral presentation of results of Y-Ni-B-C system along with those of YNi_4B at the 20th International Conference on Low Temperature Physics (LT 20), Eugene, Oregon, U.S.A., Aug. 4-11, 1993.
3. Chandan Mazumdar, R. Nagarajan, C. Godart, L.C. Gupta, M. Latroche, S. K. Dhar, C. Levy-Clement, B.D. Padalia, and R. Vijayaraghavan, Poster No. KE56, Poster presentation of results of Y-Ni-B-C system along with those of YNi_4B at the International Conference on Strongly Correlated Electron Systems (CSCES 93), San Diego, U.S.A., Aug. 16-19, 1993.
4. R. Nagarajan, Chandan Mazumdar, Zakir Hossain, S.K. Dhar, K.V. Gopalakrishnan, L.C. Gupta, C. Godart, B.D. Padalia, and R. Vijayaraghavan, Phys. Rev. Lett., **72**, 274 (1994).
5. Chandan Mazumdar, R. Nagarajan, L.C. Gupta, B.D. Padalia, and R. Vijayaraghavan, Proc. Solid State Physics Symposium of Dept. Atomic Energy, India, **33C**, 265 (1991).
6. R. Vijayaraghavan, Chandan Mazumdar, R. Nagarajan, L.C. Gupta and B.D. Padalia, Abstract No. PE3.23, International Conference on Magnetism (ICM'91), Edinburgh, U.K., 2-6 Sept. 1991.
7. R.J. Cava, H. Takagi, B. Batlogg, H.W. Zandbergen, J.J. Krajewski, W.F. Peck, R.B. van Dover, R.J. Felder, T. Siegrist, K. Mizuhashi, J.O. Lee, H. Eisaki, S.A. Carter, and S. Uchida, Nature **367**, 146 (1994).
8. Zakir Hossain, L.C. Gupta, Chandan Mazumdar, R. Nagarajan, S.K. Dhar, C. Godart, C. Levy-Clement, B.D. Padalia, and R. Vijayaraghavan, Solid State Comm. **92**, 341 (1994).
9. J.G. Bednorz and K.A. Muller: Z. Phys. **B64**, 189 (1986).
10. M.K. Wu, J.R. Ashburn, C.J. Torng, P.H. Hor, R.L. Meng, L. Gao, Z.J. Huang, Y.Q. Wang and C.W. Chu, Phys. Rev. Lett., **58**, 908 (1987).
11. R. Nagarajan, G.K. Shenoy, L.C. Gupta and E.V. Sampathkumaran, Phys. Rev **B32**, 2846 (1985).
12. Sujata Patil, R. Nagarajan, L.C. Gupta and R. Vijayaraghavan, J. Magn. Magn. Mater. **54-57**, 349 (1986).
13. Sujata Patil, R. Nagarajan, L.C. Gupta C. Godart, R. Vijayaraghavan and B.D. Padalia, Phys. Rev. **B37**, 7708 (1988).

14. Chandan Mazumdar, R. Nagarajan, S.K. Dhar, L.C. Gupta, R. Vijayaraghavan and B.D. Padalia, Phys. Rev. **B46**, 9009 (1992).
15. L.F. Matheiss et al., Phys. Rev. **B37**, 3745 (1988); R.J. Cava et al., Nature **332**, 814 (1988).
16. Chandan Mazumdar, R. Nagarajan, S.K. Dhar, L.C. Gupta, B.D. Padalia, and R. Vijayaraghavan, Proc. Solid State Physics Symposium of Dept. Atomic Energy, India, **34C**, 241 (1991).
17. Chandan Mazumdar, R. Nagarajan, L.C. Gupta, B.D. Padalia, and R. Vijayaraghavan, 37th Annual Conference on Magnetism and Magnetic Materials, Abstract No. BP14, Houston, Texas, U.S.A., Dec. 1-4, 1992.
18. K. Nihara, Y. Katayama and S. Yajima, Chem. Lett. (Chem. Soc. Japan), 613 (1973).
19. Y.B. Kuz'ma and M.P. Khaburskaya, Izv. Akd. Nauk, SSSR, Neorg. Mater. **11**, 1893 (1975).
20. M.C. Krupka, A.L. Giorgi, N.H. Krikorian and E.G. Szklarz, J. Less-Common Met. **17**, 91 (1969).
21. R.J. Cava, H. Takagi, H.W. Zandbergen, J.J. Krajewski, W.F. Peck, T. Siegrist, B. Batlogg, R.B. van Dover, R.J. Felder, K. Mizuhashi, J.O. Lee, H. Eisaki and S. Uchida, Nature, **367**, 252 (1994).
22. T. Siegrist, H.W. Zandbergen, R.J. Cava, J.J. Krajewski, and W.F. Peck, Nature **367**, 254 (1994).
23. L.C. Gupta, R. Nagarajan, S.K. Dhar, Chandan Mazumdar, Zakir Hossain, C. Godart, C. Levy-Clement, B.D. Padalia and R. Vijayaraghavan, International Conference on Advances in Physical Metallurgy, Bombay, March 9-11, 1994.
24. C. Godart, L.C. Gupta, R. Nagarajan, S.K. Dhar, H. Noel, M. Potel, Zakir Hossian, Chandan Mazumdar, C. Levy-Clement, G. Schiffmacher, B.D. Padalia and R. Vijayaraghavan, Phys. Rev **B** (1994) (in press).
25. Y. Iye, J. Phys. Chem. Solids, **53**, 1561 (1992) and references therein. See also, T. Moriya, Y. Takahashi, and K. Ueda. J. Phys. Soc. Japan, **59**, 2905 (1990); H. Kohno and Y. Yamada, Prog. Theor. Phys. **85**, 13 (1991).
26. F. Borsa,Q. Hu,K.H. Kim, B.J. Suh, D.R. Torgeson, P. Canefield, M. Xu and B. Zhong (pre-print).
27. K. Elankumaran and A.V. Mahajan et al., (to be published).
28. D.W. Cooke, J.L. Smith, S.F.J. Cox, A. Morrobel-Sosa, R.L. Lichti, T.L. Estle, B. Hitti, L.C. Gupta, R. Nagarajan, Z. Hossain, C. Mazumdar, and C. Godart, (to be published).
29. R. Movshovich, M.F. Hundley, J.D. Thompson, P.C. Canfield, B.K. Cho, and A.V. Chubukov (preprint).
30. Chandan Mazumdar and A.K. Nigam et al., (to be published).
31. See for example, Gerald Burns, in High-Temperature superconductivity: An Introduction, (Academic Press, Inc., Boston, San Diego, New York, London, Sydney, Tokoyo, Toronto, 1992) and references therein.
32. S.B. Roy, Zakir Hossain, A.K. Pradhan, Chandan Mazumdar, P. Chaddah, R. Nagarajan, L.C. Gupta and C. Godart, Physica C **228**, 319 (1994).
33. R.M. Kadam, M.D. Sastry, Zakir Hossain, Chandan Mazumdar, R. Nagarajan, L.C. Gupta, C. Godart and R. Vijayaraghavan, Physica C (1994) (in press).
34. S.K. Sinha, L.W. Lynn, T.E. Grigereit, Z. Hossain, L.C. Gupta, R. Nagarajan and C. Godart, Phys. Rev. **B** Rapid Commun., (1994) in press.
35. H. Eisaki, H. Takagi, R.J. Cava, K. Mizuhashi, J.O. Lee, B. Batlogg, J.J. Krajewski, W.F. Peck. jr. and S. Uchida (pre-print).
36. K. Nihara, T. Shishido and S. Yajima, Bull. Chem. Soc. Japan, **46**, 1137 (1973).
37. Zakir Hossain, L.C. Gupta, R. Nagarajan, P. Raj, S.K. Dhar, C. Godart, P. Suryanarayana, S.N. Bagchi, V.G. Date, D.S.C. Purushotham and R. Vijayaraghavan, Europhys. Lett., 1994 (in press).
38. J.L. Sarrao, M.C. de Andrade, J. Hermann, S.H. Han, Z. Fisk, M.B. Maple and R.J. Cava, High T_c Update, 1 June, 1994.
39. C.B. Vining and R.N. Shelton in Ternary Superconductors, Proc. Int. Conf. on Ternary Superconductors, Sept. 24-26, 1980, Lake Geneva, Wisconsin, U.S.A., Eds. G.K. Shenoy, B.D. Dunlop, F.Y. Fradin, North Holland Inc., New, York, p189.
40. K. Yvon in Ref. 39, p15.
41. Z. Fisk, D.W. Hess, C.J. Pethick, D. Pines, J.L Smith, J.D. Thompson and J.O. Willis, Science **239**, 33 (1988).

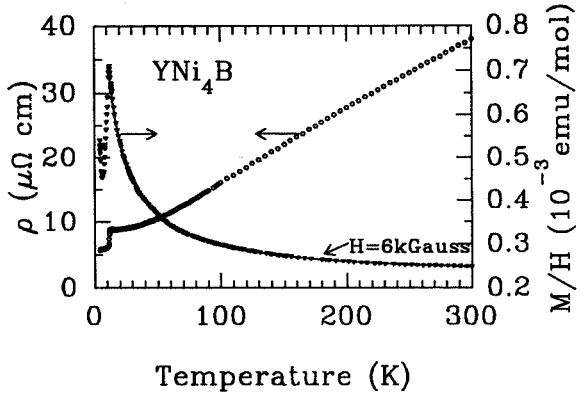

Figure 1.- Resistivity and magnetic susceptibility of our sample of YNi_4B as a function of temperature. Solid line is the Curei-Weiss fit in the range 12K to 300 K (from Ref.1)

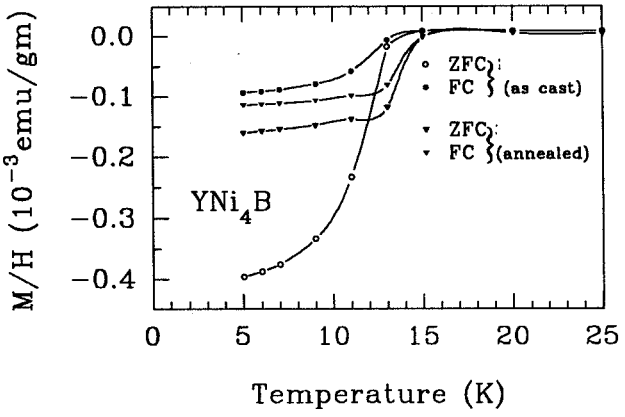

Figure 2.- Zero field cooled (shielding signal) and filed cooled (Meissner signal) diamagnetic response as function of temperature for as cast and annealed samples of YNi_4B.

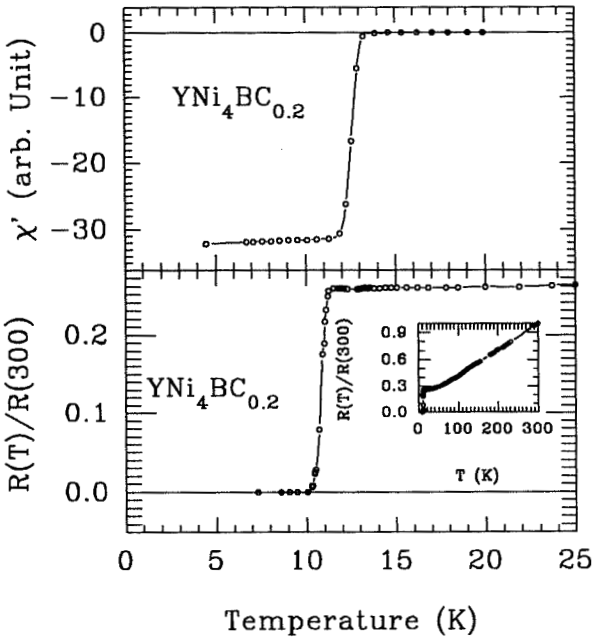

Figure 3.- a.c. magnetic susceptibility (top) and d.c. resistance (bottom) as a temperature for the sample $YNi_4BC_{0.2}$. Inset shows the resistance over the temperature range 4.2 K to 300 K.

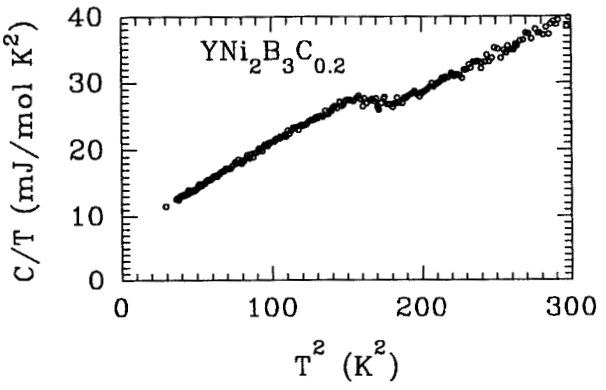

Figure 4.- Specific heat (C/T Vs.T^2) of the material with nominal composition $YNi_2B_3C_{0.2}$ (from Ref. 4).

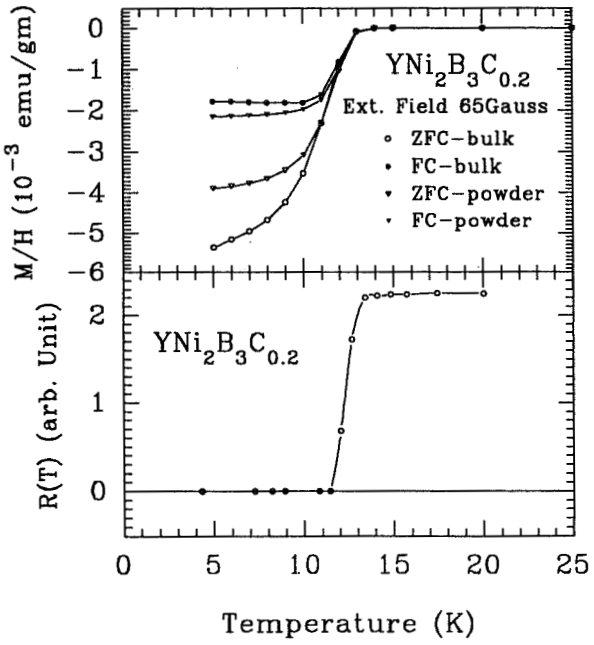

Figure 5.- Zero field cooled (shielding signal) and field cooled (Meissner signal) diamagnetic response as a function of temperature for bulk and powdered samples of $YNi_2B_3C_{0.2}$ (top). Bottom figure show resistance as a function of temperature for the bulk sample of $YNi_2B_3C_{0.2}$.

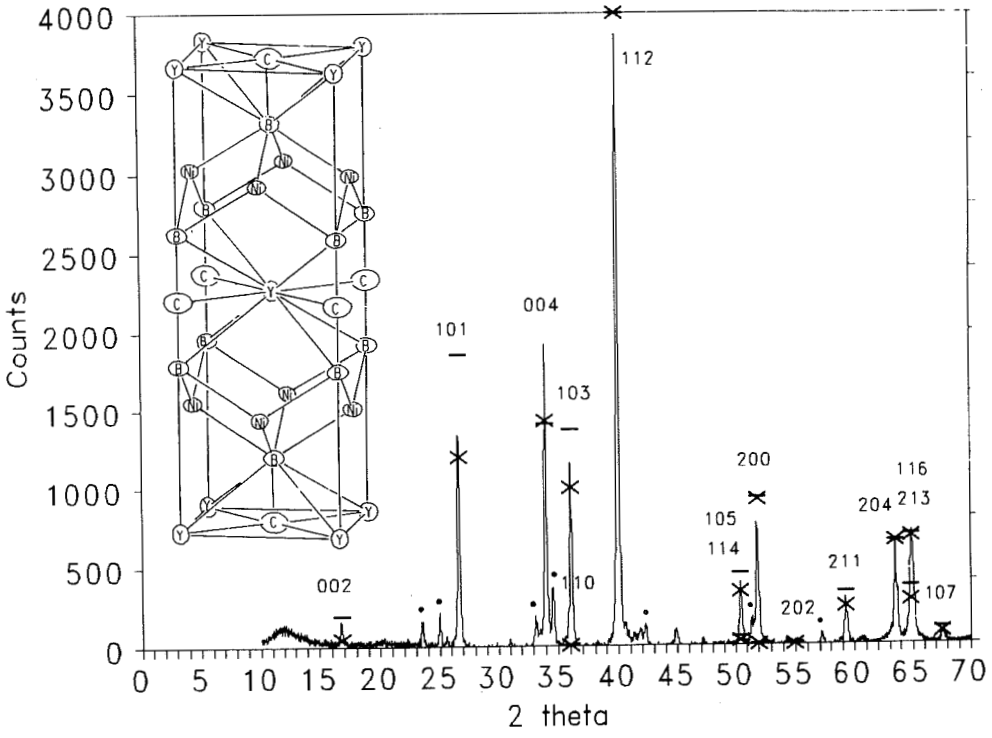

Figure 6.- Powder x-ray diffraction pattern of YNi_2B_2C. Lines corresponding to the impurity phase YB_2C_2 are indicated by solid circle above those lines. Results of our intensity calculations are shown by cross mark. Inset shows the structure of YNi_2B_2C determined from single crystal diffraction studies. Note the rather large thermal amplitude of C-atoms in the Y-C plane (represented as ellipsoids) (from Ref. 24).

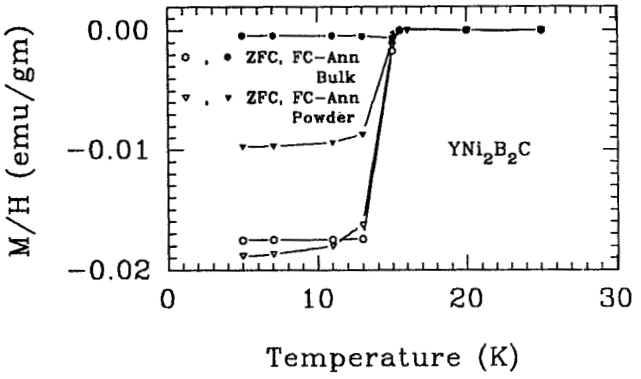

Figure 7.- Zero field cooled (shielding signal) and field cooled (Meissner signal) diamagnetic response as a function of temperature for bulk and powdered samples of annealed YNi_2B_2C. The solid lines are guide to the eye.

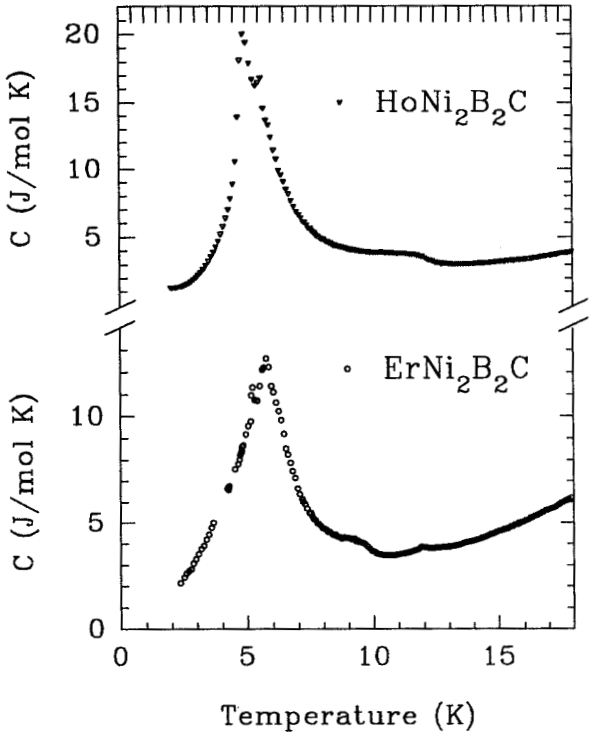

Figure 8.- Specific heat (C) of $ErNi_2B_2C$ and $HoNi_2B_2C$ as a function of temperature. The large peaks are due to magnetic ordering in these materials In $ErNi_2B_2C$, the anomaly due to SC is seen just below 10 K. In the case of $HoZNi_2B_2C_2$ it is below the limit of our observations.

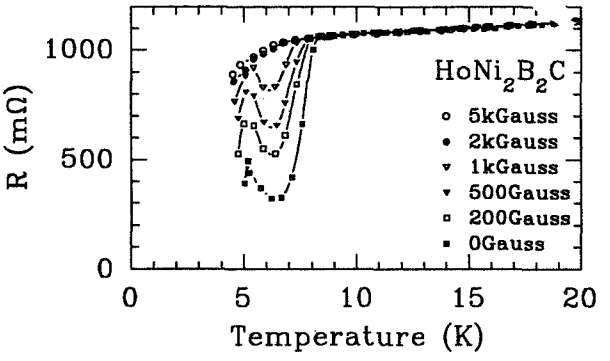

Figure 9.- Resistance as a function of temperature at various externally applied fields of $HoNi_2B_2C$. Note the double reentrant behavior for fields upto 1 KG.

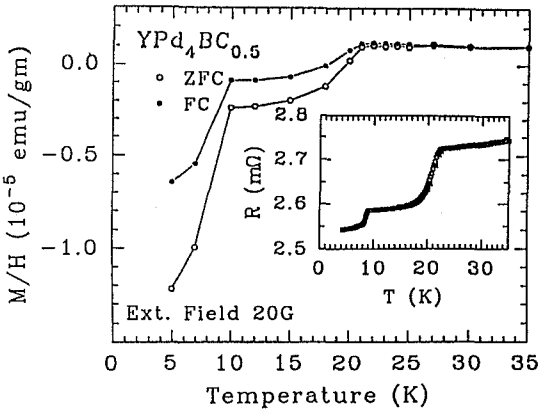

Figure 10.- Zero field cooled (shielding signal) and field cooled (Meissner signal) diamagnetic response as a function of temperature for material of nominal composition $YPd_4BC_{0.5}$. Solid lines are guide to the eye. Inset shows resistance (r) of the sample as a function of temperature (from Ref. 8). Note two superconducting transitions.

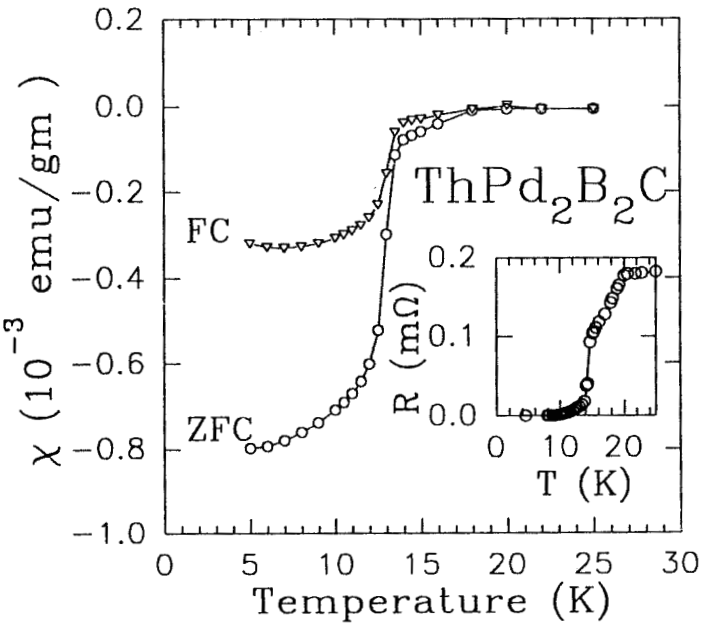

Figure 11.- Zero field cooled (shielding signal) and field cooled (meissner signal) diamagnetic response as a function of temperature for material of nominal composition $ThPd_2B_2C$. Inset shows resistance (r) as function of temperature. Note two superconducting transitions.

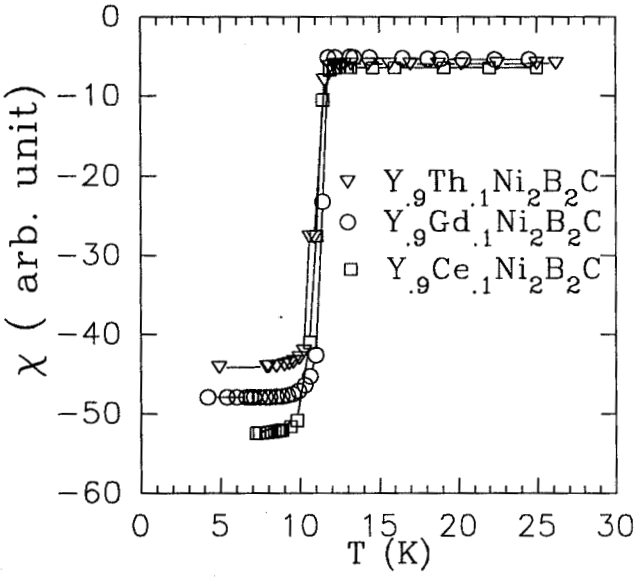

Figure 12.- a.c. susceptibility as a function of temperature for $Y_{0.9}M_{0.1}Ni_2B_2C$ (M = Th, Gd, Ce).

SINGLE SCAN
10?
531-76
514185

Electronic Structure And The van Hove Singularity Scenario In High-T_c $HgBa_2CuO_{4+\delta}$ Superconductors

by

Bal K. Agrawal & Savitri Agrawal

Physics Department, Allahabad University

Allahabad-211002, INDIA.

The electronic structure and the hole concentrations in the high Tc superconductor HgBa2CuO(4+δ) (δ = 0, 1) has been investigated by employing a first principles full potential self-consistent LMTO method with the local density functional theory. The scalar relativistic effects have been considered. The hole concentrations of the Cu-d and O-p(x,y) orbitals are seen to be larger for the HgBaCuO5 system than those of the HgBaCuO4 solid. However, the van Hove singularity (vHs) induced Cu-d and O-p peak which is seen to lie comparatively away and above the Fermi level in the δ=1 system shifts towards the Fermi level in the δ=0 system. Thus, the superconducting behaviour appears to originate from the occurrence of the vHs peak at the Fermi level. The Fermi surface nesting area in the δ=0 compound is seen to be larger than in the δ = 1 compound. The calculation reveals that the increase in pressure on the crystal enhances the hole concentrations but without showing any optimum value.

On the other hand, the vHs peak approaches to-wards the Fermi level with pressure and crosses the Fermi surface near $V/V_o \simeq 0.625$ (V and V_o are the crystal volumes at high and normal pressures, respectively). Our calculated value of the bulk modulus equal to 0.626 Mbar predicts the occurrence of this crossover at about 24 GPa which is in complete agreement with the experimental value. At this pressure the compound has maximum nesting area and self-doped behaviour.

I. INTRODUCTION :

The compound HgBa2CuO(4+δ) (δ = 0, 1) has been seen [1] to be superconducting with Tc=94°K. Schilling et al [2] have observed a Tc=133°K in a material containing HgBa2Ca2Cu3O(8+δ) and HgBa2CaCu2O(6+δ). Quite recently, values of Tc as high as 164°K at high pressure have been reported in HgBa2Ca2Cu3O(8+δ) samples [3,4].

In understanding the cause of the occurrence of superconductivity in high Tc superconductors, one can not ignore the crucial role played by the CuO2 planes. In two-dimensions, one come across with the saddle points at symmetric points of the Brillouin zone which lead to logarthimic vHs in the electron density of states obtained even after assuming only nearest-neighbour hopping. It has been seen [5] that a simple reformulation of BCS theory in the weak coupling limit considering the occurrence of a vHs near the Fermi energy may lead to quantitatively different results. The value of Tc may be much higher achieving its maximum value when the van Hove singularity coincides with the Fermi energy.

In the present communication, we investigate the occurrence of the van Hove singularity in the Hg-based single CuO2 layer compounds HgBa2CuO(4+δ) (δ=0,1). Novikov and Freeman [6] and Rodriguez et al [7] have also performed a LMTO calculation for the δ=0 compound but have not investigated the pressure effects. Our similar results for HgBa2CaCu2O(6+δ) (δ=0,1) have been reported elsewhere [8]. The present LMTO method goes beyound the usually employed LMTO method in the atomic sphere approximation which has several limitations. The method is seen to predict the electronic structure, lattice constants, elastic constants, and phonon frequencies, for the simple systems III-V and II-VI semiconducting compounds like AlAs, CdTe, GaSb, ZnSe, ZnTe, ZnS etc [9]. Also, the parent compound CaCuO2 of the recently discovered high Tc oxide superconductors has been successfully studied [10].

II. CALCULATION AND RESULTS

The crystal structures of HgBa2CuO(4+δ) (δ=0,1) possess the space group P4/mmm. The lattice parameters of the tetragonal cell are the experimentally measured values i.e., a=3.8797 A° and c=9.509 A°. In HgBa2CuO5, the atomic positions in the unit cell are Cu:(0,0,0); O(1):(0.5a,0,0); O(2):(0,0.5a,0); Ba:(0.5a,0.5a,±0.294c);

O(3):(0,0,$\pm$0.294c); Hg:(0,0,0.5c) and O(4):(.5a,.5a,.5c). For HgBa2CuO4, the atom O(4) of the HgO plane has been removed.

The basis functions with $l \leq 4$ and of energies -0.01, -1.0 and -2.3 Ry were chosen for making the expansions of the products of the LMTO envelops. The decays of these functions were taken as λ^2=-1 and -3 Ry. Each atomic sphere has thus 50 functions. The local density potential of Hedin and Lundquist [11] has been utilized. A spd basis each for the two high energies -1.0 and -0.01 Ry and a sp basis for the energy -2.3 Ry were employed for every real atom. It leads to a number 22 of LMTO's per atom.

The muffin-tin (MT) spheres chosen to fill the space were slightly non-overlapping. The radii of these atomic spheres in atomic units were Cu(2.0), O(1.655), Ba(3.35) and Hg(2.05).

The valence states considered for the various atoms are Cu(3d,4s,4p); O(2s,2p,3d); Ba(6s,6p,5d) and Hg(6s,6p,6d). The core electrons are treated not in a frozen-core approximation but are allowed to relax. A number of 72 k-points obtained by the sampling method in the irreducible part of the Brillouin zone were employed in all the calculations. The δ=0 compound shows minimum in the crystal energy at a volume ratio (V/V_o)=1.05, where V_o is the experimental crystal volume for the δ = 0.1 sample. Novikov and Freeman [6] and Rodriguez et al [7] have reported results for a different set of valence states.

(i) Electronic Structure :

The dispersion curves for a number of symmetry points lying in the two different k(x,y) planes have been depicted in Fig.1. They are Γ = (0,0,0); X = (Π/a)(1,0,0); M = (Π/a)(1,1,0); Z = (Π/a)(0,0,a/c); R = Π(1/a,0,1/c) and A = Π(1/a,1/a,1/c). The origin of the energy is taken at Fermi level (E_F).

The electronic structure is very much two-dimensional. The dispersion of the valence bands along the c-axis i.e., along the symmetry direction Γ-Z is quite small. The band structure in the two different planes along k_z are very much similar.

In Figs. 1b, 1c and 1d, we have also depicted those parts of the dispersion curves for which the probability of any wave function on an atom

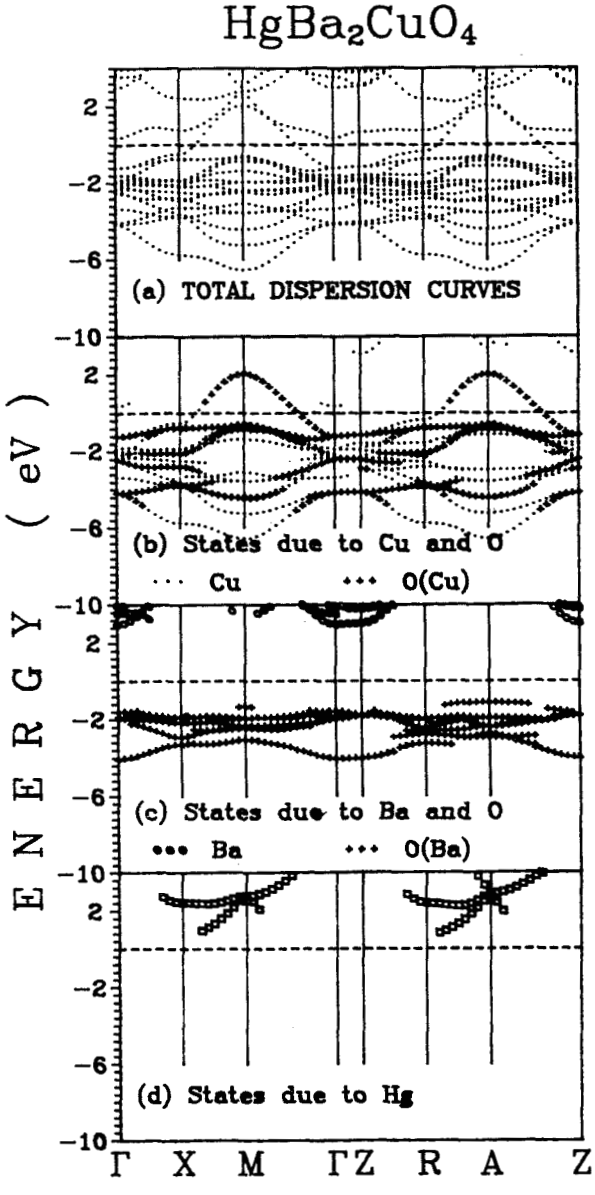

FIG.1 Electronic band structure for HgBa2CuO4 compound in two k_z - planes and also along k_z direction.

is equal or more than 0.2.

The single antibonding Cu-3d(x^2-y^2):O-2p(x, y) band crosses the Fermi surface in most of the shown symmetry directions in the k_z=0 plane [see Fig. 1(b)] and goes above E_F upto more than 2 eV.

The band structure for the HgBa2CuO5 is quite similar to that of HgBa2CuO4 except that in the former there is an overall shift of the valence bands to-wards the high energy side by 0.4 and the conduction bands by a large magnitude of about 3.5 eV.

The Hg-6p conduction states do not cross the Fermi surface making the compound not self-doped. Also no atom of the BaO and Hg planes contributes and are thus electronically inactive. In the δ=0 sample, the location of the saddle point of the crossover Cu-3d(x^2-y^2):O-2p(x, y) band changes with k_z, it varies from a value -0.51 eV at X point to -0.37 eV (k_z=0.204) at R point. On the other hand, in the δ=1 sample, they appear at 0.40 eV at X and 0.18 eV at R points, respectively.

(ii) DENSITY OF STATES :

The computed local electron density of states for the δ=0 compound is presented in Fig. 2. In the 6.0 eV wide valence band region, the main contributions arise from the Cu(3d) and the O(2p) states of the various oxygens lying in the layers of Cu-O2 and BaO. The density of states at the Fermi level in the δ=1 compound is very high equal to 7.24 states/eV as compared to 0.49 states/eV in the δ=0 sample.

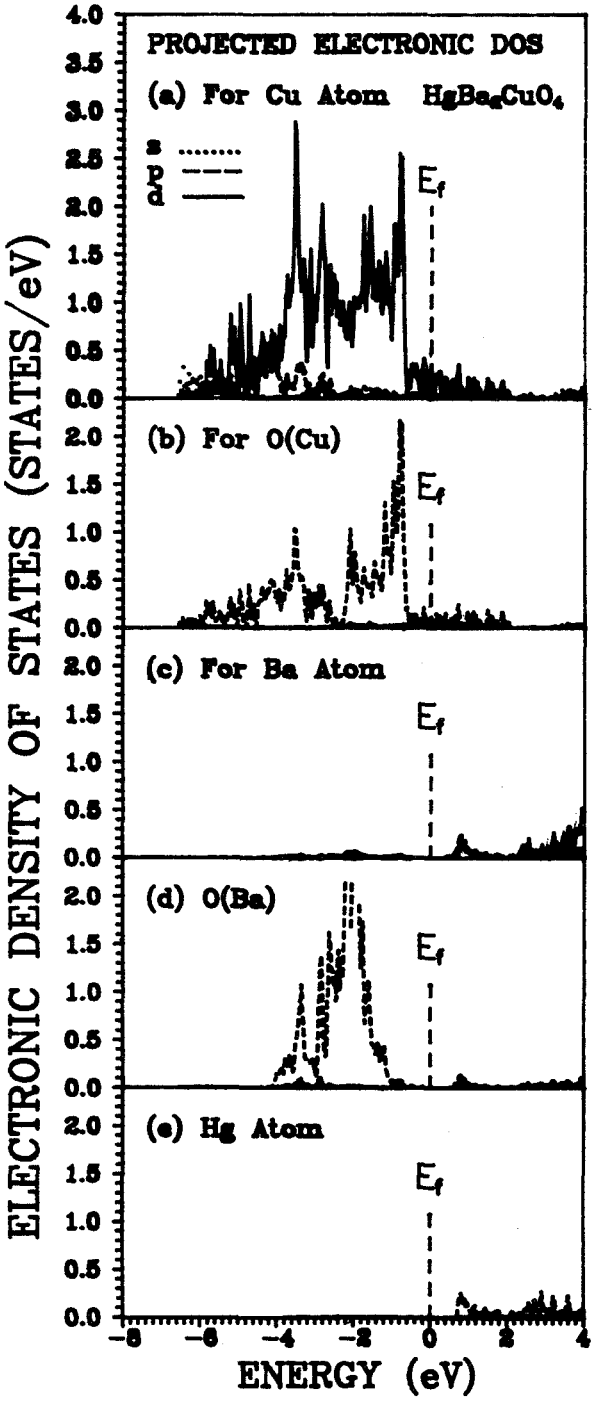

FIG.2 Projected DOS at various atoms of the HgBa2CuO4 system.

The most remarkable feature is shifting of the vHs peak originating from (Fig. 3) the Cu-3d(x^2-y^2):O-2p(xy) states. In the δ=0 compound it changes from -0.44 eV at X point to -0.37 eV at the R point which may drive the δ=0 compound approaching to-wards the superconducting behaviour. On the other hand, in the δ=1 compound these peaks appear above the Fermi level at 0.42 eV at X and 0.18 eV at R respectively. The appearence of the vHs peak above the Fermi level may result in the observed non-superconducting behaviour of the compound HgBa2CuO5 .

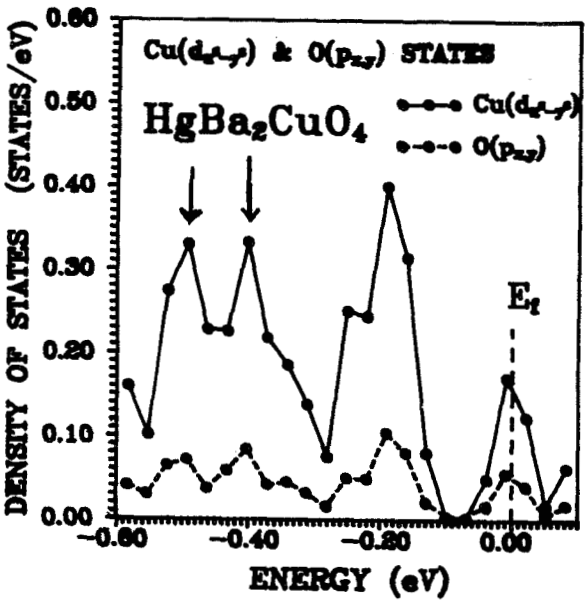

FIG.3 Cu-3d(x^2-y^2) & O-2p(x,y) density of states around the Fermi level of HgBa2CuO4 with an extended energy scale.

The other peaks like one appearing at about 0.33 eV in between the energy range 0.18 to 0.42 eV originate from the flatness of the bands in the different parts of the Brillouin zone.

(iii) FERMI SURFACE

The cross sections of the Fermi surface for the δ=0 and 1 compounds, in the two different (kx-ky) planes i.e. kz=0 and kz=0.204 are shown in Fig. 4. We find nesting along the [100] and [010] directions. The shapes of the Fermi surface are circular for δ=1 but are rounded squares in δ=0 compound. The nesting area in both the kz- planes in the δ=0 compound is greater than in the δ=1 compound. The change in the nesting area with the change of the location of the kx-ky plane along the kz-axis is quite small in δ=0 compound, a behaviour different from that seen for the δ=1 compound. The three- dimensional surface will look like a tube.

TABLE.1 : HOLE CONCENTRATIONS FOR $HgBa_2CuO_4$ AND $HgBa_2CuO_5$.

System	Atom	Orbitals	Hole Concentration
$HgBa_2CuO_4$	Cu	d	0.09
	O(Cu)	p	0.108
$HgBa_2CuO_5$	Cu	d	0.23
	O(Cu)	p	0.39
	O(Ba)	p	0.50
	O(Hg)	p	0.68

(iv) HOLE CONCENTRATIONS :

The hole concentrations at the various atomic sites are shown in Table I. The main contributions arise from the Cu(3d) and the O(2p) states.Every oxygen atoms of the unit cell contributes to-wards the hole density. The indivisual contributions of the Cu(3d) and O(2p) states are comparable.

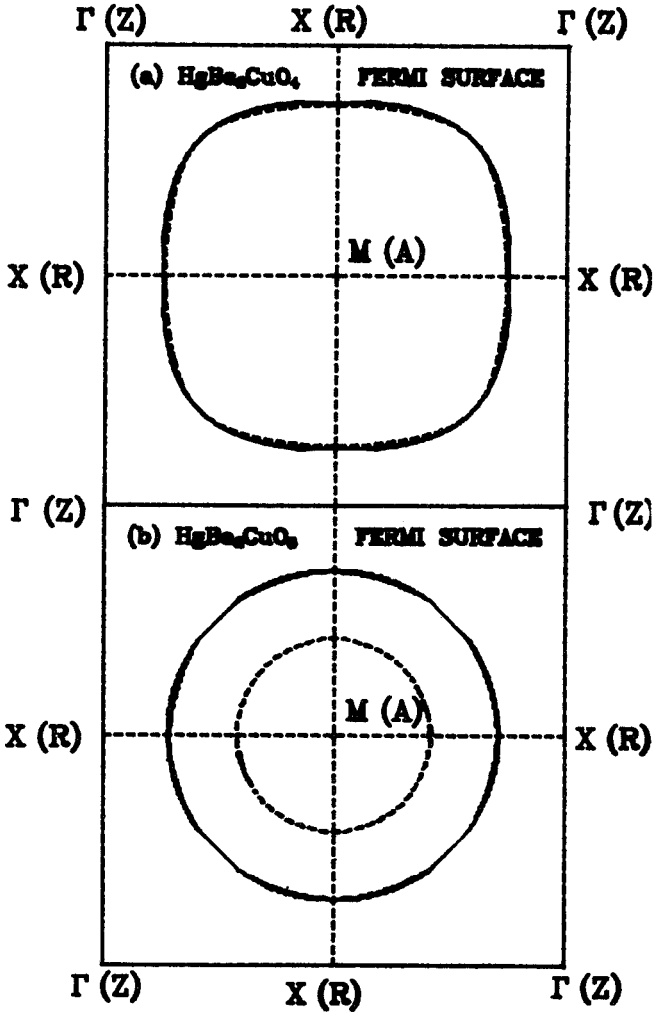

FIG.4 Cross-sections of the Fermi surface in the extended Brillouim zone scheme in two planes, kz=0 (dashed curve) and kz=0.204 (continuous curve) for (a) HgBa2CuO4 and (b) HgBa2CuO5.

(v) CHARGE DENSITY :

The charge densities around the various atoms for the δ = 0, 1 compounds are very much similar except the missing charge around O(4) atom in the δ = 0 compound. The charge density for the δ = 1 compound for the vertical plane ($1\bar{1}0$) passing through the Cu-atom shown in Fig.5 reveals that there is little charge between the Cu atom and the oxygen atom lying in the Ba-O layer (O3) because of the large separation between these atoms. Also, the binding between O3 and Hg is quite strong because of the presence of high charge density between them. The oxygen atom O4 lying in the Hg-plane is weakly bound both to the Hg and Ba atoms and is likely to be knocked out of its parent site easily.

(vi) EFFECT OF PRESSURE :

The varition of the crystal energy with the lattice volume gives a bulk modulus equal to 0.626 Mbar. The variation of the hole concentrations with pressure are depicted in Table 2. We do not find any optimum value although the hole concentration at both Cu and O atoms increase with pressure. The increase in pressure on the crystal shifts the vHs peak to-wards the Fermi level (see Fig. 6.) and near $V/V_o=0.625$, the vHs peak is pinned at Fermi level. This volume corresponds to a pressure of about 24 GPa which is in perfect agreement with the experimental obervation of Chu et al [3]. It is noted that that Hg 6(p) conduction states at the optimal volume crosses the Fermi level and makes it now self- doped, a behaviour seen [8] in the Hg based oxide superconductors containing two or more CuO2 layers. Further, the Fermi level touches the Brillouin zone boundary making the Fermi surface

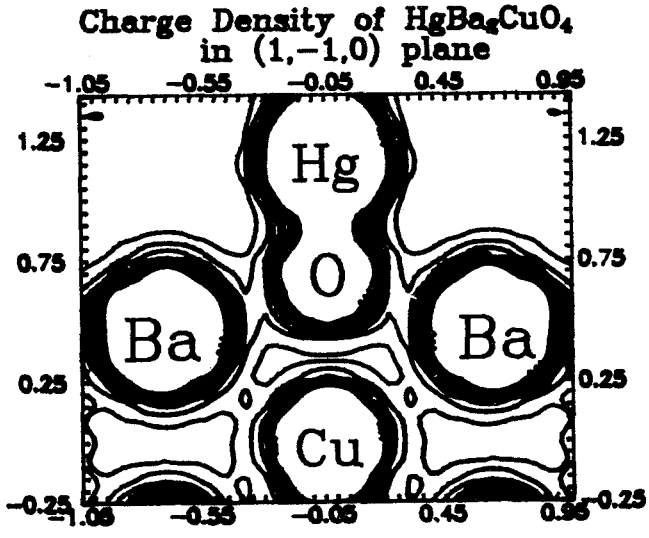

FIG.5 Distribution of the electron charge density in the (1,-1,0) plane containing Cu and O atoms of HgBa2CuO4. The contours are drawn for an interval of .015 e/(a.u.)^3 up to maximum value of 0.14 e/(a.u.)^3.

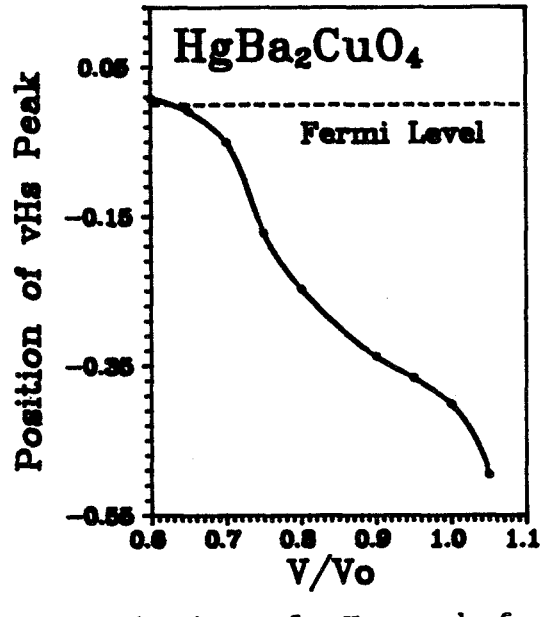

FIG 6 Deviation of vHs peak from Fermi level with pressure.

TABLE.2 : VARIATION OF HOLE CONCENTRATIONS WITH CRYSTAL VOLUME FOR $HgBa_2CuO_4$.

V/V_o	Hole Concentration		
	Cu	O(Cu)	Total
0.90	0.22	0.28	0.50
0.95	0.12	0.14	0.26
1.00	0.10	0.12	0.22
1.05	0.10	0.12	0.22

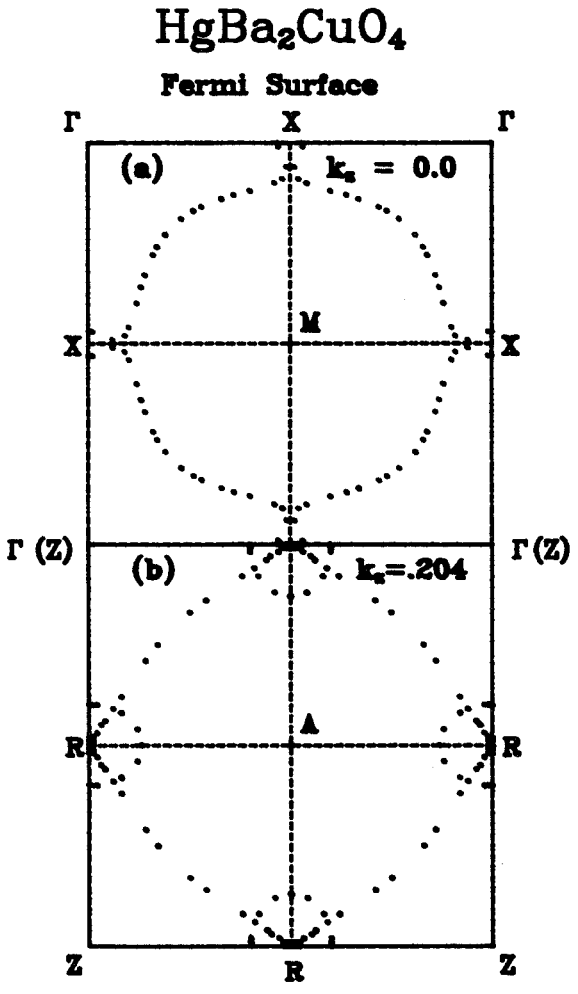

FIG.7 Cross sections of the Fermi surface for crystal volume $v/v_o=0.625$ for HgBa2CuO4.

nesting area maximum. There appear small electron pockets due to Hg 6p states at point R as shown in Fig.7.

V. CONCLUSIONS

The present results predict the occurrence of the vHs peaks above and below the Fermi level in the $\delta=1$ and $\delta=0$ compounds, respectively. This is in agreement with the observation of the superconducting behaviour in the oxygenated $HgBa2CuO4+\delta$ ($\delta=0.1$) compound. The nesting of the Fermi surface in the $\delta=0$ compound is of a higher degree than in the $\delta=1$ compound. The hole concentrations of the Cu-$d(x^2-y^2)$ and the O-p(x,y) orbitals in the $\delta=0$ compound increse with pressure on the

crystal. The deviation of the vHs peak from the Fermi level also decreases with the pressure on the crystal and the vHs is pinned at Fermi level at a pressure of about 24 GPa in perfect agreement with experimental data. The nesting area of the Fermi surface is also maximum at this optimum value.

VI ACKNOWLEDGEMENTS

The present work is financially supported by University Grants Commission, New Delhi and Department of Science and Technology, New Delhi.

REFERENCES

1. S. N. Putilin, E.V. Antipov, O. Chmaissem and M. Marezio, Nature, 362, 226(1993).

2. A. Schilling, M. Cantoni, J D Guo and H. R. Ott, Nature, B363, 56(1993).

3. C.W. Chu et al Nature, 365, 323 (1993).

4. H. Takahasi et al Physica C 218 , 1 (1993).

5. J. Labbe, and J. Bok ,Europhys, Lett., 3, 1225(1987), D. M. Newns, C.C. Tsuei, P. C. Pattnaik and C.L. Kane, Comments Condens., Matter Phys. 15, 273(1992); H. R. Krishnaswamy et al Phys. Rev., B49, 3520 (1994).

6. D.L. Novikov and A.J. Freeman Physica C 212, 233 (1993).

7. C.O. Rodriguez et al, Physica 216,12, (1993).

8. Bal K. Agrawal & Savitri Agrawal, High Tc-update May 1, 1994.

9. Bal K. Agrawal & Savitri Agrawal, Phys. Rev B45, 8321(1992); and also preprint.

10. Bal K Agrawal & Savitri Agrawal, Phys. Rev. B1, in press.

11. L. Hedin and B.I. Lundquist, J.Phys., C4, 2063 (1971).

SPACE SCAN

532-76
314207

3463307
10?

BOSON LOCALIZATION AND UNIVERSALITY IN $YBa_2Cu_{3-x}M_xO_{7-\delta}$

A. Kallio, V. Apaja and S. Pöykkö
University of Oulu, Department of Theoretical Physics, Linnanmaa, SF-90570 Oulu, Finland
(June 22, 1994)

Abstract

We consider a two component mixture of charged fermions on neutralizing background with all sign combinations and arbitrarily small mass ratios. In the two impurity limit for the heavier component we show that the pair forms a bound state for all charge combinations. In the lowest order approximation we derive a closed form expression $V_{eff}(r)$ for the binding potential which has short-range repulsion followed by attraction. In the classical limit, when the mass of embedded particles is large $m_2 >> m$, we can calculate from $V_{eff}(r)$ also the cohesive energy E and the bond length R of a metallic crystal such as lithium. The lowest order result is $R = 3.1$ Å, $E = -.9$ eV, not entirely different from the experimental result for lithium metal. The same interaction for two holes on a parabolic band with $m_2 > m$ gives the quantum mechanical bound state which one may interprete as a boson or local pair in the case of high-T_c and heavy fermion superconductors. We also show that for compounds of the type $YBa_2Cu_{3-x}M_xO_{7-\delta}$ one can understand most of the experimental results for the superconducting and normal states with a single temperature dependent boson breaking function $f(T)$ for each impurity content x governing the decay of bosons into pairing fermions. In the normal state $f(T)$ turns out to be a linear, universal function, independent of the impurity content x and the oxygen content δ. We predict with universality a depression in $T_c(x)$ with slight down bending in agreement with experiment. As a natural consequence of the model the bosons become localized slightly above T_c due to the Wigner crystallization, enhanced with lattice local field minima. The holes remain delocalized with a linearly increasing concentration in the normal state, thus explaining the rising Hall density. The boson localization temperature T_{BL} shows up as a minimum in the Hall density R_{ab}^{-1}. We also give explanation for very recently observed scaling of temperature dependent Hall effect in $La_{2-x}Sr_xCuO_4$.

I. INTRODUCTION

Despite great efforts, high-T_c superconductivity HTS is still lacking a convincing theoretical explanation that everybody can accept. There is ample experimental evidence for high-T_c, heavy fermions HF and Chevrel compounds that the properties of these systems cannot be understood with the most simple BCS model alone. More than anything the normal state properties in all these compounds deviate from BCS, which above the transition temperature T_c would predict a normal metal. The anomalies appear in the three main experiments: the NMR, the Raman and Hall experiments and to some extent in the thermal conductivity and surface resistivity.

The Hall-density ($n_H = 1/Rec$) in the ab-plane is diminishing just above T_c and shows a minimum at $T_{BL} > T_c$ and beyond the minimum it rises linearly. In the case of 123 the Hall coefficients in different direction have opposite signs $R_{ab} > 0$, $R_c < 0$ [1]. This, more than anything, requires existence of charge carriers of more than one type in these compounds. Furthermore the NMR relaxation rate $W(T)$ below T_c does not show a shoulder predicted by

BCS. At very low temperatures the relaxation rate $W(T)$ exhibits power laws with very small exponent like 1.5 as compared with exponential BCS-behaviour or linear Korringa-behaviour [2]. The Korringa law is not obeyed in the normal states. The Raman scattering shows no coherence peak at $\omega = 2\Delta$ but continuum background [3], unexplainable within the BCS.

In the case of 123-compounds all the anomalies mentioned above can be understood in terms of doubly charged boson model where the bosons exist up to temperature $T_B \approx 300 - 500$ K, much higher than T_c. Below this temperature the bosons are in chemical equilibrium with respect to reaction $B^{++} \rightleftharpoons h^+ + h^+$, where the holes are supposed to be tied to a band with parabolic dispersion relation. The chemical equilibrium can quite generally be represented by a boson breaking function $f(T)$ such that the number density of bosons and fermions are

$$\begin{aligned} n_B(T) &= n_0 f(T) \\ n_h(T) &= 2n_0\,[1 - f(T)]\,, \end{aligned} \tag{1}$$

which simply contains the charge conservation. Just like dissociation in chemistry takes place in a solvent, here the equilibrium reaction takes place in the sea of electrons.

From the Hall-experiments we have deduced that $f(T)$ is nearly linear function above T_c [4]. If the bosons and holes are tied to the ab-plane they both contribute to Hall-density and $R_{ab} > 0$. The minimum in the Hall-density is explained by the Wigner crystallization (and hence by localization) of bosons above a temperature $T_{BL} > T_c$, since their density gets smaller than the critical density for Wigner crystallization. Similarly near $T = 0$ the density of the holes gets small since $1 - f(T) \to 0$. The model therefore predicts antiferromagnetic transitions in the superconducting states. Such transitions are also often observed. Although we cannot claim that they all are connected with the proposed Wigner crystallization of the pairing fermions, it is difficult to understand why they occur near $T = 0$. In c-direction the Hall density is dominated by the background electrons, called spectators.

The plan of the paper is as follows: First we show that the existence of bosons is feasible. In fact we will calculate the relative wave function of such boson and its binding energy in the case of two charged particles with heavy mass embedded in the electron gas with neutralizing background. We do this by applying the hypernetted chain (HNC) method of classical statistical mechanics which has previously been shown to be very accurate for electron gas. In chapter III we consider boson localization and in chapter IV two types of universal behaviour in high-T_c superconductors.

II. SPECTATOR FERMION BINDING OF BOSONS

To introduce the method we repeat the steps needed to calculate energy/particle of the electron gas. Here the relevant density parameter is the r_s-value defined by the volume taken by one electron $n^{-1} = \frac{4}{3}\pi(r_s a_0)^3$, where a_0 is Bohr radius $= \hbar^2/me^2$. Another relevant quantity is the radial distribution function $g(\mathbf{r}_{12})$ which gives the relative probability of finding an other electron at the position $\mathbf{r}_2$, if there is one at the point $\mathbf{r}_1$. For uniform electron liquid $g(\mathbf{r}_{12})$ is independent of the angles $\mathbf{r}_{12}$. The corresponding probability amplitude $\psi(r_{12})$ is $\sqrt{g(r_{12})}$. With Coulomb interaction $v_c(r)$ the potential energy can be calculated exactly form

$$\frac{V}{N} = \frac{1}{2} n \int d^3r [g(r) - 1] v_c(r), \tag{2}$$

provided that function $g(r)$ is calculated from the exact ground state wave function Ψ by

$$n^2 g(r_{12}) = N(N-1) \frac{\int |\Psi|^2 d\tau_2}{\int |\Psi|^2 d\tau}, \tag{3}$$

where N is number of particles and $d\tau = d^3r_1 d^3r_2 d\tau_2$. For interactions other than Coulomb force one has $g(r)V(r)$ inside of the integrand in Eq. (2). The reason for $(g-1)v_c$ is the screening. Since $g(r) \to 1$ at large distances, this also makes the integral in Eq. (2) to converge.

Another function which, in the case of quantum liquids, is intimately connected with neutron scattering experiments, is the liquid structure factor $S(k)$ which is obtained by Fourier transform of $g(r) - 1$

$$S(k) - 1 = n \int e^{i\mathbf{k}\cdot\mathbf{r}}[g(r) - 1]d^3r. \tag{4}$$

Using the HNC-method one can calculate also the kinetic energy as functional of $S(k)$ and $g(r)$. Without repeating here all the relevant steps needed we give the final result: One can write the Euler-Lagrange equation into a form of "Schrödinger equation" for the propability amplitude $\psi = \sqrt{g}$ [5]

$$-\frac{\hbar^2}{m}\nabla^2\psi(r) + [v_c(r) + w(r) + w_e(r)]\psi(r) = 0, \tag{5}$$

where $v_c(r)$ is the Coulomb potential and the boson induced potential $w(r)$ is the Fourier transform of

$$w(k) = -\frac{\hbar^2 k^2}{4m}\left[\frac{S-1}{S}\right]^2 (2S+1). \tag{6}$$

The potential $w_e(r)$ contains higher order terms and corrections due to the Fermi statistics which are fairly small in the range $r_s > 3$. Eq. (5) is the zero energy limit of a Schrödinger equation with zero scattering length: $\psi(r) \to 1$ for large r. Since $w(k)$ is a functional of $S(k)$, the "Schrödinger equation" is highly non-linear. Simplest way to solve Eq. (5) formally is to define a correction function R by

$$\frac{\nabla^2\psi}{\psi} = \frac{1}{2}\nabla^2(g-1) + R(r), \tag{7}$$

which allows one to obtain the solution by Fourier transform of Eq. (5) (with $\gamma = 4\pi ne^2 m/\hbar^2$)

$$S(k) = \frac{k^2}{\sqrt{4\gamma + k^4 + 4k^2(m/\hbar^2 w_e(k) - R(k))}} \approx \frac{k^2}{\sqrt{4\gamma + k^4}} \tag{8}$$

In the range $r_s > 3$, which we are here interested in, both $R(k)$ and $w_e(k)$ are small, hence latter form, so-called bosonic uniform limit approximation, is quite accurate. In the uniform limit approximation by Eq. (8) two features are exact: It gives the correct k^2-behaviour for small k and produces the correct plasma frequency. Also the energy, shown in Fig. 1 compares favorably with the Monte Carlo results of Ceperley [6], which in turn is very close to the fermi hypernetted chain (FHNC) [7] result of Zabolitzky [8], which would correspond to a proper treatment of w_e and $R(k) \neq 0$ in our case. The Fermi correlations were included as a potential w_e, for which Eq. (5) gives exactly the free Fermi gas radial distribution function in the $r_s \to 0$–limit.

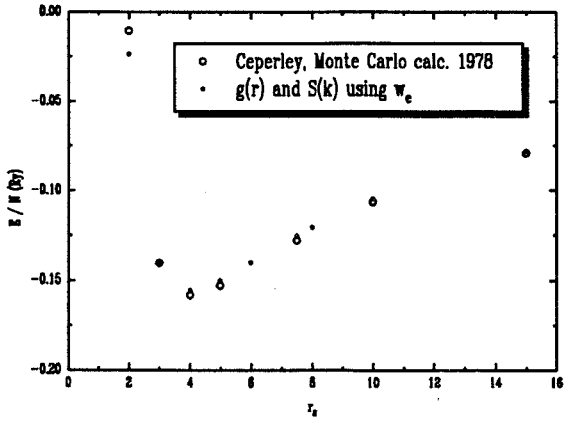

FIG. 1.

Total energy of electron gas calculated using the functions $g(r)$ and $S(k)$ solved from Eqs. (4) and (5), as compared with the Monte Carlo results of Ceperley [6]. Fermi correlation energy was added within the Lado-approximation.

The effect of screening comes out in a vivid way from Eq. (5): The free space Coulomb interaction is changed into an effective interaction $V_{eff} = v_c + w$ due to the other electrons around. In fact for large r, v_c is completely cancelled by $w(r)$ and hence $V_{eff}(r)$ has finite range.

With these preliminaries we are ready to examine what happens if we embed charged particles into the electron gas. The same treatment with radial distribution functions can be generalized for a mixture: One obtains a system of three coupled equations of the type Eq. (5). Calling the second component mass m_2, density n_2 and charge $Q_2 = Ze$ one would now need three radial distribution functions $g_{11}(r) = g(r)$ (= the electron gas) $g_{12}(r)$ and $g_{22}(r)$ and the corresponding probability amplitudes $\psi_{ij} = \sqrt{g_{ij}}$, which satisfy the following three coupled Euler-Lagrange equations

$$-\frac{\hbar^2}{\mu_{ij}}\nabla^2\psi_{ij} + \left(\frac{Q_iQ_j}{r} + w_{ij}\right)\psi_{ij} = 0, \quad i,j = 1,2 \tag{9}$$

with $\mu_1 = m$, $\mu_2 = m_2$ and $\mu_{12} = mm_2/(m+m_2) = m/(1+M)$. The detailed expressions for w_{ij} are to be found in Ref. [9]. It turns out that the set (9) has again a solution if the mass ratio $M \approx 1$, but for $M < .1$ there seems to be no solution numerically [10]. For these reason it was thought that this approach cannot be applied to a problem like the metallic hydrogen. However, since the method works so well in the single component case, the reason for this inadequacy was not fully understood earlier. Our purpose here is to show that the reason for instability is appearance of bound state in channels ψ_{22} or ψ_{12} which one simply has to treat more properly. In what follows we will show that the proper treatment is to go first to one and two impurity limits $n_2/n \to 0$. In this limit one obtains a decoupling of the three equations: First equation reduces to the background electron gas described before. For the impurity, one obtains the liquid structure factor $S_{12}(k)$ from $S(k)$ of the electron gas by

$$S_{12} = \frac{4S^2(k)}{1+MS(k)}\left[\frac{Z\gamma}{k^4} + \frac{1}{2}(1+M)\frac{R_{12}(k)}{k^2}\right] \approx -\frac{4Z\gamma S^2(k)}{k^4(1+MS(k))} \tag{10}$$

The small correction function $R_{12}(r)$ has analogous meaning as the one in Eq. (7) with the definition

$$\frac{\nabla^2\psi_{12}}{\psi_{12}} = \frac{1}{2}\nabla^2(g_{12}-1) + R_{12}(r) \tag{11}$$

and in all Fourier transforms the background electron density n is used. For small mass ratio $M \approx 0$ we obtain in the uniform limit for both $R = R_{12} = 0$ very simple form

$$S_{12}(k) = -\frac{4Z\gamma}{4\gamma + k^4}, \tag{12}$$

showing that the sign of S_{12} is opposite to charge $Q_2 = Ze$. The third component in this limit decouples also and we obtain a Schrödinger equation for the pair

$$-\frac{\hbar^2}{m_2}\nabla^2\psi_{22} + \left(\frac{Z^2Q_2^2}{r} + w_{22}\right)\psi_{22} = E\psi_{22} \tag{13}$$

with induced potential $w_{22}(k)$ in k-space

$$w_{22}(k) = -\frac{\hbar^2k^2}{4m}\left[\frac{S_{12}}{S}\right]^2(1+2MS). \tag{14}$$

With Eq. (13) we can also treat the two impurity scattering with $E \geq 0$ and the bound states, if any, with $E < 0$. In the case of finite density n_2 one would have $E = 0$ and hence $g_{12}(r) \to 1$, for large r. Here, however, we have used the formalism simply to calculate the induced potential $w_{22}(r)$ since there is no reason why $w_{22}(r)$ would have different expression for $E \neq 0$ than for $E = 0$. Eq. (13) has earlier been used by Owen [11] to calculate the Landau parameters for ^{4}He+^{3}He mixture and the expression is the same with different notation. Hence eq. (13) is

a normal, linear Schrödinger equation in the medium with induced potential calculated from HNC. For $M \to 0$, $w_{22}(k)$ is always attractive in k-space, irrespective of the sign of S_{12} and hence of the impurity charge. If one goes to finite density n_2 and Eq. (13) has a bound state, one naturally has an instability in the two fermion mixture.

Writing $Q_2^2 = Z^2e^2$ one can now calculate $w_{22}(r)$ in the uniform limit for both $S_{12}(k)$ and $S(k)$ and small M to be (with $b = \gamma^{1/4}$) inverse transform of $4\hbar^2\gamma^2/\left[mk^2(4\gamma + k^4)^{-1}\right]$ which is

$$w_{22}(r) = -\frac{Z^2e^2}{r}(1 - \mathrm{e}^{-br}\cos br) \tag{15}$$

and the effective potential becomes simply

$$V_{eff}(r) = \frac{Z^2e^2}{r}\mathrm{e}^{-br}\cos br, \tag{16}$$

showing the screening property explicitely. Notably this lowest order result is different from RKKY-type of interaction coming from Kohn-Luttinger instability [12].

This simple theory can now be applied to variety of instances. In the classical limit $M = 0$, the equilibrium distance R of the two impurities is determined by the minimum of the effective potential which is close to $bR = \pi$ and hence

$$R = 1.26r_s^{3/4}\ \text{Å}. \tag{17}$$

The corresponding cohesive energy of the pair is

$$E = \frac{1}{2}V_{eff}(R) \approx -.246Z^2r_s^{-3/4}\ \text{eV}. \tag{18}$$

Simplest case to compare with experiment here is lithium with $Z = 3$ and $r_s = 3.25$. We obtain now $R = 3.1$ Å and $E = -.9$ eV as compared with the experimental values 3.4 Å and -1.6 eV. Clearly we don't expect our result to agree with experiment in lowest order approximation but the magnitudes are correct. The calculation for lithium could in fact be performed in two ways: One could take the impurity to be He^+-ion with modified Coulomb interaction $v_c(r)$ with $Z = 1$ or else take $Z = 3$ and improve on the $S_{12}(k)$, since $S(k)$ can be calculated accurately using FHNC. By taking $Z = 1$ one avoids the exiton singularity in the 12-channel and in principle such a calculation can be performed with desired accuracy, which however is not the point here. In the original set both bound state singularities show up and we can interpret this as a sign of good accuracy rather than a deficiency of the set (9). The remedy is to treat the two fermion bound states as the second component i.e. use boson fermion mixture instead but with modified Coulomb interaction. This is exactly what has been done so far within the spectator fermion model of the new superconductors [4]

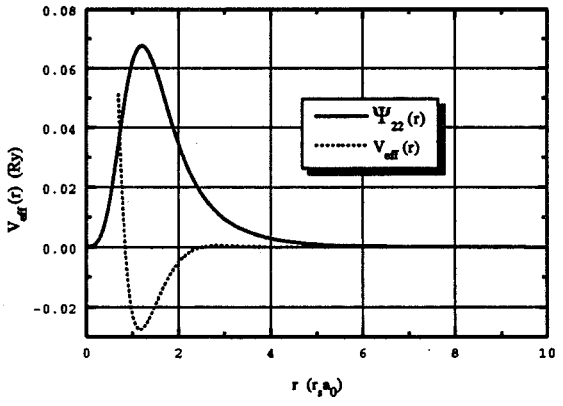

FIG. 2.

Effective potential (16) and wavefunction $\psi_{22}(r)$ for a pair of electrons or holes forming a bound boson, with $r_s = 4$ and $M = .1$.

Next we return to the high-T_c case by assuming that the impurity holes or electrons belong to a parabolic band with finite effective mass such that $M < 1$. The problem of embedding two heavy holes with effective mass m_2 is not different from the previous impurity problem and the same Schrödinger equation (13) has to be solved for the propability amplitude ψ_{22}. In Fig. 2 we show a representative case for a pair of holes or electrons forming a bound $^1S_0$-boson, using the effective potential of Eq. (16). The size is about what is needed in ceramic superconductors: Few Ångströms and the binding $2\Delta \approx 500 - 1000$ K, depending upon r_s and M. The calculation shows that the existence of such a boson or a local pair is feasible. The bosons would survive up to temperatures $k_B T_B \sim \Delta$, where T_B is the boson formation temperature. Hence we predict $T_B \sim 250 - 500$ K, which is about what one needs in high-T_c [4] or heavy fermion [13] superconductors. Furthermore the theory predicts existence of all possible combinations $[B^{++}, e^-]$, $[B^{--}, e^-]$, $[B^{++}, h^+]$ and $[B^{--}, h^+]$, since the effective interaction is always attractive. These define the electron-hole liquid (EHL) and spectator fermion (SFS) superfluid models [4]. The superfluidity of the composite bosons can be shown at $T = 0$ by calculating the superfluid fraction n_c from the one particle density matrix. Such a calculation also uses formally the impurity liquid structure factor [14] where an impurity is this time embedded into the boson system.

III. BOSON LOCALIZATION

It is well known that charged particles (bosons or fermions) on a smooth, neutralizing background become localized into a Wigner crystal (WC) at densities lower than $r_s \approx 170$ [15,16]. The limiting density n_{WC} depends upon the mass and charge of the particles. In the case of ion background additional localization is caused by ion sites, lattice defects etc.. Hence WC-localization puts an ultimate lower limit for the boson density that can still lead to superfluidity. For bosons with $Z = 2$ the limiting density turns out to be

$$n_{WC} > 2.09 \left(\frac{m_B}{m_e}\right)^3 10^{19} \mathrm{cm}^{-3}. \tag{19}$$

We use the boson mass $m_B = 2m_e$, hence the WC-localization limit is $n_B > 0.16 \cdot 10^{21}$ cm^{-3}. This should be compared with the experimental boson density $n_0 \approx 8 \cdot 10^{21}$ cm^{-3}. We anticipate that the lattice and the lattice defects localize additional portion of the bosons. The corresponding limit for the holes with $m_h = m_e$ is only $3 \cdot 10^{17}$ cm^{-3}, and we predict that the holes localize at extremely low temperatures where $n_h(T) \approx 0$. This is important for understanding of the antiferromagnetism appearing in many high-T_c and HF-compounds [13]. In what follows the holes produced in the boson decay obeying the same rule dictated by $1 - f(T)$ regardless whether they are produced from localized or delocalized bosons. Since at T_B all bosons have decayed, somewhere in between T_c and T_B there must exist a temperature T_{BL} where they all become localized. In the present calculation we will treat the localization phenomenologically by writing the number density of delocalized bosons to be

$$n_{BDL}(T) = \begin{cases} \alpha n_0 f(T)\xi(T) \approx \alpha n_0 f(T)\,(1 - T/T_{BL}), & \text{if } T < T_{BL} \\ 0, & \text{if } T > T_{BL}. \end{cases} \tag{20}$$

Here the coefficient α determines what fraction of bosons are localized already at $T = 0$. Since the localized bosons hardly show up, we cannot determine α very accurately, and the exact behaviour of the localization factor is not known. We believe that in reality $\alpha < 1$, and suggest that the localization is the main source for sample dependence observed in high-T_c materials, even for single crystals.

In the normal state only the delocalized bosons give contribution to the specific heat, Hall coefficient, resistivity, etc. The only place where the localized bosons may show up are the magnetic experiments such as NMR, where they can give contribution to the orbital shift and thereby also to the relaxation rate $1/T_1$.

The issue of boson localization can come up only in models like EHL or SFS, where the bosons exist in the normal state and suffer boson breaking. We therefore predict that HTS and HF form a laboratory where the phenomenon of localization can be studied experimentally in

details. In our earlier calculations it was difficult to understand why in the Hall effect (above T_c) only the holes contribute to the Hall-density and not the bosons. Now the observed behaviour is fully understood, including the minimum which in our model should occur near the localization temperature T_{BL}. It would otherwise be very difficult to understand why the Hall density would diminish in the range $T_c < T \leq T_{BL}$, when the temperature is increased.

IV. UNIVERSALITY

Since the dispersion relation of the fermionic excitations is unknown and likewise the band structure details, we will use the simplest possible approach of taking into account only the concentration dependencies of the experimental quantities. The temperature dependencies of concentrations in turn are determined by the boson breaking function $f(T)$ which by our earlier discussions [17] is assumed to be linear above T_c. In the normal state we write

$$f(T) = f_c \frac{1 - T/T_B}{1 - T_c/T_B}, \qquad T_c \leq T \leq T_B \tag{21}$$

The average number of holes and mobile bosons in the normal state are again given by Eqs. (1) and (20). In Eq. (21) the parameters f_c, T_c and T_B define a function which, if continued to $T = 0$, would predict that a fraction of bosons is localized already at zero temperature.

In the case of single crystal of 123 we have deduced from the experiments (Hall-effect) the values of the main parameters to be $f_c \approx 0.6$, and $T_B \equiv 280$ K. We assume that T_B is independent of impurities and likewise the linear function in Eq. (21) is assumed to be universal. These two parameters are sufficient to describe also the normal state of the impurity systems.

The idea behind universality is as follows: In the non-impurity case the boson density at $T = 0$ is n_0. The presence of plane coppers is vital for the boson formation. In the impurity case $x > 0$ a fraction of plane coppers are replaced by impurities such as Zn. Hence near the impurity sites bosons may not be formed. Therefore the boson density at $T = 0$ is diminished by a fraction ν to be $n_B(0, x) = \nu(x) n_0$. Correspondingly the density of holes is increased to $n_h(0, x) = 2n_0[1 - \nu(x)]$. In the normal state this shift of chemical equilibrium is reflected as the decrease of temperatures $T_c(\nu)$ and $T_{BL}(\nu)$, while T_B should be characteristic to each compound. As a first approximation we use the same linear function for all x, which gives us the universality.

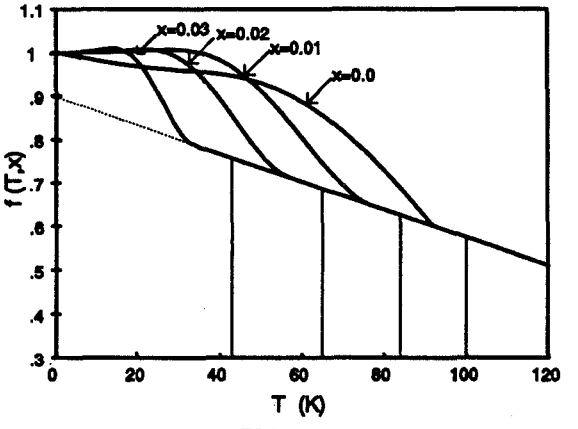

FIG. 3.

The boson breaking functions $f(T, x)$ for $YBa_2(Cu_{1-x}Zn_x)_3O_7$ with four values of x and $T_B = 280$ K. The vertical lines indicate the localization temperatures $T_{BL}(x)$. According to the universality idea the $f(T)$:s above T_c fall on the same line, which has been continued down to $T = 0$ (dotted line).

The idea of universal linear $f(T)$ above T_c is illustrated in Fig. 3. In fact we have gone one step further by assuming that the universality is true also for different oxygen contents δ, which controls the density n_0 in $YBa_2Cu_3O_{7-\delta}$. In Fig. 4 we compare the Hall density calculated using a universal $f(T)$ with the one reported by Jones *et al.* [18]. The result supports the idea of universal $f(T)$ above T_c: In the range $0 < \delta < 0.5$ the data is quite well reproduced with n_0 as the only free parameter.

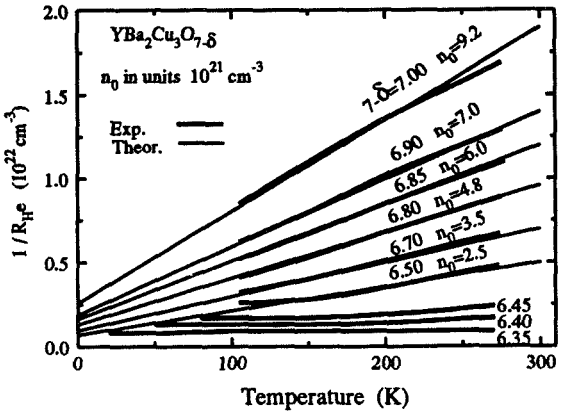

FIG. 4.

The Hall density with several oxygen contents in YBCO thin films. The short thick curves represent the experimental data of Ref. [18]. The theoretical lines were calculated using the relation $(eR_H)^{-1} = 2n_0[1 - f(T)]$ with the same linear $f(T)$ for all oxygen contents. The only changing parameter is n_0. The $f(T)$ is given by Eq. (21) with the fixed parameters $T_c = 92$ K, $T_B = 300$ K, and $f_c = 0.6$. This result demonstrates that $f(T)$ above T_c is fairly independent of the oxygen content.

The universality allows us to calculate T_c, the localization temperature T_{BL}, and f_c as a function of impurity content x from Eqs.

$$\begin{aligned} \nu f(T_{BL}(\nu)) &= f(T_{BL}(1)) \\ \nu f(T_c(\nu)) &= f(T_c(1)) \quad , \end{aligned} \tag{22}$$

where ν is related to the impurity concentration x by $1 - \nu \approx 7x$ (determined from the NMR experiment of Ref. [2]). Eqs. (22) are based on the fact that localization or the superfluid transitions take place at a fixed boson density for the same crystalline background. Using Eqs. (21) and (22) one obtains the following formula for the T_c depression:

$$T_c(\nu) = \nu^{-1}[T_c(1) - (1 - \nu)T_B], \tag{23}$$

or

$$T_c(x) = \frac{T_c(0) - 5x\ T_B}{1 - 5x}, \tag{24}$$

where $T_B \approx 300$ K and factor 5 comes from the valence counting for 123 discussed by Harashina *et al.* [20]: The Zn impurity atoms replace only coppers in the ab plane, and $\frac{2}{3}7 \approx 5$. This gives quantitative agreement with experiment [20]. The pole appearing in Eq. (24) for unphysical negative values of $T_c(x)$ causes down bending of the curve which is observable in the case of $La_{2-y}Sr_yCu_{1-x}Zn_xO_4$ in the data of the same group. Also the T_c depression of Pr and Ce substituted Bi2122 seems to bend down in a similar fashion [21]. Harashina *et al.* give an extensive discussion of the "spin gap", which they conclude to be connected with localization of holes. Here we associate the minimum in the Hall coefficient R_{ab} with boson localization, which explains in a simple way the existence of the minimum in R_{ab} near $T_{BL} \approx 100$ K in 123 [20]. From the universality idea we obtain for the localization temperature $T_{BL}(\nu)$ the relation

$$T_{BL}(\nu) - T_c(\nu) = \nu^{-1}\,[T_{BL}(1) - T_c(1)]\,. \tag{25}$$

With increasing impurity content x (decreasing ν) the separation between the localization temperature T_{BL} and T_c increases. The universality is illustrated in Fig. 3 for 123 impurity systems.

Another kind of universality in HTS has been considered by Schneider and Keller [23], who assumed that T_c has a parabolic maximum at the optimum condensate density. They found out that the rescaled T_c plotted against the muon-spin-relaxation rate of many HTS fall on a single curve. Zhang and Sato [24] have proposed that when the rescaled T_c is plotted against the hole concentration in the CuO_2-planes a universal doping curve emerges for many cuprate superconductors. Instead of the usual parabolic form, they obtain a plateau around maximum T_c. As pointed out by Awana and Narlikar [25], the weakness of such plots are the ambiguities in estimating the hole concentration. Schneider and Keller further calculate the pressure derivative $d\ln T_c/dP$ and the isotope effect coefficient $-md\ln T_c/dm$ vs. T_c. The present model obeys these universalities: the doping behaviour of T_c has been derived in Ref. [26], and the pressure derivatives were plotted in Fig. 4 of Ref. [13]. The pressure derivatives of both hole and electron doped HTS come out correctly from SFS.

In Ref. [26] the derivation of doping curves for $La_{2-x}Sr_xCuO_4$ was based on the formula $n_0 + n_e = \bar{n} = constant$ while n_0 and n_e are changed (notice the different notation). At the time of Ref. [26] the Landau damping of the sound mode was thought to be the reason why $T_c(x_B)$ is zero outside the boson concentration region $x_1 < x_B < x_2$. Now we suggest that the critical boson concentrations x_1 and x_2 correspond to the localization limits: the underdoping limit x_1 and the overdoping limit x_2 correspond to boson localization, the latter one because too few spectators remain. The localization gives the same sound velocity exponent 1/2 at both critical points [4], and we obtain a T_c formula slightly simpler than the one in Ref. [26]

$$T_c(x_B) \approx A\left[(x_B - x_1)(x_2 - x_B)\right]^{5/8}, \tag{26}$$

where A is approximately independent of concentration x_B.

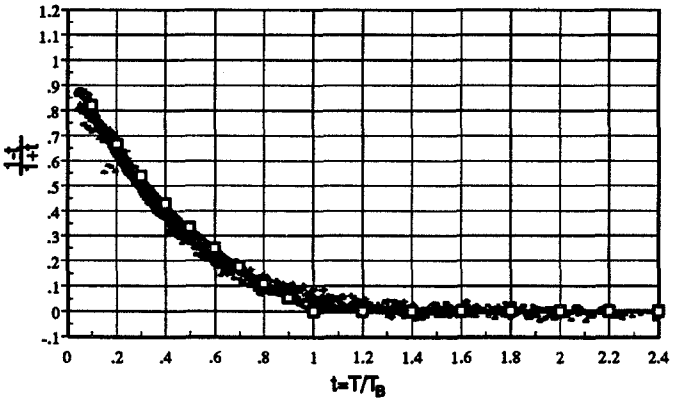

FIG. 5.
Scaling of T-dependent Hall coefficent R_H white squares respect the result from (28).

Since both n_0 and n_e change in doping we expect that also T_B, T_c and f_c in Eq. (21) will change with x. However if one uses $t = T/T_B$ with $f(t)$ universal, we may write the Hall-coefficient for $T > T_{BL}$ $R_H(t) = R_H^\infty/(1 - f(t))$, therefore

$$\frac{R_H(t) - R_H^\infty}{R_H^\infty} = \frac{f(t)}{1 - f(t)} \approx \frac{\hat{f}_c(1-t)}{1 - \hat{f}_c(1-t)} \approx \frac{\hat{f}_c(1 - t/\mu)^\mu}{1 - \hat{f}_c(1 - t/\mu)^\mu}, \tag{27}$$

which is also universal, if in Eq. (21) the quantity $\hat{f}_c = f(T_c(x))/(1 - T_c(x)/T_B(x))$ is independent of x.

Recently Hwang *et al.* [27] have reported a scaling of the in-plane temperature dependent Hall coefficent $R_H(T)$. They rescaled $R_H(T)$ in a form $[R_H(T/T^*) - R_H^\infty]/R_H^*$, giving the same T/T^* dependence for all x. R_H^* and T^* are x dependent parameters. If we identify T_B with $1.8T^*$, we obtain using $\hat{f}_c = .5$ the curve

$$[R_H(t) - R_H^\infty]/R_H^\infty = \frac{1-t}{1+t}, \tag{28}$$

which is shown in Fig. 5 to be in rather good agreement with experiment. The last, non-linear form in Eq (27) with critical exponent $\mu > 1$ would give good agreement without rescaling of t.

V. CONCLUSIONS

We conclude that simple microscopic theory predicts the possibility of boson formation in the situation where the background electron or hole liquid (the spectators) have smaller effective mass than the pairing fermions which below temperature T_B combine pairwise into bosons. Since the approximate close form effective potential $V_{eff}(r)$ by Eq. (16) gives a reasonable value for the unit cell of Li-metal and also the cohesive energy we believe that it is fairly accurate also in the quantum mechanical boson problem for one to add the effects of unisotropies present in ceramic superconductors. The knowledge of boson wave function enables one to calculate the density of states and hence $f(T)$ from the boson decay at finite temperature by simply calculating the scattering states from Eq. (13) with $E > 0$.

The present theory of boson binding is different from BCS phonon coupling and also from the bipolaron model.

[1] N. P. Ong, in: Physical Properties of High-Temperature Superconductors II, ed. D. M. Ginsberg (World Scientific, Singapore, 1990) p. 459.
[2] K. Ishida, Y. Kitaoka, T. Yoshitomi, N. Ogata, T. Kamino and K. Asayama, Physica **C 179** (1991) 29.
[3] C. Thomsen and M. Cardona, in: Physical Properties of High-Temperature Superconductors I, ed. D. M. Ginsberg (World Scientific, Singapore, 1989) p. 409.
[4] A. Kallio, V. Apaja, X. Xiong and S. Pöykkö, Physica **C 219** (1994) 340-362.
[5] A. Kallio and R. A. Smith, Phys. Lett. **68B** (1977) 315; R. Abe, Progr. Theor. Phys. **19** (1958) 407.
[6] D. Ceperley, Phys. Rev. **B 18** (1978) 3126.
[7] S. Fantoni and S. Rosati, Nuovo Cim. **25** (1975) 593; Nuovo Cim. Lett. **16** (1976) 531.
[8] J. G. Zabolitzky, Phys. Rev. **B 22** (1980) 2353.
[9] P. Pietiläinen and A. Kallio, Phys. Rev. **B 27** (1983) 224.
[10] T. Chakraborty, A. Kallio, L.J. Lantto and P. Pietiläinen, Phys. Rev. **B27** (1983) 3061.
[11] J. C. Owen, Phys. Rev. Lett. **47** (1981) 311.
[12] W. Kohn and J.H. Luttinger, Phys. Rev. Lett. **15** (1965) 524.
[13] A. Kallio and X. Xiong, Physica **C 199** (1992) 340; A. Kallio, S. Pöykkö and V. Apaja, submitted to Physica **C**.
[14] M. Puoskari and A. Kallio, Phys. Rev. **B 30** (1984) 152.
[15] E. P. Wigner, Phys. Rev. **46** (1934) 1002.
[16] K. Moulopoulos, and N. W. Ashcroft, Phys. Rev. Lett. **69** (1992) 2555.
[17] A. Kallio, V. Apaja, and X. Xiong, Physica **C191** (1992) 23.
[18] E. C. Jones, D. K. Christen, J. R. Thompson, R. Feenstra, S. Zhu, D. H. Lowndes, J. M. Phillips, M. P. Siegal and J. D. Budai, Phys. Rev. **B47** (1993) 8986.
[19] T. R. Chien, D. A. Brawner, Z. Z. Wang, and N. P. Ong, Phys. Rev. **B43** (1991) 6242; N. P. Ong, in *Physical Properties of High Temperature Superconductors II*, Ed. D. M. Ginsberg (World Scientific, Singapore, 1990) p. 459.
[20] H. Harashina, T. Nishikawa, T. Kiyokura, S. Shamoto, M. Sato, and K. Kakurai, Physica **C212** (1993) 142.
[21] V. P. S. Awana, S. K. Agarwal, A. V. Narlikar, and M. P. Das, Phys. Rev. **B48** (1993) 1211.
[22] V. Apaja, and A. Kallio, Physica **C** 209 (1993) 519.
[23] T. Schneider, and H. Keller, Phys. Rev. Lett. **69** (1992) 3374.
[24] H. Zhang, and H. Sato, Phys. Rev. Lett. **70** (1993) 1697.
[25] V. P. S. Awana, and A. V. Narlikar, Phys. Rev. Lett. **71** (1993) 303.
[26] A. Kallio, X. Xiong, Phys. Rev. **B43** (1991) 5564.
[27] H.Y. Hwang, B. Batlogg, H. Takagi, H.L. Kao, J. Kwo, R.J. Cawa, J.J. Krajewski and W.F. Peck Jr., Phys. Rev. Lett. **72** (1994) 2636.

SINGLE SCAN
J33-76
314233

THERMOMAGNETIC PHENOMENA IN THE MIXED STATE OF HIGH TEMPERATURE SUPERCONDUCTORS

E.Z.Meilikhov, RSC "Kurchatov Institute", 123182 Moscow, Russia

1. Introduction

Galvano- and thermomagnetic phenomena in conductors are usually described with the help of kinetic coefficients which are determined with the following expressions for electric field **E** and the electron fraction of the heat flow **q** [1]:

$$\mathbf{E}=\rho_{xx}\mathbf{j}+\rho_{xy}[\mathbf{k}\times\mathbf{j}]+\alpha\nabla T+QB[\mathbf{k}\times\nabla T], \quad (1)$$

$$\mathbf{q}=\Pi\mathbf{j}+E\kappa B[\mathbf{k}\times\mathbf{j}]-\kappa\nabla T+LB[\mathbf{k}\times\nabla T]. \quad (2)$$

Here ρ_{xx} and ρ_{xy} are components of the resistivity tensor; **j** is a current density; **k**=**B**/B is a unit vector parallel to magnetic field **B**; α, Q, Π, E, κ, and L are Seebeck, Nernst, Peltier, Ettingshausen, heat conductivity and Righi-Leduc coefficients, respectively. In accordance with the Onsager principle, some of these coefficients are interconnected:

$$\Pi=\alpha T, \quad E\kappa=QT. \quad (3)$$

On the other hand, there is also a connection between the electric field and the heat flow in the superconductor mixed state. If one assumes that both the electric field and the heat flow arise only under the fluxoid motion then we have Josephson formula for the electric field:

$$\mathbf{E}=-\frac{1}{c}[\mathbf{v}_f\times\mathbf{B}] \quad (4)$$

and Huebener relationship for the heat flow [2]:

$$\mathbf{q}=S_\phi T n_f \mathbf{v}_f , \quad (5)$$

where $\mathbf{v}_f$, $n_f=B/\Phi_0$ are an average motion velocity and a fluxoids density ($\Phi_0=hc/2e$ is a magnetic flux quantum), and S_ϕ is an entropy of a unit section of a fluxoid. It follows from Eqs.(4) and (5):

$$\mathbf{q}=T(cS_\phi/\Phi_0)[\mathbf{E}\times\mathbf{k}]. \quad (6)$$

For given values of the magnetic field and temperature the velocity of the fluxoid motion $\mathbf{v}_f$ depends only on the current density $\mathbf{j}$ and the temperature gradient ∇T. For a general case the dependence of $\mathbf{v}_f$ on $\mathbf{j}$ and ∇T has the form:

$$\mathbf{v}_f = a_1\mathbf{j} + a_2[\mathbf{j}\times\mathbf{k}] + a_3\nabla T + a_4[\nabla T\times\mathbf{k}] \qquad (7)$$

(a specific form of coefficients a_1, a_2, a_3, and a_4 depends on the choice of the fluxoid motion model, see below). Substituting Eq.(7) into (4) and (5), we obtain

$$\mathbf{E} = (a_2B/c)\mathbf{j} + (a_1B/c)[\mathbf{k}\times\mathbf{j}] + a_4B\nabla T - a_3B[\mathbf{k}\times\nabla T], \qquad (8)$$

$$\mathbf{q} = (n_f TS_\phi a_1)\mathbf{j} - (n_f TS_\phi a_2)[\mathbf{k}\times\mathbf{j}] + a_3\nabla T - a_4[\mathbf{k}\times\nabla T]. \qquad (9)$$

The comparison of these relations with general expressions (1) and (2) for $\mathbf{E}$ and $\mathbf{q}$ and the use of the Onsager equation (3) lead us to

$$\alpha_S = (cS_\phi/\Phi_0)\rho^S_{xy}\ , \quad Q_SB = -(cS_\phi/\Phi_0)\rho^S_{xx}\ , \qquad (10)$$

where index s marks kinetic coefficients relating to a superconductor in the mixed state. Eqs.(10) which are a consequence of the connection (6) between $\mathbf{q}$ and $\mathbf{E}$ in the mixed state of a superconductor forecast a certain correlation between "heat" and "current" coefficients (α_S, Q_S and ρ^S_{xx}, ρ^S_{xy}) and give a possibility of checking the correctness of the conception involved.

The most detailed experimental researches of kinetic coefficients in the superconductor mixed state have been carried out for high temperature superconductors [3,4] where their value is essentially higher and the temperature range accessible for measurements is noticeably wider than those for traditional superconductors. The researches revealed the real connections between kinetic coefficients to be strongly different from those predicted by relations (10). Thus, for instance, Hall resistance ρ_{xy} in the mixed state is often a nonmonotonic and even sign-reversing function of temperature and magnetic field. Meanwhile Seebeck coefficient (thermal power) usually rises monotonically with the T or B increase and its behavior, as a rule, resembles that of the longitudinal resistance: $\alpha \propto \rho_{xx}$. Besides, according to Eq.(10), the Seebeck coefficient goes to a zero on the normal state transition (since in this case entropy S_ϕ goes to a zero), although this coefficient obviously should take the value peculiar for the normal state. All this testifies to the fact that Eq.(10) is based on incorrect premises. It is clear that these are only Eqs. (4) and (5) (ensuing from an assumption that the electric field generation and the heat

transfer and, consequently, all the kinetic phenomena in the superconductor mixed state are related solely to the fluxoid motion) may be erroneous.

This approach is applicable in full measure only far from the superconducting transition, where fraction $N_n=n_n/N$ of normal quasiparticles is small (N and n_n are normal quasiparticles concentrations at $T>T_c$ and $T<T_c$, accordingly). In conformity with the weak coupling BCS theory such particles originate only due to their excitation via energy gap Δ, and hence in low temperature superconductors (with a weak electron-phonon interaction) normal quasiparticles appear in a noticeable quantity only in a direct proximity to T_c when the width of superconducting gap Δ becomes close to (or smaller than) thermal energy kT. Thus, this approach is valid almost everywhere but for a narrow temperature range near the transition.

A different situation occurs in high-temperature superconductors with a marked tendency towards a strong electron-phonon interaction resulting in the finite density of states within the energy gap [5]. In this case normal quasiparticles arise mainly owing to filling these states and their concentration is determined by a power-law dependence (e.g., by law $N_n \cong (T/T_c)^4$, known for a Gorter-Casimir two- liquid model [6]) rather than by temperature exponential dependence $N_n(T) \propto \exp(-\Delta/kT)$. The temperature range, where fraction of normal quasiparticles is large, grows much broader and there is no ground[1] to neglect their contribution into different kinetic phenomena. In Ref.[5] numerous references are made to the works which point out that the temperature dependences of thermal properties of high temperature superconductors near T_c are much better described by the Gorter-Casimir phenomenological model than by weak coupling BCS theory. In this connection the description of kinetic properties of the mixed state of high temperature superconductors requires a simultaneous and self-consisted account for the motion of fluxoids and normal quasiparticles.

The most straightforward way here is to proceed from an assumption that corresponding contributions into kinetic coefficients are independent and additive. And it exactly this way which is usually taken (see, e.g., Refs.[7 and 8]). This approach presupposes, in particular, that the presence of normal quasiparticles effects in no way the fluxoid motion (and, consequently, the electric field in a superconductor). This key

---

[1] Here by the term "normal quasiparticles" we understand not the particles which are "bound" in the fluxoid cores (with the concentration of N) but those which are outside the fluxoid cores and are "free" (their concentration is $n_n<N$).

assumption is corroborated with no due arguments and is simply postulated although it does not look absolutely obvious. So one needs to get rid of this limitation and to construct a self-consisted theory of galvano- and thermomagnetic phenomena in the superconductor mixed state within a frame work of a single model. Since at present the fluxoid motion is described approximately even in neglect for normal quasiparticles [9] a phenomenological approach analogous to that used in the classical work by Gorter-Casimir [6] might be used.

2. Seebeck and Nernst Effects

Average density $\mathbf{j}_n$ of the normal quasiparticle current is determined by the standard relationship:

$$\mathbf{j}_n=\sigma^N_{xx}\mathbf{E}+\sigma^N_{xy}[\mathbf{E}\times\mathbf{k}]-\beta_{N1}\nabla T-\beta_{N2}[\nabla T\times\mathbf{k}], \qquad (11)$$

which takes into account that conductivity (σ^N_{xx} and σ^N_{xy}) of a system of normal quasiparticles (metal) is proportional to their concentration N_n while Seebeck (α_N) and Nernst (Q_N) coefficients are independent on it[2]. Here $\beta_{N1}=\alpha_N\sigma^N_{xx}+Q_NB\sigma^N_{xy}$ and $\beta_{N2}=\alpha_N\sigma^N_{xy}-Q_NB\sigma^N_{xx}$. The electric field in a conductor with finite conductance is determined by well-known relations, namely, the Ohm's law

$$\mathbf{E}=\rho^N_{xx}\mathbf{j}_n+\rho^N_{xy}[\mathbf{k}\times\mathbf{j}_n]+\alpha_N\nabla T+Q_NB[\mathbf{k}\times\nabla T] \qquad (12)$$

for a normal metal and Josephson's formula (4) for a superconductor in the mixed state without normal quasiparticles. Here ρ^N_{xx} and ρ^N_{xy} are components of resistivity tensor of a normal metal. How could one generalize Eqs.(4), (12) corresponding to two limiting situations ($N_n=0$ and $N_n=1$) for a common case when $0<N_n<1$? In the absence of an exact answer to this question one may try the interpolation formula

$$\mathbf{E}=-f_s\left\{\frac{1}{c}[\mathbf{v}_f\times\mathbf{B}]\right\}+f_n\left\{\rho^N_{xx}\mathbf{j}_n+\rho^N_{xy}[\mathbf{k}\times\mathbf{j}_n]+\alpha_N\nabla T+Q_NB[\mathbf{k}\times\nabla T]\right\} \qquad (13)$$

where weight factors f_s and f_n have to satisfy conditions

---

[2] In normal metal α, $Q\propto kT/\varepsilon_F$ [1] where Fermi energy ε_F is determ the total concentration of charge carriers and is independent on N_n.

$f_s(N_n=0)=1$, $f_s(N_n=0)=0$, $f_n(N_n=1)=1$ which ensure the transfer of Eq.(13) into "correct" expressions (4) and (12) in the above cited limiting cases. The expression for an electric field which is obtained after substitution of Eq.(11) into (13) contains no terms proportional to ∇T (it is required for obvious equality $\mathbf{E}=0$ to take place at $\mathbf{v}_f=0$) and has the form

$$\mathbf{E} = -\frac{1}{c}[\mathbf{v}_f \times \mathbf{B}]\left(\frac{f_s}{1-N_n f_n}\right). \qquad (14)$$

As it can be seen from Eq.(14), in order to determine an electric field it is necessary to find the velocity of fluxoid motion $\mathbf{v}_f$ for which purpose let us use the equation of motion suggested in Ref.[10] (when $N_n=0$, $\nabla T=0$):

$$\eta_m\left[\mathbf{v}_s \times \mathbf{k}\right] - \eta_m\left[\mathbf{v}_f \times \mathbf{k}\right] - \eta_\perp \mathbf{v}_s - \eta_\parallel \mathbf{v}_f = 0, \qquad (15)$$

where $\eta_m=n_s e\Phi_0/c$, n_s is a concentration of superconducting carriers; $\mathbf{v}_s$ is their (average) current velocity; and $\eta_\perp$ and $\eta_\parallel$ are viscosity coefficients. The existence of normal current $\mathbf{j}_n$ (for $N_n/0$) should have brought about the appearance of a $\mathbf{v}_n$-dependent function $\Lambda(\mathbf{v}_n)$ in Eq.(17). Since at $N_n \to 1$ all the terms occurring in Eq.(17) go to a zero, the equation of fluxoid motion in this case come to relation $\Lambda(\mathbf{v}_n)=0$ coinciding with the equation of normal quasiparticles motion, i.e., to the Ohm's law (12). We may assume that at $N_n<1$ variables $\mathbf{v}_s$ and $\mathbf{v}_n$ in the motion equation are also "divided", in other words, the equation is "split" into two expressions: $\Lambda(\mathbf{v}_n)=0$ (coincides with Eq.(11)) and Eq.(15).

Now let us discuss the way of modification of the fluxoid motion equation (15) with the presence of the temperature gradient. Firstly, "thermodynamic" force $\mathbf{F}_{T1} = -S_\phi \nabla T$ must manifest itself in it. Here $S_\phi=S_\phi(T)$ is a temperature dependent entropy of a fluxoid section of a unit length. This force is an analogy [2] for Lorenz force $\eta_m[\mathbf{v}_s \times \mathbf{k}]$ and can be derive from the latter by substituting $\mathbf{v}_s \to \mathbf{v}^*=(S_\phi/\eta_m)[\nabla T \times \mathbf{k}]$. Simultaneously force $\mathbf{F}_{T2}$ analogous to "viscosity" force $-\eta_\perp \mathbf{v}_s$ from Eq.(15) should be introduced; it is derived from the latter by means of the same substitution $\mathbf{v}_s \to \mathbf{v}^*$: $\mathbf{F}_{T2} = -S_\phi(\eta_\perp/\eta_m)[\nabla T \times \mathbf{k}]$.

Another reason for appearance of "thermal" forces in the fluxoid motion equation is the origination of counterflow supercurrent in-between their normal cores [11]. If there is a temperature gradient inside the fluxoid core (that is in the

region where $N_n=1$) there appears additional normal current with the density, according to Eq.(11), equal to $\mathbf{j}_T = -\beta_{N1}\nabla T - -\beta_{N2}[\nabla T\times\mathbf{k}]$. This current is balanced with externally flowing counterflow current with an average density $\mathbf{j}_b=\mathbf{j}_{bs}+\mathbf{j}_{bn}= -\mathbf{j}_T$, which is a sum of supercurrent $\mathbf{j}_{bs}$ and normal current $\mathbf{j}_{bn}$. The superconducting component of this current equals $\mathbf{j}_{bs} = N_s\mathbf{j}_b = -N_s\mathbf{j}_T$. Similarly to the transport supercurrent $\mathbf{j}_s=en_s\mathbf{v}_s$ it is a source of forces effecting fluxoids [12]. Hence two more forces

$$\begin{aligned}\mathbf{F}_{T3} &= -(\eta_m/Ne)(\beta_{N1}[\nabla T\times\mathbf{k}]-\beta_{N2}\nabla T),\\ \mathbf{F}_{T4} &= (\eta_\perp/Ne)(\beta_{N1}\nabla T+\beta_{N2}[\nabla T\times\mathbf{k}]\end{aligned} \qquad (16)$$

should be introduced into fluxoid motion equation (15) related to the case when $\nabla T=0$. These forces are derived from Lorenz force $\eta_m[\mathbf{v}_s\times\mathbf{k}]$ and viscous force $-\eta_\perp\mathbf{v}_s$ by means of substitution $\mathbf{v}_s \to -\mathbf{v}^{**}$, where $\mathbf{v}^{**}= \mathbf{j}_{bs}/en_s = -(1/eN)\mathbf{j}_T$ [3].

Thus, in the presence of ∇T the fluxoid motion equation acquires the form:

$$\eta_m\left[\mathbf{v}_s\times\mathbf{k}\right] - \eta_\perp\mathbf{v}_s - \left[S_\phi\left(\frac{\eta_\perp}{\eta_m}\right) + \left(\frac{1}{eN}\right)(\eta_m\beta_{N1}-\eta_\perp\beta_{N2})\right][\nabla T\times\mathbf{k}] -$$

$$-\left[S_\phi - \left(\frac{1}{eN}\right)(\eta_\perp\beta_{N1}+\eta_m\beta_{N2})\right]\nabla T - \eta_m\left[\mathbf{v}_f\times\mathbf{k}\right] - \eta_\parallel\mathbf{v}_f = 0. \qquad (17)$$

Using expression $\mathbf{j}_s=en_s\mathbf{v}_s=\mathbf{j}-\mathbf{j}_n$ (where the normal current follows Eq.(11)) and substituting relationship $\mathbf{v}_s=c[\mathbf{ExB}][(1-N_nf_n)/f_s]/B^2$ ensuing from Eq.(14) into Eq.(17) we obtain the equation for the electric field. The solution of that equation in respect to $\mathbf{E}$ gives the relationship determining the transport coefficients of superconductors in the mixed state: a Seebeck coefficient (thermal power)

---

[3] The negative sign appeared in the $\mathbf{v}_s \to -\mathbf{v}^{**}$ substitution is a result of the reverse (in respect to the normal current) direction of supercurrent $\mathbf{j}_{bs}$. The nondiscrepancy of the fluxoid motion equation (17) thus obtained is confirmed by the fulfillment of the Onsager relationship for calculated kinetic coefficients (see below).

$$\alpha=N_n\left[\alpha_N(\rho_{xx}\sigma^N_{xx}+\rho_{xy}\sigma^N_{xy})+Q_N B(\rho_{xx}\sigma^N_{xy}-\rho_{xy}\sigma^N_{xx})\right] + (cS_\phi/\Phi_0)\rho_{xy} \qquad (18)$$

and Nernst coefficient

$$Q=N_n\left[Q_N(\rho_{xx}\sigma^N_{xx}+\rho_{xy}\sigma^N_{xy})-(\alpha_N/B)(\rho_{xx}\sigma^N_{xy}-\rho_{xy}\sigma^N_{xx})\right]-(cS_\phi/B\Phi_0)\rho_{xx}. \qquad (19)$$

It is easy to see that for normal metal ($N_n=1$, $S_\phi=0$) Eqs. (18) and (19) give $\alpha=\alpha_N$ and $Q=Q_N$, and in the superconducting state (no fluxoid motion, $p<p_c$ and $\rho_{xx}=\rho_{xy}=0$), as it might be expected, $\alpha=Q=0$. Thus, Eqs. (18) and (19) are true for a whole transition region of the resistive mixed state of a superconductor.

3. Heat conductivity. Peltier, Ettingshausen and Righi-Leduc Effects

Heat flow $\mathbf{q}_s$, related to the entropy transfer with moving fluxoids, equals $\mathbf{q}_s=S_\phi T n_{ef}\mathbf{v}_f$, where n_{ef} is effective density of moving fluxoids which is different from their real density $n_f=B/\Phi_0$. Nevertheless, rewriting Eq.(14) in the form $\mathbf{E}=-(1/c)[\mathbf{v}_f \times \mathbf{B}](n_{ef}/n_f)$ we come to the relation

$$\mathbf{q}_s=T(cS_\phi/\Phi_0)[\mathbf{E}\times\mathbf{k}],$$

which is an analogy to Eq.(6). As to the heat flow due to the normal quasiparticle motion, it is defined by the relationship

$$\mathbf{q}_n=\Pi_N\mathbf{j}_n+E_N\kappa_N B[\mathbf{k}\times\mathbf{j}_n]+N_n\left(-\kappa_N\nabla T+L_N B[\mathbf{k}\times\nabla T]\right), \qquad (20)$$

which accounts for κ_N and L_N being proportional to current carrier concentration N_n while Π_N and the product $E_N\kappa_N$ are independent on it.

Thus, the electron component of the heat flow in a superconductor equals

$$\mathbf{q}=\mathbf{q}_s+\mathbf{q}_n=T\left(\frac{cS_\phi}{\Phi_0}\right)[\mathbf{E}\times\mathbf{k}]+\Pi_N\mathbf{j}_n+E_N\kappa_N B[\mathbf{k}\times\mathbf{j}_n]+N_n\left(-\kappa_N\nabla T+L_N B[\mathbf{k}\times\nabla T]\right). \qquad (21)$$

To deduce corresponding kinetic coefficients is possible by means of expressing $\mathbf{q}$ in terms of total transport current $\mathbf{j}$. First let us find the connection between normal and total currents substituting Eq.(1) into Eq.(11):

$$\mathbf{j}_n=N_n\left[\mathbf{j}(\rho_{xx}\sigma^N_{xx}+\rho_{xy}\sigma^N_{xy})+[\mathbf{k}\times\mathbf{j}](\rho_{xy}\sigma^N_{xx}-\rho_{xx}\sigma^N_{xy})\right]-$$

$$-(\beta_{N1}-N_n\beta_1)\nabla T - (\beta_{N2}-N_n\beta_2)[\nabla T\times\mathbf{k}] \qquad (22)$$

where $\beta_1=(\sigma^N_{xx}\alpha+\sigma^N_{xy}QB)$, $\beta_2=(\sigma^N_{xy}\alpha-\sigma^N_{xx}QB)$. Next, substituting Eqs.(1) and (22) into (21) we come to expression (2) where Peltier coefficient

$$\Pi=N_n\left[\Pi_N(\rho_{xx}\sigma^N_{xx}+\rho_{xy}\sigma^N_{xy})+E_N\kappa_NB(\rho_{xx}\sigma^N_{xy}-\rho_{xy}\sigma^N_{xx})\right] + T(cS_\phi/\Phi_0)\rho_{xy}, \qquad (23)$$

Ettingshausen coefficient

$$(E\kappa B)=N_n\left[E_N\kappa_NB(\rho_{xx}\sigma^N_{xx}+\rho_{xy}\sigma^N_{xy})-\Pi_N(\rho_{xx}\sigma^N_{xy}-\rho_{xy}\sigma^N_{xx})\right]-T(cS_\phi/\Phi_0)\rho_{xx}, \qquad (24)$$

heat conductivity coefficient

$$\kappa=N_n\kappa_N+\Pi_N(\beta_{N1}-N_n\beta_1)+E_N\kappa_NB(\beta_{N2}-N_n\beta_2)-T(cS_\phi/\Phi_o)QB, \qquad (25)$$

and Righi-Leduc coefficient

$$LB=N_nL_NB+\Pi_N(\beta_{N2}-N_n\beta_2)-E_N\kappa_NB(\beta_{N1}-N_n\beta_1)-T(cS_\phi/\Phi_0)\alpha. \qquad (26)$$

Proceeding from the Onsager equation for a normal metal ($\Pi_N=\alpha_NT$, $E_N\kappa_N=Q_NT$) we make sure that Onsager equations (3) are also valid for above given Seebeck and Peltier coefficients (compare Eqs.(18) and (23)) as well as for Nernst and Ettingshausen coefficients (compare Eqs.(19) and (24)) for a superconductor in the mixed state. This is an evidence of inherent nondiscrepancy of the model suggested and, in particular, of a correct form of the fluxoid motion equation (17). The latter might be obtained without defining concretely expressions for "thermal" forces $\mathbf{F}_{T1}$-$\mathbf{F}_{T4}$. It would be sufficient first to obtain relations (18) and (19) for α and Q, proceeding from Onsager relations and Eqs. (23) and (24) for Π and E coefficients, and then to "restore" the fluxoid motion equation (17).

The Hall conductivity (resistance) is known to be sufficiently lower than the longitudinal conductivity (resistance) at any temperature [3,4]. It gives a possibility to simplify noticeably the expression obtained for kinetic coefficients:

$$\alpha=\Pi/T \cong N_n\alpha_N(\rho_{xx}/\rho_N)+(cS_\phi/\Phi_0)\rho_{xy} \cong N_n\alpha_N(\rho_{xx}/\rho_N), \qquad (27)$$

$$Q=(E/\kappa T) \cong N_nQ_N(\rho_{xx}/\rho_N)-(cS_\phi/B\Phi_0)\rho_{xx} \cong -(cS_\phi/B\Phi_0)\rho_{xx}, \qquad (28)$$

$$\kappa \cong N_n \kappa_N \ , \tag{29}$$

$$LB \cong N_n L_N B - T(cS_\phi/\Phi_0)\alpha \cong -N_n \alpha_N T(cS_\phi/\Phi_0)(\rho_{xx}/\rho_N) \ . \tag{30}$$

The first two of them were derived in earlier works in a not quite correct way [1, 2, 11, 13].

Let us emphasize that the expressions derived for coefficients α, Q, Π, E, κ and L are universal, i.e., independent on the choice of coefficients f_s and f_n. The latter determine only the connection between total conductivity of a superconductor in the mixed state and "partial conductivities", related to normal quasiparticles and fluxoids [14].

From the expressions obtained for kinetic coefficients α, Q, Π, E, κ, and L of a superconductor in the mixed state it is seen that each of them consists of two terms, one of which is proportional to concentration N_n of normal quasiparticles and the other is to the S_ϕ entropy of fluxoids. These two parts may be conditionally called "normal" and "fluxoid" contributions[4]. Their role in different kinetic coefficients is not identical. Longitudinal effects (described with coefficients α, Π, and κ) are defined basically with the "normal" contribution, while transverse effects (coefficients Q, E, and L) are governed by the "fluxoid" one. It is due to the following:

1) Seebeck and Peltier coefficients α, and Π : a relatively minute value of the fluxoid entropy ($cS_\phi \rho_N/\alpha_N \Phi_0 \sim R \ll \rho_{xx}/\rho_{xy}$) and a absolutely small Hall angle ($\rho_{xx}/\rho_{xy} \gg 1$); the vortices are almost immovable along the temperature gradient and transfer small (in comparison with normal electrons) energy;

2) Nernst and Ettingshausen coefficient: a relatively large value of the fluxoid entropy ($cS_\phi \rho_N/\alpha_N \Phi_0 \sim R \gg 1$) and a relatively small Nernst coefficient Q_N in the normal state ($Q_N B/\alpha_N \sim \gamma b \ll 1$); fluxoid transfer high (as compared to normal electrons) energy in the direction perpendicular to the temperature gradient;

3) Heat conductance and Righi-Leduc coefficients κ and L: all the above-said conditions and a relatively high electron heat conductance in the normal state ($\kappa_N \rho_N / T_c \alpha_N^2 \gg 1$); the vortices are

---

[4]The conventionality of this division can be seen if only from the fact that the "normal" contribution into kinetic coefficients is related to the longitudinal resistivity ρ_{xx}, which, at least to a certain extent, is determined by the fluxoid motion.

almost immovable along the temperature gradient ant transfer small (in comparison with normal electrons) energy.

A good agreement with experimental data for HTSC of different compositions has been achieved for a different selection of interpolation factors of the form $f_s=N_s^{\mu}$, $f_n=N_n^{\nu}$ [14]. The values $\mu = \nu = 1$ for $YBa_2Cu_3O_{7-\delta}$ and $\mu = \nu = 3/2$ for Bi-2223 were shown to provide the best fit.. A possible reason for these different values is the different degree of anisotropy of the two compounds in question. This problem, however, is to be further analyzed.

REFERENCES

1. A.A.Abrikosov, *Fundamentals of the Theory of Metals*, Elsevier, New York, 1988
2. Huebner R.P., *Magnetic Flux Structures in Superconductors*, Springer Verlag, Berlin, 1979
3. Dascoulidou A. et al., Physica C, 1992, v.201, p.202
4. Freimuth A., *Transport Properties in the Mixed State of High Temperature Superconductors*, Preprint, 1992
5. V.L.Ginsburg, E.G.Maksimov, SPCT, 1992, vol.5, p.1543 (in Russian)
6. C.J.Gorter, H.B.G.Casimir, Zs.Phys., 1934 vol.35, p.963; Zs.Techn.Phys., 1934 vol.15, p.539
7. Z.D.Wang, C.S.Ting, Phys.Rev.Lett., 1992 vol.69, p.1435
8. H.-C.Ri et al., Phys.Rev.B, 1991, v.43, p.13739
9. Z.D.Wang, C.S.Ting, Phys.Rev.B., 1992 vol.46, p.284
10. S.J.Hagen et al., Phys.Rev.B, 1990 vol.41, p.11630
11. A.V.Samoilov, A.A.Yurgens, N.V.Zavaritskii, Phys.Rev., 1992, v.46, p.6643
12. R.Huebener et al., *Thermoelectric and Thermomagnetic Effects in High Temperature Superconductors*, Preprint, 1992
13. R.P.Huebener, Physica C, 1990, v.168, p.605
14. Meilikhov E.Z. and Farzetdinova R.M., 1994, Physica C, v.221, p.27

SINGLE SCAN
534-76
314252

313-329

SPECTROSCOPY OF INFRARED-ACTIVE PHONONS IN HIGH-TEMPERATURE SUPERCONDUCTORS

A.P. Litvinchuk

Department of Physics, Chalmers University of Technology, S-41296 Göteborg, Sweden

C. Thomsen

Institut für Festkörperphysik, Technische Universität Berlin, Hardenbergstraße 36, D-10623 Berlin, Federal Republic of Germany

M. Cardona

Max-Planck-Institut für Festkörperforschung, Heisenbergstraße 1, D-70569 Stuttgart, Federal Republic of Germany

L. Börjesson

Department of Physics, The Royal Institute of Technology, S-10044 Stockholm, Sweden

For a large variety of superconducting materials both experimental and theoretical lattice dynamical studies have been performed to date. The assignment of the observed infrared- and Raman-active phonon modes to the particular lattice eigenmodes is generally accepted (for a reviews see Ref. [1-5]). We will concentrate here upon the analysis of the changes of the infrared-phonon parameters (frequency and linewidth) upon entering the superconducting state which, as will be shown, may provide information on the magnitude of the superconductivity-related gap and its dependence on the superconducting transition temperature T_c.

Effects of the superconductivity-induced infrared-phonon renormalization were studied experimentally most intensively for $Y_2Ba_4Cu_{6+n}O_{14+n-\delta}$ (n = 0, 1, and 2) superconductors with a double CuO_2-layer in each primitive cell. An interesting feature of the materials with single-CuO chains as structural element (n = 0 and 1) is the possibility to gradually modify their superconducting properties by varying the oxygen content; this allows to study the effects of a reduced T_c in detail even for materials of the same crystallographic structure. For n = 2, however, the presence of the double-CuO chains fixes the oxygen content and, correspondingly, T_c. Another possible way to investigate the effects of phonon renormalization and their connection to superconductivity is to study ion-substituted superconductors knowing the effects of the ions on the superconducting properties of materials from independent measurements.

Superconductivity-induced phonon self-energy effects or so called phonon anomalies were found rather soon after discovery of YBCO superconductors [6, 7]. For a number of reasons they were studied most intensively by means of Raman spectroscopy mainly because the sample requirements are easier to fulfill for Raman then for infrared spectroscopy or neutron-scattering experiments. Pronounced changes (up to 10 cm^{-1}) of the frequencies and the linewidths of the oxygen-related mode at about 340 cm^{-1} were found upon cooling below the superconducting transition temperature (note that even larger effects have been reported for the $Tl_2Ba_2Ca_2Cu_3O_{10}$ superconductor [8]). It is clear qualitatively

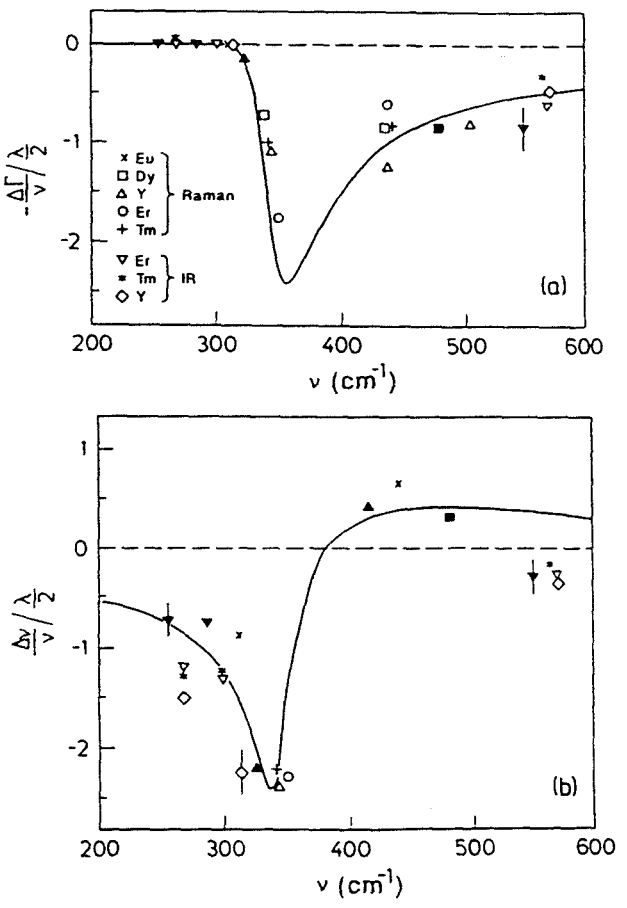

Figure 1: Calculated (after Zeyher and Zwicknagl [10]) imaginary (a) and real (b) parts of the phonon self-energies for a superconducting energy gap at $2\Delta = 316$ cm^{-1} and an impurity scattering rate $1/(2\Delta\tau) = 1$ (solid lines). Points are the experimental data (after Ref. [11-15] for Raman- as well as infrared-active (after Ref. [16]) phonons. Open points refer to ^{16}O and full - to ^{18}O substituted materials.

that if the phonon energy $h\nu_{ph}$ is larger than the magnitude of a given superconducting gap 2Δ, one expects an additional broadening of the phonon at low temperatures because new decay channels appear due to the possibility to break a superconducting pair. When $h\nu_{ph} < 2\Delta$ one expects, on the other hand, the phonon to narrow because of the reduction in the density of states in the gap and hence in the number of decay channels. At the same time phonons exhibit frequency hardening or softening depending on their position relative to the superconductivity-related gap. Of course, phonons with energies close to the gap value 2Δ should react most sensitively to the transition from normal to the superconducting state. For even-parity Raman-active phonons all the features mentioned above were calculated quantitatively by Zeyher and Zwicknagl [9, 10] in the framework of weak BCS as well as conventional strong-coupling theory.

In Fig. 1 experimental results are shown for the superconductivity-induced changes of the phonon linewidth (a) and frequency (b) for single-chain $YBa_2Cu_3O_7$, i.e., changes of the phonon parameters ($\Delta\Gamma$ and $\Delta\nu$ between T_c and $T \approx 0$). The solid lines in the figure are the results of the calculations under the assumption of a single isotropic gap. The only adjustable parameter in these calculations (except, of course, of the magnitude of the superconducting gap 2Δ which was assumed to be 316 cm^{-1} $\approx$ 39.5 meV in Fig. 1) is the electron-phonon coupling constant which from the comparison of theoretical and experimental results was found to be 0.01-0.02 for the phonon branch. These values are in good

agreement with LMTO *ab-initio* calculations.

Note again that calculations presented in Fig. 1 were done for Raman-active modes. It is interesting that the self-energy effect of the odd-parity infrared-active modes could also be described by those calculations despite of the fact that for even-parity excitations different transitions are involved in the electron-phonon interaction (including intraband transitions). So, the superconductivity related gap and even the electron-phonon coupling constants seem to be rather similar for Raman- and infrared-active modes in $YBa_2Cu_3O_7$ [16]. The only infrared data points which do not fit into the general picture are the frequency variations of the high-frequency apical oxygen vibration at about 600 cm^{-1}: this mode exhibits a frequency softening in the superconducting state instead of the predicted hardening (see Fig. 1,b). It was shown recently, however, that this specific feature could consistently be explained theoretically by taking into account the interplane charge fluctuations of the double-plane system [17, 18].

Careful experimental investigations of various superconducting materials revealed a strong dependence of the superconductivity-induced phonon self-energy effects in $YBa_2Cu_3O_{7-\delta}$ on the oxygen content δ and the presence of impurities even for the samples within the so called 90K-plateau (see, e.g., Ref. [19, 20]). It is advantageous in this sense to investigate also the double-chain $YBa_2Cu_4O_8$ superconductor which is known to have an essentially fixed oxygen content because of the presence of the double CuO-chains.

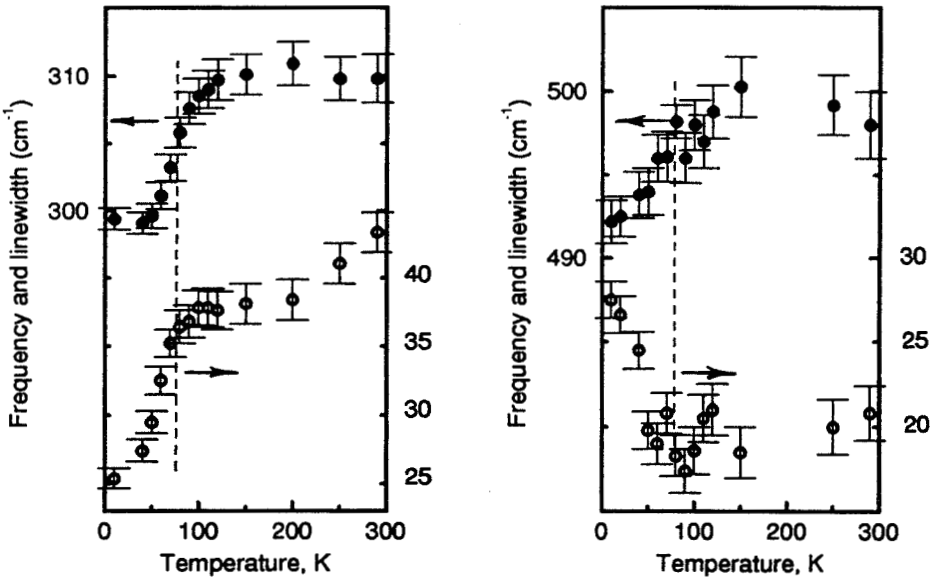

Figure 2: Temperature dependences of the frequencies (solid points) and linewidths (open points) of two oxygen-related modes of the double-chain $YBa_2Cu_4O_8$. The dashed vertical lines mark the T_c (after [25]).

It was found that the self-energy effects experienced by the $B_{1u}(z)$ infrared-phonons of the double-chain $YBa_2Cu_4O_8$ are rather similar to those observed

for the single-chain $YBa_2Cu_3O_{7-\delta}$ and discussed above [21-23]. In Fig. 2 data are presented for the frequency and linewidth variation upon cooling of two phonon modes: the plane-oxygen vibration at 300 cm^{-1} and also the CuO-chain mode [24] at about 500 cm^{-1}. A pronounced narrowing of the former upon cooling below T_c and a broadening of the latter yielded boundaries for the magnitude of the superconducting gap: 310 $cm^{-1} \leq 2\Delta \leq 497$ cm^{-1} [22]. Note that similar to the single-chain $YBa_2Cu_3O_{7-\delta}$ a frequency softening of the high-frequency mode is evident. Remarkably, for both modes shown in Fig. 2 the softening starts at temperatures well above T_c – a fact which is still under discussion and may be related to the opening of the spin-related gap above T_c in *underdoped* superconductors (see [1, 26] and references cited therein).

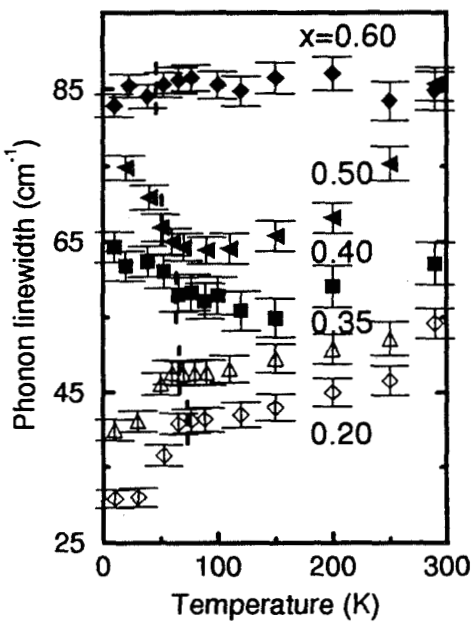

Figure 3: Temperature dependence of the full linewidth at the half-maximum of the plane-oxygen phonon of $(Pr_xY_{1-x})Ba_2Cu_4O_8$ superconductors with frequency about 300 cm^{-1}. The curves from top to bottom are offset vertically by 45, 25, 15, 10, and 0 cm^{-1}. The dashed vertical lines mark the T_c for each sample (after Ref. [27]).

Investigations of T_c-reduced (Pr- and Zn-substituted) double-chain $YBa_2Cu_4O_8$ yielded more information on the superconducting gap. Some of the results for $(Pr_xY_{1-x})Ba_2Cu_4O_8$ are shown in Fig. 3. A narrowing upon cooling of the phonon at 300 cm^{-1} for all materials with Pr-content $x < 0.35$ signals the presence of the gap at higher energies. For higher Pr-contents this mode starts to broaden below T_c. This has been interpreted as a result of the creation of a new decay channel for the plane-oxygen phonon and experimental evidence for the shift of the corresponding gap to lower energies across the phonon frequency [27].

Qualitatively similar results as regards to the effect of the reduction of T_c on the infrared-phonon self-energies were observed in the case of Zn-substituted $YBa_2Cu_4O_8$ [28]. An important experimental finding is that for both Pr- and Zn-

substitute different ions within the crystallographic structure) differs by factor of ten. As a comparison, there is no effect on the self-energies in the case of Sr substitution for Ba within a rather wide range of concentrations, which also does not influence the superconducting temperature T_c. All these facts provide convincing evidence that the discussed effects of the infrared-active phonon of $Y_2Ba_4Cu_{6+n}O_{14+n-\delta}$ are indeed superconductivity related.

Acknowledgments This work was supported by the Swedish Research Board for Natural Sciences, the Bundesminister für Forschung und Technologie under contract No. 13N5840 5 (Federal Republic of Germany) and the European Community. Part of this work was performed by one of us (A.P.L.) under the support from the Swedish Superconductivity Consortium, Max-Planck Gesselschaft (München, Federal Republic Germany) and Alexander von Humboldt Foundation (Bonn, Federal Republic Germany). He also acknowledges the hospitality of the Max-Planck-Institut für Festkörperforschung (Stuttgart, Federal Republic of Germany) where part of this work was performed.

References

[1] A.P. Litvinchuk, C. Thomsen, and M. Cardona, in *Physical Properties of High Temperature Superconductors IV*, ed. by D.M. Ginsberg (World Scientific, Singapore, 1994), p.375.

[2] D.B. Tanner and T. Timusk in *Physical properties of High Temperature Superconductors III*, ed. by D.M. Ginsberg (World Scientific, Singapore, 1992), p.363.

[3] K.F. Renk, in: *Tl-based High Temperature Superconductors*, ed. by A.H. Hermann and J.V. Yakhmi (Marcel Dekker, Inc., Publishers, New York, 1992), p.477.

[4] C. Thomsen, in *Light Scattering in Solids VI*, ed. by M. Cardona and G. Güntherodt (Springer, Berlin, Heidelberg, New York, 1991), p.285.

[5] R. Feile, Physica C **159**, 1 (1989).

[6] R.M. Macfarlane, H.J. Rosen, and H. Seki, Solid State Commun. **63**, 831 (1987).

[7] A. Wittlin, R. Liu, M. Cardona, L. Genzel, W. König, W. Bauhofer, Hj. Mattausch, A. Simon, and F. Garcia-Alvarado, Solid State Commun. **64**, 477 (1987).

[8] T. Zetterer, M. Franz, J. Schützmann, W. Ose, H.H. Otto, and K.F. Renk, Solid State Commun. **75**, 325 (1990).

[9] R. Zeyher and G. Zwicknagl, Solid State Commun. **66**, 617 (1988).

[10] R. Zeyher and G. Zwicknagl, Z. Phys. B: Condensed Matter **78**, 175 (1990).

[11] B. Friedl, C. Thomsen, and M. Cardona. Phys. Rev. Lett. **65**, 915 (1990).

[12] C. Thomsen, M. Cardona, B. Friedl, C.O. Rodriguez, I.I. Mazin, and O.K. Andersen, Solid State Commun. **75**, 219 (1990).

[13] B. Friedl, C. Thomsen, H.-U. Habermeier, and M. Cardona, Solid State Commun. **78**, 291 (1991).

[14] B. Friedl, C. Thomsen, E. Schönherr, and M. Cardona, Solid State Commun. **76**, 1107 (1990).

[15] B. Friedl, PhD. Thesis, Universität Stuttgart, 1992.

[16] A.P. Litvinchuk, C. Thomsen, and M. Cardona, Solid State Commun. **80**, 257 (1991).

[17] G. Hastreiter and J. Keller, Solid State Commun. **85**, 967 (1993).

[18] G. Hastreiter, F. Forsthofer, and J. Keller, Solid State Commun. **88**, 769 (1993).

[19] C. Thomsen, B. Friedl, M. Cieplak, and M. Cardona, Solid State Commun. **78**, 727 (1991).

[20] E. Altendorf, J.C. Irwin, R. Liang, and W.N. Hardy, Phys. Rev. B **45**, 7551 (1992).

[21] A.P. Litvinchuk, C. Thomsen, and M. Cardona, in *Sixteenth Intern. Conf. on Infrared and Millimeter Waves*, ed. by Siegrist, M.R., Tran M.Q., and Tran T.M.: Proc. SPIE **1576**, 22 (1991).

[22] A.P. Litvinchuk, C. Thomsen, P. Murugaraj, and M. Cardona, Z. Phys. B: Condensed Matter **86**, 329 (1992).

[23] A.P. Litvinchuk, C. Thomsen, M. Cardona, J. Karpinski, E. Kaldis, and S. Rusiecki, Z. Phys. B: Condensed Matter **92**, 9 (1993).

[24] C. Thomsen, A.P. Litvinchuk, E. Schönherr, and M. Cardona, Phys. Rev. B **45**, 8154 (1992).

[25] A.P. Litvinchuk, C. Thomsen, and M. Cardona, unpublished.

[26] A.P. Litvinchuk, C. Thomsen, and M. Cardona, Solid State Commun. **83**, 343 (1992).

[27] A.P. Litvinchuk, C. Thomsen, M. Cardona, L. Börjesson, M. Käll, P. Berastegui, and L.-G. Johansson, Solid State Commun. **87**, 907 (1993).

[28] A.P. Litvinchuk, C. Thomsen, M. Cardona, L. Börjesson, P. Berastegui, and L.-G. Johansson, Phys. Rev. B **50**, July, 1 (1994).

Page intentionally left blank

Physical Properties

Session PP-2 Chair: Prof. Valeri Ozhogin
Co-Chair: D. Brinkman

Page intentionally left blank

FLUX PINNING CHARACTERISTICS AND IRREVERSIBILITY LINE IN HIGH TEMPERATURE SUPERCONDUCTORS

T. Matsushita, N. Ihara and M. Kiuchi

Department of Computer Science and Electronics, Kyushu Institute of Technology,
680-4 Kawazu, Iizuka 820, Japan

ABSTRACT

The flux pinning properties in high temperature superconductors are strongly influenced by thermally activated flux motion. The scaling relation of the pinning force density and the irreversibility line in various high temperature superconductors are numerically analyzed in terms of the flux creep model. The effect of two factors, i.e., the flux pinning strength and the dimensionality of the material, on these properties are investigated. It is speculated that the irreversibility line in Bi-2212 superconductors is one order of magnitude smaller than that in Y-123, even if the flux pinning strength in Bi-2212 is improved up to the level of Y-123. It is concluded that these two factors are equally important in determination of the flux pinning characteristics at high temperatures.

INTRODUCTION

The critical current density J_c is one of the most important parameters of high temperature superconductors in their application to various fields. However, the critical current density in these materials is empirically known to be significantly degraded with increasing magnetic field at high temperatures. Such a poor critical current property is ascribed to weak pinning strength in these materials and large thermal activation of fluxoids at high temperatures. The boundary between the magnetically irreversible region with nonzero J_c and the reversible region with zero J_c in the field(B)-temperature(T) plane is called the irreversibility line. The poor critical current property in high temperature superconductors is directly concerned with their low irreversibility line.

In order to quantitatively understand the critical current property at high temperatures, it is necessary to take into account the effect of the thermally activated fluxoid motion correctly. For this purpose the collective flux creep theory [1] seems to be useful. One of the important features of this theory is that the pinning potential U_0 can be estimated in terms of the virtual critical current density J_{c0} in the creep-free case. The theoretical result of the summation of elementary pinning forces is applicable to this quntity for a superconductor with known pinning centers. On the other hand, in the case of unknown pinning centers as in most high temperature superconductors, the critical current density observed at sufficiently low temperatures where the thermal activation is not significant can be approximately used as J_{c0}. The irreversibility lines in various superconductors can be explained satisfactorily with respect to the dependences on temperature, flux pinning strength and superconducting materials [2]. Therefore, the flux pinning characteristics in the vicinity of the irreversibility line can also be expected to be analysed correctly in terms of the flux creep theory. In this paper theoretical results on various superconductors are discussed and the scaling laws of the pinning force density are compared with experimental results.

THEORY

According to the flux creep model [3], the induced electric field due to the thermally activated

fluxoid motion is given by

$$E = Ba\nu \exp\left(-\frac{U}{k_B T}\right), \tag{1}$$

where a is the hopping distance of the flux bundle, ν is the oscillation frequency of the flux bundle in the pinning potential, U is the activation energy caused by flux pinning and k_B is the Boltzmann constant. The factor of the exponential term gives the probability for flux bundle to jump over the energy barrier due to the thermal activation. From the fact that the situation changes almost periodically with respect to the displacement of fluxoids by their mean spacing a_f, it is expected that a can be approximately replaced by a_f. According to the theoretical analysis using the Fokker-Planck equation [4], the oscillation frequency is given by

$$\nu = \frac{\zeta \rho_f J_{c0}}{2\pi a_f B}, \tag{2}$$

where ζ is a constant dependent on the pinning center and takes 2π for point defects [5] and ρ_f is the flow resistivity.

The activation energy U varies when the current density J varies and its variation depends on the shape of the pinning potential. If we assume a sinusoidally varying washboard pinning potential, U is written as

$$U(j) = U_0[(1-j^2)^{1/2} - j\cos^{-1} j], \tag{3}$$

where $j = J/J_{c0}$ is the reduced current density.

According to the flux creep theory [1] the pinning potential U_0 in bulk superconductors is expressed as

$$U_0 = \frac{0.835 g^2 k_B J_{c0}^{1/2}}{\zeta^{3/2} B^{1/4}}, \tag{4}$$

where g^2 is the number of fluxoids in the flux bundle. In the original flux creep theory [1], the number g^2 was expected to be determined by the elastic correlation length as

$$g^2 = \frac{C_{66} a_f}{\zeta J_{c0} B} \equiv g_e^2, \tag{5}$$

where C_{66} is the shear modulus of the fluxoid lattice. However, it has been clarified [6] that the practical g^2 values estimated from the observed irreversibility field are smaller than g_e^2 given by Eq. (5). This tendency is more remarkable for the larger g_e^2 value and for the case of the magnetic field parallel to the c-axis [7, 8]. This behavior can be understood as the result of the irreversible thermodynamics so as to minimize the energy dissipation. That is, if the flux bundle size becomes smaller, the flexibility of fluxoids to be pinned by distributed pinning centers increases, resulting in the stronger pinning, while it leads to the smaller pinning potential due to smaller volume, resulting in the larger effect of thermal activation. Thus, the optimal condition exists and g^2 is expected to be given by [7]

$$g^2 = g_e^2 \left[\frac{5 k_B T}{2 U_e} \ln\left(\frac{B a_f \nu}{E_c}\right)\right]^{4/3}, \tag{6}$$

where U_e is the virtual pinning potential when g^2 is equal to g_e^2 and E_c is the electric field criterion for the definition of the critical current density.

In the case of magnetic field normal to the c-axis, g_e^2 is proportional to the coherence length along the c-axis. Hence, the flux bundle tends to have small sizes in two-dimensional superconductors. For the magnetic field parallel to the c-axis, the corresponding coherence length is that in the a-b plane, and the obtained U_e is very large. However, this results in quite small g^2 value from Eq. (6) [8]. It is concluded, therefore, that the two-dimensional superconductors are more strongly influenced by the thermal activation in the both field directions.

In this paper the flux pinning property in the vicinity of the irreversibility line is investigated. In this region where the current density is small, the fluxoid motion in the direction opposite to the Lorentz force is also appreciable, since the activation energy in this direction is not largely different from that in the normal direction. Hence, Eq. (1) is replaced by

$$E = Ba_{\rm f}\nu\exp\left[-\frac{U(j)}{k_{\rm B}T}\right]\left[1-\exp\left(-\frac{\pi U_0 j}{k_{\rm B}T}\right)\right]. \tag{7}$$

For the calculation of the E-J curve at desired temperature and magnetic field, it is necessary to express U_0 as a function of the temperature and the magnetic field. For this purpose, the empirical dependences are assumed for the virtual critical current density as

$$J_{\rm c0} = A\left[1-\left(\frac{T}{T_{\rm c}}\right)^2\right]^m B^{\gamma-1}\left(1-\frac{B}{B_{\rm c2}}\right)^\delta, \tag{8}$$

where A, m, γ and δ are the pinning parameters. That is, A corresponds approximately to the critical current density at 0 K and 1 T and represents the flux pinning strength of superconductors. m and γ respresent the temperature and magnetic field dependences, respectively. In the case of high temperature superconductors, the upper critical field $B_{\rm c2}$ is much larger than the irreversibility field, $B_{\rm i}$, and the parameter δ is less important. In the numerical calculation, the flow resistivity is also necessary. In this paper, we assume the Bardeen-Stephen model [9], $\rho_{\rm f} = (B/B_{\rm c2})\rho_{\rm n}$ where $\rho_{\rm n}(T) = (T/T_{\rm c})\rho_{\rm n}(T_{\rm c})$ is the normal resistivity.

We calculate the pinning force in a melt-processed Y-123, a Bi-2223 tape wire and a melt-processed Bi-2212 in this paper. The assumed parameters are listed in Table 1. The case is treated where the magnetic field is applied normal to the c-axis. In the melt-processed Y-123, fine particles of the Y_2BaCuO_5 (211) phase of 2.0 μm in diameter and 20 % in volume fraction are assumed to work as the dominant pinning centers. In the Bi-2223 tape wire and the melt-processed Bi-2212, the results observed at low temperatures are approximately used for $J_{\rm c0}$ [6, 10]. Fine particles of

	Y-123 (melt)	Bi-2223 (tape)	Bi-2212 (melt)	Bi-2212 (crystal)
$T_{\rm c}$(K)	92.0	107.7	92.8	77.8
$B_{\rm c2\|\|}(0)$(T)	644	1000	690	690
$\rho_{\rm n}(T_{\rm c})(\mu\Omega{\rm m})$	2.0	100	100	100
$AB_{\rm c2}^m(0)$	2.58×10^9	$2.54\times10^9/6.57\times10^8$	$7.52\times10^8/3.33\times10^8$	1.71×10^6
m	1.5	3.0/1.5	2.25/1.5	3.1
γ	0.5	0.63/0.5	0.79/0.5	0.98
δ	2.0	2.0	2.0	2.0
ζ	4	$2\pi/4$	2π	2π
$g_{\rm e}^2$	44.4	6.7/1.55	2.2	620
g^2	6.0	4.0/1.55	2.0	14*
reference		6	10	11
assumption		$U_0 = (U_{01}^2 + U_{02}^2)^{1/2}$	$J_{\rm c0} = (J_{\rm c1}^2 + J_{\rm c2}^2)^{1/2}$	

Tab. 1. Superconducting and pinning parameters used in the numerical analysis. Two kinds of pinning centers are assumed to work in Bi-2223 tape wire and melt-processed Bi-2212. $*g^2 = 14$ is assumed so as to get a good fit, although $g^2 = 4.0$ is theoretically predicted.

Bi-free phases observed from the microscopic observation are assumed to contribute to the flux pinning in these specimens. The mean diameter and the volume fraction assumed are 5.0 μm and 10 %, respectively. The E-J curves are calculated from Eq. (7) and the critical current density is estimated by the offset method from the point on the E-J curve at $E = E_c = 1.0 \times 10^{-5}$ V/m. The irreversibility field is defined by the magnetic field at which the critical current density is reduced to 1.0×10^5 A/m^2.

RESULTS AND DISCUSSION

Figure 1(a) shows the results of numerical calculation of the irreversibility lines in various superconductors and the corresponding experimental results are given in Fig. 1(b) [12]. In these figures, the results on a Bi-2212 single crystal with very weak flux pinning strength are also shown for comparison. It can be seen from these figures that the agreement is fairly good for various superconductors. This means that the flux creep theory explains correctly the phenomena concerned with the thermal activation of fluxoids.

The results depicted in Fig. 1(a) and 1(b) clarify that the irreversibility line strongly depends on the flux pinning strength and the superconducting material. As for the latter factor, the superconductor with the larger two-dimensionality is inferior in the irreversibility. In order to clarify this point more quantitatively, we shall discuss the theoretical prediction from the flux creep theory [1]. According to this theory the irreversibility field is approximately estimated as

$$B_i = \left(\frac{K}{T_c}\right)^{4/(3-2\gamma)} \left[1 - \left(\frac{T}{T_c}\right)^2\right]^{2m/(3-2\gamma)} \tag{9}$$

in the vicinity of the critical temperature, where K is a constant given by

$$K = \frac{0.835 g^2 A^{1/2}}{\zeta^{3/2} \ln(B a_f \nu / E_c)}. \tag{10}$$

In Eq. (10) the logarithmic term is almost constant and typically takes a value from 12 to 15. We shall compare the cases of melt-processed Y-123 and Bi-2212 superconductors as an example where the irreversibility field B_i is approximately different by a factor of 100. At high temperatures, such as the reduced temperature of $T/T_c = 0.95$(i.e., $1 - (T/T_c)^2 \simeq 0.1$), the nonsuperconducting particles are expected to be dominant pinning centers in the both superconductors. In this case, the pinning force density at low fields calculated from the direct summation is

$$J_{c0} B = \frac{\pi B_c^2 \eta \xi}{4 \mu 0 a_f D}, \tag{11}$$

where η and D are the volume fraction and the mean diameter of the nonsuperconducting particles, respectively. This leads to $m = 3/2$ and γ=1/2. Thus, we have $B_i \propto A g^4$. The A value in Bi-2212 is expected to be smaller by a factor of 7.8 than that in Y-123 due to the worse flux pinning efficiency of larger nonsuperconducting particles and their smaller concentration. In addition, the g^2 value in Bi-2212 is estimated to be smaller by a factor of 3 than that in Y-123 due to the smaller coherence length along the c-axis. This also leads to the smaller B_i by a factor of about 9. As a result, the B_i in Bi-2212 is expected to be smaller by a factor of about 70 than that in Y-123. This is in an approximate agreement with the experiments shown in Fig. 1(b).

It means that the two factors, i.e., the flux pinning strength and the dimensionality are equally important in determination of the irreversible property of superconductors. It seems to be fairly difficult to improve drastically the irreversiblity field in Bi-2212 superconductors, although it can be improved to some extent by introduction of strong pinning centers in priniciple. That is, even if the flux pinning strength in Bi-2212 is improved to the level of present Y-123, its irreversibility field is expected to be still by one order of magnitude smaller than in Y-123.

Here we shall discuss the flux pinning property in the vicinity of the irreversibility line. Figure 2(a) and 2(b) are the calculated results of the normalized pinning force density in Y-123 and Bi-2212

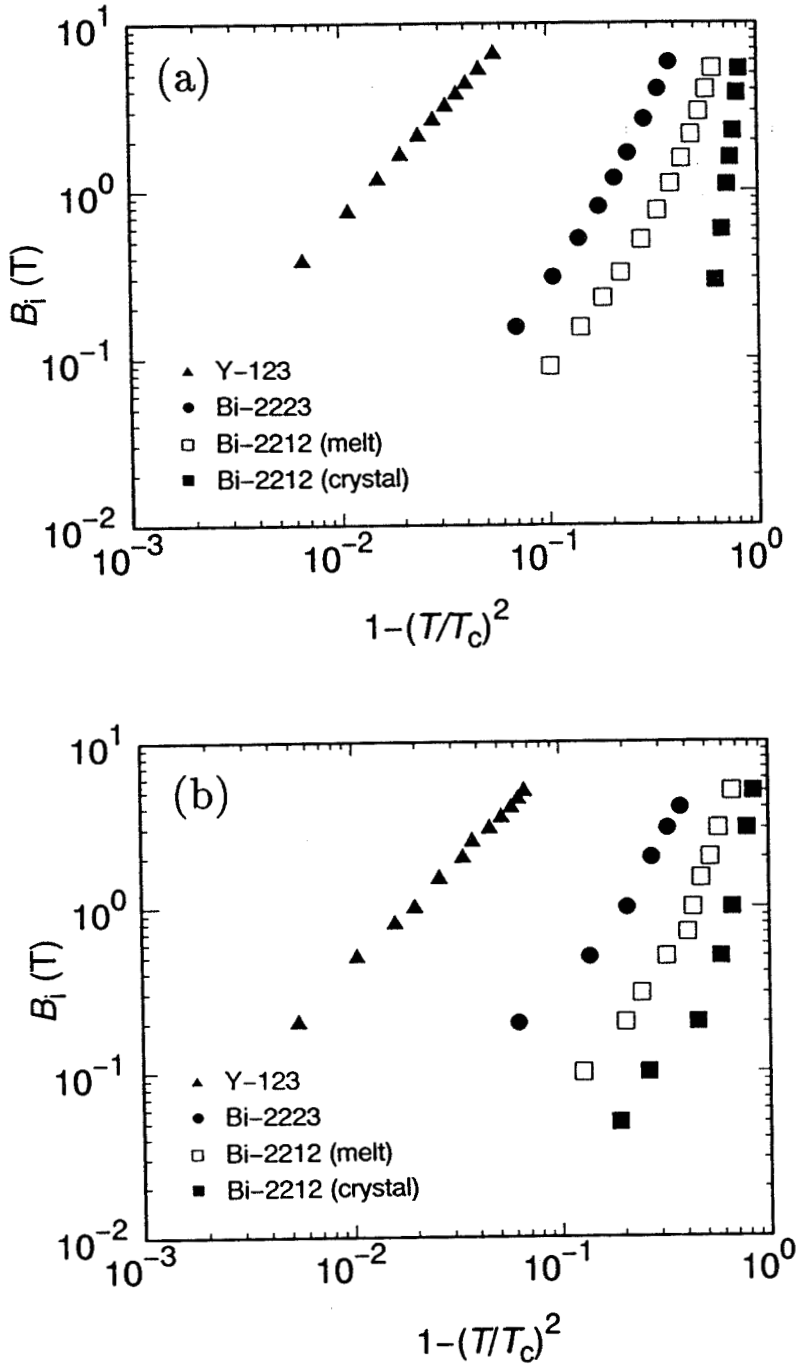

Fig. 1. (a) Calculated irreversibility lines and (b) observed irreversibility lines for melt-processed Y-123 (▲), silver-sheathed Bi-2223 tape wire (●), melt-processed Bi-2212 (□) and TSFZ-processed Bi-2212 single crystal (■).

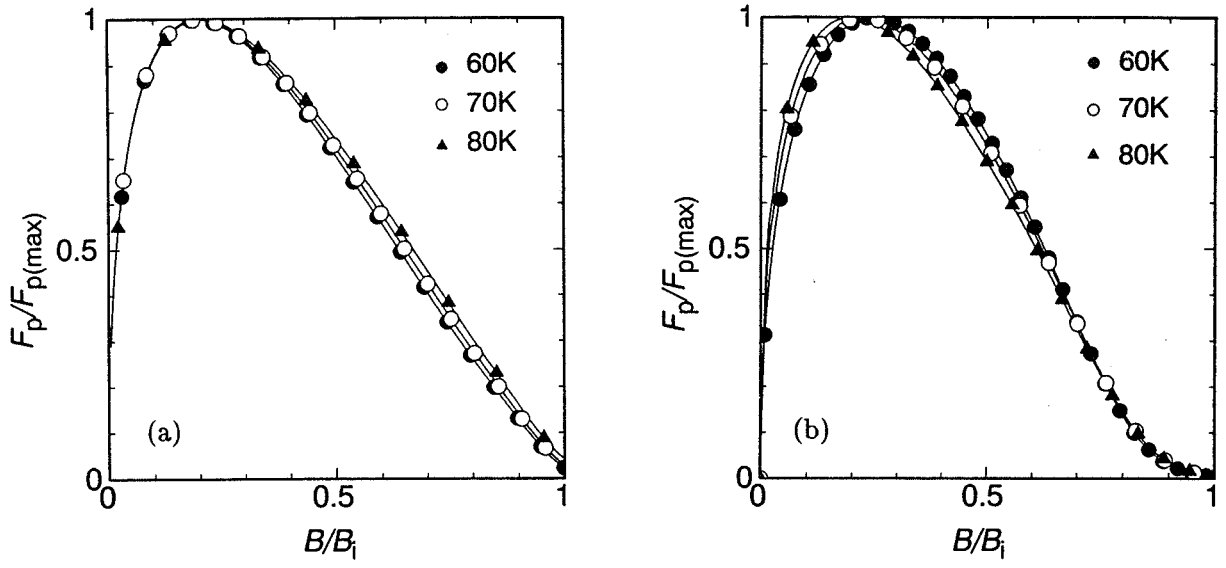

Fig. 2. Calculated scaling law of the pinning force density for melt-processed (a) Y-123 and (b) Bi-2212.

as a function of the magnetic field reduced by their irreversibility field, $b_i = B/B_i$. It is found that the results collapse approximately on a master curve in the both cases, as experimentally observed. The relation between the maximum pinning force density and the irreversibility field is shown in Fig. 3. From the results shown Figs. 2 and 3, the pinning property in the vicinity of the

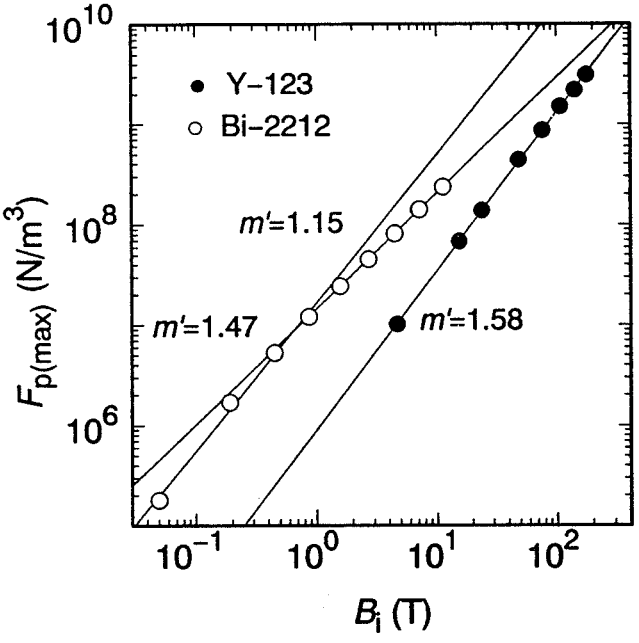

Fig. 3. Relation between the maximum pinning force density and the irreversibility field calculated for melt-processed Y-123 and Bi-2212.

irreversibility line is expressed in the form of scaling law of

$$F_p = A' B_i^{m'}(T) f(b_i), \tag{12}$$

where A' is a constant and f is a function only of the reduced field b_i shown in Fig. 2. The obtained parameter m' representing the temperature dependence is 1.58 for Y-123 and 1.15 and 1.47 in the lower and higher temperature regions for Bi-2212. The reason why the two m' values are obtained for Bi-2212 is that the dominant pinning centers are different between the lower and higher temperature regions as can be seen from the two slopes in Fig. 1(a). These m' values are smaller than $m + \gamma$ given in Table 1 representing the temperature dependence of the original pinning force density. This is caused by the fact that the temperature dependence of B_i is stronger than that of B_{c2} which is assumed as $B_{c2} \propto 1 - (T/T_c)^2$. That is, if the temperature dependence of B_i is expressed as $[1 - (T/T_c)^2]^n$, n takes 1.5 for Y-123 and 3.2 and 1.5 in the lower and higher temperature regions for Bi-2212.

From the results shown in Fig. 2(a) and 2(b), it is found that the scaling form of the pinning force density is rather independent of the superconductor, although a slightly longer tail of the pinning force density is obtained for Bi-2212. Such a common feature of the pinning property is considered to be caused by the fact that the resultant pinning property does not remember the original pinning characteristics due to the significant effect of flux creep like a shape of sand hills attacked by waves. It is seen from Fig. 3 that the obtained B_i is smaller in Bi-2212 than in Y-123 even for the same maximum pinning force density. This also suggests that the influence of flux creep is larger in Bi-2212 with the larger two-dimensionality.

Similar theoretical result is obtained also for a Bi-2223 tape wire. Here this theoretical result is compared with experimental results. Figure 4(a) and 4(b) are the observed scaling behavior of pinning force density in the Bi-2223 tape wire in the magnetic field normal and parallel to the c-axis, respectively. The temperature dependence of the irreversibility is shown in Fig. 5. The anaisotropy factor in this specimen is about 6.2 at 80 K. Figure 6 represents the relation of the maximum pinning force density and the irreversibility field in the two field directions. Using the formula given by Eq. (12), we have m'=1.4 for the field normal to the c-axis and m'=1.5 for the

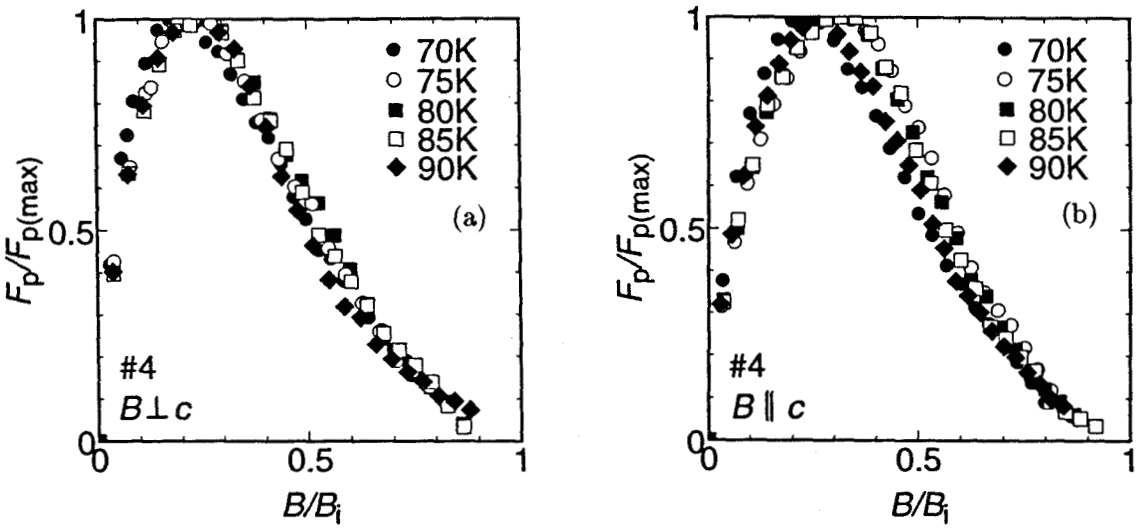

Fig. 4. Observed scaling of pinning force density in Bi-2223 tape wire in the magnetic field (a) normal to the c-axis and (b) parallel to the c-axis.

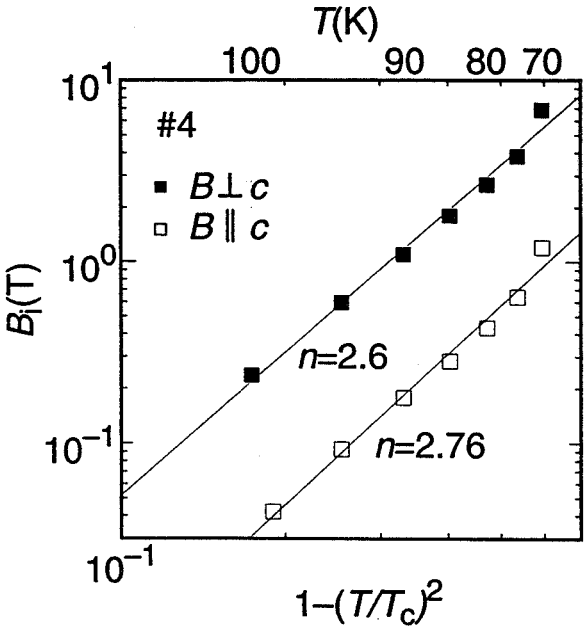

Fig. 5. Temperature dependence of irreversibility field in Bi-2223 tape wire in the two field directions.

field parallel to the c-axis. If the measurement is carried out to much higher temperature region, larger m' values are expected to be observed. In this specimen the pinning parameters observed at sufficiently low temperatures are m=3.96 and γ=0.73. Thus, the m' value is smaller than $m+\gamma$ as in the theoretical treatment for Y-123 and Bi-2212 in the above.

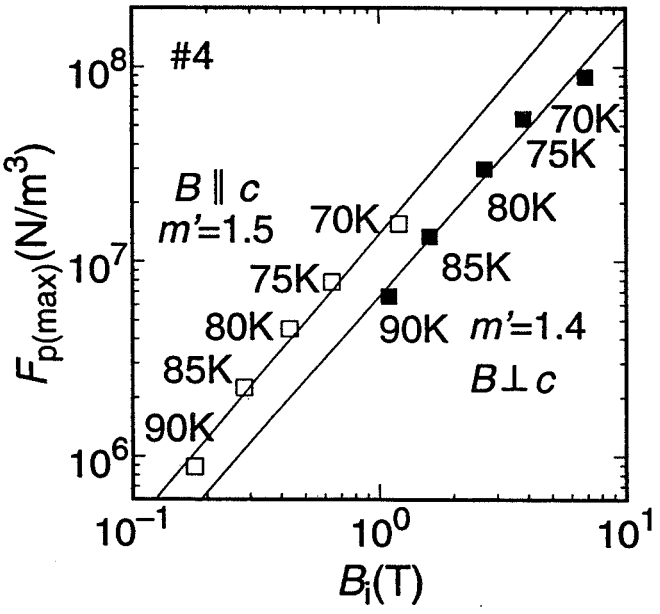

Fig. 6. Relation between the maximum pinning force density and the irreversibility field in Bi-2223 tape wire.

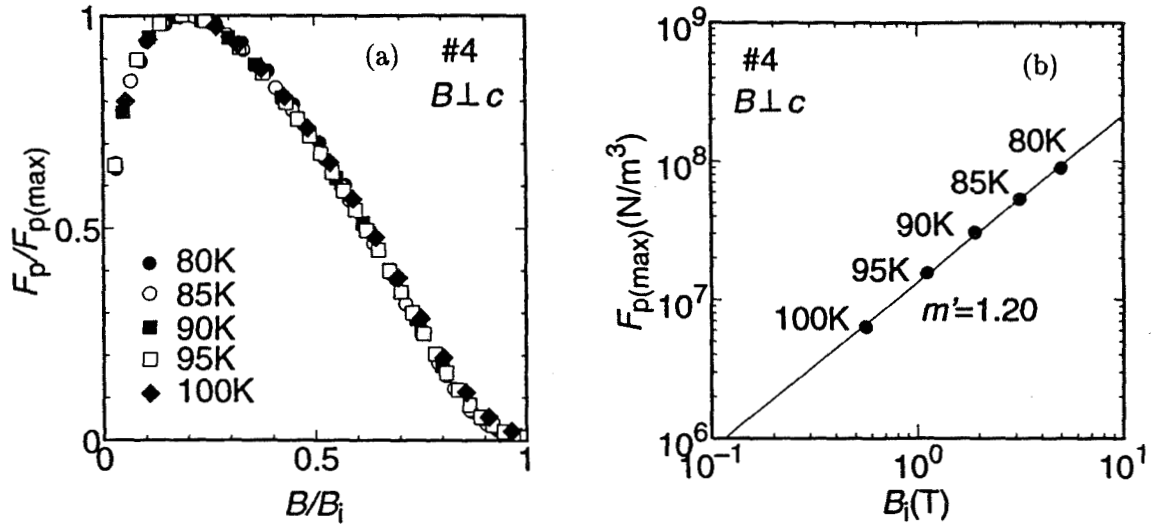

Fig. 7. (a) Calculated scaling law of the pinning force density and (b) relation between the maximum pinning force density and the irreversibility line in Bi-2223 tape wire.

Numerically calculated results for the magnetic field normal to the c-axis, corresponding to the experimental results shown in Fig. 4(a) and Fig. 6, are given in Fig. 7(a) and 7(b), respectively. The reduced field at the maximum pinning force density is approximately the same and a similar scaling curve is obtained, although the decrease of the pinning force density at high field is not large as observed. The rapid decrease in the observed result may be attributed to the distributed pinning strength due to inhomogeneity. The parameter m' obtained from Fig. 7(b) is 1.2 and is approximately the same with the observed $m' = 1.4$. Thus, the agreement between the theory and the experiment seems to be satisfactory.

The above argument shows that the flux creep theory explains systematically the phenomena concerned with the thermally activated motion of fluxoids. Satisfactory explanation can be given also on anomalous magnetic relaxation at low temperatures [7] and scaling of E-J curves [13]. Hence, this theory is expected to be applicable for the estimation of the critical current density in a superconductor with artificially introduced pinning centers that will be fabricated in the future. This will be helpful for foreseeing the attainable characteristics of high temperature superconductors on which the possibility of application of these materials entirely depend.

SUMMARY

The flux pinning property of high temperature superconductors is investigated in the vicinity of the irreversibility line using the flux creep theory. The following results are obtained:

(1) The irreversibility line depends on both the flux pinning strength and the dimensionality of superconductors due to their anisotropic structures. These factors are found to be equally important in determination of the irreversibility line. For example, the irreversibility field in Bi-2212 is estimated to be approximately one order of magnitude smaller than that in Y-123, even if the flux pinning strength in Bi-2212 is improved up to the present level of Y-123.

(2) The scaling law of the pinning force density as observed usually is obtained for various superconductors. The scaling curve is fairly insensitive to the material. This means that the original flux pinning property dependent on the material is shaded off by the strong effect of flux creep. Agreements with experiments are obtained for the case of a Bi-2223 tape wire.

(3) From these points it can be concluded that the electromagnetic phenomena concerned with thermally activated flux motion can be correctly described by the flux creep theory. This theory is expected to be useful for foreseeing the pinning property in superconductors that will be fabricated in the future.

REFERENCES

1 T. Matsushita, T. Fujiyoshi, K. Toko and K. Yamafuji, Appl. Phys. Lett. **56**, 2039 (1990).

2 For example, T. Matsushita, *Studies of High Temperature Superconductors* (Nova Science, New York, 1994) Vol. 14, p. 19.

3 P. W. Anderson and Y. B. Kim, Rev. Mod. Phys. **36**, 39 (1964).

4 K. Yamafuji, T. Fujiyoshi, K. Toko and T. Matsushita, Physica C **159**, 743 (1988).

5 A. M. Campbell, H. Küpfer and R. Meier-Hirmer, *Proc. Int. Symp. on Flux Pinning and Electromagnetic Properties in Superconductors* (Matsukuma, Fukuoka, 1985) p. 54.

6 T. Matsushita, E. S. Otabe, M. Kiuchi, B. Ni, T. Hikata and K. Sato, Physica C **201**, 151 (1992).

7 T. Matsushita, Physica C **217**, 461 (1993).

8 T. Matsushita, *Adv. in Superconductivity VI* (Springer-Verlag, Tokyo, 1994) p. 503.

9 J. Bardeen and M. J. Stephen, Phys. Rev. 140, A1197 (1965).

10 T. Matsushita, T. Nakatani, E. S. Otabe, B. Ni, T. Umemura, K. Egawa, S. Kinoichi, A. Nozaki and S. Utsunomiya, Cryogenics **33**, 251 (1933).

11 T. Matsushita, T. Nakatani, E. S. Otabe, K. Yamafuji, K. Takamuku and N. Koshizuka Jpn. J. Appl. Phys. **32**, L720 (1993).

12 T. Matsushita and N. Ihara, *Proc. Europ. Conf. Appl. Supercond.*, 1993, Göttingen, p. 779.

13 T. Matsushita and N. Ihara, to be published in *Proc. 7th Int. Workshop on Critical Currents in Superconductors*, 1994, Alpbach.

536-76

EFFECTS OF NEUTRON IRRADIATION ON THE LONDON PENETRATION DEPTH FOR POLYCRYSTALLINE $Bi_{1.8}Pb_{0.3}Sr_2Ca_2Cu_3O_{10}$ SUPERCONDUCTOR.

314309

J. G. Ossandon,[a] J. R. Thompson,[b,c] Yang Ren Sun,[b] D. K. Christen,[c] and B. C. Chakoumakos.[c]

[a]*Facultad de Recursos Naturales, Universidad de Talca, Talca, Chile,*
[b]*Department of Physics, Univ. of Tennessee, Knoxville, TN 37996-1200, U.S.A.*
[c]*Oak Ridge National Laboratory, P. O. Box 2008, Oak Ridge, TN 37831-6061*

314332

ABSTRACT

Magnetization studies of polycrystalline $Bi_{1.8}Pb_{0.3}Sr_2Ca_2Cu_3O_{10}$ superconductor, prior to and after neutron irradiation, showed an increase in J_c due to irradiation damage. Analysis of the *equilibrium* magnetization revealed significant increases in other more fundamental properties. In particular, the London penetration depth increased by ~ 15 % following irradiation with $8x10^{16}$ neutrons/cm^2. Corresponding changes were observed in the upper critical magnetic field H_{c2}. However, the most *fundamental* thermodynamic property, the superconductive condensation energy F_c, was unaffected by the moderate level of neutron-induced damage.

INTRODUCTION

Magnetometric studies have been widely used to determine the physical properties of high temperature superconductors (HTSC).[1] For example, the intragrain persistent current density $J_p(T,H)$ in the mixed state can be found from measurements of the *irreversible* magnetization by means of the Bean model, provided the grain morphology is known. The London penetration depth λ can often be obtained from the logarithmic slope of the equilibrium (*reversible*) magnetization M(H,T) using the standard London-limit formalism of Kogan et al.[2] More recent theoretical developments, however (Bulaevskii et al.[3], Kogan et al.[4]), have shown that vortex *fluctuations* are important in regions of magnetic field and temperature above the irreversibility line, where vortices are free to move to their equilibrium locations. In particular, the entropy associated with fluctuations introduces a correction to the equilibrium free energy, which modifies the

equilibrium magnetization. These modifications are most significant for highly anisotropic, layered materials, and near the superconductive transition temperature T_c. The fluctuation analysis provides a useful tool to determine the superconducting volume fraction of the material, as well as the characteristic magnetic fields and lengths. Cho *et al.*[5] showed that this formalism still applies to random polycrystals, provided the material is sufficiently anisotropic that only the component of the applied field H perpendicular to the layers is effective. Further below T_c, where fluctuation effects are less significant, the theory of Hao-Clem[6] provides an alternative formulation for determining the fundamental properties of the superconductor from studies of the reversible magnetization in the intermediate field region.[7]

In this work, the main objective is to investigate the impact of neutron-induced damage on the London penetration depth. Here we used fast neutron irradiation to modify the Bi-based superconductor $Bi_{1.8}Pb_{0.3}Sr_2Ca_2Cu_3O_{10}$. Apparently the localized damage affects the superconductor in two ways: (1) it shortens the mean free path for conduction electrons by providing scattering centers and (2) it increases the (critical and persistent) current density in the material, by providing vortex pinning sites. Here we study primarily mean free path effects, as there is little information to date regarding their impact on high-T_c superconductors.

EXPERIMENTAL ASPECTS

The sample was a polycrystalline specimen of the $Bi_{1.8}Pb_{0.3}Sr_2Ca_2Cu_3O_{10}$ (hereafter BiPb-2223) compound, containing three adjacent CuO-layers in the unit cell. This highly anisotropic superconductor initially had a diamagnetic onset transition temperature $T_c \approx 109$ K, measured at low magnetic field (≤ 4 - 10 Oe). It consisted of thin platelets with edge dimensions of ≈ 100 microns. Two pieces of the same batch were used for comparison; one of them (m = 169 milligrams) was irradiated with $\sim 8 \times 10^{16}$ [n/cm^2] fluence of fast neutrons (E > 0.1 MeV), giving roughly a 3-fold increase of irreversible magnetization M(H,T), i.e., a 3-fold increase in the critical current density J_c. The other piece (m = 85 milligrams) was left unirradiated. Both showed clear evidence of vortex fluctuation effects at temperatures of a few degrees below and above the low-field T_c.

The magnetic measurements were conducted using a multipurpose SQUID magnetometer. Both the virgin and the irradiated samples were measured in identical conditions, using a magnetometer scan length of 2 ~ 3 cm, and fixed temperature settings ranging from 40 K to 108 K. To correct for background signals, the normal state magnetic susceptibility was measured for temperatures up to 250 K; the background moment was practically independent of temperature. For most of the study in the superconducting state, the measurements were conducted in the reversible region above the irreversibility line in the magnetic phase diagram.

The equilibrium magnetization M(T,H) of the sample was calculated as the reversible magnetic moment per unit volume of BiPb-2223 compound. Normally, the total volume V_{tot} has been obtained by simply dividing the total mass of the sample by the X-ray density (in our case, 6.4 [g/cm^3]). This procedure assumes that all of the BiPb-2223 material is superconducting. The determination of the *superconducting* volume of the sample, however, is a difficult step. In this work, we obtain the fraction of the total volume (the volume ratio "ϵ" = V_{SC}/V_{tot}) that is superconducting, from the fluctuation analysis. Using the procedure described previously,[4,8] we obtain the results that ϵ was $\sim$ 0.31 for the virgin sample and $\sim$ 0.36 for the irradiated one.

THEORETICAL FRAMEWORK

According to Bulaevskii et al.[3] and Kogan et al.[4], fluctuations introduce a correction term, due to entropic effects, into the standard London-limit result M $\propto$ ln(H), where M is the mixed state reversible magnetization. With fluctuations included, one has

$$\frac{\partial M_o}{\partial \ln(H)} = \frac{\phi_o}{32\pi^2 \lambda_{ab}^2(T)}[1-g(T)], \qquad (1)$$

where

$$g(T) = 32\pi^2 k_B T \lambda_{ab}^2(T)/(\phi_o^2 s) \qquad (2)$$

The quantity M_o is the magnetization of a single crystal with H $\perp$ (layers); λ_{ab} is the magnetic penetration depth corresponding to screening by supercurrents in the ab planes; ϕ_o is the flux quantum; and s is the interlayer spacing. For BiPb-2223 containing three adjacent trilayers, we take s to be the separation of trilayers sets, 1.8 nm. At the characteristic temperature $T^* < T_c$ where $g(T^*) = 1$, M is independent of field and has the value $M^* = k_B T^*/\phi_o s = m^*/V_{sc}$. The field-independence of the mixed state magnetization at temperature T^* is a very important signature of the vortex fluctuation theory as well as the nonpertubative scaling theory.[9,10,11] This relation also provides a means for calculating the superconducting volume V_{sc} and fraction ϵ, since the other quantities are measured. The results are valid for temperatures near and below T^*, where the correction term markedly affects the deduced values of $\lambda_{ab}(T)$. The above theoretical expressions refer to the case with H $\perp$ (layers), as with a single crystal. According to Cho et al.,[5] these results still apply for a random polycrystal, if the material is sufficiently anisotropic that only the component of H perpendicular to the layers is effective. Then the magnetization M_s of a polycrystal is

$$M_s = M_o\langle\cos\theta\rangle + \langle\cos\theta\ln(\cos\theta)\rangle\frac{\phi_o}{32\pi^2\lambda_{ab}^2}(1-g) \qquad (3)$$

The brackets <...> denote an angular average with weighting factor $\sin\theta$. For random crystallites, one has $\langle\cos\theta\rangle = 1/2$; $\langle\cos\theta\, ln\cos\theta\rangle = -1/4$; $M^*_s = (1/2)M^*_o$; and $(\partial M_s/\partial \ln H) = (1/2)(\partial M_o/\partial \ln H)$. In this work we have used equations 1-3 and the weighted angular averages to obtain λ_{ab} and related properties.

For comparison, the Hao-Clem[6] analysis was used to compute the Ginzburg-Landau parameter $\kappa(T) \equiv \lambda/\xi$ and the thermodynamic critical field $H_c(T)$. The product of these two gives $H_{c2}(T) = \kappa(T)H_c(T)\sqrt{2}$. Also $\lambda(T)$, $\xi(T)$ and $H_{c1}(T)$ can be obtained from the usual G-L expressions. The procedure, which is not simple, has been described in other publications.[7] A third theoretical model used in this work was the two dimensional scaling theory.[9,10,11] Details of these analyses will be presented elsewhere.

RESULTS AND DISCUSSION

At elevated temperatures, the theory outlined above predicts that the magnetization should vary linearly with ln(H). This feature is clearly seen in Fig. 1, a semilogarithmic plot of M_s vs H for the unirradiated sample. The results for the neutron-irradiated specimen were very similar. Another feature evident in Fig. 1 is the horizontal, i.e., field independent magnetization for a temperature near 106 K. This locates experimentally T^* with the corresponding value M^*_s. From this and the relations cited, we obtained values for the superconducting volume fraction ϵ given above.

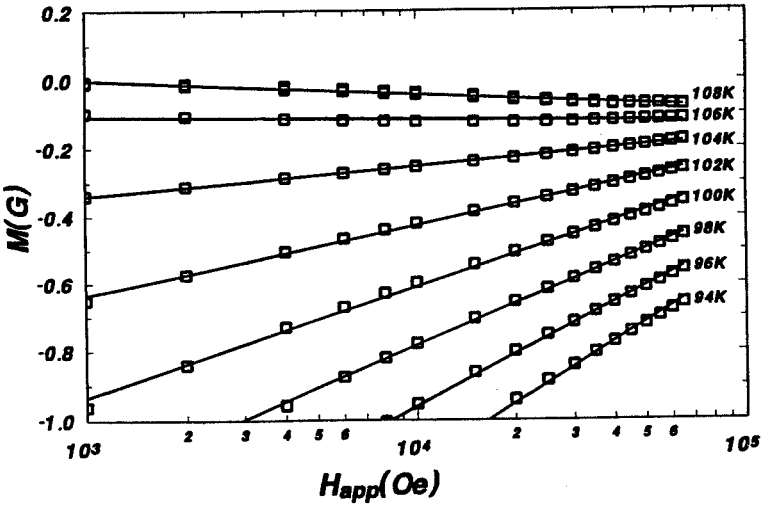

FIG. 1. Magnetization M_s versus H_{app} on a semilogarithmic scale, for non-irradiated (virgin), polycrystalline BiPb-2223 superconductor. Straight lines show the theoretical dependence at elevated temperatures.

To determine the penetration depth $\lambda_{ab}(T)$, we obtain logarithmic slopes $\partial M_s/\partial \ln H$ from the data in Fig. 1 and similar

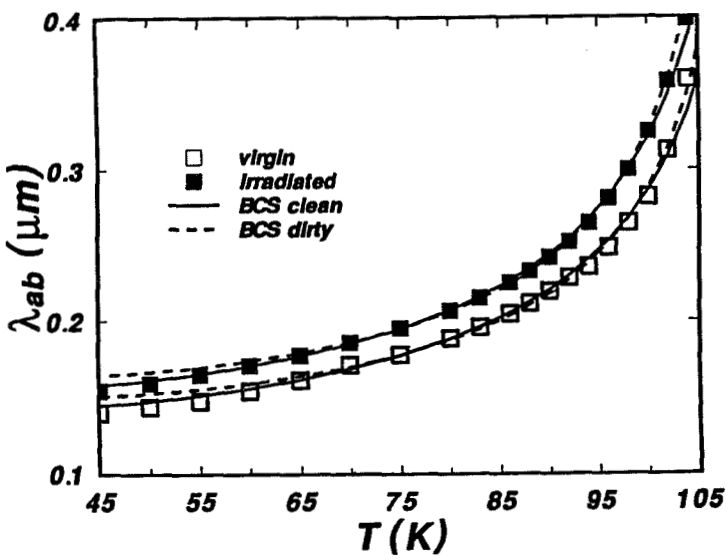

FIG. 2. $\lambda_{ab}(T)$ as a function of T from fluctuation analysis, for virgin and neutron irradiated BiPb-2223 materials. Dashed and solid lines are BCS fits to the data in the clean and dirty limits, respectively.

plots. Analysis using Eq. 1 and 2 with appropriate angular and volumetric factors "ϵ" leads directly to λ_{ab} for each isotherm. The results for the BiPb-2223 virgin and irradiated materials are summarized in Fig. 2. The solid and dashed lines are BCS temperature dependencies in the clean and dirty limits, respectively, which were fitted to the data. Points for $T > T^*$ (outside of the range of validity of the theory) were not fitted. From the BCS fits, the extrapolated $\lambda_{ab}(0)$ and the *mean field* transition temperature $T_{co,\lambda}$ (where λ diverges) are derived in both limiting cases. In the more appropriate clean limit, the respective values are 139 nm and 113.8 K for the unirradiated sample, compared with 152 nm and 112.9 K for the irradiated material. Observe that in each case, $T_{co,\lambda}$ lies several Kelvins *above* the low field diamagnetic onset T_c values, 109 and 108 K, respectively. This is another characteristic feature of the vortex fluctuation theory.

A central result of this study is the increase in London penetration depth λ upon irradiation. Qualitatively, we attribute this feature to increased "dirtiness," i.e., disorder in the material, which scatters the conduction electrons. Another feature commonly associated with electron scattering and the associated reduction on electronic mean free path is an increase in the slope of the upper critical magnetic field $H_{c2}(T)$. Further analysis using the Bulaevskii-Kogan formalism indeed revealed a substantial steepening of the slope, by approximately 25-40 %. This increase was corroborated by complementary analyses using the Hao-Clem and scaling methods. An important consistency check is provided by the thermodynamic critical field $H_c(0)$. This was calculated both from the Hao-Clem formalism and from $\lambda_{ab}(0)$ and the coherence length $\xi_{ab}(0)$. We obtain nearly the same value, $H_c(0) \approx 1.3$ T, for both the virgin and the irradiated samples. This result is consistent with the expectation that the superconductive condensation energy $F_c = H_c^2/8\pi$ should not be affected by moderate densities of neutron generated defects. Details will be presented elsewhere in a comprehensive discussion.

CONCLUSION

This work shows that neutron-generated damage increased the London penetration depth of BiPb-2223 superconductor by approximately 10 ~ 15 %. Further analysis using three independent theoretical models has shown that $H_{c2}(0)$ concurrently increased by 25% ~ 40%. However, neither the thermodynamic critical field H_c nor the transition temperature T_c were appreciably affected. The observed behavior is similar in magnitude and directions to observations[12] in A-15 superconductors. For instance, Nb_3Sn and V_3Si thin films with differing residual resistivities just above T_c showed a significant increase in $H_{c2}(0)$ (about $\approx$ 35 %) as the material goes from the clean (low resistivity) limit to the dirty (high resistivity) limit at the expense of a small decrease in T_c. The similarity of behavior suggests that the observed changes for the BiPb-2223 originate from mean free path effects. Further investigations are under way to test this hypothesis.

We thank Carlos Becerra Labra and Walter Bussenius Cortada for their collaboration. The work of J.G.O. was supported by the Chilean National Science and Technology Fund (FONDECYT Grant N° 1930210) in cooperation with the University of Talca. A portion of the work of J.R.T. and Y.R.S. was supported by the Science Alliance of the University of Tennessee. The research was sponsored by the Division of Materials Sciences, U. S. Department of Energy and technology development was funded by the U.S. Department of Energy, Office of Advanced Utilities Concepts-Superconductor Technology Program, both under Contract N° DE-AC-05-84OR21400 with Martin Marietta Energy Systems, Inc.

REFERENCES

1. J. R. Thompson, D. K. Christen, H. R. Kerchner, L. A. Boatner, B. C. Sales, B. C. Chakoumakos, H. Hsu, J. Brynestad, D. M. Kroeger, J. W. Williams, Yang Ren Sun, Y. C. Kim, J. G. Ossandon, A. P. Malozemoff, L. Civale, A. D. Marwick, T. K. Worthington, L. Krusin-Elbaum, and F. Holtzberg, "Studies of 'Non-Ideal' Superconductors using dc Magnetic Methods," in Magnetic Susceptibility of Superconductors and Other Spin Systems, ed. by R. A. Hein, T. Francavilla, and D. Liebenburg (Plenum, New York 1992), pp. 157-176.
2. V. G. Kogan, M. M. Fang, and Sreeparna Mitra, *Phys. Rev. B* **38**, 11958 (1988).
3. L. N. Bulaevskii, M. Ledvij, and V. G. Kogan, *Phys. Rev. Lett.* **68**, 3773, (1992).
4. V. G. Kogan, M. Ledvij, A. Yu. Simonov, J. H. Cho, and D. C. Johnston, *Phys. Rev. Lett.* **70**, 1870 (1993).

5. J. H. Cho, D. C. Johnston, M. Ledvij, and V. G. Kogan, *Physica C* 212, 419 (1993).
6. Z. Hao, J. Clem, M. McElfresh, L. Civale, A. Malozemoff, and F. Holtzberg, *Phys. Rev. B* **43**, 2844 (1991).
7. J. G. Ossandon, J. R. Thompson, D. K. Christen, B. C. Sales, H. R. Kerchner, J. O. Thomson, Y. R. Sun, K. W. Lay and J. E. Tkaczyk, *Phys. Rev. B* **45**, 12534 (1992).
8. J. R. Thompson, J. G. Ossandon, D. K. Christen, B. C. Chakoumakos, Yang Ren Sun, M. Paranthaman, and J. Brynestad, *Phys. Rev. B (RC)* **48**, 14031 (1993).
9. S. Ullah and A. T. Dorsey, *Phys. Rev. B* **44**, 262 (1991).
10. Z. Tesanovic, L. Xing, L. Bulaevskii, Qiang Li and M. Suenaga, *Phys. Rev. Lett.* **69** 3563 (1992). Also: Z. Tesanovic and A. V. Andreev, *Phys. Rev. B*, (accepted).
11. Qiang Li, K. Shibutani, M. Suenaga, I. Shigaki, and R. Ogawa, *Phys. Rev. B* **48**, 9877 (1993); Qiang Li, M. Suenaga, L. N. Bulaevskii, T. Hikata, and K. Sato, *Phys. Rev. B* **48**, 13865 (1993).
12. T. P. Orlando, E. J. McNiff (Jr), S. Foner, and M. R. Beasley, *Phys. Rev. B* **19**, 4545 (1979).

SINGLE SCAN
S37-76
3143326
5P.
3143337

THE THERMOPOWER IN THE TEMPERATURE RANGE T_c-1000K AND THE BAND SPECTRUM OF Bi-BASED SUPERCONDUCTORS.

V.E.Gasumyants, E.V.Vladimirskaya, V.I.Smirnov, and S.V.Kazanskiy

State Technical University, St.Petersburg 195257, Russia

The temperature dependencies of thermopower, S, in the range $T=T_c$-1000K as well as of resistivity and Hall coefficient in the range $T=T_c$-300K for the single-phase ceramic samples $Bi_2Sr_2Ca_{1-x}Nd_xCu_2O_y$ have been measured. It was found that the S(T) dependencies in normal phase have three characteristic regions. Despite the fact that the S(T) dependencies in Bi-based high-T_c superconductors (HTSC) differ essentially from ones in Y-based HTSC at $T=T_c$-300K, the main feature of theirs (S(T)=const at high temperatures) retains in samples investigated at T>620K. The results obtained have been analyzed on the basis of the narrow-band model with the use of assumption of slight asymmetry of the conductive band. The band spectrum parameters of the samples studied have been calculated. An analysis of the tendencies in these parameters changes with samples composition varying enables to make the conclusion about the similarity of the main features of the conductive band structure in Y- and Bi-based HTSC.

1. INTRODUCTION

It is hard to tell now something definitely about the band structure in Fermi level vicinity of the Bi-based HTSC. The complex experimental investigation of the transport phenomena is one of the most available method for the band spectrum study and is reasonably effective one at the same time. This is confirmed convincingly by the experience on the investigations of semiconductors and semimetals with a complicated electron spectrum. The information extracted from such an investigation becomes more detailed and unambiguous if we can vary the Fermi level position over a wide range of energy. This is usually achieved by doping material studied with donor or acceptor impurities.

Earlier we have proposed the phenomenological model of electron transport in the case of narrow conducive band [1]. This so-called narrow band model has enabled us not only to explain all the specific features of transport coefficients temperature dependencies, but also to determine the band spectrum parameters in the samples with different composition. On the basis of analysis of tendencies in these parameters change we have made some conclusions about conductive band transformation character, influence of different components of unit cell and have revealed the correlation between band spectrum parameters and critical temperature (T_c) value in the Y-based HTSC [1-3]. To realize this approach, as applied to the Bi-system, we have chosen the 2212-phase as a main object of the investigation. Compared to the 2223-phase this one is more stable that enables us to prepare highly doped samples being single-phase.

It is known that temperature dependencies of resistivity (ρ) and Hall coefficient (R) in Bi-system are like the ones in Y-system (see, for example, [4]). However the S(T) dependencies differ essentially from the ones in Y-based HTSC [5,6]. It generates a need for some additions to our model for explaining these dependencies. On the other hand data about Seebeck coefficient behavior at T>300K are practically absent in the literature although they can be quite informative in the view of band spectrum studying.

In this connection in this paper we carried out the experimental investigation of thermopower in $Bi_2Sr_2Ca_{1-x}Nd_xCu_2O_y$ (x=0-0.5) in the wide temperature range as well as analysis of the narrow band model applicability to Bi-based HTSC.

2. RESULTS AND DISCUSSION

The ceramic samples $Bi_2Sr_2Ca_{1-x}Nd_xCu_2O_y$ have been prepared by standard solid-state synthesis method from high-purity oxides and carbonates. The absence of heterogeneous phases in the appreciable amount was controlled by using the X-ray analysis as well as by comparative analysis of magnetic susceptibility and transport coefficients temperature dependencies.

Table 1
The values of transport coefficients in normal phase and critical temperature in $Bi_2Sr_2Ca_{1-x}Nd_xCu_2O_y$

x	ρ(300K), mΩ·cm	ρ(100K), mΩ·cm	S(300K), μV/K	R(300K), $\times10^{-3}cm^3/C$	T_c^m,K	T_c^o,K
0.0	1.2	0.6	-3.70	1.9	76.6	64.2
0.1	2.7	1.4	-2.08	2.9	83.9	66.0
0.2	3.0	2.0	2.17	4.2	82.6	56.9
0.3	3.5	2.9	6.30	6.8	75.9	53.9
0.4	3.8	3.7	15.82	9.6	56.0	34.2
0.5	11.1	9.4	31.10	12.5	36.0	23.5

The results of electro-physical measurements are shown in Table 1. The Nd content increase leads to increasing of the absolute values of ρ, S, and R as well as T_c depression and broadening of superconducting transition. The temperature dependencies of ρ and R are similar to the typical ones for all the HTSCmaterials. Dependencies of ρ(T) are linear in all the temperature range measured, the Hall coefficient decreases with the temperature increase, although the relative lowering of R for Bi-system is not so great as for Y-system. The S(T) dependencies are shown in Fig.1. These curves are stationary, i.e., they don't change after several temperature cyclings. It can be seen from this figure that the absolute value of S increases with x and the S(T) dependencies in normal phase have three characteristic regions. At $T=T_c$-(120-200)K the thermopower have the smooth maximum which is characteristic also to Y-system. At T=(120-200)K-620K one decreases almost

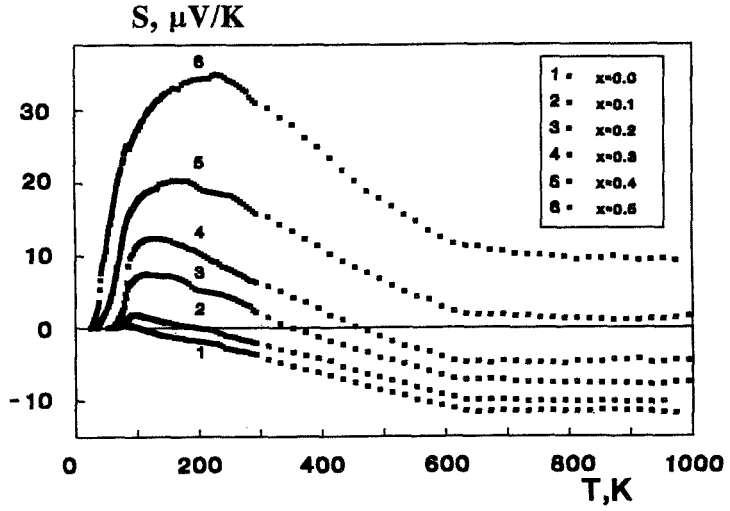

Fig.1. The temperature dependencies of thermopower in $Bi_2Sr_2Ca_{1-x}Nd_xCu_2O_y$.

linearly which is characteristic to Bi-based HTSC as compared with Y-based ones. Nevertheless the main feature of S(T) dependencies in Y-based HTSC (S(T)=const at high temperatures) retains in Bi-based HTSC at T>620K. The great length of S linear decrease region (300K) and very insignificant deviation from S=const at high temperature have engaged our attention. The last fact is forcible argument in favor of the narrow band model using because its main consequence is just independence of S in the limit of high

temperature. Furthermore, yet another fact can be noted. This is the quite drastic transition from second region of S(T) dependencies to third one with independence of the temperature of this transition (T=620K) from dopant content. It is necessary to emphasize that analogous point of drastic transition from one dependence type to another was been detected by us in Y-based HTSC [7], although at another temperature (T=350K). It is possible that existing of this point is a common feature of different types of HTSC.

For explanation and quantitative describing all the experimental data obtained we must bear in view the concrete model of band spectrum with the lowest number of fitting parameters. For this purpose we are using (as in the case of Y-based HTSC) the narrow-band model which suggests the band width to be comparable with the Fermi smearing. The analysis of the main electron transport peculiarities in case of narrow band is performed in Ref.[1]. Certain of the concepts and results of this analysis are as follows.

The model includes three phenomenological parameters. The first one is the degree of band filling with electrons that is the ratio of the free electrons number to the whole number of band states. Two other parameters are the "state density" and "conductivity" effective band widths (W_D and W_σ). These effective widths may differ from one another as well as from the whole band width W. The distinctions between W, W_D, W_σ are related to the peculiarities and differences in energy dependencies of electron state density D(E) and differential conductivity $\sigma(E)$. The comparison of W_D and W_σ values may be used to get some information on the electron kinetics, dynamics and scattering peculiarities. As shown in Ref.[1], in the case of narrow band (i.e., when the W value is not much greater than k_oT value) the spectrum details, like the D(E) and $\sigma(E)$ peculiarities, are not of great significance as long as the W_D and W_σ values. This makes possible to use the simplest approximations for these functions as rectangles with different widths. In this case we can derive the analytical expressions for chemical potential and all the transport coefficients. It is to be noted that our formulas enabled us to compute the absolute value and the sign of the Seebeck coefficient at the different temperatures, whereas the ρ and R could be computed only with an accuracy of a constant cofactor. Therefore we have used S(T) dependencies to determine the model parameters values and then we have verified their validity by comparison between the calculated and experimental dependencies of the $\rho(T)/\rho(300K)$ and R(T)/R(300K). In the limit of high temperature (when $W_D<k_oT$) Seebeck coefficient doesn't depend on temperature and is determined from formula:

$$S = \frac{k_o}{e} \cdot \ln \frac{F}{1-F}$$

It should be mentioned that the fitting parameters are believed to be temperature-independent. That means that the parameters number is less than the number of equations which we can use for their determination because we compare the calculated and experimental temperature dependencies in a wide temperature range.

When analyzed the transport coefficients in Y-based HTSC we have proposed that the conductive band is symmetric. For explanation of S(T) dependencies in Bi-based HTSC we use narrow band model too but we add assumption of slight asymmetry of the conductive band. This fact is taken into account by introducing some distance ($b \cdot W_D$, where b is asymmetry parameter) between centers of rectangles D(E) and $\sigma(E)$. In this case all the formulas from Ref.[1] retain their previous form but in formulas for transport coefficients instead of the chemical potential μ we must use now ($\mu - b \cdot W_D$).

In the framework of our model we were able to describe the temperature dependencies of thermopower in the whole temperature range adequately. The region of drastic transition S(T) from linear decrease to constant value is of particular complexity. The calculated dependencies demonstrate only smooth transition which may be due to roughness of approximation used. It is necessary to take into account the features of the band structure in more detail for the best agreement of experimental and calculated dependencies. In particular it would appear reasonable that the band spectrum parameters are temperature dependent. Nevertheless, analyzing the results obtained we can consider with reasonable

confidence that our data lend support to the validity of narrow band using for Bi-based HTSC. It is necessary to emphasize that calculated dependencies of $\rho(T)$ and $R(T)$ retain all its features in the frame of asymmetric model.

The dependencies of the main band parameters calculated from S(T) on Nd content are shown in Fig.2. It can be seen that the deviation from stoichiometry (increase of x in $Bi_2Sr_2Ca_{1-x}Nd_xCu_2O_y$) leads to increase of F value (the hole density decrease) as well as to the appreciable transformation of conductive band. The effective band width gradually increases with x, in so doing this broadening of band is accompanied by simultaneous reduction of W_σ/W_D ratio as shown by our calculations. Therefore, we could assume that

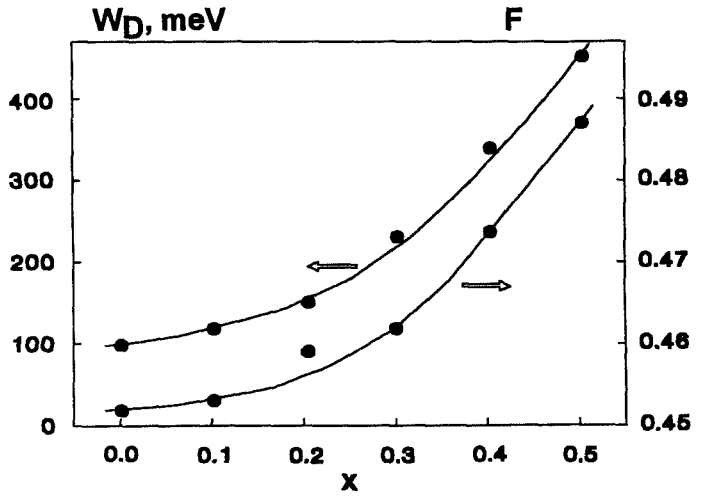

Fig.2. The band effective width and the band filling degree with electrons vs. Ca content.

increase of dopant content leads to the growth of the difference between the energy dependencies of D(E) and $\sigma(E)$ functions and as consequence the W_σ/W_D ratio changes. One of possible explanation of the band transformation revealed bases on assumption of determinant effect of lattice disordering. The rise of disorder causes the Anderson's localization of states at the band edges and increasing of total band width. Thus, the values and the changes character of band structure parameters with deviation from stoichiometry, as well as the possible reason of these changes in Y- and Bi-based HTSC are analogous. As for the band asymmetry, our calculations show this one to be very little (the energy shift of D(E) and $\sigma(E)$ rectangles relative to each other is about 3-5% from the total effective band width).

The results obtained enable us to reveal (as in the case of Y-based HTSC) a correlation between the band spectrum parameters and the critical temperature value. With the proviso that the number of states in the band remains constant, the band broadening causes the decrease of the density of states value at Fermi level. It may be one of the factor (perhaps, the main factor) leading to suppression of the T_c value with deviation from stoichiometry.

3. CONCLUSION

In summary, we have carried out the investigation of thermopower behavior in ceramic samples $Bi_2Sr_2Ca_{1-x}Nd_xCu_2O_y$ in the wide temperature range. The results obtained and their analysis allow to make the following conclusions.

1. There are two lengthy regions in the S(T) curves for Bi-2212 HTSC with different character of S behavior. The thermopower value decreases linearly with temperature up to T=620K and remains constant above this temperature.
2. The transition from one type of dependence to another is very drastic. As this takes place, the temperature of this transition (T=620K) is unchanged for the samples with different degree of the deviation from stoichiometric composition.

3. The narrow band model can be used successfully for explanation of the unusual behavior of the transport coefficients not only in Y-system, but also in 2212-phase of Bi-based HTSC. Some literature data provide reason to believe that band narrowness is the common feature of all known high-T_c materials.
4. The values and the changes character of band structure parameters with deviation from stoichiometry as well as the correlation between these parameters and critical temperature in Bi-based HTSC are analogous to the ones in the Y-system. This clearly demonstrates the similarity of main properties of charge carriers system in these types of HTSC-materials.

REFERENCES

1. V.E.Gasumyants, S.A.Kazmin, V.I.Kaidanov, V.I.Smirnov, Yu.M.Baikov, Yu.P.Stepanov, Sov.Superconductivity, 4 (1991) 1184.
2. V.E.Gasumyants, S.A.Kazmin, V.I.Kaidanov, E.V.Vladimirskaya, Sov.Superconductivity, 5 (1992) 673.
3. V.E.Gasumyants, V.I.Kaidanov, E.V.Vladimirskaya, Chinese J. of Phys., 31 (1993) 999.
4. L.Forro, J.R.Cooper, Europhys.Lett., 11 (1990) 55.
5. C.N.R.Rao, T.V.Ramakrishnan, N.Kumar, Physica C, 165 (1990) 183.
6. M.F.Crommie, A.Liu, M.Cohen, A.Zettl, Phys.Rev.B, 41 (1990) 2526.
7. V.E.Gasumyants, S.A.Kazmin, V.I.Kaidanov, A.Z.Kublanovskii, V.I.Smirnov, Sov.Superconductivity, 6 (1993) 77.

S38-76
314342
3Y3338
10R

NONEQUILIBRIUM TRANSPORT IN SUPERCONDUCTING FILAMENTS

K.Yu.Arutyunov*, N.P.Danilova*, A.A.Nikolaeva+

*Low Temp. Dpt., Phys. Faculty, Moscow State Univ., Moscow 119899, Russia.
+Appl. Phys. Inst. of Moldovian Acad. of Sciences, Kishinev 277028, Moldovia

Abstract

The step-like current-voltage characteristics of highly homogeneous single-crystalline tin and indium thin filaments has been measured. The length of the samples L~1cm was much greater than the nonequilibrium quasipartcle relaxation length Λ. It was found that the activation of successive i-th voltage step occurs at current significantly greater than the one, derived with the assumption that the phase slip centers are weakly interacting on a scale $L>>\Lambda$. The observation of "subharmonic" fine structure on the voltage-current characteristics of tin filaments confirms the hypothesis of the long-range phase slip centers interaction.

INTRODUCTION

One of the most fundamental properties of superconductors is the vanishing of the electrical resistivity for direct current I if its value does not exceed some critical threshold I_c. It was found that the destruction of superconductivity by the transport current in homogeneous bulk superconductor had a sudden feature. The phase transition could be described by the model of a spreading "hot spot". The normal phase nucleates within the field penetration layer $\sim\lambda(T)$ on the surface of the sample.

The above model does not hold for sufficiently thin superconducting wires with the transverse dimensions, comparable with the coherence length $\xi(T)$. In the latter case, only one supercurrent channel exist and therefore only an S-N-S boundary along the length of the filament could be formed. Due to strong temperature dependences of $\xi(T)$ and $\lambda(T)$ the requirement of quasi-one-dimensionality for clean I-type superconductors, as tin and indium, holds within few mK below T_c for the samples of several mkm in diameter.

The first candidates for testing were tin whiskers of about 1 mkm^2 in cross section and with a distance between potential probes less or equal to 0.5 mm. In the early experiments [1] it was found that close enough to the critical temperature T_c the V(I) curves show a wide transition with a series of regular voltage steps. Later, the same results were obtained for whiskers and microbridges of various clean superconductors (Sn, In, Pb, Zn, Al) and alloys [2].

Irrespectively of the material and its purity several basic features were outlined. At least for the first few

voltage steps the differential resistance $(dV/dI)_i$ is a multiple of differential resistance $(dV/dI)_1$ after the first step. The back extrapolation of the V(I) curve for each voltage step gives a non-zero excess current $I_o(i)$, corresponding to V=0. Thus the V(I) curve could be approximated by a set of i voltage steps:

$$V(I)=(dV/dI)_i[I-I_o(i)] \qquad (1)$$

It was found that the increments of the differential resistance $\Delta(dV/dI)_i$ and the excess currents $I_o(i)$ for each i-th voltage step are approximately constants equal to the corresponding values for the first step.

The above experimental results indicate that the formation of the steps is a repetition of the same event. The differential resistance of each i-th voltage step could be associated with the destruction of superconductivity on a normal-like length $L(i)\approx const$. The non-zero value of the excess current $I_o(i)$ indicates that the naive model of normal domains nucleation is not legal.

At present moment it may be stated that the step-like peculiarities of the voltage-current characteristics in quasi-one-dimensional superconductors could be qualitatively described by the essentially nonequilibrium process of the phase slip centers (PSC) activation. Still there are some questions which are not clear enough. One of them is the problem of the interaction of the neighboring PSC.

The early experiments with whiskers and microbridges were performed for relatively short samples, where the length of the wire L was comparable with the normal-like length $L(i)\leq 100$ mkm for clean superconductor (tin and indium). However, the predictions of some widely used theoretical models are valid only for the well-separated PSC. The assumption of the PSC isolation leads to the definite positions of the voltage steps activation $I_c(i)$.

The precise experimental test of the theories needs for long highly homogeneous filaments, where the PSC are well-separated and are not pinned to the sample imperfections.

In this article we present the results of experimental study of transport properties of thin and long tin and indium filaments in glass cover. The objects studied have some remarkable features. All the filaments are single-crystalline with mean free path comparable with the diameter of the wire. The process of filament drawing permits to produce a homogeneous wire of hundred meters in length with highly uniform parameters. The last feature gives a possibility to study samples of various types (electrical probes, length, etc..) made of a single filament with almost the same parameters: diameter, mean

free path, critical temperature, etc. The high uniformity of the filaments opens a wide range of future applications.

EXPERIMENT

In the present work thin metal wires in glass cover were studied. The filaments were prepared by drawing of molten metal in glass capillary [3]. Depending upon the metal, type of the glass, temperature, cooling and speed of the wire spinning it is possible to produce filaments with diameter of metal core from 0.6 mkm to 40 mkm and with the external diameter of glass cover from 12 mkm to 45 mkm.

X-ray analysis show that all the wires studied are single crystals.

The observation of the samples with the SEM displayed no cuts neither of the metal, nor of the glass cover (fig.1). The diameter of the filaments was measured with SEM and the distance between the voltage probes with a light microscope.

The filament with length L~1 cm was glued to sapphire stage excluding the regions for electrodes where the glass was removed with hudrofluoric acid.

After several experiments we succeeded in producing "windows" for potential probes of ~20 mkm wide.

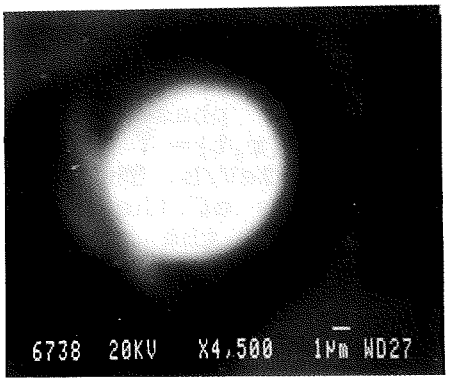

Fig.1 SEM picture of the indium filament.

The current probes were prepared by direct placing of silver paint or Wood's metal above the ends of the metal filament. The best results for potential probes were obtained by placing 8 mkm copper wire covered with a thin layer of conducting epoxy across the sample.

The temperature of the helium bath was measured with germanium thermometer and stabilized with accuracy ~1mK using PC as a PID controller. When necessary, the samples were placed inside a massive vacuum calorimeter with internal heater. The temperature of the stage was measured with additional thermometer and stabilized with the intellectual PID controller OXFORD ITC-4. The resulting typical temperature stability was about ±0.1mK.

All measurements were performed using conventional 4-probe method with accuracy 1nV. The direct measure current could be monitored with accuracy 1nA. The Earth magnetic field was reduced to ≤1mOe by superconducting shield.

THEORY

Soon after the experimental observation of a step-like V(I) structure of tin whiskers [1] several theoretical models were derived to describe the observed phenomena. One line of development [4-6] introduced the phenomenological conception of the PSC activation. Another line of work, culminating in the work [7], has been to explore the time dependent Ginzburg-Landau (TDGL) equations, and nonequilibrium extensions thereof. And the third line of theoretical investigations was summarized in [8], emphasizing the static solutions of equations taking full account of nonlinear effects of large supercurrent densities.

The phenomenological models [4-6] associates the voltage steps with activation of PSC along the one-dimensional superconductor. The PSC is a region of weakened superconductivity (the S-S'-S boundary) with the region S' of the weak core $\sim\xi(T)$. If the voltage V across the PSC is non-zero the phase $\varphi(r,t)$ of the superconducting order parameter $\Psi(r,t)=\Psi^2 e^{i\varphi(r,t)}$ increases as a function of time: $d\varphi/dt=2eV/h$. This leads to an increase of $\nabla\varphi(r,t)$ and thus increase of the supercurrent $j_s\sim|\Psi|^2\nabla\varphi$. However, with increasing j_s the absolute value of the order parameter $|\Psi|^2$ will decrease. The critical value j_c will be reached as soon as $|\Psi|^2=2/3|\Psi_o|^2$, corresponding to $\nabla\varphi\xi(T)=1/\sqrt{3}$, and the superconductor will enter the normal conducting state.

The idea of PSC is related with the assumption that the phase $\varphi(r,t)$ is periodically reduced by 2π to compensate the monotonic growth of the time-dependent phase. In order to explain the co-existence of superconductivity and non-zero voltage along the one-dimensional sample in a wide range of transport currents $I>I_c$ within the phenomenological models [4-6], one should involve the model of a two-fluid superconductivity. The superconducting and the normal current components are associated with non-stationary concentrations of Cooper pairs and quasiparticles. A few moments after the phase-slip event the normal current component I_n will carry the most part of a total current $I=I_n+I_s$: $\nabla\varphi\approx0$ in the PSC core and thus the supercurrent $j_s\sim|\Psi|^2\nabla\varphi$ is close to zero. While just before the phase-slip event the supercurrent will be close to its critical value I_c. In order the above process could be stationary in time the periodic variation of the phase $\varphi(r,t)$ by 2π should compensate the monotonic growth of the phase during one period τ_{slip}:

$$2\pi=\varphi(0)-\varphi(\tau slip) = 2e/h\int_0^{\tau_{slip}} V(t)dt=2e/h<V>\tau_{slip} \qquad (2),$$

where <V> is the time-averaged voltage across the PSC. This leads to the well known Josephson relation: $\omega_{slip}=2\pi/\tau_{slip}=2e<V>/h$.

Skocpol, Beasley and Tinkham (SBT) [5] postulated that the phase-slip event occurs within the range $\sim\xi(T)$ of the PSC core, while the non-equilibrium quasiparticles charge imbalance relax on a length scale $\Lambda=(1/3lV_F\tau_{in})^{1/2}$, where l is the mean free path, V_F- the Fermi velocity and τ_{in} is the inelastic relaxation time for normal particles. The differential resistance $(dV/dI)_i$ is associated with the resistance of the normal-like section of length $L(i)=2\Lambda$.

Later Kadin, Smith and Scocpol (KSS) developed a detailed model of a charge imbalance wave equation for a PSC connected to a transmission line [6]. The KSS model includes the SBT [5] as a limit of a diffusive decay of a charge imbalance. However, KSS showed that under some conditions the relaxation of charge imbalance may results in propagating of charge-imbalance waves on the scales much greater than the Λ of SBT model. Therefore, the KSS model predicts the long-distance interaction of the PSC.

The above simplified review of the phenomenological models [4-6] outlines the main features of the PSC conception. Theoretically more strict developments [7,8] includes the phase-slip solutions as a limit.

Introducing the TDGL equations Kramer and Baratoff [9] obtained the following results:

1) When the current I is less than some value I_1 the superconductor enters a uniform current-carrying state.

2) When the current I is larger than the threshold value I_2 the superconducting current-carrying state transforms into an expanding domain of normal phase. The threshold current I_2 coincides with the stability limit of the normal-superconducting interface studied by Likharev [10].

3) In the interval between I_1 and I_2 there exist a solution which corresponds to phase slippage. The one-dimensional sample remains superconducting over the its length, but at some point local oscillations of the order parameter $|\Psi|^2$ take place. When $|\Psi|^2$ turns to zero the phase φ experiences a jump of 2π.

The numerical solutions of the TDGL equations [11, 12] give for a PSC region size of the order $\sim\xi(T)\Gamma^{1/2}$, where Γ is the pair-breaking term: $\Gamma=(8\sqrt{5.79}\tau_{in}T_c)(1-T/T_c)^{-1/2}$. Thus the TDGL equations predict the long-range interaction. The distance of this interaction diverges rapidly at T_c.

RESULTS AND DISCUSSION

For all the wires studied the relation of the resistance at room temperature to the one at 4.2K gives the mean free path l, comparable to the filament diameter.

All the samples displayed the superconducting transition. The typical width of the transition ΔT_c is about ~0.01K. The critical temperature T_c, determined from the slope of the function $I_c^{3/2}(T_c-T)$ correlate well with the one from the R(T) transition.

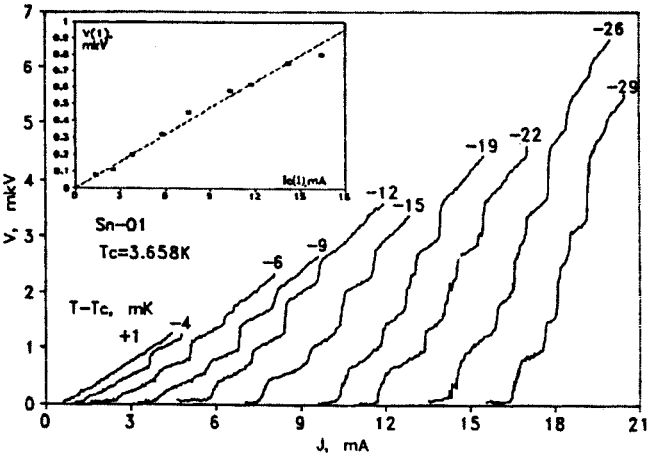

Fig.2 Current-voltage characteristic of the tin filament Sn-01 for several fixed temperatures $\Delta T = T - T_c$. The inset shows the dependence of the height of the first voltage step V(1) versus the critical current $I_c(1)$

The voltage-current characteristics at fixed temperatures close to T_c display a wide transition with pronounced step-like structure (fig.2).

The curvature of the actual V(I) characteristics (especially for high currents) indicates the existence of heating effects.

Fig.3b (left axis) shows the temperature dependences of the normal-like lengths for the first and the second voltage steps L(1), L(2) corresponding to V(I) transition of fig.2. Within experimental errors no temperature dependence could be found. The absence of temperature dependence and the values for L(i,T) correlate well with existing results for tin whiskers [2].

According to SBT model [5] the relation of the excess current to the critical value is a constant equal to $I_o(1)/I_c(1)=0.65$. Within experimental errors our results give the value $I_o/I_c \approx 0.8$ for the first step (fig.3b, right axis) which correlate with the TDGL model [13].

It is remarkable that the height of the first voltage jump $V(1)=V(I_c(1))$ follows a straight line (fig.2, inset), which holds for all tin and indium samples. Since, according to (1), $V(1) = (dV/dI)_1[1-I_o(1)/I_c(1)]I_c(1)$ this observation indicates that the temperature dependence of $(dV/dI)_1$ and $[1-I_o(1)/I_c(1)]$ compensate each other so that their product is independent of the temperature and, therefore, is constant for different critical currents $I_c(1,T)$.

The above experimental results, dealing with quanti-

ties derived from the first step of the V(I) transition: L(1), $I_o(1)/I_c(1)$, $V(I_c(1))$ correlate well with the corresponding data obtained for the short samples [2] and with theoretical models involving the isolated PSC.

However, to calculate the critical currents $I_c(i)$ for i>1, where the successive voltage steps build up, one should make some additional assumptions to improve the models of non-interacting PSC.

Tinkham [14] applied the ideas of SBT [5] to describe the current-voltage characteristics of an ideal homogeneous filament. The resulting step-like V(I) dependence is associated with successive activation of N independent PSC at critical currents $I_c(1)<I_c(2)<...<Ic(N)$:

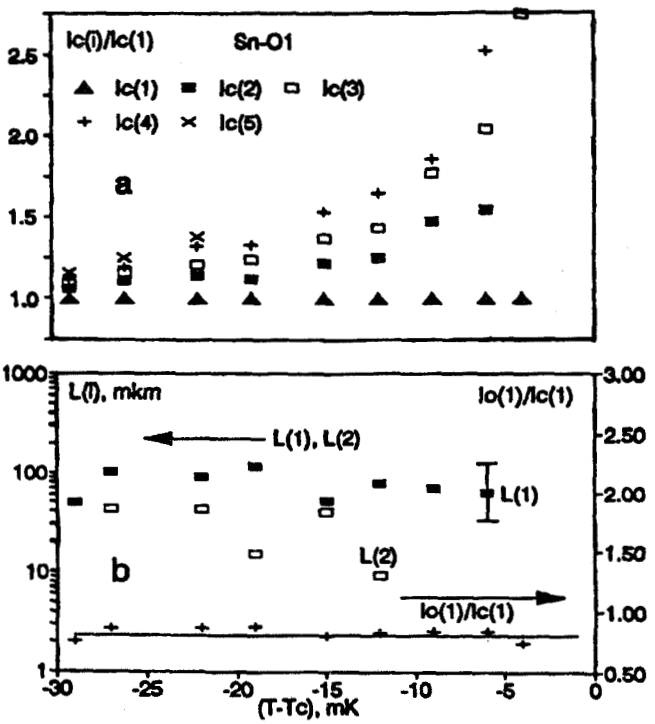

Fig.3 Temperature dependencies for the sample Sn-01 of: (a) the normalized critical currents $I_c(i)/I_c(1)$; (b) the normal-like lengths L(1), L(2) (left axis) and normalized excess current $I_o(1)/I_c(i)$ (right axis).

$$\frac{I_c(i)}{I_c(1)} = \frac{\cosh(L/2i\Lambda) - I_o(1)/I_c(1)}{\cosh(L/2i\Lambda) - 1} \qquad (3)$$

The interaction of the PSC is reduced to the activation of the successive PSC midway between existing ones. It was shown [14] that for sufficiently long filament $L/2N\Lambda>>1$ the PSC are well separated and weakly interacting. The general spacing of the predicted steps is in a qualitative agreement with experimental results, obtained for the short samples [2]. But the positions of the first steps for widely studied whiskers [2] are separated by inevitable inhomogeneities, which overwhelm the exponentially weak interaction of the ideal model [14].

The observed V(i) characteristics for our samples show regular $I_c(i)$ dependences contrary to the case of the widely studied whiskers with random PSC activation, determined by the sample imperfections.

Our results are in a disagreement with the model of the weakly interacting PSC [14]. The strong temperature and the step number i dependencies of the successive critical currents $I_C(i)/I_C(1)$ are observed (fig.3a). While according to eq.(3) neither of this dependencies should be detected.

Even utilizing the temperature dependence of the normal-like length L(1,T), which is not observed in our experiments, but is reported in literature for indium whiskers [15], one can fit the V(I) curves only by intro-ducing the "effective" averaged normal-like length $L^*(T) \approx 8*L(1,T)$ (fig.4, vertical bars). Experiments with highly homogeneous long filaments presented here permits one to neglect the pinning of the PSC to sample imperfections. Therefore increasing of the effective normal-like length $L^*(T)$ in comparison to the one derived from the differential resistance of the voltage steps: $L(i)=(L/R_n)(dV/dI)_i$, (R_n - is the full normal resistance), indicates that for higher steps the PSC are "repulsed".

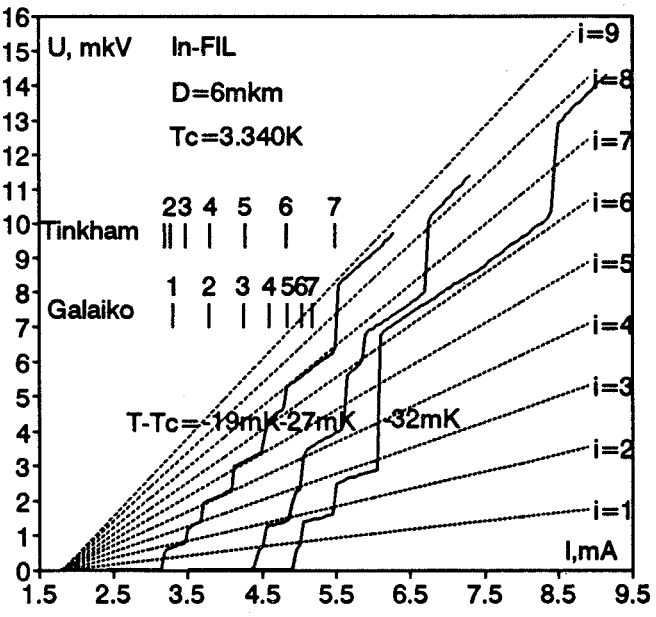

Fig.4 Current-voltage characteristics of the indium filament In-Fil for several fixed temperatures $\Delta T=T-T_c$. Vertical bars represents the calculations for the critical currents $I_c(i)$ according to Tinkham [14] and Galaiko [16, 12].

The activation of successive i-th PSC occurs at current $I_C(i)$ greater than the one derived with the assumption that the PSC are weakly interacting eq.(3) [14]. The physical mechanism of the observed enhancement of superconductivity is not clear.

One can make a surprising conclusion that the distance of the required long-range interaction is significantly greater than the normal-like length $L(i) \sim \Delta(dV/dI)_i \sim const$, corresponding to the quasiparticle relaxation length $\Lambda=L(i)/2$.

The calculations of the $I_C(i)$ dependencies, using the theoretical model of Galaiko and co-workers [16, 12], are in a qualitative disagreement with the experiment: the spacing between the voltage steps in I-scale should decrease with increasing current I, contrary to the observed V(I) characteristics (fig.4, vertical bars).

The conception of the activation of similar PSC results in equal increments of the differential resistance $\Delta(dV/dI)_i \sim const$ and excess currents $I_o(i) \sim const$ for all i voltage steps of the same V(I) characteristic. The above requirement has been confirmed at least qualitatively for a whole variety of whiskers and microbridges of different superconductors [2]. It also holds for the indium filaments studied at present work. But for tin samples we observed the "subharmonic" fine structure on the V(I) curves (Fig.5). Along with the set i of voltage steps with differential resistances $(dV/dI)_i = i*(dV/dI)_1$ and with constant value of the excess current $I_o(i) = I_o(1)$, there exist the subset n_i of the the steps with equal differential resistances $(dV/dI)_{n,i} \sim const$ and rational values of the excess currents $I_o(n,i)/I_o(1)$ (fig.5).

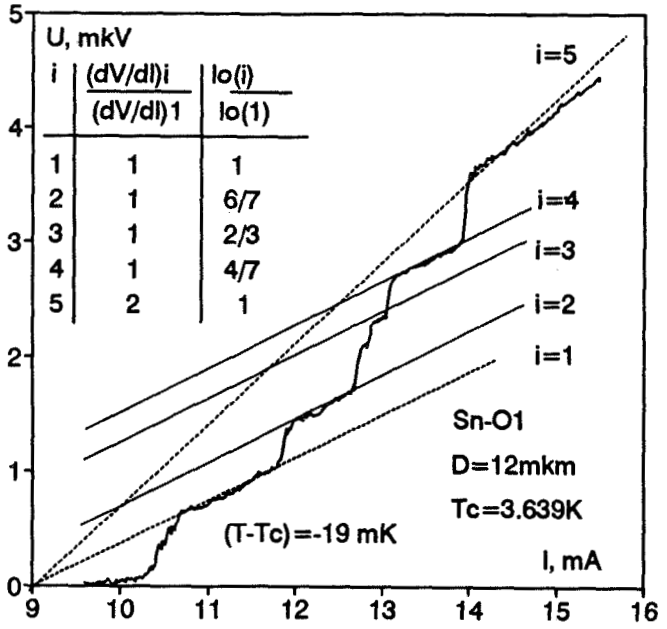

Fig.5 The V(I) curve for the sample Sn-01. The dotted lines are the guides for the eye to illustrate the existence of the voltage steps with equal differential resistance $(dV/dI)_i$, but with different excess currents $I_o(i)$.

We consider the above result as an additional manifestation of the PSC interaction. The mysterious extra long-range ($\geq$300 mkm) influence of the PSC has been observed already on tin whiskers [17]. The physical mechanism of such an interaction is not clear.

As a preliminary hypothesis we may propose the model of the PSC interacting not only via nonequilibrium quasiparticles on a scales $\sim\Lambda$, but additionally through the ac irradiation of the active PSC. To our knowledge, while the sensitivity of the PSC to the external rf has been observed (the ac Josephson effect) [5], the inverse effect of the rf generation has not been detected yet. Thus the above hypothesis needs for further experimental confirmation.

SUMMARY

The step-like current-voltage characteristics of highly homogeneous single-crystalline tin and indium thin filaments has been measured. The length of the samples L~1cm was much greater than the nonequilibrium quasipartcle relaxation length Λ.

The quality of the filaments gives the possibility to neglect the pinning of the PSC to the sample imperfections. This assumption is confirmed by the reproducibility of the results for the samples cut from different parts of the same wire and by the observation of definite dependence of the critical currents $I_c(i)$ versus the step number i.

Quantitative values, obtained from the first voltage steps of the V(I) curves (the activation of the solitary PSC) agree with the experiments reported previously for whiskers and microbridges [2] and correlate with corresponding calculations [5, 12, 15].

The observed enhancement of superconductivity for higher voltage steps and the "subharmonic" fine structure could not be understood within the existing theories of weakly interacting PSC.

ACKNOWLEDGEMENTS

The authors acknowledge Prof. Yu.P.Gaidukov, Dr. Ya.G.Ponomarev and Dr. M.Yu.Kupriyanov for valuable discussions.

REFERENCES

[1] J.D.Meyer, Appl.Phys. 2, 303, (1973)
[2] R.Tidecks, "Current Induced Nonequilibrium Phenomena in Quasi-One-Dimensional Superconductors", (Springer, 1990)
[3] N.B.Brandt, D.B.Gitzu, A.M.Josher, B.P. Kotrubenko and A.A.Nikolaeva, Sov.: "Pribory i Technika Experimenta" n.3, 256, (1976)
[4] T.J.Riger, D.J.Scalapino and J.E.Mercerau, Phys.Rev.B, 6, 1734, (1972)
[5] W.J.Scocpol, M.R.Beasley and M.Tinkham, J.Low Temp.Phys.16, 145, (1974)
[6] A.M.Kadin, L.N.Smith and W.J.Scocpol, J.Low Temp.Phys. 38, 497, (1980)
[7] L.Kramer and R.Watts-Tobin, Phys.Rev.Lett., 40, 1041, (1978)
[8] V.P.Galaiko, J.Low Temp.Phys., 26, 483, (1977)
[9] L.Kramer and A.Baratoff, Phys.Rev.Lett, 38, 518, (1977)
[10] K.K.Likharev, Sov: Pis'ima v Zh.Eksp.i Teor. Fiz, 20, 730 (1974)
[11] B.I.Ivlev, N.B.Kopnin and L.A.Maslova, Zh.Eksp.i Teor. Fiz, 78, 1963, (1980)
[12] V.P.Galaiko and N.B.Kopnin, "Nonequilibrium Superconductivity", Elsevier Sci. Publ., 1986
[13] L.Kramer and R.Rangel, J.Low Temp.Phys. 57, 391, (1984)
[14] M.Tinkham, J.Low Temp.Phys., 35, 147, (1979).
[15] R.Tidecks, G.Slama, Z. Physik B, 37, 103, (1980)
[16] E.V.Bezugly, E.N.Bratus and V.P.Galaiko, Sov: Fizika Nizkih Tempeatur, 3, 1010, (1977)
[17] R.Tidecks, J. Low Temp. Phys, 58, 183, (1985)

OMIT
7815
PAGE

THIS PAGE INTENTIONALLY LEFT BLANK

Page intentionally left blank

Fabrication Methodology

Chair: Dr. U. Balachandran

HIGH Tc SUPERCONDUCTORS FABRICATED BY PLASMA AEROSOL MIST DEPOSITION TECHNIQUE

X. W. Wang, K. D. Vuong, A. Leone, C. Q. Shen, J. Williams, and M. Coy
Alfred University, Alfred NY

ABSTRACT

We report new results on high T_c superconductors fabricated by a plasma aerosol mist deposition technique, in atmospheric environment. Materials fabricated are YBaCuO, BiPbSrCaCuO, BaCaCuO precursor films for TlBaCaCuO, and other buffers such as YSZ. Depending on processing conditions, sizes of crystallites and/or particles are between dozens of nano-meters and several micrometers. Superconductive properties and other material characteristics can also be tailored.

I. INTRODUCTION

Since the discoveries of high T_c superconductors between 1986 and 1993, different film fabrication techniques have been developed [1-3]. These techniques can be classified as thin film and thick film processes. The thin film processes include electron-beam evaporation, sputtering, and laser ablation [2,4-5]. The thick film processes include ink printing, tape casting, and plasma powder spray [6-8]. In the thin film processes, materials deposited onto the substrates can have atomic, ionic, or molecular sizes. Resulting thin films usually have high qualities and high densities. However, film growth rates in thin film processes are relatively slow, which could not be applied in large scale productions. As far as thick film processes are concerned, materials' sizes are 1-10 micrometers, film growth rates are relatively fast, but resulting films are usually inhomogeneous and porous. To find compromises between thin and thick film processes, other fabrication techniques have been developed such as pyrolysis chemical vapor deposition, mist deposition in microwave chambers [9], RF plasma mist deposition in enclosed chambers [10], and RF plasma mist deposition in atmospheric environment [11]. In this paper, we shall report new results obtained via the last process. Operational principles are briefly explained in section II, materials deposited are presented in section III, plasma-experimental conditions are given in section IV, results are summarized in section V, and future work is discussed in section VI.

II. OPERATIONAL PRINCIPLE

In this RF plasma aerosol deposition process, an aerosol mist containing desired cations is injected into a plasma region where the maximum temperature is 10,000 K and the gas pressure is slightly higher than one atmosphere. After vaporization and collision, ions or groups of ions with sufficient momenta travel towards a collector outside the plasma region. Depending on temperature profiles of the collector, nano-sized particles, particle clusters, or micro-sized deposits can be formed. In Figure 1, an experimental set up is illustrated, where the collector is a substrate with its heater block. Besides the substrate assembly, there are two other assemblies: starting material assembly and plasma

reactor assembly. The starting material assembly consists of an ultrasonic nebulizer, a solution container, a carrier gas inlet, and a mist outlet. The plasma reactor assembly consists of an RF coil with two copper leads (power supplied by an RF generator, 4 MHz, 35 kW), a plasma gas nozzle device with three plasma gas inlets, a quartz tube, a mist inlet, and a flame outlet. To prepare a solution, nitrates and/or chlorides with desired cations are dissolved in distilled water. The aqueous solution is poured into the solution container. When the ultrasonic nebulizer vibrates at a frequency of 1.63 MHz, the solution is excited into aerosol mist with droplet sizes of 5 - 10 micrometers. Under the pressure of a carrier gas (Ar), the mist is fed into the plasma reactor. After vaporization and deposition, films and/or materials are formed on the substrate (collector).

Around the middle section of the quartz tube, ion sizes are estimated to be 1 - 3 angstroms. Near the exit end of the tube (flame outlet), sizes of travelling particles are estimated to be 5 - 10 nanometers [12]. Particle clustering is expected to take place in the flame region, and nucleation is expected on the substrate. Besides substrate temperature, film morphology and grain sizes may be affected by the distance between the substrate and the flame outlet, plasma power coupled to the RF coil, plasma gas feeding rates, misting rates, and solution concentration. Oxidation process may be initiated in the quartz tube, enhanced by auxiliary oxygen supply near the flame outlet (not shown), and near the substrate.

III. MATERIALS DEPOSITED

A. BiSrCaCuO systems

In an earlier experiment, films with 2212 composition were fabricated with the plasma technique [13]. Recently, a group at SUNY Buffalo found that the 2223 fabrication window was approximately 5°C [10]. To ease fabrication conditions for large scale productions of 2223 film coatings, a bulk processing technique called two-powder process provided an alternate route [14]. In this bulk process, 2212 was first formed, 0011 was then added to form 2223.

In this work, we attemp to fabricate $Bi_{2.2-x}Pb_xSr_{2-y}Ca_{1+y}Cu_2O_8$ (2212) films; with x=0.20, 0.25, 0.30; and y = 0.25, 0.50, 0.75; as illustrated in Table I. Once 2212 film is formed, 0011 can then be added.

B. YBaCuO systems

Films of superconductive 123 phase were deposited at a substrate temperature of approximately 600°C, without post-annealing [11]. For a film deposited on MgO single crystal, superconductive transition temperature was 100 K, zero resistance temperature was 93 K, with transition width (10-90%) of 3 K [15]. It was observed that sizes of deposited oxides could be as small as 20 nanometers [16].

In this work, we attempt to fabricate nano-sized 211 powder. It is known that 211 affects the superconductivity of 123 phase. For example, the critical current (J_c) of 123 superconductor can be altered by the presence of 211 phase [17-18]. When J_c is enhanced, 211 particles are assumed to be flux pinning centers. When J_c is reduced, 211 particles are

assumed to be a micro-sized impurities blocking supercurrent flow. To clearly understand the roles played by the 211 phase, nano-sized particles are needed. Once these particles are produced with uniform particle size distributions, we can carry out well controlled doping experiments to systematically study pinning effects, kinetics, and mechanical properties.

C. BaCaCuO precursor films for TlBaCaCuO systems

In an earlier experiment, 0223 precursor films were deposited by the plasma technique. The precursor films were annealed at different substrate temperatures in a one-zone furnace to form 2212 and 2223 phases [19]. Recently, it was observed that 1223 phase has better critical current properties under high magnetic field than that of 2212 and 2223 phases. To fabricate a 1223 film, DeLuca developed a two-zone furnace technique [20].

In this work, we attempt to fabricate 0223 precursor films with different porosities and different dopants. When the porosity of a film can be tailored, we shall be able to control Tl diffusion processes in a two-zone furnace. When a metallic oxide such as silver oxide can be doped, we shall be able to align 1223 grains to enhance J_c.

D. Other buffer or hybrid materials

It has been a great challenge to coat YBaCuO on nickel containing substrates. If a buffer layer can be inserted between the substrate material and the superconductive material, this buffer layer can stop interdiffusion, can match lattice parameters, and can match thermal expansion coefficients. In this work, we attempt to deposit yttria stabilized zirconia, tin oxide, and silicon oxide. With superconductors, the last two coating layers can also be utilized as optical couplers and other hybrid optoelectronic films.

IV. PLASMA EXPERIMENTAL CONDITIONS

During plasma experiments, all parameters were optimized, as listed in Table II. In BiPbSrCaCuO experiments, nine batches of solutions were prepared according to the stoichiometric ratios listed in Table I. Each batch of films was deposited at two different substrate temperatures ranges. The low temperature range was from 400-600°C, while the high temperature range was 600-750°C. The films deposited at low substrate temperatures were heat treated in a furnace at 800°C for one hour to enhance 2212 phase formation. For comparative purposes, bulk powders were used to fabricate the superconducting phases represented by equations 1-9 [21]. These samples were prepared by a solid state reaction method. That is, powders of $CaCO_3$, CuO, $SrCO_3$, Bi_2O_3, and PbO were mixed in the ratios listed in Table I. These mixtures were then calcined and annealed in an atmospherically controlled furnace several times to form 2212 phases.

To prepare solutions for Y_2BaCuO_5, the stoichiometric ratios of Y:Ba:Cu ranged from (0.161) : (0.158) : (0.158) to (0.194) : (0.171) : (0.172). During fabrication of 211 materials, the collector (substrate) temperature was maintained at a temperature of 400 to 660°C.

To prepare solutions for BaCaCuO (0223), the mole ratio of Ba:Ca:Cu was 0.16:0.13:0.18 mole, with additional 0.01-0.02 mole of Ag in some experiments. The substrate temperatures ranged from 500 to 750°C.

To prepare yttria stabilized zirconia, zirconyl nitrate and yttrium nitrate powders (10 mol% yttrium) were mixed in the appropriate ratio and dissolved in distilled water. The substrate temperatures ranged from 600-950°C.

To prepare solution for tin oxide, $SnCl_4 \cdot 5H_2O$, HCl, and distilled water were mixed to produce solution with a concentration of 100 g/l. To prepare silica solution, a starting suspension containing silicon oxide powder (7 nm) and water was mixed to produce solution with a concentrations of 10 to 40 g/l.

V. RESULTS AND DISCUSSION

All films and materials were characterized by x-ray diffraction (XRD), energy dispersive spectroscopy (EDS), and scanning electron microscopy (SEM). Resistances of some films were measured by a four-point lead method, as a function of temperature.

1. BiPbSrCaCuO Films

From EDS measurements, all cations (metals) were observed in the BiPbSrCaCuO films. From SEM analysis, film thickness, morphology, and microstructures were studied. Film thicknesses were between 3 and 12 micrometers. As-deposited films contained plate-like crystals, with crystal sizes of 1-5 micrometers. However, crystal shapes were dependent on the cation ratios. Referring to Table I, crystals of equations 2-4, and 7-8 had more edges, indicating a more dendrite growth.

As verified by XRD measurements, when films were deposited at low substrate temperatures (<600°C), 2201 phase was the dominant phase along with 2212 and other binary and ternary phases as minor phases. After post-annealing at 800°C for one hour, 2212 phase was enhanced. However, when films were deposited at high substrate temperatures (>600°C), 2212 phase was the dominant phase in each as-deposited film as illustrated in Table I and Figure 2 (corresponding to Eqn. 7) [22]. There was also an indication of preferred 00l orientation, which indicated a possibility of liquid phase growth from small deposits in the ranges of 50 to 150 nanometers as determined from the Full Width Half Maximum (FWHM) of an XRD pattern by a program called SHADOW.

In comparison, a series of bulk processing experiments were conducted with nine identical equations listed in Table I. It took several thermal cycles to fabricate 2212 bulk materials. However, with this plasma technique, 2212 materials were synthesized within one deposition process.

2. Y_2BaCuO_5 (211)

Y_2BaCuO_5 powders were scrapped off a flat MgO collector (5cm x 5cm). XRD measurements revealed that powders were phase pure 211 when the starting material ratios were from (0.190) : (0.158) : (0.158) to (0.194) : (0.158) : (0.157) for Y:Ba:Cu, as

illustrated in Figure 3. As the ratios were outside of the range, other non-211 phases were presented as minor phases, as illustrated in Table III. The crystallite size increased from 53 to 116 nm when collector temperature increased from 500°C to 660°C. Initial SEM analysis of as-deposited powders revealed that these powders were agglomerated. Powders were then dispersed in acetone (containing Darvan 821 deflocculant), and vibrated in an ultrasonic oscillator. Particle sizes of those powders were approximately 100-300 nm, as estimated by SEM measurements.

3. BaCaCuO Precursor (0223)

For a precursor film, XRD reveals that barium copper oxide and calcium copper oxide phases were present. With silver dopant, silver metal was present from XRD pattern. The crystallite sizes ranged from 70-150 nm (from SHADOW). EDS results verified the existence of all desired cations. For the film deposited at 450°C, the particle sizes were relatively uniform (0.5-1.5 micrometers) and the film was porous. The film deposited at 650°C had particle sizes ranged from 0.5 to 10 micrometers and the film was dense. After thallination in a two-zone furnace, XRD revealed that the films were 1223 phase pure, and four-point-probe measurements revealed that zero resistance temperature was 108 K [23].

4. YSZ

Thin films of YSZ were deposited on Ni containing substrates. All as-deposited films were yttria stabilized cubic zirconia as determined by XRD. The deposition rate was dependent on the feed flow rate, reactor-substrate distance, nebulizer setting, and solution concentration. The film thicknesses ranged from 5 to 30 micrometers depending on the duration of deposition and other experimental conditions as those listed in Table I. The density and morphology of the film were dependent on the substrate temperature and deposition rate. It was observed that films deposited below 900°C have "snowflakes" appearance with low density and poor adhesion. When the substrate temperature was higher than 900°C, the film density and adhesion strength were increased. Post heat treatment slightly enhanced the density and adhesive strength of these films. Surface morphologies of the as-deposited and post heat-treated films were different. In general, the post-annealed films were more crystallized than the as-deposited films.

6. Tin Oxide and Silica

In tin oxide films, XRD revealed that the predominant phase was SnO_2 (Cassiterite - JCPDS card # 41-1445). Mossbauer spectrometry determined that the tin was in its $^{+4}$ oxidation state. The crystallite size was determined to be ~25 nm via XRD SHADOW program. SEM analysis of the films showed a particle size ranged from 0.4 to 4 micrometers. In addition, silicon oxide films were deposited on SLS glass substrates. When the solution concentration increased from 10-20g/l to 40g/l, films changed from amorphous to crystalline structures as verified by XRD and SEM.

VI. DISCUSSION

Plasma aerosol deposition technique has potential for large scale coatings such as underground superconductor cables and magnetic shieldings. To fully develop the technique into a mature process, we are currently conducting the following experiments:

1. to add (BiSrCaCuO) 0011 into 2212 to form 2223;
2. to dope nano-sized 211 powder into 123 superconductor and to compare the results with that obtained from the micro-size powder;
3. to hybridize 123 with others magnetic materials;
4. to improve the 0223 precursor film's properties by changing the experimental parameters, and to study the roles played by silver.

Acknowledgment

We would like to thank Dr. R.L. Snyder, Dr. S. Dorris, Dr. K. Gorreta, Mr. Robert Kampwirth, Mr. T. Hardy, Dr. C. Oberly, Dr. R.M. Spriggs, and Dr. L.D. Pye for their help. Part of the work was initiated at Argonne National Laboratory when Dr. X.W. Wang was a summer faculty of DOE Education Department. This work was partially supported by Argonne National Laboratory, U.S. Air Force, Center for Advanced Ceramic Technology, and NSF Industry Center for Glass Research.

REFERENCES

1. J. Talvacchio et al, "YBCO and LSCO Films Grown by Off-Axis Sputtering," in Science and Technology of Thin Film Superconductors 2, Ed. by R.D. McConnell and R. Noufi, Plenum Press, New York, 1990.
2. M. G. Krishna et al, "Single Source Electron Beam Evaporation of Bi-Sr-Ca-Cu-O Thin Films," in Science and Technology of Thin Film Superconductors 2, Ed. by R.D. McConnell and R. Noufi, Plenum Press, New York, 1990.
3. D. H. Kuo et al, "Preparation of Superconducting Tl-Ba-Ca-Cu-O Films by Diffusion Method," in Science and Technology of Thin Film Superconductors 2, Ed. by R.D. McConnell and R. Noufi, Plenum Press, New York, 1990.
4. N. G. Dhere et al, "Control of Thickness and Composition Uniformity in Sputtered Superconducting Thin Films," in Science and Technology of Thin Film Superconductors 2, Ed. by R.D. McConnell and R. Noufi, Plenum Press, New York, 1990.
5. T. Frey et al, "In-Situ Deposited Superconducting Laser Ablated Thin Films of $Y_1Ba_2Cu_3O_{7-x}$ and $Bi_{0.8}Pb_{0.2}Sr_{0.8}Ca_1Cu_{1.6}O_x$," in Science and Technology of Thin Film Superconductors 2, Ed. by R.D. McConnell and R. Noufi, Plenum Press, New York, 1990.
6. U. Balachandran et al, "Sintering $Bi_2Sr_2CaCu_2O_y$ Pellets and Thick Films," in Superconductivity and Ceramic Superconductors, Vol. 13, Ceramic Transaction, Ed. by K.M. Nair and E.A. Giess.

7. D. W. Johnson et al, "Processing and Jc Considerations in High-Temperature Superconductors," in Superconductivity and Ceramic Superconductors, Vol. 13, Ceramic Transaction, Ed. by K.M. Nair and E.A. Giess.
8. T. Okada, H. Hamatani, and T. Yoshida, "Radio-Frequency Plasma Spraying of Ceramics," J. Am. Ceram. Soc., **72** [11] 2111-16 (1989).
9. A. Koukitu et al, Jpn. J. of Appl. Phys. **28**, L1212 (1989).
10. A. Shah, S. Patel, E. Narumi, and D. T. Shaw, "In situ, rf plasma deposition of $Bi_2Sr_2Ca_2Cu_3O_x$ thin films at atmospheric pressure," Appl. Phys. Lett. **62** (19) 2422-24, 1993.
11. X.W. Wang, H.H. Zhong, and R.L. Snyder, Appl. Phys. Lett. **57** (15) 1581 (1990).
12. T. Yoshida, "The Future of Thermal Plasma Processing," in Materials Transactions, JIM, Vol. 31, No. 1 (1990), pp. 1-11.
13. R.L. Snyder, X.W. Wang, and H.H. Zhong, U.S. Patent No. 5,120,703, June 1992.
14. Process developed by S. Dorris and B.C. Prorok at Argonne. For detailed information, see, for example, B.C. Prorok, "Formation of the $Bi_2Sr_2Ca_2Cu_3O_x$ Superconductor by a Two Powder Process," U. of Illinois at Chicago, 1993.
15. H.H. Zhong, X.W. Wang, J. Hao, and R.L. Snyder, "Deposition of Superconductive YBaCuO Films at Atmospheric Pressure by RF Plasma Aerosol Technique," in Superconductivity and Its Applications, Ed. by Y.H. Kao, A.I. Kaloyeros, and H.S. Kwok, AIP Conference Proceedings 251, Buffalo, NY 1991.
16. J. Hao, X. W. Wang, and R. L. Snyder, "RF Plasma Aerosol Deposition of Superconductive $Y_1Ba_2Cu_3O_{7-x}$ Films at Atmospheric Pressure," in Proceeding of the Fourth National Thermal Spray Conference, Pittsburg, PA, 4-10 May 1991.
17. Donglu Shi, S. Sengupta, and J.S. Luo, "Extremely fine precipitates and flux pinning in melt-processed YBa2Cu3Ox," Physica C213 (1993) 179-184.
18. S. Jin, T.H. Tiefel, and G.W. Kammlott, "Effect of Y_2BaCuO_5 inclusions on flux pinning in $YBa_2Cu_3O_{7-x}$," Appl. Phys. Lett. **59** (5), 1991.
19. H.M. Duan, B. Dlugosch, A.M. Hermann, X.W. Wang, J. Hao, and R.L. Snyder, "Superconducting TlBaCaCuO Thin Films From BaCaCuO Precursors," in Superconductivity and Its Applications, Ed. by Y.H. Kao, A.I. Kaloyeros, and H.S. Kwok, AIP Conference Proceedings 251, Buffalo, NY 1991.
20. J.A. DeLuca, P.L. Karas, J.E. Tkaczyk, P.J. Bednarczyk, M.F. Garbauskas, C.L. Briant, and D.B. Sorensen, Physica C 205, 21 (1993).
21. Unpublished results from X.W. Wang's experiments performed at Argonne National Lab between May and June 1993.
22. The crystallite size for 2212 film (eqn. 7) was ~128 nm as determined from SHADOW. Also the electrical resistance was measured by a four-point lead method. For as-deposited films, superconductive transition temperature was 100 K for Equation 5 and 90 K for Equation 2. The zero resistance temperature was 58 K and 60 K for Equation 5 and Equation 2, respectively.
23. Work performed by Mr. Robert Kampwirth at Argonne National Laboratory.

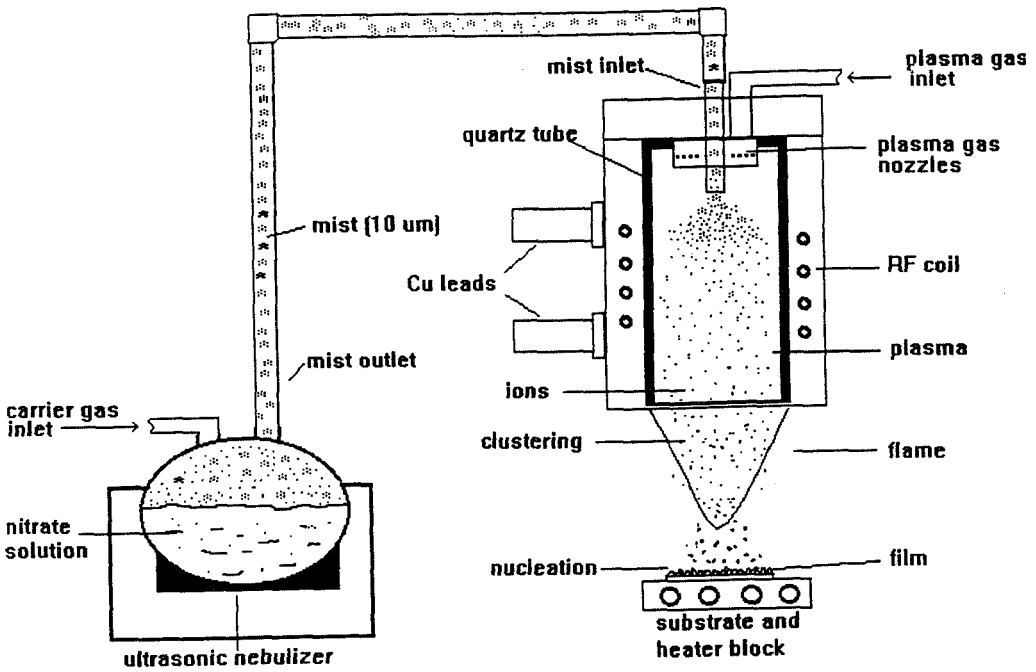

Figure 1. Plasma aerosol deposition experimental set-up.

Table I. Formulae of Nine Equations (Bi:Pb:Sr:Ca:Cu) and Relative Concentrations of 2212 Phases.

Equation #	x	y	Formula Ratio	2212*	2201	Ca_2CuO_3
1	0.20	0.25	2:0.20:1.75:1.25:2	89%	11%	0%
2	0.25	0.50	1.95:0.25:1.50:1.50:2	94%	4%	2%
3	0.30	0.75	1.90:0.30:1.25:1.75:2	93%	5%	2%
4	0.20	0.50	2:0.20:1.50:1.50:2	93%	6%	1%
5	0.25	0.75	1.95:0.25:1.25:1.75:2	86%	10%	1%+
6	0.30	0.25	1.90:0.30:1.75:1.25:2	95%	4%	1%
7	0.20	0.75	2:0.20:1.25:1.75:2	97%	2%	1%
8	0.25	0.25	1.95:0.25:1.75:1.25:2	95%	4%	1%
9	0.30	0.50	1.90:0.30:1.50:1.50:2	90%	8%	2%

* The relative percentages of various phases were estimated from relative heights of the 100% peaks.
+ other peaks observed

Table II. Film Deposition Conditions for Superconducting and Nonsuperconducting Materials.

Parameter	Bi-2212	Y_2BaCuO_5	$Ba_2Ca_2Cu_3O_x$	YSZ	SnO_2 / Silica
Power Setting %	35	35	30	30	40
Axial Argon Flow Rate (L/min)	5	7	7 - 9	7	5
Swirl Argon Flow Rate (L/min)	10	7 - 10	8 - 10	10	7.5
Swirl/Tangential O_2 Flow Rate (L/min)	15	10 - 15	15 - 20	10	12.5
Feed Argon Flow Rate (L/min)	4	2.5 - 4	3.5 - 5	2.5	2.5
Nebulizer Setting (%)	80	80	75	80	50 / 100
Substrate Distance (cm)	13	12	13	12	11
Substrate Temp. (°C)	400 - 750	400 - 660	500 - 750	600 - 950	400 - 500
Solution Conc. (g/l)	100	120	100	75 - 100	100 / 10-50

Table III. Solution Ratios and Substrate Temperatures Effect of Impurity and Crystallite Size.

Experimental #	Solution Mole Ratio (Y:Ba:Cu)	Substrate Temp (°C)	Impurity	Crystallite Size (nm)
1	0.190 : 0.158 : 0.158	660	0	105
2	0.190 : 0.158 : 0.158	500	10% Y2O3	116
3	0.190 : 0.158 : 0.158	500	10% Y2O3	102
4	0.161 : 0.158 : 0.158	400	30% 123	66
5	0.190 : 0.171 : 0.172	530	15% 123	56
6	0.190 : 0.164 : 0.163	600	15% 123	80
7	0.190 : 0.159 : 0.157	550	10% 123	72
8	0.194 : 0.158 : 0.157	570	0	70
9	0.192 : 0.158 : 0.157	500	0	53

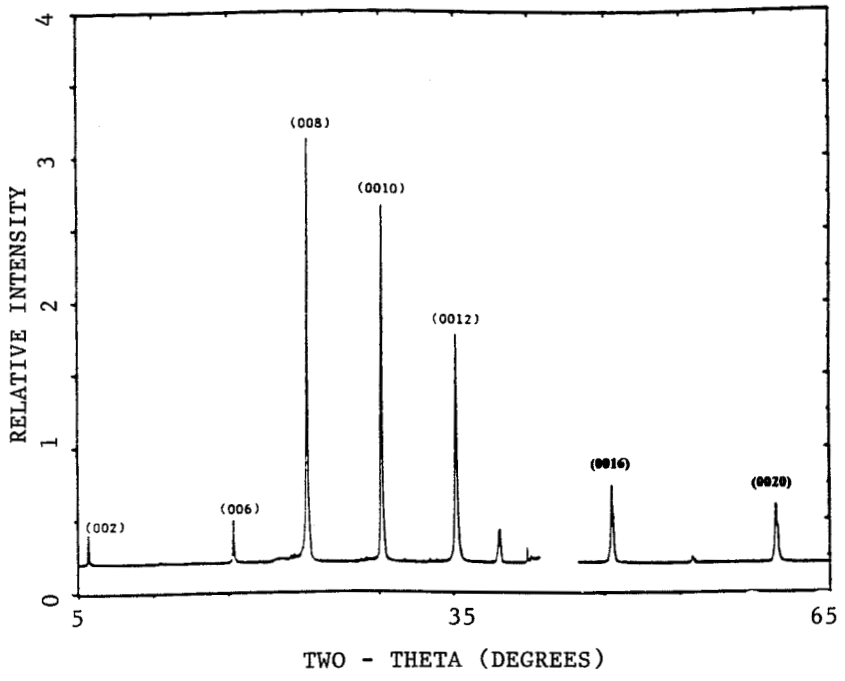

Figure 2. XRD pattern of 2212 film (eqn. 7). The peak at ~38 degree two-theta is due to MgO substrate. The peaks (omitted) between 42 and 45 degrees two-theta are also due to MgO substrate.

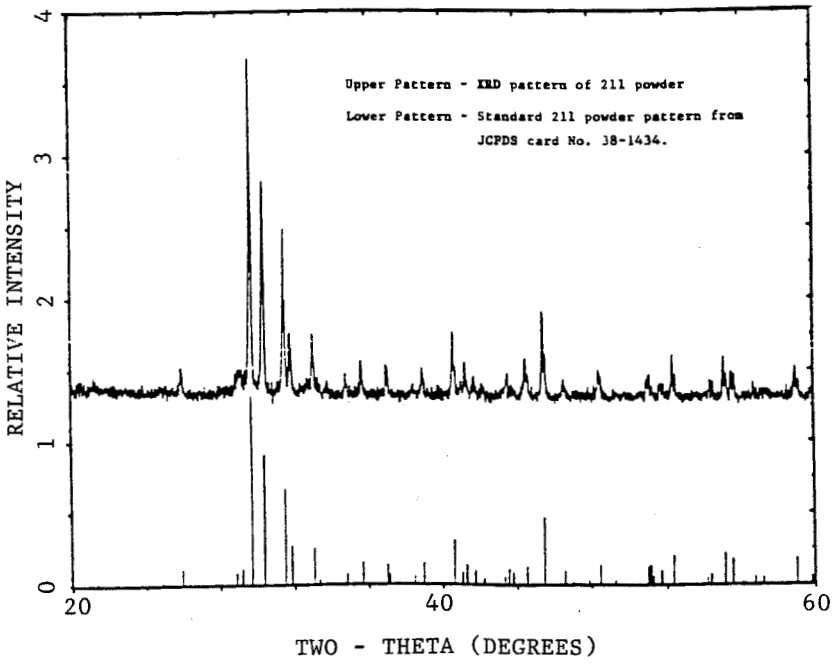

Figure 3. XRD pattern showing phase pure 211 powder (expt. #1).

Partial Melting of Bulk Bi-2212

B. Heeb and L.J. Gauckler

Nichtmetallische Werkstoffe, ETH Zürich, Sonneggstr. 5, CH-8092 Zürich, Switzerland

Abstract

Dense and textured Bi-2212 bulk samples have been produced by the partial melting process. The appropriate amount of liquid phase necessary for complete densification has been adjusted by controlling the maximum processing temperature. The maximum temperture itself has to be adapted to several parameters as powder stoichiometry, silver addition and oxygen partial pressure. Prolonged annealing at 850 and 820 °C and cooling in N_2 atmosphere led to nearly single phase material with T_c=92 K. Critical current densities j_c of 2'200 A/cm^2 at 77 K/0 T have been achieved in samples of more than 1 mm thickness. Reducing the thickness below 0.4 mm enhances j_c considerably to values > 4'000 A/cm^2. The addition of 2 wt% Ag decreases the solidus temperature of the Bi-2212 powder by 21 °C. Therefore, the maximum heat treatment temperature of Ag containing samples can be markedly lowered leading to a reduction of the amount of secondary phases. In addition, Ag enhances slightly the texture over the entire cross-section and as a result j_c at 77 K/0 T.

Introduction

Melt processing of Bi-2212 ($Bi_2Sr_2CaCu_2O_x$) is a common fabrication technology to produce superconducting devices with a dense, weak-link free microstructure. Various geometries have been produced by this technique: (a) Thick films on Ag-substrates are fabricated by the so-called *partial melting* route [1,2] leading to an excellent grain alignment and high critical current densities at 77 and 4.2 K even in long tapes. (b) Ag sheathed wires are produced by a very similar process [3-5]. So far, good superconducting properties in long lenghts have been achieved at temperatures between 4.2 and 25 K. (c) Massive devices, e.g. tubes and rings for current leads and limiters, have been fabricated by *complete melting* at temperatures above 1000 °C. For these geometries, the high temperatures are required to achieve the appropriate viscosity to form the desired shape [6], but they promote oxygen loss during melting and the development of an unfavorable microstructure with coarse secondary phases even after prolonged annealing at temperatures above 800 °C [7-9]. As a consequence, the critical current density at 77 K remains limited. Nevertheless, technical devices are feasible with bulk materials due to components with large cross-section carrying high currents.

The purpose of this study is to apply the partial melting process to produce bulk Bi-2212 material in order to avoid the disadvantages of the complete melting. The heat treatment was optimized in order to enhance the critical current density of massive

devices at 77 K. Since Ag was used as container material, special emphasis was laid on the control of its influence on the processing parameters and the resulting properties.

Experimental

a. Powder preparation

Powder with the stoichiometry $Bi_{2.2}Sr_{2.0}Ca_{1.0}Cu_{2.0}O_x$ was prepared by the standard calcination process. The appropriate amounts of Bi_2O_3[a] , $SrCO_3$[b] , $CaCO_3$[c] and CuO[d] were mixed and calcined at 750 °C for 18 h, at 800 °C for 36 h, at 820 °C for 85 h and at 850 °C for 96 h in a flowing gas mixture of 20% O_2 and 80% N_2 with intermediate grindings. This powder stoichiometry was chosen, because it is reported to be within the single phase region of Bi-2212 [10]. In addition, the Bi-excess reduces the amount of Bi-free secondary phases of melt processed Bi-2212 [11]. The nearly single phase calcined powder was ball milled in hexan for 2 hours, dried and sieved passing completely the 32 µm sieve. To a part of the calcined powder 2 wt% Ag was added in form of Ag_2O. The Ag_2O powder[e] was mixed with the Bi-2212 powder on a roll mill for 3 h, resulting in a homogeneous mixture of the two powders. The Ag_2O is decomposed during heating leading to finely dispersed Ag particles of a few microns on the 2212 powder particles.

DTA measurements revealed a solidus temperature of the powder of 881 °C in air and 892 °C in oxygen, respectively. The addition of 2 wt% silver led to a decrease of the solidus temperature to 871 °C in oxygen.

To control the quality of the powder a pressed pellet was sintered at 850 °C for 96 h in air and drop quenched in liquid N_2. The sample was single phase (a=0.541 nm, c=3.086 nm) and showed a T_c of 95 K.

b. Sample preparation and characterization

Pellets with a diameter of 13 mm and variable thickness were uniaxially pressed at a pressure of 150 MPa, put into Ag crucibles and subjected to the heat treatment, which consisted of three main steps:

- Partial melting at 880 to 905 °C for 2 h in oxygen to densify the samples.
- Annealing at 850 °C for 48 h in oxygen after cooling at a cooling rate of 30 °C/h to form a high volume fraction of the 2212 phase [12]. A second annealing step of 80 h at 820 °C in oxygen or air followed.
- Cooling at a rate of 300 °C/h to room temperature; the atmosphere was changed to nitrogen ($p_{O_2} \approx 10^{-3}$ atm) at 700 °C in order to optimize the oxygen stoichiometry.

---

[a] PCF, 99.9% purity
[b] Solvay Barium Strontium GmbH, > 99.9%
[c] Solvay Barium Strontium GmbH, > 99.9%
[d] Cerac Inc., > 99.8%
[e] Fluka Chemika, > 99.0%

The microstructure of the samples was investigated by light microscopy, X-ray diffraction (XRD) with CuK_α radiation and Si as internal standard, and scanning electron microscopy (SEM). To achieve information about the microstructure of the entire volume, the sample thickness was reduced by removing material in steps of 100 μm by polishing. Chemical compositions of phases were determined by EDX at an acceleration voltage of 25 kV. The ZAF correction was applied to the intensities of the BiM_α, SrL_α, CaK_α, and CuK_α lines, and the compositions calculated by means of internal standards.

The critical temperature T_c was determined resistively by the conventional four-probe method or by AC susceptibility. The measurements of the critical current density j_c were performed magnetically in an AC magnetometer at f=4 Hz using the 1 μV/cm criterion. The samples were immersed in a bath of liquid nitrogen. The current densities were calculated from the width ΔM of the measured M(H) loops. Since granularity was never found in melt processed Bi-2212 [13] ΔM must be due to macroscopic currents only.

Results and Discussion

a. Microstructure

The maximum heat treatment temperature is the crucial processing parameter for the microstructural development of melt processed Bi-2212. For thick films it has been shown that only a narrow temperature range is suitable to achieve dense mircrostructures with high critical current densities [2,14]. Similar behavior was observed for bulk material. In Figure 1 the fracture cross-section of a sample processed at T_{max}=905 °C is shown. The typical microstructure of melt processed Bi-2212 consisting of bundles of 2212 grains with parallel c-axis and separated by (001) twist boundaries [13] can be recognized. It is completely dense and no major secondary phases can be detected. SEM observations in the backscattering mode revealed the chemical composition to be very homogenous throughout the cross-section. These findings were further confirmed by XRD showing that only traces of 3430 are present as secondary phase beside the 2212 phase with a=0.541 nm and c=3.087±0.002 nm. The chemical composition of the 2212 phase is $Bi_{2.13}Sr_{2.06}Ca_{1.06}Cu_2O_x$ and is close to the composition of the starting powder.

In contrast to the bulk, both the surface and the interface to the Ag substrate show a considerable amount of secondary phases. At the surface the Bi-free 0$\underline{14}$x$\underline{24}$ phase was found; its appearance is mainly attributed to Bi-loss during processing. At the interface the 2201 and the Cu-free 3430 phase were present as secondary phases. In addition, the very large FWHM (0.63°) of the (008) peak of the 2212 phase as well as the EDX analysis showing a chemical composition of $Bi_{2.82}Sr_{2.31}Ca_{1.03}Cu_2O_x$ indicate a high density of 2201 intergrowths inside the 2212 grains. However, the second phase rich layers at the suface and interface have a thickness of less than 100 μm.

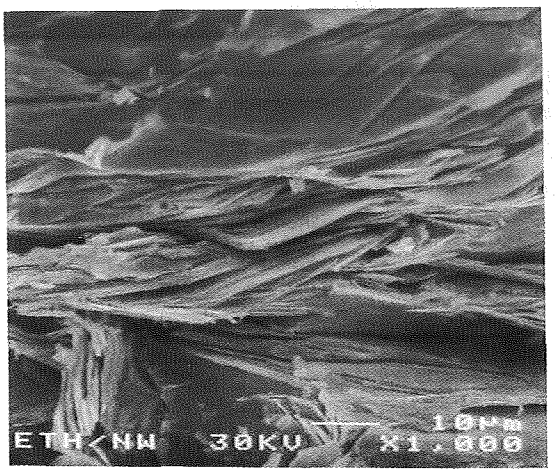

Fig.1: SEM picture of the cross-section of a Bi-2212 bulk sample processed at T_{max}=905 °C.

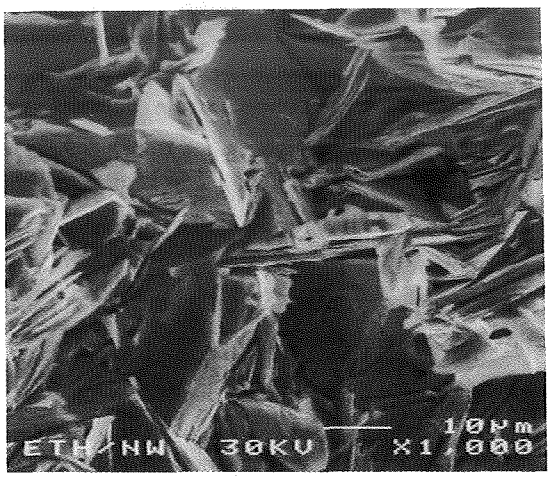

Fig.2: SEM picture of the cross-section of a Bi-2212 bulk sample processed at T_{max}=880 °C.

Reducing the maximum processing temperature led to a decrease of the amount of liquid phase and to a dramatically reduced density. Figure 2 shows the fracture cross-section of a sample heated to T_{max}=880 °C. Only a thin layer of approx. 10 to 20 µm at the Ag interface is molten and densified, whereas the bulk is only sintered and remained porous. Obviously, two solidus temperatures can be found in this sample; affected by the Ag substrate, Bi-2212 near the interface begins to melt at a markedly lower temperature than the rest of the sample. However, the small amount of liquid phase produced is inadequate to promote the densification of the entire sample. Therefore, a processing temperature exceeding the solidus temperature by about 15 °C is considered to be appropriate for complete densification of bulk Bi-2212, even in Ag crucibles. This difference is larger than the 3-7 °C reported for thick films [2,14].

As mentioned earlier, doping $Bi_{2.2}Sr_2CaCu_2O_x$ with 2 wt% Ag decreases the solidus temperature by 21 °C to 871 °C in oxygen atmosphere. Taking into account that the proper amount of liquid phase can be achieved by the previously mentioned 15 °C above solidus, the maximum temperature of the partial melting process was reduced to 885 °C. Indeed, this low temperature led to the complete densification of the samples and to a considerably smaller amount of secondary phases, especially of the Bi-free 014x24 at the surface and 2201 at the Ag/Bi-2212 interface.

In Figure 3 the melting behavior of Bi-2212 on Ag substrates as a function of the partial melting temperature is summarized. Without Ag addition (figure 3a) a temperature around 905 °C is necessary for complete densification of the sample. At this temperature, the surface is overheated and the Ag/Bi-2212 interface suffers a substantial Bi-loss leading to an enhanced volume fraction of secondary phases in these layers. As it will be shown later, these layers are the most textured ones and so possible regions of high current carrying capacity. Therefore, an improvement of the melting process in regard of the microstructural development of surface and interface seems to be advantageous for the enhancement of the current density.

Lowering the maximum processing temperature T_{max} to 880 °C does not solve the problem. The microstructure of the interface layer is certainly improved, but the amount of liquid phase is insufficient to densify the whole sample. Therefore, such low temperatures can only be used for the fabrication of thick films which consist entirely of Ag/Bi-2212 interface. The second, more promising way to improve the microstructure of bulk material is the addition of 2 wt% Ag to the powder (figure 3b). It lowers the solidus temperature of the entire sample and eliminates the inhomogenous melting. At the same time, the processing temperature is comparable to the one used for the partial melting of thick films. Therefore, the volume fraction of secondary phases at the interface due to overheating and at the surface due to Bi evaporation can be markedly reduced.

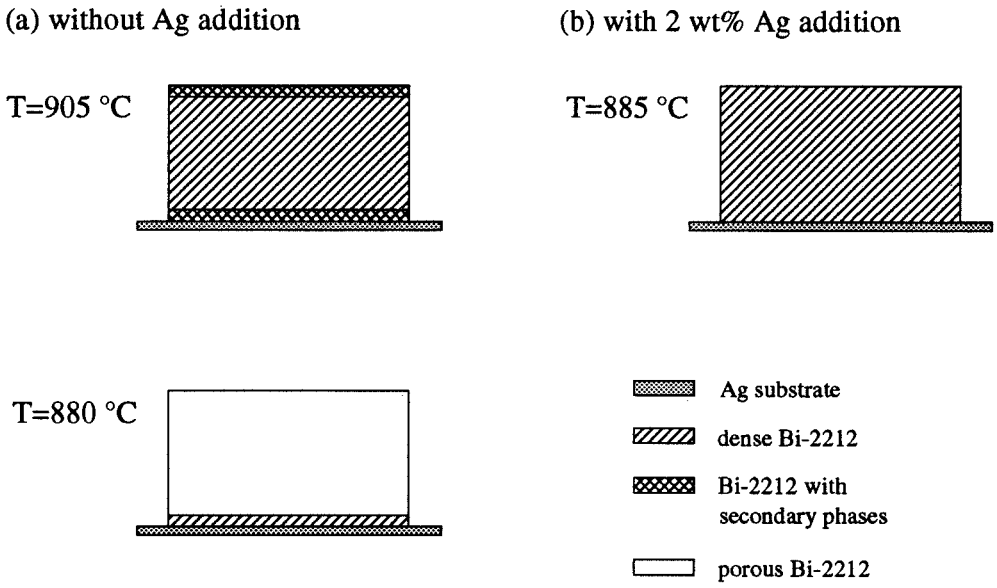

Fig.3: Schematic drawing of the melting behavior of Bi-2212 bulk samples on Ag substrates (a) without and (b) with 2 wt% Ag addition.

b. Texture

Figure 4 shows the dependence of the degree of texture[a] on the distance from the Ag/Bi-2212 interface. The high value of f=0.99 at the interface expresses an almost perfect alignment of the (ab)-plane parallel to the Ag substrate. However, the highly textured layer has only a thickness of less than 100 μm. Comparable good grain alignment is found at the sample surface.

[a] Quantification of the texture from XRD measurement: $f = \Sigma Intensities(00l)_{2212}/\Sigma Intensities(hkl)_{2212}$

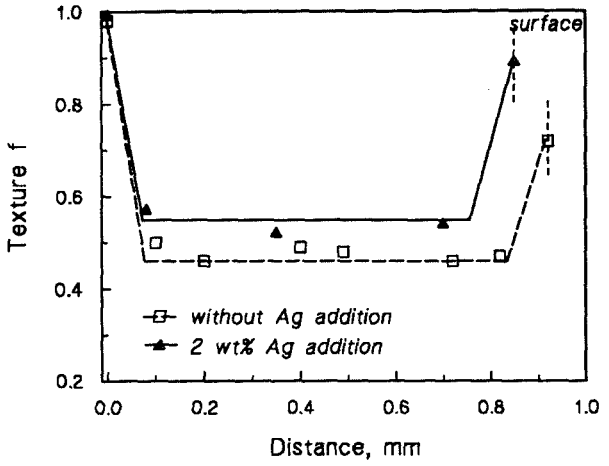

Fig.4: Degree of texturing from the Ag/Bi-2212 interface to the surface of melt processed Bi-2212 with and without Ag addition

The degree of texturing in the bulk is lower, but constant over the entire cross-section. The parameter f showing values of 0.5 lays markedly above the value of an unoriented powder specimen with f=0.14 and a little above f of a pressed and sintered specimen (f=0.47). This indicates that a considerable degree of texture in the bulk is already formed by pressing which is intensified by the partial melting process. Excellently textured layers are induced by the Ag substrate as well as by the free surface. The Ag addition slightly enhances the degree of alignment over the entire cross-section.

c. Properties

Table 1 shows the critical temperatures T_c of melt processed and sintered Bi-2212. All heat treatment schedules including partial melting lead to the same T_c of 92 K. This temperature is somewhat lower than T_c = 95 K of the sintered and drop quenched sample without Ag addition, but equal to the T_c of sintered Bi-2212 with 2 wt% Ag addition. This indicates, that the oxygen stoichiometry of the partially molten Bi-2212 is well adjusted, but T_c is slightly lowered due to the influence of Ag taken up from the substrate during partial melting and/or added to the starting powder.

Heat treatment	Ag addition, wt%	T_c, K
Partial melting	--	91.5 - 92
	2	92
Sintering	--	95
	2	92

Table 1: Dependence of T_c on heat treatment conditions and Ag addition

The critical current density j_c being the most important design parameter of system components was determined at 77 K, the envisaged operating temperature. Figure 5 shows the j_c dependence on the sample thickness d after partial melting in oxygen and annealing at 850 °C in oxygen as well as at 820 °C in air. The maximum processing

temperature was 905 °C for pure Bi-2212 samples and 885 °C for Ag containing samples. For sample thicknesses d≤0.4 mm j_c increases strongly with decreasing sample thickness. Values above 4'000 A/cm^2 can be reached. For samples with d>0.4 mm the dependence of j_c on component dimensions is much reduced but still present. Critical current densities larger than 2'000 A/cm^2 can be obtained in specimens of more than 1 mm thickness after this process.

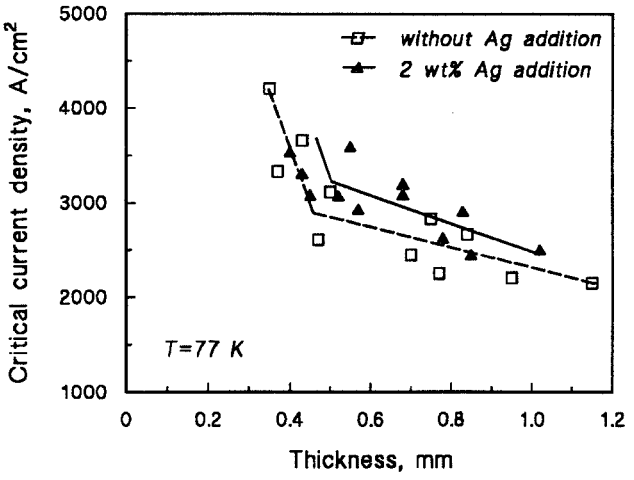

Fig.5: Dependence of j_c (77 K/0 T) on sample thickness for partially molten Bi-2212 with and without Ag addition (incl. air annealing)

The Ag addition enhances j_c for all sample sizes. Since T_c of all samples is equal, we conclude that the increase is connected with the improved microstructure, namely phase composition and texture.

Assuming that self-field effects can be neglected at the present sample size of d<1.2 mm, j_c is mainly influenced by the phase composition and texture. As we have shown before, the samples are nearly single phase and the texture is constant over the main part of the cross-section. Therefore, the increase of j_c with decreasing thickness might be attributed to the increasing contribution of the highly aligned layer at the Ag/Bi-2212 interface with decreasing overall sample thickness.

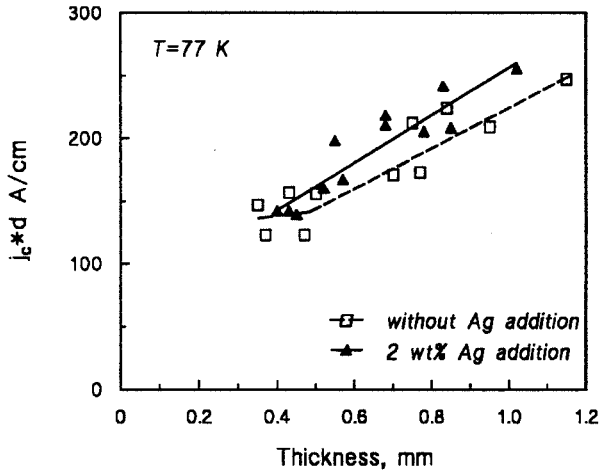

Fig.6: Dependence of j_c*thickness (77 K/0 T) on sample thickness for partially molten Bi-2212 with and without Ag addition (incl. air annealing)

Figure 6 shows the dependence of the product j_c*d on sample thickness. This product is of interest for technical devices. It gives an indication how much current can be transported in a conductor of a certain width. The increase of j_c*d with increasing sample thickness is remarkable and the maximum has not been reached with d=1.2 mm. This behavior clearly demonstrates that bulk Bi-2212 is well suited for high current applications. The loss of critical current density can be over-compensated by increasing the thickness. For comparison, the best thick films have $j_c > 10^4$ A/cm^2 [2,14], but their j_c*d is in the region of 30-40 A/cm, almost an order of magnitude smaller than in bulk material.

In Figure 7 the thickness dependence of j_c of the samples with the final annealing at 820 °C in oxygen instead of air (figure 5) is shown. Again, the maximum processing temperature was 905 °C for pure Bi-2212 samples and 885 °C for Ag containing samples for samples annealed in O_2 at 820 °C.

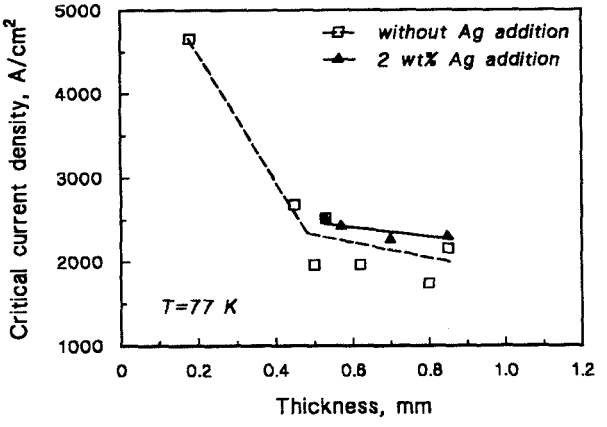

Fig.7: Dependence of j_c (77 K/0 T) on sample thickness for partially molten Bi-2212 with and without Ag addition (oxygen annealing)

The critical current density for all sample thicknesses is significantly reduced. Since macroscopic differences like T_c, texture or phase compositions cannot be observed, the influence of the oxygen annealing is not understood so far. More careful investigations of the micro- and nanostructure is necessary to explain the advantage of air annealing. Of course, the lower j_c values lead also to lower j_c*d as illustrated in figure 8.

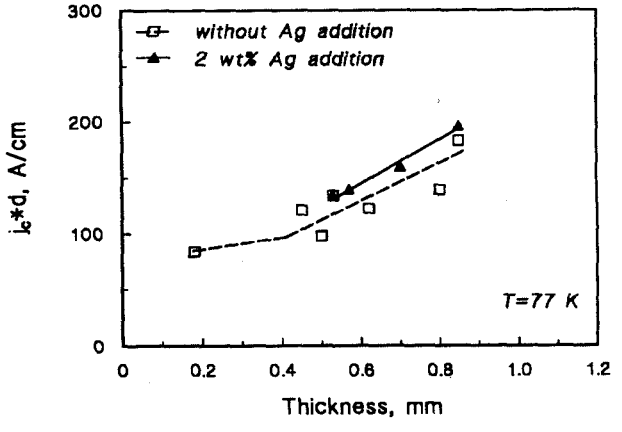

Fig.8: Dependence of j_c*d (77 K/0 T) on sample thickness for partially molten Bi-2212 with and without Ag addition (oxygen annealing)

Conclusions

Partial melting is an appropriate processing technology to produce dense bulk Bi-2212 with nearly single phase microstructures. It leads to a considerable texture over the entire cross-section. A particularly pronounced degree of grain alignment is found at the Ag/Bi-2212 interface and the surface. Therefore, avoiding secondary phases in this layer enhances the current density in thin samples (d<0.4 mm), in which the interface layer contributes substantially to the total current. The addition of 2 wt% Ag is shown to be a useful measure for this purpose.

The maximum processing temperature has to be approx. 15 °C above the solidus temperature in order to achieve a sufficient amount of liquid phase promoting the densification of the sample. Annealing including a step at 820 °C in air is superior to annealing only in oxygen atmosphere. Cooling in N_2 is sufficient to obtain a high T_c. No further heat treatment is necessary to adjust the oxygen stoichiometry.

Critical current densities j_c (77 K/0 T) above 4'000 A/cm^2 are achieved for a sample thickness d<0.4 mm. The addition of 2 wt% Ag enhances j_c slightly. Increasing the thickness leads to a reduction of j_c. However, because the thickness dependence becomes small for d>0.4 mm, bulk Bi-2212 with high critical currents can be produced by partial melting .

Acknowledgments

This work is supported by ABB (CHCRC.M3). The authors are grateful to Dr. W. Paul (ABB) and Th. Lang for helpful discussions.

References

[1] J. Kase, K. Togano, H. Kumakura, D.R. Dietderich, N. Irisawa, T. Morimoto, H. Maeda, *Jpn. J. Appl. Phys.* **29** (1990) L1096.
[2] J. Shimoyama, K. Kadowaki, H. Kitaguchi, H. Kumakura, K. Togano, H. Maeda, K. Nomura, *Appl. Supercond.* **1** (1993) 43.
[3] J. Tenbrink, M. Wilhelm, K. Heine, H. Krauth, *IEEE Trans. Mag.* **27** (1991) 1239.
[4] S. Hayashi, T. Hase, K. Shibutani, T. Egi, Y. Masuda, R. Ogawa, Y. Kawate, *Processing of Long Lengths of Superconductors* (TMS, Warrendale, 1994), p.81.
[5] C.-T. Wu, K.C. Goretta, M.T. Lanagan, A.C. Biondo, R.B. Poeppel, ib. p.101.
[6] J. Bock, H. Eckhardt, S. Elschner, *Advances in Superconductivity V* (Springer, Tokyo, 1993), p.643.
[7] B. Heeb, L.J. Gauckler, H. Heinrich, G. Kostorz, *J. Electr. Mater.* **22** (1993) 1279.
[8] T.G. Holesinger, D.J. Miller, L.S. Chumbley, *IEEE Trans. Appl. Supercond.* **3** (1993) 1178.
[9] J. Bock and E. Preisler, *High Temperature Superconductors: Materials Aspects* (DGM, Oberursel, 1991), p.215.
[10] P. Majewski and B. Hettich, *Layered Superconductors: Fabrication, Properties and Applications* (MRS Symp. Proc. 275, Pittsburgh, 1992), p.627.
[11] S. Wu, J. Schwartz, G.W. Raban Jr., *Physica C* **213** (1993) 483.
[12] B. Heeb, L.J. Gauckler, H. Heinrich, G. Kostorz, *J. Mater. Res.* **8** (1993) 2170.
[13] W. Paul and Th. Baumann, *Physica C* **175** (1991) 102.
[14] D. Buhl, Th. Lang, B. Heeb, L.J. Gauckler, to be published in *Physica C.*

N. MAKI et al. Proceedings 4th World Congress on Superconductivity, Orlando, Flolida (1994)

247-76
3144 68

CORRELATION BETWEEN FABRICATION FACTOR AND SUPERCONDUCTING PROPERTIES OF THE TL- AND BI- BASED HIGH-Tc SUPERCONDUCTOR

CLOSE
34330
16 p.

Naoki MAKI, Michiya OKADA, Toshiya J. DOI, Tsuneyuki KANAI,
Jun'ichi SATO*,
and Kazutoshi HIGASHIYAMA

Hitachi Research Laboratory, Hitachi Ltd.
Ohmika-cho 7-1-1, Hitachi, Ibaraki 319-12 Japan

**Advanced Research Laboratory, Hitachi Cable Ltd.*
Kidamari-cho 3550, Tsuchiura, Ibaraki 300 Japan

ABSTRACT

Large critical current densities (Jc) were obtained in c-axis oriented Tl-1223/Ag composite tapes fabricated by spraying methods without a vacuum. Transport measurements at 77K under a zero field indicated a Jc of 9×10^4 A/cm^2 and 7×10^3 A/cm^2 at 1T for the tapes fabricated by spray pyrolysis . The novel GPM method was also applied for Bi-2212/Ag PIT composite wire, and found to be very effective for improving the distribution of voids, which caused from the melt-solidifying process. The GPM showed a marked effect for obtaining homogeneous long wire. A 1T class coil was successfully fabricated with monocore wire.

1. INTRODUCTION

It is well known that the Bi-system wires with high critical current density Jc's are much preferable for applications in high magnetic field regions at cryogenic temperature below 20K than Tl-system superconductors from the viewpoint of process easiness realizing good crystal alignment enabling a large current flow, however, the Bi-system superconductors can not be useful in liquid nitrogen temperature applications due to the weak pinning characteristics caused from the two dimensional vortex structure. In the latter case, Tl-1223 with Tc 122K, having strong pinning characteristics (with more three dimensional vortex structure), is thought to be the best candidate. Since, Tl-1223 requires ,however, the three-dimensional crystal alignment for overcoming the grain boundary weak links, the wire fabrication processes are thought to be restricted in a field of the thin film technologies.

In this paper, we show the following two novel processing for both Bi- and Tl- system HTS's,

(1) GPM(gas pressurized melt) process for Bi-2212/Ag solenoid coil using PIT

(2) Spray pyrolysis method for Tl-1223 on silver substrate in ambient pressure conditions.

2. *Bi-2212 GPM Process*

It is well known the Bi-2212/Ag wire with high critical current density Jc can easily be obtained through the partial-melting process.[1] However, the most serious problem of the process is thought to be the oxygen release which causes "*swell*" on the wire. So far, we have already reported that the oxygen release can be reduced using the Bi-2212 powders with Ag,[2] calcined at temperatures around melting point, under a high oxygen partial pressure (100% O_2 - 1 atm). In order to achieve a good superconducting property in a long wire, it is necessary to improve microstructural homogeneity in the longitudinal direction of the wire. In followings, we will discuss the effect of the GPM (Gas Pressurized Melt Process) for Bi-2212/Ag, on microstructure.[3]

2.1 *Experimental*

Commercial powders of 3N pure oxide were mixed in a nominal composition of Bi_2 Sr_2 Ca_1 Cu_2 $Ag_{0.2}$ O_y and calcined twice at 810℃ for 10h. Silver tubes with outer diameter of 6mm, filled with the powder, were processed by drawing to get 0.7mm and 1.2mm outer diameter and 25m length wires. The round wire was cut into 3cm lengths for short sample. As-drawing 25m long wires (1.2mm o.d.) were wound into solenoid type. The fabricated solenoid coil is shown in Fig.1. Both short wires and the coils were partially melted for 10 minutes from 865℃ to 885℃. Short wires were calcined under various conditions of oxygen concentration and total gas pressure. Coils were melted under both atmospheric pressure and a pressurized atmosphere, using GPM. The transport critical current was measured by a four-probe method at 4.2K with a 1 μV / cm criterion for short wires, and with a $10^{-13}\Omega \cdot m$ criterion for coils. The voids distribution inside Ag-sheath was observed using X-ray radiography (Voltage : 180kV, current : 5mA, target : W).

2.2 *Results and discussion*

Since the oxygen partial pressure during melt process affect a release of oxygen gas from Bi-2212 crystals, oxygen partial pressure, pO_2, should be changed to appear the effect on void formation and superconducting properties. It was found that the high Jc values of over 10^5 A/cm^2 were obtained using GPM under a pO_2 of 1.0 to 3.0 atm. And, we investigated the details of the effect of total gas pressure under the condition of pO_2=1.0～1.2atm. Under the total gas pressure over 3.0 atm with a constant pO_2, relatively high Jc values are obtained in a wide temperature range with a little scatterings. According to the X-ray radiography, the distribution of voids in wires melted at P_{total} of 6.0 atm estimated to be smaller than those of melted at the atmospheric pressure (P_{total}=1.0 atm) .Therefore, the GPM method which melted under pO_2 of 1.0 to 3.0 atm and Ptotal over 3.0 atm, are prerequisites for getting wires with the high Jc values and homogeneous distribution of voids. We also fabricated small solenoid coils melted under both ambient and the GPM atmosphere. Fig.2 shows the distribution of voids in both coils. Horizontal axis shows the average length of the voids in the longitudinal direction of the wire, and vertical axis shows the number of the voids. The properties of the coil melted under the atmospheric pressure are markedly depends on the cross-sectional locations. For example, outer-most side, the Jc was lowest, which

corresponds to the void concentration of 50 mm long in fig.2. Microstructures and Tc of the coil were homogeneous, however, the distribution of the voids governed the V-I properties. On the other hand, voids of the coil processed through the GPM method were 10mm long at most. Therefore, the GPM method seems to be very effective for improving the distribution of voids, and makes easy for obtaining homogeneous long wire. The coil, using a 5 pieces of 25m long wire, generated a maximum magnetic field of 1.1T at a current of 88A.

3. *Tl-1223/Ag composite tape*

In order to apply high-Tc superconductors to magnets operable in liquid nitrogen, a considerable length of wire must be fabricated with a transport Jc of at least 10^4 A/cm^2 in magnetic fields of 1 T or greater. Key to the fabrication of practical high-Tc superconducting wires is to prepare polycrystalline conductors which have good intergranular connectivity and high flux pinning characteristics. Although YBCO[4] and Tl-1223[5)-7)] has strong pinning force at 77K, the transport capabilities of wires fabricated by the powder-in-tube method are seriously impaired by weak-link behavior resulting from poor intergranular connectivity. In contrast, large transport Jc values have been reported for YBCO thin films epitaxially grown on oxide single crystals[8)] and even for those grown on metal with a biaxial aligned buffer layer[9)] by physical or chemical vapor deposition. It is important to align the in-plane a- and b-axes of individual grains by using thin film processes in order to inhibit weak-link behavior. Such processes, however, which must be performed under high-vacuum conditions, may not be suitable for wire applications, where long length, high productivity and low cost are required.

The spray pyrolysis method is a film fabrication technique which do not require a vacuum, and which therefore make it possible to produce long lengths of tape shaped wires. In this paper, we report a high Jc value for Tl-based superconductors/Ag composite tapes prepared by spraying methods under ambient pressure, thus verifying the high potential of these methods.

3.1 *Experimental*

The precursor films containing appropriate proportions of all the metals except Tl were deposited under ambient pressure. The deposited films are porous, and so they were pressed or rolled to make them denser and then fired in a controlled thallium oxide vapor.

For the spray pyrolysis, a 0.02 mol/l aqueous solution was prepared from $Ba(NO_3)_2$, $Sr(NO_3)_2$, $Ca(NO_3)_2.4H_2O$ and $Cu(NO_3)_2.3H_2O$ with a metal stoichiometric ratio of Ba:Sr:Ca:Cu=1.6:0.4:2:3. The spray solution was converted into a mist with an ultrasonic transducer. The mist was introduced onto the Ag tape which was heated to 700℃. The deposited precursor oxide films were fired at 860℃ for 30 hours in a controlled thallium oxide vapor. The film thickness was approximately 1 μm.

The transport Jc of the films was measured by using the standard four probe method with a criterion of 1 μV/cm. The crystal structure and composition were analyzed by X-ray diffraction (XRD) and energy-dispersive X-ray analysis (EDX). Their microstructure was observed with a scanning electron microscope (SEM) and X-ray pole-figure analysis.

3.2 *Results and discussion*

Figure 3 shows the XRD pattern of Tl-1223/Ag composite tape prepared by the spray pyrolysis method. All the peaks can be assigned to the (00l) diffraction of the Tl-1223 phase, except for the (hkl) diffraction of Ag metal. The film was confirmed to consist of single phase Tl-1223 with c-axis crystal orientation. The specimen for Jc measurements was cut from the 1 m long composite tape. The Jc variation was within 5 % for all the pieces. The highest Ic value of any sample was 6.0 A and its Jc was $9x10^4$ A/cm^2 at 77 K without a magnetic field. Figure 4 shows the magnetic field dependence of the Tl-1223/Ag composite tape with the field applied parallel to the c-axis. The Jc at 1T was $7x10^3$ A/cm^2 which is 10 times the value of our silver sheathed Tl-1223 wire. To improve the Jc for practical high-Tc superconducting wire, it is important to achieve three dimensional alignment of the in-plane a-axes (biaxial orientation) of individual Tl-1223 grains.

Recently we have found that biaxially oriented Tl-1223 films can be successfully formed on a $SrTiO_3$(100) single crystal substrate by spray pyrolysis. Figure 5 shows the magnetic field dependence of Jc for Tl-1223 film with the field applied parallel and perpendicular to the c-axis up to 8T at 77K. The curves reveal a relatively weak dependence under low fields. When the fields were applied parallel to the c-axis, Jc reached $5x10^4$ A/cm^2 at 1T. The gentle magnetic field dependence of Jc below 1T for the biaxial oriented Tl-1223 film suggests that the weak-link problem is almost eliminated in the film.

To achieve biaxial orientation in Tl-1223/Ag composite tapes, the "buffer layer" or "metal substrate" itself have to be aligned biaxially. Iijima et al.[9] reported the successful growth of a biaxially aligned YSZ buffer layer on a hastelloy substrate by the ion-beam assisted deposition process, and biaxially aligned YBCO films with high transport Jc values were formed on it.

YBCO films grown by the laser ablation method on Ag(001), Ag(110) and Ag(111) single crystal substrates show specific in-plane epitaxial orientation with respect to the crystallographic axes of the substrate[10]. This result has important consequences in terms of in-plane alignment on metal substrates. It is well known that a (100)[001] texture can be easily formed by rolling and annealing with fcc metals such as Cu where the metal surface consists of a square arrangement of atoms. In the case of Ag, the annealed texture is different from that of Cu, which is mainly (110)[112] and which is described as a rectangular lattice. Yoshino et al.[11] showed that YBCO films grown on a (110) textured Ag substrate by ionized-cluster-beam-deposition, were aligned with in-plane orientation. However, this textured substrate was not suitable for use with our spraying method because of its instability of texture and surface irregularity at higher temperature. We examined the optimum rolling and annealing conditions with which to obtain the (100) texture. Figure 6 shows the XRD (θ-2θ) pattern and surface morphorogy of the nearly (100) textured Ag substrate. The texture and surface flatness of the Ag substrate remained even at 850℃ which corresponds to the heating temperature for the precursor films.

The results of this study demonstrate the considerable potential of the spray pyrolysis method, which does not require a vacuum, for the fabrication of practical superconducting wires and tapes.

4. *Acknowledgments*

The authors would like to thank Dr.K.Aihara of Hitachi Research Laboratory for useful discussions.

5. *References*

1)J. Kase, K. Togano, H. Kumakura, D. R. Dietderich, N. Irisawa, T. Morimoto and H. Maeda : Jpn. J. Appl.Phys. 29 (990) L1096.

2)T.Kanai and T. Kamo : Supercond. Sci. Technol. 6(1993)510.

3)T.Kanai and N.Inoue : J. Mat. Sci. : to be published

4) M. Murakami, M. Morita, K. Doi, K. Miyamoto and H. Hamada: Jpn. J. Appl. Phys. 28 (1989) L339.

5) D. H. Kim, K.E.Gray, R. T. Kampwirth, J. C. Smith, D. S. Richeson, T. J. Marks and M. Eddy: Physica C 177 (1991) 431.

6) T. J. Doi, M. Okada, A. Soeta, T. Yuasa, K. Aihara, T. Kamo and S. Matsuda: Physica C 183 (1991) 67.

7) R. S. Riu, D. N. Zheng, J. W. Loren, K. A. Mirza, A. M. Campbell and P. P. Edwards: Appl. Phys. Lett. 54 (1989) 760.

8) B. Roas et al.: Appl. P. on Superconductivity (ISS '93), Hiroshima, October, 1992 p119.

9) Y. Iijima, N. Tanabe, O. Kohno and Y. Ikeno: Appl. Phys. Lett. 60 (1992) 769.

10) J. D. Budai, R. T. Young and B. S. Chao: Appl. Phys. Lett. 62 (1993) 1836.

11) H. Yoshino, M. Yamazaki, H. Fuke, T. D. Thanh, Y. Kudo, K. Ando and S. Oshima: Abstracts of 6th Int. Symp. on Superconductivity, Hiroshima, October, 1992, p119.

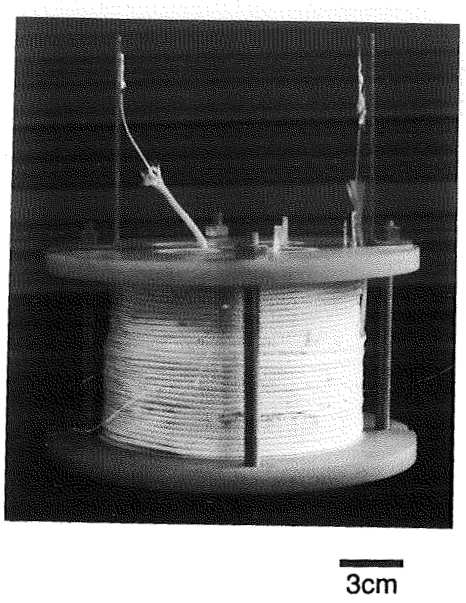

Fig.1 Photograph of the Bi-2212/Ag coil

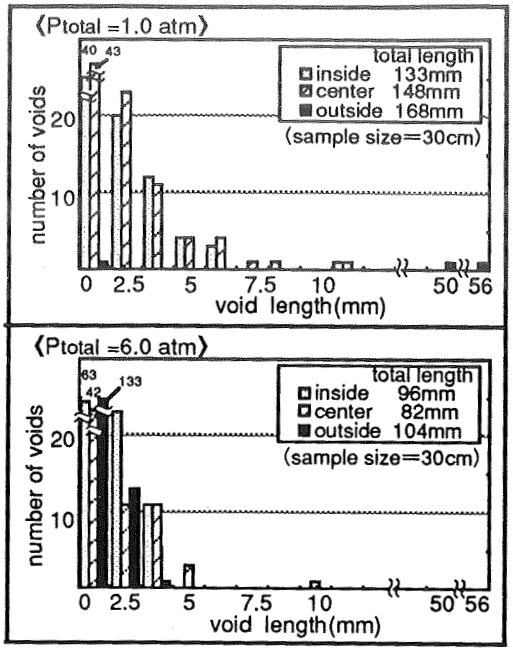

Fig.2 Void distribution of coils

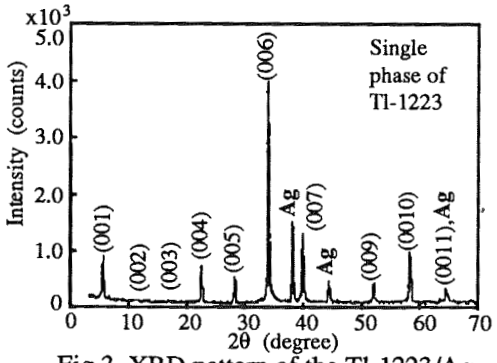

Fig.3 XRD pattern of the Tl-1223/Ag prepared by spray pyrolysis method

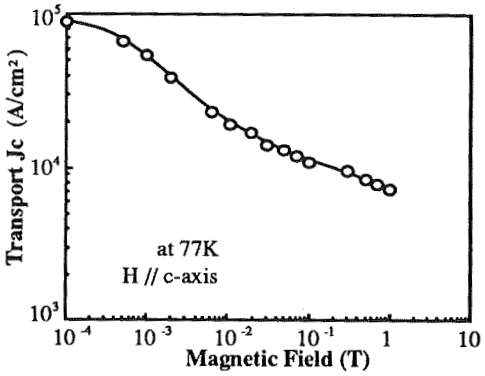

Fig.4 Jc versus field for the Tl-1223/Ag prepared by spray pyrolysis method

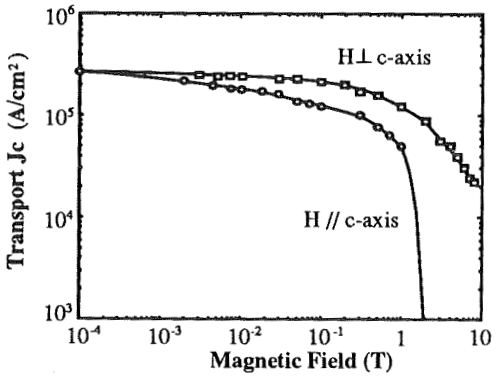

Fig.5 Jc versus field for the Tl-1223 on STO(100) prepared by spray pyrolysis method

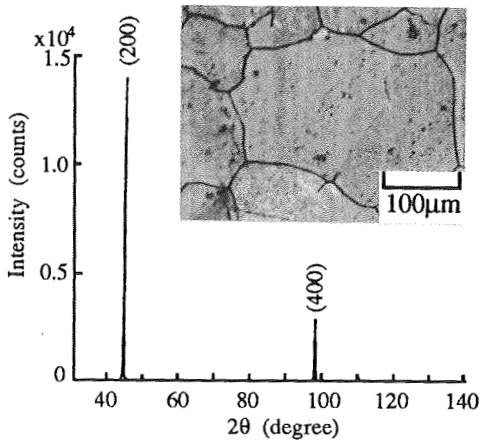

Fig.6 XRD pattern and surface morphorgy of the nearly (100) textured Ag substrate

Index

Page intentionally left blank

INDEX

A

Agrawal, Bal K. 300, 555
Agrawal, Savitri 300, 555
Aldinger, Fritz 483, 490, 677
Alzayed, N. 743
Angus, V. 423, 470
Anischenko, S. E. 574, 585
Apaja, V. 209, 308
Apte, P. R. 241, 762, 770
Arndt, G. Dickey 158
Arutyunov, K. Yu 359
Atlan, D. 470
Azuma, M. 529

B

Balachandran, U. 639
Balint, A. 730
Bankuti, J. 730
Baumann, Philip D. 400
Baziljevich, M. 106
Beales, T. P. 650
Bencze, Laszlo 56, 126
Bestgen, H. 677
Bhalla, A. S. 188
Bhasin, K. B. 611
Bhatnagar, A. K. 241, 762, 770
Bingham, W. G. 410
Bona, Maurizio 65
Borjesson, L. 328
Bratsberg, H. 106
Brinkmann, D. 273
Buhl, D. 685, 753

C

Cardona, M. 328
Chaikovsky, V. I. 574
Chakoumakos, B. C. 347
Chen, C. M. 694
Chorey, C. M. 611
Christen, D. K. 347
Chrzanowski, J. 423, 470
Chu, Wei-Kan 157
Cluff, J. A. 633
Collings, E. W. 138
Coy, M. 372
Cragg, A. R. 450
Cragg, R. A. 423, 470
Crapo, Alan 158
Curzon, A. E. 423

D
D'Souza, C. P. 243, 762, 770
Danilova, N. P. 359
Denisov, A. G. 568
Dhar, S. K. 284
Doi, Toshiya J. 391

E
Eichelberger, B. Davis, III 198
Elifritz, Thomas Lee 500
Elschner, S. 677
Enisz, M. 712
Ewert, S. 460

F
Fan, Chang-Xin 594
Fei, X. 743
Fife, A. A. 423, 450, 470
Foster, Charles 158
Frenck, H. J. 460
Fu, C. M. 694, 703
Fu, C. M.

G
Gasumyants, V. E. 356, 537
Gauckler, L. J. 382, 685, 753
Geerkens, A. 460
Giber, J. 116
Gobl, Nandor 56, 126
Godart, C. 284
Goretta, K. C. 633, 661
Gou, Y. S. 694, 703
Grant, P. D. 450
Greaves, C. 546
Guo, Ruyan 188
Guo, Y. 743
Gupta, L. C. 284

H
Habib, F. 423, 470
Hahakura, S. 510
Halasz, I. 116
Haldar, Pradeep 624, 639
Han, S. G. 594
Havenhill, A. 743
Hawsey, Robert A. 624
He, W. S. 743
Heeb, B. 382, 685, 753
Heinrich, B. 423, 450, 470
Hetland, P. O. 106
Higashiyama, Kazutoshi 391
Hirabayashi, H. 75
Hiroi, Z. 510, 529
Hoehn, J. G., Jr. 639

Hong, Gye-won 3
Horvath, E. 56
Hossain, Zakir 284

I
Ihara, N. 337
Irwin, J. C. 423, 470
Ishida, K. 529
Iyer, A. N. 639

J
Jeng, W. J. 703
Jennings, R. A. 546
Johansen, T. H. 106
Joo, J. 633
Juang, J. Y. 694, 703

K
Kaesche, Stefanie 490
Kallio, A. 209, 308
Kamyshin, V. V. 574
Kanai, Tsuneyuki 391
Kaufmann, H. J. 232
Kawashima, T. 522
Kazanskiy, S. V. 356
Khabayev, P. V. 574, 585
Kimball, Foster 416
Kirschner, I. 48, 56, 116
Kishio, K. 510
Kitaoka, Y. 529
Kitazawa, K. 510
Kiuchi, M. 337
Kotsis, I. 712
Kudeliya, A. M. 568
Kuk, Il-Hyun 3
Kumar, A. Anil 601
Kumar, D. 770
Kyotani, Yoshihiro 96, 167

L
Lanagan, M. T. 633
Lang, Th. 685, 753
Larkin, S. Y. 574, 585
Lemanov, V. V. 180
Leone, A. 372
Levy-Clement, C. 284
Li, Jiang 601
Lieurance, Dennis 416
Lin, H. C. 694
Lighthipe, R. W. 410
Litvinchuk, A. P. 328
Liu, Jianxiong 158

Liu, R. S. 10
Lu, D. F. 60, 594
Lucas, M. S. P. 743

M

Majewski, Peter 483, 490, 677
Maki, Naoki 391
Matheisen, Axel 84
Matsui, Y. 522
Matsushita, T. 337
Mazumdar, Chandan 284
McCormack, J. S 650
Meilikhov, E. Z. 318
Meng-Burany, S. 423
Meszaros,, C 730
Meven, M. 460
Miller, D. J. 661
Miranda, F. A. 611
Mishra, V. K. 24
Moon, F. C. 148
Motowidlo, Leszek R. 624, 639
Multani, Manu 24

N

Nagarajan, R. 284
Naugle, D. G. 222
Nikolaeva, A. A. 359

O

Obot, Victor 158
Okada, Michiya 391
Oltarzhevskaya, Yelena T. 739
Oravetz, D. 712
Orlova, T. S. 232
Ossandon, J. G. 347
Ozhogin, V. 37

P

Padalia, B. D. 284
Pai, S. P. 241, 762, 770
Palotas, Bela 126
Pandey, R. K. 433
Park, Jong-Chul 3
Parks, Drew 158
Patrina, I. B 537
Perin, Romeo 65
Pinto, R. 241, 762, 770
Poykko, S. 209, 308
Predtechensky, M. R. 440
Purandare, S. C. 241, 762, 770

R
Radzikhovsky, V. N. 568
Raina, K. K. 433
Rao, Appajosula S. 260
Rathnayaka, K. D. D. 222
Reichle, D. 743
Ren, Yanru 661
Ren, Z. F. 158
Riise, A. B. 106
Rix, Craig 416
Ruan, J. Z. 417, 594
Ruse, A. B. 593

S
Sali, Robert 722
Sasakawa, Yohei 167
Sato, Jun'ichi 391
Sawh, Ravi 158
Schonhuber, P. 148
Shen, C. Q. 372
Shimoyama, J. 510
Singh, J. P. 633
Smal, A. N. 440
Smirnov, B. I. 232
Smirnov, V. I. 356
Sokolowski, Robert S. 624
Srinivas, S. 241, 762, 770
Su, H.-L. 483
Sugawara, Yoshinori 167
Sumption, M. D. 138
Sun, G. F. 594
Sun, Yang Ren 347
Szalay, A. 712

T
Takano, M. 510, 529
Takayama-Muromachi, E. 522
Takezawa, Setsuo 167
Tatarenko, Valentine A. 739
Thompson, J. R. 347
Thomsen, C. 328
Tsysman, Constantin L. 739
Tukhto, O. M. 440

U
Uen, T. M. 694, 703

V
Vajda, Istvan 56, 126
Varlamov, Yu D. 440
Varshney, Usha 198
Vasanthamohan, N. 632
Vasil'Eva, I. G. 440
Vatnik, S. M. 440

Vijayaraghavan, R. 284
Vladimirskaya, E. V. 356, 537
Vlogaert, Jos 65
Vuong, K. D. 372

W
Wang, C. A. 661
Wang, C. M. 10
Wang, J. H. 661
Wang, X. W. 372
Watson, P. W., III 222
Weinstein, Roy 158
Wenning, B. D. 405
Williams, J. 372
Williams, S. P. 546
Won, Dong-Yeon 3
Wong, K. K. 743
Wong, K. W. 594, 633
Wu, K. H. 694, 703

X
Xin, Y. 633, 743
Xing, W. 450
Xing, W. B. 423, 470

Y
Yamaura, K. 510
Ying, Z. Q. 743

Z
Zhang, Ming Fang 601
Zhou, H. 423, 470
Zhou, Hu 450
Zuo, F. 250

REPORT DOCUMENTATION PAGE

Form Approved
OMB No. 0704-0188

Public reporting burden for this collection of information is estimated to average 1 hour per response, including the time for reviewing instructions, searching existing data sources, gathering and maintaining the data needed, and completing and reviewing the collection of Information. Send comments regarding this burden estimate or any other aspect of this collection of information, including suggestions for reducing this burden, to Washington Headquarters Services, Directorate for information Operations and Reports, 1215 Jefferson Davis Highway, Suite 1204, Arlington, VA 22202-4302, and to the Office of Management and Budget, Paperwork Reduction Project (0704-0188), Washington , DC 20503.

1. AGENCY USE ONLY (Leave Blank)	2. REPORT DATE	3. REPORT TYPE AND DATES COVERED
	April 1995	Conference Publication - June 27-July 1, 1994

4. TITLE AND SUBTITLE

Proceedings of the 4th International Conference and Exhibition: World Congress on Superconductivity - Volume I

5. FUNDING NUMBERS

6. AUTHOR(S)

Kumar Krishen and *Calvin Burnham, Editors

7. PERFORMING ORGANIZATION NAME(S) AND ADDRESS(ES)

Technology Transfer and Commercialization Office
Lyndon B. Johnson Space Center
Houston, TX 77058

8. PERFORMING ORGANIZATION REPORT NUMBERS

S-792

9. SPONSORING/MONITORING AGENCY NAME(S) AND ADDRESS(ES)

National Aeronautics and Space Administration
Washington, DC 20546-0001

10. SPONSORING/MONITORING AGENCY REPORT NUMBER

CP-3290
Volume I

11. SUPPLEMENTARY NOTES

*World Congress on Superconductivity, Houston, TX 77227-7805

12a. DISTRIBUTION/AVAILABILITY STATEMENT

Unclassified/Unlimited
Available from the NASA Center for AeroSpace Information
800 Elkridge Landing Road
Linthicum Heights, MD 21090-2934
(310) 621-0390 Subject Category: 76

12b. DISTRIBUTION CODE

13. ABSTRACT *(Maximum 200 words)*

This document contains papers presented at the 4th International Conference Exhibition: World Congress on Superconductivity held at the Marriott Orlando World Center, Orlando, Florida, June 27-July 1, 1994. This conference encompassed research, technology, applications, funding, political, and social aspects of superconductivity. Specifically, the areas of research, technology, and development covered during the conference included high-temperature materials, thin films, C-60 based superconductors, persistent magnetic fields and shielding, fabrication methodology, space applications, physical applications, performance characterization, device applications, weak link effects and flux motion, accelerator technology, superconductivity energy, storage, future research and development directions, medical applications, granular superconductors, wire fabrication technology, computer applications, technical and commercial challenges, and power and energy applications. The key objective of this conference was to provide a forum for the world community to share technological results of recent advances made in the field of superconductivity and to discuss translation of the research to technology which will benefit humanity. More than 150 presentations were made at this conference.

14. SUBJECT TERMS	15. NUMBER OF PAGES
High-Temperature, Superconductivity, physical properties, fabrication methodology, devices, applications, thin films, performance characterization	420
	16. PRICE CODE

17. SECURITY CLASSIFICATION OF REPORT	18. SECURITY CLASSIFICATION OF THIS PAGE	19. SECURITY CLASSIFICATION OF ABSTRACT	20. LIMITATION OF ABSTRACT
Unclassified	Unclassified	Unclassified	Unlimited